

Ultra Clean Processing of Semiconductor Surfaces XIII

Edited by
Paul W. Mertens
Marc Meuris
Marc Heyns

Ultra Clean Processing of Semiconductor Surfaces XIII

Selected, peer reviewed papers from the
13th International Symposium on
Ultra Clean Processing of Semiconductor Surfaces
(UCPSS),
September 12-14, 2016, Knokke, Belgium

Edited by

Paul W. Mertens, Marc Meuris and Marc Heyns



Copyright © 2016 Trans Tech Publications Ltd, Switzerland

All rights reserved. No part of the contents of this publication may be reproduced or transmitted in any form or by any means without the written permission of the publisher.

Trans Tech Publications Ltd
Churerstrasse 20
CH-8808 Pfaffikon
Switzerland
<http://www.scientific.net>

Volume 255 of
Solid State Phenomena
ISSN print 1012-0394
ISSN cd 1662-9787
ISSN web 1662-9779

(Pt. B of Diffusion and Defect Data - Solid State Data (ISSN 0377-6883))

Full text available online at <http://www.scientific.net>

Distributed worldwide by

Trans Tech Publications Ltd
Churerstrasse 20
CH-8808 Pfaffikon
Switzerland

Phone: +41 (44) 922 10 22
Fax: +41 (44) 922 10 33
e-mail: sales@scientific.net

and in the Americas by

Trans Tech Publications Inc.
PO Box 699, May Street
Enfield, NH 03748
USA

Phone: +1 (603) 632-7377
Fax: +1 (603) 632-5611
e-mail: sales-usa@scientific.net

Preface

The International Symposium on Ultra Clean Processing of Semiconductor Surfaces (UCPSS) is a bi-annual conference organized by imec since 1992. The scope of the symposium includes all issues related to contamination, cleaning and surface preparation in mainstream large-scale Integrated Circuit manufacturing. For the first editions, typically silicon was the main semiconductor of interest. As currently other semiconducting materials such as SiGe and SiC, Ge and III-V are being considered for future generation devices, the scope was broadened to include these materials. Parallel to the fast moving CMOS industry also the photovoltaic industry has recognized the need for improvements in cleaning, and this topic was included.

The thirteenth international symposium on Ultra Clean Processing of Semiconductor Surfaces (UCPSS 2016) was held in Knokke, Belgium on September 12-14, 2016. The symposium was preceded by a tutorial session, given on September 11th by leading experts in the field.

The symposium proceedings cover different aspects of ultra-clean technology for large scale integration on semiconductors, cleaning and contamination control in both the front-end-of-line (FEOL) and the back-end-of-line (BEOL) processing as well as cleaning for semiconductor photovoltaic applications.

This includes studies on general topics such as particle removal using acoustic enhancement, removal of metallic contamination, pattern collapse of fine flexible and fragile features, wetting and drying, contamination control and contamination metrology. FEOL and BEOL contributions cover: surface chemistry of silicon and other semiconductors, cleaning related to new gate stacks, cleaning at the interconnect level, resist strip and polymer removal, cleaning and contamination control for various new materials and cleaning after Chemical-Mechanical-Polishing (CMP).

The meeting was attended by participants from all over the world, with a representation from most of the leading cleaning equipment manufacturers and leading integrated device manufacturers as well as staff from academia and R&D-centers. This attendance is an indication of the interest in the topic and the huge cleaning challenges in future technologies. The symposium fosters also the participation of PhD students. For the seventh time a student paper award contest was organized and *2 outstanding student contributions* and one *best student paper* were selected.

New developments in electronic micro and nano-systems evolve in increasingly diverging directions, involving nano-meter scale features and novel materials, tailored to specific applications. This leads to new tailored cleaning requirements and challenges. We believe UCPSS and similar symposia contribute significantly to the search for new solutions to these new challenges. In this perspective we invite you to the 14th edition of this symposium to be held in 2018. Information concerning future and past editions of this symposium can be found on www.ucpss.org.

Paul Mertens, Marc Meuris and Marc Heyns
Proceeding Editors

Committees

Conference Chairman

Paul Mertens (imec)

Programme Committee

Anthony Muscat (University of Arizona)
Takeshi Hattori (Hattori Consulting International)
Jerzy Ruzyllo (Penn State University)
Geunmin Choi (SK Hynix)
Mauro Alessandri (STMicroelectronics)
Kuntack Lee (Samsung)
Ara Philipossian (University of Arizona)
Jef Poortmans (imec)
Jochen Rentsch (Fraunhofer ISE)
Paul Mertens (imec)

Scientific Advisory Committee

Marc Heyns (imec)
Bernd Kolbesen (J.-W. Goethe University)

Local Organizing Committee

Kurt Wostyn (imec)
Antoinne Pacco (imec)
Guy Vereecke (imec)
Marc Meuris (imec)
Rita Vos (imec)
Paul Mertens (imec)
Marc Heyns (imec)

Logistic Support

Kathleen Vanderheyden (imec)
Fred Loosen (imec)
Charlotte Schaek (Medicongres)
Werner Van Cleemputte (Medicongres)

Review Committee

Members of the Programme Committee
and

Martin Knotter (NXP)
Quoc Toan Le (imec)
Steven Brems (imec)
Guy Vereecke (imec)
Rita Vos (imec)
Antoine Pacco (imec)
Kurt Wostyn (imec)
Dennis van Dorp (imec)
Marc Meuris (imec)

Sponsors

This symposium has been financially supported by the following companies:

		
 		
		 Pall Corporation
 Product Systems Inc.		
	engineer approved™	

			 Mastering silicon data together	
---	---	---	--	---

Table of Contents

Preface	v
Committees, Sponsor	vi

Chapter 1: FEOL: Surface Chemistry Group IV Semiconductors

Wet Selective SiGe Etch to Enable Ge Nanowire Formation

F. Sebaai, L. Witters, F. Holsteyns, K. Wostyn, J. Rip, Y. Yukifumi, R.R. Lieten, S. Bilodeau and E. Cooper	3
--	---

Silicon Surface Passivation in HF Solutions for Improved Gate Oxide Reliability

P. Garnier	8
------------------	---

Surface Preparation Quality before Epitaxy our Paper's

P. Garnier	13
------------------	----

Study of Oxygen Concentration in TMAH Solution for Improvement of Sigma-Shaped Wet Etching Process

Y.G. He, H.X. Liu, J.L. Liu, J.G. Wu, C. Haigermoser, F. Liu, M.S. Zhou and W. Lu	18
---	----

The Effect of Rinsing a Germanium Surface after Wet Chemical Treatment

Y. Yoshida, H. Takahashi, M. Sato, J. Snow, F. Sebaai and F. Holsteyns	22
--	----

Effect of Dilute Hydrogen Peroxide in Ultrapure Water on SiGe Epitaxial Process

T. Masaoka, N. Gan, Y. Fujimura, Y. Ogawa, K. Wostyn, A. Pacco, Y. Yoshida and F. Holsteyns	27
--	----

Surface Passivation of New Channel Materials Utilizing Hydrogen Peroxide and Hydrazine Gas

D. Alvarez Jr, J.J. Spiegelman, A.C. Kummel, M. Edmonds, K. Sardashti, S. Wolf and R. Holmes	31
---	----

Tris(Trimethylsilyl)Germane (Me₃Si)₃GeH: A Molecular Model for Sulfur Passivation of Ge(111) Surfaces

G. Okorn, R. Fischer, B. Steller, P. Engesser and H. Okorn-Schmidt	36
--	----

Applications for Surface Engineering Using Atomic Layer Etching - Invited Paper

J. Papalia, N. Marchack, R. Bruce, H. Miyazoe, S. Engelmann and E.A. Joseph	41
---	----

Chapter 2: FEOL: Surface Chemistry Groups III-V Compound Semiconductors

Towards Atomic-Layer-Scale Processing of High Mobility Channel Materials in Acidic Solutions for N5 and N7 Technology Nodes

D.H. van Dorp, S. Arnauts, G. Abrenica and F. Holsteyns	51
---	----

Comparison of the Chemical Passivation of GaAs, In_{0.53}Ga_{0.47}As, and InSb with 1-Eicosanethiol

Y. Contreras, P. Mancheno-Posso and A.J. Muscat	55
---	----

Digital Etching of GaAs Materials: Comparison of Oxidation Treatments

M. Rebaud, M.C. Roure, V. Enyedi, L. Borowik, E. Martinez, L. Toselli and P. Besson	61
---	----

Thin Layer Etching of Silicon Nitride: Comparison of Downstream Plasma, Liquid HF and Gaseous HF Processes for Selective Removal after Light Ion Implantation

N. Belmiloud and N. Kenkare.....152

Extended-Nanofluidic Devices and the Unique Liquid Properties - Invited Paper

K. Mawatari and T. Kitamori..... 157

Chapter 6: Mechanical Fluid Effects, Nanoparticles**Measurement of the Frictional Force between PVA Roller Brushes and Semiconductor Wafers with Various Films Immersed in Chemicals**

K. Nishio, T. Sanada, S. Hamada, H. Hiyama and A. Fukunaga..... 163

Removal of Bull's Eye Signature by Optimizing Wet Cleans Recipe

D. Bhattacharyya, P. Muralidhar and M. Conrad 168

Toward CO₂ Beam Cleaning of 20-nm Particles in Atmospheric Pressure

J.N. Kim, J.H. Lee, S.H. Kim, J.K. Kim, K.H. Choi and H.Y. Kim..... 172

Liquid Cell Platform to Directly Visualize Bottom-Up Assembly and Top-Down Etch Processes inside TEM

Z. Aabdin, X.M. Xu, U. Anand, F. Holsteyns and U. Mirsaidov 176

A Study on the Electrostatic Discharge (ESD) Defect in SOH Mask Pattern Cleaning

D.W. Ko, T.H. Hwang, S.H. Han, C.H. Kim and B.S. Ryu 182

Post-CMP Cleaners for Tungsten at Advanced Nodes

R.R. Lieten, D. White, T. Parson, S.N. Jenq, D. Frye, M. White, L. Teugels and H. Struyf..... 186

Advanced Cryogenic Aerosol Cleaning: Small Particle Removal and Damage-Free Performance

C. Mbanaso, J.W. Butterbaugh, D.S. Becker, W.P. Printz, A.L.P. Rotondaro, D.W. Bassett, G.P. Thomes, B.D. Schwab, C.A. Rathman and J.M. Lauerhaas..... 195

Developments for Physical Cleaning Sample with High Adhesion Force Particles and Direct Measurement of its Removal Force

E. Tokuda, T. Sanada, F. Iwata, C. Takato, H. Hiyama and A. Fukunaga 201

Characterization of Cavitation in a Single Wafer or Photomask Cleaning Tool

X. Chen, P. Yam, M. Keswani, N. Okada and C.I. Zanelli 207

Chapter 7: Interconnect Cleaning**Molecular Simulation Contribution to Porous Low-k Pore Size Determination after Damage by Etch and Wet Clean Processes - Invited Paper**

L. Broussous, M. Lépinay, B. Coasne, C. Licitra, F. Bertin, V. Rouessac and A. Ayral 215

Rapid Recovery Process of Plasma Damaged Porous Low-k Dielectrics by Wet Surface Modifying Treatment

A. Iwasaki, A. Higuchi, K. Komori, M. Sato, E. Kesters, Q.T. Le and F. Holsteyns..... 223

Characterization of Etch Residues Generated on Damascene Structures

Q.T. Le, E. Kesters, I. Hoflijk, T. Conard, M. Shen, S. Braun, Y. Burk and F. Holsteyns..... 227

Evaluation of Post Etch Residue Cleaning Solutions for the Removal of TiN Hardmask after Dry Etch of Low-k Dielectric Materials on 45 nm Pitch Interconnects

M. Payne, S. Lippy, R.R. Lieten, E. Kesters, Q.T. Le, G. Murdoch, V.V. Gonzalez and F. Holsteyns..... 232

Optimization of Cu/Low-k Dual Damascene Post-Etch Residue and TiN Hard Mask Removal

A. Kabansky, G. Westwood, S. Tan, F. Kovacs, D. Lou, J. Han, G. Delgadino and H.W. Chang.....237

TiN Metal Hardmask Etch Residues Removal with AlN Etch

H. Cui.....242

High Throughput Wet Etch Solution for BEOL TiN Removal

C.J. Hsu, C.J. Wang, S.H. Tu, M. Payne, E. Cooper and S. Lippy.....245

Impact of Dissolved Oxygen in Dilute HF Solution on Material Etch

E. Kesters, A. Iwasaki, Q.T. Le and F. Holsteyns251

The Effect of Inhibitors on Co Corrosion in Alkaline Post Cu-CMP Cleaning Solutions

P. Hsu, P.R. Bernatis, K. Huang and C. Yen255

Oxygen Control for Wet Clean Process on Single Wafer Platform

L. Broussous, K. Hoarau, C. de Buttet and S. Zoll260

Study of TiW Conditioning through Different Wet and Dry Treatments to Promote Ni Electroless Growth

I. Venegoni, F. Scimè, E. Ravizza, S. Spadoni, F. Pipia, P. Colpani and M. Alessandri265

Post CMP Wet Cleaning Influence on Cu Hillocks

A. Votta, F. Pipia, L. Livellara, M. Caminati, S. Spadoni, E. Ravizza, S. Grasso, M. Bollin, M. Moroni, M. Alessandri and P. Colpani270

Minimizing Wafer Surface Charging for Single-Wafer Wet Cleaning for 10 nm and beyond

K. Sano, R. Dylewicz, X. Man, D. Mui, J. Zhu and M. Kawaguchi277

Chapter 8: 3D Integrated Structures

Silica Formation during Etching of Silicon Nitride in Phosphoric Acid

D.W. Bassett and A.L.P. Rotondaro285

Low Undercut Ti Etch Chemistry for Cu Bump Pillar under Bump Metallization Wet Etch Process

S. Capecci, T. Atanasova, R. Willeke, M. Parthenopoulos, C. Pizzetti and J. Daviot.....291

Chapter 9: Metrology, Specification and Control of Contamination

Electrical Characterization of As-Processed Semiconductor Surfaces - Invited Paper

J. Ruzyllo and P.J. Drummond299

Atomic Resolution Quality Control for Fin Oxide Recess by Atomic Resolution Profiler

T.G. Kim, H.Y. Ryu, K. Kenis, A.J. Jo, S.J. Cho, S.I. Park, S. Schmidt and B. Irmer304

Specification of Trace Metal Contamination for Image Sensors

P.W. Mertens, S. Lavizzari and S. Guerrieri.....309

Metal Removal Efficiency in High Aspect Ratio Structures

P. Garnier and H. Fontaine.....313

Quantitative Analysis of Trace Metallic Contamination on III-V Compound Semiconductor Surfaces

K. Saga and R. Ohno.....319

A Mathematical Model Forecasting HF Adsorption onto Cu-Coated Wafers as a Function of the Airborne Concentration and Moisture

F. Herrán, H. Fontaine, P. González-Aguirre, C. Beitia, J. Ohlsen and J. Lundgren 323

Chapter 10: Photovoltaics

Oxidation of Si Surfaces: Effect of Ambient Air and Water Treatments on Surface Charge and Interface State Density

H. Angermann, P. Balamou, W.J. Lu, L. Korte, C. Leendertz and B. Stegemann 331

Surface Optimization of Random Pyramid Textured Silicon Substrates for Improving Heterojunction Solar Cells

B. Stegemann, J. Kegel, L. Korte and H. Angermann 338

‘Just-Clean-Enough’: Optimization of Wet Chemical Cleaning Processes for Crystalline Silicon Solar Cells

M. Haslinger, M. Soha, S. Robert, M. Claes, P.W. Mertens and J. John 344

Progress in Cleaning and Wet Processing for Kesterite Thin Film Solar Cells

B. Vermang, A. Mule, N. Gampa, S. Sahayaraj, S. Ranjbar, G. Brammertz, M. Meuris and J. Poortmans 348

Chapter 11: Non-Wafer Cleaning, Mask Cleaning

Optimization of EUV Reticle Cleaning by Evaluation of Chemistries on Wafer-Based Mimic Test Structures

A. Pacco, D. Dattilo, R. Jonckheere, J. Rip, U. Dietze, J. Kruemberg and F. Holsteyns 357

Ultra-Trace Sulfate Ion Removal on Photomasks for Haze Reduction

E. Guo, C. Wang, S. Qian, M. Wang, H. Zhang, K. Wu, J. Shen, W. Jiang and F. Xu 361

172 nm Excimer Radiation as a Technology Accelerator for Bio-Electronic Applications

A. Schäfert and H. Wiesmann 366

Chapter 12: Contamination Control of Wafer Ambient

Electrolyzed Water for Efficient Metal Removal

J. Oshinowo, A.K. Neelsen, M. Fryda, L. Rebstock and U. Quarti 375

Contamination Control for Wafer Container Used within 300 mm Manufacturing for Power Microelectronics

G. Schneider, T.Q. Nguyen, M. Taubert, J. Bounouar, C. Le-Guet, A. Leibold, H. Richter and M. Pfeffer 381

Inline FOUP Cleaner - The New Type FOUP Cleaner for the Next Generation

S.G. Gwon, K.B. Lee, B.J. Lee and G.M. Choi 387

Keyword Index 391

Author Index 397

CHAPTER 1:

FEOL: Surface Chemistry Group IV Semiconductors

Wet Selective SiGe Etch to Enable Ge Nanowire Formation.

Farid Sebaai^{1, a}, Liesbeth Witters¹, Frank Holsteys¹, Kurt Wostyn¹,
Jens Rip¹, Yoshida Yukifumi², Ruben Lieten³, Steven Bilodeau⁴,
Emanuel Cooper⁴

¹ Imec vzw, Kapeldreef 75, B-3001 Heverlee, Belgium

² SCREEN Semiconductor Solutions Co., Ltd., 480-1, Takamiya, Hikone, Shiga, 522-0292, Japan

³ Entegris, GmbH, Hugo-Junkers-Ring 5, Gebäude 107/W, 01109 Dresden, Germany

⁴ Entegris, Inc, 7 Commerce Drive, Danbury CT 06810, US⁴

^aFarid.Sebai@imec.be

Keywords: Si_{0.5}Ge_{0.5} and Si_{0.3}Ge_{0.7} isotropic etch, alkaline conditions, optimized semi-aqueous chemistry, Ge selectivity, Ge nanowire, alkaline, gate-all-around, GAAFETs, CMOS

Abstract. For the Ge nanowire formation in a gate-all-around (GAA) integration scheme, a selective etch of Si_{0.5}Ge_{0.5} or Si_{0.3}Ge_{0.7} selective to Ge is considered. Two wet process approaches were evaluated: a boiling TMAH as a commodity chemistry is compared with a formulated chemistry using a multi-stack SiGe/Ge layer as a test vehicle. The boiling TMAH exhibits an anisotropic etch of the SiGe whereas the formulated semi-aqueous chemistry removes the sacrificial SiGe by an isotropic etch which makes the process suitable for a Ge nanowire release process.

Introduction

Improving the performance of CMOS devices imposes an aggressive downscaling of the dimensions together with the introduction of high-mobility-channels materials like Ge, which has already shown significant promise [1, 2]. To reduce the supply voltage and to provide a better electrical control over the channel and thus reducing the leakage current and overcoming short-channel effects while continuing the scaling, FinFETs have been introduced. The distinguishing characteristic of the FinFET is that the gate is wrapped around the conducting channel “fin”. Eventually, to allow further scaling lateral gate-all-around FETs will be introduced, also known as lateral nanowires or nanosheets. These GAA Fets are similar in concept to FinFETs, except that the gate material surrounds the channel region on all sides. These nanowires allow relaxed channel dimensions with respect to the fin thickness while still avoiding short-channel effects. [3-5] The formation of Si, SiGe or Ge nanowires requires the development of new selective etch processes, such as Si etch selective to SiGe in order to form SiGe nanowires or SiGe selective etch to Ge to form Ge nanowires. In this work, a wet selective etch solution to enable the Ge nanowire formation is proposed by comparing two different wet etch solutions: an alkaline versus a semi-aqueous based solution. For both approaches, a wet etch process of Si_{0.5}Ge_{0.5} or Si_{0.3}Ge_{0.7} selective to Ge is investigated.

Experimental

A multilayer stack of Si_{0.5}Ge_{0.5}/Ge and Si_{0.3}Ge_{0.7}/Ge was deposited by epitaxy on 300 mm Si wafers and then patterned into parallel fins, as described in Figure 1. Top-view and cross-section SEM (scanning electron microscopy) imaging is used to reveal the selective etching of the multi-stack SiGe/Ge layers.

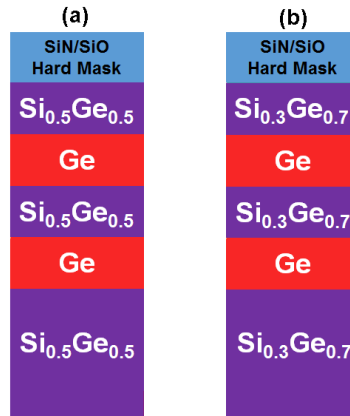


Figure 1: Description of the (a) $\text{Si}_{0.5}\text{Ge}_{0.5}/\text{Ge}$; and (b) $\text{Si}_{0.75}\text{Ge}_{0.25}/\text{Ge}$ nanowire stacks used for selective etch evaluation.

Two approaches for wet selective etching were investigated: 1) using a boiling TMAH 25% and 2) using a formulated chemistry. The commodity chemistry used in this work is alkaline: boiling TMAH 25%. The formulated chemistry evaluated in this work is semi-aqueous and designed by Entegris. These chemistries were tested in a beaker and on a 300 mm single wafer tool (SU3200) from SCREEN.

Ge nanowire formation under alkaline conditions

It has already been shown by Wostyn [6], that $\text{Si}_{0.5}\text{Ge}_{0.5}$ can be etched selectively to Ge in boiling TMAH wt25%. Using TMAH at boiling conditions helps maximize the SiGe etching rate and reduce the dissolved oxygen content, which is responsible for some Ge loss. In Figure 2, the $\text{Si}_{0.5}\text{Ge}_{0.5}/\text{Ge}$ multi-stack structures are immersed for 10 or 20 minutes in TMAH wt25 % solution. The results confirm the anisotropic etch behavior of the SiGe 50% under alkaline conditions.

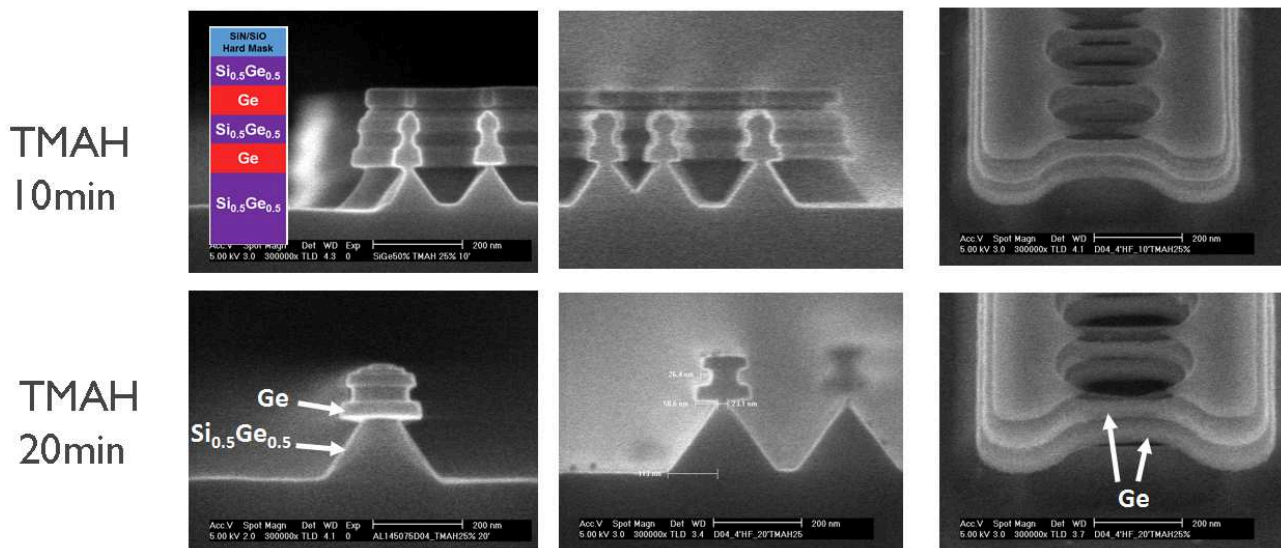


Figure 2: Top view of the $\text{Si}_{0.5}\text{Ge}_{0.5}/\text{Ge}$ multi-stack immersed in 10 or 20 minutes boiling TMAH wt 25%.

The Si etch in an alkaline solution is highly anisotropic, with more than one order of magnitude difference between the fast and slow etching crystal planes. Small variations in nanowire aspect ratio, either due to fin width or sacrificial layer thickness variations, will have a large impact on the time required for complete removal of this sacrificial layer. Due to the anisotropic etch properties in combination with the extreme conditions required for selective $\text{Si}_{0.5}\text{Ge}_{0.5}$ etch in alkaline solutions, an isotropic etchant without TMAH is therefore preferred.

Ge nanowire formation under semi-aqueous conditions

Formulations using hydrogen peroxide to oxidize Si and Ge combined with fluoride to etch the oxidized material have long been used as the basis for a selective etch [7,8]. This approach results in selective removal of high Ge content alloys relative to high Si content alloys. We have used a Si selective oxidizer combined with a Ge etch inhibitor to reduce the Ge oxidation rate and enable a formulation that selectively etches high Si content SiGe alloys. With this approach we have been able to achieve a blanket film etch rate selectivity for $\text{Si}_{0.40}\text{Ge}_{0.60}$ relative to Ge of 22:1.

Figure 3 (a) shows a SEM top view of our $\text{Si}_{0.5}\text{Ge}_{0.5}/\text{Ge}$ multi-stack test vehicle for 25 nm CD lines after different immersion times in the optimized semi-aqueous solution. The SEM images indicate that an immersion time of 3 min is required to fully remove the $\text{Si}_{0.5}\text{Ge}_{0.5}$ around two Ge nanowires without significant Ge loss. Further, the cross section SEM shown in figures 3 (b), confirms the Ge nanowire formation. Different from TMAH, an isotropic SiGe etch behavior has been observed, which will help the Ge nanowire formation without any spatial limitations [6].

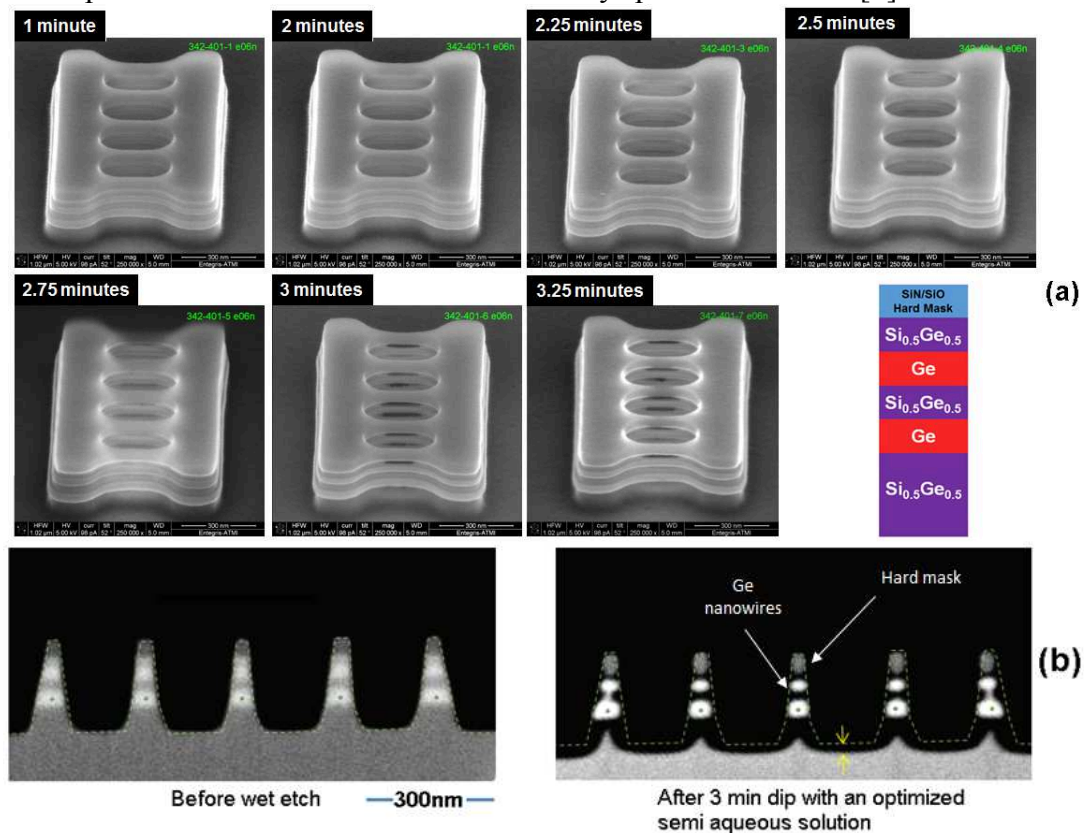


Figure 3: (a) SEM top view of the $\text{Si}_{0.5}\text{Ge}_{0.5}/\text{Ge}$ multi-stack for 25 nm CD lines using an optimized formulated semi-aqueous chemistry at different immersion times. (b) Cross section SEM of a $\text{Si}_{0.5}\text{Ge}_{0.5}/\text{Ge}$ multi-stack for 25 nm CD lines using a 3 minutes immersion time for the same chemistry.

In a second stage, the wet etch performance of the optimized semi-aqueous chemistry is being verified on a 300mm single wafer tool. By measuring the etch rate as a function of temperature on $\text{Si}_{0.25}\text{Ge}_{0.75}$ blanket wafers, an activation energy of ~ 26 kJ/mol is determined (Figure 4a). This indicates that the process is based on a surface reaction controlled mechanism without mass transport limitations ($E_a > 15.5$ kJ/mol indicates full kinetic control) [9]. In Figure 4b, it is verified that the rotation speed does not influence the $\text{Si}_{0.25}\text{Ge}_{0.75}$ etch rate (~ 6.2 nm/min) and Ge loss (~ 0.7 nm/min).

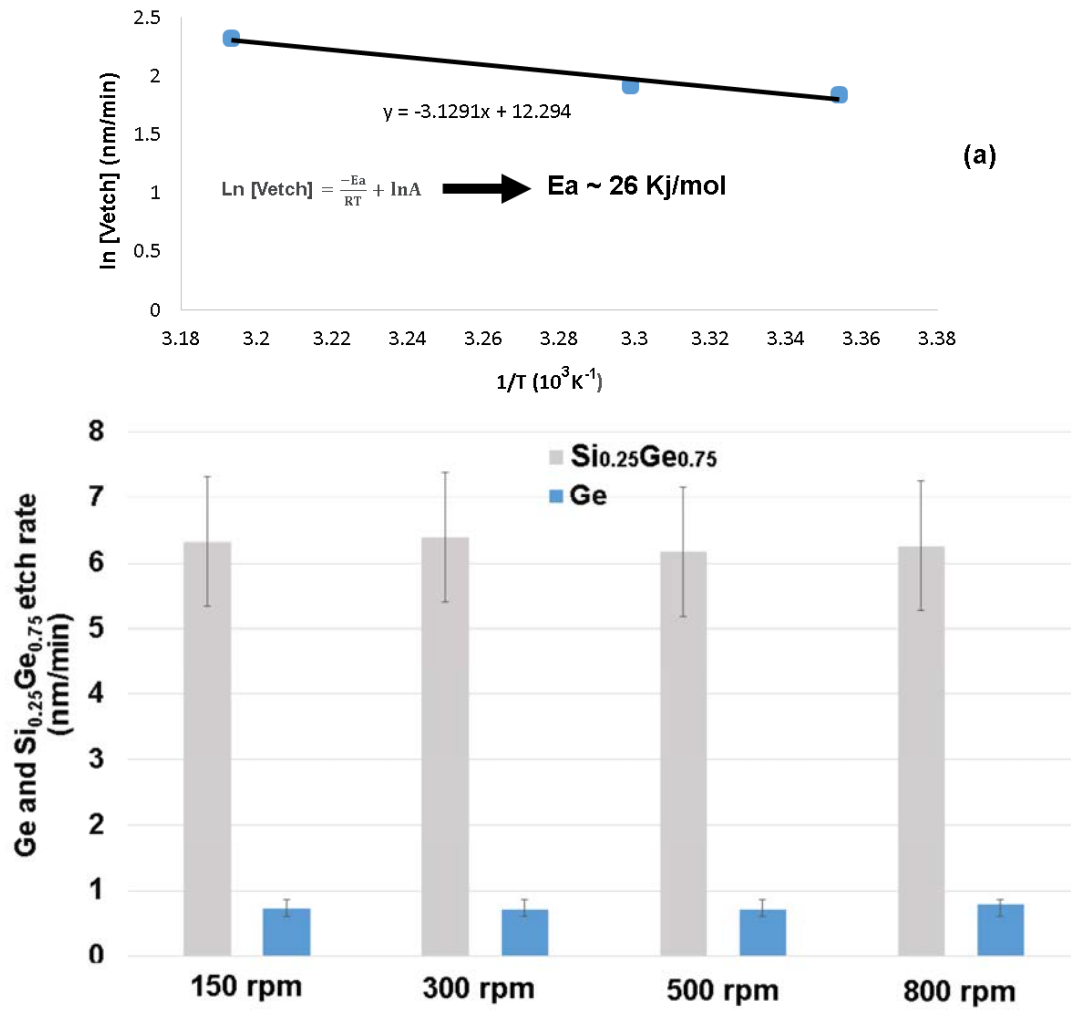


Figure 4: (a) Arrhenius plot of the $\text{Si}_{0.25}\text{Ge}_{0.75}$ etching with the optimized semi-aqueous chemistry. (b) $\text{Si}_{0.25}\text{Ge}_{0.75}$ etching rate and Ge loss vs the rotation speed using the optimized semi-aqueous chemistry

Finally, the etching behavior of the optimized semi-aqueous chemistry on the $\text{Si}_{0.5}\text{Ge}_{0.5}/\text{Ge}$ and $\text{Si}_{0.3}\text{Ge}_{0.7}/\text{Ge}$ multilayer stack using a 7min 30sec process time like shown on Figure 5. This process time allows to fully release Ge nanowires having a CD of 50 and 100nm. For such a long process time, some Ge loss was observed when comparing the width of the hard mask to the width of the released Ge nanowire.

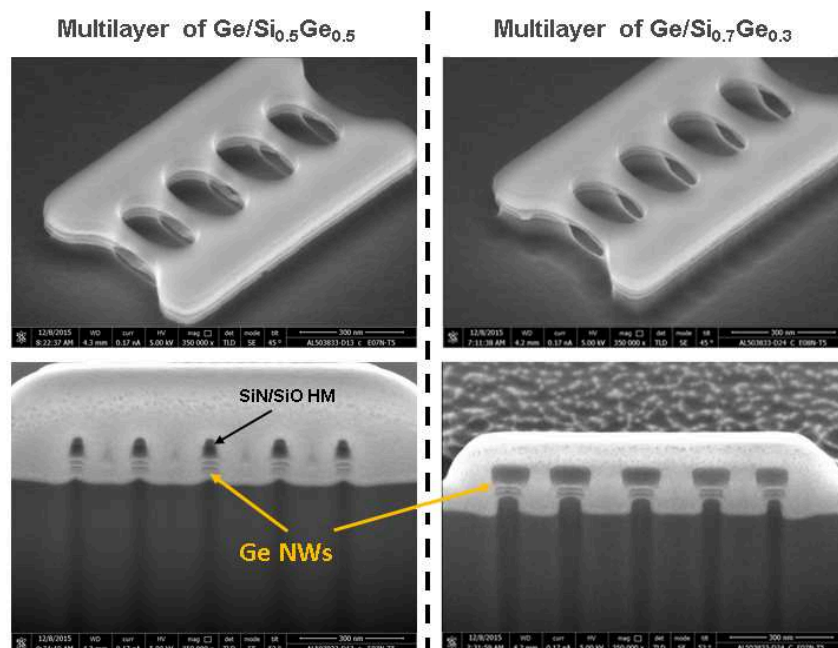


Figure 5: Top view and cross section SEM of the Si_{0.5}Ge_{0.5}/Ge and Si_{0.3}Ge_{0.7}/Ge multilayer stack after processing for 7min 30sec by an optimized semi-aqueous formulated chemistry.

Conclusion

The formulated semi-aqueous chemistry shows clear benefits in Ge nanowire formation over the alkaline solution by removing the sacrificial SiGe by an isotropic etch. The chemical reaction for SiGe etch is kinetically controlled, which makes the process suitable for single wafer processing. Since the process is not purely selective to Ge, it is advised to target a process time close to the targeted dimensions in order to limit Ge loss.

References

- [1] J. Mitard, 2013 Symposium on VLSI Technology, pT20-T21
- [2] P. Hashemi, Electron Device Letters 33(2), 2012.
- [3] Isaac Lauer, 2015 Symposium on VLSI Technology, pT140-T141
- [4] H. Mertens, 2015 Symposium on VLSI Technology, pT142 - T143
- [5] Yao-Jen Lee, presented at IEDM 2015, Washington DC (Dec 2015)
- [6] K. Wostyn, ECS Transactions, 69 (8) 147-152 (Oct 2015).
- [7] T. K. Carns, Journal of The Electrochemical Society, Vol. 142, No. 4, April 1995.
- [8] B. Holländer, Journal of The Electrochemical Society, 157 _6_ H643-H646 _2010.
- [9] P.H.L. Notten, J.E.A.M. van den Meerakker, J.J. Kelly: Etching of III-V Semiconductors: an Electrochemical Approach, Elsevier Advanced Technology Oxford 1991.

Silicon Surface Passivation In HF Solutions for Improved Gate Oxide Reliability

Philippe Garnier

STMicroelectronics Crolles2, 850 rue Jean Monnet 38921 Crolles, France

philippe-e.garnier@st.com

Keywords: HF based solutions, silicon surface passivation, gate oxide reliability

Abstract. The silicon surface passivation with diluted HF solutions is hereby explained. Without a very stable, correct Si-H surface passivation, a rough silicon surface can be obtained, leading to poor gate oxide integrity or bad epi film quality. Detailed mechanism are depicted and solutions to obtain best Si-H passivated surface are given.

Introduction

Silicon oxide etch by hydrofluoric acid is a very complex reaction, previously detailed in the literature [1]. With the transistors dimensions shrink, a continuous effort in reducing the STI (Shallow Trench Isolation) divot depth is undertaken. This paper gives some directions to reach this goal without degrading the quality of silicon interfaces, especially during gate oxide cleans.

Experimental

Surface preparations used to generate a double or triple gate oxides integration scheme [2] are considered in this work. Indeed they're the main contributors of this divot's generation in a CMOS integration.

All the presented experiments focus on the pre I/O (Input / Output function) gate oxide clean. It consists in the removal of a sacrificial oxide. But the results can be extrapolated to other silicon oxide wet etches on top of silicon surface. Wet etch processes have been conducted in 300mm wet benches or spin dry single wafer tools with diluted HF. Excepted from figure 4, all the data have been obtained with HF concentration of 0.25w%. And oxide over etch is presented here in terms of etched equivalent thermal oxide thickness.

Results and discussion

Although gaseous methods enable a very reduced STI divot [3], aqueous HF based chemistry is still widely used to etch silicon oxides. Therefore a strong care is put on reducing the total oxide etch budget. But, this needs to be done accurately, especially for pre gate oxide cleans. Generally, a sacrificial silicon oxide is removed to regrow an excellent quality thermal oxide. Very diluted HF have been widely used to reduce the silicon roughness. Indeed in presence of dissolved oxygen in the HF, silicon is locally corroded. Nonetheless, since more than 10 years, facilities can supply blended chemicals with extremely low dissolved oxygen. Inappropriate surface treatments during the gate oxide cleans can lead to reliability degradation (NBTI) [4, 5]. Surface degradation can also be observed in line. Figure 1 presents an I/O (Input / Output) gate oxide growth thickness versus the sacrificial oxide over etch. Targeted gate oxide thickness is 58Å. Smallest over etch generate out of control of about 2 Å thickness, affecting both reliability and performances of the grown gate oxide.

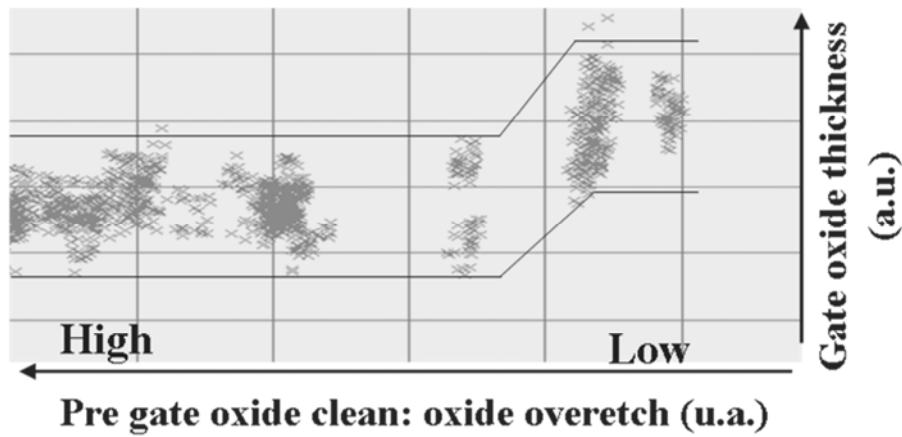


Figure 1: I/O Gate oxide thickness monitoring versus pre clean oxide etch budget

Hence, it's key to understand the silicon surface passivation mechanism occurring during a silicon oxide etch with HF (figure 2). After the silicon oxide is removed, a transitory state generates Si-F bonds. Final Si-H passivation is obtained with longer etch. Whereas Si-H bond is relatively stable, Si-F is easily reconverted to a silanol (Si-O-H) group during HF rinse.

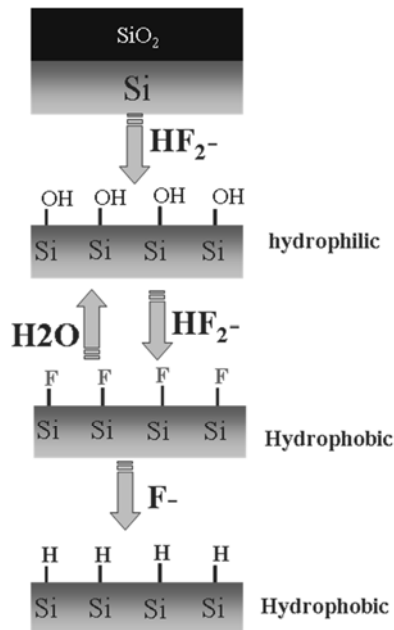


Figure 2: SiO₂ etch in aq. HF – simplified reactions
Last reaction being kinetically limited

It's tempting to use extremely diluted HF to improve etching uniformity but it increases the risks of getting incomplete Si-H passivation. Figure 3 shows both the silicon chemical oxide and grown gate oxide thicknesses versus the sacrificial silicon oxide over etch.

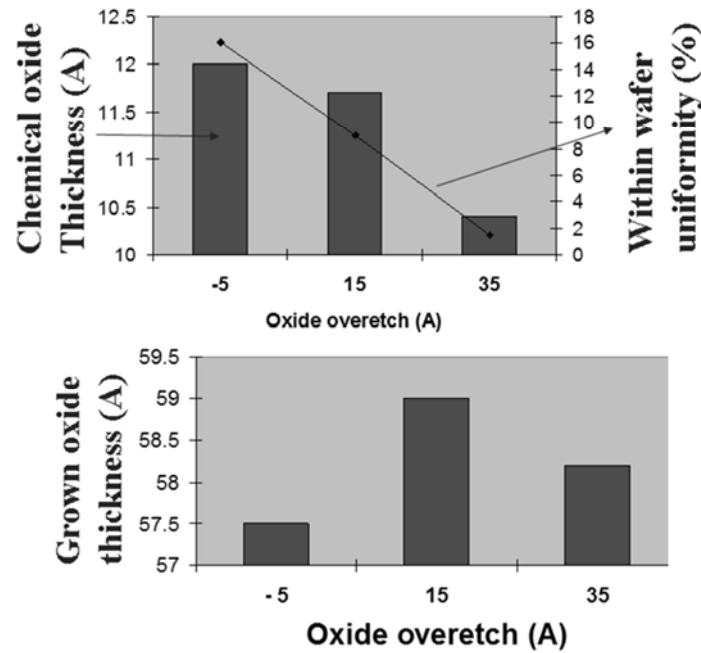


Figure 3: Ellipsometry data

- a) chemical oxide thickness and uniformity versus sacrificial over etch (top graph)
- b) grown gate oxide thickness versus sacrificial oxide over etch (bottom graph)

On both graphs, the left value represents an incomplete etch. A thin non uniform oxide residue slows the gate oxide growth giving the thinnest grown thickness between the three samples. With short oxide over etch, the film is efficiently etched away but relatively thick non uniform chemical and gate oxides are found. Finally, the sample with the highest over etch gives a perfect thin uniform chemical oxide and a good quality gate oxide

Surface characterization with HF last recipes enable a better understanding of the present phenomenon. Figure 4 confirms a short over etch with very diluted HF doesn't correctly passivate the silicon surface and leads to silanol bonds islands so to a rough surface, affecting the transistors' reliability. At this low HF concentration a relatively high oxide over etch is required to get smooth totally deoxidized surface. Such a high over etch is often incompatible with the process integration, leading to a significant deep STI divot.

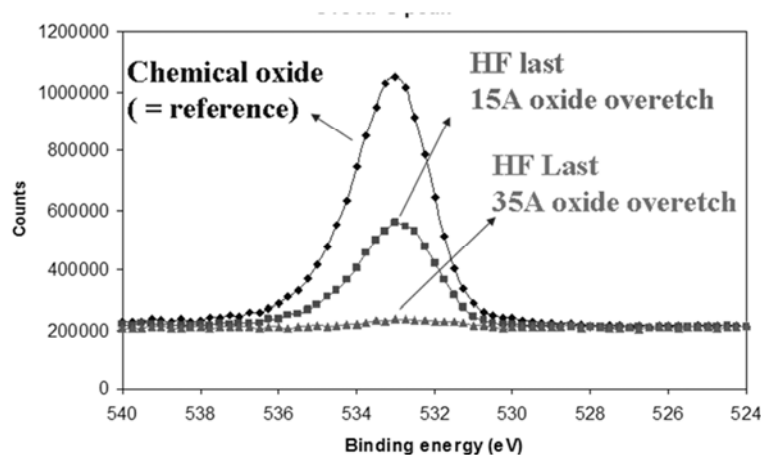


Figure 4: O1s peak (XPS): silicon surface after sacrificial silicon oxide removal by HF 0,25% with various over etches

Increasing the HF concentration enables a complete silicon passivation, drastically minimizes the over etch, and keeps an excellent gate oxide interface (figure 5).

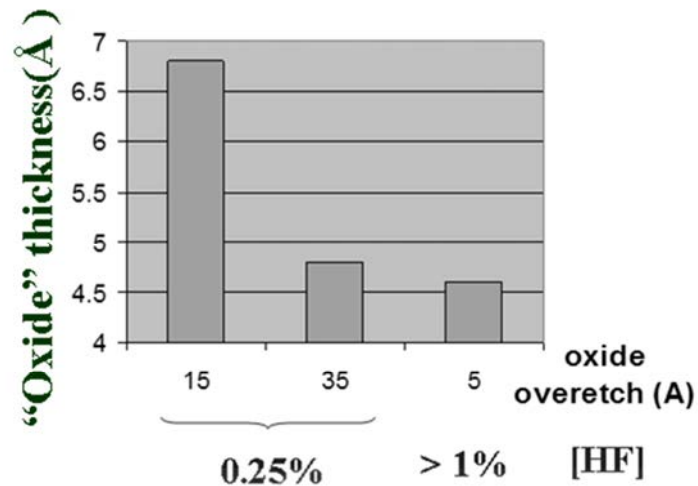


Figure 5: [HF] effect on HF last after desoxidation (ellipsometer)

Nonetheless, the short over etch method has one advantage. It can reveal a silicon oxide interface quality. Hence, sacrificial oxide grown with RTO (Rapid Thermal Oxidation) and furnace tools have been compared (figure 6). Both samples have exact same thickness and are etched away with HF 0,25% with a short over etch (15Å) to study the silicon surface. Whereas furnace has uniform interface, RTO exhibits a central signature that might be attributed to an initially silicon richer area during the oxide growth.

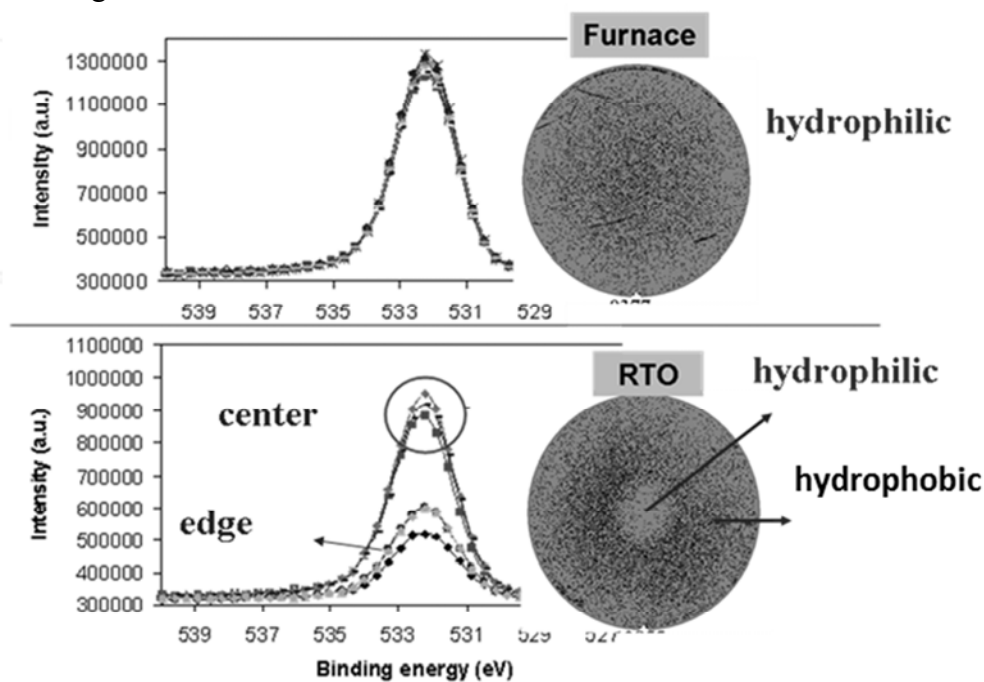


Figure 6: Si after HF Last desoxidation (over etch 15Å)

O1s XPS and surfscan (35nm particles on Si)

Top: starting from furnace thermal oxide

Bottom: starting from Rapid Thermal Oxide

Summary

A trend is observed in the integrated circuits industry to reduce the STI divot by lowering the cumulated oxide etch budget. This needs to be done without degrading the silicon surface quality. This requires to accurately select the HF concentration. Silicon oxides grown on undoped silicon surface can be correctly removed with almost no over etch when HF concentration is higher than 0,5%. Indeed, the Si-H silicon passivation reaction is kinetically driven and requires enough F⁻ ions

to be completed. Relatively high enough HF concentration immediately passivate the silicon surface, minimizing the silicon roughness and STI divot. This is key to enable an excellent gate oxide integrity.

References

- [1] M.Knotter. Etching mechanism of vitreous silicon dioxide in HF-based solutions. J. Am. Chem. Soc., 122 (18), (2000), pp 4345-4351
- [2] P.Garnier. Surface preparation challenge on nitrided gate oxides. Solid State phenomena, Vol. 134, (2007) p. 71-74
- [3] Y.Hagimoto, Evaluation of the plasmaless gaseous etching process, Solid State phenomena, Vol. 134, (2008), pp. 7-10
- [4] F. Tardiff, optimization of HF and oxidant last wet cleanings before 7nm gate oxide. ECS Fall, (1995), Vol. 95-2
- [5] Da-Yuan Lee & al. Impacts of HF etching on Ultra-thin core gate oxide integrity in dual gate oxide CMOS technology. Plasma and process-induced damage, (2003), 8th international symposium, pp 77-80

Surface Preparation Quality before Epitaxy

Philippe Garnier

STMicronics Crolles2, 850 rue Jean Monnet 38921 Crolles, France

philippe-e.garnier@st.com

Keywords: epitaxy, watermarks, silicon surface passivation, HF Last

Abstract. “HF Last” process are widely used as pre epi cleans. They enable a Si-H surface to grow a perfect Si layer by epitaxy. Nonetheless, such hydrophobic wafers are extremely sensitive to watermarks formation during the wafer drying. A design of experiments has been used to determine which parameters impact their formation on a single wafer cleaning tool. Plus, the silicon surface stability has been compared between this tool and an immersion batch cleaning tool.

Introduction

Pre epi clean requires an excellent Si-H silicon surface passivation to ensure best epi layer quality. This is even more severe for a low temperature bake epitaxy where oxygen and carbon contaminants are usual on the silicon surface. More and more, batch surface preparation tools are substituted by spin dry single wafer tools. Indeed they are less prone to metal and particles cross contamination. This paper deals with the silicon surface quality before an epitaxy: both in terms of defectivity (watermarks) and silicon passivation stability between the cleaning and the epitaxy.

Experimental

Two kind of usual cleaning tools are compared: a batch immersion FC3000 tool and spin drying single wafer SU3000 tools, both from Screen firm. The wet bench used a HF 0.25% and the single wafer tools a 0.5%. Epitaxy is grown on an Epsilon from ASM with various conditions depending on the grown film nature.

Results and discussion

WM(Watermarks) are the most severe defects affecting a pre epi clean quality. They're created either from a bad wafer drying or droplet back splashes. They're seldom observed on hydrophilic surfaces (figure 1). However, they're more often found on hydrophobic silicon, polymers [1], and even more on either hydrophobic / hydrophilic mixed surfaces, or high topography surfaces. For this reason, pattern poly silicon gates are used to compare the wafer drying performances of several cleaning tools. The patterned wafers are submitted to a HF Last process and their defect density is then checked with a standard defects inspection tool.

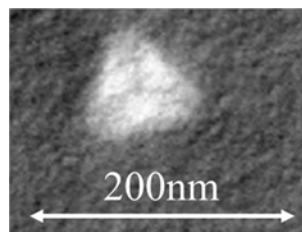


Figure 1: WM on hydrophilic HF-SC1-HCl cleaned blanket wafer

WM are made of varied nature silicates [2] [3]. On our patterned wafers, four kind of shapes are found (figure 2). First, few extremely flat defects are found, made of SiO_x material. The optical contrast made them easier to find on patterned than blanket wafers. Solid porous SiO_x silicates are the most numerous. Few perfect dendrites defects originate from a round water droplet evaporation. At last, very few crystalline Si-F made defects are found. Their shape depends on the atmospheric

and liquid droplets composition during the wafer drying, especially the often present ammonia and HF chemicals.

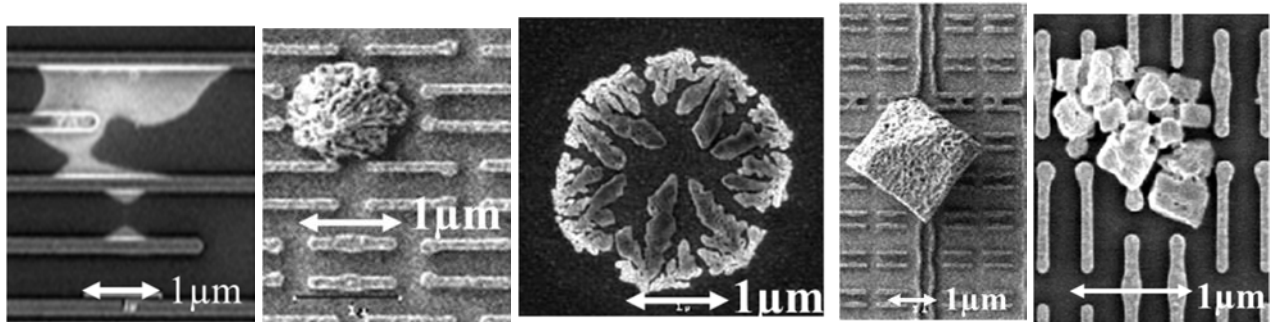


Figure 2: WM on poly silicon patterned gates after HF 0.5% last on single wafer tool:

From left to right: flat silicates, solid porous silicates, dendrites, Si-F crystalline (both right pictures)

The smaller the pitch between two patterns, and the higher their aspect ratio, the higher the probability to generate WM due to a stronger water retention onto the surfaces (figure 3).

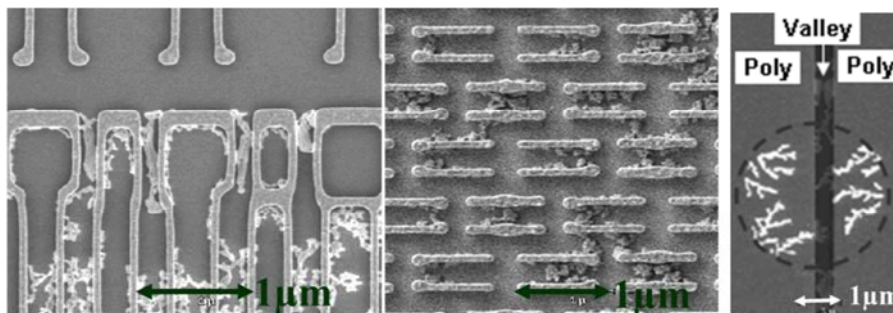


Figure 3: Stronger water retention & high surface tension, hence WM with small pitch and higher aspect ratio structures

To determine parameters influencing WM generation on a Screen single wafer tool, a design of experiments is defined. This toolset has a SP(Shield Plate) (figure 4) enabling a N₂ inert atmosphere during the drying. Indeed, oxygen and light are two known WM generators on silicon surfaces.

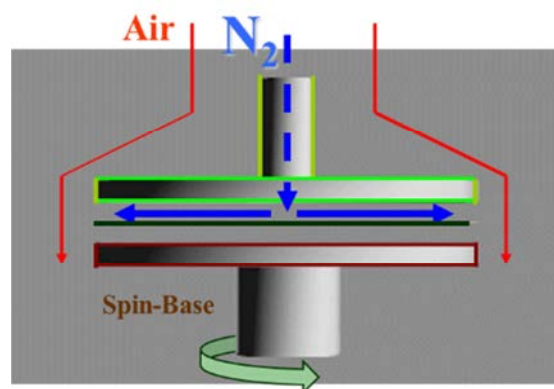


Figure 4: DNS Shield plate concept for improved wafer drying a single spin drying wafer

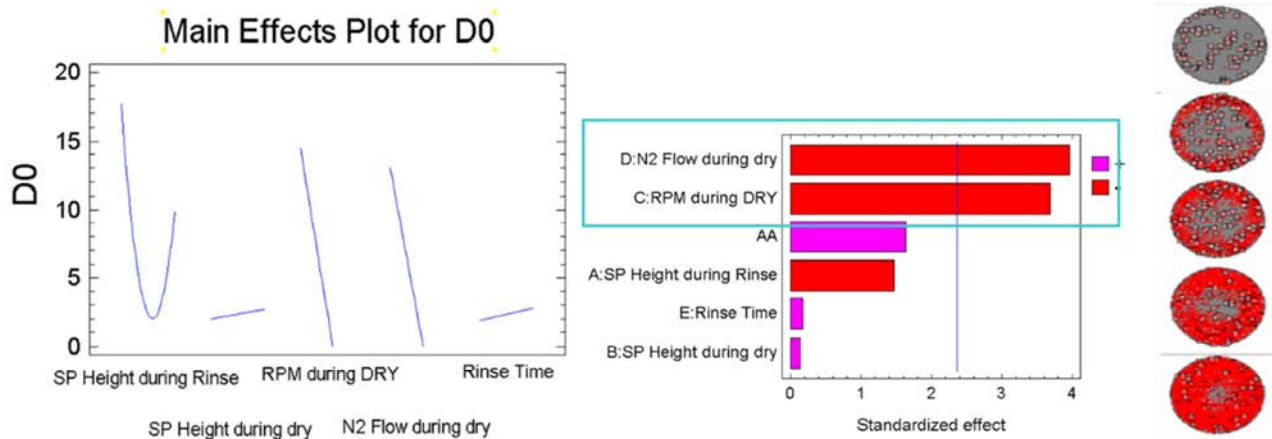


Figure 5: Design of experiments: watermarks D0(defect density /cm²) vs tested parameters (left)
Parameters significance (center), wafer mapping variation (right)

Several parameters are studied. First the SP height during the final rinse and drying steps, the rotation speed and the N2 flow (liters /min) during the drying step, and the rinse time (figure 5). WM mapping exhibit a concentric shape with high defects from the wafer edge. Only the rotation speed and N2 flows have significant impact on the WM. Hence, a plane of the design of experiments is drawn showing the impact of these two key parameters (figure 6). The higher they are, the lower the watermarks defect density. Indeed, much less humidity will remain on and close to the wafer. However the process window is extremely limited for these sensitive tested wafer patterns. IPA is highly recommended to enlarge it.

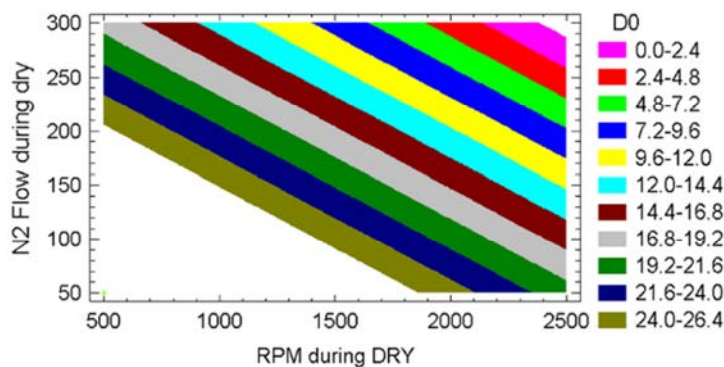


Figure 6: Selected plane with two main influent parameters on WM: D0 vs rpm & N2 flow during wafer drying

Finally, epitaxy quality reflects the surface preparation performed before its growth (figure 7) especially with a low temperature or no epi pre bake. The quality of the grown silicon layer looks similar between a HF last from a wet bench or a single wafer tool. SIMS method analyze a too small area to be reliable. The real quality difference is evidenced by a KLA Tencor surfscan measurement at 90nm. Typical respective toolset mapping can be observed: a handling contamination in the wet bench, and a spiral spin drying mapping on the single wafer tool

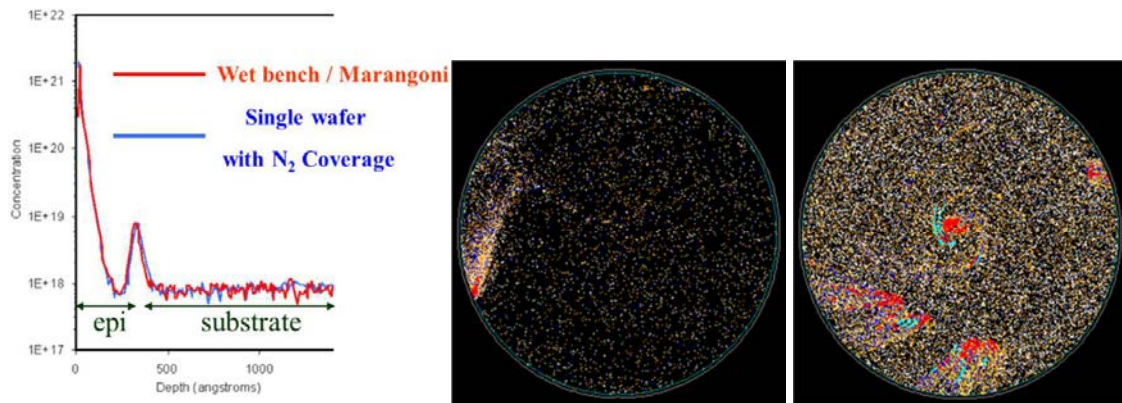


Figure 7 : 650°C Si epitaxy without H₂ bake:

[O] SIMS comparison after epitaxy between both HF Last process
90nm defects map after HF Last & this epitaxy on wet bench (left) and single wafer (right)

At last, the HF last Si-H passivation stability is compared between three samples (figure 8): from the Marangoni like wet bench, to the single wafer N₂ only drying and IPA followed by N₂ drying. SiO_x island are regrown along queue time after HF Last. Following the O1s peak on silicon surface along the queue time is relevant to follow this very slow re oxidation. From far, the Marangoni like dryer shows the best Si-H passivation. Far being is the single wafer tool. A 8s IPA dispense during the wafer drying doesn't improve the surface quality compared with N₂ only standard drying. Longer IPA dispense (up to 20s) gives similar results.

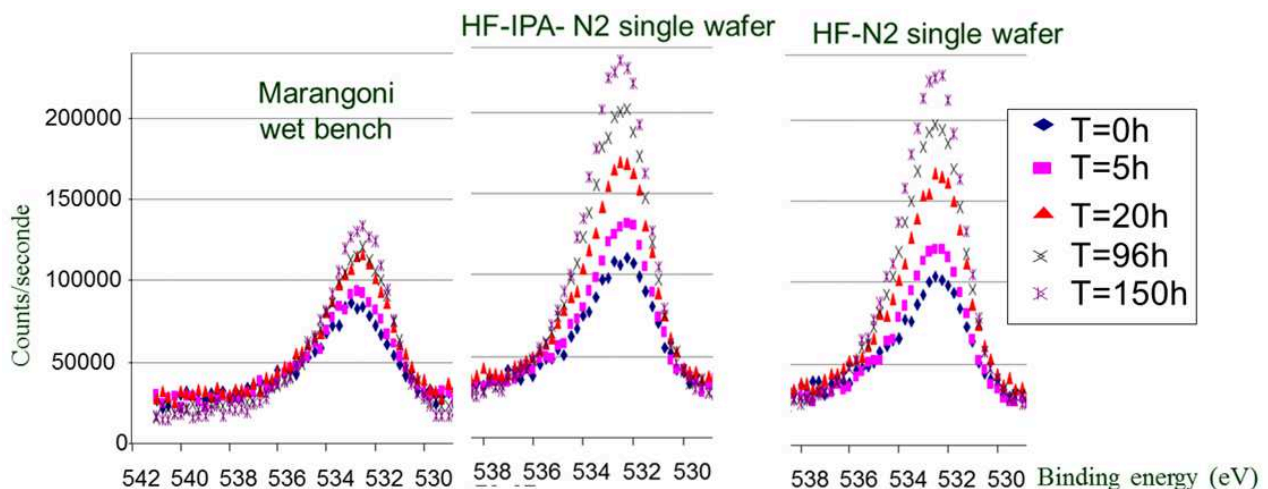


Figure 8: XPS O1s peak time evolution of silicon surface after various HF last

Even if single wafer cleaning tools present a significant much lower defect density and reduced risks of particles and metals cross contamination compared with wet benches, their wafer drying still requires some drastic improvements. Indeed the oxygen control during the wafer drying isn't as optimized as in a low pressure dryer of a wet bench. Some dry alternatives brings some solutions [4].

Summary

Pre epitaxy cleans are still made thanks to a wet HF last. The surface preparation in the semiconductors have massively evolved from the batch cleaning to single wafer tools, since these latest reduce significantly the defect density. Although this is true for most of the cleaning applications, this is less obvious for the pre epitaxy cleans. Indeed, the wafer drying performance of a Marangoni like drying system still exceeds the performance of a spin drying system (N₂ only or IPA drying). Controlling the atmosphere on a spin drying system that processes wafers one after the other is challenging. For this reason, watermarks and Si-H surface passivation during a HF last

process are still two main key challenges. Nowadays, deep competition or complementarity exist between HF Last only and combination with dry process.

Acknowledgment

We gratefully acknowledge G. Briend for the sustaining of some key experiments and discussion.

References

- [1] J.H. Kim, Understanding the relationship between the evaporation behavior of water droplets and the formation of stains on polymer surfaces, *Langmuir* 23(11), (2007), pp 6163-9
- [2] H. Namba, Insights into Watermark Formation and Control, *Solid State Phenomena Vols. 103-104*, (2005), pp 83-86
- [3] K. Miya, Effective Rinse Aiming at Water-Mark-free Drying for Single-Spin Wet Cleaning Process, *Solid state phenomena, Vols. 103-104*, (2015), pp. 79-82
- [4] M. Labrot, Low thermal budget for Si and SiGe surface preparation for FDSOI technology, *Applied surface science*, (2016)

Study of Oxygen Concentration in TMAH Solution for Improvement of Sigma-Shaped Wet Etching Process

Yonggen He^{1, a}, Huanxin Liu¹, Jialei Liu¹, Jingang Wu¹
Christian Haigermoser², Feng Liu², Meisheng Zhou², Wei Lu²

¹ Semiconductor Manufacturing International Corporation, No. 18, Zhangjiang Road,
Pudong New Area, Shanghai, China

² Lam Research (Shanghai) Corporation, No. 177, Bibo Road, Shanghai, China

^aAllan_He@SMICS.COM

Keywords: TMAH, sigma wet etching, oxygen

Abstract: Tetramethylammonium hydroxide (TMAH) is a common etchant for Sigma shape formation in IC manufacturing. The impact of oxygen dissolved in TMAH solution on process was studied in this paper. A novel O₂ gas injector was developed to improve the process stabilization by control of the oxygen concentration in TMAH solution

Introduction

For faster speed and smaller scaling of the device, Source/Drain sigma-shaped recess with embedded SiGe structures were introduced by IC manufacturers to maximize the silicon strain in the channel region in P-type transistors. Tetramethylammonium hydroxide (TMAH) is commonly used as a major wet etchant to realize the sigma shape formation. Normally, only concentration and temperature of the TMAH solution are monitored and controlled by manufacturers to achieve the desired performance. However, it has been found recently [1] that ambient oxygen dissolved in TMAH solution is also contributed to the wet etching conditions and even influence the final device performance.

This study focuses on the correlation between TMAH oxygen concentration and critical process parameters such as etch rate, device stress and electrical performance, discovering an effective method to establish a stable TMAH etching process.

Experimental

300 mm wafers with a 300nm thick Undoped Poly film were prepared to perform TMAH etch rate tests. SiGe Stress and electrical parameters were collected from state of art 28nm device wafers. These wafers were processed in a LAM single wafer cleaning system (LAM DV-Prime) with 2.38% TMAH solution and an oxygen sensor was installed in the tank for real-time monitoring of the oxygen concentration. In order to adjust the oxygen concentration in the TMAH solution, an O₂ gas injector was developed and implemented onto the TMAH filling line in the tool. The total amount of O₂ injected during filling could be controlled by O₂ flowrate and time setting.

Results and Discussion

First of all, the etch rate trend during the same TMAH bath lifetime was investigated. As shown in Fig. 1, the etch rate decreases quickly in the first two hours, then tends to be stable. On the other hand, the oxygen concentration in TMAH increases correspondingly.

Ion chromatography data of the TMAH solution (Fig. 2) revealed that the NH₄⁺ concentration remained almost the same during 20 hours bath lifetime, suggesting that the etch rate drop could be caused by the change of oxygen concentration, rather than by a TMAH condition shift.

In order to understand the oxygen behavior in the TMAH solution more clearly, different amounts of O_2 (controlled by 0.1 slm flowrate with different filling times) were injected into TMAH when it was filled into the tank. Fig. 3 illustrates that the oxygen concentration varies with the amount of injected O_2 in the beginning hours, but finally tends to reach the same level, which indicates that the oxygen in the TMAH solution exchanges with the ambient atmosphere and finally becomes saturated.

The influence of oxygen in the TMAH solution on device stress was described in Fig. 4. Less oxygen resulted in higher silicon stress because of the increased sigma trench depth. A 15% stress deviation could be calculated comparing fresh TMAH (6 ppm oxygen) with stable TMAH (8 ppm oxygen) within the same bath lifetime.

It is believed that oxygen during filling influences the TMAH etch rate in the beginning of the bath lifetime. The N_2 protection or the delivery of the TMAH from the facility reduced the oxygen concentration, which made the etching performance of TMAH solution unstable throughout the whole bath lifetime.

More oxygen in TMAH solution will produce more silicon oxide when processing on bare silicon surface, both Silicon and oxide could be etched by OH radical in alkaline solution by typical equations as followings:



The etch rate ratio between Silicon and SiO_2 in alkaline solution was reported to be from 100 to 1000 [2], which explains why the etch rate is lower when oxygen concentration is higher because of more growth of the oxide. In practical applications, stable etch rate is more meaningful so that the constant oxygen concentration in alkaline solution would be a critical factor for process control.

By injecting O_2 into the TMAH solution with a specific optimized amount (e.g. 0.1slm \times 385sec in this case), the stability of the TMAH solution was improved and the run-to-run variation was minimized within the same bath

The result of this improvement was demonstrated by Idsat comparison shown in Fig. 5. By injection of oxygen to stabilize the TMAH etching performance, the device performance (Idsat) showed a better distribution.

Conclusion

The oxygen exchange with the ambient atmosphere causes an unstable etching performance of the TMAH solution, influencing the silicon device stress and final electrical performance. By studying the oxygen behavior in the TMAH solution and developing an effective O_2 control method, the TMAH etching stability could be improved and a better device distribution could be achieved.

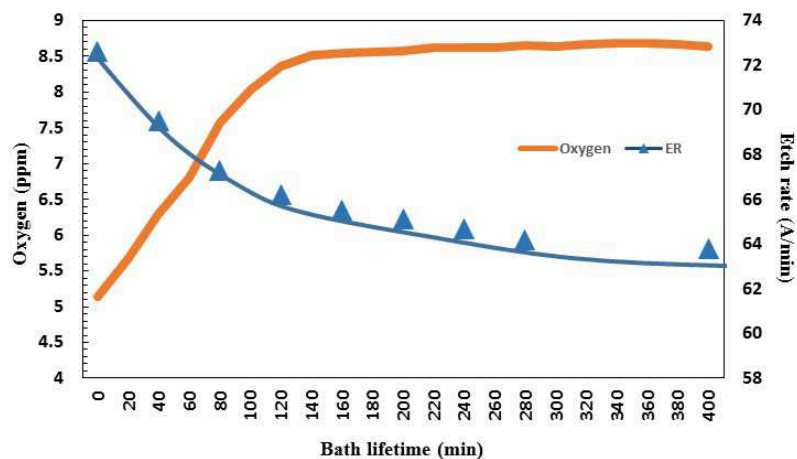


Figure 1: TMAH poly etchrate and oxygen concentration during the same bath lifetime.

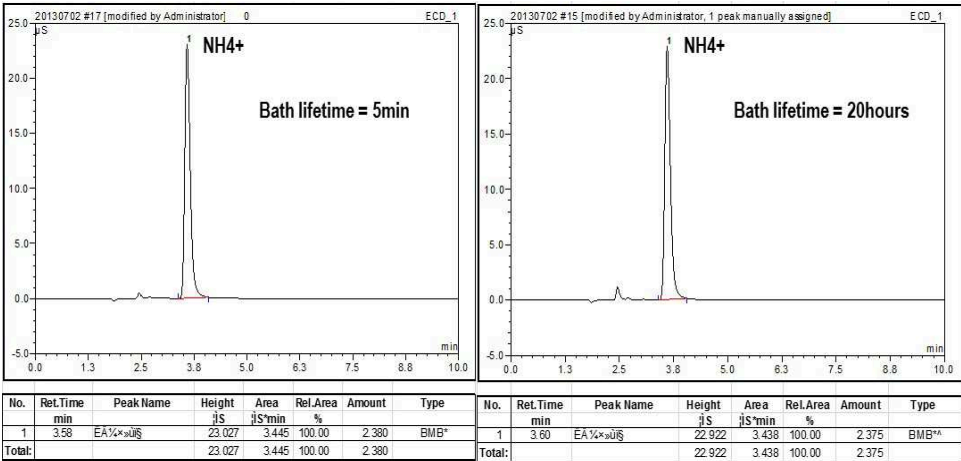


Figure 2: NH_4^+ ion concentration comparison at different bath lifetimes.

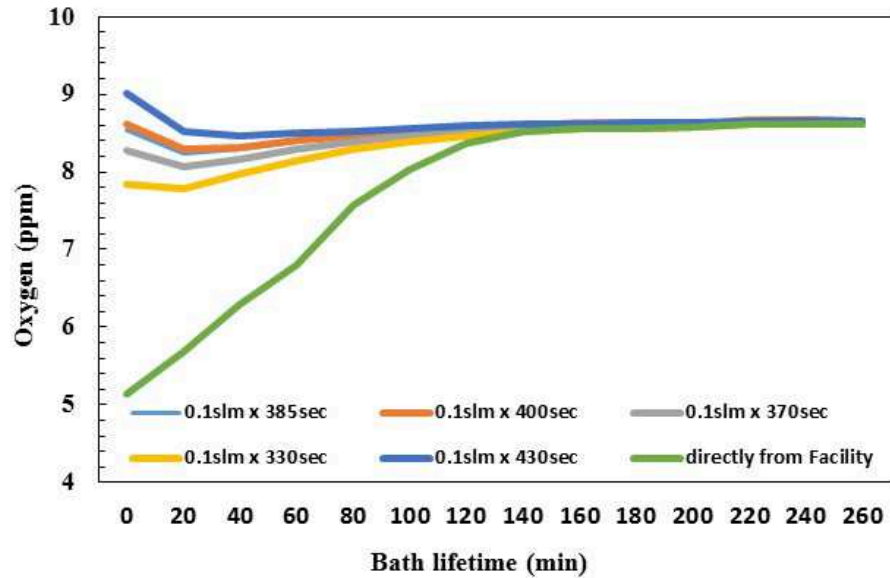


Figure 3: Oxygen concentration trend with different O₂ injection amounts.

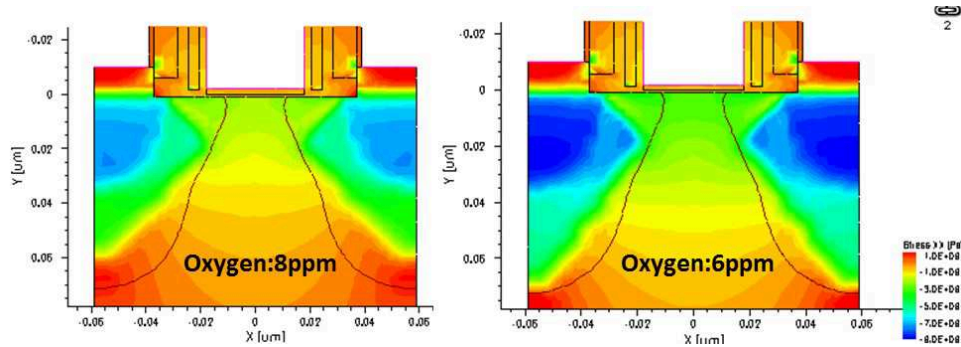


Figure 4: Si Stress comparison after TMAH etching with different oxygen concentrations (Oxygen 8ppm vs 6ppm)

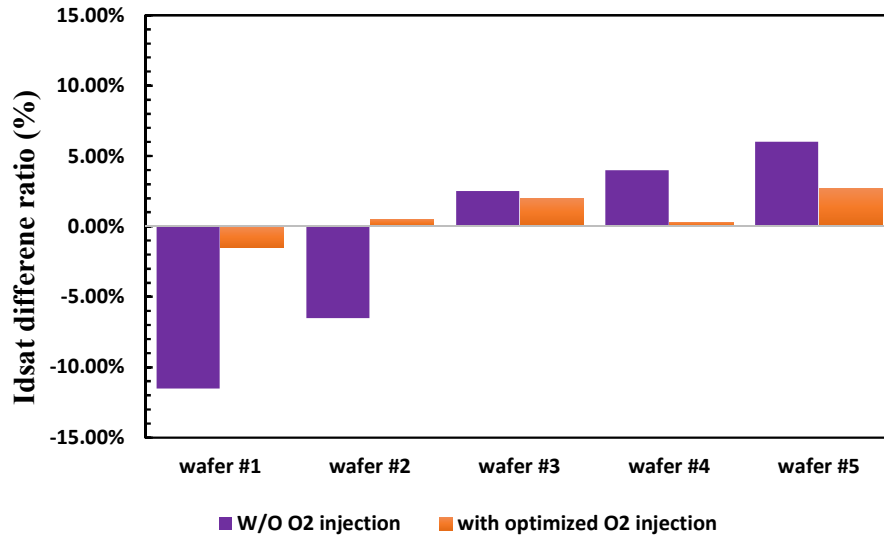


Figure 5: Idsat comparison of device wafers processed with/without O₂ injection within the same TMAH bath.

References

- [1] Euing Lin, Ted Guo, C.C. Chien, M.H. Chang, Wesley Yu, N.H. Yang, J. F. Lin, J.Y. Wu, Kenneth M. Robb, Alessandro Baldaro, Solid State Phenomena, Vol. 219 p.78 (2014)
- [2] H.Seidel, L.Csepregi, A.Heuberger, Anisotropic Etching of Crystalline Silicon in Alkaline Solutions, J. Electrochem Soc., Vol. 137 p.3620 (1990)

The Effect of Rinsing a Germanium Surface after Wet Chemical Treatment

Yukifumi Yoshida^{1, 2 a}, Hiroaki Takahashi¹, Masanobu Sato¹,
 Jim Snow¹, Farid Sebaai² and Frank Holsteyns²

¹ SCREEN Semiconductor Solutions Co., Ltd., 480-1, Takamiya, Hikone, Shiga, 522-0292, Japan

² imec vzw, Kapeldreef 75, 3001 Leuven, Belgium

^ayu.yoshida@screen.co.jp

Keywords: germanium surface, wet-chemical treatment, carbonated water, rinse effect

Abstract. The impact of rinsing liquid for Germanium surface after wet chemical treatment is described. The different Ge loss after processing with different rinse (UPW and CO₂ water) were determined and the different surface morphologies on the Ge surface after processing with different chemicals (AOM, HF and HCl) were determined by XPS. It was found that the investigation of surface morphology after chemical treatment is necessary to understand the rinse effect and the results showed the CO₂ water rinse can decrease and suppress Ge loss at chemical treatment..

Introduction

In recent years novel approaches for the nanofabrication of semiconductor devices are being studied. These include integration schemes such as FinFET (beyond Si: optionally adopting a replacement fin process flow), Gate-first approach replacement metal gate (RMG), and novel materials such as germanium and III-V compounds such as InGaAs, GaAs, InP, and InAlAs [1]. The introduction of Ge and short channel structures for CMOS devices has generated interest in terms of advantage in electron and hole mobility's. However, the use of Ge in CMOS integration is a new challenge in wet processing due to its ease of oxidation and high solubility of the formed oxide products in aqueous solutions.

In one of the typical Ge FinFET process flows, several wet surface cleaning steps need to be considered, e.g. post CMP clean, STI etch back, dummy gate oxide removal and post spacer etch. It is essential to understand the Ge surface chemistry to find the proper cleaning and rinsing chemistries to minimize Ge loss. In particular, Ge loss from the rinsing solution will be a critical concern in these smaller devices.

The influence of chemical treatment on Ge surfaces has previously been reported [2]. However the combination of the treatment with the rinsing step has not been clearly investigated. Therefore, this study focuses on the challenges to investigate a wet cleaning process to prevent the Ge loss from the combination of conventional wet chemistries with a post-rinse step.

Experimental

For this work 1000 nm Ge deposited on a 300 mm Si wafer in an ASM Epsilon 3200®AP/BP epi reactor was used. Subsequently 400 nm of the Ge surface layer was removed by chemo-mechanical polishing (CMP) to provide a low surface roughness. Prior to the Ge loss experiments, the surface was pre-cleaned by a sequential process with HF (1.5 wt%) and ozonated water (1 ppm O₃). Wet processing was carried out in a single wafer cleaning tool (SCREEN Semiconductor Solutions Co., Ltd., SU-3200) using diluted AOM (a mixture of NH₄OH/H₂O and O₃/H₂O; 1:60 and 1ppm), HF (1.5 wt%) and HCl (1.5 wt%) for cleaning and etching, and ultra-pure water (UPW) and carbonated UPW (CO₂ water; 0.2 MΩcm) for rinsing all of room temperature. The Ge etch rates were calculated by weight loss measurements (METRYXMENTOR SF3 (300)) using equation (see Eq.1).

$$R_E = \frac{4\Delta m}{\rho\pi d^2} \quad (1)$$

where R_E is the equivalent amount of Ge loss (\AA), Δm is the change in mass, ρ is the density of Ge and d is the diameter of the wafer. The Ge surface after wet-chemical treatment was studied by X-ray photoelectron spectroscopy (XPS). Coupon samples were cleaved from a 300-mm Ge-deposited wafer and subsequently immersed in different chemical solutions described above. After N_2 drying (without UPW or CO_2 water rinse), these samples were immediately loaded into the XPS load lock and transferred to the main chamber to characterize the Ge surface condition. A Theta300 system with a monochromatized Al $K\alpha$ X-ray source (1486.6 eV) from ThermoFinnigan was used. The exit angle was 78 degrees as measured with respect to the normal of the sample and the spot diameter was 400 microns.

Results and Discussion

Impact of rinse treatment. The Ge loss for a UPW and a carbonated UPW (CO_2 water) treatment was measured. The reference was a Ge surface treated by 1.5 wt% HF followed by 1 ppm of O_3 water resulting in a hydrophilic surface. Figure 1 shows the influence of process time on the weight loss for a UPW and a CO_2 water rinse. The loss increases in both cases with increasing process time. The CO_2 water treatment results in a higher oxide loss as compared to the UPW treatment. This can be explained by a pH effect. The oxide layer present on the Ge surface after the pre-cleaned has a higher solubility in lower pH solutions [3]. The results further show that the rinsing process time is an important parameter in limiting Ge loss and must therefore be limited.

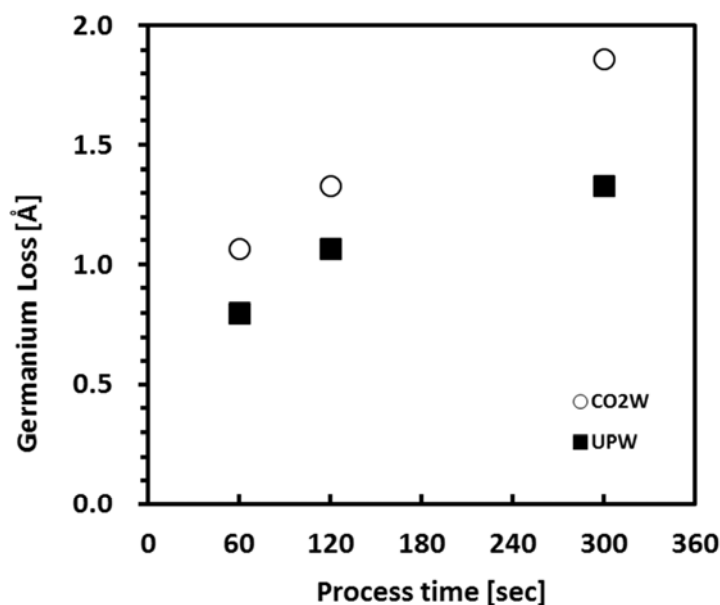


Figure 1: Germanium loss processed by UPW (close square) or CO_2 water rinse (open circle) on a pre-cleaned surface processed by the sequential with HF (1.5 wt%) and ozonated water (1 ppm O_3).

The results described below are confirmed by XPS analysis. The surface sensitive angle (78 deg) measurement result was used for the atomic concentration of each Ge^{x+} amount on substrate surface. Figure 2 a) shows the $\text{Ge}^{x+}/\text{Ge}(0)$ ratio where $1 \leq x \leq 4$ as a relative measure for the total amount of oxide present on the Ge surface. The total amount of oxide clearly decreases after processing in UPW and the amount of oxide loss is higher in the case of CO_2 water. Figure 2 b) shows the $\text{Ge}^{x+}/(\text{Ge}^{x+}_{\text{total}})$ ratio for each of the Ge oxidation states ($1 \leq x \leq 4$) as an indication for the oxide composition. The reference sample after the pre-clean shows that the oxidation state of Ge is mainly composed of Ge^{1+} , Ge^{3+} and Ge^{4+} . After an UPW rinse treatment Ge^{4+} shows the most significant decrease, which is expected due to the highest solubility of the GeO_2 with respect to the Ge suboxides. A similar trend observed for the CO_2 water treatment.

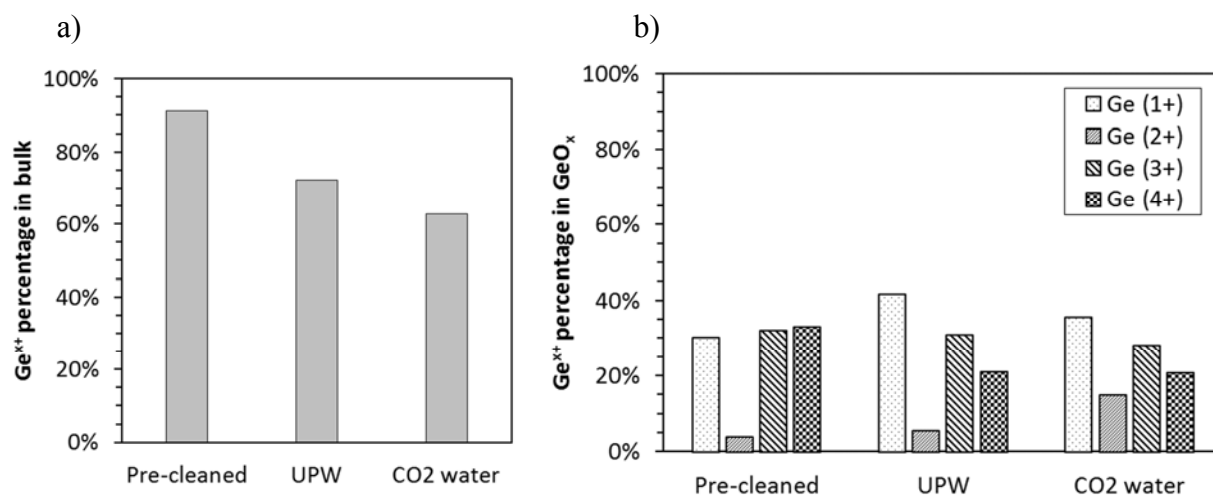


Figure 2: a) $\text{Ge}^{x+}/\text{Ge}(0)$ ratio (1 ≤ x ≤ 4) indicative for the total amount of oxide present on bulk Ge for the HF (1.5 wt%) / ozonated water (1 ppm O_3) reference and UPW and CO_2 water rinse treatment. b) $\text{Ge}^{x+}/(\text{Ge}^{x+}_{\text{total}})$ ratio's (1 ≤ x ≤ 4) as a measure for the oxide composition with UPW and CO_2 water rinse treatment.

Impact of chemical treatment. In a next series of experiments, the Ge loss was further investigated. The reference was a Ge surface treated by 1.5 wt% HF followed by 1 ppm of O_3 water resulting in a hydrophilic surface. Figure 3 shows the Ge loss after a chemical treatment of 60 seconds followed by a short UPW rinse for the following sequences; AOM-UPW rinse, HF-UPW rinse and HCl-UPW rinse. The good particle removal performance and observed Ge loss ($\sim 11 \text{ \AA}$) for the AOM treatment is in good agreement with other work [4]. The significant higher Ge loss for the AOM solution as compared to the HF and HCl treatment, is related to the presence of an oxidizing agent. The lower loss observed for the HCl treatment as compared to the HF immersion, is possibly a concentration effect (0.49 M HCl versus 0.86 M HF).

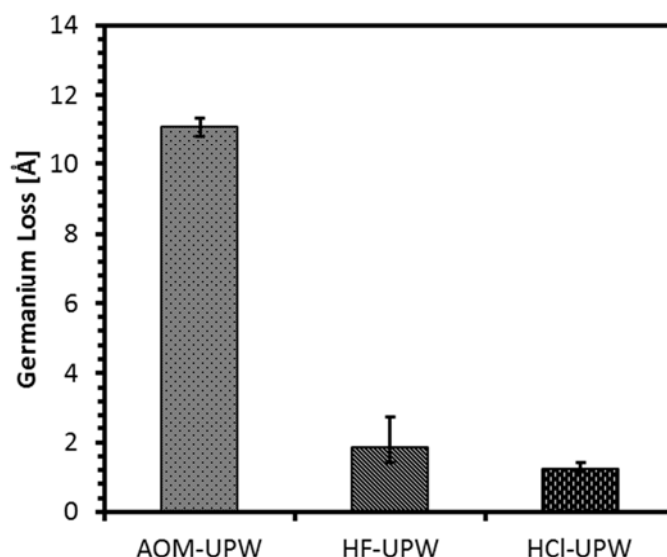


Figure 3: Germanium loss after a AOM process ($\text{NH}_4\text{OH}:\text{H}_2\text{O}$ (1:60) + 1 ppm $\text{O}_3/\text{H}_2\text{O}$), HF (1.5 wt%) or HCl (1.5 wt%) with UPW rinse on a pre-cleaned surface. the pre-clean consisted of a 1.5 wt% HF followed by 1 ppm $\text{O}_3/\text{H}_2\text{O}$.

Figure 4 a) shows the $\text{Ge}^{x+}/\text{Ge}(0)$ ratio obtained by XPS quantification. The surface sensitive angle (78 deg) measurement result was used for the atomic concentration of each Ge^{x+} amount on substrate surface. The pre-cleaned surface (1.5 wt% HF followed by 1 ppm of O_3 water) shows the highest amount of oxide present at the interface. Oxide loss is observed after both alkaline and acidic treatment: the solubility of Ge oxides in these media is higher than in UPW. The HF treatment showed the lowest amount of GeO_2 and hence the HF treatment showed higher oxide loss than the HCl treatment confirming the results shown in Figure 3. Figure 4b) shows that for all chemical

treatments the Ge^{4+} oxide gives relatively the lowest contribution in terms of oxide composition, which is expected due to its highest solubility. More detailed studies on the impact of the chemical treatment on the final oxide composition are currently ongoing.

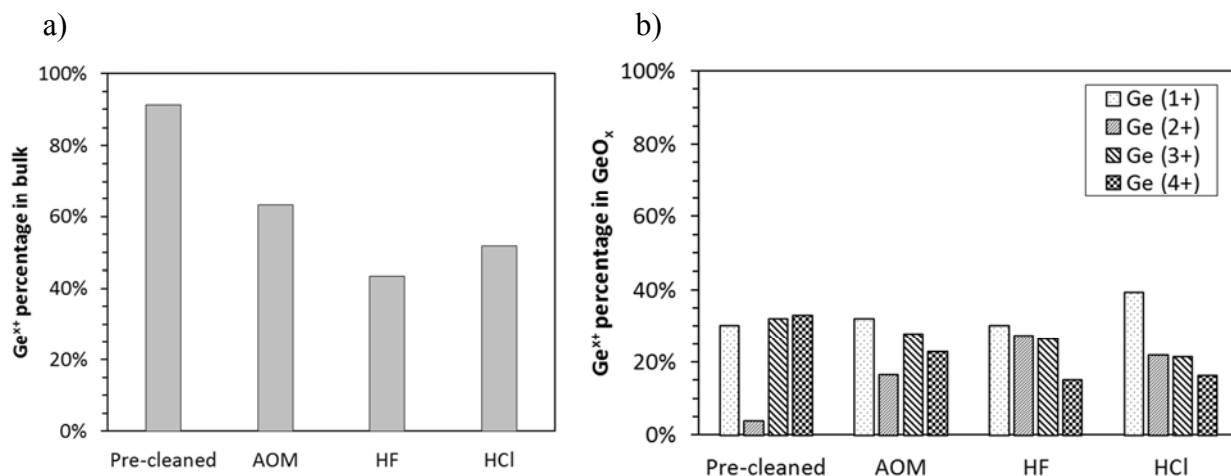


Figure 4: a) $\text{Ge}^{x+}/\text{Ge}(0)$ ratio ($1 \leq x \leq 4$) indicative for the total amount of oxide present in bulk with AOM (Ammonia and Ozonated water Mixture; 1:60 and 1ppm), HF (1.5 wt%) or HCl (1.5 wt%) without rinse. b) $\text{Ge}^{x+}/(\text{Ge}^{x+}_{\text{total}})$ ratio's ($1 \leq x \leq 4$) as a measure for the oxide composition with AOM (Ammonia and Ozonated water Mixture; 1:60 and 1 ppm), HF (1.5 wt%) or HCl (1.5 wt%) without rinse.

Impact of rinse after chemical treatment. The Ge loss on a pre-cleaned Ge surface (1.5 wt% HF followed by 1ppm of O_3 of water) was measured after different chemical treatments. Figure 5 shows the Ge loss after 60 seconds of chemical treatment followed by a UPW or CO_2 water rinse. Interestingly, when an AOM treatment is performed, a lower loss is observed when a CO_2 water rinse is applied instead of a UPW rinse. The loss could be limited to 9 Å in the former case. This may indicate that the history of the wafer may have an effect on the total Ge loss. When a HF treatment is performed after the pre-clean, CO_2 water gives no beneficial effect in terms of limiting oxide loss. In good agreement with Figure 4a) the oxide loss after HCl treatment is lower than that for HF treatment. We observed that the Ge loss could be minimized when a CO_2 rinse was performed after the HCl treatment supporting that the chemical surface condition may have an influence on the loss observed. This phenomenon is not fully understood at present and will be examined in future work.

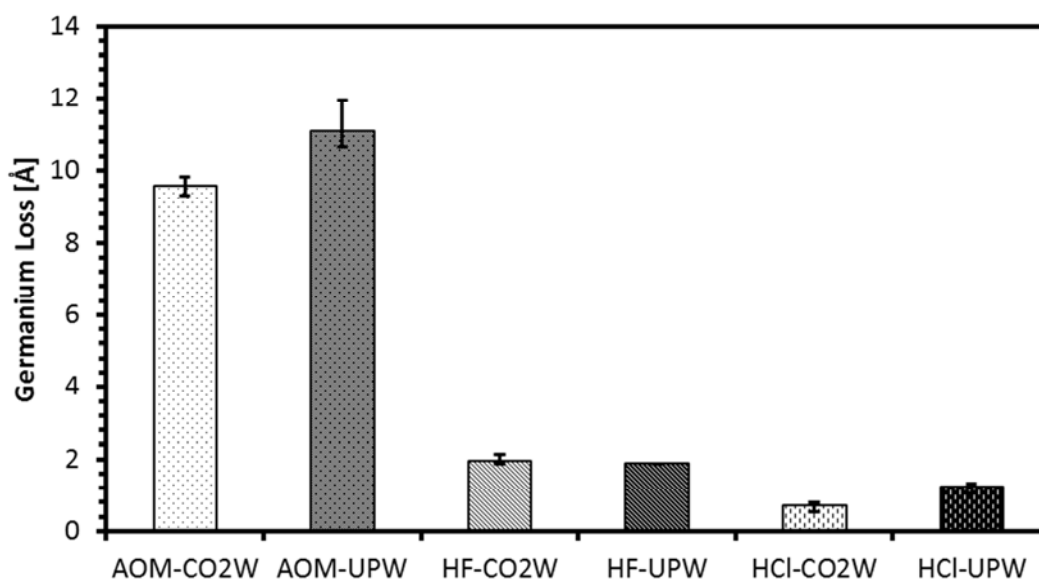


Figure 5: Germanium loss processed by AOM (Ammonia and Ozonated water Mixture; 1:60 and 1ppm), HF (1.5 wt%) or HCl (1.5wt%) with UPW or CO_2 water rinse on pre-cleaned surface processed by the sequential with HF (1.5 wt%) and ozonated water (1ppm O_3).

Conclusion

The impact of rinse solution for Ge surface was investigated. The CO₂ water treatment showed higher Ge loss than the UPW treatment by a pH effect. Only the water treatment increases Ge loss with increasing process time, thus the rinsing process time is an important parameter in limiting Ge oxide loss. Next, the impact of the rinse solution for a Ge surface was investigated with alkaline cleaning chemical (AOM) and acidic conventional chemicals (HF and HCl). The different surface morphologies on the Ge surface after processing with different chemicals were determined by XPS; all chemical treatments showed the relatively lowest Ge⁴⁺ oxide contribution in terms of oxide composition, which is expected due to its highest solubility. This study indicates that the investigation of surface morphology after chemical treatment is necessary to understand the rinse effect. CO₂ water rinse can decrease Ge loss by 2 Å after an AOM chemical cleaning process. Furthermore, CO₂ water rinse can suppress the Ge loss at HCl chemical treatment.

Acknowledgements

The author would like to acknowledge Dennis van Dorp and Sophia Arnauts from imec for fruitful discussion.

References

- [1] P. W. Mertens, R. Vos, W. Masayuki, S. Arnauts, H. Takahashi, D. Tsvetanova, D. Cuypers, S. Sioncke, N. Valckx, S. Brems, M. Hauptmann and M. Heyns, ECS Trans., 41(5), 3 (2011).
- [2] J. Kim, Germanium Surface Cleaning and Preparation Methods for Semiconductor Applications,
- [3] M. Pourbaix, Atlas of electrochemical equilibria in aqueous solutions
- [4] H. Takahashi, M. Wada, J. Snow, R. Vos, P. W. Mertens, H. Shirakawa and S. Nadahara, ECS Trans., 41(5), 163 (2011)

Effect of Dilute Hydrogen Peroxide in Ultrapure Water on SiGe Epitaxial Process

Toru Masaoka^{1,a}, Nobuko Gan¹, Yu Fujimura¹, Yuichi Ogawa¹, Kurt Wostyn², Antoine Pacco², Yukifumi Yoshida³, and Frank Holsteyns²

¹ Kurita Water Industries Ltd., 1-4-10, Nakano, Nakano-ku, Tokyo, 164-0001, Japan

² imec vzw, Kapeldreef 75, 3001 Heverlee, Belgium

³ SCREEN Semiconductor Solutions Co., Ltd., 480-1, Takamiya, Hikone, Shiga, 522-0292, Japan

^a tooru.masaoka@kurita.co.jp

Keywords: pre-epi clean, HF last, ultrapure water, hydrogen peroxide, silicon(111)

Abstract. Ultrapure water contains dilute hydrogen peroxide as an impurity. In order to clarify an impact of the dilute hydrogen peroxide on cleaning processes, a SiGe epitaxial layer was deposited on a Si(100) wafer which surface was treated by HF last process with hydrogen peroxide contained UPW or hydrogen peroxide removed UPW. The defect in the SiGe epitaxial layer was reduced when the hydrogen peroxide removed UPW was used.

Introduction

Ultrapure water (UPW) is a solvent which has been widely used for rinsing and chemical diluting in semiconductor cleaning process. Recently purity of the UPW has become quite high due to an improvement of water treatment technology. For example metal contamination in the UPW at leading semiconductor fab is now less than ppt level. Meanwhile, hydrogen peroxide (H₂O₂) in the UPW which is generated as a byproduct by an UV oxidation process, one of the water treatment processes, has been becoming a new issue. The H₂O₂, about 5-20 ppb in UPW in general [1], has a risk of having negative impacts on the surface of the semiconductor material such as corrosion during its cleaning process. Therefore, International Technology Roadmap for Semiconductors (ITRS) committees has decided to define the H₂O₂ concentration in the UPW in their guidelines [2]. Although, decomposition and analysis method of the H₂O₂ in the UPW have been reported, no studies have ever tried to evaluate its impact on the cleaning process especially for using 300mm wafer [3].

In this paper we have evaluated the impact of water quality on an HF last process because it offers a sensitive test vehicle for evaluating drying performance [4]. In addition HF last process performance has been evaluated by epitaxy since SiGe-on-Si epitaxy is very sensitive to the surface cleanliness prior to epitaxy [5]. In the last part we present FTIR-ATR results on Si (111) substrates. A perfect Si (111) surface is terminated by a mono-hydride resulting in a very narrow Si-H absorption peak. Here we evaluated the impact of water quality on the evolution of this Si-H absorption peak and show how H₂O₂ in the UPW can affect the Si surface properties.

Experimental

HF last process. 300 mm Si (100) wafers were used. The wafer was processed in dilute HF (HF 0.8 % and HCl 0.4 %) by using a single wafer cleaning tool (SCREEN SU-3100). To evaluate the impact of residual H₂O₂ on HF-last processes, UPW supplied by the general cleanroom supply (hereinafter general UPW) was compared with UPW provided by a Kurita water unit (hereinafter H₂O₂ removed UPW) during HF point-of-use mixing and rinse. The Kurita water unit is equipped with NanoSaver®, a H₂O₂ decomposition catalyst. The catalyst reduces the residual H₂O₂ present in the UPW provided by the general UPW (H₂O₂ conc. 8-10 ppb) to below the detection limit (H₂O₂ <1 ppb). Dissolved oxygen (DO) concentration of both UPW at Point-of-Entry was < 1 ppb.

Process performance. The HF-last process quality was evaluated by comparing the number of added defects or by SiGe epitaxy. The numbers of added defects on a Si (100) wafer were quantified by

surface light scattering using a KLA-Tencor Surfscan SP3 in UHS (Ultra High Sensitivity) mode. Added defects were quantified up to 21nm LSE (Latex Sphere Equivalent). Alternatively HF last quality was quantified by SiGe epitaxy. 80nm thick epitaxial $\text{Si}_{0.8}\text{Ge}_{0.2}$ was deposited on a Si (100) wafer. Prior to the epitaxial growth, the wafers were cleaned using an O_3 -last imec clean [6]. Subsequently the chemical oxide was removed using and HF last and loaded to the epitaxial deposition tool with minimal delay (ASM Epsilon 3200, delay time < 10min). $\text{Si}_{0.8}\text{Ge}_{0.2}$ deposition was done either directly after loading or after a GeH_4 -HCl-based in-situ clean. The GeH_4 -HCl-based in-situ clean enabled to remove residual O on the Si substrate prior to SiGe epitaxy [7]. SiGe epi quality was analyzed by surface light scattering measurements (KLA-Tencor Surfscan SP3) using the hazeline area method, previously found to correlate with Si (100) pre-epi-clean quality prior to $\text{Si}_{0.8}\text{Ge}_{0.2}$ epitaxy [8]. The oxygen concentration at the interface between SiGe epi and Si (100) surface, a measure of pre-epi clean quality, was quantified by dynamic Secondary Ion Mass Spectrometry (SIMS).

Hydride terminates on Si (111). Mono-hydride terminated 150 mm Si (111) wafers were prepared by NH_4F (40 %). Subsequently the wafers were in an HF solution (0.5 %, time = 15 min) with variable H_2O_2 concentration (<1–300 ppb). The wafers were treated in a closed acrylic chamber in order to avoid oxygen diffusion during HF exposure. The DO concentration of the chamber was 60 ppb. After the process, Fourier Transform IR-Attenuated Total Reflection (FTIR-ATR) was used to quantify the changes to the mono-hydride terminated Si (111).

Results and discussion

SiGe epitaxy. Figure 1 shows a hazeline image after SiGe epitaxial growth using a dHF process combined with a GeH_4 -HCl-based clean. Previously an increase in hazeline area was found to correlate with an increase in interfacial O, so correlating with the pre-epi-clean efficiency and SiGe epitaxial quality [8]. The hazeline area measurements were converted into a radial distribution (see Figure 2). From the wafer center up to a radius of approximately 100mm, the hazeline density decreases upon removal of the residual H_2O_2 in the general DIW, indicating an improvement in pre-epi-clean efficiency for H_2O_2 removed UPW compared with general UPW.

Table I compares the O concentration at the Si substrate / epitaxial-SiGe interface after HF last using general or H_2O_2 removed UPW. Epitaxial SiGe was deposited either directly on the HF-last Si substrate or after a GeH_4 -HCl-based in-situ clean. No significant differences were found in interfacial O between HF-last surfaces prepared either using general UPW or H_2O_2 removed UPW. These results indicate that the improvement in SiGe epitaxial quality is by H_2O_2 removed UPW compared to general UPW is either unrelated to the residual O on HF-last surfaces or due to differences in residual O at levels below the detection limit ($\sim 10^{12}$ at/cm²). In the past it was found that the number of SiGe defects did not correlate with interfacial oxygen concentration once the interfacial oxygen concentration reached values in the 10^{12} at/cm² range [9].

Added defects on HF-last Si (100) surfaces. Figure 3 shows the surface defect measurement results of the Si (100) wafer which is processed by dHF using general UPW or H_2O_2 removed UPW. No significant difference could be found down to 21nm LSE defect size. This result indicates that residual H_2O_2 in the UPW at concentrations in the <10 ppb range does not cause measurable differences in watermark formation for LSE sizes down to 21nm or the number of added defects is dominated by a different source. The impact of watermarks less than 21nm LSE on epitaxial quality could also be much larger compared to other defect classes (e.g. particles) as their physical size is typically much larger than the size determined by surface light scattering.

Hydride termination on Si (111). The FTIR-ATR spectra of the Si (111) wafer before and after processing in dHF with H_2O_2 concentrations in the range of <1 – 300ppb are shown in Fig. 4. Table II shows the absorbance value of the silicon mono-hydride (2082 cm⁻¹) and silicon di-hydride (2099 cm⁻¹) peak and the ratio for each condition.

By the NH_4F preparation, the Si (111) surfaces has become mono-hydride terminated, as seen by a sharp absorption peak(2082 cm⁻¹), indicative of a surface morphology dominated by terraces and a

low density of steps and kinks [10]. Upon exposure of the surface to a dHF solution containing < 1 ppb H_2O_2 results in a decrease in the mono-hydride absorption peak with a concurrent increase in the di-hydride peak. This increase is attributed to the presence of 60 ppb DO during HF exposure. Upon exposure of the mono-hydride terminated surface to HF with 60 ppb DO and increasing H_2O_2 concentration, the mono-hydride absorption peak decreases further while the di-hydride peak increases. The decrease and increase in respectively silicon mono-hydride and di-hydride absorption peak indicates a decrease and increase in respectively terraces and surface steps [10]. This is in agreement with the change in microroughness of Si surfaces upon exposure to HF/oxidizer chemical mixtures such as HF/ H_2O_2 and HF/ O_3 [11]. It may be assumed that the decrease of the mono-hydride termination and simultaneous increase of the di-hydride termination by both DO and H_2O_2 mean a less homogeneous Si (111) surface termination such as the micro roughness. Although this learning on Si (111) surfaces cannot be easily transferred to the difference in SiGe-on-Si epi quality found on Si (100) surfaces for HF last processes using general or H_2O_2 removed UPW, the results suggest the difference could be due to a change in Si (100) surface morphology and/or a difference in Si (100) silica (i.e. watermark) formation when comparing general and H_2O_2 removed UPW.

Conclusion and future work

The SiGe epitaxial quality at 300 mm wafer scale has been improved by H_2O_2 removed UPW ($\text{H}_2\text{O}_2 < 1$ ppb) compared with general UPW which contains 8-10 ppb H_2O_2 . While a reproducible improvement in SiGe epitaxial quality was found when removing the residual H_2O_2 during the HF-last process, no change in interfacial O, nor the number of added defects $\geq 21\text{nm}$ LSE on Si (100) was found. ATR-FTIR measurements indicate an impact of dissolved oxygen and H_2O_2 on the Si (111) surface morphology. More work is needed to link the changes seen on Si (111) surfaces and the impact of water quality on SiGe-on-Si epi quality.

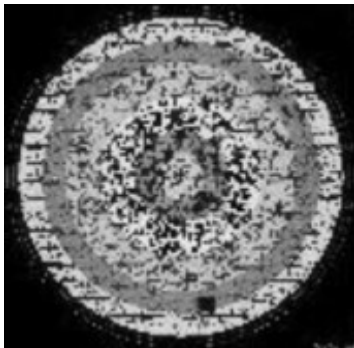


Figure 1: Hazeline image on the wafer by surface measurements after SiGe epitaxial growth. White area means a haze of the wafer surface.

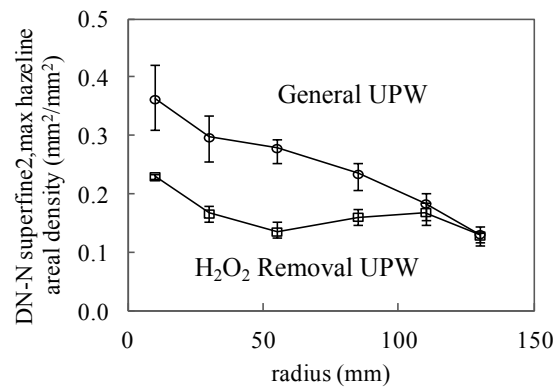


Figure 2: SiGe epi quality at radius distribution of the wafer.

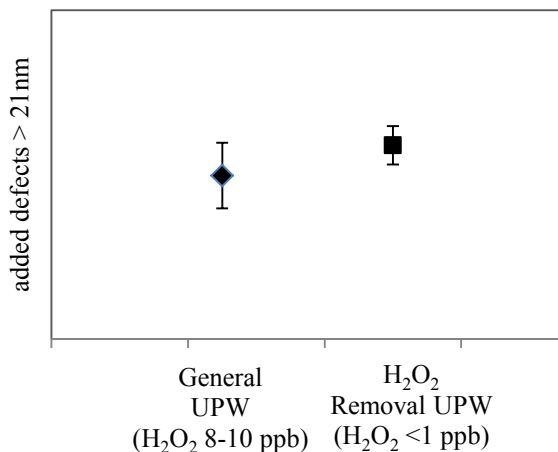


Figure 3: Defect adds up to 21 nm on Si (100) wafer after DHF process.

Table I. Interfacial O concentration (atoms/ cm^2) between the Si substrate and SiGe epitaxial layer as determined by SIMS.

	HF last	HF + GeH ₄ -HCl (600°C, 75s)
General UPW	10^{14}	$<10^{12}$
H_2O_2 -removed UPW	10^{14}	$<10^{12}$

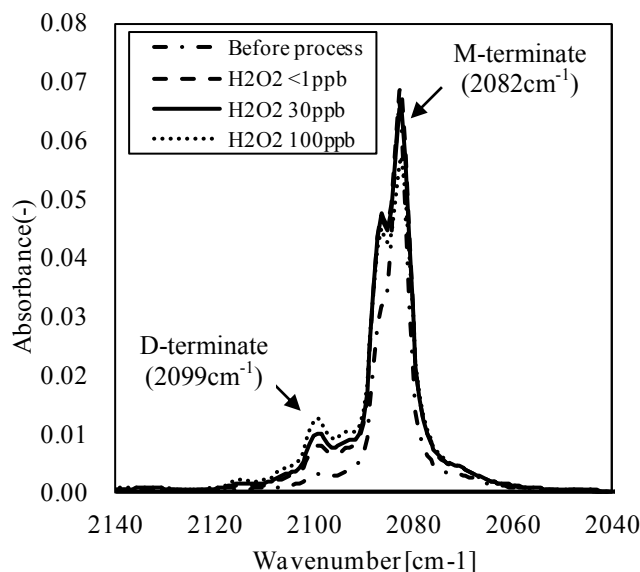


Figure 4: FT-IR-ATR spectra of Si (111) before and after processed by DHF with different H_2O_2 concentrations.

Table II: Peak absorbance of Mono-hydride and Di-hydride on Si (111) wafer after DHF process with different concentration of H_2O_2 .

	M-terminate (2082 cm^{-1})	D-terminate (2099 cm^{-1})	M/D ratio
Before process	0.0630	0.0029	21.5
H_2O_2 < 1ppb	0.0690	0.0080	8.64
H_2O_2 30ppb	0.0659	0.0101	6.55
H_2O_2 100ppb	0.0571	0.0125	4.58
H_2O_2 300ppb	0.0526	0.0125	4.20

References

- [1] Y. Miyazaki et al., "Advanced Hydrogen Peroxide Removal Technology Using Nano-sized Pt particle Catalyst Supported on Anion Exchange Resin", *ULTRAPURE WATER Micro conference 2013*
- [2] V. Libman et al., "UPW ITRS and SEMI: Synergy of Enabling Advanced Existing and Future Technologies", *ULTRAPURE WATER Micro conference 2015*
- [3] V. Libman et al., *ECS Transactions*, 69 (8), 17-28 (2015)
- [4] Y. Yoshida et al., *ECS Transactions*, 69(8), 29-35 (2015)
- [5] K. Sano et al., *Solid State Phenomena*, 145, 173-176 (2009)
- [6] Karen A. Reinhardt and Werner Kern, *Handbook of Silicon Wafer Cleaning Technology*, (2008)
- [7] K. Wostyn et al., *Solid State Phenomena*, 219, 20-23 (2015)
- [8] K. Wostyn et al., *ECS Transactions*, 64(6) 989-995 (2014)
- [9] Wang et al. *J. Electrochem. Soc.*, 143, 2387 (1996)
- [10] M.A. Hines, *Annu Rev Phys Chem.*, 54, 29-56 (2003)
- [11] Karen A. Reinhardt and Richard F.Reidy, *Handbook of cleaning for semiconductor manufacturing*, (2011)

Surface Passivation of New Channel Materials Utilizing Hydrogen Peroxide and Hydrazine Gas

Dan Alvarez, Jr.¹, Jeffrey J. Spiegelman^{1, a}, Andrew C. Kummel²,
Mary Edmonds², Kasra Sardashti², Steven Wolf², and Russell Holmes¹

¹ RASIRC Inc., San Diego, CA, USA

² University of California, San Diego

^ajeff@rasirc.com

Keywords: Hydrogen Peroxide, Hydrazine, InGaAs, SiGe, passivation, cleaning, surface preparation, In Situ passivation, Gas Phase surface preparation, self-limiting oxidation

Abstract. In situ gas phase passivation methods can enable new channel materials. Toward this end pure anhydrous HOOH and H₂NNH₂ membrane gas delivery methods were developed. Implementation led to Si-OH passivation of InGaAs(001) at 350C and Si-N-H passivation of SiGe(110) at 285C. XPS and initial electrical characterization has been carried out. Feasibility for in situ dry surface preparation and passivation was demonstrated.

Introduction

New in situ gas phase passivation methods can enable new channel materials that will allow better carrier confinement and mobility. These new methods will ideally provide one to three mono-layers of passivation material on multiple types of surfaces and crystallographic faces: InGa_{1-x}As, In_xGa_{1-x}Sb, In_xGa_{1-x}N, SiGe, and Ge. Si-OH and Si-N-H are leading passivation candidates, as they can provide barrier properties preventing metal migration as well as functionalization for subsequent deposition of High *k* materials. Our approach involves the use of a novel oxidant, anhydrous hydrogen peroxide HOOH(g) or a nitriding agent, in this case hydrazine H₂NNH₂(g), to create terminating Si-OH or Si-NH layers available for additional functionalization.

Challenges

Though theoretically appealing, an early problem encountered in this approach was the lack of vaporization sources for pure anhydrous HOOH and H₂NNH₂ gases. Hydrogen peroxide (HOOH)/Water (H₂O) mixtures in liquid form are generally used in semiconductor manufacturing for cleaning and surface preparation. Thirty percent and fifty percent two-component liquid sources for gas phase mixtures have been investigated in a few studies with moderate success [1,2]. Especially noteworthy are Kummel's findings that the use of hydrogen peroxide leads to a 3x increase in oxygen surface density on Ge versus water [3].

Membrane Technology

In practice H₂O₂/H₂O mixtures have found limited utility in the gas phase due to process problems attributed to the presence of water. Ideally anhydrous hydrogen peroxide liquid would be used as the source, however it is highly unstable and potentially explosive due to its propensity to decompose rapidly when not buffered with water. Our approach entails the use of a membrane delivery system where 99.6% hydrogen peroxide is dissolved in an organic solvent (Figure 1a). Hydrogen peroxide gas permeates the membrane and is delivered to the process chamber, while the solvent does not permeate and remains in the liquid state.

Next generation devices have low thermal process constraints. Hydrazine (H₂NNH₂) is highly reactive and appears to be the ideal low temperature nitrogen passivation source. However, it is highly flammable, toxic and current commercial materials lack sufficient purity. In an analogous approach to hydrogen peroxide, we have developed a new method and formulation for the delivery

of anhydrous hydrazine by the use of an inert organic solvent and membrane delivery system (Figure 1b). Precursor vapor pressure is maintained at levels viable for current passivation process requirements. Moreover, the addition of a high boiling point solvent raises the solution flash point, reducing explosive risk.

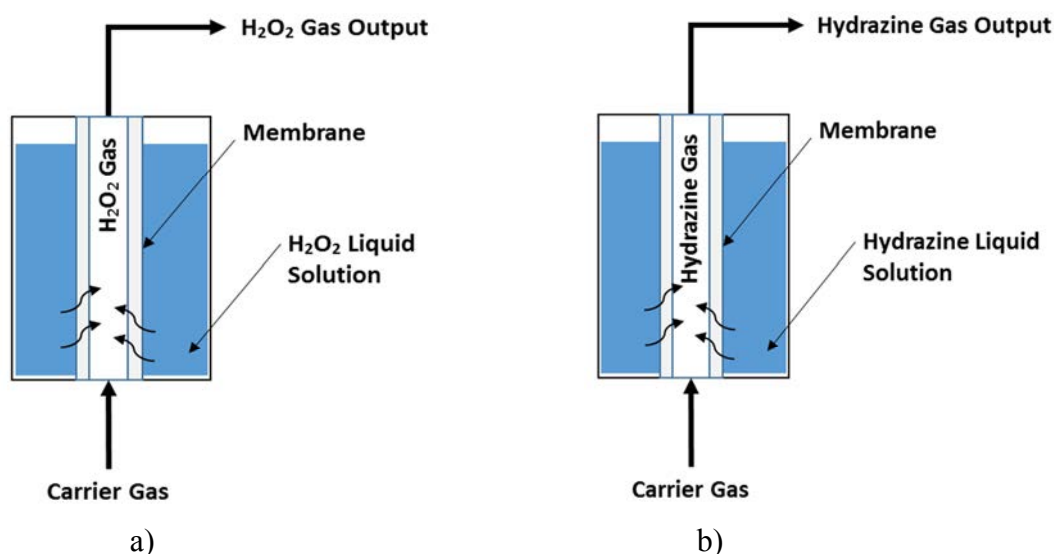


Figure 1. Novel Precursor Membrane Delivery System for a) anhydrous hydrogen peroxide (H_2O_2) and b) anhydrous hydrazine (H_2NNH_2).

Passivation Methods

Implementation of our novel sources focused on the passivation of InGaAs(001) and SiGe(110) surfaces.

A saturated Si-OH passivation layer was deposited on InGaAs(001)-(2x4) at a substrate temperature of 350°C. XPS in combination with STS/STM were employed to characterize the electrical and surface properties of the saturated Si-OH layer on InGaAs(001)-(2x4). Oxidation by anhydrous hydrogen peroxide is self-limiting where underlying substrate damage is avoided. In contrast, oxidation with the use of $\text{HOOH}/\text{H}_2\text{O}$ gas mixtures shows oxidation of Indium with the resulting formation of Indium oxide.

The 350°C self-limiting surface passivation procedure included a decapped $\text{In}_{0.53}\text{Ga}_{0.47}\text{As}(001)-(2 \times 4)$ surface dosed with total 87.6 MegaLangmuir Si_2Cl_6 followed by 210.55 MegaLangmuir total anhydrous $\text{HOOH}(\text{g})$. Complete surface saturation of Si-O_x on InGaAs(001)-(2x4) was determined to occur once no further increase in the O 1s peak was seen with additional anhydrous $\text{HOOH}(\text{g})$ doses (Figure 2).

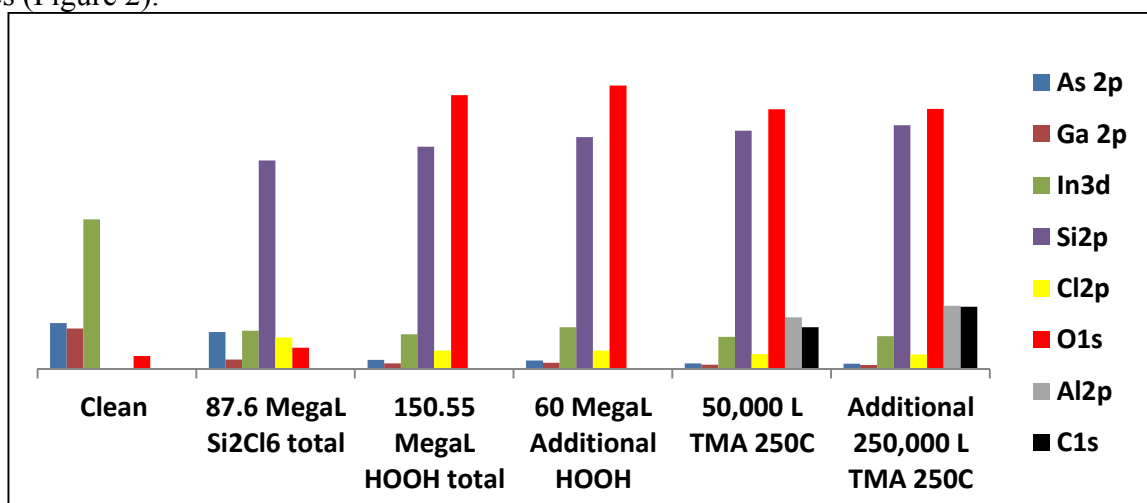


Figure 2. XPS characterization of the InGaAs(001) passivation study.

Following Si-OH surface saturation, 300,000 L TMA was dosed at 250°C, and XPS showed the emergence of Al 2p and C 1s peaks indicative of TMA surface nucleation. The surface was then dosed with 500 L atomic H at 250°C to replace the methyl groups on the surface aluminum with -H termination as well as remove any residual chlorine left on the surface. STS (Figure 3) shows that after hydrogen peroxide exposure, the surface Fermi level shifts toward the valence band due to the surface induced dipole from the presence of -OH and -O- groups. Subsequently, after capping with Aluminum, the surface Fermi level shifts back toward the conduction band.

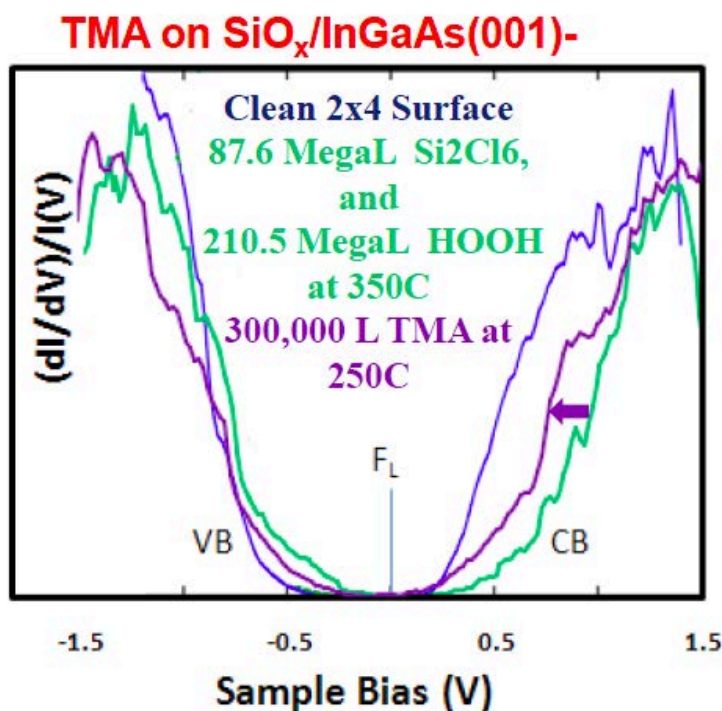


Figure 3. STS of a) Clean InGaAs(001) surface(blue), b) Shift toward the valence band due to the surface induced dipole after HOOH exposure, c) Shift back toward the conduction band after capping with TMA.

Figure 4 shows the XPS results from a similar experiment performed with aqueous 30% $\text{H}_2\text{O}_2/\text{H}_2\text{O}$ vapor. Here, the appearance of a large InO_x peak is observed after exposure to hydrogen peroxide. In this case, it is evident that sub-surface oxidation has occurred and InO_x has migrated to the surface. Therefore, while the use of anhydrous hydrogen peroxide leads to self-limiting surface oxidation, the presence of water is a detriment and damages the surface.

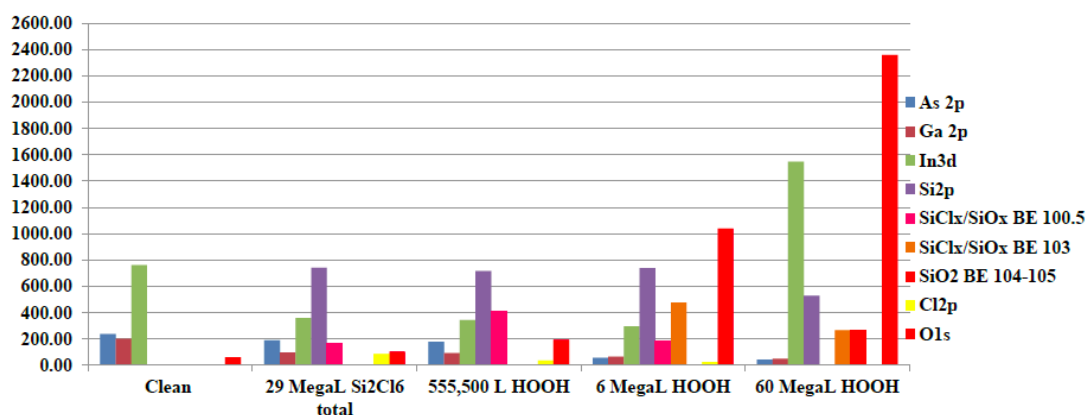


Figure 4. XPS of a $\text{Cl}_x\text{Si}/\text{InGaAs}(001)$ surface treated with 30% $\text{H}_2\text{O}_2/\text{H}_2\text{O}$. Indium migrates to the surface and forms InO_x .

The next part of our study focused on developing a low temperature silicon nitride passivation process for SiGe substrates. A silicon nitride passivation layer on semiconductor surfaces can serve several practical uses, such as acting as a diffusion barrier or channel passivation layer prior to dielectric deposition in FinFets or MOSFETs. When employed as a channel passivation layer, further reaction with an oxidant, such as anhydrous hydrogen peroxide, can leave Si-N-OH termination, which allows for further functionalization. STM/STS and XPS were employed to characterize SiN_x film growth on Si_{0.5}Ge_{0.5}(110).

The silicon nitride passivation procedure was carried out at a substrate temperature of 275°C and was performed on a p-type Si_{0.5}Ge_{0.5}(110) surface (Figure 5). After a 315 MegaLangmuir anhydrous hydrazine dose, XPS showed N-H_x surface termination, and removal of half of the initial carbon contamination. A subsequent 21 MegaLangmuir Si₂Cl₆ dose followed by 17 cycles of 3 MegaLangmuir hydrazine and 3 MegaLangmuir Si₂Cl₆ led to increased silicon nitride growth as shown by a large increase in XPS Si 2p and N 1s peaks, as well as a decrease in the Ge 3d substrate peak. STS of the atomic hydrogen cleaned surface (Figure 6) shows that the surface Fermi level is pinned at the midgap, the SiN_x on SiGe(110) looks slightly more p-type with a bandgap size of 0.8-0.9 eV.

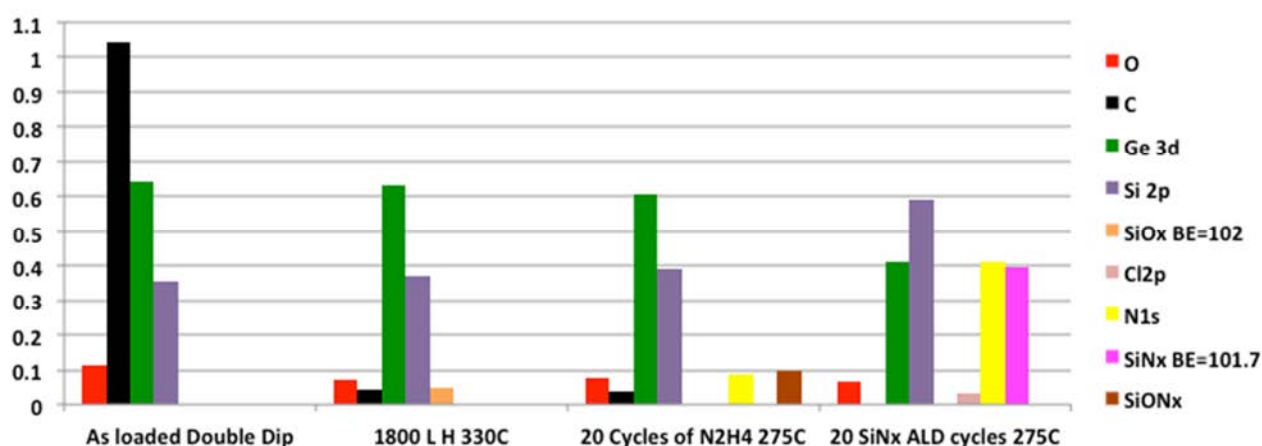


Figure 5. XPS characterization of the SiGe(110) passivation study.

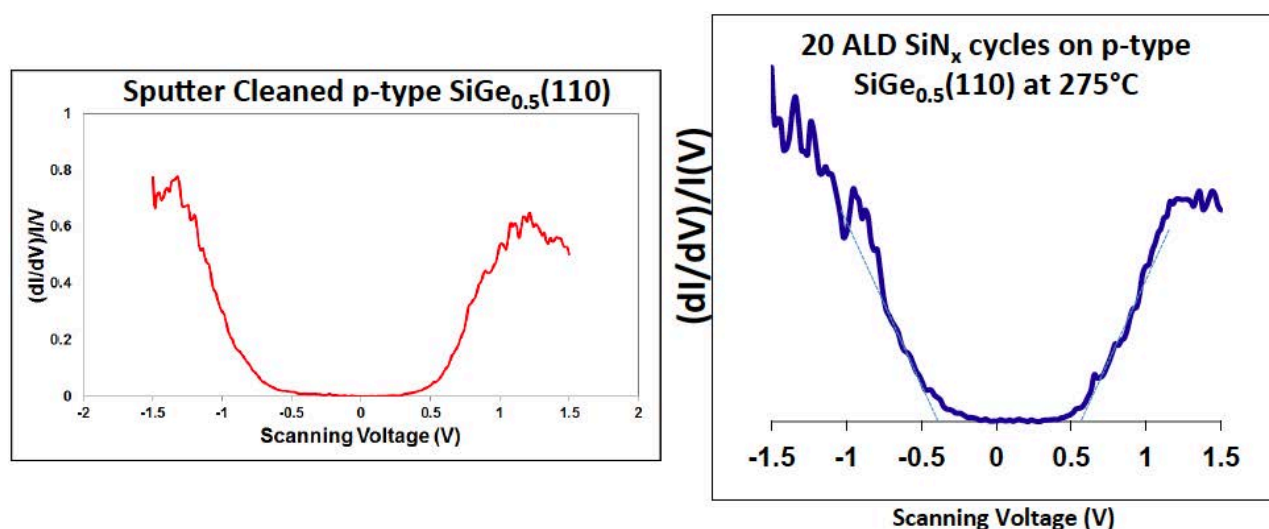


Figure 6. XPS of Cleaned Surface and SiN_x surface.

Conclusion

In conclusion, the in situ dry cleaning and passivation requirements of future generation materials have made obvious the need for new gaseous passivation sources. We have demonstrated the ability to deliver anhydrous hydrogen peroxide and hydrazine with novel membrane delivery methods. Feasibility for in situ dry surface preparation and passivation has been demonstrated by the deposition of very thin layers of Si-OH and Si-NH without sub-surface damage.

References

- [1] B. B. Burton, S. W. Kang, S. W. Rhee and S. M. George, *J. Phys. Chem. C*, 113(19), 82490–8257 (2009).
- [2] M. J. Choi, H. H. Park, D. S. Jeong, J. H. Kim, J. S. Kim and S. K. Kim, *Appl. Surf. Sci.*, **301**, 451-455 (2014).
- [3] T. Kaufman-Osborn, E. A. Chagarov and A. C. Kummel, *J. Chem. Phys.*, **140**, 204708 (2014).

Tris(Trimethylsilyl)Germane ($(\text{Me}_3\text{Si})_3\text{GeH}$): A Molecular Model for Sulfur Passivation of Ge(111) Surfaces

Gilbert Okorn ^{1,a}, Roland Fischer ¹, Beate Steller ¹, Philipp Engesser ²
and Harald Okorn-Schmidt ²

¹ Institute for Inorganic Chemistry, Graz University of Technology, Stremayrgasse 9/V, A-8010
Graz, Austria

² LLRC OG, Gerlitzengeweg 10, A-9020 Klagenfurt, Austria

^a gilbert.okorn@student.tugraz.at

Keywords: germanium, sulfur, surface passivation, kinetics, activation parameters, NMR spectroscopy, molecular model

Abstract. Tris(trimethylsilyl)germane, $(\text{Me}_3\text{Si})_3\text{GeH}$, was employed as a molecular model compound for hydrogen terminated Ge(111) surfaces. Time and temperature dependent NMR spectroscopy yielded rate constants for the reaction between $(\text{Me}_3\text{Si})_3\text{GeH}$ and elemental sulfur and allowed for the determination of the activation energy for this molecular model reaction to mimic germanium surface passivation.

Introduction

Since a few years, germanium is encountering a renewed interest as semiconducting material for highly integrated circuits due to its superior conductivity compared to silicon. Unlike silicon, where the formation of a dense native oxide prevents further oxidation at ambient conditions, germanium is significantly more sensitive towards environmental reactions. Moreover, native germanium oxide layers are hydrolytically labile. Nevertheless, germanium forms dense and relatively inert sulfide layers, hence surface passivation via sulfide layer formation is being studied including process avenues through wet chemical treatment of germanium wafers. [1] Such wet chemical protocols include the processing with e.g. ammonium sulfide as sulfur source. [2] Although relatively stable surface passivation layers can be obtained by this or similar wet chemical reactions, the careful control of process parameters proves of utmost importance to ensure homogeneous protection and to avoid surface particle contamination by formation and deposition of elemental sulfur. Despite the extensive exploration of sulfur based wet chemical surface passivation processes, the actual mechanism, reaction kinetics and activation parameters of the rate determining step remain largely unknown. In this context, we investigated the reaction of tris(trimethylsilyl)germane, $(\text{Me}_3\text{Si})_3\text{GeH}$, as a molecular model compound for a hydrogen terminated germanium(111) surface with elemental sulfur. [3]

Results and Discussion

Treatment of hydrogen terminated germanium surfaces with various sulfur sources constitutes the method of choice for wet chemical surface passivation. Despite intensive investigations, details about the mechanism, the actual chemically active species, reaction kinetics and activation energies remain largely undisclosed.

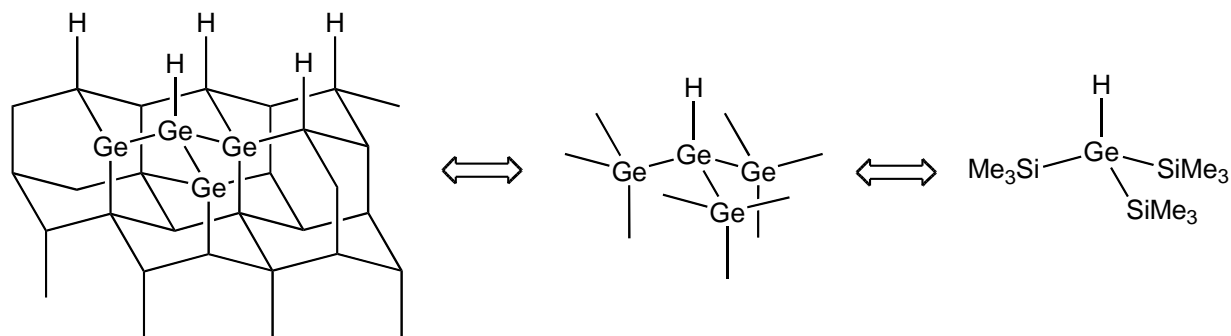


Figure 1. Tris(trimethylsilyl)germane as a model compound for surface reactions on Ge(111).

As surface reactions are difficult to assess directly, we set out to investigate the reaction of tris(trimethylsilyl)germane [4], $(\text{Me}_3\text{Si})_3\text{GeH}$, **1**, towards sulfur reagents by means of heteronuclear NMR spectroscopy and use it as a molecular model substance for a hydrogen terminated Ge(111) surface. (c.f. Figure 1)

In our model compound, the germanium atoms attached to the central Ge-H functionality have been replaced by trimethylsilyl groups as the Me_3Si -groups provide the rather unique opportunity to simultaneously study three different NMR active nuclei (^1H , ^{13}C , ^{29}Si) but have nearly no impact on the chemical reactivity of the Ge-H functionality when compared to $(\text{Me}_3\text{Ge})_3\text{GeH}$ [5,6]. In initial attempts to assess the reactivity of $(\text{Me}_3\text{Si})_3\text{GeH}$ against sulfur sources, solutions of tris(trimethylsilyl)germane in aliphatic and aromatic hydrocarbon solutions, ethers etc. were treated with excess of thoroughly degassed aqueous solutions of ammoniumsulfide, $(\text{NH}_4)_2\text{S}$. When two-phase mixtures were formed, the reaction mixtures were vigorously agitated for extended periods (up to 12 hours) to ensure potential phase transfer. However, no conversion of **1** was observed in any case. We therefore exclude a nucleophilic substitution reaction at germanium by sulfide ions. Exposure of the reaction mixtures to air, addition of hydrogen peroxide or organic peroxides, however, resulted in the formation of tris(trimethylsilyl)germathiol, **2**, and formation of the respective germanol $(\text{Me}_3\text{Si})_3\text{GeOH}$. Treatment of $(\text{Me}_3\text{Si})_3\text{GeH}$ with peroxides in the absence of sulfur sources also leads to $(\text{Me}_3\text{Si})_3\text{GeOH}$ but results furthermore in oxygen insertion into the Ge-SiMe₃ bonds.

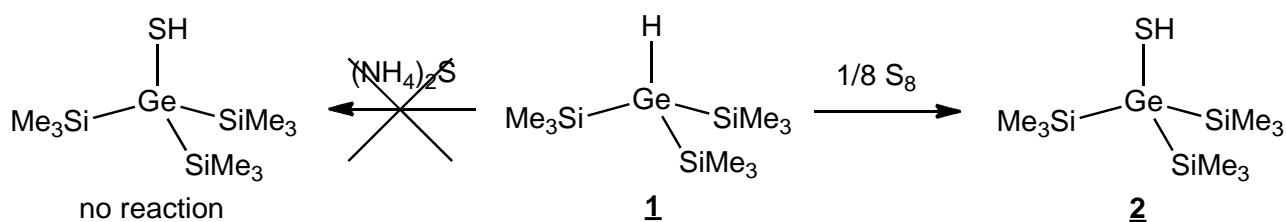


Figure 2. $(\text{Me}_3\text{Si})_3\text{GeH}$ reacts with sulfur to give $(\text{Me}_3\text{Si})_3\text{GeSH}$ but is inert towards $(\text{NH}_4)_2\text{S}$.

Similarly, treatment of aqueous $(\text{NH}_4)_2\text{S}$ solutions with hydrogen peroxide followed by addition of **1** in organic solutions and mixing the layers has similarly led to $(\text{Me}_3\text{Si})_3\text{GeSH}$. The stepwise procedure was found to be superior as the formation of oxygen containing side products was then significantly reduced. [7] We therefore concluded a radical type reaction between $(\text{Me}_3\text{Si})_3\text{GeH}$ and sulfur as the actual chemically active species. Consequently, the reaction between **1** and elemental sulfur in polar and non-polar organic solvents was investigated, where only in the case of non-polar solvents significant conversion was achieved. NMR spectroscopic investigations revealed the direct formation of $(\text{Me}_3\text{Si})_3\text{GeSH}$ from **1** at rates suitable for kinetic measurements and base line separation in ^{29}Si NMR spectra allowed for signal integration. Interestingly, $(\text{Me}_3\text{Si})_3\text{GeSH}$ is surprisingly stable towards hydrolysis in solution and attempts to oxidize **2** to yield the respective disulfide $(\text{Me}_3\text{Si})_3\text{GeSSGe}(\text{SiMe}_3)_3$ or to synthesize the sulfide $(\text{Me}_3\text{Si})_3\text{GeSGe}(\text{SiMe}_3)_3$ remained fruitless so far, which is unexpected as bridging sulfide are employed in standard surface passivation models. [3]

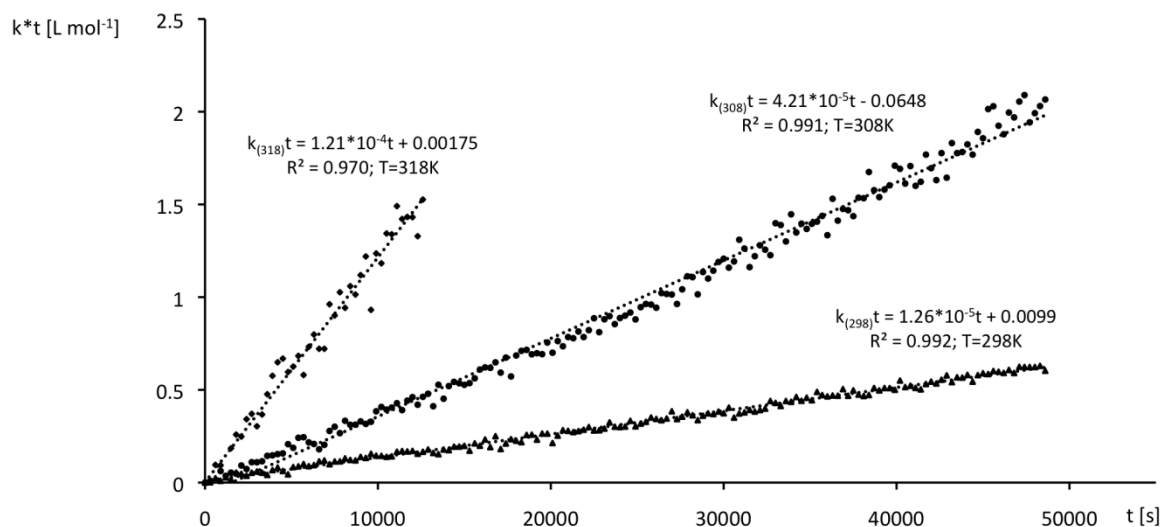


Figure 3. Plot of kt against t for samples 1-3.

In order to follow the formation of **2** under concurrent consumption of **1**, NMR samples of **1** in 2.20 weight percent solutions of elemental sulfur in benzene- d_6 were prepared and ^{29}Si NMR spectra were recorded at 5 minute intervals for up to 14 hours. From these, the rate of conversion from **1** to **2** was determined via peak integration. Evaluation of the rate constants following an overall 2nd order rate law, and first order with respect to **1** and sulfur, yielded rate constants of $1.26 \times 10^{-5} \text{ L mol}^{-1} \text{ s}^{-1}$ (298K), $4.21 \times 10^{-5} \text{ L mol}^{-1} \text{ s}^{-1}$ (308K) and $1.21 \times 10^{-4} \text{ L mol}^{-1} \text{ s}^{-1}$ (318K).

$$\frac{d[(\text{Me}_3\text{Si})_3\text{GeSH}]}{dt} = -k[(\text{Me}_3\text{Si})_3\text{GeH}][\text{S}] \quad (1.a)$$

$$\square \quad kt = \frac{1}{[\text{S}]_0 - [(\text{Me}_3\text{Si})_3\text{GeH}]_0} \ln \left[\frac{[(\text{Me}_3\text{Si})_3\text{GeH}]_0 / [(\text{Me}_3\text{Si})_3\text{GeH}]_t}{[\text{S}]_t / [\text{S}]_0} \right] \quad (1.b)$$

Equation 1. Assumed differential (a) and integrated (b) rate laws used to extract rate constants.

Based on thus extracted rate constants at 298, 308 and 318 K, the Eyring activation parameters for the conversion of **1** with sulfur have been derived. For details c.f. Table 1.

Table 1. Kinetic data for the conversion of $(\text{Me}_3\text{Si})_3\text{GeH}$ with sulfur in benzene- d_6

	Sample 1	Sample 2	Sample 3	Sample 4
Temp. [K]	298	308	318	318
$[(\text{Me}_3\text{Si})_3\text{GeH}]_0 [\text{mmol mL}^{-1}]$	0.515	0.454	0.290	0.368
$[\text{S}]_0 [\text{mmol mL}^{-1}]$	0.440	0.431	0.283	0.075
$k [\text{L mol}^{-1} \text{ s}^{-1}]$	$1.26(2) \times 10^{-5}$	$4.21(6) \times 10^{-5}$	$1.21(7) \times 10^{-4}$	$1.48(5) \times 10^{-4}$
$\Delta H^\ddagger [\text{kJ mol}^{-1}]$	86.9			
$\Delta S^\ddagger [\text{J mol}^{-1} \text{ K}^{-1}]$	-47			

The rate law according to equation 1 is further corroborated by comparison of samples 3 and 4, where the initial sulfur concentration in 3 was reduced to 25% in 4, yet to leave the rate constant almost unaltered within the experimental accuracy. From the temperature dependence of the rate constants the activation parameters have been estimated employing Eyring theory (c.f. the Eyring plot in Figure 4). According to figure 5, the enthalpy of activation accounts to 86.9 kJ/mol which is in good agreement with other radical reactions involving **1**. The entropy of activation amounts to a moderately negative value of $-47 \text{ J mol}^{-1} \text{ K}^{-1}$, which is again in fair agreement with an associative,

bimolecular, mechanism leading to a lower overall entropy due to formation of a di-nuclear activated complex where tris(trimethylsilyl)germane and sulfur participate in the rate determining step.

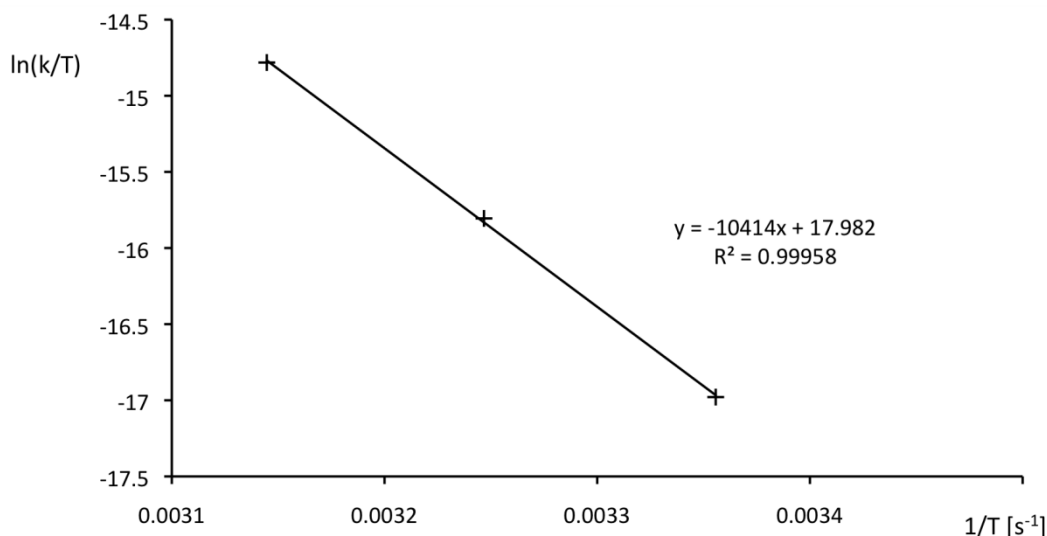


Figure 4. Eyring Plot for the reaction of $(Me_3Si)_3GeH$ with sulfur.

Experimental

Tetrakis(trimethylsilyl)germane [8] and tris(trimethylsilyl)germane [4] were synthesized following reported procedures. Sulfur and aqueous ammoniumsulfide were obtained from Sigma Aldrich. Aqueous $(NH_4)_2S$ was used as received, sulfur was recrystallized from hot toluene. Deuterated solvents were purchased from Deutero GmbH. Unless otherwise stated, all solvents were dried and degassed prior to use. All manipulations were carried out using standard Schlenk techniques, NMR sample preparation was accomplished in a nitrogen filled glove box (MBraun UniLab). NMR spectra were recorded on a Varian Mercury 300 MHz spectrometer (1H 300.23 MHz, ^{13}C 75.50 MHz, ^{29}Si 59.64 MHz). All spectra are referenced to solvent residual peaks of the deuterated solvent. ^{29}Si spectra were recorded using the 1D DEPT sequence [9] with polarization transfer delays optimized for Me_3Si groups. Prior to the experiments, temperature calibration was performed using Varian ethylene glycol standard samples.

In a typical experiment 110 mg (0.375 mmol) of tris(trimethylsilyl)germane were added to a saturated solution (500 μ l; 2.20 weight percent of sulfur as determined gravimetrically, 0.302 mmol) of elemental sulfur in dry, degassed benzene- d_6 and placed in a screw cap NMR tube. Immediately after mixing of the compounds, the array of NMR spectra was recorded at the temperatures given in the text.

To ensure sufficient mixing of the organic and aqueous layer, reactions between tris(trimethylsilyl)germane (110 mg dissolved in 500 μ l of benzene- d_6) and aqueous ammonium sulfide were vigorously stirred with a magnetic stir bar and, after phase separation, were monitored NMR spectroscopically after intervals of 1 hour. No reaction progress, however, was observed in the absence of oxygen or other oxidizing agents. When the reaction was carried out in air, however, slow transformation of tris(trimethylsilyl)germane into tris(trimethylsilyl)germane thiol $(Me_3Si)_3GeSH$ was observed, but was accompanied by partial oxidation of Si-Ge bonds to yield the siloxane specie $(Me_3SiO)_n(Me_3Si)_{3-n}GeEH$ ($E=O, S$).

Attempts to oxidize $(Me_3Si)_3GeSH$ with air, aqueous hydrogen peroxide and mCPBA (meta chloro perbenzoic acid) to yield the disulfide $[(Me_3Si)_3GeS]_2$ remained unsuccessful. To test the hydrolytic stability of $(Me_3Si)_3GeSH$, water and THF were added to solutions of $(Me_3Si)_3GeSH$ in benzene- d_6 to ensure phase homogeneity. No hydrolysis products, however, were observed NMR spectroscopically within 1 week.

Summary

Tris(trimethylsilyl)germane was investigated as a molecular model for the surface passivation of hydrogen terminated germanium(111). Temperature dependent NMR spectroscopic investigations provided detailed kinetic information and indicate a reaction between elemental sulfur and Ge-H groups as the key step in wet chemical passivation of germanium with sulfur groups. The activation parameters for the respective solution based reaction have been determined and are expected to be transferable to technologically relevant surface reactions.

References

- [1] C. Claeys, E. Simonen, Eds., *Germanium Based Technologies: From Materials to Devices* (Elsevier, Oxford, 2007)
- [2] J. Buriak, Chem. Rev., 102 (2002), p, 1271.
- [3] D. Lee, K. Kubo, T. Kanashima, M. Okuyama, Jap. J. App. Phys., 51 (2012), 04DA06.
- [4] J. Fischer, J. Baumgartner, C. Marschner, Organometallics, 24 (2005) p. 1263.
- [5] C. Chatgililoglu, M. Ballestri, J. Escudié, I. Pailhous, Organometallics, 18 (1999) p.2395.
- [6] a) M. B. Taraban, O. S. Volkova, A. I. Kruppa, T. V. Leshina Radical Reaction Mechanisms of and at Organic Germanium, Tin and Lead, p 580-631 b) M. W. Carland, C. H. Schiesser *Synthetic Uses of R_3MH ($M=Ge, Sn, Pb$)*, p 1401-1483 in: *The Chemistry of Organic of Germanium, Tin and Lead Compounds II* (Z. Rappoport, Ed.) (Wiley, Chichester, 2001).
- [7] J. Lalevée, N. Blanchard, B. Graff, X. Allonas, J. P. Fouassier, J. Organomet. Chem., 693 (2008) p. 3643.
- [8] A. G. Brook, F. Abdesaken, H. Söllradl, J. Organomet. Chem. 299 (1986) p. 9.
- [9] D. M. Doddrell, D. T. Pegg, M. R. Bendall, J. Magn. Reson., 48 (1982) p.323.

Applications for Surface Engineering using Atomic Layer Etching

John Papalia, Nathan Marchack, Robert Bruce,
Hiroyuki Miyazoe, Sebastian Engelmann, and Eric A. Joseph^a

¹ IBM T.J. Watson Research Center, Yorktown Heights, NY, USA

^a ejoseph@us.ibm.com

Invited paper, previously published in SPIE 9782, Advanced Etch Technology for Nanopatterning V, 97820H (2016)

Keywords: Selectivities, atomic layer etch, pattern transfer, discharge chemistry, high aspect ratio patterning

Abstract. Over the course of the past few years, the semiconductor industry has continued to invent and innovate profoundly to adhere to Moore's Law and Dennard scaling. At each of the technology nodes starting with 45nm, new materials and integration techniques, such as high-K & metal gates, double patterning techniques, and now 3D FinFet / Trigate device geometries are being introduced in order to maintain device performance. This places a large burden on unit process development to accommodate and deliver advanced process capability and is growing the need for the ultimate etch solution: etching with atomic layer precision. Atomic layer etching is a promising path to answer the processing demands of thin high mobility channel devices on the angstrom scale. Self-limiting reactions, discrete reaction & activation steps, or extremely low ion energy etch plasmas are some of the pathways being pursued for precise sub-nanometer material removal. In this invited paper, previously published in SPIE, the ability to achieve atomic layer etch precision is reviewed in detail for a variety of material sets and implementation methods.[1] For a cyclic approach most similar to a reverse ALD scheme, the process window to achieve a truly self-limited atomic layer etch process is identified and the limitations as a function of controlling the adsorption step, the irradiation energy, and the reaction process are examined. Alternative approaches, including processes to enable pseudo-ALE precision, are then introduced and results from their application investigated. While these new plasma-enhanced atomic layer etch (PE-ALE) processes show encouraging results, most patterning applications are best realized by optimizations through discharge chemistry and/or plasma parameters. Significant improvements however were obtained when applying PE-ALE approaches to small pitch patterns. In particular the increased selectivity to OPL seems to offer a potential benefit for patterning high aspect ratio features.

Introduction

Atomic Layer Deposition (ALD) has been widely accepted as a technique to overcome deposition challenges for high aspect ratio features.[2] A complementary etching technique has not, until recently, been established.[3] While potential benefits of atomic layer etch processes have been formulated,[4,5] a clear approach to reaching those benefits had not been identified. Currently, various approaches including thermal, wet chemical, and plasma based process techniques are all under investigation to enable atomic scale etch precision for advanced technology nodes. [5,6,7,8] For one particular plasma enhanced Atomic layer etching technique (PE-ALE), competing deposition and etch processes commonly found in fluorocarbon plasma processes are separated in time. This was first demonstrated by Metzler et al.[9] and has also been evaluated for device patterning.[10] An inert plasma is maintained at all time, while alternating cycles of a precursor pulse and an etch step with increased ion energy are applied to the wafer. While this approach does not offer atomic layer control in the deposition cycle, the following etch cycle offers high enough selectivity to the original substrate to show self-limiting behavior. As such, a quasi- or pseudo-ALE approach has been established and the potential benefits on device processing have been reported.[11] The impact of PE-ALE on patterning applications however, has not been fully

examined. Hence, the ability to simultaneously pattern multiple materials was investigated in this work. We also investigated the performance of PE-ALE during standard trilayer patterning processes at varying pitch sizes.

Experimental

We used conventional inductively coupled plasma (ICP) sources that are able to operate the plasma and gas injection in the desired cyclic operation. Source power (W_s), bias power (W_b), substrate temperature, and processing times were varied to investigate the process parameter space. Process development was executed based on scanning electron microscopy (SEM) analysis of etch features post process. No in-situ characterization was possible due to operational limitations.

The experimental structures used consisted of patterns defined by a 193nm lithography process for 200 nm and 400 nm pitch features and e-beam lithography for small pitch features (<50 nm line/space pitch). LER/LWR analysis has been performed using Summit.

Cyclic operation of the plasma will be referred to as PE-ALE, whereas the conventional continuous wave operation (all gases in parallel) is referred to as CW.

Results and Discussion

Exploration of PE-ALE process space for patterning. Due to the cyclic nature of the (PE-)ALE process, there is a larger parameter space than one would typically have with a CW etch process. Our typical PE-ALE recipes involve a four-step process: passivate, purge, etch, purge. Initial work on the impact of etch step time, substrate temperature and the effect of profile feature has been previously reported.[10] Springboarding from these initial findings, using C_4F_8 as precursor gas, we optimized our process further by reducing the reactor volume and also the precursor chemistry. We were able to use these processes to demonstrate a successful etch stop on SiN, as shown in Figure 1. While we are able to characterize the physical morphology of these etch processes, our chemical analysis and evaluation is hampered by the lack of in-situ characterization.

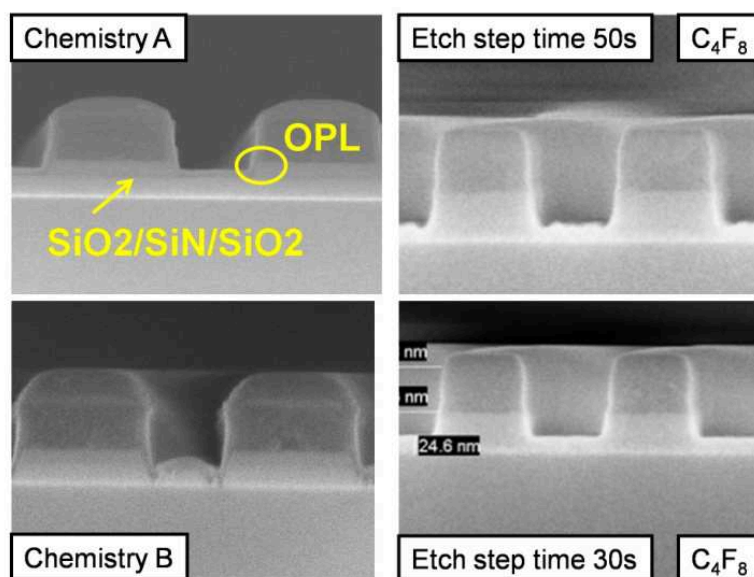


Figure 1: PE-ALE impact of gas chemistry.

The process of Chemistry A was further investigated by wafer uniformity measurements. Figure 2 shows the measured selectivities and uniformities of the PE-ALE process and its corresponding CW processes. While we can see excellent selectivity of the PE-ALE process to OPL, only moderate selectivity to SiN was found. Additionally, we measure very good uniformity across wafer. When operating in CW mode, we noted a complete loss of selectivities as well as a significant increase in uniformity (CW, low bias). When an increase in bias power is applied, we achieve a significant improvement of selectivities. In no case was good selectivity to TiN observed.

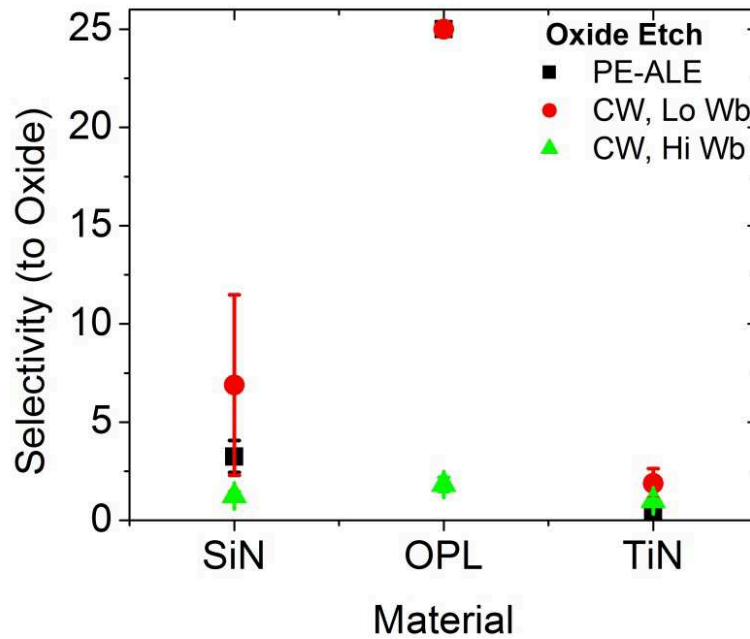


Figure 2: Selectivities for oxide etch of chemistry A in PE-ALE and CW modes.

An opposite approach was undertaken for Nitride etching (Figure 3). An existing CW process that demonstrates moderate selectivity was converted to a PE-ALE for comparison.

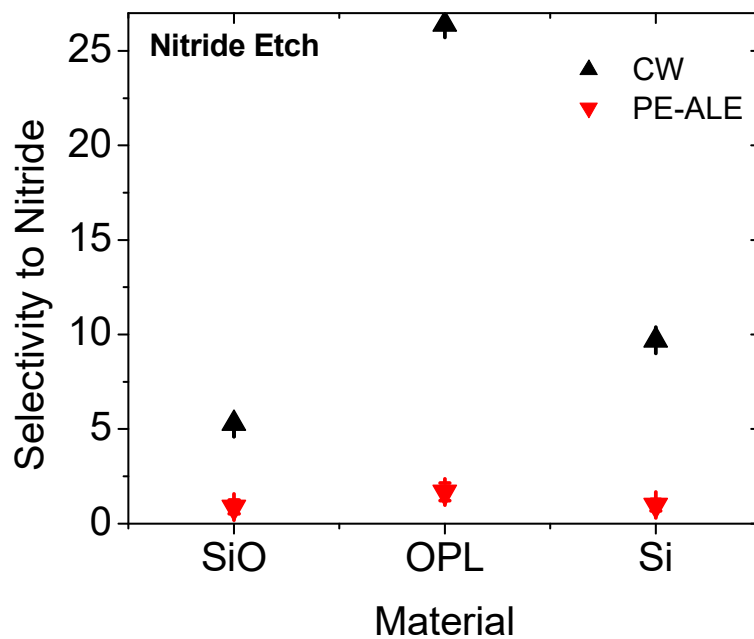


Figure 3: Selectivities for nitride etch in PE-ALE and CW modes.

As we can see in Figure 3, no selectivity can be obtained by simply applying a cyclic process methodology to a selective CW process. Instead, in-situ optimization of deposition and etch fluxes is necessary to improve the ease of application to patterning processes.

Multi-Color Selectivity. In both cases studied, oxide as well as nitride etching, the most promising approach for multi-color patterning was enabled through optimization of the chemistry in addition to optimization of the other plasma parameters. For the patterning of oxide materials, further optimization of the discharge chemistry based on results reported in Figure 2 was explored (Figure 4). While excellent selectivity to OPL material was observed in both cases, a further selectivity increase to SiN materials was observed by discharge chemistry optimization. In the same manner,

an optimization of the process selectivities based on the data reported in Figure 3 was also executed (Figure 5). Chemistry C (Figure 5) was chosen as ideal chemistry to pattern nitride materials.

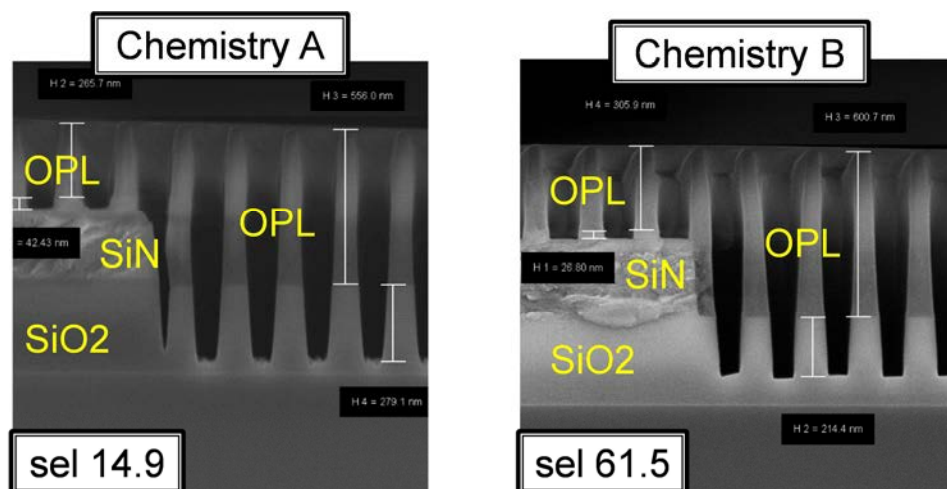


Figure 4: Selectivities for oxide etch by optimizing discharge chemistry.

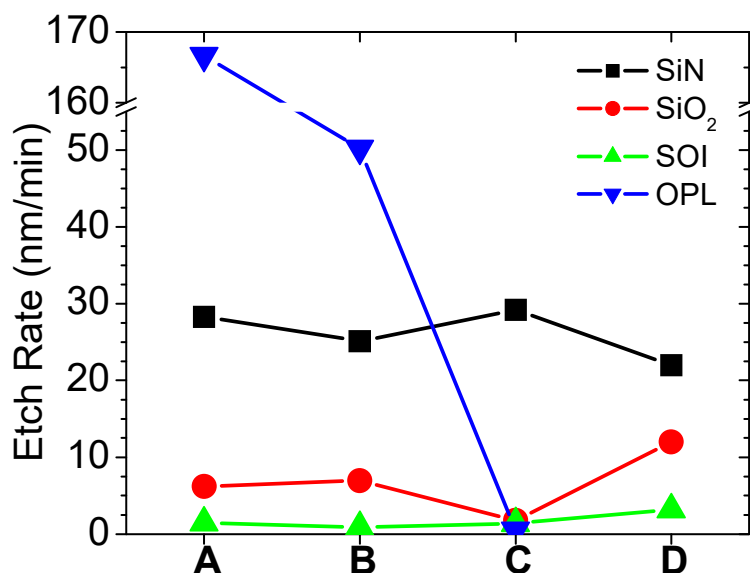


Figure 5: Etch rates for nitride etch by optimizing discharge chemistry. Chemistries A through D each represent a different hydrofluorocarbon utilized.

Critical dimensions of SiARC as observed under precursor chemistry changes. When working through a multistep etch process, it can be difficult to specifically attribute at which point Critical Dimension (CD), Line Width Roughness (LWR), and Line Edge Roughness (LER) begin to drift away from the ideal. This work has explored a typical stack of SiARC, PR, OPL and Material X on Si, where material X may be TiN, TEOS, SiN, or any of a number of other materials. We explored both CW and PE-ALE processes with specific focus on their effect on SiARC CD, LWR, and LER values.

The CW process, which utilizes CF₄/CHF₃ chemistry, is our baseline. This baseline demonstrates an immediate and obvious decrease in all three critical values after processing (SiARC etch). The PE-ALE processes tested utilized a direct substitution for the precursor chemistry with no further attempts at optimization. Overall, the LWR/LER increased, regardless of which chemistry was applied (Figure 6). One possible explanation for this increase is that the vacuum ultraviolet (VUV) of the background inert plasma maintained throughout the entire process may play a crucial role in these processes.

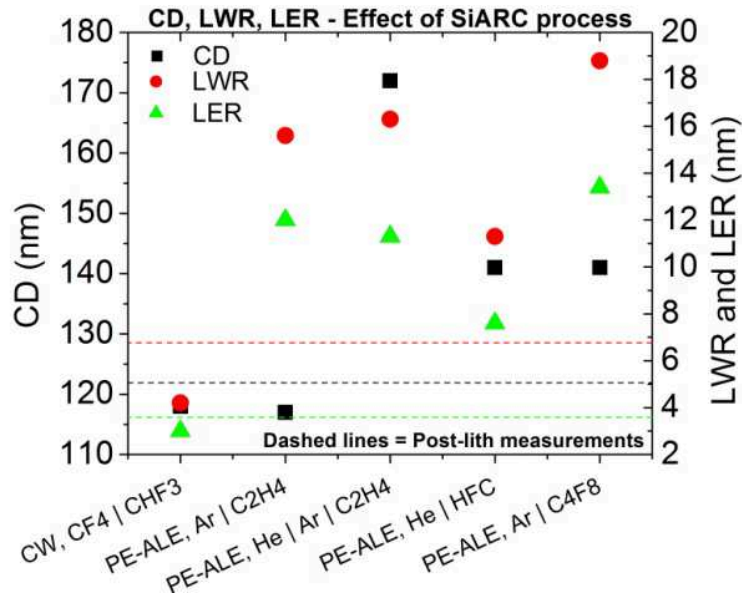


Figure 6: Variation of CD, LWR and LER of 200nm pitch features during the SiARC etch step, across multiple PE-ALE chemistries.

Initial experiments were performed on large features: 100nm lines at 200nm pitch. These same processes were applied to small pitch wires - 21nm wires at 44nm pitch - written by e-beam. It was found that while CD increased significantly on the optical features, there was, conversely, a slight drop in CD accompanied by only a slight increase in LWR and LER (Table 1) in the case of the e-beam features.

Table 1: Comparison of CD, LWR and LER changes relative to large (200nm) and small (44nm) pitch features. All values are in nm.

	200nm Pitch			44nm pitch		
	CD	LWR	LER	CD	LWR	LER
Post-Lith	122	6.8	3.7	21.1	5.0	3.5
PE-ALE SiARC (Ar C ₄ F ₈)	141	18.8	13.4	18.8	8.7	5.3
CW SiARC	118	4.2	3.0	17.4	7.5	5.1

OPL Open studies. Just as we did with SiARC, we also explored the effect of the PE-ALE processes on the opening of the OPL layer. These OPL recipes were tested on samples which had their SiARC opened with the standard CW SiARC open recipe previously discussed.

It should be reiterated that during the PE-ALE process there is no fluorocarbon precursor flowed during the deposition step. Despite this, a significant increase in CD is found in the PE-ALE processes, unlike in the CW process which shows a CD decrease. It was previously expected that the CD increase seen in the PE-ALE SiARC process was caused by fluorocarbon deposition. However due to the CD increase seen in these fluorocarbon-free OPL etch processes, this original conclusion may not explain the entirety of the physics at play and warrants further investigation. For the PE-ALE OPL samples, the specific case of the He/Ar background plasma is exceptionally bad with regards to feature changes (Figure 7).

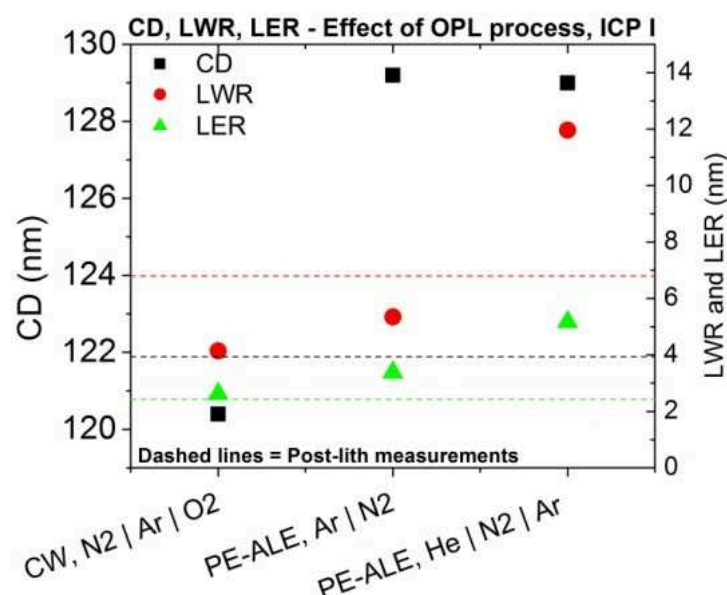


Figure 7: Effect of various PE-ALE OPL open processes on CD, LWR and LER of 200nm pitch features.

As with the SiARC experiments, these OPL processes were applied to small pitch (e-beam) features. In the case of the e-beam written features, the OPL budget is quite small, therefore selectivity and mask retention become critical factors in these etches. Here we found that the PE-ALE processes improved OPL retention, especially as substrate temperature was decreased (Figure 8). It was also found that there was a difference in FC deposition species which is believed may be contributing to the drop in CD and LER, relative to the CW process.

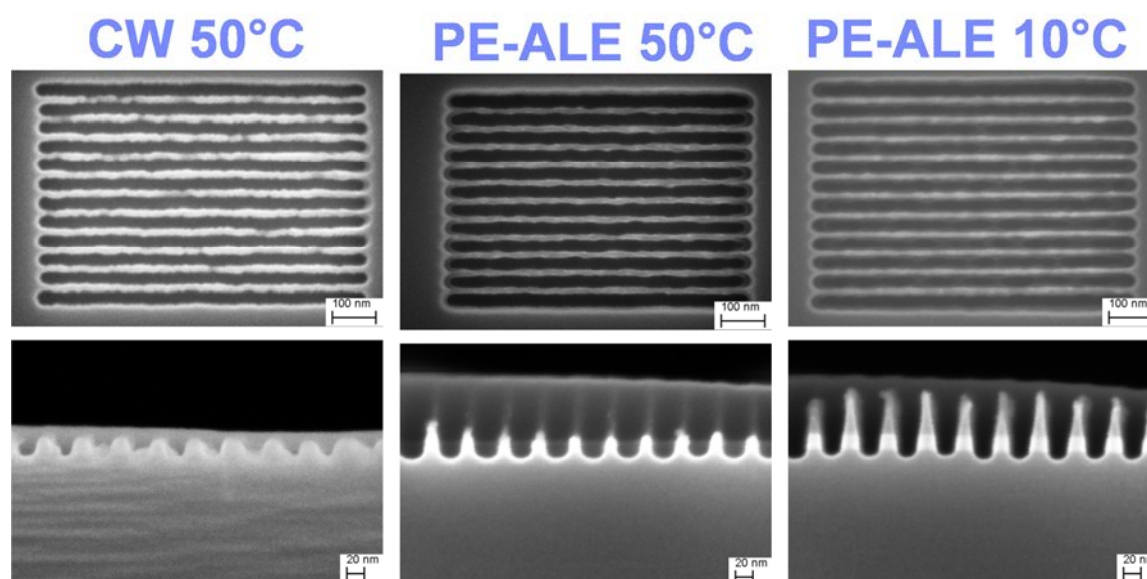


Figure 8: OPL retention variation difference between CW and PE-ALE process, and PE-ALE process at different substrate temperatures.

FC deposition species was analyzed via XPS, comparing PE-ALE processes to our baseline CW process. It was found that there is significantly more CF_3 speciation in the PE-ALE processes than in the CW process. How these species are able to reach the bottoms of a high-aspect pattern is not understood. It is also not currently understood what effect these species have on the pattern itself.

Interaction with OPL of conventional patterning etch. We endeavored to explore how etchant byproducts interact with the OPL of a patterned TiN wafer, utilizing 40nm of TiN that was directly etched using Cl_2/Ar chemistry. This particular etch was seen to be non-uniform and columnar in nature. The most striking aspect of this etch was the poor profile and significant residue found after processing.

Conversely, we explored the same system using our PE-ALE process. In this case, the etch front progressed uniformly and was well controlled. The final etch profile was good, with very little overetch into the oxide under the TiN. Here the most striking aspect was the complete lack of surface residue after processing.

To better understand the effect of these etches on the OPL (in particular the chemical characteristics of the sidewalls of the etched features) the exposed features and sidewalls were analyzed via XPS. It was found that the CW etch (Figure 9) left significantly higher Ti and O moieties at the expense of carbon than did the PE-ALE etch (Figure 10). This could suggest intermixing (re-sputtering) of the metal with the OPL mask. This is further observed in these samples after they were dry stripped (via remote plasma), where the two processes yield very different OPL residues.

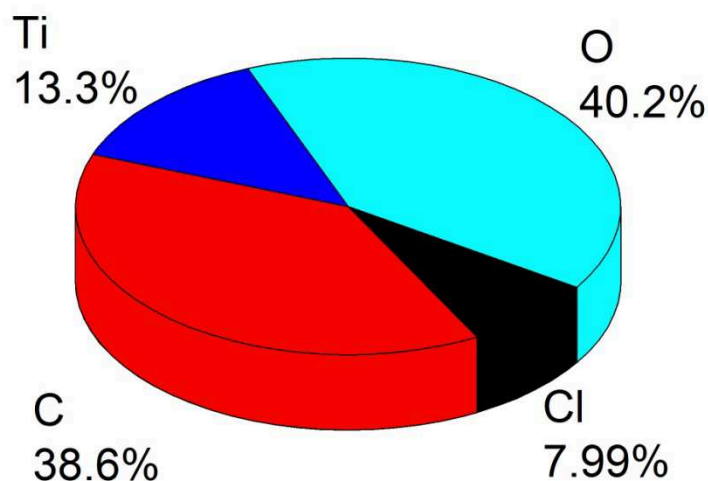


Figure 9: Species found on CW etched TiN sample, as determined by XPS.

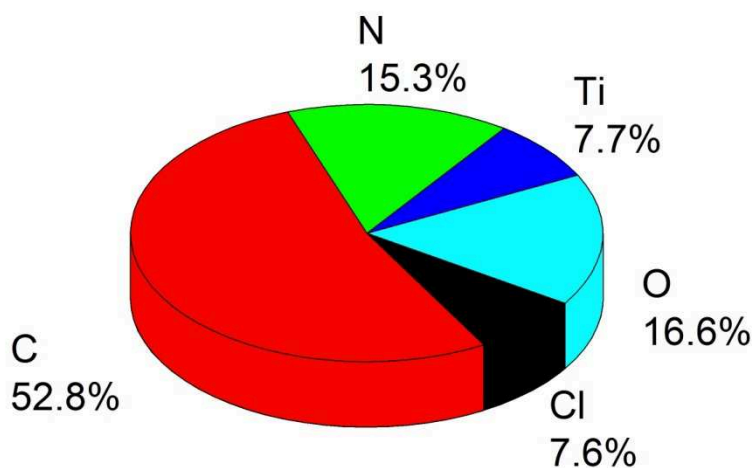


Figure 10: Species found on PE-ALE etched TiN sample, as determined by XPS.

CONCLUSION

We have evaluated current PE-ALE processes for patterning applications. For oxide multicolor selectivity schemes, we were able to show that selectivities of over 20:1 can be obtained for conventional processes based on chemistry and discharge parameter optimization, while PE-ALE processes offer much better across wafer uniformity. For Nitride applications significant improvements were shown by chemistry optimization, whereas a simple transfer of the chemistry to the PE-ALE approach did not yield better selectivities.

PE-ALE processes have also been applied to trilayer processing. Significant increase in CD, LER and LWR has been observed for PE-ALE approaches at large pitch, suggesting a possible issue with VUV damage during PE-ALE. At small device pitch, significantly improved performance was observed for PE-ALE processes. The greatest benefit was observed for employing PE-ALE at the final substrate etch, where an LER improvement of over 25% was achieved. Furthermore the PE-ALE approach also showed much greater control in the reduction of particle contamination following a soft-masked etch of TiN mask material.

ACKNOWLEDGEMENTS

This work was sponsored in part by the National Science Foundation under award No. CBET-1134273 and the US Department of Energy (DE-SC0001939). The devices were fabricated in the Microelectronics Research Laboratory (MRL) at the IBM T. J. Watson Research Center. The authors are grateful to the members of the YKT plasma group, including K. Uppireddi, W. Graham, B. To, E. Sikorski, A. Jagtiani, S. Choi and J. Mykytenko. The authors also like to thank Scott Waltion (NRL), Prof. Oehrlein and D. Metzler (UMD), Zeon Corporation (M. Nakamura, T. Suzuki, A. Itou, T. Jimbo et al.), TEL (M. Yamazaki, T. Nozawa, K. Moyama et al.) and the YKT AMAT support team (J. Hustins, J. Rinnovatore, G. Bain, A. Rodriguez) for parts of this work. The authors would also like to thank the MRL staff & MRL management for support of this work.

References

- [1] Papalia, et al, Proc. SPIE 9782, Advanced Etch Technology for Nanopatterning V, 97820H (2016)
- [2] R.W. Johnson et al., MAT. TOD. 306, 1-11 (2014)
- [3] C. Huffman et al., ECS J. Solid State Sci. Technol. 2015 volume 4, issue 6, Y7
- [4] C.T. Carver et al., ECS J. Solid State Sci. Technol. 2015 volume 4, issue 6, N5005-N5009
- [5] S.U. Engelmann et al., ECS J. Solid State Sci. Technol. 2015 volume 4, issue 6, N5054-N5060
- [6] D. H. van Dorp et al, ECS J. Solid State Sci. Technol. 2015 volume 4, issue 6, N5061-N5066
- [7] Y. Lee et al, ECS J. Solid State Sci. Technol. 2015 volume 4, issue 6, N5013-N5022
- [8] K. Kanarik et al., JVST A 33, 020802 (2015)
- [9] D. Metzler et. al., JVST A32, 020603 2014
- [10] D. Metzler, et al., JVST A 34, 01B102 (2016)
- [11] J.K. Kim et al., J. Vac. Sci. Technol. A 31(6), 061302 (2013)

CHAPTER 2:

FEOL: Surface Chemistry Groups III-V Compound Semiconductors

Towards Atomic-Layer-Scale Processing of High Mobility Channel Materials in Acidic Solutions for N5 and N7 Technology Nodes

Dennis H. van Dorp^{1,*}, Sophia Arnauts¹, Graniel Abrenica^{1,2},
and Frank Holsteys¹

¹imec, Kapeldreef 75, B-3001 Leuven, Belgium

²Katholieke Universiteit Leuven, Celestijnenlaan 200F B-3001, Leuven, Belgium

*vandorpd@imec.be

Keywords: atomic layer etching, surface preparation, cleaning, channel materials

Abstract. In this work the etching kinetics of Ge (100) is studied in acidic solutions containing and oxidizing agent. It is shown that the etch rate in the low etch-rate range is controlled by the concentration of the acid, oxidizing agent and the hydrodynamics of the system. The surface termination during etching has strong impact on the etching kinetics. Finally, we discuss the stability of the Ge (100) surface in water and relate this to the low solubility of the Ge suboxides.

Introduction

Complementary metal-oxide semiconductor (CMOS) science and technology has been dominated by silicon for many decades now. After the 130nm node, equivalent scaling based on judicious materials selection took over from dimensional scaling: straining the Si channel by means of epitaxial strained SiGe source and drain structures boosted mobility and hence drive currents (90-65 nm node), high-k oxides helped reducing gate leakage (65-45 nm node), Trigate or FinFET transistors allow better electrostatic control (22-10nm nodes). For nodes below 10 nm however, further progress requires even higher charge carrier mobilities than what can be delivered by strained Si [1, 2]. The most promising candidate materials which are currently under investigation are Ge for pMOS and III-V (InP and especially InGaAs) for nMOS, usually integrated by selective epitaxial growth on Si platform wafers [3].

For device manufacturing a large number of wet-chemical processing and etching steps are required (e.g. rinsing steps, layer selective etching, trimming, recess etching, smoothening, oxide and (sub)surface damage removal) [4]. Due to the aggressive scaling, an etching control up to the (sub)atomic-layer-scale becomes ultimately necessary. The increased complexity of material properties (e.g. the solubility of group III versus group V oxides or GeO₂ versus GeO_x oxides, impact of cations on the dissolution mechanism, electroless mechanisms, and so on) makes the design of suitable wet chemical etchants challenging. Clearly, a thorough insight in the basic etching kinetics and mechanisms is required to meet the technological milestones foreseen for the near future.

In this work we will give an overview of the dissolution kinetics and chemical stability of Ge in ultra-pure water and HCl solution in the presence of H₂O₂ and O₂ as the oxidizing agent. Besides the striking similarity between Ge and III-As in HCl based chemistries, the etching control of the group IV semiconductor up to (sub) atomic-layer-scale shows that aqueous systems are excellent candidates for advanced CMOS processing.

Experimental

Single side polished p-type bulk 2" (100) Ge wafers (Umicore) were used. The dopant density was ~1E17/cm³). The etching experiments were performed at room temperature in a clean room environment in a dedicated polyvinylidene fluoride (PVDF) cell. The etch rates were determined by ICP-MS measurements [5]. For the oxide removal experiments, the surface was oxidized in a saturated O₃/H₂O solution prior to HCl immersion. The chemicals were purchased from Sigma

Aldrich and were of p.a. quality: 37% HCl (12.0 M) and 30% H₂O₂ (9.7 M). The XPS measurements were carried out in a Theta300 system from ThermoFinnigan using a monochromatized Al K α X-ray source (1486.6 eV) and a spot size of 400 microns. The samples were transported in an N₂ atmosphere to the XPS set-up. The total air exposure was kept to less than 5 minutes.

Results and discussion

Figure 1a shows the influence of the wafer rotation rate on the etch rate of Ge in ultra-pure water (UPW) for different H₂O₂ concentrations. Ge is chemically stable in water: a loss of ~0.02 nm/min was measured. It is noted that the solution was not degassed prior to immersion of the sample (the background O₂ and H₂O₂ concentration in UPW is about 2 μ M and 0.5 μ M, respectively). Upon addition of H₂O₂, the semiconductor is etched. For all the H₂O₂ concentrations studied, mass transport effects are observed; the etch rate increases by a factor of ~2 when the rotation rate is increased from 0 rpm to 200 rpm. For >200 rpm the etch rate is essentially independent of rotation rate. In this range Ge dissolution is kinetically controlled, a condition required for uniform wafer processing [6].

Atomic-layer-scale etching ($v_{\text{etch}} \sim 0.3 \text{ nm min}^{-1}$) is observed for 0.1 mM H₂O₂ in H₂O. The etch rate of Ge in water increases to 3 nm min⁻¹ for 3 mM H₂O₂. A comparable result is observed for the low H₂O₂ concentration range in 1M HCl solution (Figure 1b). However, the influence of the hydrodynamics of the system is more pronounced for higher H₂O₂ concentrations. In the case of 20 mM H₂O₂ the wafer needs to be rotated at ≥ 750 rpm to render dissolution kinetically controlled. The latter was supported by Arrhenius analysis: an activation energy of 32 kJ/mol was found (Figure 1c). For both H₂O and 1M HCl, the surface is hydrophilic during etching, confirming the presence of oxides on the semiconductor surface. Figure 1d shows the influence of the H₂O₂ concentration on the etch rate under kinetically controlled conditions. The presence of HCl strongly affects the etching kinetics. For ≥ 5 mM H₂O₂/H₂O the etch rate reaches a plateau value of about 3.5 nm/min indicating that the oxide solubility is limiting. As the Cl⁻ ion is a more efficient complexing agent, the etch rate is not limited for 1M HCl: v_{etch} increases rapidly with increasing H₂O₂ concentration. Similar to the etching of III-As, the etching kinetics depends strongly on the wetting properties of the Ge surface. For high HCl concentration, the surface becomes hydrophobic and the etch rate is significantly lowered (Figure 1c). Sun and co-workers confirmed with synchrotron radiation photoelectron spectroscopy measurements that Cl is present on Ge (100) surface after HCl immersion, most likely as a result of Cl-passivation of the dangling surface bonds [7]. We suspect that the lower electronegativity of Cl with respect to the OH group, stabilizes surface bonds and hence lowers the chemical reactivity; mass transport effects are less pronounced (not shown). Although the observed trend is strikingly similar to that for III-As [6, 8], higher HCl concentrations are required due to the low solubility of GeO_x ($x < 4$) as compared to group III and V oxides (see next section) [9].

Figure 2 shows Ge 3d core level XPS spectra recorded after O₃/H₂O treatment followed by immersion in 1M HCl (a) and 12 M HCl (b) for 5 minutes. For low HCl concentration, all the Ge oxidation states were detected: oxide removal is clearly not effective. Most of the oxide could be removed by immersion in 12M HCl. In this case only the Ge¹⁺ oxidation state was observed. At this moment we cannot exclude that the Ge¹⁺ is formed during the short air exposure between immersion and the XPS the measurement. The inset shows the Cl 2p peak revealing the presence of Cl at the surface. Surface sensitive measurements indicate that about one monolayer of Cl is present. These results have implications for atomic-layer-scale processing of Ge in acidic solutions (Figure 2c). The low solubility of the suboxides (in contrast to GeO₂) stabilizes the semiconductor in O₂ saturated UPW: Ge loss is limited to 0.15 monolayer minute⁻¹. However, in HCl solution (≥ 6 M) the solubility of the suboxides is sufficiently high and the etch rate can be controlled up to 0.6 monolayer minute⁻¹. As degassing of the HCl solution by N₂ purging lowers the etch rate, it can be concluded that O₂ serves as an oxidizing agent for Ge. These results further suggest that in case Ge loss needs to be minimized to negligible amounts, oxygen free processing will be essential.

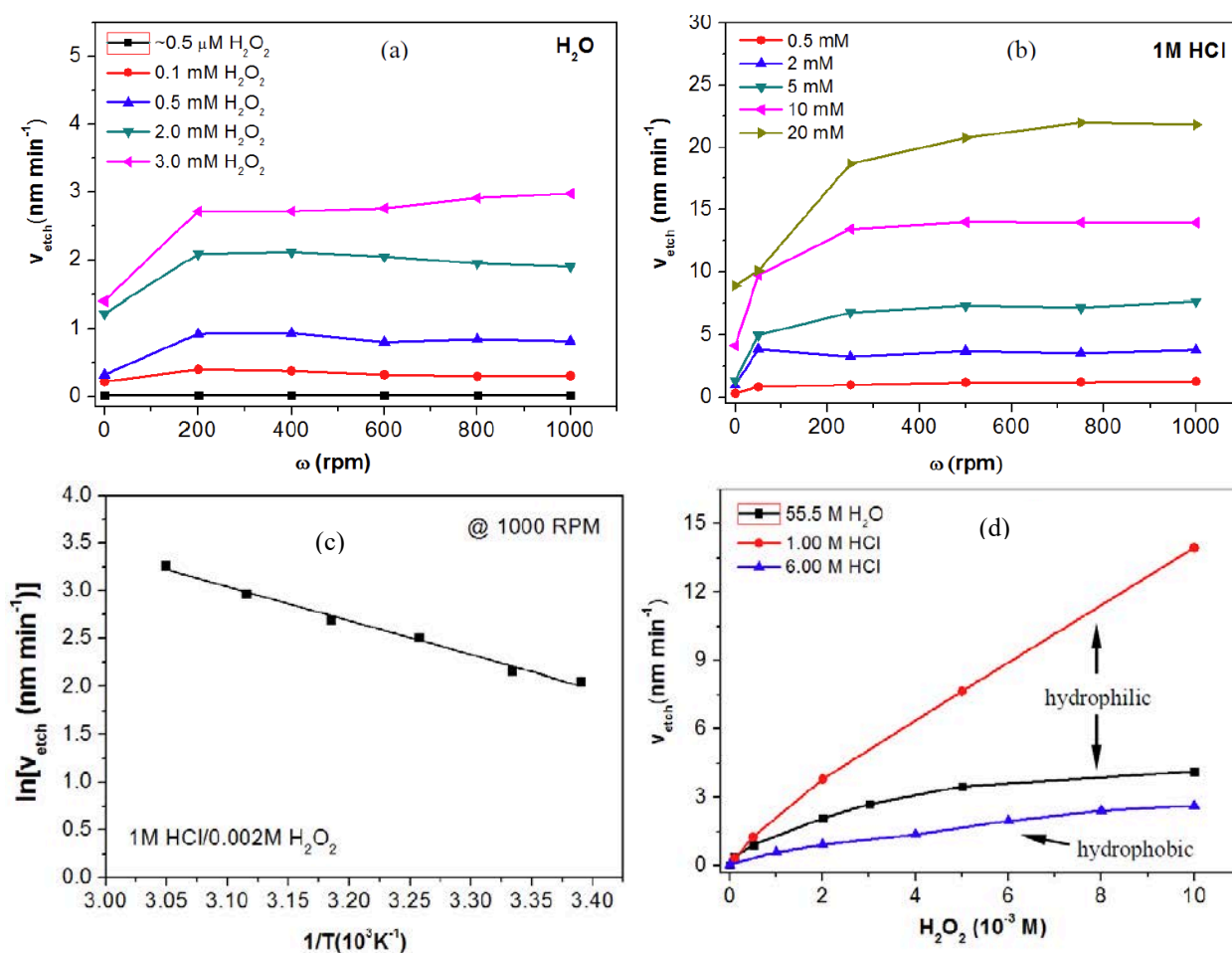


Figure 1. The etch rate of Ge (100) as a function of rotation rate in H_2O (a) and 1 M HCl solution (b) for various H_2O_2 concentrations. In (c) and Arrhenius plot is shown. The influence of the H_2O_2 concentration on the kinetically controlled etch rate for Ge (100) in HCl solution and H_2O is shown in (d).

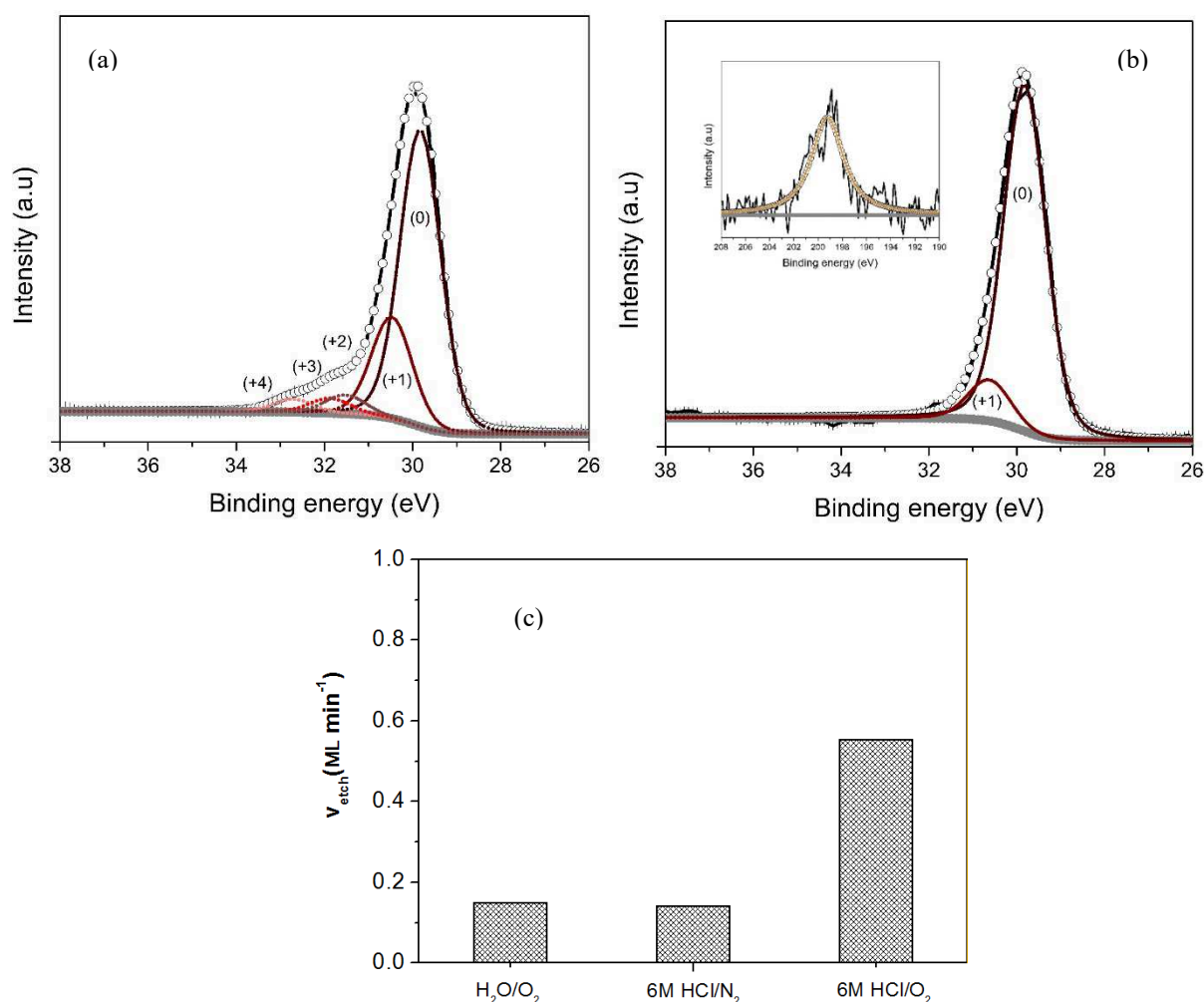


Figure 2: Ge 3d core level photoelectron spectra of Ge (100) surfaces after O₃/H₂O treatment followed by immersion in 1 M HCl (a) and 12 M HCl (b) for 5 minutes. The inset shows the Cl 2p core level peak. In (c) Ge loss is shown for various solutions. The sample was immersed for 60 minutes prior to ICP-MS analysis.

References

- [1] J.A. del Alamo, *Nature*, **479** (2011), 317.
- [2] R. Pillarisetty, *Nature*, **479** (2011), 324.
- [3] M. Heyns and W. Tsai, *MRS Bulletin* **34** (2009) 485
- [4] K.A. Reinhardt and R.F. Reidy: *Handbook of Cleaning for Semiconductor Manufacturing - fundamentals and Applications* (John Wiley and Sons, U.S.A., 2011).
- [5] D.H. van Dorp, S. Arnauts, F. Holsteys and S. De Gendt, *ECS J. Solid State Sci. Technol.*, **4** (2015), N5061.
- [6] J. Rip, D. Cuypers, S. Arnauts, F. Holsteys, D.H. van Dorp, S. De Gendt, *ECS J. Solid State Sci. Technol.*, **3** (2014), N3064.
- [7] S. Sun, Y. Sun, Z. Liu, D-I. Lee, S. Peterson and P. Pianetta, *Appl. Phys. Lett.* **88** (2006), 021903.
- [8] D. H. van Dorp, S. Arnauts, D. Cuypers, J. Rip, F. Holsteys, S. De Gendt, and J. J. Kelly, *ECS J. Solid State Sci. Technol.*, **3** (2014), P179.
- [9] B. Onsia, T. Conard, S. De Gendt, M. Heyns, I. Hoflijk, P. Mertens, M. Meuris, G. Raskin, S. Sioncke, I. Teerlinck, A. Theeuw, J. Van Steenberg, C. Vinckier, *Solid State Phenomena*, **27** (2005).

Comparison of the Chemical Passivation of GaAs, In_{0.53}Ga_{0.47}As, and InSb with 1-Eicosanethiol

Yissel Contreras, Pablo Mancheno-Posso, and Anthony J. Muscat^{a*}

^a Department of Chemical and Environmental Engineering
The University of Arizona, Tucson, Arizona 85721, USA

*muscat@erc.arizona.edu

Keywords: Gallium arsenide, indium antimonide, indium-gallium arsenide, chemical passivation, self-assembled monolayer, 1-eicosanethiol, x-ray photoelectron spectroscopy.

Abstract Self-assembled 1-eicosanethiolate layers were deposited on the oxide-free (100) crystal planes of GaAs, In_{0.53}Ga_{0.47}As, and InSb to protect the surfaces. The layer prevented re-oxidation in air for 30 min on GaAs but only 8 min on In_{0.53}Ga_{0.47}As based on the O 1s x-ray photoelectron spectroscopy state. The layer protected InSb from reoxidation for only 4 min based on the O Auger state. Well-ordered monolayers formed on GaAs and In_{0.53}Ga_{0.47}As based on transmission Fourier transform infrared (FTIR) spectroscopy. A partially ordered layer was formed on InSb based on attenuated total reflection FTIR. The increased reoxidation rate of InGaAs and InSb is due to the larger lattice parameter of these surfaces and their In content, which forms weaker bonds to S, Ga, and Sb compared to Ga bonding to As and S.

Introduction

Future generations of transistor technology need materials with improved electrical properties. III-V semiconductors are candidates because of their higher electron and hole mobilities that increase switching speed and reduce power consumption [1]. However, III-V oxides create interface states that are detrimental to the electrical performance of the transistor. One approach after removing the oxides is to protect the surface with a functional layer that prevents oxide re-growth. This layer can be a diffusion barrier for oxygen in air or a kinetic barrier that prevents the reaction of surface atoms. The deposition of a monolayer of S using Na₂S·9H₂O or (NH₄)₂S passivates the surface [2,3] but does not provide a diffusion barrier. Alkanethiols (CH₃(CH₂)_n-SH) were chosen because they potentially provide both a diffusion barrier (C chain) and chemically passivate the surface through thiolate (R-S⁻) bonding with surface atoms [4]. This work compares the resistance to oxidation in air of the (100) crystal planes of GaAs, In_{0.53}Ga_{0.47}As, and InSb covered with a 1-eicosanethiol (CH₃(CH₂)₁₉SH) self-assembled monolayer (SAM).

Experimental Procedure

Materials. Semiconductor grade acetone, hydrogen peroxide (H₂O₂, 30%), hydrochloric acid (HCl, 36%), and hydrofluoric acid (HF, 49%) were obtained from Honeywell. 1-Eicosanethiol (ET, CH₃(CH₂)₁₉SH, 98%) was obtained from Alfa Aesar and ethanol (anhydrous, 99.5%) and ammonium hydroxide (28%-30% NH₃ basis) from Sigma-Aldrich. Ultrapure water (UPW, 18 MΩ-cm) was used as a solvent and for rinsing steps. All the chemicals were used as received.

Passivation. GaAs(100) (undoped, Freiburger Compound Materials) and InSb(100) (undoped, Xiamen) wafers were cut into 1 x 1.5 cm² coupons and cleaned by sonication in acetone and water for 1 min each. In_{0.53}Ga_{0.47}As(100) epitaxial layers on InP substrates (1000 nm thick, undoped, IntelliEpi), were cut into 1 x 1.5 cm² coupons and immersed for 1 min in 1:1:10000 v/v NH₄OH:H₂O₂:H₂O at room temperature, followed by a 1 min immersion in UPW. After rinsing with UPW and drying with N₂, the GaAs and InSb samples were immersed consecutively in 0.28 M HF for 1 min and 1.0 M H₂O₂ for 2 min, with water rinse and N₂ drying in between. This sequence was repeated twice. After immersion in the same HF solution for 1 min, samples were transferred, without rinsing or drying, to 1.0 M HCl for 1 min and subsequently transferred to 4 mM (GaAs) or

0.1 mM (InSb) ET in ethanol, where the samples were treated for 20 min (GaAs) or 20 h (InSb). A lower ET concentration was used on InSb because multilayer formation was observed on this surface when treating in 4.0 mM solutions, even for a short period of time (20 min). The $\text{In}_{0.53}\text{Ga}_{0.47}\text{As}$ samples were immersed twice in 0.28 M HF, with UPW rinsing and N_2 drying in between, without any rinse after the second HF step. Finally the InGaAs samples were treated for 20 h in 4 mM ET in ethanol. A thin film of the HCl or HF solution was carried over on the sample into the ET solution to avoid exposure to air. The samples were swished in fresh ethanol for 5 s (GaAs) or 30 s (InSb and InGaAs), dried with N_2 and loaded into an ultra-high vacuum system for surface analysis.

Characterization. X-ray photoelectron spectroscopy (XPS) was performed using a Physical Electronics (Model 549) instrument equipped with a non-monochromatic Al/Mg X-ray source and a double-pass cylindrical mirror analyzer. XPS spectra were obtained with the Al $K\alpha$ source (1486.6 eV) at a 0.1 eV resolution and a pass energy of 50 eV. The As 3d photoelectron line at 41.1 eV was used to correct for sample charging of GaAs and $\text{In}_{0.53}\text{Ga}_{0.47}\text{As}$, and the Sb 3d_{3/2} line at 537.0 eV was used for InSb. The Au 4f_{7/2} line at 84.0 eV (FWHM = 1.94 eV) was used for calibration. A Shirley background correction and peak fitting using Voigt lineshapes were done using Igor Pro (WaveMetrics, Inc., v.6.2). Fourier-transform infrared spectroscopy (FTIR) was done using a single beam spectrometer (Nicolet Nexus 670) equipped with a MCT detector. Transmission FTIR spectra were acquired at normal incidence at 4 cm⁻¹ resolution and 200 scans were co-added. Attenuated total reflection (ATR) FTIR spectra were recorded for InSb samples 50 mm × 10 mm in size by using a trapezoidal Ge crystal (50 mm × 10 mm × 3 mm with 45° bevels) as the internal reflection element. The angle of incidence of the beam was 60° and the spectra were processed with ATR correction with the analysis software OMNIC (v.6.2).

Results and Discussion

The Ga 2p, As 2p, and O 1s XPS spectra for GaAs(100) surfaces after the last HCl immersion, and after immersion in ET solution followed by 3 min, 30 min, and 120 min of exposure to air are shown in Figure 1. After immersion in HCl, the Ga 2p region shows a peak at 1117.1 eV due to bulk Ga from the substrate [5]. The peak at a binding energy shift of +1.1 eV from the bulk Ga peak is due to Ga_2O_3 species [5,6]. The peak in the As 2p state at 1323.0 eV is assigned to the contribution of both bulk As and the As-As dimer state [6]. The second peak at higher binding energy is due to the contribution of As_2O_3 (+3.2 eV) and As_2O (+1.3 eV) species [5,6]. The corresponding O 1s state shows a peak at 531.1 eV due to Ga and As oxides. After immersion in ET and 3 min of air exposure, oxygen is below the detection limits as shown by the O 1s region. The peaks due to oxide states in the Ga 2p and As 2p regions were not detected. The peak shifted by +1.3 eV from the bulk As peak is due to As-S bonds [7]. After 30 min of exposure, the same peaks due to bulk As-Ga and As-S bonds are observed and oxygen is maintained below detection limits. After 120 min of exposure, high binding energy peaks are observed in the Ga 2p and As 2p region due to the formation of Ga-O (+0.8 eV), As_2O_3 (+3.2 eV), and As_2O species (+1.3 eV) [5,6]. The corresponding O 1s state shows a peak at 531.2 eV due to the re-growth of Ga and As oxides.

The In 3d, Ga 2p, As 2p, and O 1s XPS spectra for $\text{In}_{0.53}\text{Ga}_{0.47}\text{As}$ (100) surfaces after the last HF immersion, and after immersion in ET solution followed by 4 min, 8 min, and 60 min of exposure to air are shown in Figure 2. Peaks corresponding to bulk In in the 3d region were assigned at 444.0 eV and at 451.5 eV for the 3d_{5/2} and 3d_{3/2} spin orbit splitting states. The bulk In 3d_{5/2} peak has been assigned previously at 444.4 eV in $\text{In}_{0.53}\text{Ga}_{0.47}\text{As}$ [8]. The position for In_2O_3 was set at 452.1 eV. The Ga 2p and As 2p bulk states were assigned at 1117.1 eV and 1322.9 eV, respectively, and the Ga^{3+} and As^{3+} states at 1118.3 eV (+1.2 eV binding energy shift) and 1326.0 eV (+3.1 eV shift). From the spectra in Figure 2, the main surface oxides present 4 min after HF etching and UPW rinse correspond to As and Ga in the 3+ state. Additional In states were not resolved due to the proximity of the bulk and oxide peak positions, but the small shift in the position of the In 3d peaks to higher binding energies is indicative of the formation of In_2O_3 . The surface was covered with an oxide layer after only 4 min exposed to air during sample transfer from

the liquid solution to the vacuum chamber. The corresponding O 1s state shows a peak at 531.5 eV due to In, Ga, and As oxides. After a 20 h immersion in ET and 3 min of air exposure, oxygen is below the detection limits as shown by the O 1s region. The peaks due to oxide states in the Ga 2p and As 2p regions were not detected. The peak at a shift of +1.2 eV from the bulk As peak is due to As-S bonds. After 8 min of exposure, the same peaks due to bulk As-Ga and As-S bonds are observed and oxygen is detected in the O 1s region. A small As₂O₃ peak at +3.1 eV from the bulk As peak was resolved. After 60 min of exposure, high binding energy peaks are observed in the Ga 2p and As 2p region due to the formation of Ga₂O₃ (+1.2 eV) and As₂O₃ (+3.1 eV) species (+1.3 eV). The corresponding O 1s state shows a peak at 531.5 eV due to the re-growth of Ga and As oxides.

The Sb 3d, In 3d, and O Auger XPS spectra for InSb(100) surfaces after the last HCl immersion, and after immersion in the ET solution followed by 3 min, 8 min, and 20 min of exposure to air are shown in Figure 3. After immersion in HCl, the spin-orbit coupled bulk Sb 3d_{5/2} state is at 527.7 eV (previously reported at 528.0 eV, [9]). The Sb 3d_{3/2} state was fixed at 537.0 eV. The bulk In 3d_{5/2} state was assigned at 444.0 eV (444.0 eV for a native oxide surface has been reported [9]), and the In 3d_{3/2} state is at 451.5 eV. The states at 530.5 eV (+2.9 eV) and 540.0 eV (+3.0 eV) to higher binding energies are due to Sb oxide and sulfide. The peak at ~530.5 eV contains contributions from the O 1s, Sb-O, and Sb-s states. Contributions from Sb⁺³ and Sb⁵⁺ have been reported at 530.5 eV and 531.4 eV [10]. The O 1s state has been reported at 532 eV [10] and at 531 eV [11] in InSb. In 3d oxide states were not resolved, and the bulk In peaks did not shift to higher binding energy. From these results, the InSb surface was oxidized after a 3 min exposure to air. After the sample was treated for 20 h in ET, smaller Sb 3d peaks were observed at high binding energies. In fact, the Sb 3d_{5/2} state is slightly shifted to a lower binding energy (530.0 eV, +2.4 eV) because of the presence of Sb-S bonding instead of Sb-O bonding. After 8 min of air exposure, oxygen is detected in the Auger region and the high binding energy Sb 3d_{5/2} peak (+2.4 eV) increased and shifted towards 530.5 eV, indicating formation of Sb oxides. This trend increases after a 20 min air exposure with further increase of the O Auger state and the high binding energy Sb 3d_{5/2} peak (+2.9 eV).

The surfaces are terminated by group-V atoms after the halogen acid immersions and thiol deposition. The immersions in HCl and HF leave an As-rich layer on GaAs (As 2p/Ga 2p peak area ratio = 1.8) and a Sb-rich layer on InSb (Sb 3d/In 3d ratio = 1.3). The HF etch leaves an As-rich layer on InGaAs (As 2p/Ga 2p ratio = 5.9, As 3d/In 3d ratio = 2.9). After immersion in ET for 20 min (GaAs) and 3-4 min of air exposure, the GaAs surface is still rich in As atoms (As 2p/Ga 2p = 1.5), and remains As-terminated after 30 (As 2p/Ga 2p = 1.7) and 120 (As 2p/Ga 2p = 1.4) min of exposure. Both In_{0.53}Ga_{0.47}As and InSb surfaces keep their group-V atom termination after the thiol deposition. On InGaAs, the As 2p/Ga 2p ratio = 3.0, and the As 3d/In 3d ratio = 2.9 after a 20 h thiol deposition. For InSb, the Sb 3d/In 3d ratio is 1.5 after a 20 h immersion. The group V atom terminates the surface after the halogen acid last step and adsorption of the eicosanethiolate layer preserves this termination.

Figures 4-6 show the transmission FTIR spectra for native oxide GaAs and treated in 1-eicosanethiol for 20 min as well as In_{0.53}Ga_{0.47}As and InSb cleaned using a halogen acid last step and treated in 1-eicosanethiol for 20 min or 20 h. For GaAs, the asymmetric methyl stretch is observed at 2960 cm⁻¹, and the methylene stretches are found at 2918 cm⁻¹ (asymmetric) and 2950 cm⁻¹ (symmetric). On In_{0.53}Ga_{0.47}As the asymmetric methyl stretch is observed at 2960 cm⁻¹, and the methylene stretches are found at 2918 cm⁻¹ (asymmetric) and 2950 cm⁻¹ (symmetric), while on InSb, absorbance peaks at 2957 cm⁻¹, 2925 cm⁻¹, 2850 cm⁻¹, and 2847 cm⁻¹ are observed. The presence of the symmetric methylene stretch at wavenumbers of 2920 cm⁻¹ and lower is indicative of a crystalline-like layer [4], as opposed to a liquid-like, disordered layer at wavenumbers of 2928 cm⁻¹ [12].

The formation of As-S bonds (bond dissociation energy = 379.5 kJ/mol) is not thermodynamically favorable compared to Ga-S bonds (393 kJ/mol), but the GaAs and In_{0.53}Ga_{0.47}As surfaces are rich in As atoms after the HF and HCl cleans. The re-oxidation of the

GaAs and $\text{In}_{0.53}\text{Ga}_{0.47}\text{As}$ surfaces occurs by the attack of molecular oxygen and formation of As-O bonds (484 kJ/mol), which are more favorable than As-S bonds. Formation of Sb-S bonds (378.7 kJ/mol) is more thermodynamically favorable than In-S bonds (287.9 kJ/mol), and re-oxidation occurs by formation of Sb-O bonds (434 kJ/mol). Also, In forms weak bonds to Ga and Sb (94 kJ/mol and 152 kJ/mol, respectively), which results in oxygen attacking back bonds more easily on surfaces that contain In. The FTIR spectra in Figures 4-6 show that the ET layer is less ordered and dense on InSb. The asymmetric methylene stretch for ET on InSb is at 2925 cm^{-1} , which is indicative of a liquid-like layer [12,13]. Oxygen diffusion is faster through a disordered layer and more sites are available for reaction [13]. Based on FTIR, the ET layers on GaAs and $\text{In}_{0.53}\text{Ga}_{0.47}\text{As}$ are both ordered, but the In content makes the InGaAs surface more easily attacked by oxygen or water in air. In the case of InSb, the higher In concentration increases the reoxidation rate. Adsorption of the alkanethiolate molecules on GaAs (lattice constant = 5.4 \AA) induces a surface reconstruction that promotes the formation of a dense and ordered monolayer [4]. Alkanethiolate adsorption could induce larger surface reconstructions on $\text{In}_{0.53}\text{Ga}_{0.47}\text{As}$ (5.9 \AA) and InSb (6.5 \AA) that are not as favorable to monolayer formation due to their larger lattice constants. All three materials have zinc blende structures. The atomic surface density on the (100) plane is $6.8 \times 10^{14}\text{ atoms/cm}^2$ for GaAs, $5.7 \times 10^{14}\text{ atoms/cm}^2$ for InGaAs, and $4.7 \times 10^{14}\text{ atoms/cm}^2$ for InSb. The trend in the atomic densities correlates with the lower FTIR peak intensities indicative of the alkanethiolate layer and the propensity for reoxidation of the underlying surfaces.

Conclusions

GaAs, $\text{In}_{0.53}\text{Ga}_{0.47}\text{As}$, and InSb were chemically passivated for different times by an ET layer. The maximum passivation time for GaAs(100) was 30 min, whereas for $\text{In}_{0.53}\text{Ga}_{0.47}\text{As}$ and InSb the surface was protected for 8 and 4 min, respectively. The quality of the ET layer on GaAs and $\text{In}_{0.53}\text{Ga}_{0.47}\text{As}$ was higher than that on InSb. This is due to the larger lattice constant of InSb, which is incommensurate with a crystalline-like monolayer of ET. Despite the good quality of the ET layer on $\text{In}_{0.53}\text{Ga}_{0.47}\text{As}$, the presence of In and the smaller density of available surface sites leads to a higher re-oxidation rate.

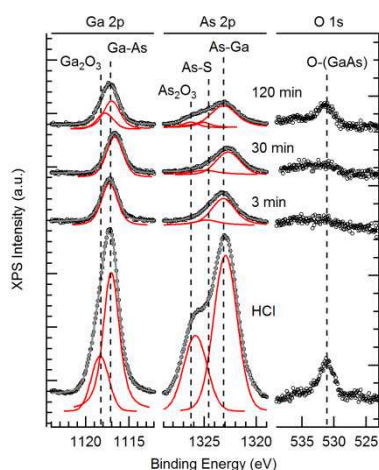


Figure 1: XPS spectra of GaAs(100) after the last HCl immersion without water rinse, and after a 20 min immersion in 4.0 mM ET followed by 3 min, 30 min, and 120 min of air exposure. Circle markers correspond to data and solid lines to fitting results. Dashed vertical lines are guides to the eye for peak positions.

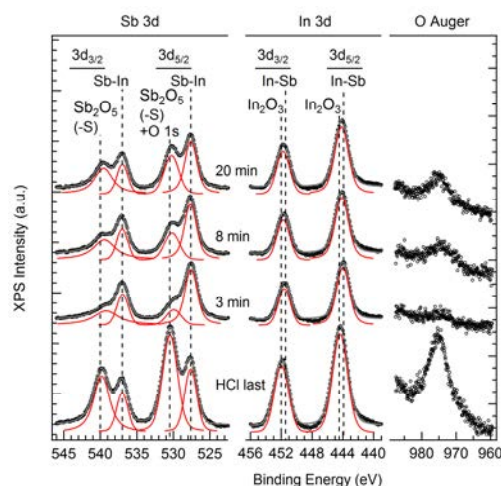


Figure 2: XPS spectra of InSb(100) after the last HCl immersion, and after a 20 h immersion in 0.1 mM ET followed by 3 min, 8 min, and 20 min of air exposure. Circle markers correspond to data and solid lines to fitting results. Dashed vertical lines are guides to the eye for peak positions.

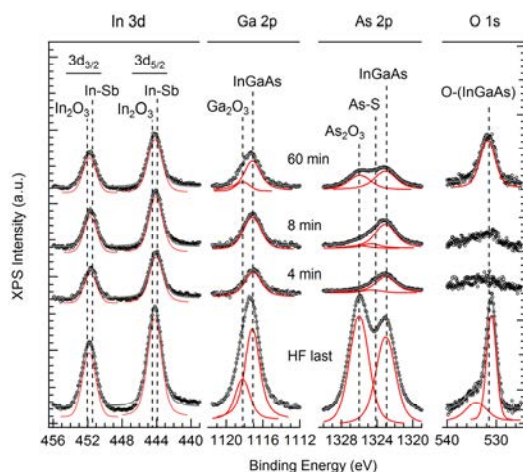


Figure 3: XPS spectra of $\text{In}_{0.53}\text{Ga}_{0.47}\text{As}(100)$ after the last HF immersion, and after a 20 h immersion in 4.0 mM ET followed by 4 min, 8 min, and 60 min of air exposure. Circle markers correspond to data and solid lines to fitting results. Dashed vertical lines are guides to the eye for peak positions.

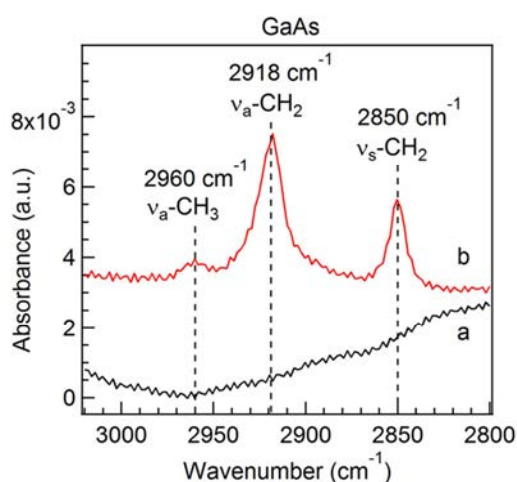


Figure 4: Transmission FTIR spectra of a) native oxide $\text{GaAs}(100)$, and b) GaAs immersed in 4 mM ET for 20 min.

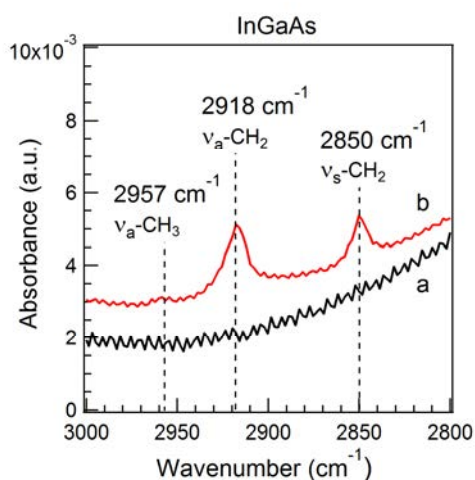


Figure 5: Transmission FTIR spectra of $\text{In}_{0.53}\text{Ga}_{0.47}\text{As}(100)$ a) as received (covered with oxide), and b) after immersion in 4 mM ET for 20 h.

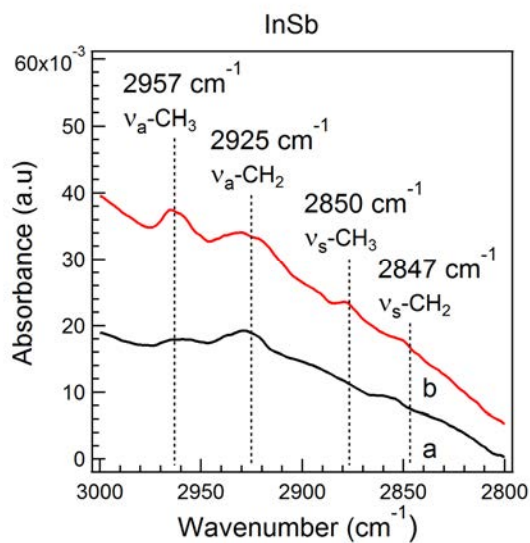


Figure 6: ATR FTIR spectra of $\text{InSb}(100)$ a) after cleaning in HCl and reoxidation, and b) after immersion in 0.1 mM ET for 20 h.

References

- [1] J. del Alamo. *Nature* **479** (2011), p. 317.
- [2] C. J. Sandroff, M. S. Hegde, L. A. Farrow, C. C. Chang, and J. P. Harbison: *Appl. Phys. Lett.* **54** (1989), p. 362.
- [3] Y. Nannichi, J. Fan, H. Oigawa, and A. Koma: *Jpn. J. Appl. Phys.* **27** (1988) p. 2367.
- [4] C. McGuiness, A. Shaporenko, M. Zharnikov, A. Walker, and D. Allara: *J. Phys. Chem. C* **111** (2007) p. 4226.
- [5] B. Brennan, M. Milojevic, C. Hinkle, F. Aguirre-Tostado, G. Hughes, and R. Wallace: *Appl. Surf. Sci.* **257** (2011), p. 4082.
- [6] S. McDonnell, H. Dong, J. M. Hawkins, B. Brennan, M. Milojevic, F. S. Aguirre-Tostado, D. M. Zhernokletov, C. L. Hinkle, J. Kim, and R. M. Wallace: *Appl. Phys. Lett.* **100** (2012), p. 141606-1.
- [7] H. A. Budz, M. C. Biesinger, and R. R. LaPierre: *J. Vac. Sci. Technol. B*, **27** (2009), p. 637.
- [8] H. Oh, S. A. B. Suleiman, and S. Lee: *J. Electrochem. Soc.*, **157** (2010), p. H1051.
- [9] T. V. Lvova, M. S. Dunaevskii, M. V. Lebedev, A. L. Shakhmin, I. V. Sedova, and S. V. Ivanov: *Semiconductors*, **47** (2013), p. 721-727.
- [10] D. M. Zhernokletov, H. Dong, B. Brennan, J. Kim, and R.M. Wallace: *J. Vac. Sci. Technol. B*, **30** (2012), p. 04E103.
- [11] P. D. C. King, T. D. Veal, M. J. Lowe, and C. F. McConville: *J. Appl. Phys. B*, **104** (2008), p. 083709.
- [12] G. Neshet, A. Vilan, H. Cohen, D. Cahen, F. Amy, C. Chan, J. Hwang, and A. Kahn, *J. Phys. Chem. B* **110** (2006), 14363.
- [13] Y. Contreras and A. J. Muscat, *Appl. Surf. Sci.* **370** (2016), p. 67-75.

Digital Etching of GaAs Materials: Comparison of Oxidation Treatments

Mickaël Rebaud^{1,a,*}, Marie-Christine Roure^{1,b}, Virginie Enyedi^{1,c},
Lukasz Borowik^{1,d}, Eugénie Martinez^{1,e}, Laura Toselli^{1,f} and Pascal Besson^{1,g}

¹Uni. Grenoble Alpes, F-38000 Grenoble, France

CEA, LETI, MINATEC Campus, F38054 Grenoble, France.

^amickael.rebaud@cea.fr, ^bmarie-chistine.roure@cea.fr, ^cvirginie.enyedi@cea.fr,

^dlukasz.borowik@cea.fr, ^eeugenie.martinez@cea.fr, ^flaura.toselli@cea.fr, ^gpascal.besson@cea.fr

Keywords: Gallium arsenide, III-V materials, surface passivation, digital etching.

Abstract. Oxidation of a GaAs surface was performed with liquid H₂O₂, gaseous O₂ and O₃ in order to identify the best solution for digital etching. The oxide layer formed with H₂O₂ is Ga-rich and exhibits surface roughening which can be understood by oxide hydrolysis/condensation model. Roughening makes aqueous H₂O₂ irrelevant as an oxidizing agent for repeated oxidation steps. On the other hand, a smooth oxide layer can be obtained with gaseous O₂ and O₃. Thickness of the formed oxide layer is controlled by time exposure to the oxidizing agent. The nature of the oxide was analyzed by X-Ray Photo-electron Spectroscopy and is also time-dependent.

Introduction

The cleaning of GaAs with a controlled consumption of material is a key point for its industrial development. Chemical cleaning solutions are generally composed of mixed compounds and designed to assume two main roles: (i) pH or complexing effects are controlled by acid or basic chemicals with a huge impact of the involved counter-ion; (ii) strong oxidizing agent, like H₂O₂, is often used to modify the extreme surface of the substrate in order to enhance its reactivity with the liquid media. However, without extreme dilution of standard 30% H₂O₂ (1/5000), etch rates of GaAs in non-neutral solution are not compatible with micro-electronic applications [1]. Prepare such a highly diluted solution has a low reliability and is tricky to manage. This may highly impact processes reproducibility.

An alternative to mixed chemistries is to separate the cleaning process in multiple steps. An oxide layer with a controlled thickness is firstly grown. Oxide dissolving chemistries with specific properties (pH control, complexing effect) can subsequently be used on this oxide layer. Chemicals should not react with the bulk material. The overall material consumption of this two-steps treatment is thus defined by the oxide thickness. The digital etching [2] avoids concomitant reactions of substrate oxidation and dissolution which lead to high etch rates. This study thus focuses on different ways to form such a controlled oxide layer on GaAs surface with different oxidizing agents (liquid H₂O₂ and gaseous O₂ or O₃). The most relevant oxidizing agent for further processing will be highlighted.

Experimental

4 inches GaAs (100) oriented Zn-doped (10¹⁸ cm⁻³) substrates provided by AXT are used. The surface was prepared by chemical mechanical polishing refresh followed by a scrubber step. Air-aged samples were degreased by acetone, ethanol and iso-propanol sequence prior to measurements. To obtain an oxide free surface, samples were treated in 1M NH₄OH for 10 min followed by a rinsing step in Running Ultra-Pure Water (RUPW) with a low content of dissolved oxygen obtained by an high surface exchanger nitrogen bubbling ([O₂] = 0.3 ppm) [3]. Oxide growths were subsequently conducted with less than 2 minutes of air exposure. For controlled oxidations, 10% H₂O₂ bath, O₂ from clean-room environment air and O₃ carried to a closed chamber from an external plasma generator were used.

XPS spectra were collected in a PHI VersaProbe II Scanning XPS Microprobe system using a monochromatic Al K α X-ray source (1486.7 eV) and a take-off angle of 45°. Ga 3d and As 3d spectra were collected with a constant pass energy of 23.5 eV leading to an overall energy resolution of 0.6 eV. The peak positions were calibrated using the C1s core level spectra (284.8 eV) as a reference. The XPS curves fitting was carried-out with the CasaXPS 2.3.16 software using Voigt functions and a Shirley background subtraction. The air exposure was minimized to less than 5 minutes after treatments.

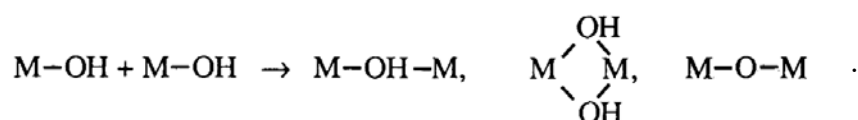
AFM images were acquired on a Bruker Dimension FastScan and treated with NanoScope Analysis 1.5 software.

Ga and As species dissolved from one GaAs wafer in 10L static H₂O₂ 10% bath were followed by Induced Coupled Plasma Mass Spectrometry analysis (ICPMS). The chemical bath was stirred up prior to each 10mL solution sampling.

The oxide thickness evolution as a function of time was followed by ellipsometry in a cleanroom environment with a model of one oxide layer on a bulk substrate.

Results and discussions

GaAs in H₂O₂. One approach to form an oxide layer on the surface is to use hydrogen peroxide. The pH of H₂O₂ is in a range from 4.7 (clean room reagent at 30%) to 7 (pure water). From a molecular point of view, an issue might arise if attention is given to the solubility of each kind of oxidized species (GaOx and AsOx) in this range of pH (Fig. 1). Both oxidized arsenide species can be considered as totally soluble while pure Ga₂O₃ is insoluble and its hydrated form Ga(OH)₃ has a very low solubility. In order to confirm these thermodynamic data, a GaAs wafer was exposed to a large excess of H₂O₂ (10%) to ensure oxide formation despite oxide dissolution. From this oxide, the dissolution of Ga and As species was followed by ICPMS (Fig. 2). In the early stages, a significant amount of As is detected while Ga remains under the Low Limit Detection (LLD) of the analytical method. Arsenide species are preferentially desorbed from the oxide layer confirming their higher solubility. To understand this phenomena, hydrolysis/condensation equilibria of an oxide has to be taken in consideration (Eq. 1 [5]).



Considering initial As-O-Ga bonds (Fig. 3A), these bonds should be hydrolyzed to release soluble As³⁺ and As⁵⁺ species (Eq. 1 from right to left) found in the three first ICPMS measurements. Free hydrolyzed GaOx and AsOx are generated at the surface. Highly soluble AsOx species are removed from the oxide (Fig. 3B) which leads to surface enrichment in Ga-OH bonds (Fig. 3C). Low solubility of GaOx species (in this near neutral pH) suggests that Eq. 1 is displaced towards the right side when Ga³⁺ is involved as “M”. As a results, the surface passivates following oxide condensation of GaOx species with AsOx entrapment (Fig. 3D). This explains why, after 3 days, concentration of dissolved gallium is between those of Ga₂O₃ and Ga(OH)₃ at pH = 5.1 (corresponding to a Ga³⁺ saturated solution) while concentration of dissolved arsenide is far from the expected thermodynamic equilibrium. The analysis of the surface (Table 1) treated with H₂O₂ shows a clear gallium enrichment with a high amount of gallium involved in GaOx. This confirmed the formation of a gallium rich oxide layer.

From this mechanism, free hydrolyzed GaOx can have a short displacement before finding condensation sites. In early stages, island shaped structures are observed which are followed by deep etched areas when passivation is reached (Fig. 4). These highlighted phenomena might happen to a lesser extent in the case of repeated short exposures to quasi-neutral aqueous oxidizing solutions. The surface will be damaged if several digital etching cycles are needed for a cleaning sequence.

Table 1: Surface composition of different samples extracted from Ga 3d and As 3d XPS spectra.

Surface treatment	Ga (%)	Ga _{bulk} (%)	GaO _x (%)	As (%)	As _{bulk} (%)	AsO _x (%)
NH ₄ OH with RUPW	52	97	3	48	98	2
NH ₄ OH with RUPW and 2 hours in 10% H ₂ O ₂	68	40	60	32	53	47

Oxidation with gases. As roughening occurs according to hydrolysis and condensation reactions which involve water as a reactant, oxidation in dry gaseous phase at low temperature is more suitable for respectful surface roughness. Whatever the gaseous treatments, no variation in surface roughness is noticed (Table 2).

Table 2: Surface roughness of GaAs after different treatments (values obtained by averaging two 20 μm x 20 μm images realized on each sample)

Surface treatment	Roughness (rms) [nm]	Rmax [nm]
Incoming substrate	0.240	2.44
NH ₄ OH with RUPW and 30 minutes to air exposure	0.247	2.31
NH ₄ OH with RUPW and 30 minutes to O ₃ exposure	0.231	2.14

A sufficient thickness of oxide is required for chemical dynamics to take place on the substrate surface in a dissociated oxidation/dissolution process. Control on the oxide layer thickness allowed to manage the amount of removed material for each cycle.

Oxide can be grown on GaAs by simple air exposure at room temperature [6]. On Fig. 5, we can see that after NH₄OH treatment, the thickness of the oxide layer grown in air follows a logarithmic trend. Oxidation rate is decreasing while oxide thickness is increasing. In the early stages of air oxidation, control of oxide thickness is thus hard to achieve. On the other hand, oxide thickness obtained in a 30 minutes time range is not exceeding 1.0 nm. Time required to obtain such a thickness (or more) does not allowed the use of oxygen from air as an oxidation step for digital etching.

On the same range of treatment time (2 minutes and 30 minutes), oxide layers obtained with gaseous O₃ are thicker than those obtained with O₂ (Fig. 5) according to a higher oxidation potential of O₃ molecule. Self-passivation of the oxide film is not reach (even with 30 minutes of exposure to O₃). This implies that reliable and thicker layer can be form with short O₃ process time compare to ambient air oxidation.

Changes of surface chemical composition with different exposure time to O₃ are shown on As 3d and Ga 3d photo-electron spectra (Fig 6). Each chemical component is fitted with a 3d_{5/2} and 3d_{3/2} doublet that is constrained to have a 3:2 peak area ratio and equal FWHM for the two peaks of the doublet. Peak separation is 0.69 eV for As species and 0.45 eV for Ga species. Components from the bulk material have binding energies of 40.9 eV (± 0.2 eV) for As and 19.0 eV (± 0.2 eV) for Ga. After oxide removal with NH₄OH/RUPW rinse and 2 minutes of exposure to O₃, oxide signal exhibits only one component. Chemical shift is about +3.2 eV for As and +1.1 eV for Ga. These peaks are attributed to As (III+) and Ga (III+) species. With longer exposure to O₃, oxide signal rises. This corresponds to an increase of the oxide thickness. Moreover, an additional component with a chemical shift of +4.5 eV is observed on As 3d spectra and is considered as As (V+) species. Lu and co-workers [7] shown that As (V+) species are preferentially formed on the extreme surface of the substrate. Complete fit of As 3d spectra need a last component with a chemical shift of +0.7 eV. From this chemical shift, the associated species should be elemental arsenide or arsenide sub-oxides (< III+). No visible change on chemical shift of Ga (III+) species can be observed. For digital etching application, as As (V+) species have a higher solubility than As (III+) species, their presence in the oxide layer can be helpful for the oxide dissolution step. Long time exposure to O₃ thus leads to a thick oxide layer containing highly soluble As (V+) species.

Conclusion

In order to reach a controlled consumption of GaAs for cleaning applications, processes made of dissociated oxidation/dissolution are promising. Aqueous oxidation implies reversible hydrolysis/condensation reactions which can lead to surface roughening due to the difference of solubility of each kind of oxides in near neutral pH range. To overcome this problem, low temperature gaseous oxidations are preferred.

No self-passivation of the oxide layer was achieved with gaseous oxidizing agents as expected for a strict digital etching. Oxide thickness is however controlled by the nature of the oxidizing agent and the exposure time. With O_2 from air, only thin oxide layers (< 1 nm) are obtained in a reasonable industrial timeframe. Such an oxide layer might not be sufficient for chemical dynamic to take place in the second step of digital etching. With O_3 as an oxidizing agent, thicker oxide layer (over 1.5 nm) can be produced with only 2 minutes of exposure. This makes O_3 valuable for an industrial process.

The oxide thickness increases with increasing time exposure to O_2 or O_3 . Material consumption can thus be managed as its only depends on oxide thickness in digital etch.

In terms of chemical composition, As V⁺ species appears on thick oxides. As highly oxidized arsenide species are very soluble, their presence will promote oxide dissolution during the second step of digital etching.

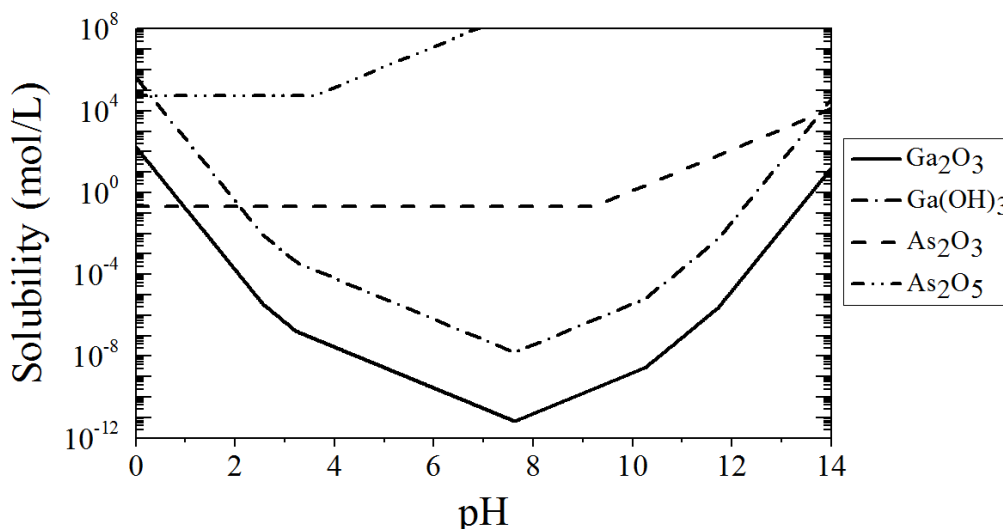


Fig. 1: Solubility of stable oxidized species of gallium and arsenide in function of pH (data taken from [4])

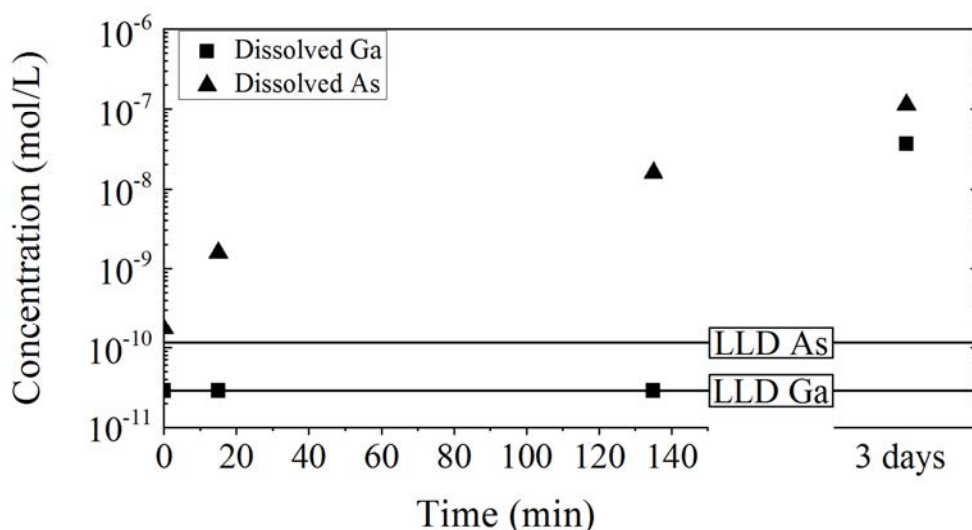


Fig. 2: Kinetic of dissolution of GaAs in stagnant H_2O_2 10%

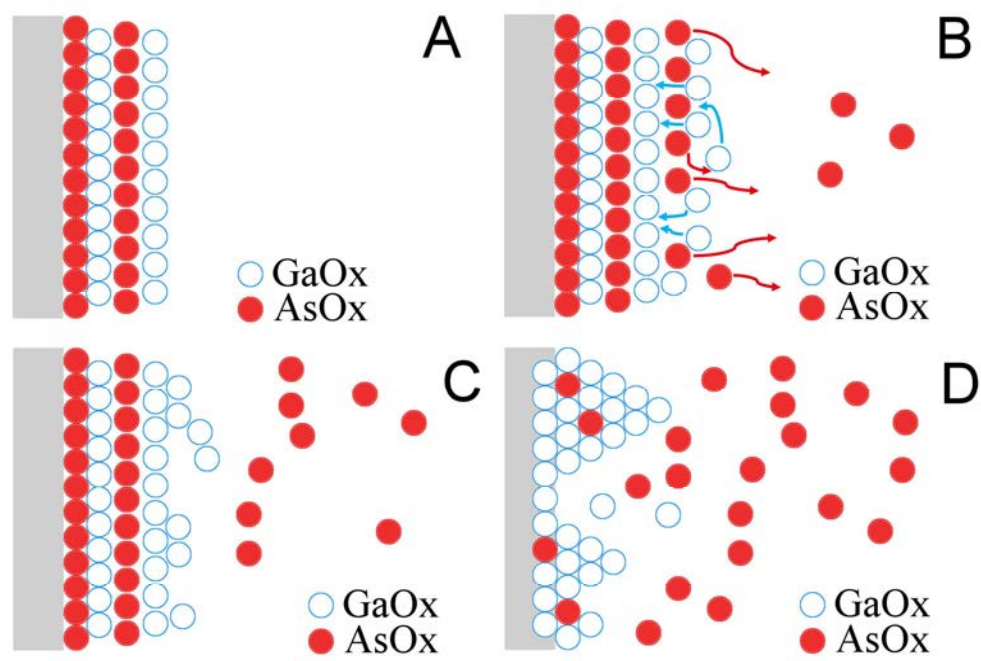


Fig. 3: Illustration of the mechanism of GaAs passivation in aqueous concentrated H_2O_2

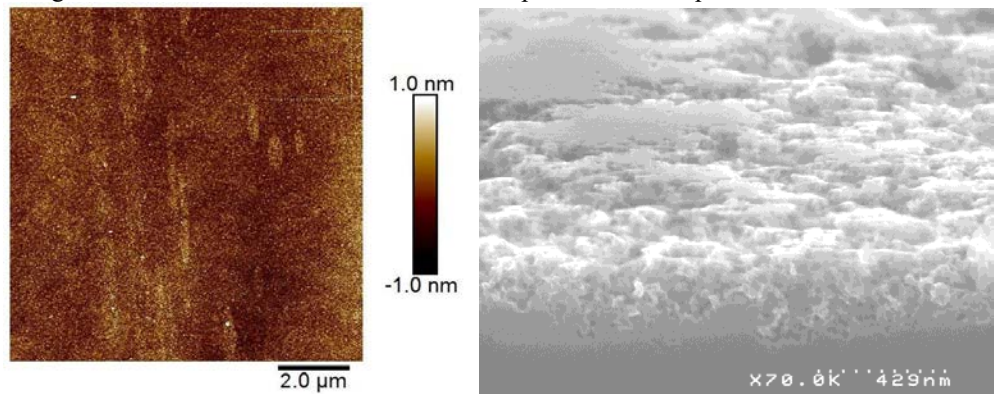


Fig. 4: (left) $10\ \mu\text{m} \times 10\ \mu\text{m}$ AFM scan of GaAs surface after 15 min in 10% H_2O_2 ($R_{\text{rms}}=0.33\ \text{nm}$, $R_{\text{max}}=11.3\ \text{nm}$), (right) SEM image after 72h

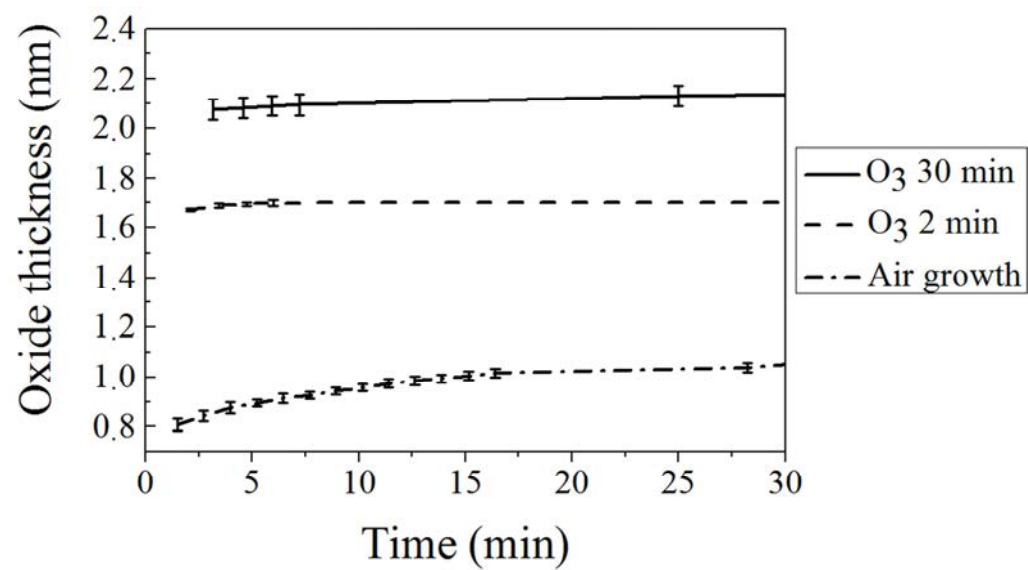


Fig. 5: Time dependance of the top layer oxide thickness in a clean-room environment after different treatments

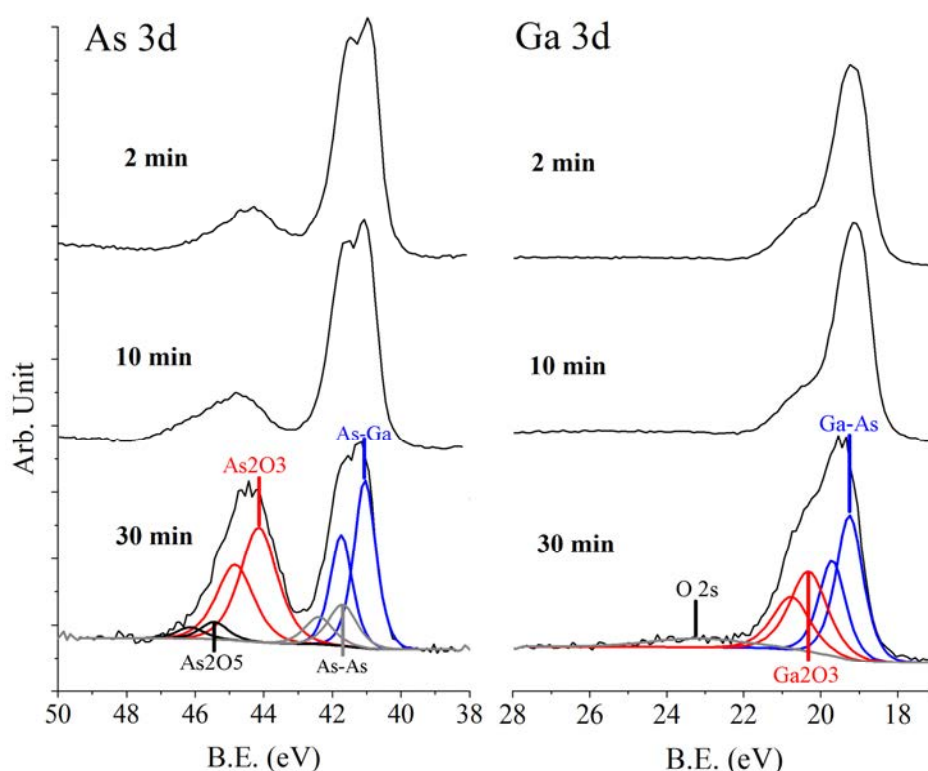


Fig. 6: As 3d and Ga 3d XPS spectra after different time exposure to gaseous O_3

References

- [1] S. Sioncke, D. P. Brunco, M. Meuris, O. Uwamahoro, J. Van Steenberghe, E. Vrancken, M. M. Heyns, Etch Rate Study of Germanium, GaAs and InGaAs: A Challenge in Semiconductor Processing, *Solid State Phenomena*, 145 (2009) 203-206.
- [2] G. C. DeSalvo, C. A. Bozada, J. L. Ebel, D. C. Look, J. P. Barrette, C. L. A. Cerny, R. W. Dettmer, J. K. Gillespie, C. K. Havasy, T. J. Jenkins, K. Nakano, C. I. Pettiford, T. K. Quach, J. S. Sewell, G. D. Via, Wet chemical digital etching of GaAs at room temperature, *Journal of The Electrochemical Society*, 143(11) (1996) 3652-3656.
- [3] M. Rebaud, M.C. Roure, V. Loup, Ph. Rodriguez, E. Martinez, P. Besson. Chemical treatments for native oxide removal of GaAs wafers. *ECS Transactions*, 69(8) (2015) 243–250.
- [4] M. Pourbaix, Atlas of electrochemical equilibria in aqueous solutions, National Association of Corrosion Engineers, Houston, 1974, pp. 429-434 & 517-523.
- [5] J. P. Jolivet, De la solution à l'oxyde - Condensation des cations en solution aqueuse, in: *Chimie de surface des oxydes*, Ed EDP Sciences, Les Ulis France, 1993, pp. 2.
- [6] F. Lukes, Oxidation of Si and GaAs in air at room temperature. *Surface Science*, 30 (1972) 91-100.
- [7] Z. H. Lu, B. Bryskiewicz, J. McCaffrey, Z. Wasilewski, M. J. Graham, Ultraviolet-Ozone oxidation of GaAs(100) and InP(100), *Journal of Vacuum Science & Technology B*, 11(6) (1993) 2033-2037.

CHAPTER 3:

FEOL: Etching

Thin Layer Etching of Silicon Nitride: Comparison of Downstream Plasma, Liquid HF and Gaseous HF Processes for Selective Removal After Light Ion Implantation

Olivier Pollet^{1, a}, Nicolas Posseme¹, Vincent Ah-Leung¹
and Maxime Garcia Barros²

¹ CEA, LETI, MINATEC Campus, 17 rue des Martyrs, 38054 Grenoble Cedex 9, France

² ST Microelectronics, 850 Rue Jean Monnet, 38920 Crolles France

^aolivier.pollet@cea.fr

Keywords: silicon nitride, spacer, layer modification, light ion implantation, selective removal, thin layer etching, gas-phase HF

Abstract. To overcome challenges related to spacer etching in sub-14nm FDSOI technologies, a novel approach was developed to achieve thin layer etching. This process is based on a prior modification of silicon nitride through light ion implantation in a plasma etch chamber, followed by selective removal of the modified layer. Several removal techniques were evaluated, relying on downstream plasma or hydrofluoric acid either in liquid or gas-phase.

Introduction

For technology nodes beyond 14nm silicon nitride spacer etching has become a major challenge. Conventional plasma etching techniques based on CHF_3/O_2 cannot achieve thorough nitride removal on horizontal surfaces without inducing either CD loss or Si/SiGe source/drain recess. This leads to either gate leakage increase or poor raised source/drain epitaxy. To overcome atomic scale control issues faced with continuous plasma processes, several techniques aiming at achieving atomic layer etching or thin layer etching were recently described [1]. An original etching approach has been reported which consists in modifying the silicon nitride through H_2 ion implantation by plasma (ICP or CCP) and then selectively removing the modified fraction of the layer thanks to chemical etching [2]. Layer modification depth is controlled thanks to plasma parameters (bias voltage and process time). This unconventional technique was demonstrated on 14nm FDSOI logic device and showed less than 1nm spacer CD loss, less than 0.6nm SiGe recess which enabled defect-free source/drain epitaxy [2]. Mechanisms for silicon nitride modifications and selective removal are discussed in this article by comparing downstream plasma, liquid-phase HF and gas-phase HF as removal techniques.

Experimental

Experiments were carried out on 300mm silicon wafers deposited with 40nm LPCVD silicon nitride. Layer modification was done by hydrogen implantation in a commercially available capacitively-coupled plasma chamber. Selective removal of implanted vs non-implanted nitride relied on HF at different concentrations, either in liquid or gas-phase, or on remote plasma (using NF_3/NH_3 gas mixture combined with annealing). Film modification and removal mechanisms were investigated thanks to ellipsometry, AFM, MIR, ATR, FTIR, XPS and SEM observations.

Results and discussion

SiN layer characterization after modification. ATR and MIR spectra recorded on SiN layer after hydrogen implantation in a CCP chamber are shown in Figure 1. They exhibit a noticeable increase in Si-H and N-H peaks (respectively 2200cm^{-1} and 3300cm^{-1} [3]) after H_2 plasma with respect to pristine material. Additionally Si-N peak observed at 1100cm^{-1} on as-deposited SiN turns into a

larger peak with a slight shift in wavenumber after implantation, revealing silicon oxidation since this new peak at 1050 cm^{-1} corresponds to Si-O stretching mode vibration. Silicon nitride oxidation after hydrogen implantation is confirmed by XPS analyses carried out pre and post-treatment in CCP chamber (Figure 2). While the pre-treatment spectrum shows one single peak at Si-N binding energy (102eV), the post-treatment analysis reveals two peaks at 102eV (Si-N) and 103eV (Si-O).

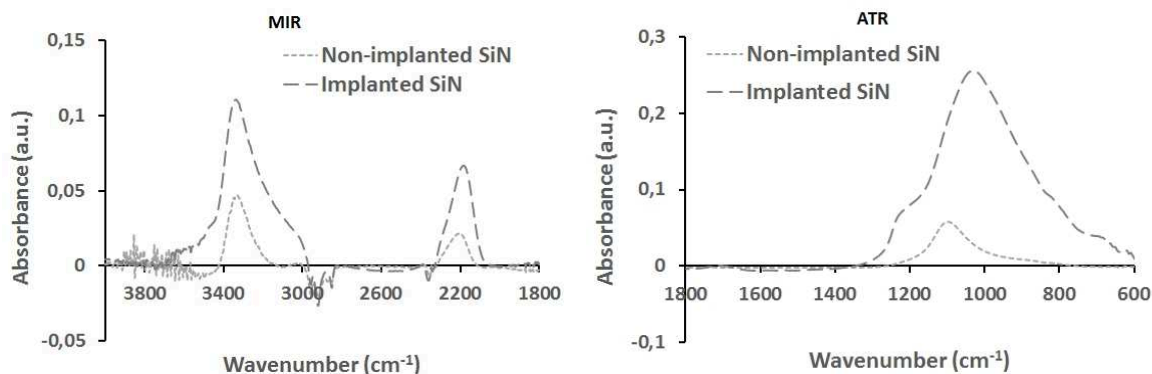


Figure 1: MIR (left) and ATR (right) spectra recorded on SiN without and with hydrogen implantation

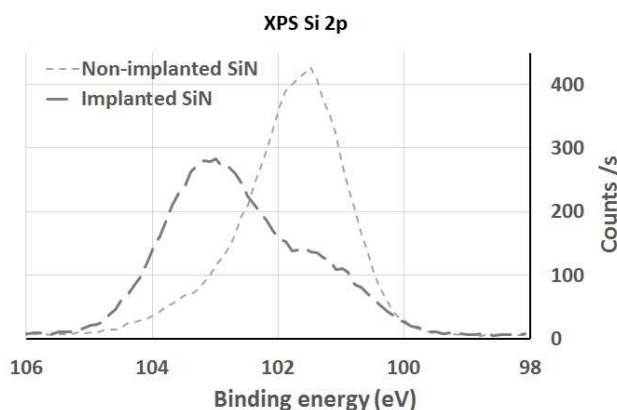


Figure 2: XPS Si-2p analyses of SiN layer pre and post- H_2 implantation in CCP chamber

To figure out the depth of modification within the silicon nitride layer a simple test consisting in etching the layer in dilute HF (1% weight concentration) for different times was used. As long as the modified fraction of the material is being etched away the etch rate is substantially higher than that of pristine SiN. Once the etch rate drops to that of pristine SiN, the modified layer has been thoroughly removed. This method was used to plot an abacus of the modification depth as a function of bias voltage and process time which are the two main parameters influencing the implantation depth and dopant dose.

In following analyses CCP chamber parameters were set in order to achieve a depth of modification equal to 20nm.

Post-modification removal. Several techniques were evaluated to remove the implanted silicon nitride layer. Since the targeted application is the fabrication of spacers above the transistor gate, the removal process must be selective to unmodified SiN (i.e. the spacer material), silicon dioxide (gate hardmask and STI) and Si/SiGe (source/drain materials). Of course the removal process should not leave any residues on surface either.

The first method tested was liquid-phase hydrofluoric acid which does etch H_2 plasma treated SiN as explained above. A decent selectivity to non-implanted SiN as high as 8 was measured with this

removal process while infra-red spectra recorded after HF treatment showed complete disappearance of peaks representative of layer modification: the IR spectra after HF are identical to those of as-deposited SiN for both MIR and ATR with lower intensities due to the thickness decrease compared to the initial layer. The weakness of this removal process remains its low selectivity to silicon dioxide which is lower than 2 (implanted LPCVD nitride to thermal oxide). Though by carefully controlling the liquid-phase HF process in time and concentration, spacer etching on 14nm transistor gate was demonstrated while preserving SiO₂ hardmask from excessive etching, without spacer foot formation and with a subsequent defect-free source/drain epitaxy as can be seen on TEM picture in Figure 3.

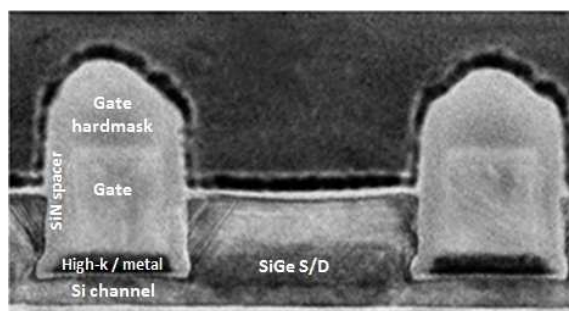


Figure 3: TEM picture of 14nm FDSOI transistor gate. Spacer etching was performed by H₂ plasma implantation followed by liquid-phase HF etching

Because of the lack of selectivity to silicon dioxide with the liquid-phase HF process, other methods were tested to etch away the modified SiN layer. Those rely on dry treatments such as remote plasma or gas-phase HF.

Figure 4 shows IR analyses (MIR and oblique transmission FTIR) carried out on silicon nitride after reaction in NF₃/NH₃/He remote plasma. New peaks at 770cm⁻¹ and 1440cm⁻¹ appear after treatment by remote plasma which correspond respectively to Si-F and N-H (wagging mode) bonds. Additionally the absorbance at 3300cm⁻¹ of the N-H bond in stretching mode is increased to a large extent compared to that observed after hydrogen implantation which, combined with the advent of the wagging mode of the same bond, suggests the formation of ammonium ions NH₄⁺. Therefore infrared analyses point towards the formation of ammonium hexafluorosilicate (NH₄)₂SiF₆ by reaction between the modified SiN layer and radicals formed in NF₃/NH₃/He remote plasma. This compound was previously reported to form by reaction of a hydrogenated silicon nitride film with a fluorinated plasma [3]. Data in the literature state that ammonium hexafluorosilicate decomposes into SiF₄ and NH₃, which are both volatile species, as temperature rises [4] therefore the reacted layer can then be eliminated by means of a thermal anneal. Infrared spectra recorded after annealing wafers above 100°C for 120 seconds indeed no longer exhibit the absorbance peaks described above and spectra become very similar to those recorded on as-deposited SiN thereby demonstrating effective removal of the SiN modified layer. However there is still one major weakness in applying NF₃/NH₃ based remote plasma to perform spacer etching in that the etch rate of silicon dioxide is significantly higher than that of H₂-implanted SiN which induces an unacceptable consumption of gate hardmask and shallow trench insulation. This is illustrated in Figure 5 comparing film consumptions during a 45s remote plasma exposition for pristine, implanted SiN and SiO₂ as a function of NF₃ ratio in the gas flow.

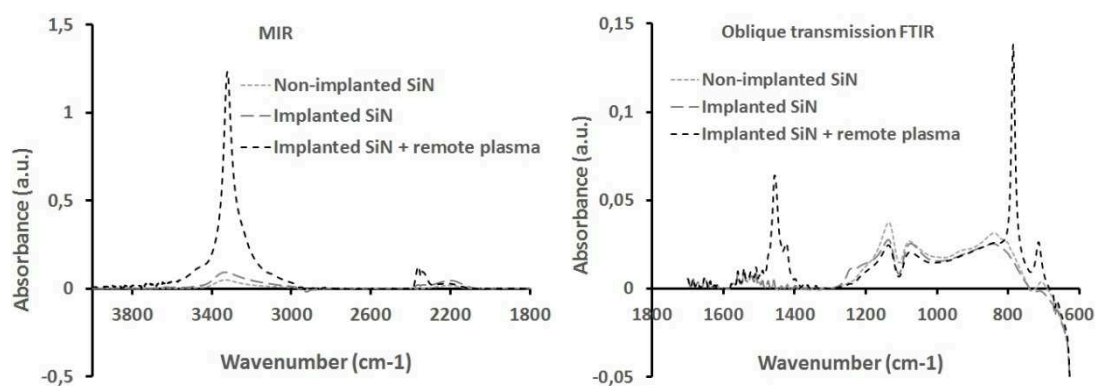


Figure 4: MIR (left) and oblique transmission FTIR (right) spectra of SiN layer after H₂ implantation and reaction with remote NF₃/NH₃ plasma. Non-implanted SiN spectrum showed for reference

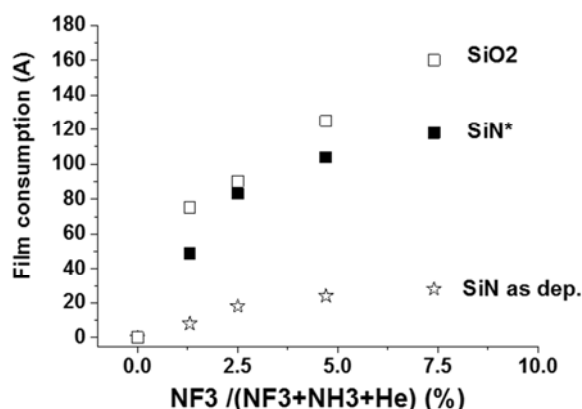


Figure 5: Etched amounts of SiO₂, pristine SiN and H₂-implanted SiN in NF₃/NH₃/He remote plasma as a function of NF₃ ratio. Downstream plasma exposition was followed by a 2min / 100°C annealing step to remove byproducts

To overcome this major drawback of poor selectivity to SiO₂ in both liquid-phase HF and remote NF₃/NH₃ plasma, an alternative dry process, based on gaseous HF, was developed in order to fulfill spacer etching requirements, i.e. remove the H₂-implanted SiN with a high selectivity to pristine SiN and SiO₂. Surface chemical composition was probed by infrared spectroscopy after reaction of modified SiN with gaseous HF under optimized conditions, which revealed again the formation of the ammonium hexafluorosilicate compound as is observed in the case of the remote plasma technique: the same absorbance peaks at 1440cm⁻¹ and 3300cm⁻¹ (N-H vibration in respectively wagging and stretching mode) and 770cm⁻¹ (Si-F bond) are present on IR spectra.

Conversely infrared spectra recorded on silicon dioxide after the same gaseous HF and remote plasma processes unveil a very different surface composition depending on the process (Figure 7). In the case of gas-phase HF, IR absorbance measured by Attenuated Total Reflection in the 600-1800cm⁻¹ region exhibits the same representative peaks as those observed on unprocessed SiO₂, i.e. the Si-O bending and Si-O-Si stretching vibration modes (respectively 800cm⁻¹ and 1090cm⁻¹). A slight increase in intensity of the 1050cm⁻¹ peak may reflect formation of a reaction byproduct on surface after gas-phase HF to a limited extent, but obviously no major modification of the SiO₂ layer occurs by treatment with gaseous HF. The result obtained with remote plasma is drastically different in that high intensity peaks appear at 770cm⁻¹, 1440cm⁻¹ and 3300cm⁻¹, thereby highlighting the formation of (NH₄)₂SiF₆ similarly to what happens with H₂ plasma treated SiN processed in remote plasma. This result is a major difference between the gas-phase HF process and remote plasma and the fact that no reaction occurs with silicon dioxide in gaseous HF is likely to translate into high selectivity which is desirable for spacer etching.

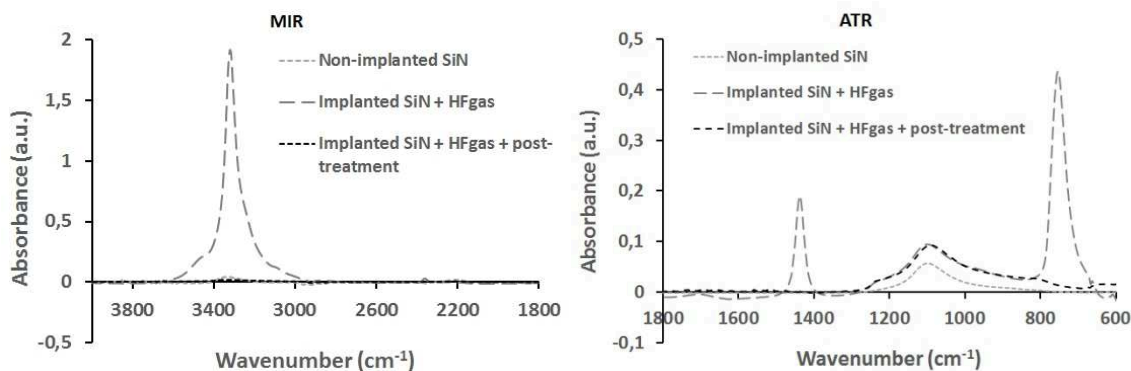


Figure 6: MIR and ATR spectra of SiN layer implanted by H_2 ions in plasma chamber after reaction in gaseous HF and post-treatment

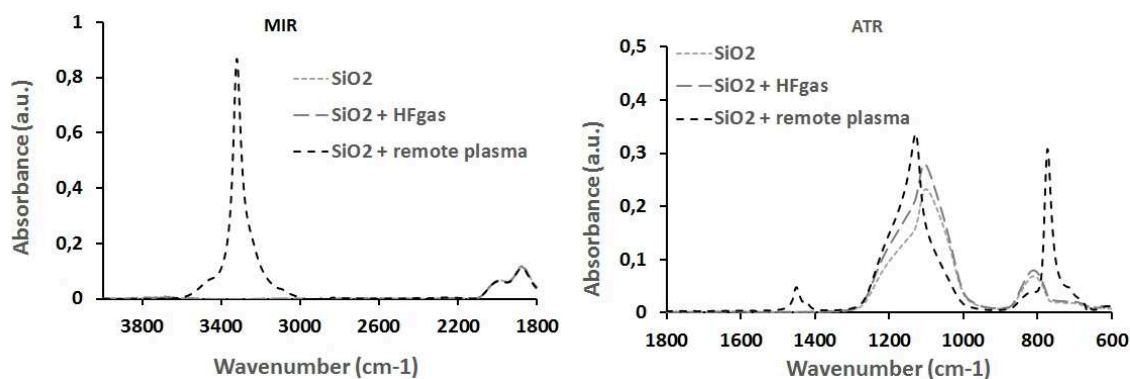


Figure 7: MIR and ATR spectra for SiO_2 after treatment with gaseous HF and remote NF_3/NH_3 plasma

Nevertheless this method also requires a thermal post-treatment to dispose of the ionic $(NH_4)_2SiF_6$ compound and recover a pristine SiN surface as can be seen in IR absorbance plots in Figure 6 where related peaks are no longer present after post-treatment and the corresponding spectra are quite similar to those of as-deposited SiN. To confirm the suitability of this method for spacer etching, silicon dioxide, pristine silicon nitride and modified silicon nitride were all three processed for a fixed time while HF concentration in the gas phase was varied in order to figure out etching selectivities as a function of process parameters. The resulting chart in Figure 8 shows that gaseous HF process can achieve a high selectivity to both SiN and SiO_2 (respectively 31 and 39 at $0.5C_0$ in normalized HF concentration) together with a large process window since HF concentration can be doubled with respect to optimum conditions and still maintain selectivity above 10. Therefore, considering these excellent selectivity values and the intrinsically infinite selectivity of hydrofluoric acid to Si and SiGe the optimized gaseous HF process is thoroughly suited for spacer etch applications.

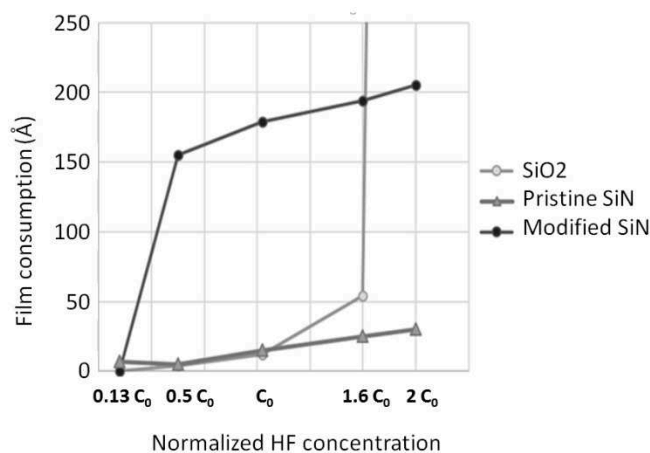


Figure 8: Etched amount of SiO_2 , pristine SiN and modified SiN as a function of HF concentration in gas-phase HF process

Conclusions

An original thin layer etching method has been developed for silicon nitride targeting spacer etching applications for 10nm technology node and beyond. This relies on the prior modification of a controlled thickness of silicon nitride by means of hydrogen implantation in a capacitively-coupled plasma chamber followed by the selective removal of the modified fraction of the layer thanks to a gaseous HF process combined with a post-treatment. This sequence outperforms plasma etch processes currently used for spacer fabrication in terms of selectivity to other materials exposed at this stage of transistor manufacturing and offers a much broader process window. Evaluation of the optimized process sequence on device wafers is underway in order to demonstrate that it does not induce spacer CD loss or foot formation and to verify the compatibility of this method with downstream source/drain epitaxy.

References

- [1] G.S. Oehrlein, D. Metzler, C. Li, ECS J. Solid State Sc., 4 (6), pp. N5041-N5053, 2015
- [2] N. Posseme, O. Pollet, S. Barnola, Appl. Phys. Lett. 105, 5 (2014).
- [3] V.P. Tolstoy, I.V. Chernyshova, V.A. Skryshevsky, *Handbook of Infrared Spectroscopy of Ultrathin Films*, (John Wiley & Sons, 2003)
- [4] W.R. Knolle, R.D. Huttemann, J. Electrochem. Soc., 135 (10), pp. 2574-2578, 1988
- [5] D.L. Perry, *Handbook of Inorganic Compounds*, 2nd Ed. (CRC Press, 2011)

Selective Etching of Silicon Oxide Versus Nitride with Low Oxide Etching Rate

Hsing-Chen Wu^{1, a *}, Sheng-Hung Tu^{1, b} Min-Chieh Yang^{1, c}
and Emanuel Cooper^{2, d}

¹Entegris Inc., Taiwan Technology Center, 1F, no. 669, Sec. 4, ZhongXing Road, Zhudong Town, Hsinchu County 310, Taiwan (R.O.C.)

²Entegris Inc., 7 Commerce Drive, Danbury, Connecticut 06810 USA

^aMegan.Wu@entegris.com, ^bSpencer.Tu@entegris.com, ^cJack.Yang@entegris.com,

^dEmanuel.Cooper@entegris.com

Keywords: Wet etching, silicon oxide, silicon nitride, solvent, fluoride, BOE solution.

Abstract. This paper describes both aqueous and solvent-based formulations aimed at etching silicon oxide (SiO_x) with etching rates (E/R) of the order of 10-20 Å/min with selectivity greater than 5 with respect to silicon nitride (SiN_x). Diluted hydrofluoric acid (dHF) with very low pH was tried first but the selectivity was found to increase only with higher SiO_x E/R. Solvent-based formulations derived from previous work also behaved in a similar way, however its SiO_x E/R could be reduced by modifying the total fluoride concentration inside formulation. Finally, we found that low SiO_x E/R could also be implemented in the diluted buffer-oxide etch (BOE) solution and the selectivity could be adjusted by addition of a specific surfactant at a very low concentration level.

Introduction

With the continued demand for improving device performance, scaling down device dimension has long been critical. Tight control of etching rates or pre-deposition surface cleaning became more important. It has been realized that etching with high selectivity between silicon oxide and nitride films in aqueous fluoride solution was difficult to be achieved. Fluoride-contained aqueous solutions are known to remove silicon oxide (from thermal oxide to PETEOS-like materials) rapidly by properly choosing different conditions such as: concentration, pH, dissociation constant (for instance, solvent content) and temperature. It is also known that acidic fluoride will attack silicon nitride to various degrees and generally shows low selectivity between SiO_x to SiN_x . Harrap has reported high Si_3N_4 : SiO_2 selectivity of 85:1 in a highly diluted hydrofluoric acid solution of 0.0075% at 85 °C, however the etch rate of nitride was very low (6 Å/min) [1].

From the equilibrium of fluoride species and the preferred reactivity to silicon nitride/ silicon oxide by monofluoride/ difluoride species, it's suggested that highly diluted HF (< 0.01%) would show mainly monofluoride and favor nitride etching. Besides, increase temperature would increase both nitride/ oxide etch rates but nitride was faster than oxide. If a low oxide etch rate was required, low pH will preferred to neutral species that diminish the reactivity. Addition of solvent that reduce solution polarity can also shift the equilibrium to neutral species and change the reactivity in a non-linear manner [1-2].

The present paper describes selective removal of SiO_x materials with E/R around 10 Å/min, with the associated requirements of > 5:1 selectivity to SiN_x and good compatibility to poly-silicon (poly-Si) and silicon carbonitride (SiCN). First, efforts were made to explore possible answers using aqueous-based formulation due to concern about cost and the impact on the environment. Diluted HF solutions in different pH ranges were tried, but the SiO_x etch rate (E/R) was too high to be acceptable. On the other hand, formulations related to HF and its ammonium salts in a solvent-based system with low deionized water (DIW) content (< 10%) were tested as extension of our previous study that was applied in an anhydrous environment [3]. Finally, modifications for diluted BOE solutions with screening of different surfactants were also investigated in this paper.

Experimental details

In the aqueous formulations, different amounts of 36% hydrochloric acid (36% HCl, BASF) were added in order to reduce the pH of diluted HF solutions with HF concentrations from 0.05% to 1%. The solvent-based formulations were prepared using 49% hydrofluoric acid (49% HF, BASF), and the fluoride-containing ammonium salts were referred as salt M and N (Alfa Aesar). Solvent 1 was less than 20% (Aldrich), solvent 2 may vary from 70-80% (JT Baker), and the total DIW content was less than 10%. Dilution of BOE solutions was proceeded into two ways, one by directly diluting the whole solutions by 10-fold (BOE: DIW = 1: 9 in wt %, indicated by "10X" in the following paper). The other way was by taking 1/10 of raw materials of NH_4F and HF then adding the expected amount of cationic surfactants (S1-S4, <0.05%) with different hydrophobic chains. All test wafers were provided by the customer. Etch rates were measured by ellipsometer (J.A. Woollam), with different reaction time ranges from 0.5-2 min owing to different initial film thicknesses which were 30-300 Å for SiO_x and 40-300 Å for chemical vapor deposition (CVD) SiN_x . Both oxide and nitride etch rates were calculated by the film loss divide by reaction time. A surface pre-treatment of SiN_x film was done by dipping SiN_x film in 1:100 dHF for 30 sec, the results were included in next section of this paper. Surface tension was measured by force tensiometer (KRÜSS, K11). All processes were performed in Teflon or PFA beaker with stirring rate of 360 rpm, at room temperature (RT, 21 ± 1 °C), rinsing with DIW, and blowing dry with nitrogen.

Results and Discussions

It was found that acidic dHF solutions ($\sim 0.1\%$) showed low selectivity (0.8-0.9) between SiO_x and SiN_x . In neutral pH they did etch oxide and nitride, but exhibited very low etch rates at RT. Therefore, dHF solutions with concentration of 0.1ϕ to 2ϕ % were split (ϕ was a factor between 0.1-1) and adjusted to very low pH of 0.5 by adding 36% HCl. Compared with HCl, HF can be considered a weak undissociated acid; therefore the HCl amount required to bring a given HF solution to pH=0.5 can be obtained by simple calculation. As illustrated in Figure 1, SiO_x E/R was very low (1.7 Å/min) with $[\text{HF}] = 0.1\phi$ % and selectivity to SiN_x was 0.5; the selectivity became greater than 1 when $[\text{HF}] > 0.3\phi\%$. When increasing HF concentration, SiO_x E/R were found to rise quickly relative to SiN_x , and the selectivity of $\text{SiO}_x/\text{SiN}_x$ also increased from 0.5 to 3.8; however, SiO_x E/R already reached 150 Å/min at this point. It means that higher SiO_x E/R can get higher selectivity in this system, but such high oxide E/R has far deviated from its target E/R of 10 Å/min.

For the solvent-based formulation, fluoride sources were defined in a way similar to the description in a previous patent [3]. Parameters were defined as follows: (1) The total wt% of fluoride ($[\text{F}]_{\text{Total}}$), and (2) The ratio of the fluoride-contained salt M to HF or salt N to HF. For the solvent parts, solvent 1 was fixed at values in the 10-20% range; solvent 2 was allowed to vary slightly to balance the total solution to 100%, due to the presence of water in some fluoride species used here. SiO_x E/R was monitored in $[\text{F}]_{\text{Total}}$ of $0.5x$ to $1.5x$ with different ratios between salt M and HF; the results are summarized in Figure 2, where SiO_x E/R is found to increase as $[\text{F}]_{\text{Total}}$ increased. In addition, within the same $[\text{F}]_{\text{Total}}$, it was observed that SiO_x E/R slowly dropped with increasing the ratio of salt M to HF.

The $\text{SiO}_x/\text{SiN}_x$ selectivity is illustrated in Figure 3. The trend of selectivity change is similar to SiO_x E/R, but with more fluctuations caused by the SiN_x E/R. Since it is known that silicon nitride surface presents a thin layer of surface oxide, a pre-treatment of SiN_x was done by dipping SiN_x coupon in 1:100 dHF for 30 sec, then processing in the same oxide etching solution. The pretreated SiN_x E/R was about 4-fold lower than the un-pretreated one. If the surface oxide of SiN_x can be well controlled, the selectivity should be even better. As revealed in Figure 3, there are many points showing selectivity higher than 5; however, these points also show SiO_x E/R higher than 20 Å/min when comparing with Figure 2. For example, see the case of $[\text{F}]_{\text{Total}} = 0.5x$ with salt M: HF = 0.2λ : 1, in which selectivity was 5.12 but SiO_x E/R has been >35 Å/min as indicated in Figure 2. From the previous cases of acidic dHF and solvent-based formulations described above, it is clear that the trends for lower SiO_x E/R and higher selectivity are contrary to each other. Working below RT would

make more formulations practical, but the necessary equipment is not widely available in manufacturing plants.

On the other hand, we next attempted to replace HF by salt N, beginning with low $[F]_{\text{Total}}$ with high salt M to salt N ratio. The results are listed in Table I, where the $[F]_{\text{Total}}$ values were x and $0.75x$ with ratio of $2\lambda:1$. In this range, SiO_x E/R could be less than 20 \AA/min with selectivity around 5. Compared to the salt M: HF case, using salt M: salt N showed lower oxide E/R and slightly higher selectivity, which may be the effect of less water content inside the final formulation. The compatibility tests for etch rates of poly-Si and SiCN at RT gave E/R's of 1.06 and 0.28 \AA/min , respectively.

The final trials were performed with modified diluted BOE solutions. A common BOE solution comprises a 6:1 volume ratio of 40% NH_4F (AF) in water to 49% HF in water. Besides, addition of surfactants into BOE solutions is generally known to improve the wettability and provide a high etching selectivity ratio of an oxide film to a nitride film [4-5]. Cationic surfactants with different hydrophobic chain (S1 to S4) were applied for reducing the surface tension of solutions and for adjusting $\text{SiO}_x/\text{SiN}_x$ selectivity. First, different fluoride sources were compared at a common content of $2\sigma\%$ of S1 inside (due to very low concentration of surfactant was added, surfactant was prepared in a stock solution with $2\sigma\%$, where σ is a factor less than 1). Fluoride sources were tried as: AF, (AF + HF), and [AF + hexafluorosilicic acid (AF + HFSA))] with 10X dilution as listed in No.1-3 of Table 2, where α is the HF% we used and ζ is the HFSA% which is equal in molarity to $\alpha\%$ of HF. The results revealed that neutral pH of AF solution showed E/R $<1 \text{ \AA/min}$ for both SiO_x and SiN_x ; even when heating up to 50°C , the E/R was still $<2 \text{ \AA/min}$. On the other hand, in the cases of AF plus HF or HFSA, the SiO_x E/R were 14-15 \AA/min , and selectivity to two kinds of SiN_x films can be easily >5 , or even >10 . Since the performance of HF and HFSA was similar, HF was preferred due to its cost and lower trace metal level; the remaining issue was the high surface tension for the solution after 10X dilution.

It is assumed that direct 10X dilution of the BOE solution would increase the surface tension due to the left surfactant concentration was only 1/10 of the original solution. In order to keep low surface tension of the solution, the surfactant concentration should be used as an independent variable. Thus chemical preparation was done by taking 1/10 amount of both AF and HF together with total $2\sigma\%$ of S1 inside the formulation as listed in No.4 in Table 2, where $\beta = \alpha/10$. However, there was only small surface tension drop in No.4 but its SiO_x E/R was increased more than 2-fold compared to No.2. Besides, influences on SiO_x E/R by reducing [AF] or [HF] were tested as listed in No.5-6 in Table 2 where [HF] and [AF] were reduced for 1/3 and 1/6 compared to No.4. The results showed that both factors could decrease SiO_x E/R, but based on the total reduced concentration, reducing HF might be more effective than reducing AF.

Based on the previous observation, screening other surfactants was the first priority for reducing the solution surface tension. As shown in Table III, [HF] was lowered to one-third of β , and surfactants S1-S4 were tried with concentration from 2σ to $6\sigma\%$, and only a solution with S4 at a level of $2.2\sigma\%$ could get a surface tension of less than 40 mN/m . Then an additional split in the HF concentration with $4.4\sigma\%$ S4, as listed in Table IV, showed lowest SiO_x E/R of about 12 \AA/min with selectivity of 6.3 in the case of $[\text{HF}] = \beta/3$; both E/R and selectivity can be repeated with average value of $11.3 \pm 0.9 \text{ \AA/min}$ and selectivity of 7.9 ± 3.2 . The trend of oxide E/R vs. the selectivity is still consistent with the previous cases, i.e. higher oxide E/R correlates to higher selectivity to nitride.

Conclusions

The trend of SiO_x E/R and its selectivity to SiN_x in the three systems presented in this study was consistent, i.e. with higher SiO_x E/R we also obtained higher selectivity; however, the requirement of a relative low E/R of SiO_x makes reaching the selectivity goal difficult. We found both solvent-based and aqueous BOE-based formulations in which SiO_x E/R was about 14 and 11 \AA/min , respectively, with selectivity to SiN_x greater than 5.

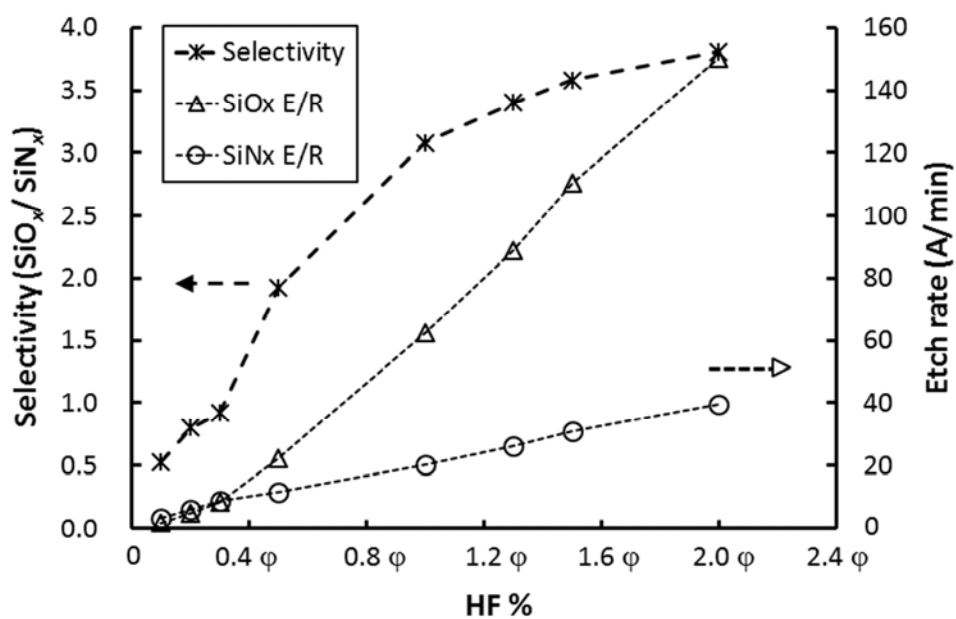


Figure 1: Etch rates for SiO_x and SiN_x and selectivity of SiO_x/ SiN_x with different [HF] at pH=0.5.

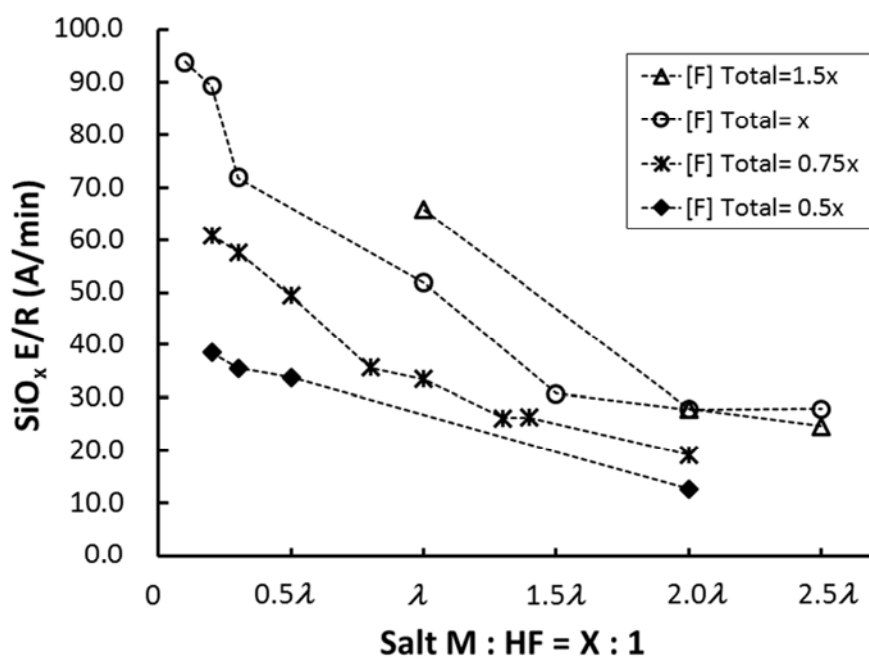


Figure 2: SiO_x etch rate of total fluoride concentration of 0.5x-1.5x% with different salt M to HF ratio.

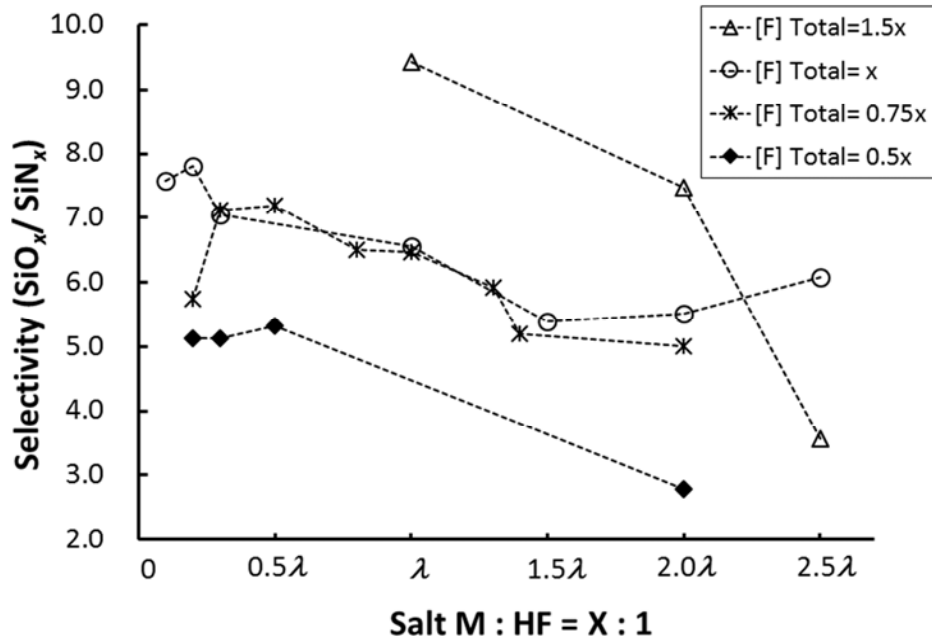


Figure 3: Selectivity ($\text{SiO}_x/\text{SiN}_x$) of total fluoride concentration of 0.5x-1.5x% with different salt M to HF ratio.

Table I: Etching rates and selectivity when using (salt M: salt N) and (salt M: HF) as oxide etchants.

[F] _{Total} (%)	Salt M: Salt N ratio	Salt M: HF ratio	SiO _x E/R (Å/min)	SiN _x E/R (Å/min)	Selectivity (SiO _x /SiN _x)
x	2λ:1	-	16.67	3.02	5.52
0.75x	2λ:1	-	14.41	2.97	5.42
x	-	2λ:1	28.87	3.58	5.40
0.75x	-	2λ:1	19.22	3.84	5.00

Table II: pH, etching rates, and surface tension of modified BOE solutions with different fluoride sources. (*Ori: original solution, **10X: 10-fold diluted solution, #β=α/10)

No.	DIW	40% AF	49% HF	34% HFSA	σ % S-1 stock soln.	pH		Etch rates		Surface tension of (10X) soln. (mN/m)
						Ori.*	10X**	SiN _x	SiO _x	
								(Å/min)		
1		60			2	7.0	6.5	0.61	0.67	73.93
2	Balance	60	α		2	6.4	5.3	1.62	14.60	72.82
3	to	60		ζ	2	6.0	5.0	1.51	15.83	73.78
4	100%	6	β [#]		2	5.2		1.89	37.15	69.01
5		6	(2/3)β		2	5.5		1.26	23.16	68.68
6		5	β		2	5.2		1.44	25.86	68.35

Table III: Surface tension of solutions with lower [HF] and pH of solution with surface tension less than 40 mN/m. (#β= α/10)

No.	DIW	40% AF	49% HF	σ % S1 stock soln.	σ % S2 stock soln.	1.3σ % S3 stock soln.	1.1σ % S4 stock soln.	Surface tension of soln. (mN/m)	pH
								(mN/m)	
1		6	β [#] /2.5	2				68.85	
2		6	β /3	2				70.44	
3	Balance	6	β /3		2			66.53	
4	to 100%	6	β /3			2		58.77	
5		6	β /3				2	39.98	5.5
6		6	β /3	6				65.03	
7		6	β /3		6			56.60	

Table IV: pH, etching rates, and surface tension of modified BOE solutions with different [HF].

No.	DIW	40% AF	49% HF	1.1σ % S4 stock soln.	pH	Surface tension	Etch rates		Selectivity (SiO _x / SiN _x)
							SiN _x	SiO _x	
		(%)				(mN/m)	(Å/ min)		
1	Balance	6	β/ 2	4	5.5	33.29	2.28	22.16	9.73
2	to	6	β/ 2.5	4	5.7	34.16	1.96	17.33	8.82
3	100%	6	β/ 3	4	5.7	34.03	1.95	12.24	6.27

References

- [1] V. Harrao: *Semiconductor Silicon 1973*, edited by. H. R. Huff and R. R. Burgess, Princeton, NJ, USA, 1973, p. 354
- [2] D. Martin Knotter, Nigel Stewart, and Ian Sharp, *Solid State Phenomena*, 103-104 (2005) 103-106.
- [3] Martha. Rajaratnam , David.D. Bernhard, and David.W. Minsek, PCT WO 2007/044447 A2.
- [4] Jung H. Lim, Dae H. Kim, Chang J. Yoo, and Seong H. Park, US 20120070998 A1.
- [5] Chang-S. Mun, Hyung-H. Ko, Woo-G. Shim, Chang-K. Hong, and Sang-J. Choi, US 20060183297 A1.

Metrology for High Selective Silicon Nitride Etch

Chuannan Bai, Guang Liang, and Eugene Shalyt*

ECI Technology, 60 Gordon Drive, Totowa, New Jersey 07512

*eshalyt@ecitechnology.com

Keywords: Silicon Nitride etch, low temperature etching, phosphoric acid, organo-silicon, selectivity, metrology, Near Infrared (NIR)

Abstract. This paper demonstrates a variety of metrology methods for high selective silicon nitride etch in different process baths. Capability of measuring full matrix components is also presented. For the measurement of H_3PO_4 and H_2O , both NIR spectroscopy and conductivity methods work well. Si measurement in the etchant that contains an organo-silicon compound requires a new reagent development in comparison with the original reagent method developed for regular process contains inorganic Si only.

Introduction

Selective Silicon Nitride etch has been a building block of semiconductor manufacturing for many years. Traditionally, concentrated phosphoric acid at nearly boiling temperature (165°C) is used [1]. Recent semiconductor processes such as 3D Memory and FinFET logic require an enhancement in $\text{Si}_3\text{N}_4:\text{SiO}_2$ selectivity in excess of 100. Selectivity is traditionally adjusted through increasing the levels of dissolved SiO_2 to suppress further SiO_2 etch. However, Si has very low solubility in H_3PO_4 and easily crystallizes/reattaches itself above 100 ppm. The required $\text{Si}_3\text{N}_4:\text{SiO}_2$ selectivity may be attained via etchants that are comprised of an organo-silicon compound, phosphoric acid, and water [2,3]. Organosilicate improves the solubility of Si, enabling both high selectivity and etch rate. An alternative approach to enhance selectivity is to use lower temperature processes ($<130^\circ\text{C}$), which also suppresses SiO_2 etch and provide excellent selectivity, but at presumably lower overall etch rates. Another advantage of the lower temperature is that there is no damage to surrounding silicon dioxide and metal silicide structures [4].

While overall etch rate is dominated by the combination of process temperature and % H_2O , selectivity is controlled by the Si level. Water content can be monitored through conductivity, refractive index, or the preferred method, non-contact Near Infrared (NIR) Spectroscopy. There is a variety of commercial analyzers for this purpose. The main challenge is measurement of Si. We have previously described an automated method for analysis of Si in traditional Si_3N_4 etching solutions [5]. However, high selectivity processes present new metrology challenges.

H_3PO_4 and H_2O Measurement

H_3PO_4 and its counterpart H_2O are measured by both NIR spectroscopy and conductivity methods. Table I summarizes the performance of the two methods

Table I. Overview of methods for the analysis of H_3PO_4

Method	Accuracy (wt%)	Standard deviation (wt%)	Type	Time per analysis	Targeted Group
NIR	0.1	0.05	Non-reagent	Real-time (sec)	O-H
Conductivity	0.2	0.1	Non-reagent	Real-time (sec)	H_3O^+ , H_2PO_4^- , HPO_4^{2-}

NIR Spectroscopy. Near-infrared (NIR) spectroscopy has been successfully implemented for real-time monitoring of various cleaning and etching solutions used in the semiconductor industry [6]. The NIR spectroscopy method at ECI utilizes a broad range of spectra combined with multivariate calibration techniques to extract the desired chemical information (see Eq. 1). In a simplified form, the algorithm is based on determining the optimum set of coefficients to provide the best correlation:

$$c_{\text{analyte}} = c_{\lambda_1} \times A_{\lambda_1} + \cdots c_{\lambda_i} \times A_{\lambda_i} + \cdots c_{\lambda_n} \times A_{\lambda_n} + c_0 \quad (1)$$

where c_{λ_i} is the coefficient at wavelength λ_i and A_{λ_i} is the absorbance at wavelength λ_i . A sample is examined as it flows through the inert flow cell. The InGaAs array-based spectrometer with thermoelectric temperature tuning feature contains no physically moving hardware parts, providing robust analysis especially beneficial to process control in the IC fabrication environment. The application is fully automated and allows continuous measurements under “in-flow” conditions. Entire system miniaturization, real-time results, “non-reagent”, and the “non-contact” nature of the probe make this technique highly attractive. Figure 1 compares H_3PO_4 results between on-line automated NIR method and off-line ICP-MS. The on-line results are comparable to those of ICP-MS, but with much better time response (< 5 min) and automated sampling/feedback (lab analysis by ICP-MS can take several weeks with fab logistics).

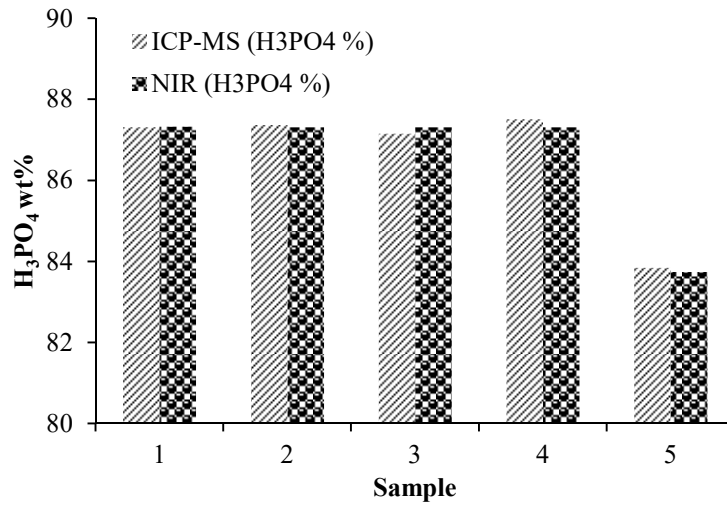


Figure 1: H_3PO_4 results comparison (NIR and ICP-MS)

Conductivity. Conductivity represents mobility of the ions under the driving force of an electrical field and is highly sensitive to temperature (see Eq. 2):

$$\text{Conductivity} = A * (1 + B * \Delta T) \quad (2)$$

Modern temperature control devices enable efficient temperature control so that the effect of temperature is greatly suppressed. Figure 2 shows a typical conductivity calibration curve with temperature correction, which has a good correlation with H_3PO_4 concentration.

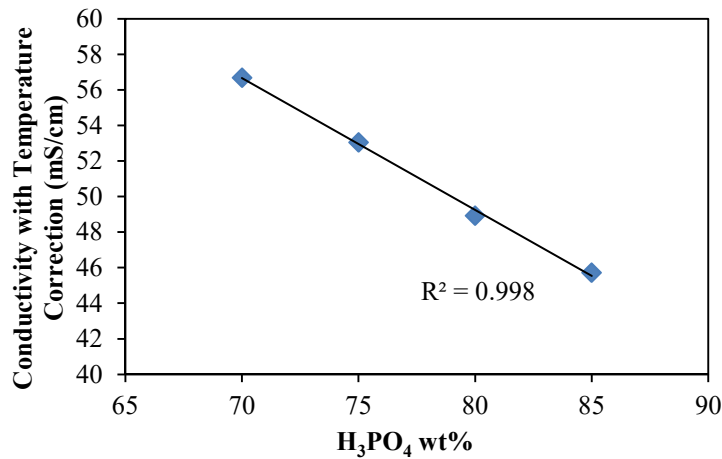


Figure 2: Conductivity calibration curve with temperature correction

Si Measurement

Silicon is measured by adding predetermined concentrations of fluoride ions to a predetermined volume of etchant solution, and measuring the potential of a fluoride ion specific electrode (FISE) in this test solution. Reaction with silicon ions in the test solution reduces the concentration of fluoride ions, which are present in stoichiometric excess. This enables the silicon concentration of the etchant solution to be determined from the difference between the predetermined and measured concentrations of fluoride ions in the test solution. Under ideal conditions, the potential (E) of a FISE is given by the well-known Nernst equation:

$$E = E^{\circ} - (2.303 RT/F) \log [F^-] \quad (3)$$

In practice, Nernstian slopes for fluoride detected by a FISE typically deviate somewhat from the theoretical value (59 mV/decade) due to incomplete dissociation of the fluoride compound (HF, for example), variations in the concentrations of other species involved in the equilibrium (H^+ ion from phosphoric acid, for example), and/or non-ideal solution behavior (non-unity activity coefficients, for example). By optimizing the fluoride ion concentration, a linear correlation between the Si concentrations and FISE potentials can be obtained.

Si Measurement in Low Temperature Etch. Si is measured in a wet bench low temperature hot phosphoric etch process. Figure 3 shows field measurement data for Si with labeled process activities. The expected Si rise caused by wafer runs (greyed blocks under “1st Batch”, “2nd Batch”, and “3rd Batch”) match the measured Si up trending results (blue line with markers) well. In this study, the 1st and 2nd batches are “seed” layers used just to build up the required silica level in solution based on end user’s feedback. Only during processing of the 3rd batch is the required selectivity attained. In addition, the Si results of ~0.2 normalized from the fresh bath after the 3rd batch process indicates the process tank did not recover to the original baseline where Si was at 0-0.1 normalized. Therefore, additional tank cleaning may be required between batches.

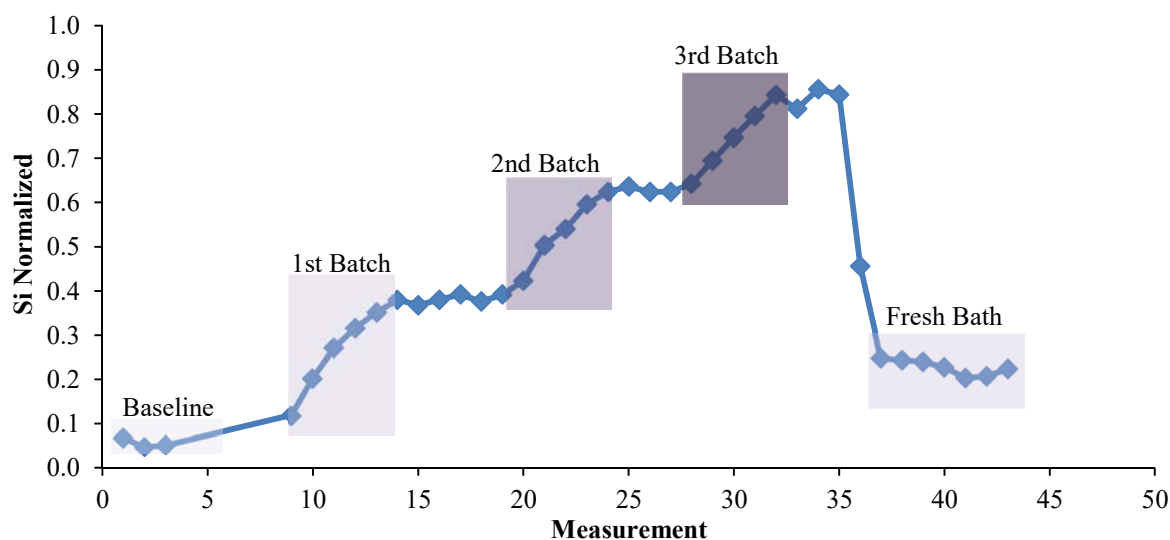


Figure 3: Monitoring Si concentration in low temperature hot phos process

Organosilicate Measurement. In the etchant that contains an organo-silicon compound, the Si concentration is much higher (>10 times) than that in a regular hot phos process. In this case, more fluoride must be added to digest excessive amounts of Si. Moreover, this digestion requires significantly longer time and there are precipitations during the reaction, which are two major disadvantages for on-line automated analysis. To improve the Si analysis performance, carboxylic acids were added into the fluoride reagent matrix [7]. The effect of carboxylic acids was studied in comparison with the regular Si method mentioned above. Figure 4 shows this correlation when two different carboxylic acids were used. For the reagent solutions comprising 10.0 g/L KF in the acids, the calibration plots in Figure 4 are linear and practically identical for both acids. Figure 4 also

shows the efficacy of adding carboxylic acids. It is evident that the sensitivity of the FISE potential to the concentration of silicon ions in the etchant solution (mV/ppm) is a factor of two greater for the reagent solutions comprising a carboxylic acid ($\sim 0.1\text{mV/ppm}$) compared to that for the reagent solution not comprising a carboxylic acid ($\sim 0.05\text{mV/ppm}$), as indicated by the slopes of the plots in Figure 4. A higher fluoride concentration is used in carboxylic acid matrices as the digestion is faster and free of Si precipitation. Sensitivity is further studied with various fractions of acetic acid in the reagent. Figure 5 shows the descending trend of sensitivity to the Si concentration as the volume fraction of the acid decreases.

The accuracy of this method with $\sim 90\%$ of carboxylic acid in reagent is evaluated by off-line ICP-MS method, which is shown in Figure 6. Samples were obtained from an actual process tank. The results from this improved fluoride method match those from ICP-MS. Good stability of organosilicate results by the same method with carboxylic acid in reagent is shown in Figure 7. This test was performed on samples with a known prepared concentration for a period of one week. All measured results have an accuracy of $< 2\%$ (solid lines on Figure 7).

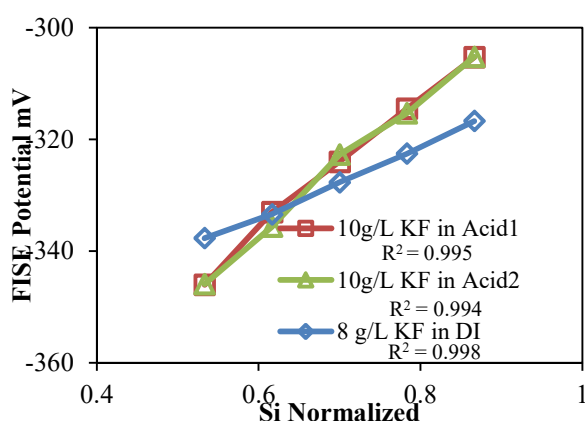


Figure 4: Correlations between FISE signals and silicon concentrations in carboxylic acids and water matrices

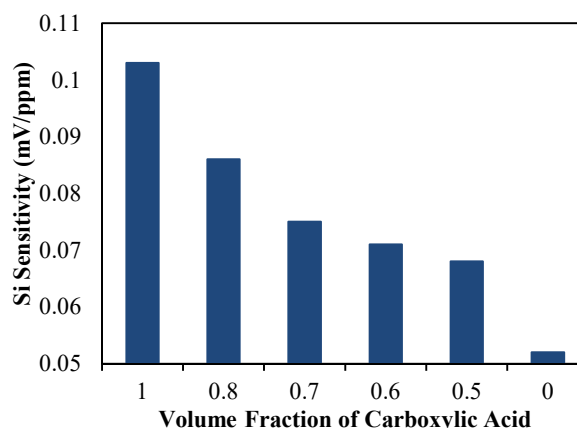


Figure 5: Sensitivity to Si concentration vs. different volume fraction of carboxylic acid

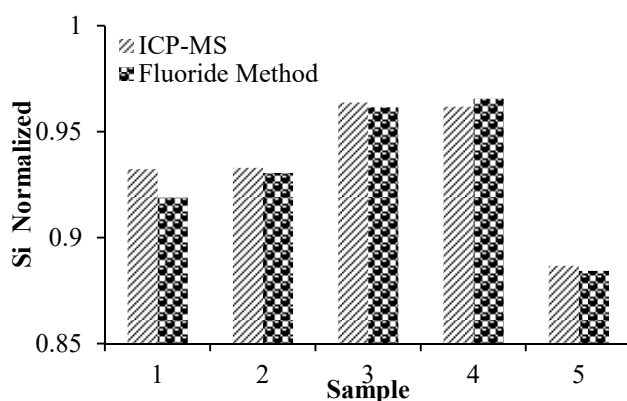


Figure 6: Organosilicate results from fluoride method containing carboxylic acid in comparison with ICP-MS

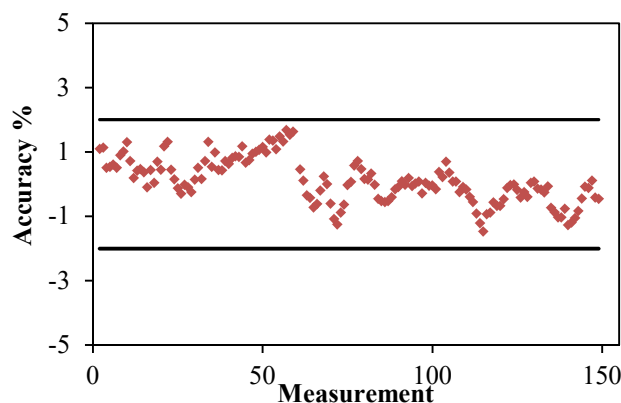


Figure 7: Organo-Si stability for a period of one week by the fluoride method containing carboxylic acid. The prepared Si concentration is used to evaluate accuracy.

Conclusions

A variety of methods have been developed to measure the silicon nitride etch process bath in real time. Results from these analyses can be used for tight process control to achieve high selectivity for silicon nitride removal.

References

- [1] S.J. Baffat, M.S. Lucey, M.R. Yalamanchilli Hot Phosphoric Acid APC for Silicon Nitride Etch. Semiconductor International, 8/1/2002
- [2] Hong et al. Compositions for etching and methods of forming a semiconductor device using the same US Patent 9,136,120
- [3] Cho et al. Etching composition and method for fabricating semiconductor device using the same US Patent 8,821,752
- [4] Nowling et al. Low Temperature Etching of Silicon Nitride Structures Using Phosphoric Acid Solutions US Patent 8,716,146
- [5] Shalyt et al. Analysis of silicon concentration in phosphoric acid etchant solutions US Patent 8,008,087
- [6] E. Shalyt, G. Liang, P. Bratin, C. Lin: Real Time Monitoring for Control of Cleaning and Etching solution (Proceed. of SPWCC Conference, USA, 2007).
- [7] Shalyt et al. Analysis of silicon concentration in phosphoric acid etchant solutions United States Patent Application 20160018358

Study on the Etching Selectivity of Oxide Films in Dry Cleaning Process with NF_3 and H_2O

Sung-Min Kang^{1,2}, Tae-Hyung Kim², and Taesung Kim^{1,a}

¹ SKKU Advanced Institute of Nanotechnology, Sungkyunkwan University, #300 Cheoncheon-Dong, Jangan-Gu, Suwon, Gyeonggi-Do, 440-746, Korea.

²Memory Division, Device Solution Business, Samsung Electronics Co., LTD, San #16 Banwol-Dong, Hwasung, Gyeonggi-do, 445-701, Korea.

^aE-mail: tkim@skku.edu

Keywords: Cleaning, Dry Cleaning, NF_3 -based Gas Cleaning, Selectivity, Oxide Film Etching, $\text{NF}_3+\text{H}_2\text{O}$ Dry Cleaning, HF-Solution.

Abstract. Dry cleaning process has been limited to particular field of removing native oxide because it has low etching selectivity for various oxide films. To increase etching selectivity, we added H_2O steam feeding step before NF_3 feeding step. From the experimental, we can change selectivity between oxide films from tens to hundreds.

Introduction

The structure of memory devices is becoming more and more complex as the pattern size gets thinner. While the types of oxides used in semiconductors are increasing in their diversity, specific etch rates per films, which can be expressed as selectivity, are becoming more critical. Wet cleaning process is face the chemical limits because it use DIW (De-Ionized Water) rinse process and drying process. The surface tension cause such as water-mark and pattern collapse problem [1, 2]. Recently, gas dry cleaning process use the HF or NF_3 is studied in semiconductor manufacturing to oxide etching[3]. But dry cleaning process has been limited to particular field of removing native oxide because it has low etching selectivity for various oxide films. Figure 1 shows the difference of selectivity for various oxide films and silicon nitride with respect to thermal oxide between the dry cleaning (HF or NF_3 gas) and wet cleaning (HF solution). In general, selectivity of dry cleaning is very low, limited to processes used. At various oxide films open structure. For example in air-gap structure in NAND flash devices[4]. It is difficult to etch the only selected oxide film without other oxide film damages. The study is conducted in order to overcome the current limit of selectivity in dry cleaning.

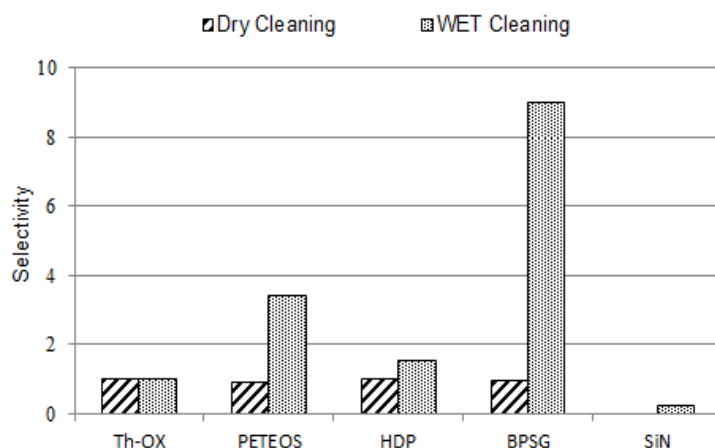


Figure 1. Selectivity of Dry cleaning vs Wet cleaning (Relative to themal oxide)

Experimental setup

We grew several kinds of oxide films on boron doped Si(100) wafer. Tonen Silazane – Silazane of Tonen Chemical Corporation (TOSZ), room temperature atomic layer deposition (RT-ALD) : 25 °C, high temperature atomic layer deposition (HT-ALD) : 650°C, and high temperature oxidation (HTO) : 790 °C. We used dry cleaning system manufactured by Applied Materials (AMAT, USA). Base process pressure, wafer stage temperature and NF_3 flow rate were 8 Torr, 12 °C and 15 sccm. The helium gas flow rate and RF power were fixed to 2500 sccm and 250 W. We added H_2O steam feeding step before NF_3 feeding step and changed process parameters such as pressure, wafer stage temperature, NF_3 flow rate and H_2O flow rate.

Results and discussions

In the dry cleaning process, NF_3 and NH_3 gas react with SiO_2 layer on top of the oxide film generating $(\text{NH}_4)_2\text{SiF}_6$, as reaction byproduct [5]. Then the reaction continues with NF_3 and NH_3 gas diffusing through the byproducts layer and reacting with the oxide layer underneath. When the initial reaction is quick, the byproduct layer is built up quickly also. The thicker the by-product layer, the harder for the reaction gases to diffuse through it, resulting in a reduction of the etchrate[5].

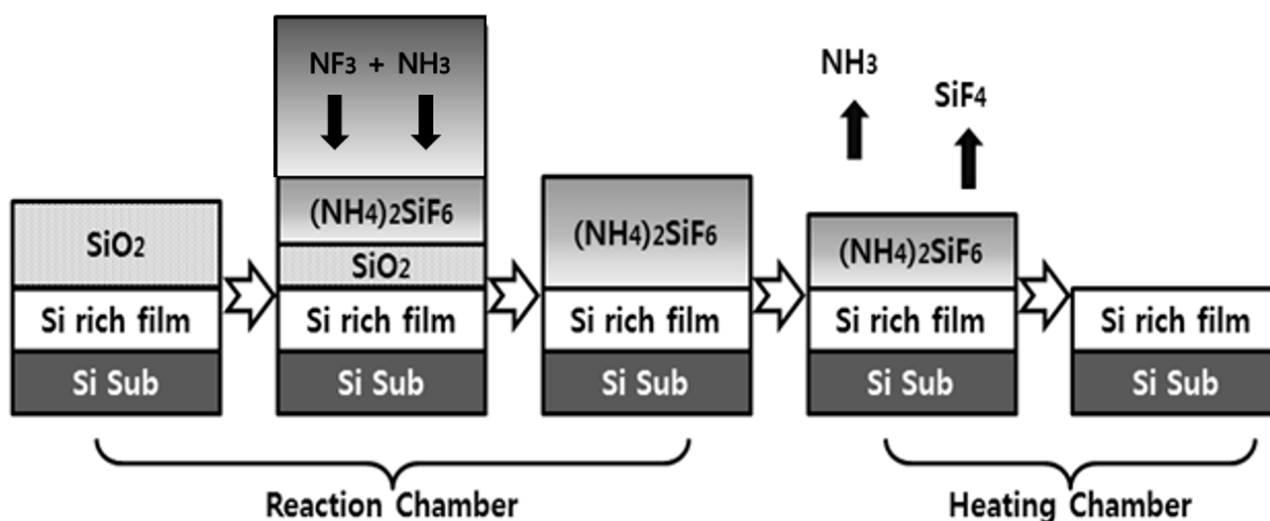


Figure 2. Selectivity and Etching Amount according to the NF_3 process flow

But, adding H_2O steam to the gas etching process (dry cleaning) is being tested as a way of improving etching selectivity among different oxide films. Before feeding the NF_3 gas step, hot H_2O steam feeding step is added. Figures 3 and 4 show how the NF_3 flowrate and H_2O flowrate behave during the gas etching process, in which the etch-rate selectivity between different oxide films is improved by mixing NF_3 and H_2O . When reducing the flow rate of NF_3 as shown in figure 3, the total etched thickness is reduced but the selectivity between oxide films is increased. Figure 4 shows that the total etch amount is increased by increasing the H_2O flow rate but the selectivity is decreased. Figure 5 shows that the total etch amount is increased by increasing process pressure but the selectivity is decreased.

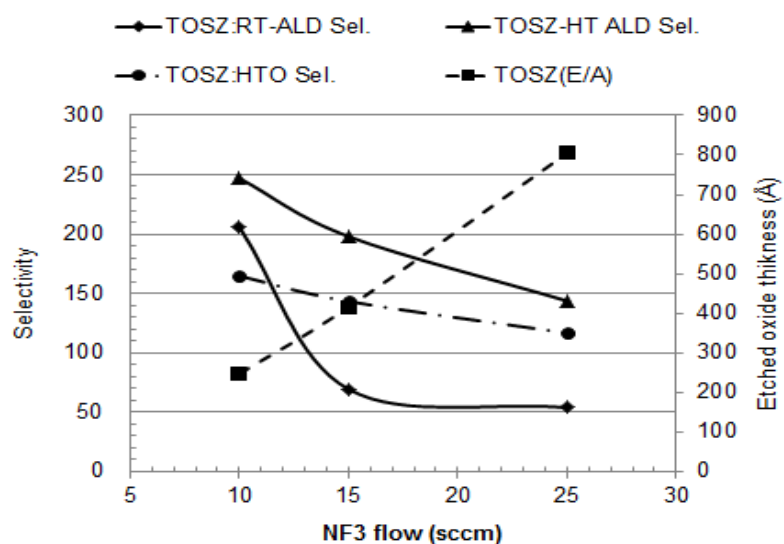


Figure 3. Selectivity and Etching Amount according to the NF₃ flow rate (Relative to TOSZ)

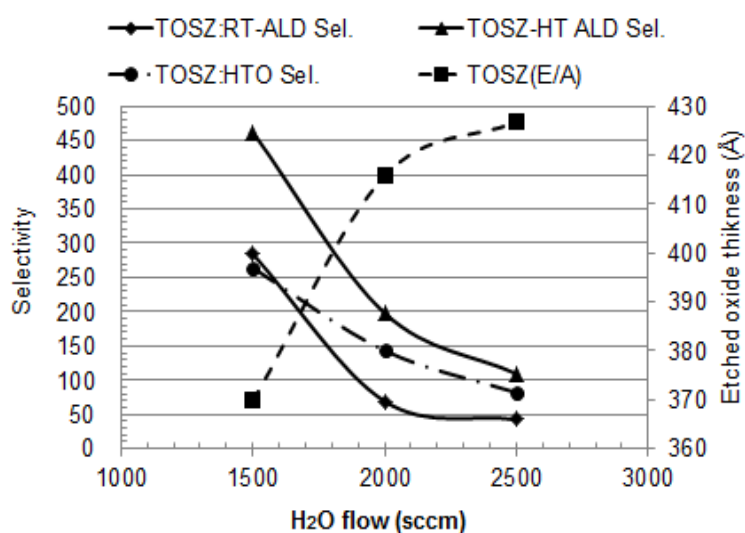


Figure 4. Selectivity and Etching Amount according to the H₂O flow rate (Relative to TOSZ)

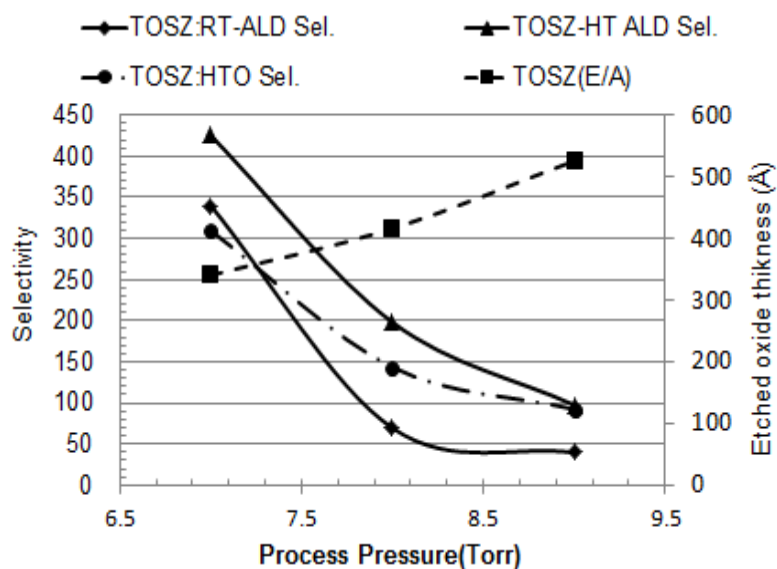


Figure 5. Selectivity and Etching Amount according to the Process Pressure (Relative to TOSZ)

As shown in figure 3, 4 and 5, when we change the process conditions (NF_3 , H_2O , pressure) selectivity between oxide films is changed from tens to hundreds. The reaction process with H_2O added is as shown below, leading to the formation of oxide etchants (HF , HF_2^-) [6].

1. $\text{NF}_3 \rightarrow \text{NF}_2^* + \text{F}^*$ (Radical)
2. $2\text{H}_2\text{O} + 4\text{F}^* \rightarrow 4\text{HF} + \text{O}_2$
 $\text{HF} \rightarrow \text{H}^+ + \text{F}^-$
 $\text{F}^- + \text{HF} \rightarrow \text{HF}_2^-$
3. $2\text{HF} + 2\text{HF}_2^- + 2\text{H}^+ + \text{SiO}_2 \rightarrow \text{H}_2\text{SiF}_6 + 2\text{H}_2\text{O}$

Such reaction is very similar to the reaction that occurs in liquid HF chemical solution. Therefore, this reaction requires an initiation step, which creates H_2O condensed film on the oxide layer surface. The OH bonded in Si structure affects creation of the reaction intermediate. Thus, the more OH bonding exist in the film, the higher etch-rate is obtained by HF . We found that the adding the H_2O steam pre-flow step before NF_3 flow step can make a difference in oxide surface hydroxylation level and this can be the tuning knob for the etch-rate selectivity. These various process conditions can be simplified into a single index; Relative Humidity (RH).

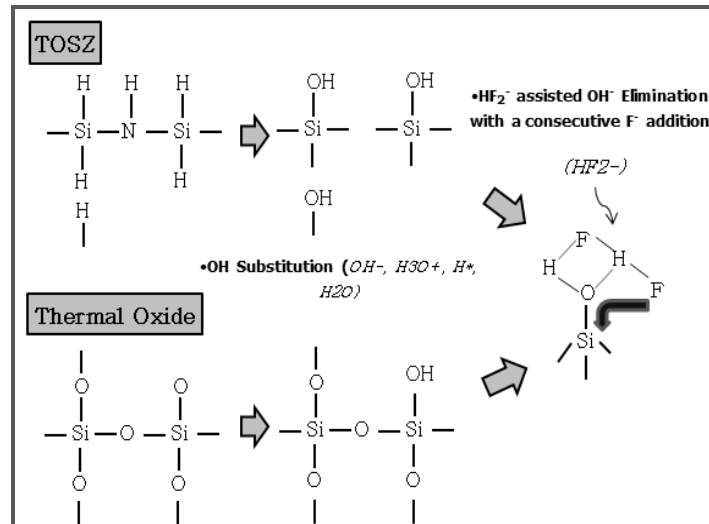


Figure 6. Schematic of oxide film etching

Table1. Summary of experiment.

Parameter	Test Condition	Etch Rate	Selectivity	Comment
Pressure	Decrease	Decrease	Increase	RH ↓
H_2O Flow rate	Decrease	Decrease	Increase	RH ↓
Temperature	Decrease	Increase	Increase	RH ↓
NF_3 Flow rate	Decrease	Decrease	Increase	F^* Radical ↓

Conclusions

In some cases, conventional dry cleaning could not be implemented in processing of multi-oxide film structure because of the low selectivity. However, it is confirmed throughout this experiment that the oxide film etch-rate selectivity can be controlled (increased) by supplying high-temp H_2O steam into the process chamber before the etching source gases (NF_3) are supplied [7]. This phenomenon is explained by differences in hydroxylation level of different types of oxide films at surface, which

make differences in the reaction speed between the oxide film and the etching gases. The etchrate selectivity showed relation in some extends with process variables such as etching gas (NF_3) flow rate, chamber pressure, or H_2O supply flowrate. Among all the process variables counted, the amount of H_2O supply had the most significant relation toward the selectivity control. Still, adding the H_2O pre-flow before NF_3 gas flow step in dry cleaning process has shown the potential to be useful. This process can remove the ILD oxide film without damaging the pattern liner or stopper films. Also it can remove the bulk of trench-fill oxide without damage of ONO (Oxide-SiN-Oxide) and tunnel oxide at Air-gap structure in NAND-flash devices [4].

References

- [1] S. Farshid Chini, Alidad Amirfazli, J. Micro/Nanolith. MEMS MOEMS, **11** (3), (2012). p. 033003
- [2] G. Liu, J. Zhou, Y. Xiong, X. Zhang and Y. Tian, Nanotech., **22**, 30, (2011)
- [3] T. Hattori, ECS Trans, **25** (5) (2009), p. 3-14
- [4] J. Hwang, J. Seo, Y. Lee, S. Park, J. Leem, J. Kim, T. Hong, S. Jeong, K. Lee, H. Heo, H. Lee, P. Jang, K. Park, M. Lee, S. Baik, J. Kim, H. Kang, M. Jang, J. Lee, G. Cho, J. Lee, B. Lee, H. Jang, S. Park, J. Kim, S. Lee, S. Aritome, S. Hong and S. Park, IEEE International Electron Devices Meeting (IEDM), (2011) p. 9.1.1 - 9.1.4
- [5] H. J. Oha, J. H. Lee, ECS Trans. **61** (2014), p. 1-8
- [6] T. Hayashi, J. Nanomed. Nanotechol, **S:15**, (2013), p. 001,
- [7] C. Zhang, G. Hatipoglu and S. Tadigadapa, J. Microelectromech. S, **24**, (2015)

Titanium Nitride Hard Mask Removal with Selectivity to Tungsten in FEOL

Hsing-Chen Wu^{1, a *}, Sheng-Hung Tu^{1, b} Min-Chieh Yang^{1, c}
and Emanuel Cooper^{2, d}

¹Entegris Inc., Taiwan Technology Center, 1F, no. 669, Sec. 4, ZhongXing Road, Zhudong Town, Hsinchu County 310, Taiwan (R.O.C.)

²Entegris Inc., 7 Commerce Drive, Danbury, Connecticut 06810 USA

^aMegan.Wu@entegris.com, ^bSpencer.Tu@entegris.com, ^cJack.Yang@entegris.com,
^dEmanuel.Cooper@entegris.com

Keywords: titanium nitride, tungsten, hard mask, selective etching.

Abstract. This paper describes etching of titanium nitride (TiN) highly selective to tungsten (W), where the TiN etch rate (E/R) was about 100 Å/min and W E/R was less than 1 Å/min at 60°C. The formulation concept was adapted from the Entegris TK-10 series, but it was modified to fit the criteria for front-end application. No damage to tantalum nitride (TaN) was required during the etching process but silicon oxide compatibility requirement was relaxed. By replacing W inhibitors with more suitable ones, W loss was well controlled, while the particle issue previously found in the scale up lots was also solved.

Introduction

In the back-end of line (BEOL) process, titanium nitride (TiN) has been used as hard mask (HM) for metal 1 (M1) patterning in the dry etching process. This is then followed by a wet etching process to remove the TiN HM totally (or partially) and to clean off the post-etching residues. Consequently, tungsten metal would be exposed during this wet process, thus low W etch rate was necessary. This problem has been solved by the published Entegris TK-10 series, applied successfully in BEOL [1].

However, in the front-end of line (FEOL) applications, new materials are introduced continuously for improving device performance. In 10 nm or more advanced node, some metals that appeared in BEOL in the past have been moved into FEOL or the “middle-end of line” (MEOL) process, including W, Co, Al, TaN, TiN, TiAl, Ta, etc. For example, W is used in the replacement gate process and TiN can be used as work functional metal (WFM); together they can be combined for the needs of specific processes in FEOL. Could it be possible to provide the same solution used in BEOL for FEOL application? The extension is not automatically applicable, since the criteria levels of trace metal contamination and particle tolerance are much more stringent in FEOL than in BEOL.

Entegris TK-10 series were developed for TiN HM removal with compatibility with W and low-k dielectric (k value=2.8). There is no request of low-k dielectric compatibility for the application here to TiN removal process. Consequently, the original inhibitor system inside TK-10 formulation would be modified to fit the FEOL criteria. The formulation approach for TK-10 to remove TiN was oxidizing TiN, then etching the oxidized TiO_x by etchant. However, the combination of oxidant and etchant can also attack W; as a result, choosing adequate oxidant and W inhibitor to reduce W loss became very important.

The present paper describes a modified formulation named TK10X7 that was derived from the TK-10 series for a specific FEOL application. It is an aqueous-based formulation with the same formulation concept as in TK-10 series, but it has been optimized to fit FEOL specifications. The final formulation showed TiN E/R around 100 Å/min and CVD W E/R less than 1 Å/min, ALD W E/R less than 2 Å/min, and nearly zero damage to TaN at 60 °C.

Experimental details

It is known that W is etched by peroxide, thus oxidant A was “inherited” as the same functional group used in TK-10, pH adjustors were screened by using strong acids, and types of etchants were tried with different concentrations. W inhibitors were screened and finally surface-active compounds were chosen that present different carbon numbers in their hydrophobic part. Etch rates were calculated by film thickness loss measured by X-Ray fluorescence (XRF) or ellipsometer (J.A. Woollam). Surface tension was measured by force tensiometer (KRÜSS, K11). Liquid particle counter (LPC) model was RION KE-40AF. The pH was measured by using narrow-range pH indicator paper.

Results and Discussions

Since the oxide inhibitors inside TK-10 for BEOL application had a different criteria from FEOL, in order to make it applicable for FEOL application, the first priority here was to change the etchant system. Etchants 1-4 were tested (E1-E4) with the same molar concentration, in which E1 and E3 showed TiN E/R of $<30 \text{ Å/min}$, while E2 and E4 showed TiN E/R $>80 \text{ Å/min}$ at 60°C . The results are summarized in Table I where the etchant molar concentrations of etchants have been converted to wt% and the W E/R were obtained in the presence of 3 α % W inhibitor B-1. E2 showed the highest TiN ER, but its W E/R was also higher; thus we chose E4 as the final etchant due to concern about the tungsten loss.

A comparison of TiN and W etch rates tested in different pH adjustors is illustrated in Figure 1(a) and 1(b), where the etchant [E4] was $x\%$ with 3 α % W inhibitor B-1 and processing temperature was 60°C . The TK-10 data points are also marked on the figures for reference (labeled as Δ). It is known that the oxidation ability is generally pH dependent [2-3]. Here acid-1 and acid-2 are of approximately the same strength and their solutions are at about the same pH, but acid-2 is more sterically hindered and therefore the etch rate is lower. The etching rate performances for both TiN and W were found to be better for acid 2, in which TiN E/R is higher and W E/R is lower. It indicated that the structure of acid is more important than its pKa. Appropriate pH range is important in this system since oxidation ability for the oxidant is affected by pH and thus the etch rates for metals will be changed. The prototype of formulations has been fixed at this time, and its E/R data are summarized in Table II.

Scaled-up samples were prepared in our alpha-scale laboratory, and sent to single-wafer tool (SWT) for on-site demonstration. Before shipping, internal filtration was adjusted and finally incorporated in the manufacturing process as following: beginning with 50/ 20 nm size filters until LPC was <100 at particle size of $0.1 \mu\text{m}$, then replacing with 10 nm filter and circulating for 24 hr. The detailed lot information is listed in Table III. Within these sample lots, two W inhibitors of B-1 and B-2 were tried and they differed in the hydrophobic carbon chain length, with B-1 containing the longer hydrophobic chains.

The on-wafer particle data for the scaled-up batches were measured by SP3 for particle size $>30 \text{ nm}$. The results are summarized in Figure 2, in which the initial state (circulation in SWT within one-day) of on-wafer particle counts is compared for the 1st to 7th batches, where batches 1-3 were using W inhibitor B-1 and batches 4-7 were using inhibitor B-2. As revealed in Figure 2, in the cases using W inhibitor B-1, there are still >1000 particles in the 1st batch, and only the 3rd batch showed initial on-wafer particle less than 300, which was due to longer circulation time with the 10 nm filter - for four days before testing in customer's tool. This indicates that longer filtration time could reduce the particle count.

Considering the particle issue, it is reasonable to speculate that the high particle counts may have resulted from micelles of W inhibitor since it is essentially a surfactant. Literature reported that the critical micelle concentration (CMC) of the surfactants applied here would reduce a factor of around four as increasing every two carbons in the hydrophobic end of surfactant [4], thus prompting us to replace the W inhibitor from B-1 to B-2, since B-1 contains longer carbon chain lengths than

B-2. It is rational to expect those longer carbon chains in B-1 would form micelle more easily and result in higher particle counts. There were failed experiments for protecting W in scaled-up lots due to the filtration step in which the filter was believed to adsorb part of the W inhibitors and resulted in high W E/R.

Due to the concern about adsorption, we designed a three-fold higher concentration of $6\alpha\%$ of B-2 than beaker tests (where $2\alpha\%$ was used) for the first scaled-up batch that was referred as the 4th batch in Table III. As illustrated in Figure 2, the initial on-wafer particle count could be reduced to <300 . Then we further lowered the concentration of B-2 to $2\alpha\%$ in the 5th batch; the performance for W E/R of the 5th batch was still <1 Å/min with the initial particle count data at ~ 120 . However, when we tried to reduce B-2 to $0.5\alpha\%$ in the 6th batch, functional test results showed slight increasing to W E/R of 1.3 Å/min and no more improvement in particle performance was found.

It is evident that if the filtration step or the filter condition may influence the W protection, it is necessary to set up an analytical technique to quickly evaluate whether the scaled-up products are “in spec” or not. Surface tension is thought to be a quickly way for confirming the result. Different concentrations of W inhibitors B-1 to B-3 (molecular weight $B-1 > B-2 > B-3$) were added in TK10X7-based solution and the surface tension was measured. The results are summarized in Figure 3, where x-axis is the surfactant concentration presented in logarithmic scale. Surface tension decreases with increasing surfactant concentration, until a turning point where the dropping rate becomes very slow or even zero, meaning that the CMC of the surfactant has been reached. When the concentration higher than the CMC, the micelles were formed and very slow or no more decrease in surface tension [5]. As mentioned before, CMC of surfactant decreases with carbon-chain length, thus CMC for W inhibitors would be $B-3 > B-2 > B-1$, as illustrated in Figure 3. Although B-1 showed the lowest CMC in TK10X7, it's still higher than $5\alpha\%$ ($5\alpha\%$ was the highest concentration we applied in this system for the three surfactants), and the CMC for B-2 and B-3 were even higher. In brief, the concentration of W inhibitors used in our formulations has not reached the CMC, and even though the CMC may lower at high temperature (eg., the process temperature 60 °C.), the formed micelle would be very hard to detect with an estimated size of about 4 nm in diameter.

On the other hand, W E/R were also monitored in the same conditions as in Figure 3, the presented data only tested by using inhibitor B-2 since there are less particle or filtration issues with it in the scaled-up process. The relation between W E/R and surface tension is displayed in Figure 4; at surface tensions greater than 50 mN/m, W E/R decreased with the decrease in surface tension. In addition, W E/R was <1 Å/min and stayed at the same level at surface tensions about 45 - 50 mN/m or below. When converting the x-axis from surface tension to surfactant %, W E/R showed a steep drop before $\alpha\%$, and then gradually decreased as increasing surfactant %, as illustrated in Figure 5. The two regression lines (indicated by dash line) were estimated to intersect at 0.75α , which refers to the surfactant concentration where W E/R would be <1 Å/min. As mentioned above, surface tension measurement could be applied as a quick way to monitor the scaled-up batch for its W compatibility after filtration, since the etch rate was proved to correlate with surface tension.

Finally, a summary of TK-10 series from the early stage by using peroxide to the non-peroxide based X series (X4 and X7) were listed in Table IV, where the trace metal level, LPC performance, on-wafer particle and the W compatibility were arranged for comparison. It clearly highlights the improvements made going from the previous versions to TK10X7 and why the modifications introduced in this paper make it more suitable for FEOL applications.

Conclusions

An aqueous, low cost formulation designed for TiN removal with high compatibility to W was achieved. Modification for etchant and optimization of W inhibitor bring the trace metals and particle performance to levels that could be acceptable in FEOL applications. Based on the formulations of our previous TK-10 series, TiN, W, and TaN etch rates were screened in solutions containing oxidant

and etchant in low pH. CMC study of W inhibitors with low concentration, surface tension drop caused by surfactants and their influence on W etch rates were also investigated.

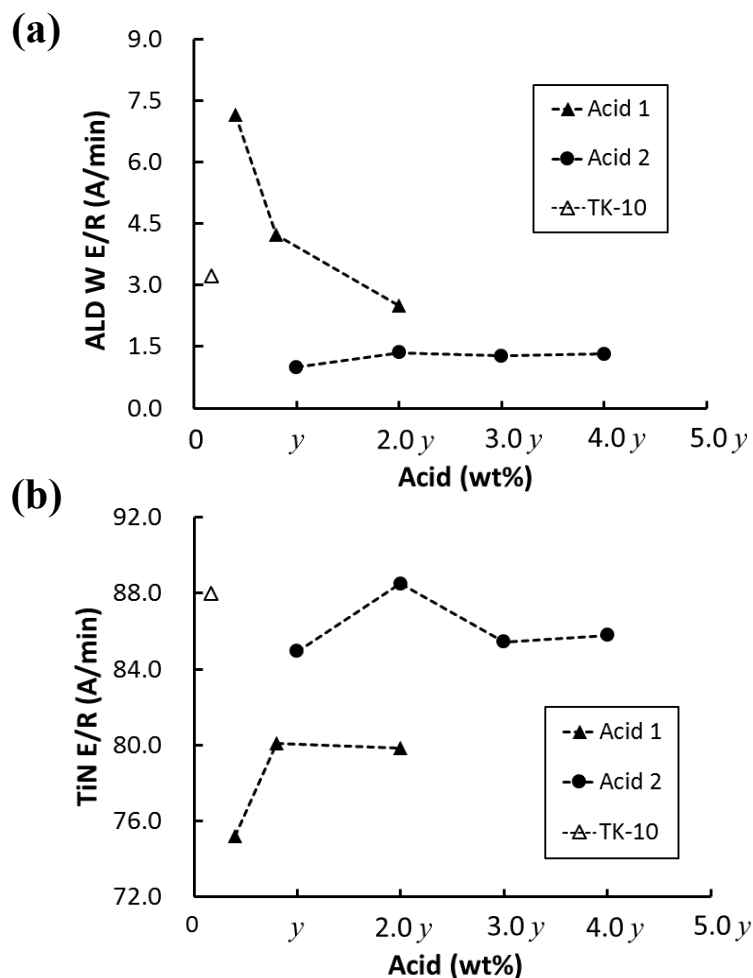


Figure 1: (a) TiN and (b) ALD W etch rate obtained using different acids in TK10X7. The data points for TK-10 are also marked in the figures by the Δ symbol.

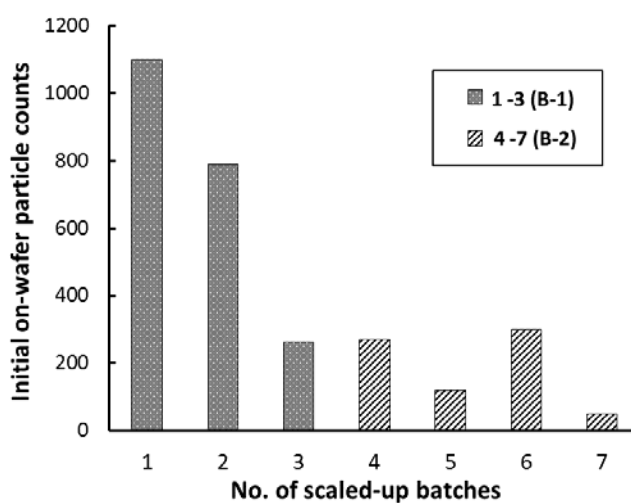


Figure 2: Initial (day 0 to day 1) on-wafer particle counts of the scaled-up batches measured in SWT by SP3. W inhibitor B-1 was used in batches of 1-3, and B-2 was used in batches of 4-7.

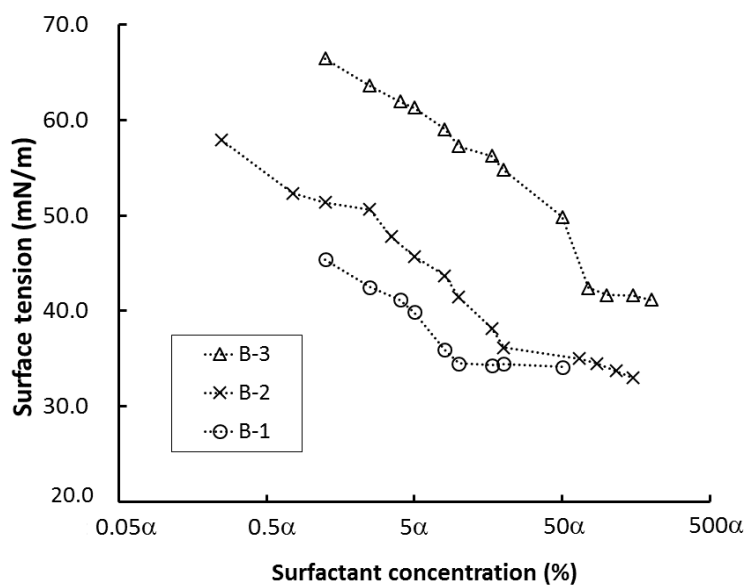


Figure 3: Surface tension of different W inhibitors with different concentrations in TK10X7 based solutions. The turning points for the zero slope indicate the approximate CMC of the corresponding surfactants.

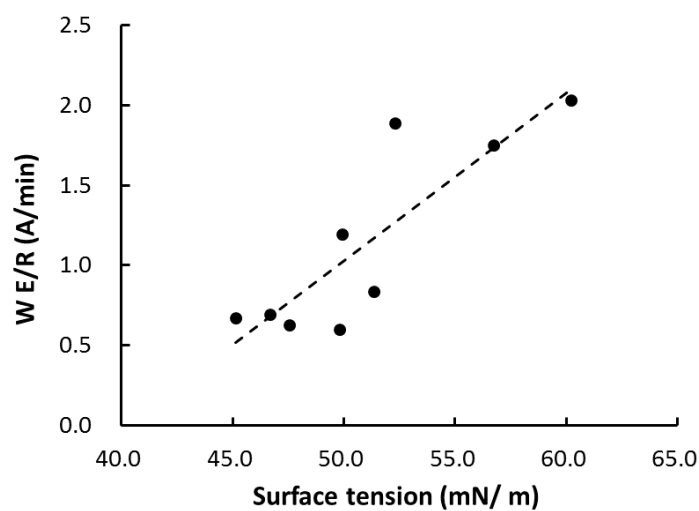


Figure 4: W etching rate (E/R) vs. different surface tensions obtained by adding W inhibitor B-2 into TK10X7.

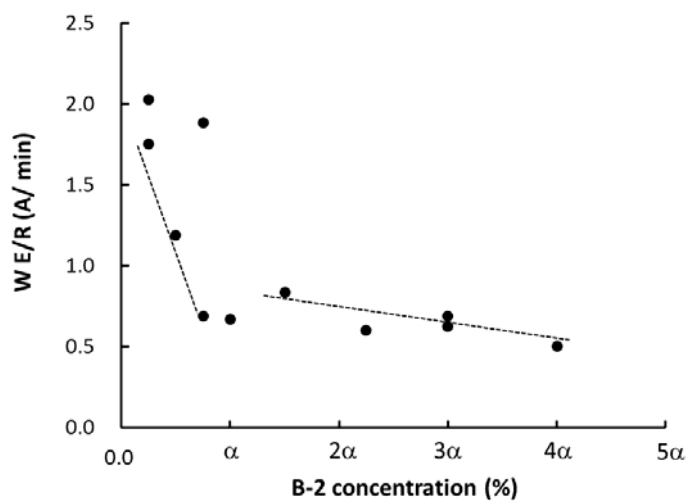


Figure 5: W etching rate (E/R) vs. different concentrations of W inhibitor B-2.

Table I: TiN and W etch rates of different etchants with the same mole number in TK10X7 based formulations at 60 °C. W etching rates were obtained in the presence of 3 α % W inhibitor B-1.

Etchants	wt%	TiN E/R (Å/min)	W E/R (Å/min)
1	2.0 <i>x</i>	27.94	0.25
2	2.8 <i>x</i>	97.55	3.04
3	5.0 <i>x</i>	14.20	0.34
4	<i>x</i>	84.94	1.07

Table II: TK10X7 etching rate data at 60°C.

Formulation	Etching rates (Å/min)				
TK10X7	TiN	CVD W	ALD W	TaN	PETEOS
	87.3 \pm 3.4	0.86 \pm 0.13	0.8 \pm 0.06	0 \pm 0.11	3.7 \pm 1.0

Table III: Filtration and blending information of the 1st- 7th scaled-up lots.

Sample lot	Filter size (nm)	Filtration time (day)	W-inhibitor used	[W inhibitor]
1	50/20 +10	1	B-1	3 α
2		1	B-1	3 α
3		4	B-1	3 α
4		1	B-2	6 α
5		1	B-2	3 α
6		1	B-2	0.5 α
7		1	B-2	3 α

Table IV: Performance comparison of TK10X7 with the previous versions.

Formulations	H ₂ O ₂ -based	TK10X4	TK10X7
Trace metal level	All trace metal < 10 ppb	Some with ppm level	All trace metal < 10 ppb
LPC performance	< 10 @ 0.1 μ m	~15 @ 0.1 μ m	< 10 @ 0.1 μ m
On-wafer particle	< 30 @ 30 nm	> 2000 @ 30 nm	< 300 @ 30 nm
W compatibility	No	Yes	Yes

References

- [1] Jeffrey A. Barnes, Emanuel I. Cooper, Li-min Chen, Steven Lippy, Rekha Rajaram, Sheng-Hung Tu, US 20150027978 A1.
- [2] Antonin Berka, Jaroslav Vulterin, and Jaroslav Zýka, Newer Redox Titrants: International Series of Monographs in Analytical Chemistry, 22 (1965) 66.
- [3] Jean-Louis Burgot, Ionic Equilibria in Analytical Chemistry, Springer Science & Business Media, 2012, pp. 359.
- [4] D.Fennell Evans, Martin Allen, B.W. Ninham, and Abdel Fouda: J. Solution Chem. 13 (1984) 87.
- [5] Pei.-Chuan. Li, Experimental measurements for thermodynamic properties of micellization of surfactants, Department of Engineering, National Taiwan University, Master's Thesis (2002).

Analysis of Si Wet Etching Effect on Wafer Edge

Suguru Saito^a, Atsushi Okuyama, Kenji Takeo,
Yoshiya Hagimoto, and Hayato Iwamoto

Sony Corporation

RDS Platform Device & Material R&D Group

4-14-1 Asahi-cho, Atsugi-shi, Kanagawa, 243-0014 Japan

^aSuguru.Saito@jp.sony.com

Keywords: wet etching, back-grinding, stress relief, vertical step, HF/HNO₃, fluid velocity, wafer edge, liquid simulation, etching rate, concave-convex shape

Abstract. We investigated the effect of Si wet etching on the vertical step at wafer edge. We found that the concave-convex shape appeared at the wafer edge after Si etching by the Atomic Force Microscopy analysis. From the liquid simulation and the detailed evaluation of Si etching rate, we revealed that the concave-convex shape was formed by the distribution of the fluid velocity at the wafer edge.

Introduction

Packaging technology has become more and more important with the miniaturization of electronic devices. Providing thinner substrates is essential for this technology and the wet etching process followed by the back-grinding is widely used for the wafer thinning process [1]. The purpose of the wet etching is relieving stress and damage caused by back-grinding and they are increasingly significant with the demand for the thinner and smaller devices. In the process of the back-grinding, wafers develop a knife-shaped edge and it can negatively affect the performance of the following processes. For example, an edge bead phenomenon, which is when the liquid surface tension and the edge shape cause the resist thickness to increase at the wafer edge, has been reported in the lithography process [2]. For wet etching, it is important to control the liquid film thickness to ensure high uniformity of the etching in single wafer silicon etching. However, the knife-shape of a wafer edge can affect the distribution of liquid film thickness in that region. In this report, we investigate the effect of the edge shape on the wet etching process performance by detailed observation of the edge shape of wafers after a single wafer wet etching process.

Experiment

We prepared silicon wafers which have vertical step at the wafer edge in order to enable the evaluation of the edge shape influence. The depth of the vertical step was about 90 μm . Wafers were etched by a single wafer wet etching system using an HF/HNO₃ mixture and a chemical temperature of about 30°C. Etched amount of silicon was about 20 μm . We observed the step shape of the samples before and after the wet etching. We also analyzed fluid velocity using the liquid simulation in order to consider the etching mechanism at the vertical step.

Results

Profile of the edge shape before and after Si etching.

At first, we evaluated the step of the samples by Scanning Electron Microscopy and Optical Microscopy. However, we could not observe the step shape in detail since it is too large in planar direction and too small in vertical direction. Therefore, we evaluated the step shape by Atomic Force Microscopy (AFM). AFM images and profiles at the step are provided in Figure 1. As shown, the step is a perpendicular shape before Si etching and changes to a concave-convex shape after Si etching. It is considered that this phenomenon is caused by chemical reaction and fluid film at the vertical step.

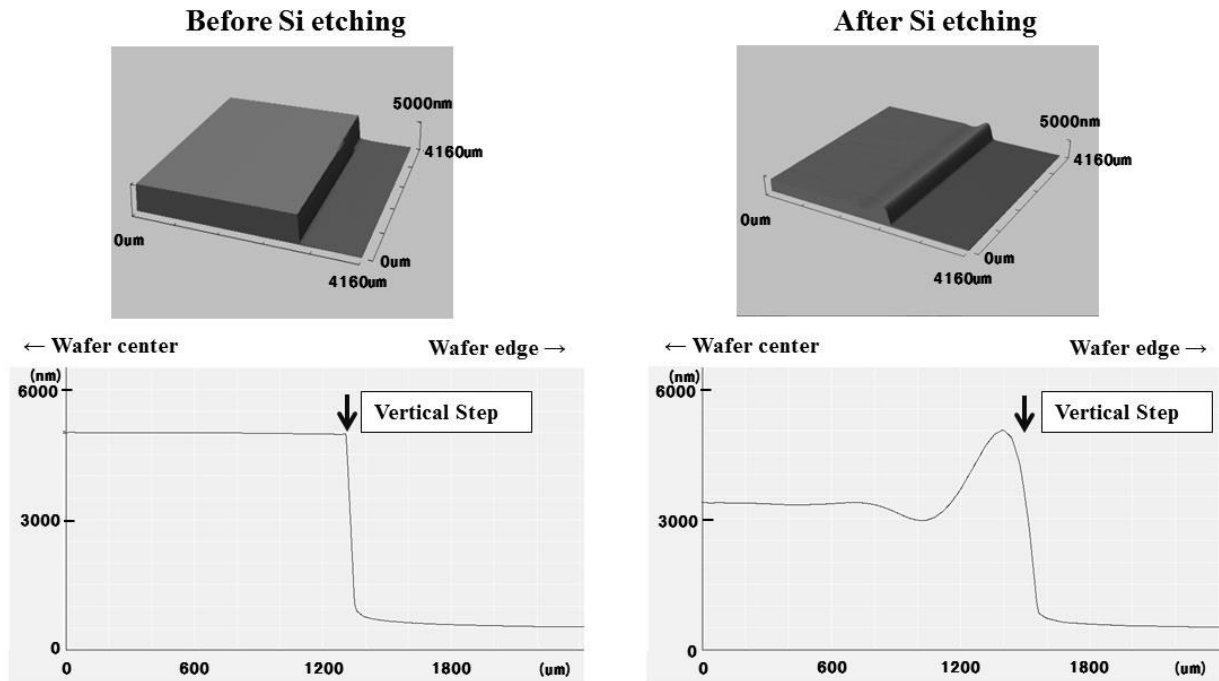


Figure 1: Profile of the vertical step before and after Si etching.

Relationship between fluid velocity and etching rate.

In the case of single wafer wet etching, the Si etching rate depends on the fluid velocity. The Si etching reaction by using HF/HNO₃ is infinitely fast, so the reaction rate is determined by the chemical supply rate to the wafer surface [3].

In our experiment, we evaluated the relationship between etching rate and fluid velocity. The fluid velocity on a wafer was calculated using a liquid simulation under the conditions listed in Table 1 [4]. The etching profile was obtained from measurements of wafer thickness before and after etching. Figure 2 show the etching profile and fluid velocity distribution on the wafer. Both were high at the center region of the wafer and low at the edge, suggesting a high correlation between fluid velocity and etching rate.

Table 1: Simulation conditions.

Solution	Density	Viscosity	Flow	Wafer rotation speed
HF/HNO ₃ mixture	1.48 g/cm ³	1.93 cP	3.0 L/min	450 rpm

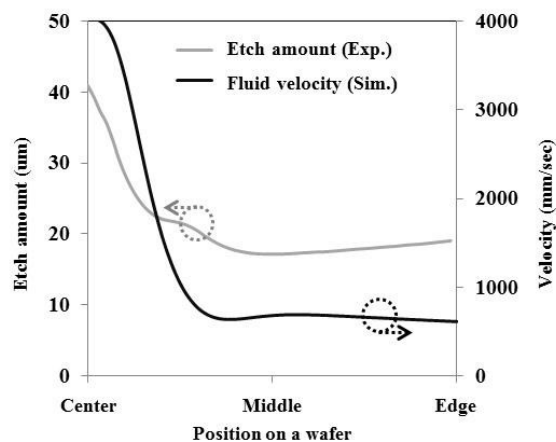


Figure 2: Relationship between etching rate and fluid velocity on a whole wafer.

Liquid simulation at vertical step region.

We analyzed the fluid velocity distribution at the vertical step region using FLOW-3D, a general-purpose liquid analysis simulator. Figure 3 shows 2D (X, Z) model space settings. The total

number of meshes in the 2D space is 450,000. The gray pattern in the figure is the vertical step region. Liquid inflow moves from the left boundary of the simulation space. Simulation parameter settings including liquid physical parameters, inflow conditions, and step shape values are listed in Table 3. We used an uncompressed flow model simulation solver based on Navier-Stokes equations with volume-of-fluid (VOF) algorithms for liquid-air free surface handling.

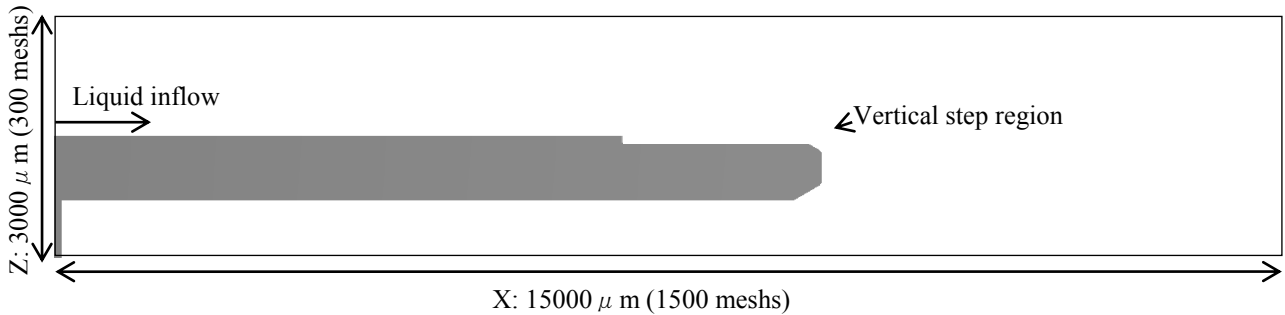


Figure 3: Liquid simulation space settings (2D model).

Table 2: Liquid simulation parameter settings.

Film thickness	Settings	Parameters	Settings	Step shape	Settings
Initial	0 μm	Viscosity	1.93 [cP]	Height	90 μm
Inlet	91 μm	Surface tension	42.1 [dyn/cm]	Angle	90°
On wafer	~91 μm	Contact angle	5 [degree]		
		Density	1.48 [g/cm ²]		
		Acceleration (+X)	50,000 [cm/sec ²]		
		Inlet velocity	62.44 [cm/sec]		

Figure 4(a) shows the liquid simulation and (b) shows the distribution of fluid velocity of the Z (film thickness) direction at the inflow region. The velocity is fast at the air-liquid interface but slow at the solid-liquid interface. We assume that etchant is supplied to the wafer surface from the vicinity of the solid-liquid interface, so to discuss the relationship between etching rate and fluid velocity at the wafer surface, we evaluated the distribution of velocity at the vicinity of this interface. Figure 5 shows the distribution of velocity at a distance of 15 μm from the solid-liquid interface. The distribution of velocity around the vertical step is characteristic; in particular, velocity is extremely fast at the vertical step, slow at the inside, and fast toward the wafer center. These results suggest that the characteristic distribution of fluid velocity is formed by the vertical step.

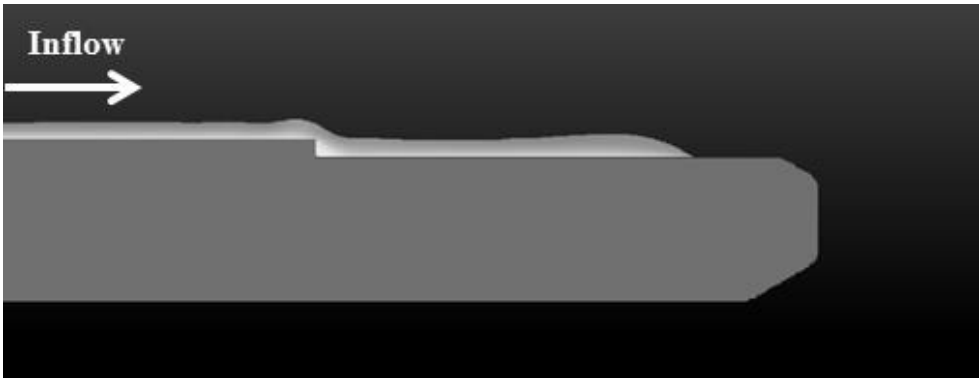


Figure 4(a): Result of liquid simulation.

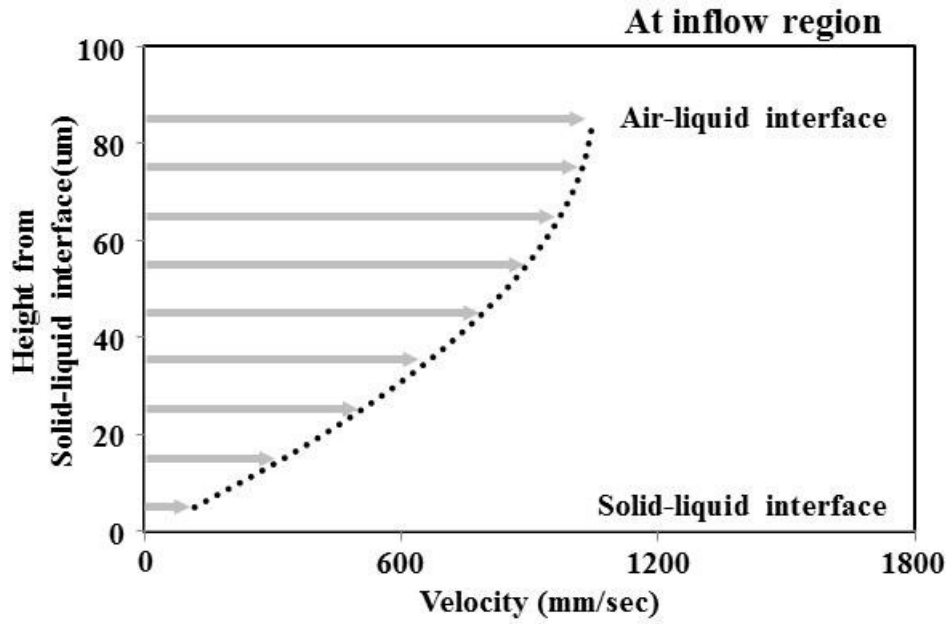


Figure 4(b): Distribution of fluid velocity of Z direction.

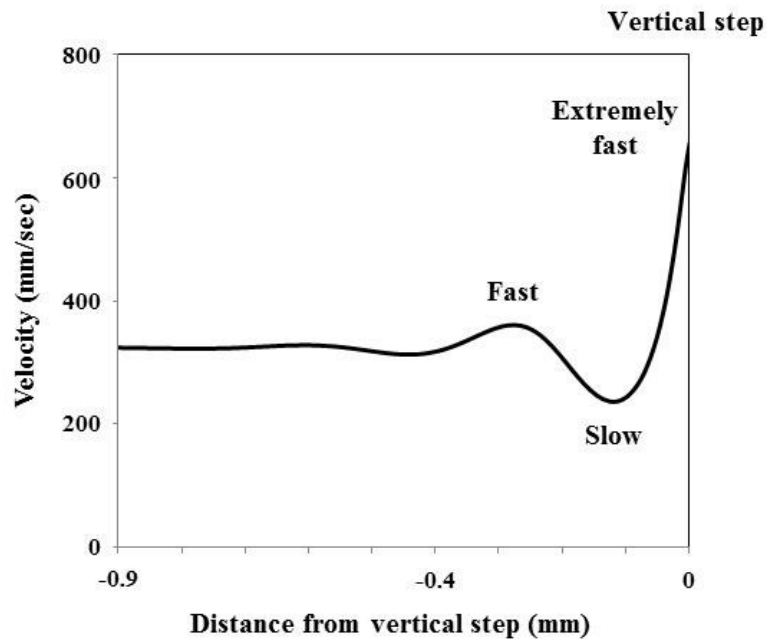


Figure 5: Distribution of fluid velocity 15 μm from the solid-liquid interface.

Discussion

Etching mechanism at vertical step region.

Si wet etching by HF/HNO₃ solution is given by equations (1) and (2) [5]. First, Si is oxidized by HNO₃, and SiO₂ is formed on the Si surface. Next, SiO₂ is etched by HF contained within the solution. By these two reactions, Si etching is progressed continuously.



Figure 6 shows the possible reason why the characteristic shape is formed at the vertical step after Si etching. The liquid velocity is changed by the vertical step, and change of the etchant amount supplied to the wafer surface causes the difference of etching rate. We therefore conclude that the

characteristic concave-convex shape is formed by the difference of etching rate due to the change of local liquid velocity.

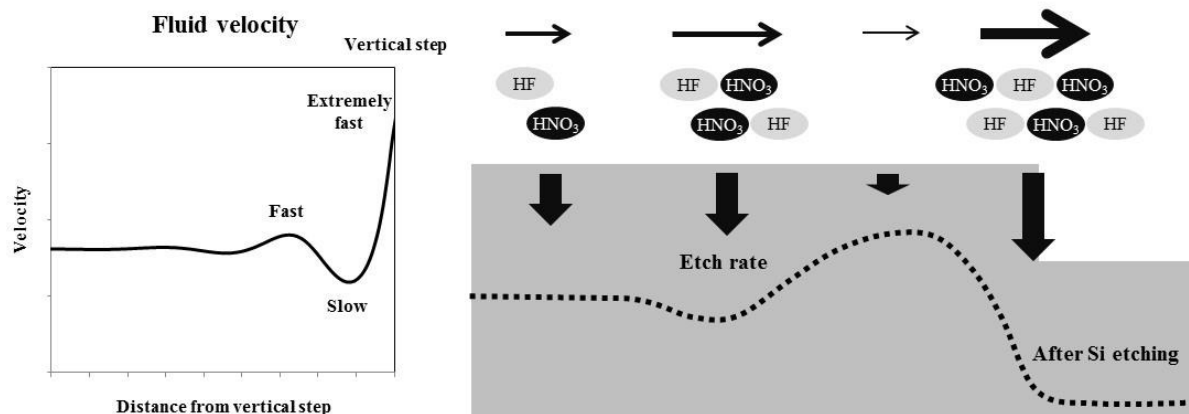


Figure 6: Etching mechanism at vertical step region.

Summary

In this work, we examined the effect of Si wet etching on the vertical step at wafer edge. AFM analysis after Si etching revealed a characteristic convex-concave shape. After examining the Si etching reaction and comparing fluid velocity with etching rate on a whole wafer, we confirmed that the etching rate was correlated strongly with fluid velocity. In addition, from the results of a liquid simulation, we found that the characteristic distribution of velocity is formed by the vertical step. We conclude that the concave-convex shape is formed by the local fluid velocity changing around the vertical step region.

References

- [1] Hendrix, M., et al., "Advantages of wet chemical spin-processing for wafer thinning and packaging applications." *Electronics Manufacturing Technology Symposium, 2000. Twenty-Sixth IEEE/CPMT International*. IEEE, 2000.
- [2] Okuda, S., et al., "Influence of edge beveling in small diameter wafer for resist coating," *The 74th Japan Society of Applied Physics Autumn Meeting Proceedings*, 2013.
- [3] Kaneko, K., et al., *ECS Transactions* 2.6 (2007): 295–303.
- [4] Kim, Tae-Sung and Kim, Moon-Uhn, *Fluid Dynamics Research* 41.3 (2009): 035504.
- [5] Schwartz, B. and Robbins, H., *Journal of the Electrochemical Society* 108.4 (1961): 365–372.

CHAPTER 4:

FEOL: Photoresist Removal, General Cleaning

Middle of Line (MoL) Cleaning Challenges in Sub-20nm Node Device Manufacturing

SherJang Singh^{1,a}, Pranesh Muralidhar¹, Samuel Mallabar¹, Silas Scott¹

¹ GLOBALFOUNDRIES US Inc. 300 StoneBreak Rd. Extension, Malta, NY, USA

^aSherJang.Singh@GlobalFoundries.com

Keywords: Wet Cleans, Middle of Line, MoL, Salicidization, Contact Cleans, CMP defects, Wafer Edge particles, Bevel particles

Abstract. In advanced technology nodes (sub 20nm), the gate & active contact architecture has become very complex. This architecture not only introduced new materials but also integrated additional patterning mask layers. This necessitated a separate Middle of Line (MoL) zone whereas conventionally contact integration used to be a Front End of Line (FEoL) process. This paper discusses wet cleaning challenges in MoL that were unforeseen with conventional contact architecture. Typical chemistries such as Sulfuric Peroxide Mixture (SPM), dilute Hydrofluoric Acid (dHF), Aqua Regia, Standard Clean 1 (SC1), etc. that were used for contact cleaning or in salicidization process are found to be too aggressive due to smaller process window, shrinking Critical Dimensions (CD), and other challenges arising from overall tighter tolerances. As a result of device scaling, most of the MoL mask patterning is done with immersion lithography and double patterning techniques such as Litho-Etch Litho-Etch (LELE) are also needed. Immersion lithography is very sensitive to pre-litho backside and frontside particles which make pre-litho cleaning in MoL very critical as well. Also due to lack of high aspect ratio features in MoL (mostly contact holes), physical particle removal techniques such as droplet spray and MegaSonic can be very effectively used to achieve higher Particle Removal Efficiency (PRE). This paper summarizes such different scenarios & related challenges.

Background

Most of the advanced technology node semiconductor device manufacturing has adopted the gate-last approach which utilizes an RMG (Replacement Metal-Gate) process. The gate last method prevents unnecessary thermal loading on the high-k gate material and the metal layers; typically induced due to high-temperature activation of the doping regions. In gate-last processes, junctions are salicidized after RMG requiring a different patterning approach for the active regions, i.e. an additional TS (Trench Silicide) mask is used [1]. Thus the contact to the active regions is split into two levels. First the TS is formed and filled with tungsten which is followed by conventional contact patterning (figure 1). Figure 1.a depicts a simplified MoL process flow for advanced nodes. In conventional nodes, the contact to gate and the active regions are made through one single contact mask layer which is further connected to BEOL (Back End of Line) metal layers. In the advanced nodes, a trench is first patterned onto the active area which is then cleaned and salicized and further filled with tungsten (W). The gate area is masked during the trench patterning process. After the W CMP (Chemical Mechanical Planarization), a contact to the trench & gate is patterned separately which is followed by etch and cleaning.

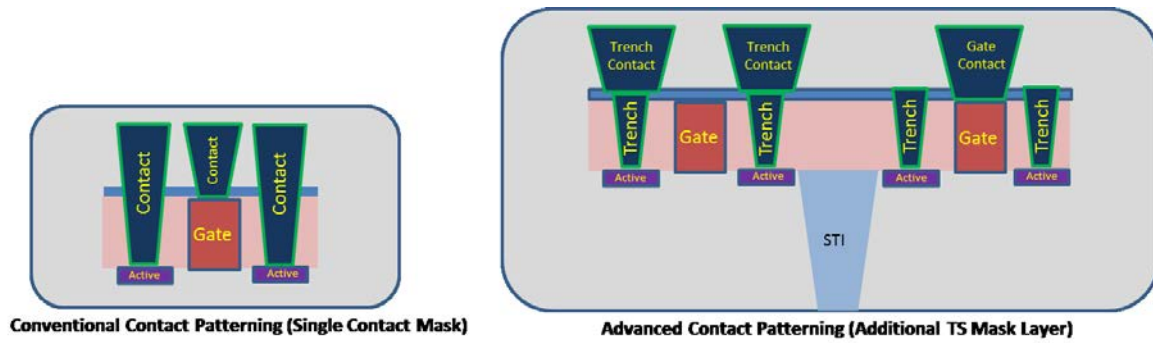


Figure 1.a: Middle of Line (MoL) contact architecture (simplified) for advanced scaling and conventional technology nodes



Figure 1.b: Figure showing a simplified Middle of Line (MoL) process flow.

Methods & Results

Challenge 1-Using SPM in MoL: Contacts to active areas are salicidized to reduce parasitic resistance and improve device speed. The salicide process involves depositing a thin metal film followed by a series of annealing and etch processes to form a metal silicide in the active regions of the device [2]. Before this process begins, the bottom of the contact needs to be free of any contamination to form defect free interconnects. Therefore aggressive clean chemistries such as hot SPM (Sulfuric Peroxide Mixture) are typically preferred [3]. Gate is completely encapsulated during active region (source/drain) salicidization process. However gate encapsulation is always prone to weak points due to unavoidable upstream defectivity and process marginalities. Figure 2 shows two possible mechanisms that can potentially compromise the encapsulation. Aggressive chemistries such as hot SPM can worsen or dissolve these weak points/defects and open a channel to the gate region thus etching out gate material. Figure 3 shows the cross-sectional and planar TEM of the device area of interest. Both the TEM images show a leakage path between TS (trench) & PC (gate). As mentioned earlier, salicidization process involves multiple film deposition, clean, etch & anneal steps. The device wafers were hammered (intentional aggravated process) through the various process steps of salicidization process to recreate the defect mode as shown in figure 2 & 3. The hot-SPM cleaning step was found to be the major cause for creating leakage paths. Figure 4 shows the results of SPM clean hammer test where consecutive cleaning cycles introduced more missing gate defects.



Figure 2: Figure showing possible models of marginal gate encapsulation that may allow SPM to generate a leak path between trench (TS) & gate (PC) a) SPM dissolvable contamination post gate CMP b) Point voids in Inler Layer Dielectrics (ILD).

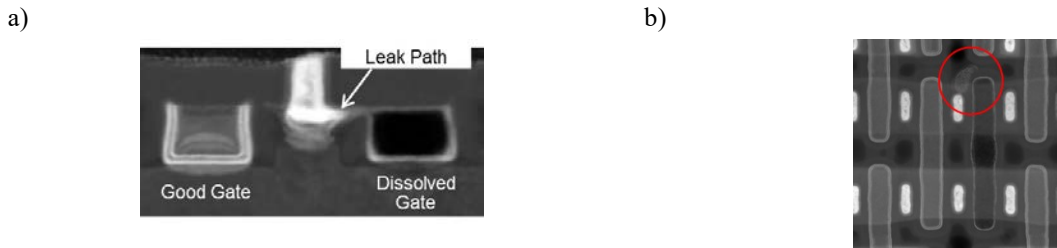


Figure 3: TEM images on product showing leak path for SPM chemical and missing gate stack a) Cross-Sectional TEM b) Surface TEM

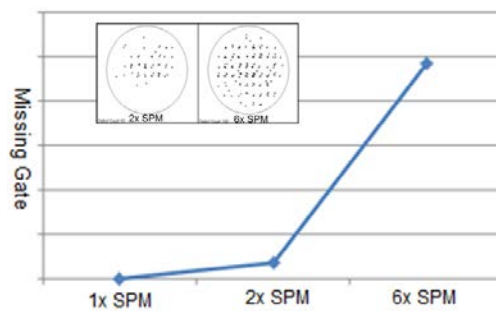


Figure 4: Plot showing results of hammer test done to validate the pre-salicidization clean (hot-SPM) attack with dark gate defect map after 2x & 6x SPM cleans.

Challenge 2- TS CMP interaction with Particles: In advanced MOL scheme an additional Chemical Mechanical Planarization (CMP) step is inserted post trench filling (step 7 in figure 1.b). The contamination induced from this step is very much dependent on upstream trench salicidization cleaning (step 5) [5]. Figure 5.a below shows an example of a defect that was introduced during trench salicidization process and later re-distributed during trench fill CMP. TEM analysis of a product failure site as shown in figure 5.b confirms the same site to create a short between TS contacts.

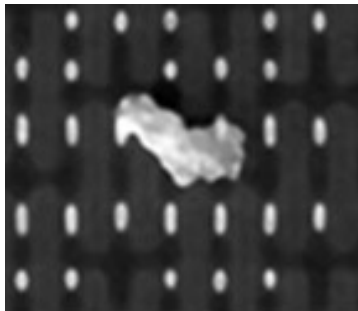


Figure 5.a: Post fill CMP SEM images showing flake

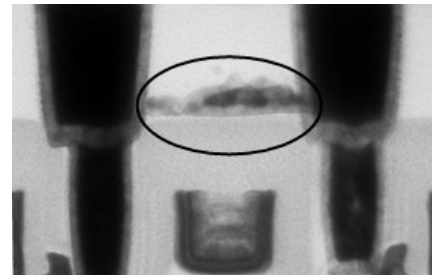


Figure 5.b: TEM cut image of a Product Failure site showing a flake shorting trench silicide contacts

Since the salicidization process involves multiple metal layer depositions it is important to remove all unreacted metal residues from across the wafer uniformly. The upstream wafer bevel/edge defect

can be redistributed by post fill CMP process. An optimized post salicidization clean process to remove the bevel/edge metal residues significantly reduces the flakes/particles defect post fill CMP step. Figure 6 shows comparison between old and new post salicidization clean process and figure 7 shows the impact of this improved process on downstream post fill CMP particles.

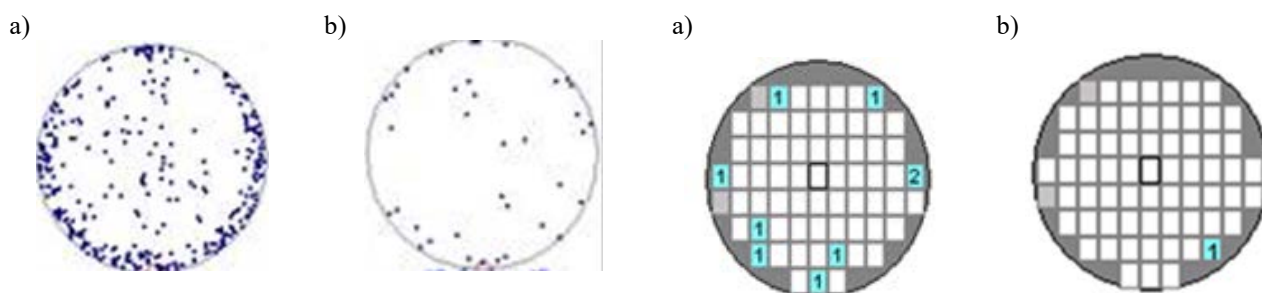


Figure.6: a) Blanket wafer particle/flake data (30nm) comparing old process and b) new process.

Figure.7: a) Product wafer particle/flake data comparing old process and b) new process.

Challenge 3- Gate & Trench Fill Material Compatibility: Aluminum (Al) and Tungsten (W) are widely used gate and trench fill metals. During the contact cleaning (step 10 in figure 1.b) trench filled W metal and gate filled Al metal are exposed [6]. Cleaning chemistry chosen for this step has to be carefully optimized to avoid metal attack. NH_4OH as well as SC1 (Standard Clean 1, i.e. $\text{NH}_4\text{OH} + \text{H}_2\text{O}_2 + \text{H}_2\text{O}$) are common cleaning chemistries to remove post etch residues as well as particles. Figure 8.a shows the TEM image of a failed site where W is seen missing in the trench while it is still intact in the contact which suggests that the trench W is eroded before the contact filling. W missing induced from contact cleaning can be analyzed & quantified at post trench CMP inspection. Figure 8.b shows an example of such inspection where W missing is clearly visible. Figure 8.c shows effect of NH_4OH cleaning on the W missing defects. W missing increases progressively with multiple NH_4OH based hammer test.

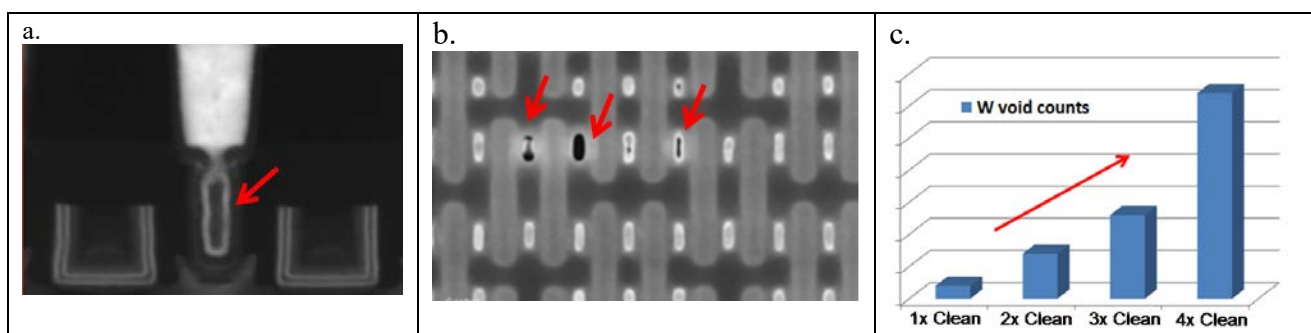


Figure 8. a) TEM image of a failed bit site in PFA (Product Failure Analysis) showing W missing from the trench. b) SEM image example of W missing through the trench post W trench CMP (step 7 in figure 1.b) c) Plot showing number of W void defects as a function on number of NH_4OH cleans.

Figure 9 shows SEM images of Al filled gate before and after cleaning with NH_4OH based MoL chemistries. NH_4OH based chemistries were found to attack Al metal as well. Therefore contact cleaning needs to be carefully optimized while considering chemical compatibility with various exposed materials.

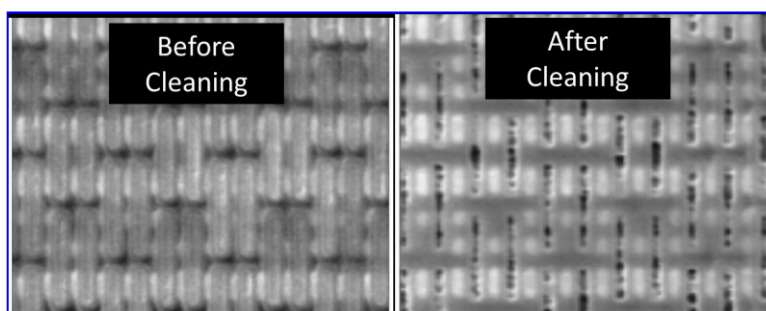


Figure 9. SEM showing Al filled gates before and after NH_4OH cleaning

Challenge 4- Pre-Litho & Post-Etch Particles: MoL contact lithography has always been a critical patterning step. In advanced nodes, MoL structures require tighter CD and overlay controls as well as new patterning films. A particle free surface is paramount to high quality lithography patterning [7]. Figure 10 below shows an impact of pre-litho particles on MoL patterning. Even sub 100nm particle can create patterning defects. This requires advanced cleaning methods to be employed before MoL lithography.

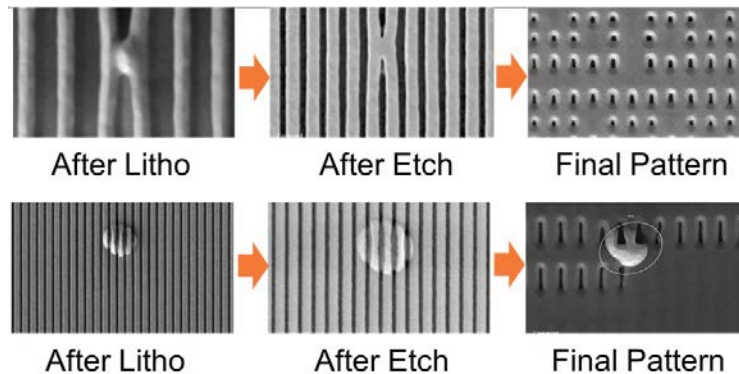


Figure 10: SEM images showing effect of pre-litho particles on litho patterning before and after etch.

Since pre-litho surfaces are blank films, physical particle removal techniques such as MegaSonic and jet spray (nanospray, etc.) can be successfully leveraged. Moreover in MoL layers, high aspect ratio features are absent and most of the integrated architecture has only contact holes exposed post etching. Therefore physical particle removal techniques can be used not just to the benefit of improved particle removal efficiency but also as a method to reduce clean process adds. Figure 11 shows a comparison between particle adds from two post MoL etch clean processes with and without use of jet spray techniques. It is evident that use of jet spray nozzle tremendously improves particle adds without any damaging side effects.

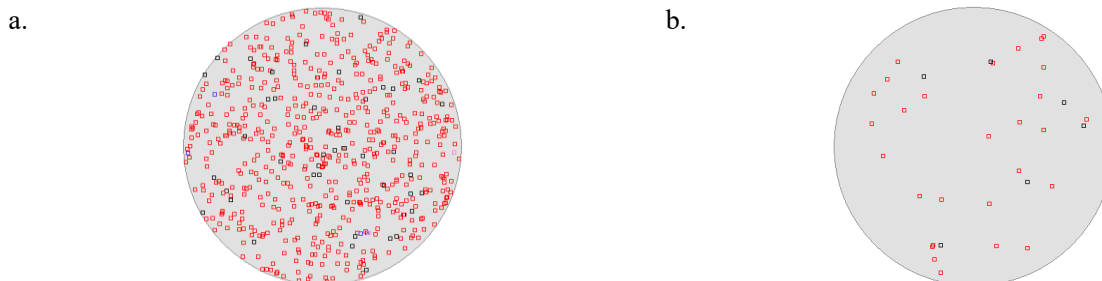


Figure 11: a) Particle add (> 30nm) map of a post etch clean process without physical particle removal b) with spray jet added in the process

Summary

With the increased complexity of contact architecture, contact cleaning becomes more critical in preventing contact opens as well as in maintaining the structural integrity by eliminating risks of contact to gate shorts and trench fill erosion. This paper lists various MoL cleaning challenges. Aggressive chemistries such as hot SPM can dissolve weak points/defects in gate encapsulation and open a channel to the gate region thus etching out gate material. Post salicidization clean is found to be very critical and if not optimized, it can lead to particle re-distribution during downstream trench fill CMP steps. NH_4OH based conventional chemistries can attack trench fill and gate fill metals such as W and Al, thus chemistries need to be carefully chosen when such materials are exposed. Pre-litho surface particles can lead to patterning issues thus physical techniques such as MegaSonic and NanoSpray should be leveraged as MoL architecture does not have high aspect ratio features exposed. Such techniques not just improve particle removal efficiency, but they also reduce process adds.

References

- [1] Cappellani, A.; et. al., "45nm High-k + metal gate strain-enhanced transistors," VLSI Technology, 2008 Symposium on, pp.128-129, Issue Date: 17-19 (June 2008)
- [2] Wong et. al. ;"Low contact resistance metal contact" US Patent No.: US 7,749,890 B2 (2010)
- [3] Karen Reinhardt, Werner Kern, "Handbook of Silicon Wafer Cleaning Technology", William Andrew, (2008)
- [4] K.N. Chauhan, V. Sih, T. Bhat, M. H. Kang, E. Kabutoya, G. Cheng, "Removing Organic Residues Using Backside Brush Scrubber Clean", ECS Trans, Electrochemical Society, Volume 69, pp. 109-115, (2015)
- [5] SherJang Singh, et. al. "Optimized salicide clean to reduce post fill defectivity," 2015 26th Annual SEMI Advanced Semiconductor Manufacturing Conference (ASMC), Saratoga Springs, NY, pp. 372-374, (2015)
- [6] SherJang Singh, et. al. "Optimizing Middle of Line (MoL) Contact Cleaning to Preserve Tungsten (W) Integrity in Advanced Technology Nodes" ECS Transactions, Electrochemical Society, 69(8):301-306, (2015)
- [7] SherJang Singh, et. al. "Pre-Litho Surface Preparation: Comparison of MegaSonic Vs NanoSpray in a Single Wafer Clean Tool" Sematech's Surface Preparation and Cleaning Conference, Saratoga Springs, NY (2015)

Characterization and Development of High Dose Implanted Resist Stripping Processes

Marion Croisy^{1,2,3,a*}, Cécile Jenny^{1,b}, Claire Richard^{1,c}, Denis Guiheux^{1,d},
Alain Campo^{2,e}, Erwine Pargon^{3,f} and Nicolas Possémé^{2,g}

¹STMicroelectronics, 850 rue Jean Monnet, 38926 Crolles Cedex, France

²CEA-Leti, 17 avenue des Martyrs, F-38054 Cedex 09, Grenoble, France

³CNRS-LTM, Université Grenoble Alpes, CEA-Leti Minatec 17 rue des Martyrs, F-38054 Grenoble Cedex, France

^amarion.croisy@st.com, ^bcecile.jenny@st.com, ^cclaire-therese.richard@st.com,

^ddenis.guiheux@st.com, ^ealain.campo@cea.fr, ^ferwine.pargon@cea.fr, ^gnicolas.posseme@cea.fr

Keywords: dry strip, residues, photoresist, implant, crust layer, high dose

Abstract. With the increase of implantation dose in new technologies, implanted photoresist stripping is even more challenged in terms of efficiency and substrate consumption. In this work, the effect of implantation parameters (energy and implanted specie) on the photoresist modifications are studied and several plasma chemistries are evaluated to remove it. A good removal efficiency with a low substrate consumption has been found with H₂-based processes especially N₂H₂.

Introduction

Stripping of photoresist after High Dose Implantation (HDI) is becoming a critical step with the increase of both implantation acceleration energy and dose. During the implantation, the photoresist surface is exposed to energetic ion bombardment and a modified layer (called “crust”) is formed. This crust is difficult to remove by conventional dry strip processes.

The main requirements of stripping processes are: to remove completely the photoresist without leaving residues on the surface, to avoid the formation of added defectivity such as blisters, to minimize the consumption and oxidation of underlying materials (Si substrate, epitaxial SiGe) and to avoid dopants loss and redistribution on the implanted areas.

N₂/H₂ and O₂/N₂ plasmas are commonly used in dry strip processes. O₂/N₂ is known to achieve a high ashing rate and consume the non-modified photoresist preferentially [1] while non-oxidizing plasmas are less reactive to strip the photoresist but are very efficient to remove the crust [2].

In this paper, we focused on the stripping efficiency of oxidizing and reductive plasma chemistries. First, several characterization techniques have been used to evaluate the physical and chemical modifications induced in the photoresist by the implantation step. The impact of both dopant energy and chemical nature have been investigated. Based on this understanding, several plasma chemistries are investigated for removing the implanted resist properly with no remaining residues and minimal substrate loss.

Experimental set up

In this work, 200nm-thick 248nm photoresist (PR) coated on 300mm wafers and commonly used for Complementary Metal Oxide Semiconductor applications has been exposed to either As or P implantation processes with an energy of 4 or 9 keV and a dose between 1.5 and 2.10¹⁵ atoms/cm². Several characterizations techniques (TEM, ToF-SIMS...) have been used to analyze the physical and chemical modifications of the PR exposed to the implantation process. TEM allows to determine the modified layer thickness and the implantation depth respectively. ToF-SIMS is used to get information on chemical profiles in the implanted PR but also to analyze residues

composition. These analyses are performed with an Ion-TOF TOF-SIMS⁵ instrument with a dual beam acquisition and detection of the negative ions only. A Bi⁺ beam at 25 kV is used for both analyses, with a 50 x 50 μm^2 raster. For the implanted PR characterization, a 50 μs cycle time is used with a 128 pixels resolution whereas for the residues analysis, the cycle time is 90 μs and the resolution 1024 pixels. The sputtering is performed using a Cs (500 eV) beam, with a 300 x 300 μm^2 raster for the photoresist and a 300eV beam with a 300 x 300 μm^2 raster for the residues. An electron flood gun with -20 V bias is also used to overcome charging problems.

Oxidizing and non-oxidizing dry strip processes are developed in Gamma GxT tool (Lam Research) on patterned 300mm wafers. Dry stripping processes efficiency is evaluated by CD-SEM observations on a Hitachi 5001 tool.

Experimental results

Implanted Resist characterization. A methodology has been set up to study the influence of implantation parameters (dopant specie and ions energy) on the PR modifications. TEM analyses on resist blanket wafers allow to determine the modified layer thickness for several implantation conditions (Table 1). An example of TEM picture is presented on Figure 1 and allows to discriminate two distinct areas: the underlying non-modified layer (“bulk”) and the crust on the PR surface.

Table 1 TEM analyses: crust thickness depending on implantation parameters

Implanted specie	Energy (keV)	Crust thickness (nm)
P	4	7
P	9	18
As	4	8
As	9	17

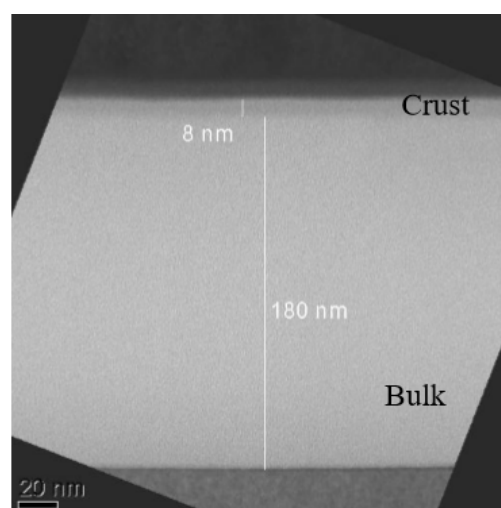


Figure 1 TEM picture of implanted PR (As 4keV)

For both As and P-implanted PR, the crust thickness depends on the implantation energy. At higher energy, the dopants go deeper into the photoresist which is modified on a thicker layer. On the other hand, the dopant specie (As or P) does not influence the crust thickness. However, XRR measurements (not shown here) show a higher density for the As-implanted photoresist.

ToF-SIMS analyses have been performed on As and P-implanted photoresist. Figure 2 presents the depth profiles for an energy of 4 keV.

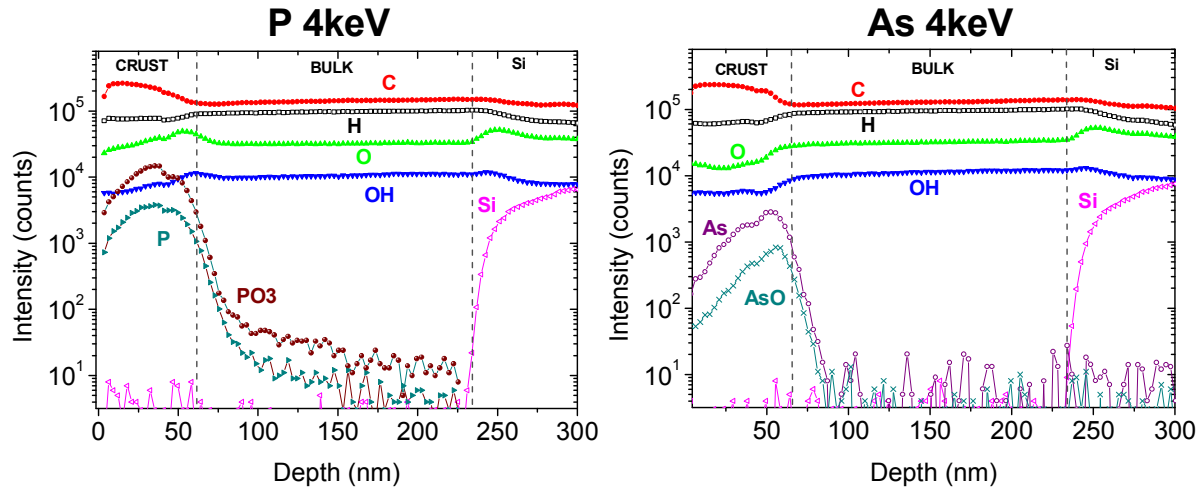


Figure 2 ToF-SIMS analyses of implanted PR : P 4keV 1.5×10^{15} at/cm² (left), As 4keV 2×10^{15} at/cm² (right)

Similar chemical modifications of the PR are observed for both implantations. The first 60nm of the photoresist analyzed by ToF-SIMS correspond to the crust observed in TEM picture and are depleted in O and H and enriched in C and dopants (either As or P). It should be noted that the crust thickness obtained by the ToF-SIMS analyses do not correspond to the thicknesses given by the TEM. Indeed, the depths given in Figure 2 are calibrated considering the sputtering rate of the non-modified resist which is certainly higher than the sputtering rate of the crust layer. Thus, the crust thickness given by the ToF-SIMS is overestimated.

These analyses clearly show that the photoresist is modified on the first 50nm whereas the dopants are located until 100nm. This means that the resist is not modified on the entire implanted depth.

Another interesting point is that dopants are present in their oxidized and metallic forms in the crust. ToF-SIMS experiments performed with As and P-implanted resist at an energy of 9keV show similar chemical depth profiles, except for the modified depth which is thicker.

Dry strip process development. The dry strip efficiency is evaluated for the same 200nm-thick photoresist with As and P implantation at both 4 and 9 keV using CD-SEM top-down observations. The results obtained for N₂/H₂ plasma are presented on Figure 3.

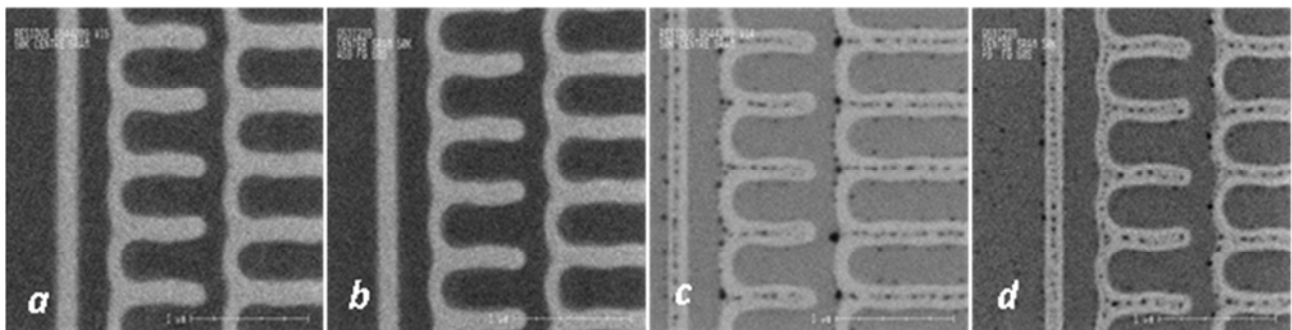


Figure 3 CD-SEM top view observations after N₂/H₂ dry strip process with several implantation energies
a) As 4keV b) As 9keV c) P 4keV d) P 9keV

N_2/H_2 is found to be very efficient to remove As-implanted photoresist for both 4keV and 9keV energies and there is no residues left. On the other hand, little black residues on both implanted and non-implanted areas are observed when the resist is implanted with phosphorus.

These black residues have been identified by ToF-SIMS analyses as phosphorus oxides. They are likely coming from the implanted photoresist because they are not observed on the wafer surface after the same process without photoresist.

These results indicate that N_2/H_2 chemistry is not efficient to remove phosphorus oxides coming from the crust, while we assume that it can eliminate arsenic oxides. However, a SPM-SC1 wet cleaning (SPM 5:1 at 80°C and SC1 1:2:80 at 65°C) following the dry strip process (Figure 4) can remove them completely.

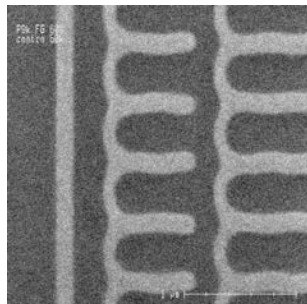


Figure 4 CD-SEM top view observation after N_2/H_2 dry stripping followed by a SPM-SC1 wet cleaning of P-implanted photoresist at 9keV

Concerning the O_2/N_2 dry strip chemistry, two kinds of residues are observed for both As and P implantations (Figure 5).

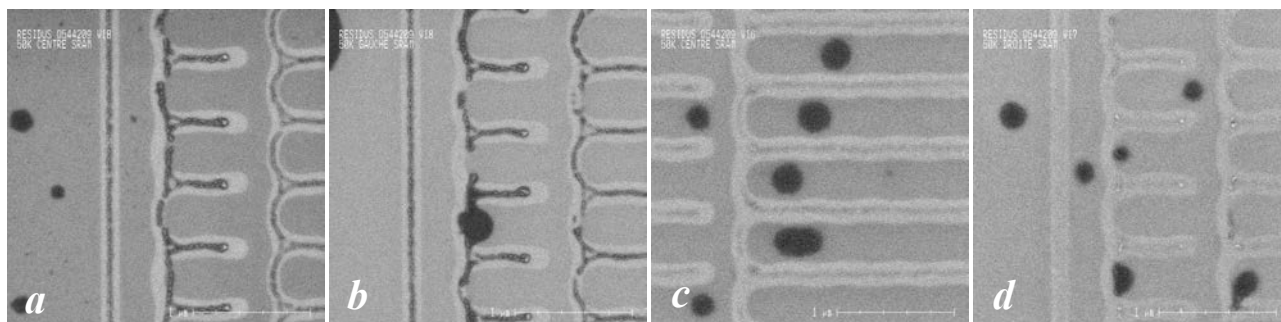


Figure 5 CD-SEM top view observations after O_2/N_2 dry strip process with several implantation energies
a) As 4keV b) As 9keV c) P 4keV d) P 9keV

Black residues larger but similar to those obtained with N_2/H_2 plasma are observed as well as small residues present on the non-implanted area previously protected by the photoresist.

The black residues have also been analyzed by ToF-SIMS (Figure 6) for P 4keV condition and identified as phosphorus oxides. O_2/N_2 plasma is not efficient to remove oxidized dopants present in the implanted resist and certainly contributes to the oxidation of the metallic dopants also present. That could explain why the black residues are larger with O_2/N_2 process.

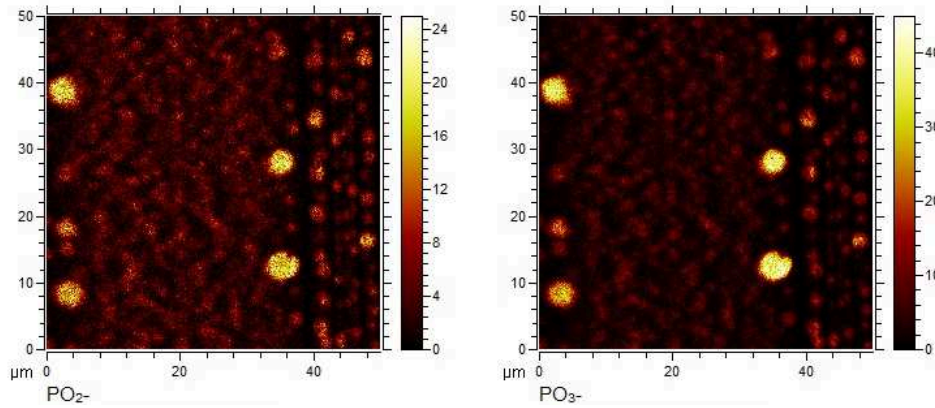


Figure 6 ToF-SIMS 3D view of PO_2^- and PO_3^- residues after O_2/N_2 dry strip

No chemical information could be obtained for the other small residues present on the non-implanted area but they are likely coming from the crust which is known to be hardly removed by O_2 -based plasma chemistries.

After a wet cleaning, the black residues identified as oxidized dopants are efficiently removed for both As and P-implanted resist, but the small residues attributed to the crust layer remain on the non-implanted areas (Figure 7).

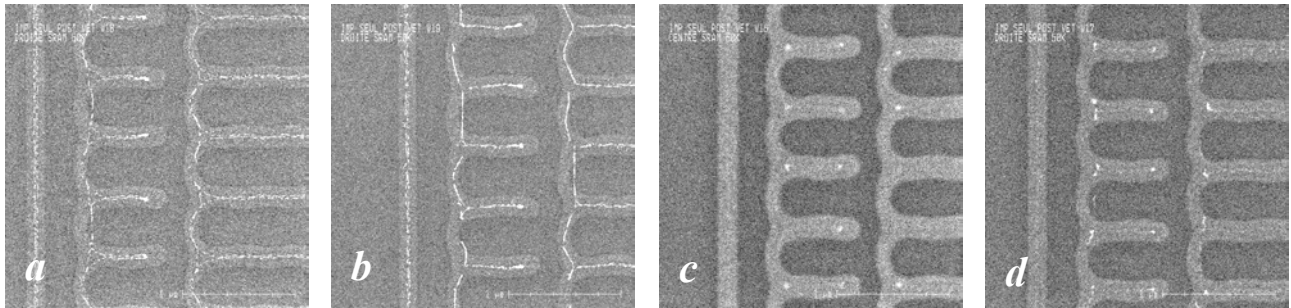


Figure 7 CD-SEM top view observations after O_2/N_2 dry strip followed by a SPM-SC1 wet clean
a) As 4keV b) As 9keV c) P 4keV d) P 9keV

To evaluate stripping chemistries, the effect on substrates (spacer, Si, epitaxial material like Boron-doped SiGe called SiGeB) is also an important parameter which has to be taken into account. Several phenomena are commonly observed: the oxide growth at the surface and the substrate consumption. Table 2 presents the results obtained on Boron-doped SiGe blanket wafers after N_2/H_2 and O_2/N_2 plasma processes. As expected, the oxide growth is higher with the oxidizing plasma. N_2/H_2 is more promising because of the minimal consumption and oxidation phenomena induced in Boron-doped SiGe.

Table 2 Ellipsometric thickness measurements of oxide growth and Boron-doped SiGe consumption with N_2/H_2 and O_2/N_2 processes

	Oxide growth (Å)	SiGeB consumption (Å)
N_2/H_2	12	2
O_2/N_2	32	7

Finally, the comparison between the two commonly used chemistries N_2/H_2 and O_2/N_2 indicates that N_2/H_2 is the most efficient to remove implanted photoresist without consuming substrate like Boron-doped SiGe. Even if some phosphorous-oxides residues could remain after dry strip process, they are entirely removed by the wet cleaning. With O_2/N_2 plasma, residues assumed to come from the crust layer are still observed on the non-implanted regions even after a wet cleaning.

However, some added defectivity called blisters can be observed after several N_2/H_2 plasma processes [3].

Other chemistries are thus evaluated to remove implanted photoresist with at least the same efficiency as N_2/H_2 and without blisters formation.

Alternative dry strip chemistries either reductive (He/H_2 or Ar/H_2) or oxidizing (N_2O , O_2/Ar , O_2/He) have been investigated with phosphorus implanted at 4keV (Figure 8).

H_2 -based chemistries show interesting results with no remaining black residues after dry strip process (Figure 8a and 8b) even if some residues remains on the non-implanted area (light area on Figure 8). These residues are likely coming from the crust which was not stripped efficiently even after a wet cleaning. However, He/H_2 is clearly more efficient than Ar/H_2 and the stripping efficiency could be improved for instance by increasing H_2 ratio.

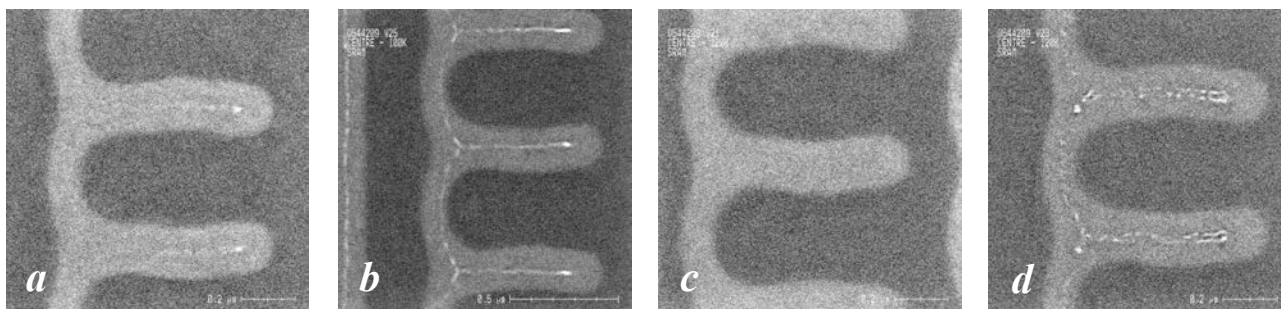


Figure 8 CD-SEM top view observations after a) He/H_2 b) Ar/H_2 c) N_2O d) O_2/He dry strip process of a P-implanted PR (4keV)

Remaining crust is also observed for O_2/He as well as for O_2/Ar and $N_2/H_2/O_2$ (data not shown). Only N_2O allows to remove the crust properly. Furthermore, for all these O_2 -based chemistries, black residues of phosphorus oxide are seen at the edge of wafer after dry strip. So far, N_2/H_2 plasma followed by a wet cleaning remains the most efficient dry strip process

Conclusions

The photoresist mask is highly modified by the implantation step. A cross-linked carbon layer depleted with H and O but enriched with As or P dopants is formed on the resist surface. The dopants are present both in their elemental and oxidized forms. Several plasma chemistries have been tested to remove the implanted resist. After dry strip process, two kinds of residues can be observed according to the plasma chemistry used: black residues identified as oxidized dopants which are easily removed by a wet clean and smaller residues attributed to the crust. So far the most efficient dry strip process is N_2/H_2 plasma but such process can introduce some blister defects. Some alternative chemistries show interesting preliminary results especially N_2O and He/H_2 and further investigations are ongoing on these chemistries especially to evaluate the sensitivity to blisters.

References

- [1] B. Thedjoisworo, D. Cheung & V. Crist, J. Vac. Sci. Technol. B Microelectron. Nanometer Struct. **31**, 021206 (2013).
- [2] K. Kinoshita & P. Engesser, ECS J. Solid State Sci. Technol. **2**, Q34–Q39 (2013).
- [3] C. Jenny & al., Plasma Etch and Strip in Microtechnology, 27-28th April 2015, Leuven Belgium

Chemical Infiltration through Deep UV Photoresist

Philippe Garnier*, Marc Neyens

STMicroelectronics Crolles2, 850 rue Jean Monnet 38921 Crolles, France

philippe-e.garnier@st.com

Keywords: 248nm Deep UV resist, HF, BOE, BHF, resist lift off, PALS, resist free volume

Abstract. Still nowadays in integrated circuits manufacturing, few materials patterns are defined by a wet etch on patterned deep UV photoresist. From dies to dies generation, an optical performance improvement is required, hence an evolution with thinner and thinner positive resist. This makes these latter more sensitive to wet chemical etchant through the polymer, reducing their protection of the underneath material. Following characterizations enable a clear understanding of BHF (Buffered HF) benefits versus diluted HF during a gate oxide definition.

Introduction

Gate oxides areas are still nowadays defined thanks to a combination of a photo lithography and a wet etch. Indeed this latter is preferred to plasma etching to avoid any transistor channel roughness and reliability degradation [1]. During this soft mask patterning, the gate oxide under the resist can be degraded by two different mechanisms: either a lateral wet etchant infiltration at the PR(Photo resist) / gate oxide interface [2], or a vertical diffusion of chemicals down to this same interface. Diffusion kinetics and characterization have already been proposed [3] [4]. A deeper understanding of the gate oxide degradation by HF based chemicals infiltration through the resist is hereby discussed.).

Experimental

248 nm deep UV commercial resists are considered with a thickness range from 200nm to few microns. Wet etchants used for the gate oxide patterning are either HF or BHF. Otherwise stated, BHF ratio is 1/7/160 (HF/NH₄F/H₂O). Both chemicals are dispensed on a single wafer spin dryer. Since focus is only targeting vertical infiltration through resist, wafers have only been coated with blanket resist without any exposure to UV. Since no pattern exist, no lateral infiltration occur. Gate oxide is a 7,5 nm thick grown SiO₂ made by RTO(Rapid Thermal Oxidation).

Results and discussion

Gate oxide patterning usually use either HF or BHF. This latter has shown better robustness than HF towards resist lift off during past empirical case studies depending on its dilution [5]. However BHF can roughen the silicon, and is much more sensitive to doped silicon corrosion linked with wafer charging [6], due to its much high conductivity than diluted HF. Hence, HF still has some advantages.

The degradation of the resist protection has already been discussed with resist blisters apparition [7]. This phenomenon is more often observed since the resists are thinner and thinner to meet optical performances. This occurs when the wet etchant has completely diffused through the resist and begins to degrade the underlayer. The most challenging task is to detect this degradation. Figure 1 shows resist blisters after a resist exposure to liquid HF. The blisters are only revealed under the SEM exposure. This is probably due to a resist swelling. Infra Red measurements have determined the resist core nature isn't modified during the HF diffusion inside the polymer. Nevertheless, some components like plasticizers, charges, ... can out diffuse during the contact with HF. Moreover the polymer will lose its mechanical properties if the wet etchant penetrate the polymer, due to polymer

chains relaxation. The SEM probably brings locally enough energy to swell the resist, decorating the degraded layer areas under the resist.

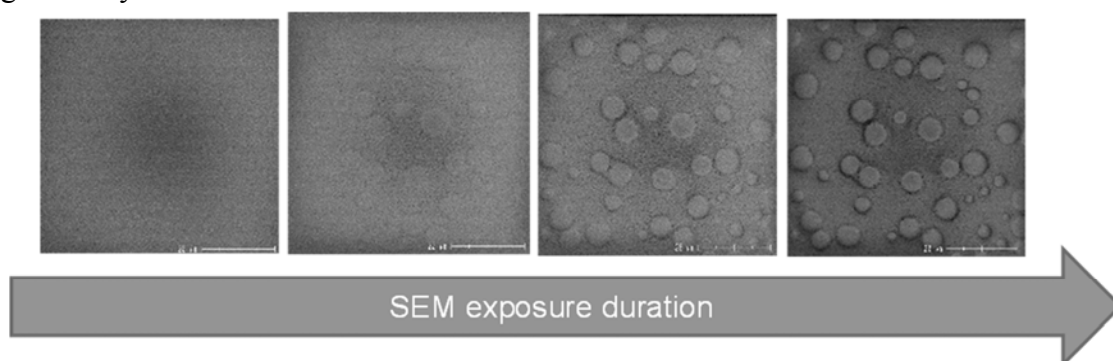


Figure 1: Resist blister evolution under SEM exposure (up to 1min). scale = 20 μ m

Several methods are proposed to study the resist protection degradation (figure 2). The most reliable is the electrical test of transistors, nonetheless the duration between these tests on products and the gate oxide definitions is usually of one month. Hence the degradation is caught very late and represents a huge cost in case of degraded resist protection events.

Transistor	Chemicals diffusion through PR	Gate oxide Surface analysis	Resist / Gate oxide interface: acoustic analysis
Electrical test	ATR-MIR	AFM	Gigasonic echo
	Gravimetry	Tof-SIMS	Acoustic microscopy 50MHz
	Tracers (neutrons)	Microscopy	Acoustic picosecond laser

Figure 2: Characterization methods either for chemical diffusion through PR or interface degradation

Other methods enable to study the chemicals diffusion through the PR, or the interface degradation by acoustic methods. Hereby focus lays on the gate oxide surface degradation once the chemicals have just reached the underlayer.

A HF0,5% 2 liters / min dispense is applied on a resist blanket with various duration. Then the resist is stripped with a DMSO / TMAH solvent in order to characterize the gate oxide surface. First, AFM scans 80 x 80 microns areas (figure 3). A 0,4nm thickness degradation is already measured after 400s HF dispense. At longer HF dispense, the gate oxide degradation is huge. Large circles are observed where the gate oxide is completely removed.

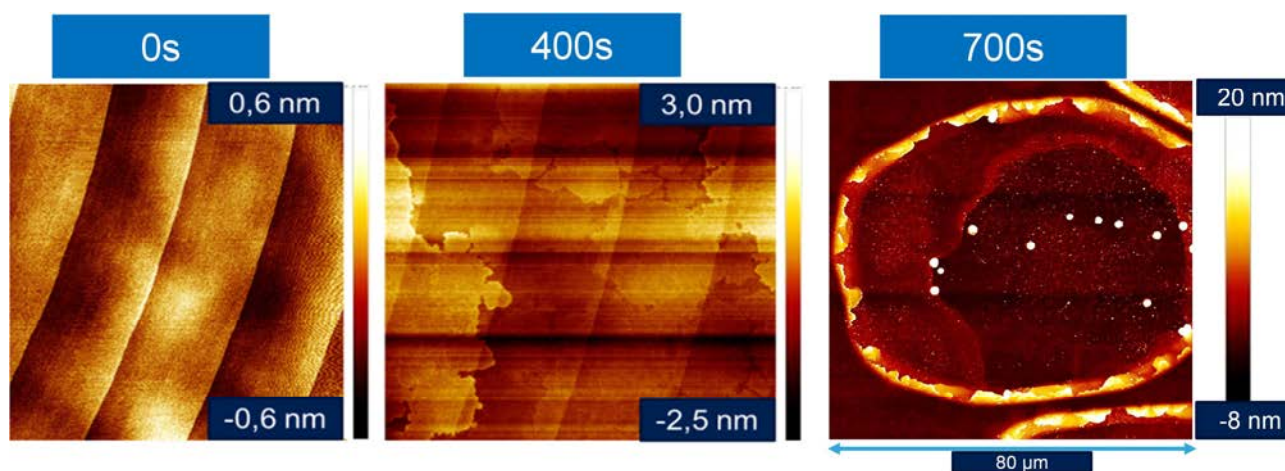


Figure 3: AFM: Gate oxide surface degradation along HF0,5% contact time with PR

Moreover, a 3D AFM profile enables a better visualization of the surface degradation but also evidences the re-deposition of wet etch by-products (figure 4). Indeed the SiO₂ layer is locally etched away where the fluorine based species have reached this interface. ToF SIMS gives an idea of the formed by product nature, made of Si, O and F.

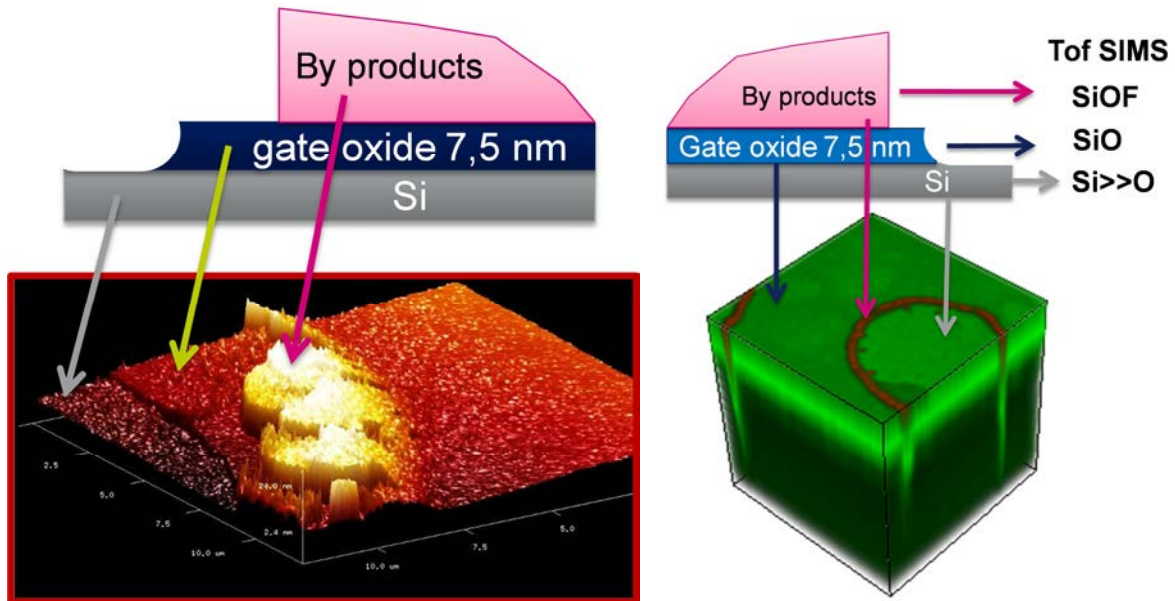


Figure 4: Gate oxide surface characterization after HF0,5% 700s on resist & resist strip: 3D AFM (left) & ToF SIMS profile composition (right)

Finally HF versus BHF infiltrations are compared through the same PR for an equivalent wet etch target of SiO₂ (figure 5). Whereas numerous resist blisters appear with HF0,5%, the resist protection appears perfect with BHF under a microscope. This is confirmed by transistors electrical testing: PR can stand a large BHF process window but very limited one with HF0,5%.

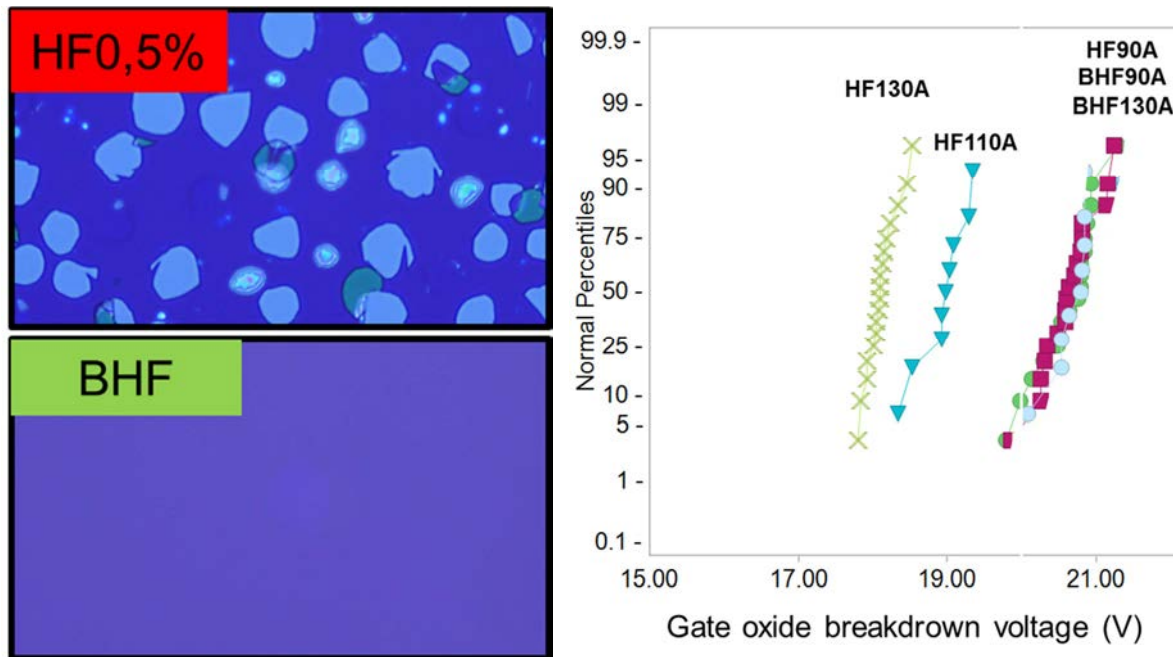


Figure 5: HF0,5% vs BHF – same SiO₂ 110A etch target dispense on same resist: microscopic observation (left) and gate oxide reliability comparison (right)

To understand these observations, the free volume of various polymers used in lithography has been established. First, ellipso-porosimetry method has been attempted but was unsuccessful because of resist swelling when solvents have been used. Secondly, VEPALS (Variable Energy Positron

Annihilation Lifetime Spectroscopy) has been used on two different commercial polymer formulations: a 215nm thick, 248nm Deep UV resist and a 56nm thick developable bottom anti-reflective layer. The two samples have been measured for various positron energy up to 2.1 keV. Only the o-Ps(ortho-positroniums) pick-off annihilation with middle lifetime have been considered since they are characteristics of the diffusion in free volume holes of the studied layers. The FVH (Free Volume Hole) is determined using spherical dimensions, based on the Tao-Eldrup model. The measured FVH is about 0,28nm (figure 6) for the resist and slightly lower for the dbarc layer.

This value is compared with the molecules present in the system. Whereas main fluorine species in the discussed BHF are HF₂⁻ and F⁻ ions [8], HF and H₂F₂ dimer compose HF_{0,5}%. Due to their respective size, HF can easily penetrate through this resist, unlike HF₂⁻ which is drastically restrained by steric hindrance and bad ionic affinity towards many electronegative bonds of the resist. Moreover the by products from gate oxide etch are probably made of SiF₆²⁻ ions, too big to diffuse back into the resist, so precipitate on the under layer. Experimentally, even if the dbarc is four times thinner than the discussed resist, thanks to a lower FVH, the HF diffusion through this polymer is well delayed.

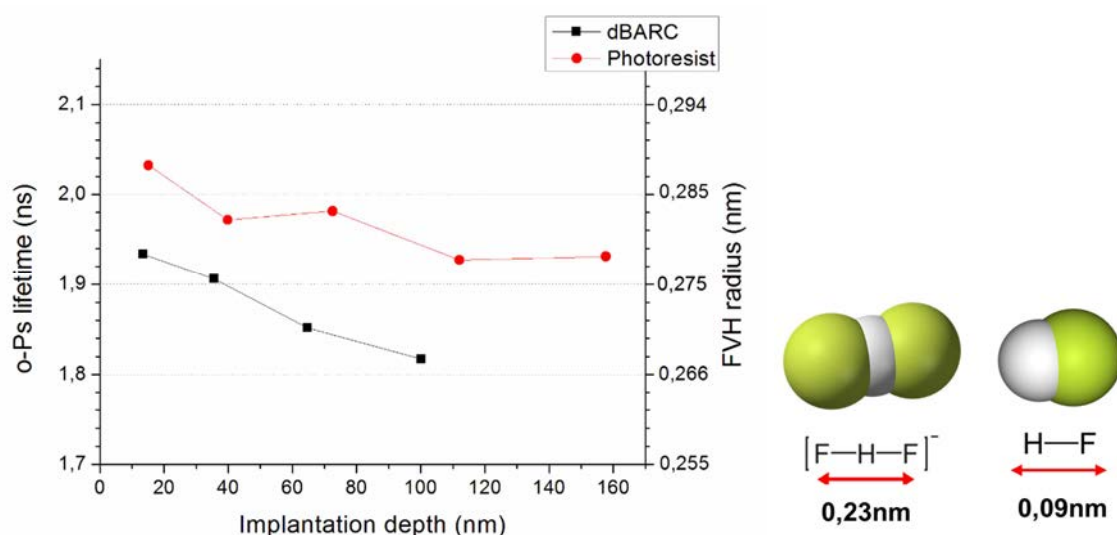


Figure 6 : PR FVH (Free Volume Hole) measured by PALS (left) & discussed molecules dimensions

Summary

Resist – wet etch couple is key in the gate oxide patterning. Indeed the resist must fully protect the under layer during the whole etch. Resist thickness is continuously thinner and thinner to follow the optical performances driven by the node evolution: from few microns down to few hundreds of nanometers. This makes the under layer protection by the resist more sensitive to wet etchant diffusion. Gate oxide patterning is usually performed with a 248nm DUV resist and either HF or buffered HF. Empirical experiments in the late 1990's proved I-line resist were more sensitive to HF and low pH buffered HF than pH > 3 buffered HF. Similar facts were also observed later for 248nm DUV resists. For the first time, we have hereby demonstrated the relationship between measured resist free volume and these empirical observations. Indeed, fluorinated wet etchant with pH < 3 is mostly made of HF molecules, that are small enough to quickly diffuse through the resist free volume. The SiF₆ based by-products are then trapped under the resist and precipitate. On the contrary, high pH BHF penetration is limited through the resist thanks to HF₂⁻ bigger ions size. Although transistors reliability tests remain the best standard method, the hereby discussed methodology could be used in the integration phase mode to select best resist / wet etchant couple. To conclude, even if BHF is safer regarding resist protection, HF is still preferred for channel quality interface.

Acknowledgment

We gratefully acknowledge the support of V. Joseph for the BHF experiments and N. Djourellov, INRNE-BAS, Sofia, Bulgaria for the PALS measurements

References

- [1] J.P. Carrere, CMOS gate oxide defects induced by pre-gate plasma process, Microelectronic engineering, 84, (2007), pp 2109-2112
- [2] P. Garnier, Photoresist adhesion during wet etch on single wafer tool, Solid state phenomena, Vol. 145-146, (2009) pp. 219
- [3] M. Neyens, Wet etchant diffusion through photoresist during gate oxide patterning, ECS Trans., Vol 69, (2015), pp 177-183
- [4] M. Foucaud, Investigation of the TiN/photoresist interface degradation during a wet etch, Microelectronic Engineering 135 (2015), pp 7-12
- [5] A. Beverina, 'Resist / Wet Etch' Couple for Dual Gate Oxide, Solid state phenomena, Vol.92, (2003), pp 235-238
- [6] B. Palla, Sources and Solutions for Silicon Pitting Defects Originating from Wet Chemical Processing, SPCC conf. 2015
- [7] C. Virgilio, Acoustic Characterization of Patterning Degradation during Wet Etching, ECS Trans. Vol. 69, (2015), pp 185-190
- [8] Y. Le Tiec, the chemistry of co-injected BOE, ECS Trans., Vol. 99, (2000), pp 377-384.

Efficient Photoresist Residue Removal with 172nm Excimer Radiation

Andreas Schäfert^{1, a,*}, Hartwig Wiesmann²

¹ Ushio Deutschland GmbH., Münchener Str. 10, 85643 Steinhöring, Germany

² Ushio Europe B.V, Breguetlaan 16-18, 1438 BC Oude Meer, The Netherlands

^aandreas.schaefer@ushio.de

Keywords: Excimer, VUV Cleaning, 172nm radiation, photoresist residue removal

Abstract The publication reviews the technique of photoresist residue removal with 172nm excimer radiation. The emission principle of excimer lamps is explained as well as the multi-step cleaning mechanism with vacuum UV radiation (VUV cleaning). Based on this principle, the effect on actual photoresist molecules of wafer cleaning applications is shown. The removal rate for typical resists is plotted as a function of dose as well the SEM picture of a wafer before and after the treatment is presented. As a conclusion, the chances and possible limitations for the usage of this technique are presented.

Introduction

In the last decade, excimer radiation sources have gained more and more impact in many fields of surface cleaning, surface activation and hydrophilization like semiconductor and flat panel display production [1] but also in exotic applications like the photofunctionalization of human implants for an enhanced healing pace [2]. All these applications are based on the effect of high-energy radiation in combination with oxygen radicals which are made out of the air by the radiation. This functional principle also offers a promising possibility for photoresist residue removal. It keeps the advantages of all excimer applications like instant-on functionality, high efficiency, high-speed applications, high process safety and no damaging of the substrate. Tests have been performed which showed very good results, in laboratory investigations as well as in micro electronic production.

Emission principle of dielectric barrier discharge excimer lamp

The functional principal of excimer lamps is based on cold high-frequency plasma located typically between two (one inner and one outer) quartz glass tubes (see Fig. 1). A metal electrode is mounted within the inner tube, while a second metal mesh electrode is mounted outside of the outer tube. The space between the quartz glass tubes is filled with a gas, either a noble gas or a noble gas halide compound. A high AC-voltage (typically some kV) is applied between the electrodes and therefore a number of micro discharge plasmas are generated between the two dielectrics (dielectric barrier discharge). These discharge plasmas excite the gas atoms of the discharge gas to instantaneously produce the excimer state. When the excited state of atoms decays into the ground state, a photon with the characteristic energy of the discharge gas is emitted. Therefore, the emitted spectral distribution is very narrow around the wavelength, set by the energy difference between the excited and the ground state of the specific discharge gas. The emitted spectrum can therefore be selected by the chosen discharge gas. Most commonly used is a xenon-filling, which results in an almost monochromatic 172nm radiation with efficiencies theoretically up to 67% [3]. The wavelength can be used widely for all kind of surface cleaning, activation and hydrophilization.

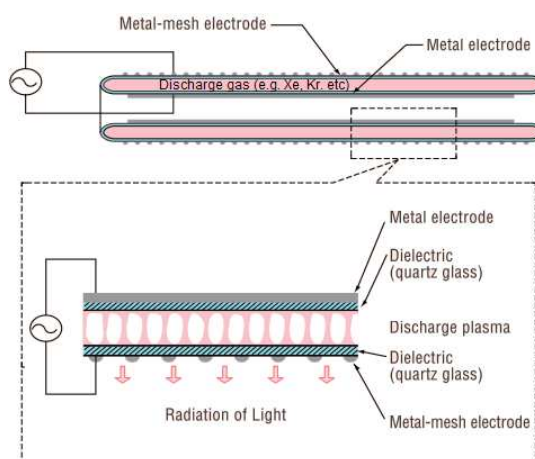


Fig. 1: Sketch of excimer lamp (based on [1])

Principle of VUV cleaning with 172nm excimer radiation

VUV cleaning with 172nm excimer radiation is a two-step process which is able to split organic molecules and remove the residues from the substrate.

It must be taken into account that only absorbed photons can contribute to the process. For organic molecules the extinction coefficients ϵ at 172nm are mostly higher 1000 [4]. In combination with the fact, that scattering is not a dominant source for extinction in most cases this means, that the radiation is absorbed effectively in the organic matter. VUV cleaning was first published by Falkenstein 2001 [5] and is in use already in various applications [6][1].

The VUV cleaning process is illustrated in Fig. 2.

In a first step, the bindings of organic molecules on the surface to be cleaned are split directly by the highly energetic 172nm photons. In table I is illustrated, that all major organic bonds except the C=O double binding can be split in this way.

Next to the organic molecules on the substrate, also the O_2 molecules in the air layer between the excimer module and the substrate are split and therefore radical atomic oxygen is produced which partly transforms with O_2 to ozone.

The radical atomic oxygen as well as the ozone transform the residues (C, C=O, O, H) of the split organic molecules into gaseous CO_2 , O_2 , H_2O and therefore removes them from the surface.

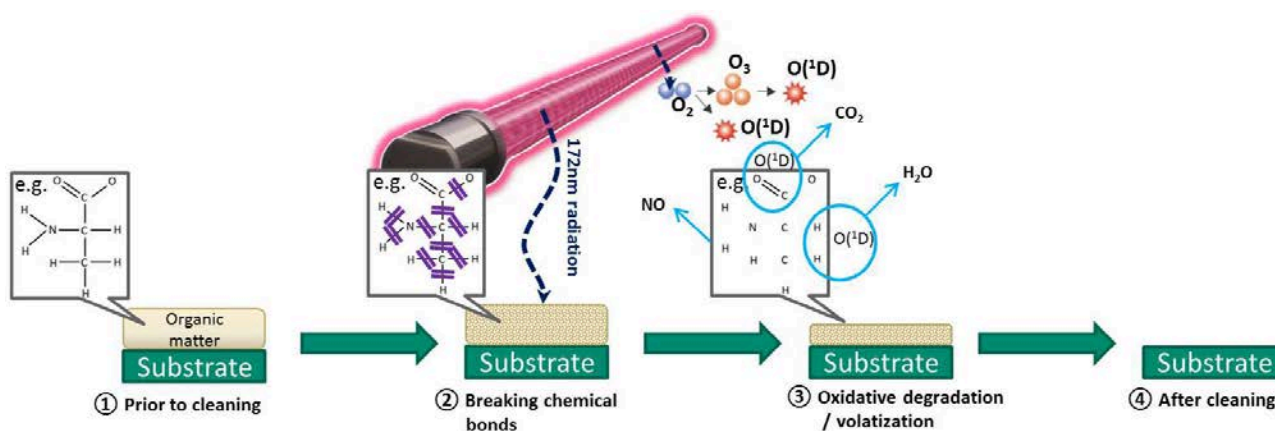


Fig. 2: Principle of VUV cleaning with 172nm excimer radiation as a two-step process (based on [1])

Table I: Binding energy of typical organic bindings compared to the photon energy of a 172nm photon (7.23eV). Green numbers indicate that the binding can be split by the photon. The only binding which cannot be split is marked by an arrow (based on [7]).

Binding	MeanBinding energy [eV]	Binding	MeanBinding energy [eV]
C—C	3.61	O—O	1.51
C=C	6.36	O=O	5.16
C—F	5.07	H—O	4.80
C—H	4.28	H—F	5.88
C—Cl	3.51	H—Cl	4.47
C—N	3.16	H—N	4.05
C—O	3.71	Si—O	6.49
C=O	7.72 ←		

Effect on photoresists

Photoresists are compounds of polymers like PMMA, PMGI, Novolac or epoxy resins, solvents like Cyclopentanone or Gamma-Butyrolactone and photosensitive ingredients [8]. Typical photoresists are for example SU-8 (based on epoxy resin) or DUV.

These organic molecules are composed of C, O and H bonds, so that absorbed 172nm photons can directly crack them. Therefore the typical VUV-Cleaning approach works as described in the previous section. The principle of the molecule fragmentation by 172nm radiation is sketched in Fig. 3.

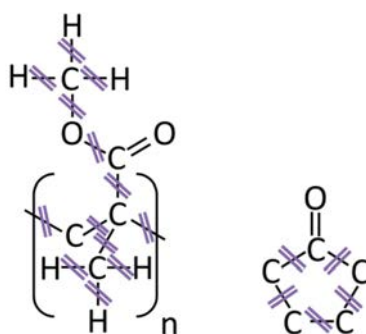


Fig. 3: Structure of typical photoresist components PMMA (left) and Cyclopentanone (right) and all bonds, which can be directly cracked by 172nm radiation, indicated by a double line. The residues can all be oxidized to H_2O , O_2 and CO_2 and therefore be removed from the surface.

Application of 172nm excimer radiation for photoresists removal

Tests have been performed both, in laboratory as well as already in microelectronic production machineries. To find the required 172nm radiation intensity the removal rate was measured as a function of the applied dose for different typical photoresists. The results presented in Fig. 4 show that with a high-intensity excimer systems ($400\text{mW}/\text{cm}^2$ at window) about 10nm thickness of photoresists residuum can be removed per second. The substrate was situated in 1mm distance from the window during the test. The whole process is very sensitive concerning the distance between the substrate and the excimer window due to the high absorption rate of 172nm radiation in air as illustrated in Fig. 5. The curve is not a pure e-function which can be explained by the fact that with the changing 172nm intensity also the oxygen radical concentration, which has a higher absorption coefficient as oxygen, changes as a function of the distance to the window. However if such a close distance between substrate and window is not possible the distance can be enlarged by the application of a controlled N_2 and O_2 purging between the window and the substrate with an optimized mass ratio of these two gases.

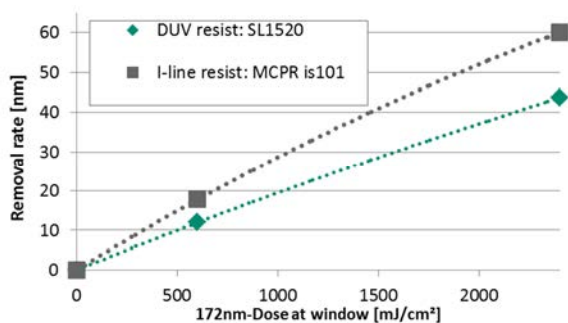


Fig. 4: Photoresist removal rate as a function of the 172nm excimer radiation dose for two typical resists (SL1520 and a MCPRITM series photoresist from The Dow Chemical Company)

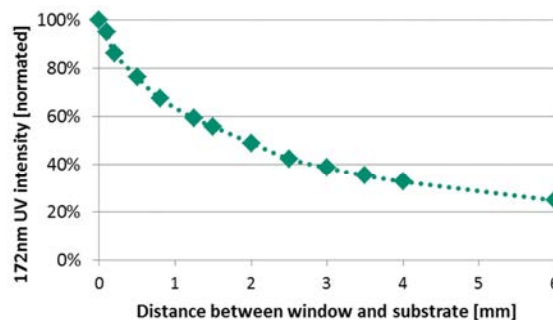


Fig. 5: Fraction of 172nm radiation intensity on the substrate compared to the initial value as a function of the distance to the excimer window measured in atmospheric air

To visualize the photo residual removal effect in the real application a positive edged pattern before and after the VUV cleaning with 172nm radiation was investigated with secondary electron microscopy as shown in Fig. 6. It can be seen clearly that the residuals can be removed efficiently and without residues.

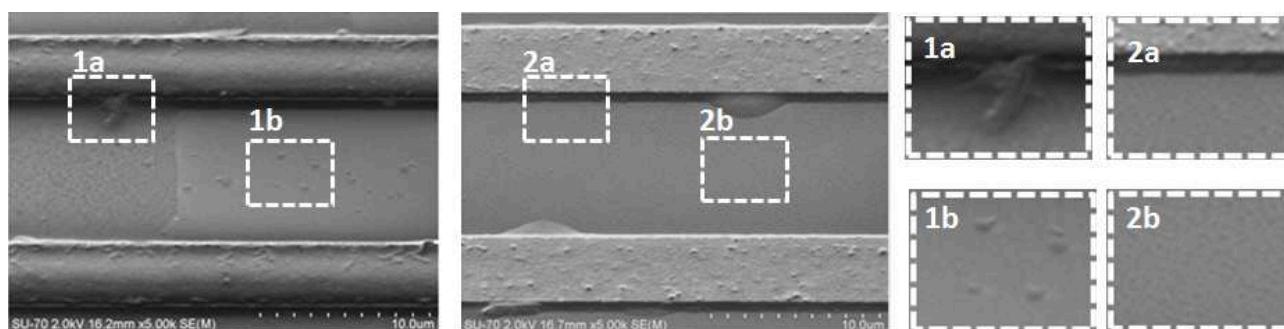


Fig. 6: SEM picture of a positive edged pattern before [left] and after [right] 172nm excimer radiation in atmospheric air. Two comparable frames are zoomed in to emphasize the differences

Summary and outlook

The test shows that 172nm excimer radiation is an efficient way of photo resist residue removal which is already in use in first plants. The main advantages are that the process is highly reproducible, needs no consumables and cleans the surface without secondary residues. As the 172nm radiation can be monitored in real time with sensors in the excimer module a stable process can be ensured easily. However due to a variety of different photo resists with different thicknesses and different geometries it is crucial that the necessary 172nm UV dose is investigated for each specific application to achieve best results.

References

- [1] USHIO Inc., Excimer irradiation unit, Tokyo, 2011
- [2] H. Aita et al., *Biomaterials* **30** (6), 83 (2009)
- [3] Sz. Beleznaï et. al., *J. Phys. D: Appl. Phys.* **41** (11), 6 (2008)
- [4] M. Hesse et. al., *Spectroscopic Methods in Organic Chemistry*, 2nd Ed. (Thieme; Stuttgart, 2008), pp. 1-24
- [5] Z. Falkenstein et. al., *Proc. SPIE* **4440**, 246 (2001)
- [6] K. Tanaka et. al., *Japanese Journal of Applied Physics* **46** (1), 6150 (2007)
- [7] F. Neufingerl et. al, *Chemie I - Allgemeine und anorganische Chemie*, 2nd. Ed. (Jugend & Volk, Wien 2007), p.47
- [8] E. Roßhaupter et. al., *Chemie in unserer Zeit* **5** (5), 147 (1971)

CHAPTER 5:

Processes of Wetting and Drying

Deep Trench Isolation and Through Silicon Via Wetting Characterization by High-Frequency Acoustic Reflectometry

C. Virgilio^{1, a}, L. Broussous², P. Garnier², J. Carlier¹, P. Campistron¹,
V. Thomy³, M. Toubal¹, P. Besson⁴, L. Gabette⁴ and B. Nongaillard¹

¹ Université de Valenciennes et du Hainaut-Cambrésis, Institute of Electronics, Microelectronics and Nanotechnology, IEMN, UMR 8520, Le Mont Houy 59313, France

² STMicroelectronics, 850 rue Monnet, F-38926 Crolles, France

³ Institute of Electronics, Microelectronics and Nanotechnology, Univ. Lille, UMR 8520 - IEMN, F-59000 Lille, France

⁴ CEA/LETI - Minatec, 17 rue des martyrs, 38054 Grenoble cedex 09, France

^aChristophe.Virgilio@etu.univ-valenciennes.fr

Keywords: Deep Trench Isolation, Through Silicon Via, wetting kinetics, high aspect ratio, acoustic reflectometry

Abstract. Wetting efficiency of microstructures or nanostructures patterned on Si wafers is a real concern in integrated circuits manufacturing. We present here a high-frequency acoustic method which enables the local determination of the wetting state of a liquid on real DTI and TSV structures. Partial wetting states for non-hydrophobic surfaces or low surface tension liquids are detectable with this method. Filling time of TSV structures has also been measured.

Introduction

With node evolution and the miniaturization of the components, aspect ratios of micro/nanostructures in electronic device are becoming higher and higher. Efficient wet etching or cleaning of these structures is determined by a complete wetting of the patterns which is very challenging at the micro/nanometer scale [1] and an adequate drying to avoid pattern collapse. Structures in DRAM with high aspect ratios are particularly subjected to these cleaning / drying issues [2, 3]. At the nanometer scale, for image sensor devices, Deep Trench Isolation structures (DTI) with high aspect ratios (around 20) need a good cleaning to avoid bad pixels isolation and then display issues like the apparition of white pixels on images. At the micrometer scale, Through Silicon Via (TSV) specific patterns are needed for ultra-small form factor packaging (processors and memory products), with aspect ratios up to 10. In these structures wetting kinetics also remains badly known. Theoretical models [4, 5, 6] and experimental works enable to predict and find the wetting time of micro/nanostructures like nanotrenches [7], microholes [8] and nanopillars [9]. However, very local measurement of the wetting of the bottom of the nanostructures or the wetting kinetics of a single microstructure is harder to obtain. High-frequency acoustic reflectometry can solve the latter problem. In the present work, this method has been used to determine the static wetting states of real DTI structures and wetting kinetics of real TSV structures.

Experimental Setup

The acoustic method proposed consists in the evaluation of the reflection of a high-frequency longitudinal acoustic wave (gigahertz range) on the structured interface (DTI or TSV) between bare silicon and a liquid droplet (Figure 1). An acoustic wave is generated by piezoelectric transducers fabricated on the wafers backside. This method has been previously used to characterize the wetting of silicon hydrophobic pillars at the micrometer scale [10] and nanometer scale [11] and the degradation of deep UV photoresist by etching solutions [12].

For the DTI case, a Finite Difference Time Domain (FDTD) model has been developed to predict the behavior of the emitted wave and predict the frequency needed to separate the reflected echoes (top and bottom of the DTI) in the time domain [13]. At 5 GHz frequency, the wavelength in the silicon is sufficiently small (1.7 μm) compared to DTI depth to have a good echoes separation. Thus, transducers working at 5 GHz have been designed and fabricated. For the TSV case, transducers working at 3 GHz have been used (in this case, too high frequency is not needed due to the higher TSV depth). In the two cases, the acoustic signal reflection occurring at the bottom of the structures will be characterized by monitoring the electrical reflection coefficient of the transducer to know if the liquid has reached the bottom of the structures.

Piezoelectric transducers fabrication: a ground electrode is first deposited on silicon by thermal evaporation (Ti / Pt: 10 nm / 50 nm). The shape and size of the transducers are then designed by a photolithography step (a circle with diameter of 100 μm) and ZnO is deposited by magnetron sputtering. Finally, the top electrode is also deposited by thermal evaporation (Pt: 50 nm) and transducers are obtained thanks to lift off technique. The DTI and TSV structures were etched into a Si wafer (frontside) with standard lithography and silicon etch processes, then cleaned with standard solutions such as SPM and SC1, that allow to grow a chemical oxide on Si surface. For some experiments, additional oxygen plasma was performed in order to remove atmospheric volatile contamination after long waiting time, and recover hydrophilic surface state. For the hydrophobic case, additional treatment is performed with PFTS (perfluorodecyltrichlorosilane). The contact angle on a flat silicon surface is 120° with water. Samples without any treatment will be referred to as “non-hydrophobic”.

Patterns are respectively crossed trenches 200 nm wide and 4 μm deep and a network of circular holes with a (diameter, depth) of (5 μm , 55 μm) and (20 μm , 95 μm). A TSV network of squares of side of 20 μm and depth of 95 μm is also studied.

The reflection coefficient is measured with different water / ethanol and water / isopropanol (IPA) mixtures (tunable surface tension) deposited as droplets on the wafer frontside. Cassie state (liquid droplet stands on top of the roughness trapping air pockets between the asperities) and Wenzel state (liquid imbibition is complete) are then detectable.

DTI Wetting States: Static Case

Measurements of the acoustic reflection coefficient at the bottom of the DTI are presented in Figure 2. All measurements on DTI structures have to be compared with those performed on the same wafer in non-etched area (flat surface). Theoretically, the reflection coefficient values measured on DTI structures should perfectly match with the one on the flat surface in a total wetting state. The variation of the reflection coefficient on the flat surface is due to the variation of the mechanical impedance of the mixture according to the ethanol concentration [14].

For the PFTS case, the reflection coefficient value is 1 with water which indicates that the liquid is in Cassie state, i.e. “non-wetting” situation, as expected after this surface treatment. For an ethanol concentration between 30% and 50% which corresponds to a surface tension between 35.0 mN.m^{-1} and 29.2 mN.m^{-1} , the reflection coefficient rapidly decreases from 1 to 0.93 which is characteristic of a Cassie / Wenzel transition. In Cassie state, air fills the DTI structures so the reflection of the acoustic wave is total, but in Wenzel state, air replacement by liquid implies a lower quantity of reflected energy (transmission of energy in the liquid is improved). Then, the slight increase observed for ethanol concentration higher than 50% can be compared to the same evolution obtained on a planar surface. However, the values beyond the transition are higher than those measured for a total wetting in the flat surface case. Therefore, it means that air is still present in the network and wetting is partial.

For the untreated case, the reflection coefficient is lower than the one corresponding to the PFTS treated structures and there is no Cassie / Wenzel transition anymore. Liquid wetting in the

structures is thus obtained for water and all the water / ethanol mixtures. However, we also note that reflexion coefficient values are still higher than for the reference flat surface case and the FDTD-simulated one with water in Wenzel state. We can conclude that the total wetting of the network is never achieved in the two cases even with the lower surface tension liquid (21.7 mN.m^{-1} for pure ethanol). This trend could be explained by the collapse of the thinnest part of the network during transducers fabrication. In fact, the use of liquids during the photolithography and lift off steps can imply pattern collapse if the drying of the structures is non-uniform. Moreover, the V-shape of the bottom of the trenches can make the liquid penetration harder in these areas (Figure 3).

TSV Filling Kinetics: Dynamic Case

Principle. As the depth of the TSV is about a hundred of micrometers combined with a closed hole geometry, the wetting states determination is not always instantaneous anymore. Once the liquid droplet is deposited on the wafer frontside, the reflection coefficient at the bottom of the TSV can vary over time. This variation represents the time needed for the full release of the air trapped in the bottom of the holes. The transducer size enables the wetting characterization on a dozen of holes simultaneously for TSV networks with holes diameter of $5 \mu\text{m}$ and on a single hole for $20 \mu\text{m}$ holes diameter.

5 μm diameter round TSV. Results with water / ethanol and water / IPA mixtures without hydrophobic treatment are presented in Figure 4. It is considered that the wetting is total when the value of the reflection coefficient at the bottom of the TSV is constant over time and reaches the value of the reflection coefficient at the top of the TSV (0.86 for water and 0.91 for pure alcohols). With pure water, the time needed to perform the full wetting of the structure is between 120s and 400s. It is possible to reduce the filling time by increasing IPA concentration of the mixture or using pure alcohols (immediate wetting with pure alcohols). We can notice that the wetting time is not significantly reduced with water / ethanol mixture compared to water / IPA mixtures. Applying an oxygen plasma treatment on the TSV before liquid deposition enables to drastically improve structures wetting kinetic. In this case, the surface is cleaner (atmospheric contamination removal) and hydrophilic and only 10 seconds is needed to fill the holes with water. In this case, the use of alcohols to reduce the filling time is not meaningful. With PFTS hydrophobic treatment, wetting is possible only for IPA and ethanol concentration higher than 60 % with filling times comparable to non-hydrophobic case.

20 μm diameter round TSV. Measurements have been performed for holes in the same array and in arrays at different locations in the center of the wafer. The filling time with water is a hundred of seconds, even after an oxygen plasma treatment but it is not exactly the same for each hole. In Figure 5: at 170s, the filling is completed for hole 2 but it is not for hole 1 (located in the same array than hole 2) and hole 3 (in a different array). These variations in wetting times are due to the very local surface state which is not exactly the same for each hole. We can notice that without oxygen plasma, the liquid penetration is sometimes but not always possible or is tending to infinite time because the wetting behavior is very sensitive to pollution and surface state for this depth. In the previous $5 \mu\text{m}$ TSV case, the wetting measurement was averaged on many holes, so this local effect cannot be seen. Optical observations of the surface with liquid shows that air bubbles have escaped from the holes for a hundred of seconds (Figure 6). This range of time is in agreement with the filling time determined by the acoustic method which let us think that holes filling duration is determined by non-dissolved air escaping. Moreover, by considering only air dissolution, theoretical calculations show that a few hours are requested to fully fill one hole with water [6]. This result reinforces the hypothesis of the non-dissolved air escaping. With hydrophobic treatment, wetting is impossible even with pure alcohols.

20 μm side square TSV. Measurements have been performed again with and without oxygen plasma treatment. Unlike the round TSV case, the liquid penetration is always possible and faster. It

is quite instantaneous for IPA (only a few seconds) and lasts about 20 seconds with water even without oxygen plasma treatment. This result shows the impact of the hole shape on imbibition phenomena and then its importance on cleaning process duration. Theoretically, the filling speed of an open square capillary tube can be calculated and it is higher than the one for a round capillary tube [15]. In our case, the geometry of the structures is closed but the filling speed tendency is the same. With hydrophobic treatment, wetting is impossible even with pure alcohols.

Conclusion

Wetting characterization of real DTI and TSV structures with high aspect ratios has been performed by high-frequency acoustic reflectometry. The method enables the determination of static wetting states when the depth of the structures is a few microns. It has been showed that DTI wetting depends on surface state and liquid surface tension. Full wetting was never achieved maybe due to patterning issues. For TSV structures with depth of a hundred of micrometers, as wetting state was not stable with time, it was also possible to determine the wetting kinetics. Even with a hydrophilic surface, round-shaped TSV wetting was completed in a hundred of seconds. This time goes down to 10 seconds for square-shaped TSV and imbibition phenomenon seems driven by local air evacuation. If the surface is hydrophobic, the liquid penetration can be impossible if the TSV depth is too high even with very low surface tension liquids like ethanol or IPA. Now, TSV wetting kinetics has to be performed including a liquid flow on the wafer to recreate industrial cleaning conditions. Wetting characterization of smaller holes with diameters close to those of CMOS contacts (about 50 nm) will also be completed.

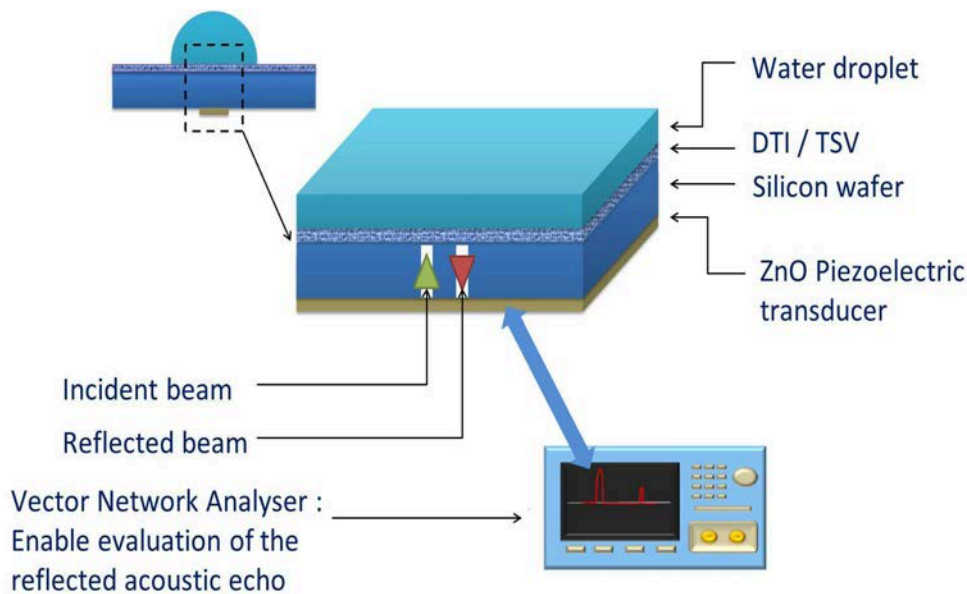


Figure 1: High-frequency acoustic reflectometry principle

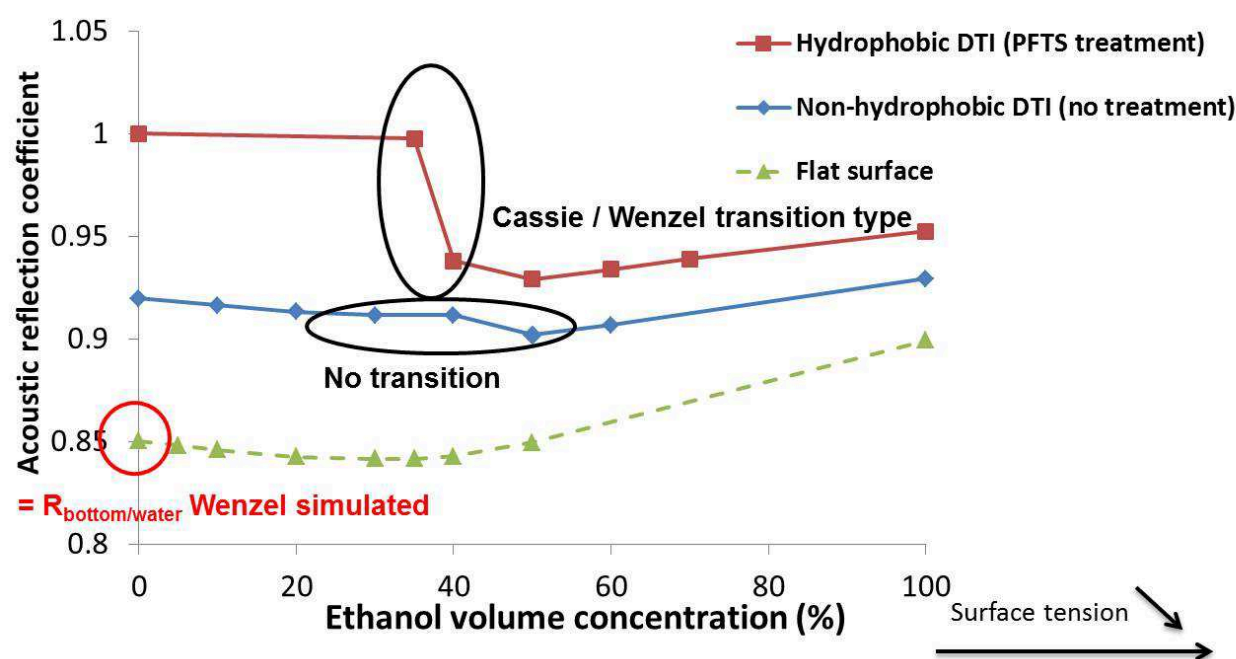


Figure 2: Measured acoustic reflection coefficient on the bottom of the DTI for different ethanol / water mixtures

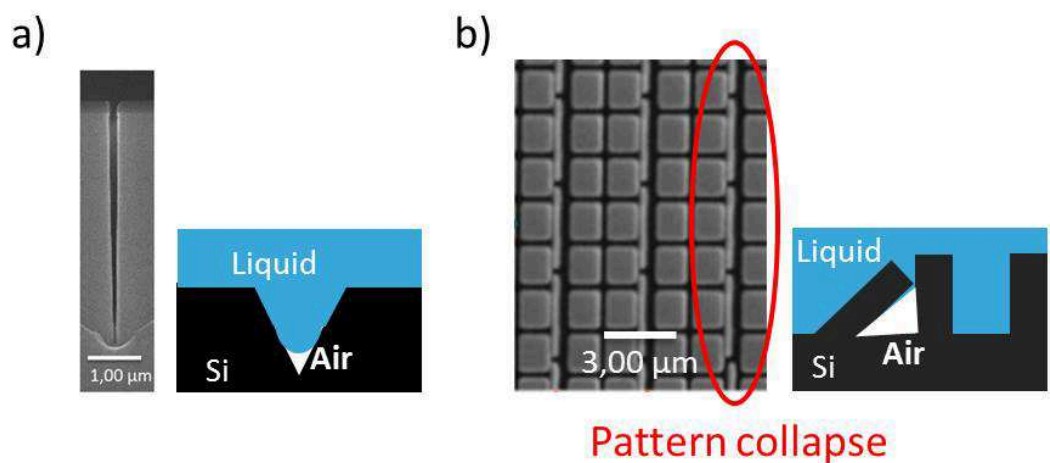


Figure 3: SEM cross section and scheme of the V-shape of a DTI trench (a) and SEM top view and scheme of the of the DTI network with pattern collapse (b)

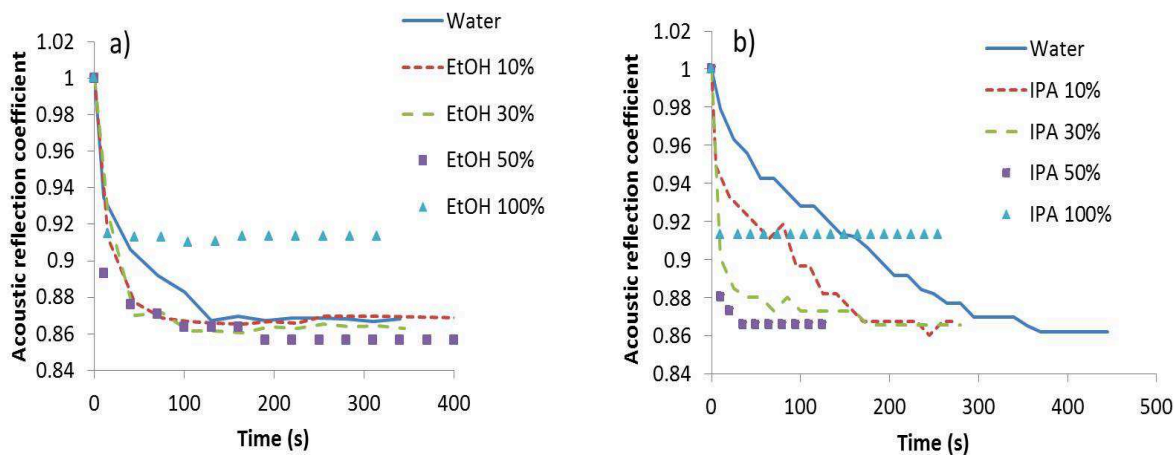


Figure 4: Measured acoustic reflection coefficient on the bottom of the 5 μm diameter non-hydrophobic TSV network versus time for different water / ethanol (a) and water / IPA (b) mixtures

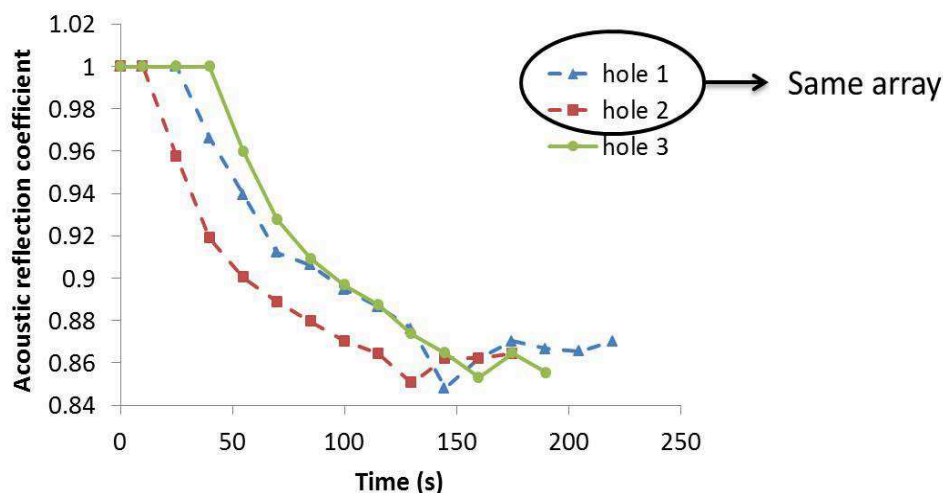


Figure 5: Measured acoustic reflection coefficient on the bottom of three different 20 μm diameter TSV holes versus time with water after an oxygen plasma treatment (measurements performed on the same wafer)

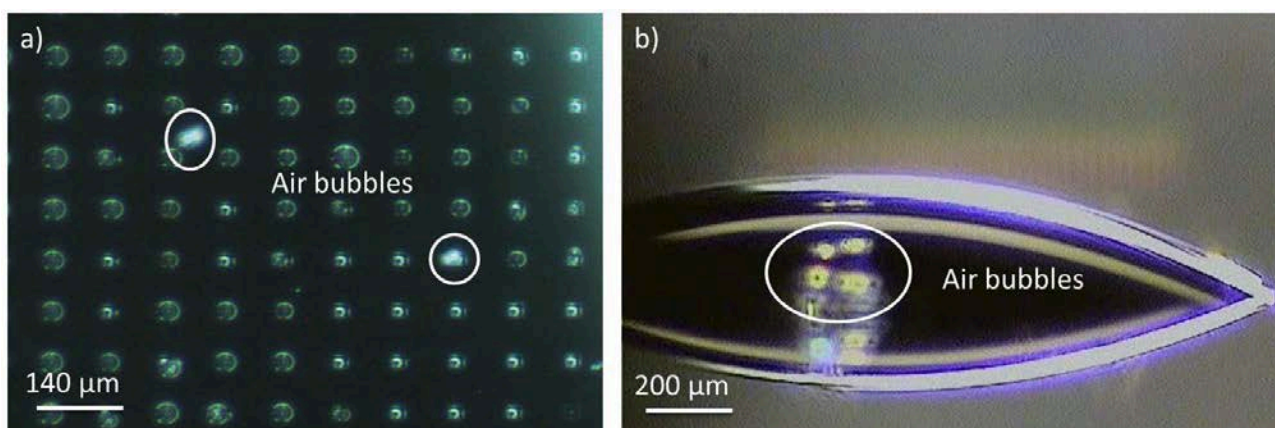


Figure 6: Optical visualisation of air bubbles release with water deposited on 20 μm diameter non-hydrophobic TSV network: top view (a) and side view (b)

References

- [1] X. M. Xu, G. Vereecke, E. van den Hoogen, J. Smeers, S. Armini, T. Delande and H. Struyf, *Solid State Phenomena* **195**, 235-238 (2012).
- [2] R. Hanestad, B. Schwab, J. W. Butterbaugh, K. T. Lee, W. G. Shim, S. Y. Kim and Y. P. Han, *Solid State Phenomena* **92**, 203-206 (2003).
- [3] A. Pacco, M. Wada, T. Bearda and P. Mertens, *Solid State Phenomena* **145-146**, 87-90 (2009).
- [4] I. Nakao, H. Umimoto, S. Odanaka, T. Ohzone and H. Esaki, *J. Electrochem. Soc.* **137** (7), 2303-2305 (1990).
- [5] D. Chandra and S. Yang, *Langmuir* **27**, 2303-2305 (2011).
- [6] M. T. Spuller and D. W. Hess, *Journal of The Electrochemical Society* **150** (8), 476-480 (2003).
- [7] J. Haneveld, N. R. Tas, N. Brunets, H. V. Jansen and M. Elwenspoek, *Journal of Applied Physics* **104**, 014309 (2008).
- [8] K. Ota and A. Tsutsumi, *ECS Trans.* **11** (2), 299-306 (2007).
- [9] G. Vereecke, XiuMei Xu, W. K. Tsai, Hui Yang, S. Armini, T. Delande, G. Doumen, F. Kentie, Xiaoping Shi, I. Simms, K. Nafus, F. Holsteys, H. Struyf and S. De Gendt, *ECS Journal of Solid State Science and Technology* **3** (1), 3095-3100 (2014).

-
- [10] N. Saad, R. Dufour, P. Campistron, G. Nassar, J. Carlier, M. Harnois, B. Merheb, R. Boukherroub, V. Senez, J. Gao, V. Thomy, M. Ajaka and B. Nongaillard, *Journal of Applied Physics* **112**, 104908 (2012).
- [11] S. Li, S. Lamant, J. Carlier, M. Toubal, P. Campistron, XiuMei Xu, G. Vereecke, V. Senez, V. Thomy and B. Nongaillard, *Langmuir* **30**, 7601-7608 (2014).
- [12] C. Virgilio, P. Garnier, M. Foucaud, A. Devos, D. Pinceau, J. Carlier, P. Campistron, B. Nongaillard, M. Neyens and L. Broussous, *ECS Trans.* **69** (8), 185-190 (2015).
- [13] C. Virgilio, J. Carlier, P. Campistron, M. Toubal, P. Garnier, L. Broussous, V. Thomy and B. Nongaillard, *International Journal of Mechanical, Aerospace, Industrial, Mechatronic and Manufacturing Engineering* **10** (3), 484-489 (2016).
- [14] D. Royer and E. Dieulesaint, *Onde Élastiques dans les Solides—Tome 1: Propagation Libre et Guidée* (Masson, Paris, 1996).
- [15] M. Dong and I. Chatzis, *Journal of Colloid and Interface Science* **172**, 278-288 (1995).

Pattern Collapse of High-Aspect-Ratio Silicon Nanostructures – A Parametric Study

Nandi Vrancken^{1,2}, Guy Vereecke², Stef Bal³, Stefanie Sergeant⁴,
Geert Doumen², Frank Holsteyns², Herman Terryn¹, Stefan de Gendt²,
and XiuMei Xu^{2,a}

¹ Vrije Universiteit Brussel, Pleinlaan 2, 1050 Elsene

² Imec, Kapeldreef 75, 3001 Leuven, Belgium

³ KU Leuven, Celestijnenlaan 200F, 3000 Leuven, Belgium

⁴ UC Leuven-Limburg, Herestraat 49, 3000 Leuven, Belgium

^a xiumei@imec.be

Keywords: High aspect ratio structures, wetting, pattern collapse, Cassie-Baxter, Wenzel, surface modification, contact angle, ATR-FTIR.

Abstract. This work focuses on capillary-induced collapse of high-aspect-ratio silicon nanopillars. Modification of the surface chemistry is demonstrated to be an efficient approach for reducing capillary forces and consequently reduce pattern collapse. Special effort is spent on determination of the wetting state of chemically modified surfaces as complete structure wetting is of utmost importance in wet processing. In light of this, an ATR-FTIR based method has been developed to unambiguously distinguish between wetting and non-wetting states.

Introduction

High-aspect-ratio (HAR) micro- and nanostructures have been widely used in various applications, including microelectronics, microfluidic devices, (biomedical) sensors, energy storage and photovoltaics [1–4]. During the fabrication or application of these structures, a liquid environment is often encountered, which poses great challenges to maintain the structural stability. Specifically, with decreasing size of the structures and increasing aspect ratio, the surface to volume ratio increases and therefore surface effects may become a dominant factor affecting the mechanical stability. During wet processing, capillary forces acting on the structures may result in pattern collapse. Formation of such capillary-force induced aggregates is particularly pronounced in the case of dense arrays of HAR – structures and is considered as a critical failure mechanism in device fabrication [5]. Surface modification of HAR-structures by deposition of organic layers has a potential to reduce pattern collapse greatly, but may result in superhydrophobic conditions [6]. Such superhydrophobic property prevents aqueous solutions to penetrate in between the structures and can thus severely reduce the effectiveness of wet processing steps. Therefore the goal of this work is to gain more insight in the mechanism of nano-scale wetting and pattern collapse for the development of efficient and damage free wet processing for HAR nanostructures.

Experiments and discussion

Silicon nanopillars of aspect ratios up to 20 are used as test structures in this work [7]. The structure dimensions are summarized in Table I and a SEM image of the AR 10 test structures is shown in Figure 1. Modification of the surface chemistry and surface hydrophobicity is achieved by UV/O₃ treatment for 15 minutes at ambient temperature and by vapor-phase deposition of volatile silane derivatives for 1h at 140°C. Liquid-phase depositions cannot be used, as these could already induce collapse of the test structures. A list of the deposited silane-derivatives and their respective water contact angles on blanket substrates is given in Table II.

Table I: Structure specifications.

Aspect ratio	Height (nm)	Average diameter (nm)	Pitch (nm)
5	240	46	90
10	380	37	90
18	490	27	90

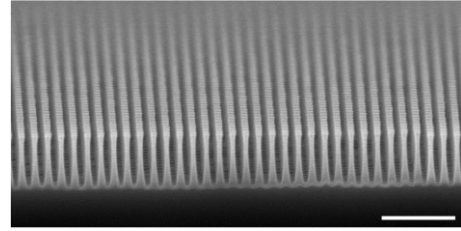


Figure 1: XSEM image of the AR 10 test structures. Scale bar is 500 nm.

Table II: Overview of the surface treatments (deposition of silane-derivatives and UV/O₃-cleaning) and the measured water contact angles on flat Si(100) substrates.

Abbreviation	Chemical name	Water contact angle on Si (°)
UV / O ₃		< 5
PEG	Polyethyleneglycol trimethoxy silane	~ 44
CUTS	11-cyanoundecyltrichlorosilane	~ 68
N ₃	Azido undecyltrimethoxy silane	~ 82
PETS	Phenethyltrichlorosilane	~ 88
BUTS	11-bromoundecyltrichlorosilane	~ 91
FDTs	1H,1H,2H,2H-perfluorodecyltrichlorosilane	~ 110

During liquid evaporation at the final stage of wet processing, liquid-air interfaces formed at the tips of the nanostructures give rise to capillary forces that could cause the structures to deflect and eventually to aggregate with nearby structures. In the case of nanopillars, the magnitude of the capillary force approximately scales according to: [8]

$$F_{cap} \propto \frac{2\pi \gamma R^2 \cos^2(\theta)}{\sqrt{d^2 - 4R^2}}, \quad (1)$$

where γ is the surface tension of the wetting liquid, θ the static contact angle measured on a flat surface of the same material, d the center-to-center distance between two adjacent pillars and R the pillar radius. As can be seen from Eq (1), for given dimensions of nanopillars, there are two approaches to reduce the capillary force: (1) use of solvents with lower surface tension (γ), e.g. organic compounds like isopropyl alcohol (IPA) and (2) surface modification to increase the contact angle (θ). The effectiveness of these approaches is compared in Figure 2. For silicon nanopillars of the same dimensions (AR 10: height 380 nm, average diameter 37 nm), replacing deionized water (DIW) (figure 2-a) by IPA (figure 2-b) reduces the cluster size formed after drying, but there is only a limited improvement because capillary forces can be reduced only by a factor of 3 ($\gamma_{H_2O} = 72 \text{ mNm}^{-1}$, $\gamma_{IPA} = 21 \text{ mNm}^{-1}$ at 298K). In contrast, surface modification can be more efficient in reducing capillary forces, as can be seen from the comparison of the UV/O₃ treated samples (figure 2-a and figure 2-b) with the one functionalized by BUTS (figure 2-c), and this allows for extending the processing window.

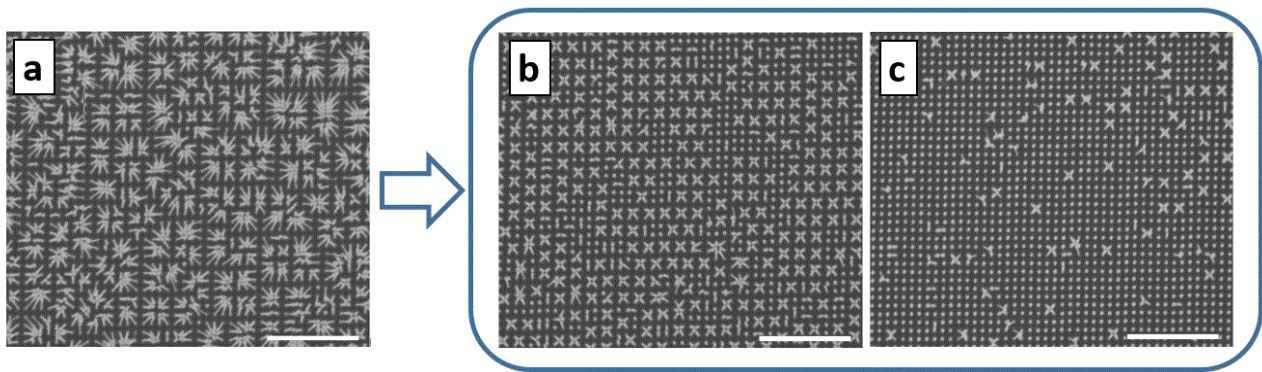


Figure 2: Reduction in pattern collapse upon changing the wetting liquid or modification of the surface with 11-bromoundecyltrichlorosilane (BUTS) for AR 10 structures. Scale bars are 1 μm . (a): UV/O₃ + DIW. All pillars collapsed and large aggregate clusters are formed. (b): UV/O₃ + IPA. A clear improvement is observed compared to (a), but still many pillars are collapsed. (c): BUTS + DIW. Most of the pillars remain freestanding. Increasing sample hydrophobicity is very efficient to reduce pattern collapse.

Pattern collapse after wetting and drying is characterized through statistical analysis of SEM-images in MATLAB[®]. The average cluster size is defined as the total number of pillars in each image divided by the total number of clusters. For AR 18 nanopillars, the variation of the average cluster size with contact angle is depicted in Figure 3. Generally, increasing hydrophobicity results in smaller clusters and less damage. For more hydrophobic surface terminations with CA > 80°, many of the pillars are still freestanding, indicating that surface modification is a promising approach for controlling pattern collapse. Although only marginal collapse is observed for superhydrophobic nanostructures, special care needs to be taken to avoid this wetting state as the lack of water penetration for the will result in a poor processing efficiency.

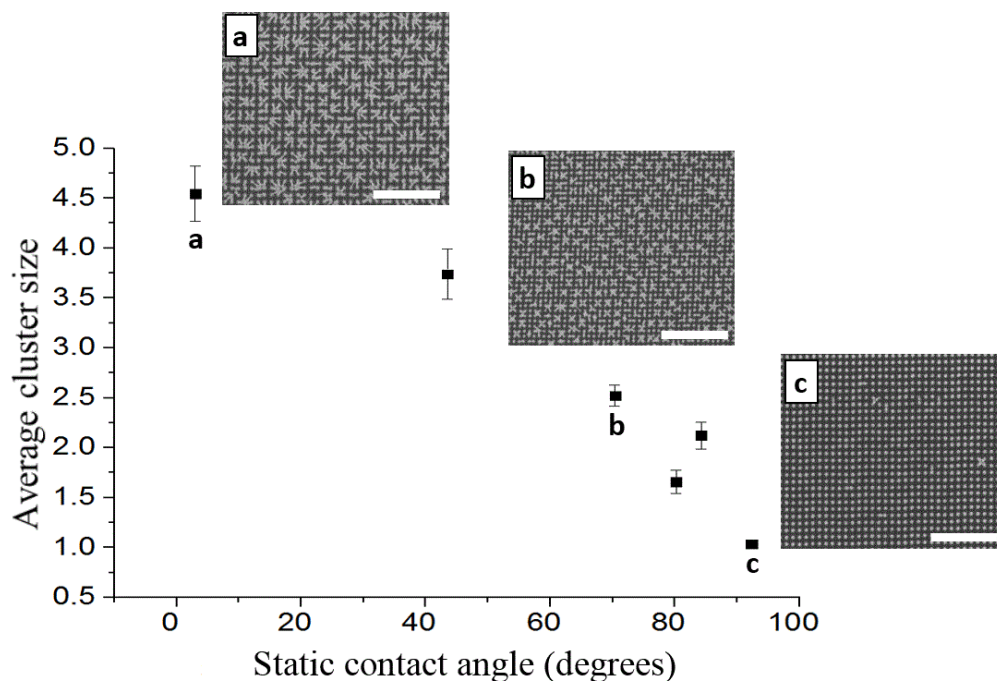


Figure 3: Variation of average cluster size as a function of water contact angle for the AR 18 structures. Static contact angles are measured on blanket silicon substrates with different silane depositions using a OCA200 system. Water drops of 1 μl size are used in the measurements. (a): UV/O₃ treated sample. (b): 11-cyanoundecyltrichlorosilane (CUTS) – deposited sample. (c): 1H,1H,2H,2H-perfluorodecyltrichlorosilane (FDTs) -deposited sample. Scale bars of the insets are 1 μm .

The most commonly used approach to estimate wetting properties is contact angle measurement. Contact angles above 140° are generally considered as characteristics of non-wetting states (Cassie-Baxter regime [9]), whereas static contact angles below 140° are attributed to good wetting-states (Wenzel [10] or Hemi-Wicking [11] regimes). Although this approach is relatively fast and easy to use, it does not provide an unambiguous determination of the wetting state. The value of 140° is rather arbitrarily chosen, and Wenzel states exhibiting static contact angles above 140° have been reported [12]. In order to accurately determine the wetting state, ATR-FTIR is used in this work. Crystals, made from silicon wafers patterned with nanostructures of AR 5, are placed in a liquid cell where the in situ ATR-FTIR spectrum is collected. Two main water peaks can be distinguished: the broad OH-stretching band around 3300 cm^{-1} and the OH-bending band at 1640 cm^{-1} . If the structures are fully wetted (Wenzel or Hemi-Wicking), as in the case of UV/O₃ treated crystal, a characteristic spectrum similar to water spectra on the blanket references is obtained. In the case of superhydrophobic wetting states for structures deposited with FDTs, an air layer is present in between the structures, which drastically decreases the intensity of water peaks. As the penetration depth of the evanescent wave is proportional to the wavelength, there is more attenuation at shorter wavelengths. This results in a change in the relative intensity ratio of the two water peaks, from ~ 2.7 for full wetting case to ~ 1 for non-wetting case, as illustrated in Figure 4. This difference in peak intensity ratio enables an accurate determination of the wetting states in between nanostructures. The nanoscale wetting states combined with the analysis of pattern collapse give a complete methodology for characterizing the effectiveness of different surface modifications on pattern collapse.

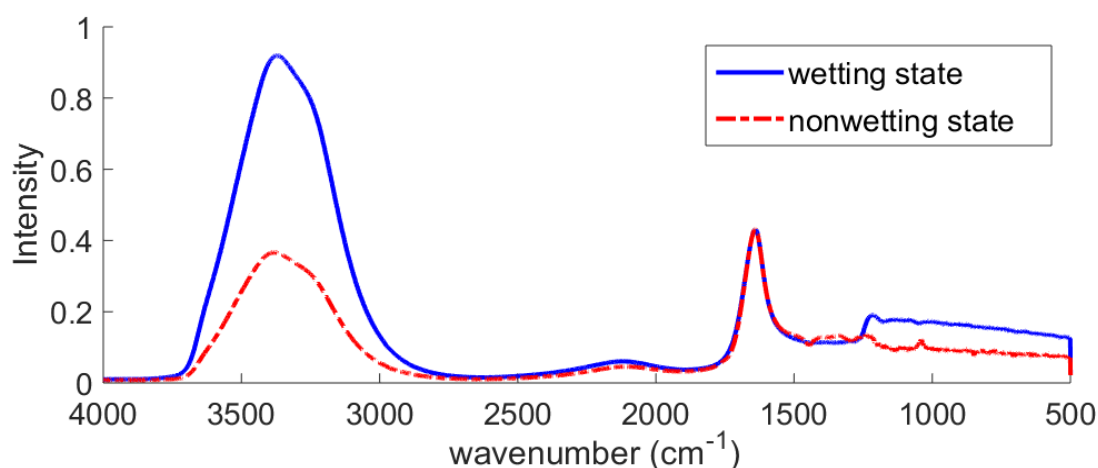


Figure 4: Normalized Water spectra collected on the AR 5 structures for a UV/O₃-treated crystal (good wetting) and 1H,1H,2H,2H-perfluorodecyltrichlorosilane-deposited (nonwetting) crystal.

Summary

Structural aggregation as a result of capillary forces is a major issue in the fabrication and wet processing of high-aspect-ratio nanostructures. IPA drying, as currently used in industry can only provide roughly three-fold reduction in capillary forces and will not be sufficient for more challenging high aspect ratio structures. The main purpose of this work is the achievement of a more fundamental understanding of the physical mechanisms behind the phenomena of wetting and pattern collapse, required to overcome the detrimental effects associated to structural aggregation. Surface modification to increase surface hydrophobicity is proven to be a more efficient method to reduce pattern collapse in HAR nanostructures. Increasing superhydrophobicity strongly reduces capillary forces and thus reduces the tendency to form structural aggregates. However close attention needs be paid to avoid superhydrophobic states, as these would lead to low processing / cleaning efficiencies. Accurate determination of the nanoscale wetting state was successfully

achieved by ATR-FTIR, based on the relative intensity ratio of the water peaks. The ATR-FTIR wetting study together with statistical analysis of pattern collapse allows for fine-tuning the surface chemistry to reduce pattern collapse, while still maintaining good wetting. For industrial applications, it is important to develop new rinsing liquids that could simultaneously tune the hydrophobicity of the structures during rinsing steps, and the removal of organic residues afterwards is also critical. These aspects will be studied in a future work.

Acknowledgements

Nandi Vrancken acknowledges the Fonds voor Wetenschappelijk Onderzoek (FWO) for a PhD grant.

References

- [1] L.C. Taylor, N. V. Lavrik, and M.J. Sepaniak, *Anal. Chem.* **82**, 9549 (2010).
- [2] O. du Roure, A. Saez, A. Buguin, R.H. Austin, P. Chavrier, P. Silberzan, and B. Ladoux, *Proc. Natl. Acad. Sci. U. S. A.* **102**, 2390 (2005).
- [3] M.G. Kim and J. Cho, *Adv. Funct. Mater.* **19**, 1497 (2009).
- [4] X. Li, *Curr. Opin. Solid State Mater. Sci.* **16**, 71 (2012).
- [5] G. Vereecke, X. Xu, W.-K. Tsai, H. Yang, S. Armini, T. Delande, G. Doumen, F. Kentie, X. Shi, I. Simms, K. Nafus, F. Holsteys, H. Struyf, and S. De Gendt, *ECS Trans.* **58**, 171 (2013).
- [6] V. Kumar, K.N. Bhat, and N. Nipun Sharma, *J. Adhes. Sci. Technol.* **29**, 308 (2014).
- [7] X. Xu, G. Vereecke, C. Chen, G. Pourtois, S. Armini, N. Verellen, W.K. Tsai, D.W. Kim, E. Lee, C.Y. Lin, P. Van Dorpe, H. Struyf, F. Holsteys, V. Moshchalkov, J. Indekeu, and S. De Gendt, *ACS Nano* **8**, 885 (2014).
- [8] H. Cooray, P. Cicuta, and D. Vella, *J. Phys. Condens. Matter* **24**, 284104 (2012).
- [9] A.B.D. Cassie and S. Baxter, *Trans. Faraday Soc.* **40**, 546 (1944).
- [10] R.N. Wenzel, *Ind. Eng. Chem.* **28**, 988 (1936).
- [11] J. Bico, C. Tordeux, and D. Quéré, *Europhys. Lett.* **55**, 214 (2001).
- [12] A. Lafuma and D. Quéré, *Nat. Mater.* **2**, 457 (2003).

Influence of CO₂ Gas Atmosphere on the Liquid Filling of Superhydrophobic Nanostructures

Guy Vereecke^{1,a}, Haroen Debruyn², XiuMei Xu¹, Frank Holsteys¹
and Stefan De Gendt^{1,3}

¹ imec, Kapeldreef 75, 3001 Leuven, Belgium

² Katholieke Hogeschool Leuven, Herestraat 49, 3000 Leuven, Belgium

³ Chemistry Department, Katholieke Universiteit Leuven, Celestijnenlaan 200F, 3001 Leuven, Belgium

^a guy.vereecke@imec.be

Keywords: wetting, superhydrophobic, nanostructures, CO₂ gas, ATR-FTIR.

Abstract. The introduction of 3-D nanostructures in semiconductor manufacturing may create wetting issues in aqueous processing. In this work we evaluated the use of a CO₂ gas atmosphere to promote the wetting of superhydrophobic nanopillars, relying on the high solubility of CO₂ in aqueous solutions. The patterned surface was first flushed with CO₂ gas, before dispensing the aqueous solution that was saturated with N₂ and switching the gas flow from CO₂ to N₂. The liquid penetration was characterized by monitoring the disappearance of CO₂ gas using ATR-FTIR. Results showed only a modest improvement in wetting, presumably due to a fast N₂-CO₂ gas exchange at the wetting front.

Introduction

With the continuous downscaling to smaller feature sizes of microelectronic devices, the semiconductor industry has entered the nano-age. The fundamental limitations encountered with silicon in planar devices has motivated the introduction of new materials and new 3-dimensional transistor architectures. One of the most recurring process step is the removal of residues generated by patterning processes. Typically, aqueous based chemistries are used for cleaning since they present a lower environmental impact and cost of ownership. However their high surface tension creates a new challenge on nano-patterned surfaces covered with hydrophobic residues. Indeed surface structures are known to enhance the hydrophobic character of surfaces with a contact angle $\theta > 90^\circ$, ultimately leading to a superhydrophobic behavior with no wetting of the open space in-between the structures [1]. Moreover recent studies have shown that even inherently hydrophilic surfaces ($\theta < 90^\circ$) can become hydrophobic as a consequence of structuring [2-5]. Incomplete wetting during a cleaning step would result in inefficient residue removal and unacceptable defectivity. While the common use of surfactants to decrease the surface tension and promote wetting is not always applicable any more, as this may leave residues in poorly rinsed nano-spaces [6].

In this work we evaluated the use of a CO₂ gas atmosphere to force the wetting of superhydrophobic structures, without the use of surfactants. The high solubility of CO₂ in aqueous solutions has been shown to promote a void-free filling of nanofluidic channels [7]. Here the patterned surface was first flushed with CO₂ gas, before dispensing the aqueous solution that was saturated with N₂, with the purpose that the dissolution of the trapped CO₂ gas would force the liquid to penetrate in-between the structures and lead to a complete wetting. Structures consisted of nanopillars that were rendered superhydrophobic by SAM-grafting. The liquid penetration was characterized by ATR-FTIR. Results showed only a modest improvement in wetting, presumably due to a fast N₂-CO₂ gas exchange at the wetting front.

Materials and methods

Silicon nanopillars of 90nm pitch, with a diameter of about 31nm and a height of about 416nm ($AR = 13$) were etched using a Lam Research 2300 Kiyo® C series conductor etch system [8]. The fabrication process ended up with an O_2 plasma strip. Pillars were functionalized with a vapor phase deposited self-assembled monolayer (SAM) of FDTS (1H,1H,2H,2H-perfluorodecyltrichlorosilane) to give them superhydrophobic properties [4]. Static contact angle measurements of sessile drops on functionalized blanket reference samples and nanopillars were carried out using a Dataphysics OCAH 230 system, lending $\theta \approx 110^\circ$ and 149° , respectively. The absence of liquid filling the space in-between the pillars was confirmed by optical reflectance measurements in a previous study [4]

CO_2 gas disappearance upon wetting with UPW was monitored by ATR-FTIR on a Nicolet 5700 spectrometer from Thermoelectron Corporation, equipped with a liquid nitrogen cooled mercury-cadmium-telluride detector. ATR crystals were polished from patterned wafers and mounted in a flow cell [5]. Crystals had a window angle of 30° and a length L of 53mm, lending 18 reflections at an angle of 60° on the patterned surface in the liquid cell (Figure 1). The evanescent wave had a penetration depth of about 301nm in gas at the wavenumber of the monitored CO_2 peaks ($\sim 2350cm^{-1}$), ensuring a high sensitivity for monitoring the space in-between the nanopillars. The cell was connected to a flow setup for the make-up of CO_2 -saturated UPW and the fast switching between CO_2 and N_2 gas flows (Figure 2). The setup was equipped with a magnetically levitated centrifugal pump providing a stroke-free flow through the cell (Levitronix BPS-i30). Tests were performed at room temperature ($T = 22^\circ C$), with spectra acquired at a resolution of 0.5 ($0.25cm^{-1}$).

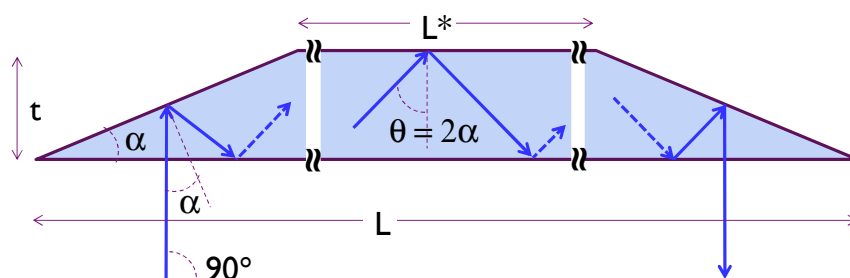


Figure 1: Geometrical description of ATR crystals. The IR beam enters and leaves the crystal from the backside at an angle of 90° . The internal reflection angle at the top surface is twice the angle of the polished slanted edges. Total reflection occurs for all internal reflections. The crystal makes the floor of the liquid flow cell placed on top.

A wetting test consisted of 3 steps:

1. the space in-between the nanopillars was filled with CO_2 gas by flushing the cell at a flow rate of 100sccm; the replacement of air by CO_2 was monitored till equilibrium was achieved, ensuring that the space in-between the nanopillars was completely filled with CO_2 gas;
2. the cell was filled with N_2 -saturated UPW at a flow rate of 100mL/min to cover the superhydrophobic nanopillars with a liquid film; then, as soon as the ATR crystal was fully covered by the solution, the CO_2 gas flow was replaced with a N_2 gas flow to avoid the saturation of the water with CO_2 and enhance the dissolution of the trapped CO_2 gas; the disappearance of CO_2 in the gas and liquid phases was monitored till equilibrium was achieved;
3. the cell was flushed with CO_2 gas to replace N_2 in the solution and in any remaining gas pocket in-between the nanopillars. Here, the appearance of a CO_2 gas peak in the FTIR spectra would give a clear evidence of non-wetted spaces in-between the pillars, as the thickness of the liquid film (5mm) was too thick to allow detecting the CO_2 gas above the film by the evanescent waves.

At the end of each step a spectra was acquired with a long acquisition time (28min) to provide a high signal/noise ratio.

Finally, a reference spectrum was acquired for water on a flat ATR crystal. Also water and CO₂ reference spectra were acquired for nanopillars in the superhydrophobic state. In this purpose a test was performed with CO₂-saturated UPW under a CO₂ gas flow. Under this condition no wetting occurred ($Y=1$ in Figure 3 and 5) and the CO₂ peak area after wetting corresponded to the volume in-between the nanopillars.

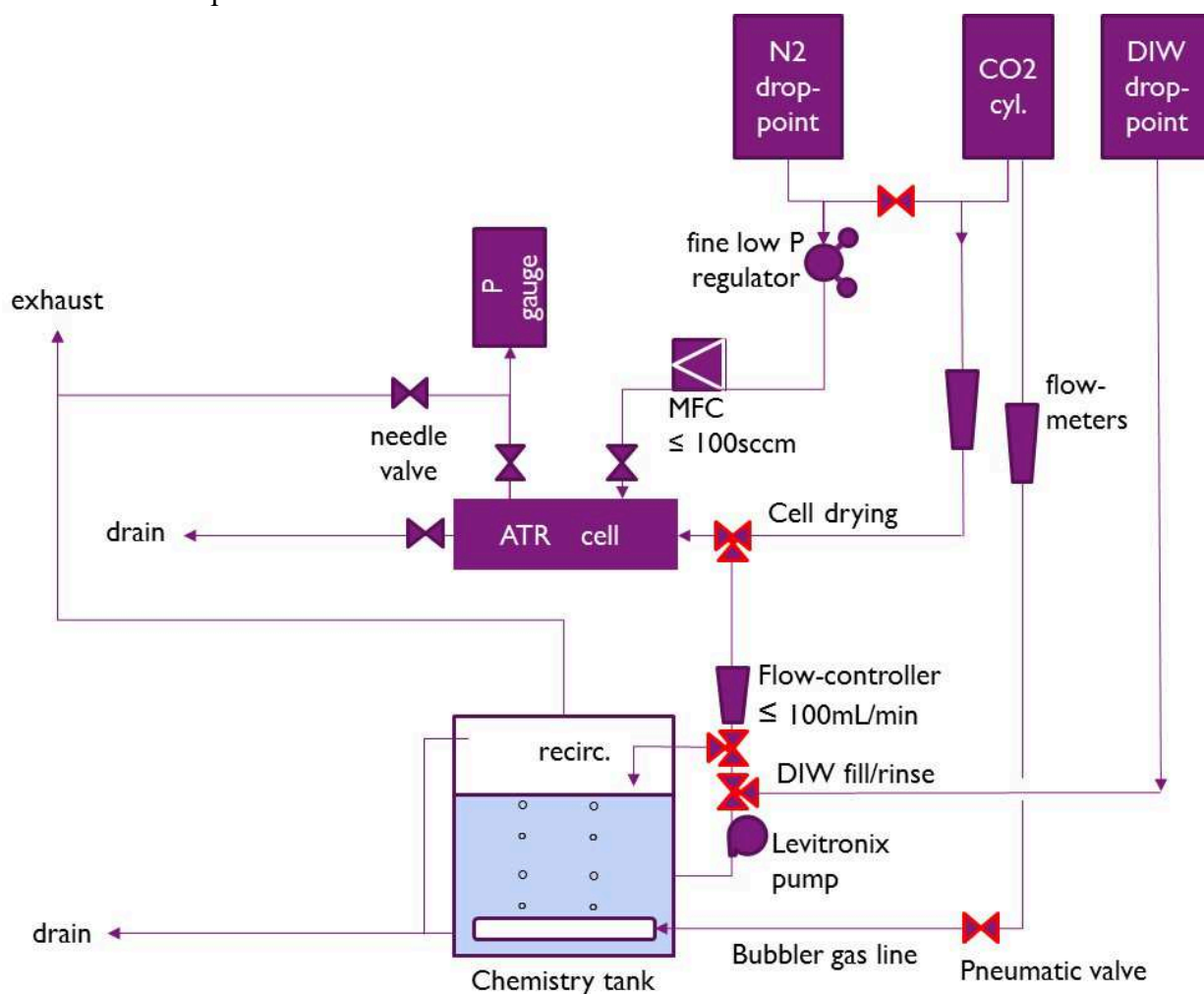


Figure 2: Schematic diagram of the ATR flow cell setup.

Results and discussion

Three tests were performed to check for the wetting of superhydrophobic nanopillars using the CO₂ gas method. Poor wetting was first evidenced by the ratio of H₂O bands intensities (Figure 3). Water presents two bands in the mid-IR, a broad intense stretching band at about 3300cm⁻¹ and a smaller bending vibration band at 1640cm⁻¹, with IR penetration depths of about 160 and 480nm, respectively. The difference in penetration depth renders the stretching band more surface sensitive compared to the bending band. Figure 3 gives a comparison of the spectra of non-wetted pillars with that of water, showing the relative decrease of the H₂O band at 3300cm⁻¹ from the presence of gas in-between the pillars: the intensity of the stretching band decreases as the water layer is positioned further away from the ATR crystal surface. A similar decrease was observed for pillars at the end of step 2 and step 3, indicating little if no wetting (Figure 3).

A more quantitative picture was obtained from the CO₂ spectra. The presence of CO₂ gas was evidenced by its resolved rotational fine structure peaks (CO stretching vibration mode, 2300-2380cm⁻¹) as opposed to the non-resolved band of dissolved CO₂ (2343cm⁻¹). The presence of CO₂

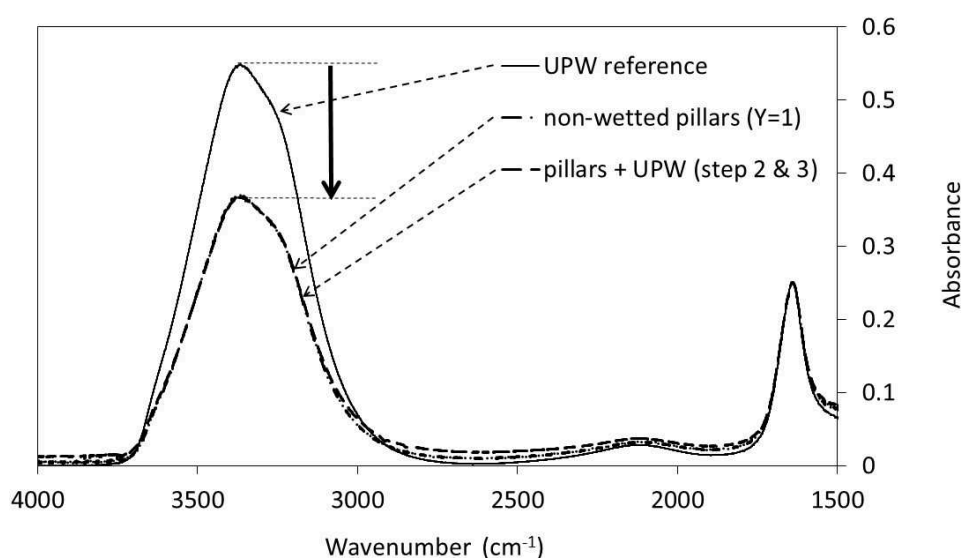


Figure 3: Typical ATR-FTIR spectra of H₂O on a flat Si surface (UPW reference), on non-wetted superhydrophobic nanopillars (Y=1), and as acquired at the end of the 2nd and 3rd steps of a wetting test. The spectra have been normalized with respect to the low frequency H₂O band. The arrow indicates the relative decrease of the stretching band when the space in-between nanopillars is not wetted.

gas at the end of a test (step 3) indicated that no complete wetting of the structures had been obtained (Figure 4). Remaining gas pockets that had been filled with N₂ in step 2 were filled back with CO₂ during step 3. Normalizing the results with respect to the superhydrophobic state provided a more quantitative interpretation (Figure 5). In this purpose the ratio between the CO₂ intensity before and after wetting determined in the superhydrophobic state reference test was used to set the ‘no wetting’ level in the wetting tests (Y=1 in Figure 5). In the test shown in Figure 5 no significant penetration of the liquid in the volume in-between the nanopillars was observed: the CO₂ gas level rose back to Y=1 during the final CO₂ purge (step 3). A summary of results obtained in the 3 tests performed is given in Table 1. Wetting was characterized by the relative decrease in the CO₂ gas peak area between step 3 and the reference level for no wetting (Y=1 in Figure 5). Only little wetting was caused by the method proposed by Tamaki et al. [7]. This indicates that the N₂/CO₂ gas

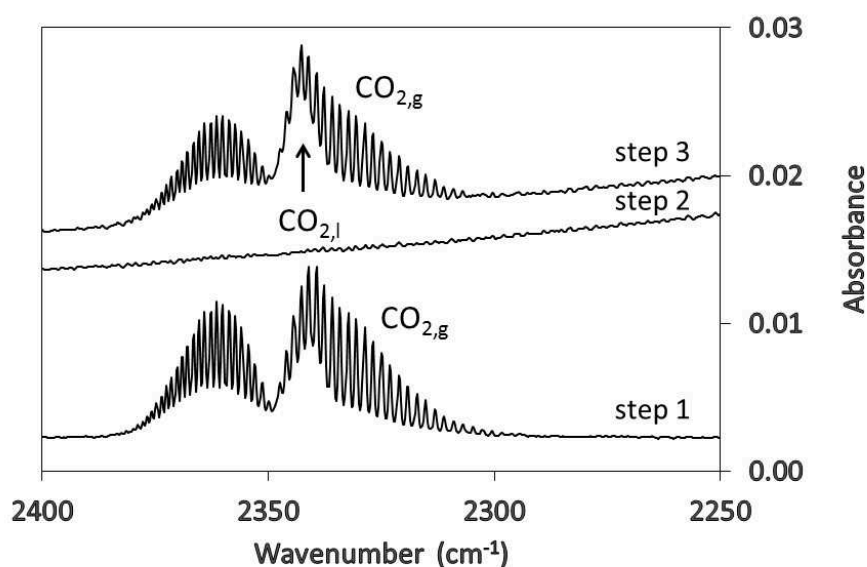


Figure 4: Typical ATR-FTIR spectra of the CO₂ stretching band, acquired at the end of the 3 steps of a wetting test. With an evanescent wave penetration depth of about 300nm, the signal originates from the volume in-between and just above the nanopillars, and not from the gas phase above the liquid film (step 3).

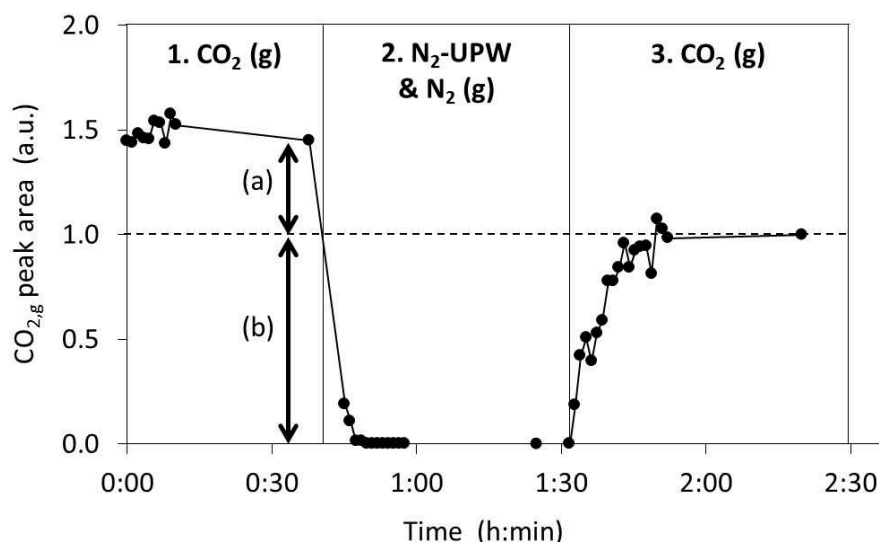


Figure 5: Normalized CO_2 gas intensity as a function of time in a wetting test. The separations between the 3 steps are outlined with full vertical lines. The reference ‘no wetting’ level for the volume in-between nanopillars is given by the horizontal dotted line ($Y=1$). In step 1, this line separates the contributions from the volume above (a) and in-between (b) the nanopillars to the measured intensity (a)+(b).

exchange at the wetting front interface was not much influenced by the difference in solubility of N_2 and CO_2 in water, and that N_2 dissolved in the liquid film replaced CO_2 in the spaces in-between nanopillars nearly as fast as CO_2 was dissolving in the liquid film. It should be noted that our nanospaces were closed, as opposed to the nanofluidic channels used in [7]. This may have affected the time evolution of the CO_2 gas concentration in the vicinity of the wetting front. In conclusion the method may be useful only for nanostructures with a much smaller open volume than tested here.

Table I: Summary of wetting tests.

Test	Wetting (%)
1	12
2	6
3	0

Conclusions

We have evaluated the use of CO_2 gas to force the wetting of superhydrophobic structures, without the use of surfactants. The patterned surface was first flushed with CO_2 gas, before dispensing the aqueous solution that was saturated with N_2 and switching the gas flow from CO_2 to N_2 . ATR-FTIR results showed only a modest improvement in wetting, presumably due to a fast N_2 - CO_2 gas exchange at the wetting front. The method may only be useful for nanostructures with a much smaller open volume than tested here.

Acknowledgements

The authors thank Geert Doumen from imec for helping with construction of the ATR flow cell setup and Adrian Ljutic from Levitronix for providing a magnetically levitated centrifugal pump.

References

- [1] P.-G. de Gennes, F. Brochard-Wyart and D. Quéré: *Capillarity and Wetting Phenomena: Drops, Bubbles, Pearls and Waves* (Springer, 2004).
- [2] M.E. Abdelsalam, P.N. Bartlett, T. Kelf, and J. Baumberg: *Langmuir* **21** (2005), p. 1753.
- [3] P.M. Harder, T.A. Schedd, and M. Colburn: *J. Adhesion Sci. Technol.* **22** (2008), p. 1931.
- [4] X. Xu, G. Vereecke, C. Chen, G. Pourtois, S. Armini, N. Verellen, W.-K. Tsai, D.-W. Kim, E. Lee, C.-Y. Lin, P. Van Dorpe, H. Struyf, F. Holsteys, V. Moshchalkov, J. Indekeu, S. De Gendt: *ACS Nano* **8**(1) (2014), p. 885.
- [5] G. Vereecke, XiuMei Xu, W.K. Tsai, Hui Yang, S. Armini, T. Delande, G. Doumen, F. Kentie, Xiaoping Shi, I. Simms, K. Nafus, F. Holsteys, H. Struyf, and S. De Gendt: *ECS J. Solid State Sci. Technol.* **3**(1) (2014), p. N3095.
- [6] Q.T. Le, V. Jeannot, M.R. Baklanov, R. Vanderheyden, W. Boullart, and S. Vanhaelemeersch: *Electrochem. Solid-State Lett.* **9**(4) (2006), p. F17.
- [7] E. Tamaki, A. Hibara, H.-B. Kim, M. Tokeshi, T. Ooi, M. Nakao, and T. Kitamori: *Anal. Sci.* **22** (2006), p. 529.
- [8] I. Vos, D. Hellin, J. Vertommen, M. Demand and W. Boullart, *ECS Trans.* **41**(5) (2011), p. 189.

Some Critical Issues in Pattern Collapse Prevention and Repair

XiuMei Xu^{1,a}, Nandi Vrancken^{1,2}, Guy Vereecke¹, Samuel Suhard¹,
Geoffrey Pourtois¹ and Frank Holsteys¹

¹ imec, Kapeldreef 75, B-3001 Leuven, Belgium

² VUB, Pleinlaan 2, 1050 Elsene, Belgium

^a xiumei@imec.be

Keywords: High aspect ratio (HAR) structures, pattern collapse, structural strength, molecular dynamics (MD) simulations

Abstract In semiconductor fabrication, pattern collapse of high aspect ratio structures after wet processing is a major problem that could reduce production yield. In this work, several critical issues which limit our understanding of pattern collapse phenomenon are discussed together with some recent results of experiment and modeling. Special efforts have been put to update some of the most recent developments in characterization techniques.

Introduction

In wet processing, pattern collapse is a commonly observed phenomenon in which clustering of micro- or nano-structures is induced by capillary forces [1–4]. Pattern collapse is more pronounced for non-rigid nanostructures such as photoresist and low-k dielectric structures, or structures with very high aspect ratios (AR). As CMOS scaling continues to sub-10 nm technology nodes, due to the large surface area to volume ratio, pattern collapse of silicon FinFET structures with a moderate AR could occur even after drying with hot isopropyl alcohol (IPA). Using dry treatments to break the covalent bonds formed between bridging nanostructures and thus to repair pattern collapse has a potential to extend the applicability of current drying techniques to more challenging nanostructures. For process development, it is important to understand the roles of capillary interactions, surface adhesion and mechanical strengths of nanostructures on pattern collapse formation and repair. In this work, some of our recent development on characterization methods together with some experimental and modeling results will be discussed.

Results and discussions

For patterned substrates, as structures are fixed at one end, the bending and aggregation of structures result from the competition between capillary forces and the elastic restoring forces. Figure 1 shows dark field optical microscope images obtained at different stages of water evaporation on densely packed silicon micropillars (diameter: 1 μm , height: 45 μm).

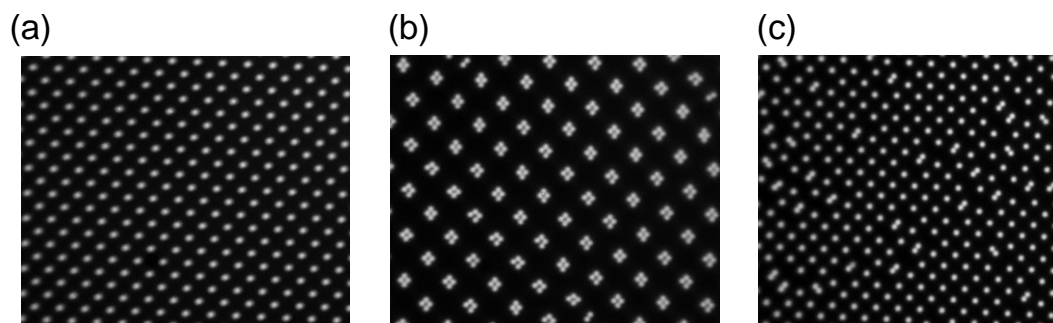


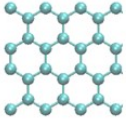
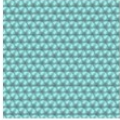

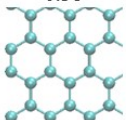
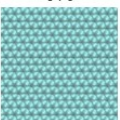

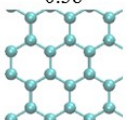
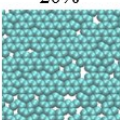

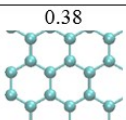
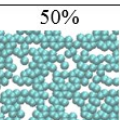

Figure 1 Optical microscopic images showing formation of pattern collapse during water evaporation on silicon micropillars, (a) when pillars are fully immersed in water, (b) when pillars protrude from water layer, and (c) after pillars are completely dried. Note that water film cannot be resolved in these dark field microscope images.

When fully immersed in water (Figure 1-a), the pillars remain intact due to the absence of capillary interfacial forces. Upon evaporation, a sudden bending and clustering of nearby pillars is observed, which indicates the presence of strong capillary forces acting on the structures that dominate over the elastic restoring force (Figure 1-b). The pillars are found to maintain the same clustering configurations till almost the end of evaporation. Interestingly, it is observed that most pillars can return to the initial free standing states after complete drying (Figure 1-c). This indicates that in the absence of capillary force, the surface adhesion between these aggregated pillars is not sufficient to counterbalance the elastic restoring force. These results clearly underline the importance of in-situ characterization in understanding the dynamic force balance that dictates the final configuration of pattern collapse.

For nanostructures with dimensions below the optical diffraction limit, in-situ characterization becomes very challenging. Even to determine whether liquids could penetrate in between nanostructures is not so straightforward [5]. However, it is extremely important to ensure complete wetting on nanostructures as unexpected capillary forces and damages can be resulted from a partial wetting state. Using silicon nanopillar arrays (pitch: 90 nm, diameter: 30 nm, various heights), we have developed several techniques that could be used to measure wetting states at the nanoscale. With optical reflectance measurements, the nanoscale water penetration depths have been measured and the wetting transition from complete wetting to the superhydrophobic state has been determined by varying the surface chemistry with different silanes [6]. For silicon pillars grafted with FDTs (1H,1H,2H,2H-perfluorodecyltrichlorosilane), a high frequency acoustic method [7] and an ATR-FTIR [8] based technique have been developed to accurately determine the critical alcohol-water concentration that is needed to break the superhydrophobic state. All these different wetting characterization methods have shown a consistent deviation from the classical wetting models, indicating a change in wetting property of the nanostructures [6]. Therefore contact angle measurements do not always represent the real wetting states in between nanostructures [5], and special efforts need to be taken to ensure complete wetting in the first place before any work on drying can be undertaken.

Most of the theoretical works on pattern collapse are based on pair-wise capillary interactions and a static force balance. On one hand, capillary interactions on nanostructures are always calculated from apparent contact angles, which are measured on a blanket substrate of the same material. On the other hand, contact angles at the nanoscale can be very different from their macroscopic counterparts. During the fabrication, there are inevitable modifications of the structure surface with respect to the planar silicon wafer, such as different surface densities from different crystal plane orientations or surface defects. The effects of atomic scale surface modification on wetting have been studied by molecular dynamics (MD) simulations using the LAMMPS package [9]. More simulation details can be found in our previous publication [6]. Table 1 compares the surface energies and water contact angles with different surface lattice densities and atomic vacancies. As can be seen, these surface modifications could change the surface wetting property significantly, and thus they could have a big impact on the capillary interaction. Surface adhesion is another important, yet very often overlooked aspect. As shown in Figure 1, although the deflection of pillars is initially induced by capillary forces, the final state, however, is determined by the balance between elastic restoring energy and surface adhesion energy that holds the pillar tops together. It is well known that surface adhesion depends not only on chemical composition, but also on surface morphology and contact deformation. However, the underlying mechanism behind this complex physicochemical interaction is still not well understood, which makes quantitative analysis of pattern collapse very challenging.

Table 1. MD simulations showing the influence of atomic scale surface perturbation on wetting properties. The surface lattice density, atomic vacancy fractions in the top layer, surface energy and contact angles on the modified flat surfaces are compared.

Surface density (\AA^{-2})	Top layer vacancy fraction	Surface energy (mJ/m^2)	Contact angle on modified flat surface (θ)
0.47 	0% 	206.9	74.1° 
0.38 	0% 	135.1	93.3° 
0.38 	20% 	90.2	107.0° 
0.38 	50% 	43.5	128.7° 

For structures collapsed after wet processing, the usage of dry treatments to break the covalent bonds formed between bridging structures has a potential to repair pattern collapse. Figure 2 shows a comparison of the aggregated morphology of silicon nanopillars (diameter: 30 nm, height: 480 nm) after rinsing and dry in IPA (Figure 2-a) and sequentially after vapor HF etching (Figure 2-b). By removing native oxide from the pillar surface, the adhesion between pillars is reduced and pattern collapse can be repaired to some degree.

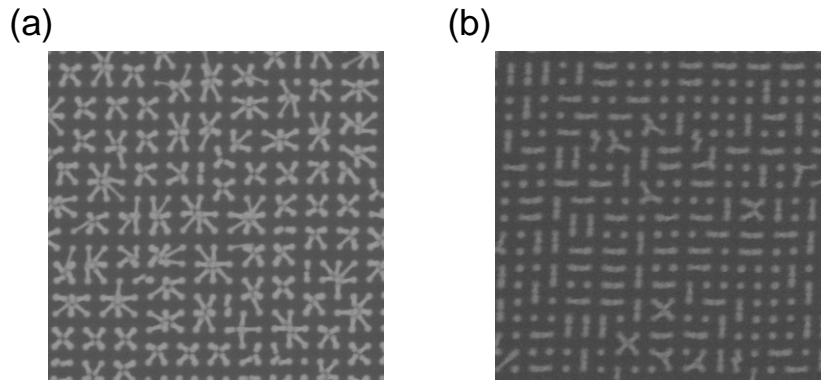


Figure 2 SEM images showing (a) pattern collapse of silicon nanopillars after rinsing and dry in IPA, and (b) the same sample in (a) after a sequential vapor HF treatment.

The repair efficiency depends on 1) the etch efficiency at the contact area and 2) the balance between elastic restoring energy and surface adhesion. For the latter aspect, the mechanical property of nanostructures plays an important role, and it is found that the repair of heavily bended structures is very challenging. Recently, direct mechanical characterizations of individual nanowires under uniaxial tension, compression or bending have been carried out in SEM or TEM [10–13]. It has been found that stress could induce plastic deformation [10] or show large anelastic behaviors for silicon nanowires [11]. As in-situ mechanical characterization is not a commonly available

technique, molecular dynamics (MD) simulations can be a powerful tool to obtain mechanical properties of nanostructures with a reasonable accuracy. MD simulations have been carried out for silicon nanowires orientated in $\langle 100 \rangle$ direction. An empirical Tersoff potential is used to simulate the interatomic interaction for silicon [14]. In these simulations, a force is applied to the top of the nanowire and the equilibrium deflection and bending stress are calculated at 300 K under an NVT ensemble. Figure 3 shows the maximum von Mises stress as a function of the applied force for a silicon nanowire with a diameter of 2 nm. In the elastic regime, the bending stress increases monotonically with the applied force. An abrupt transition is observed with a further increase in the amplitude of the external force, which indicates an onset of plastic deformation. In this regime, nanowires cannot return to their original position after unloading and relaxation. A notable change in crystal lattice is observed from the cross-sectional atomic structures as shown in the inset of Figure 3, as in agreement with other studies [10]. Such unexpected plastic deformation of heavily bended nanostructures poses great challenges for pattern collapse prevention and repair.

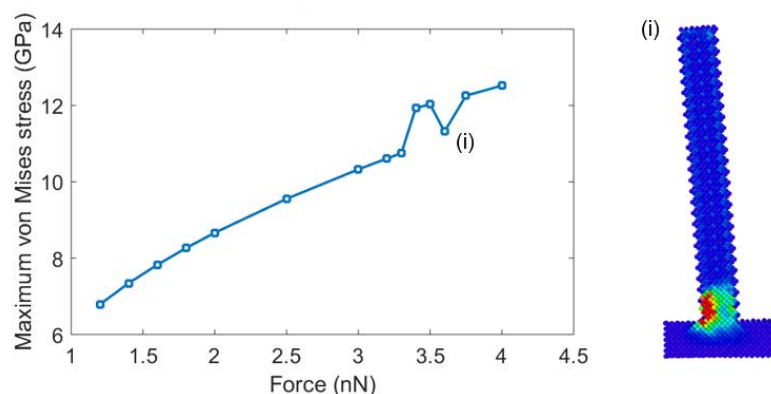


Figure 3 Bending stress of silicon nanowire as a function of the applied force from molecular dynamics simulations. The inset shows atomic structures of a relaxed nanowire after plastic deformation.

Summary

In this work, we have discussed several critical issues, which limit our understanding of pattern collapse phenomenon. For nanostructures, there is a lack of in-situ characterization techniques that could help us to understand the dynamic force balance. The lack of nanoscale surface wetting and adhesion characterization makes quantitative analysis of pattern collapse very challenging. Mechanical characterization of nanostructures is another critical aspect that needs more in-depth investigation. Although many of the physicochemical mechanisms and properties behind pattern collapse phenomenon remain unclear, the emerging nanoscale characterization techniques could bring more insights into theoretical studies as well as practical applications.

Acknowledgements

Nandi Vrancken acknowledges the Fonds voor Wetenschappelijk Onderzoek (FWO) for a PhD grant.

References

- [1] D. Chandra, S. Yang, *Langmuir* 25 (2009) 10430–4.
- [2] N. Tanaka, Toshihiko; Morigami, Mitsuaki; Atoda, *Jpn. J. Appl. Phys.* 32 (1993) 6059–6064.
- [3] T. Kondo, S. Juodkazis, H. Misawa, *Appl. Phys. A Mater. Sci. Process.* 81 (2005) 1583–1586.
- [4] D. Wu, N. Fang, C. Sun, X. Zhang, *Sensors Actuators, A Phys.* 128 (2006) 109–115.
- [5] X.M. Xu, G. Vereecke, E. van den Hoogen, J. Smeers, S. Armini, T. Delande, H. Struyf, *Solid State Phenom.* 195 (2012) 235–238.

-
- [6] X. Xu, G. Vereecke, C. Chen, G. Pourtois, S. Armini, N. Verellen, W.-K. Tsai, D.-W. Kim, E. Lee, C.-Y. Lin, P. Van Dorpe, H. Struyf, F. Holsteys, V. Moshchalkov, J. Indekeu, S. De Gendt, *ACS Nano* 8 (2014) 885–93.
 - [7] S. Li, S. Lamant, J. Carlier, M. Toubal, P. Campistron, X. Xu, G. Vereecke, V. Senez, V. Thomy, B. Nongaillard, *Langmuir* 30 (2014) 7601–8.
 - [8] N. Vrancken, *Manuscr.* (2016).
 - [9] S. Plimpton, *J. Comput. Phys.* 117 (1995) 1–19.
 - [10] D.-M. Tang, C.-L. Ren, M.-S. Wang, X. Wei, N. Kawamoto, C. Liu, Y. Bando, M. Mitome, N. Fukata, D. Golberg, *Nano Lett.* 12 (2012) 1898–1904.
 - [11] G. Cheng, C. Miao, Q. Qin, J. Li, F. Xu, H. Haftbaradaran, E.C. Dickey, H. Gao, Y. Zhu, *Nat. Nanotechnol.* (2015) 1–6.
 - [12] L. Wang, K. Zheng, Z. Zhang, X. Han, *Nano Lett.* 11 (2011) 2382–2385.
 - [13] Y. Zhu, F. Xu, Q. Qin, W.Y. Fung, W. Lu, *Nano Lett.* 9 (2009) 3934–3939.
 - [14] Tersoff J., *Phys. Rev. B* 38 (1988) 9902–9905.

Watermark-Free and Efficient Spray Clean on Hydrophobic Surface with Single-Wafer Technology

^{1,a}N.Belmiloud, ²N.Kenkare

¹Screen SPE Germany, Fraunhofer straÙe 7, D - 85737 Ismaning, Deutschland

²Globalfoundries, Wilschdorfer LandstraÙe 101, 01109 Dresden, Deutschland

^a n.belmiloud@screen-spe.eu

Keywords: particles, hydrophobic, zeta-potential, single-wafer, spray clean.

Abstract The interaction of spray-based physical clean and hydrophobic surfaces is studied on a single-wafer technology. A model simulating a rolling water marble on a rotating disk describes accurately the footprint of watermarks. Contrary to its oxide, on a silicon surface the adhesion of particles does not depend on the pH value but on the rotation speed. This newly proposed method, based on the simultaneous combination of spray and liquid dispense is then compared to the standard IPA-based process. Despite the non-usage of solvents, the substrates show similar particles level, defectivity and epi-growth quality.

Introduction

As the technology node scales down to 14nm and beyond, removal of particles from wafer surface without etchloss and surface state change is critical. Deposition of particles on wafers is mainly governed by intermolecular forces. For hydrophobic surface, the interaction between organic and apolar surfaces is strong. Moreover, surfaces like HF-last silicon or copper are highly sensitive 1) to watermarks due to residual droplets or 2) to pitting due to electrostatic charges. On batch technology, megasonic clean generates dramatic damages and watermarks. Here, we will propose a chemical-free technique for an efficient spray cleaning on hydrophobic surface with minimizing the watermarks and enhancing the particles performance while not changing the surface termination. First, the source of the adhesion of nano-particles onto surface is explained according to its wetting properties and second, we propose a solution based on CO₂ water (CO₂W) physical clean combined together with a liquid-shield configuration to reach excellent performance without isopropanol (IPA).

Adhesion of Particles onto surface: hydrophilic vs. hydrophobic cases.

The zeta potential is a measure of the magnitude of the electrostatic potential (repulsion-attraction) between particles. The pH and ionic strength/species of the surrounding liquid can modify drastically the interaction between particles and wafers because it determines the electro-kinetics in the vicinity of the wafer surface. The DLVO theory (named after Dejarguin, Landau, Verwey and Overbeek) looks at the imbalance between 2 forces: the Van der Waals (VdW) and the electrostatic interactions due to the adsorbed double layer around the particles [1].

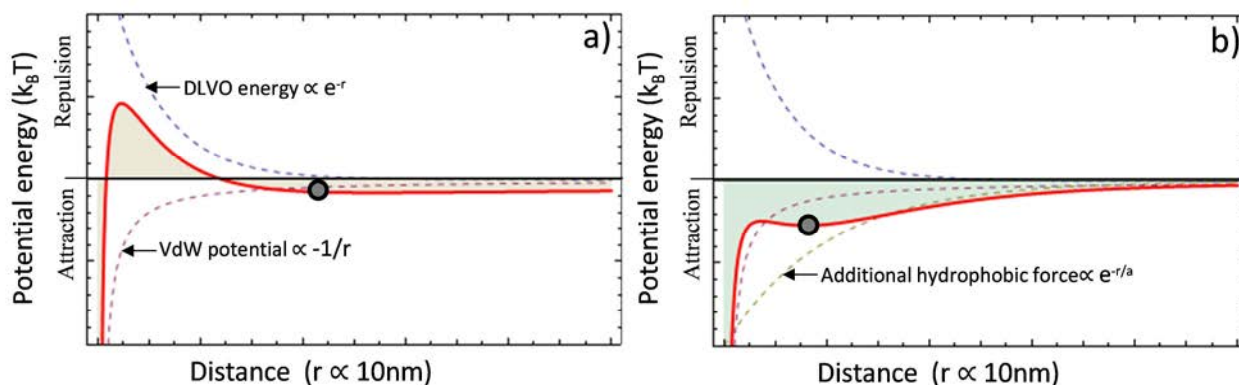


Figure 1: Schematics of the interaction potential between a particle and a surface a) hydrophilic case b) hydrophobic interaction. The particle is symbolized by the black dot. a and r are an arbitrary constant and the distance between surface and particles respectively.

In Figure 1a, the particle (dark circle) is attracted to the surface by Van der Waals forces but repelled by electrostatic forces and stays at the 2^{ndary} minimum of the total potential. This minimum is not so pronounced. Therefore the interaction between surface and particles is weak and can be counterbalanced easily by a physical clean. Besides, it was shown that the attractive interaction between hydrophobic organic molecules in water is strong, long range, decaying exponentially with distance and have strengths of a few $k_B T$ - comparable in energy to hydrogen bonds [1,2]. In figure 1b, the addition of a third hydrophobic force shifts the energy potential into the attraction area and unbalances the DLVO forces. The physical removal of an organic particle on hydrophobic surfaces requires a high amount of energy. The weak spontaneous wetting property makes also inefficient the elimination of the particles by liquid convection or adsorption. Nevertheless, a spray clean is theoretically able to force the wetting and impose locally some hydrodynamical and mechanical forces onto the particles-surface system. By controlling the droplets speed, size and flux, the utilization of the energy from the droplet impact has been proven to be an efficient technique for the removal of particles without pattern damage [3]. In the other hand, watermarks and pitting issue were reported [4].

Watermarks impact heavily the surface preparation of hydrophobic surfaces. First, during evaporation, non-volatile contaminant present in the water precipitate and generate residues, then these drying spots act as a mask for the next processes. Second, the residual droplets locally change the surface termination and oxidize the surface, thus inhibiting epitaxial growth. Indeed water acts as a catalyst for the oxidation of silicon by dissolved oxygen [5, 6]. Watermarks are more problematic on hydrophobic surface than on hydrophilic surface because evaporation time increases monotonically with the contact angle [5]. Higher the hydrophobicity, longer is the evaporation, hence longer the liquid/substrate chemical interaction. On single wafer technology, this issue is even more pronounced as a droplet remains on the frontside of a flat horizontal surface, whereas on batch, the wafer surface is vertical during wet cleaning. Several root causes are commonly observed: dripping nozzle, unsuitable drying sequence and mist condensation. The reported solutions are mostly the decrease of the contact angle with solvent (eg. IPA dry) and the removal of the dissolved oxygen (eg. low oxygen configuration with degassing units).

Experiment: Physical clean on hydrophilic and hydrophobic surface.

Hydrofluoric acid (HF), hydrochloric acid (HCL) and CO₂W are the only components in our single wafer processes under study. Chemicals are kept at constant temperature. CO₂W removes electrostatic charges. HCL aims to change the pH of the solution to affect the DLVO forces. HF removes the native oxide and makes the wafer hydrophobic with a contact angle (CA) around 80°. The etchloss average and non-uniformity were monitored on thermal oxide silicon wafers and are of the same order in all experiments on single wafers. The particles level is measured via light-point defects detection and map-to-map comparison at sub 40nm size. To evaluate the distribution mode

(eg. radial, centerspot, ring), the wafer surface is divided into 10 rings of same area ($\sim 71\text{mm}^2$). For each zone, the number of particles is plotted against the related binned radius.

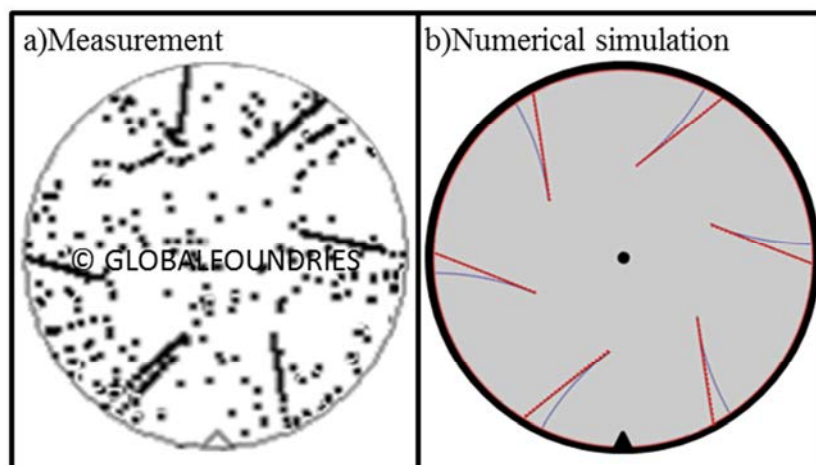


Figure 2: Particles maps on hydrophobic wafers processed on single wafer: a) measured particles maps, b) numerical simulation of rolling droplet at 5 different initial positions: fast rpm (red dashed straight lines) and slow rpm (blue curvy lines).

In the first part of our investigation, the instability of HF-Last process with bare silicon wafers is investigated. The particles maps show unpredictably some streaks as it can be seen in figure 2.a. The CA hysteresis is pretty low and the adhesion forces can be allegedly assumed to be negligible in comparison with centrifugal forces. Therefore, a water droplet on a hydrophobic wafer at a high spin velocity can be simulated as a liquid marble on a rotating plate. In Figure 2b, this physical model is in a good accordance with the maps. The influence of the speed can be seen: higher the speed, straighter the trajectories. This demonstrates that these signatures come from the footprints of rolling droplets on a rotating hydrophobic wafer at high rpm.

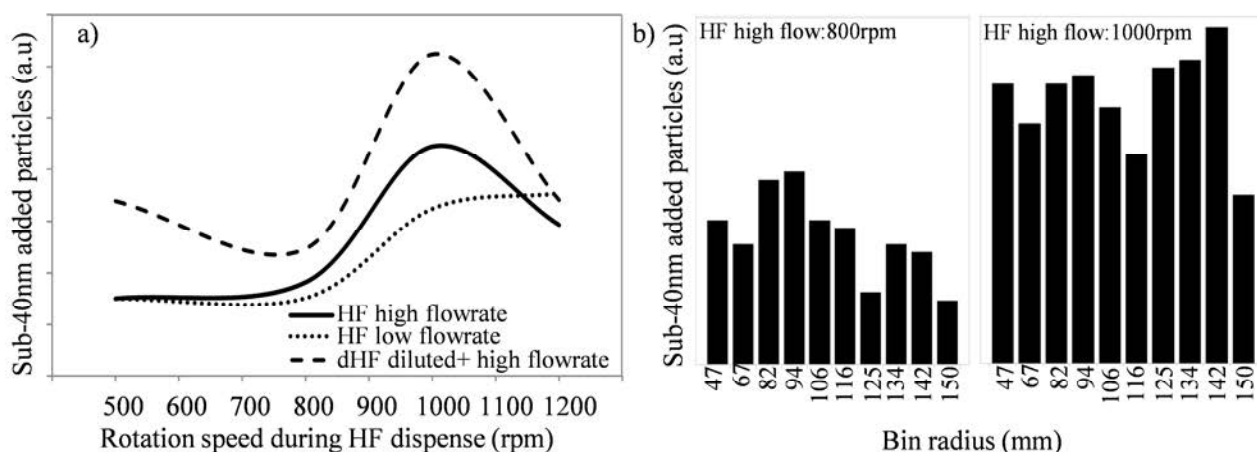


Figure 3: a) Particles count vs. rotation speed measured on hydrophobic silicon wafers. The time of HF and diluted HF were adjusted to have the same amount of material loss. The effect of flowrate and dilution are also reported. b) Particles count per zone of same area vs distance from the center.

Furthermore, the process parameters during the HF step are examined. The flowrate and spin-velocity during the HF step influence the total number of added particles (Figure 3a). The force of friction from the liquid acting on the wafer depends on spin velocity and flowrate. In the case of diluted HF, the time dispense is longer and so was the friction. Friction raises surface charges, ie. triboelectricity. In Figure 3.b, the particles density is uniform onto the surface. The slight difference in speed between 1000 and 800rpm leads to an important reduction of the particles count. Sub-40nm particles were electrostatically attracted during HF dispense. During the rinse, CO_2W removed the generated surface charges but not the particles which stay onto the surface due to the strong hydrophobic interaction.

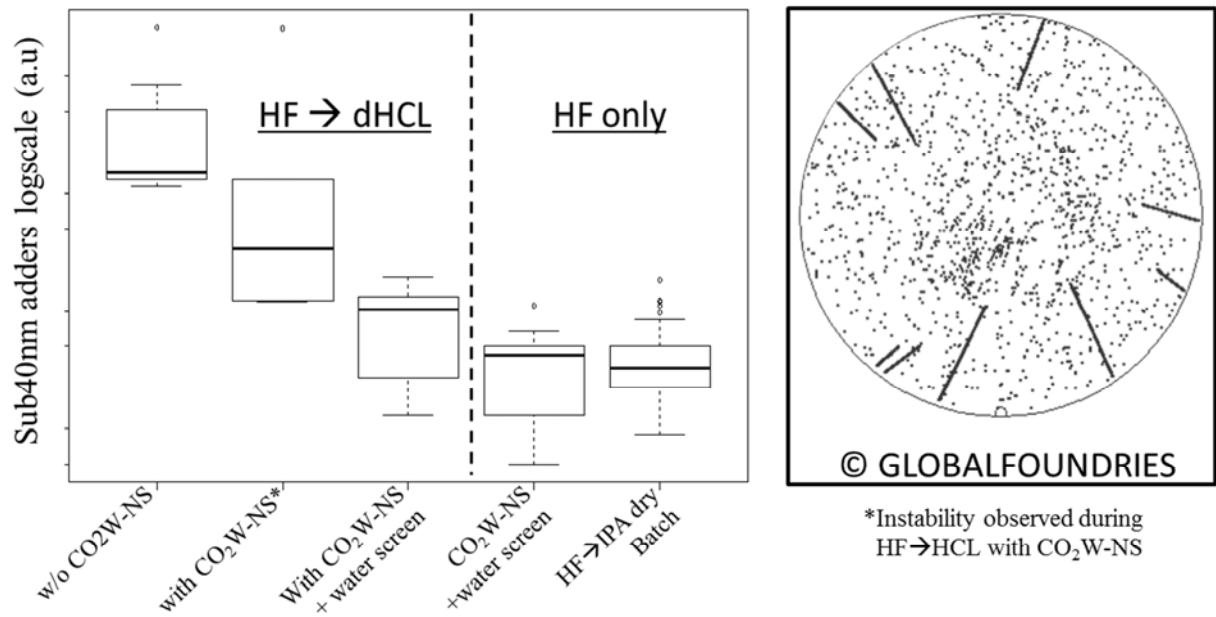


Figure 4: Added particles count for different processes based on a HF (800rpm) then HCL sequence on single wafers tools. Comparison is made with HF process on batch tool where IPA is used during drying.

Now, a final physical clean is inserted to decrease again the level of particles at 800rpm. In figure 4, the application of a spray decreases the particles baseline. Still, the hydrophobicity of the wafer makes the process unstable and vulnerable to watermarks. The similarity between the maps in Figure 2 and 4 reveals that residual droplets yield to bad performance. To prevent droplets from condensing directly on the wafer, we dispense simultaneously water to guarantee a partial liquid screen on the wafer. This synchronized combination of spray and liquid-screen allows better and more robust performance than standard configurations. And yet, there is no IPA dry (Isopropanol) to lower the surface tension and subsequently improve the wettability and the drying efficiency of the process. This process performs as well as batch process where IPA is used and where also the hydrophobicity forbids megasonic to be applied.

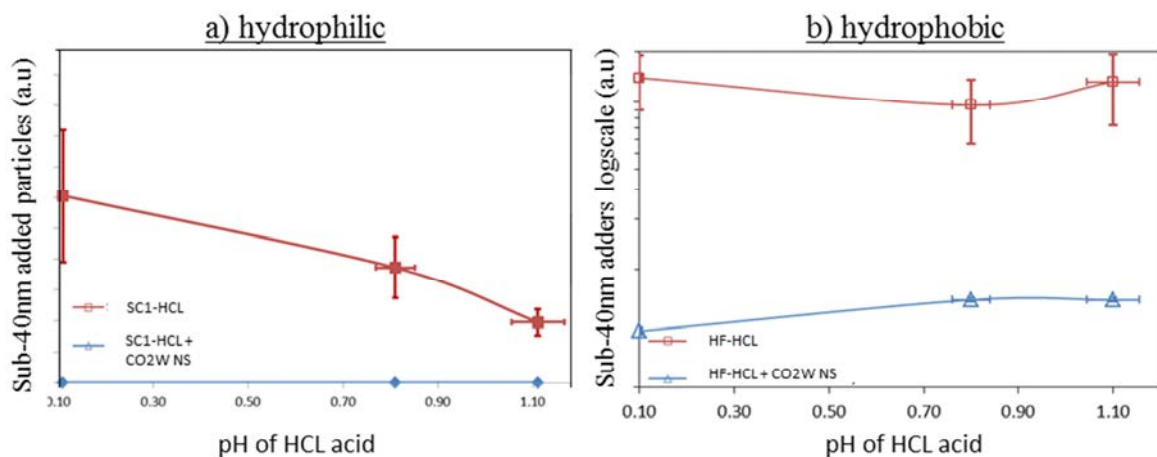


Figure 5: Particles count vs pH of diluted HCL acid on: a) hydrophilic oxidized silicon wafers: SC1-dHCL b) hydrophobic de-oxidized silicon wafers: HF-HCL with and w/o spray + water screen.

Then, the influence of the pH is discussed on chemically oxidized (SiO₂) and de-oxidized (Si) bare silicon wafers. In the hydrophilic case, wafers were processed first with an alkaline oxidizing (SC1: NH₄OH/H₂O₂ mixture) solution at a constant pH of 9.4, then it is followed by an acidic step of HCL. In Figure 5a, lower the pH, higher the number of particles in agreement with the zeta potential model. In figure 5b, the level of particles is higher and there is no dependence on pH. The hydrophobic forces are dominant and stronger. In both cases, when a CO₂W physical clean is inserted after the HCL step, there is no more dependence making the process more stable and cleaner.

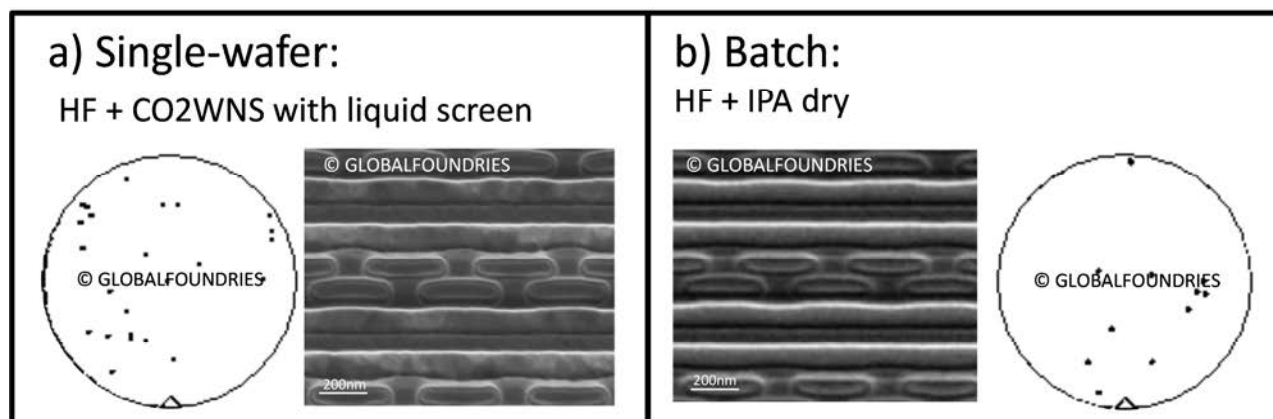


Figure 6: Defectivity maps in bright field and SEM pictures on a) Single wafer with HF-CO₂WNS+liquid screen configuration and on b) batch with HF-IPA dry.

Finally, to confirm the good performance, the newly developed process is used as a clean prior to SiGe (silicon germanium alloy) epitaxial growth on silicon. For a high quality crystalline layer, epitaxial growth requires excellent surface preparation with low particles level, metallic impurities and roughness. The patterned wafers were inspected after the low-bake epi-process with a bright field optical scan. Each defect is mapped and reported with a SEM image. As it can be seen in Figure 6, the good performance of the HF-CO₂WNS with water-screen on Single wafer is confirmed. It has similar performance to the batch. When defect are reported, slight differences are observed in the SEM images when the lines get closer and the opening smaller. This can be attributed to an increase of the roughness generated by a higher etchrate on single wafer or the time exposure with the HF solution.

Conclusion

This investigation explains how dispense time, flowrate, spin-velocity, pH impact on the particles performance of single-wafer technology. A lower rpm during HF results in a significant decrease of the particles. It has been demonstrated that the source of the unstable spray is due to rolling droplets on hydrophobic surface at high rpm. A physical clean combined with a liquid shield effect is mandatory to drastically improve the particles performance on substrates that are sensitive to watermarks. On hydrophobic as well as on hydrophilic surfaces, particle performance was drastically enhanced thanks to a simultaneous combination of etchless spray/rinse that does not modify the surface chemistry and can be fine-tuned to avoid pattern damage. Despite the absence of IPA and low oxygen settings, good epitaxial growth quality and morphology were obtained, demonstrating the ability of the studied configuration to perfectly dry a hydrophobic surface without any organic solvents and any oxidation issues.

References

- [1] Israelachvili, J., Intermolecular and Surface Forces, 3 ed. Academic Press London (2011)
- [2] Hupka, Lukasz, et al., Solid State Phenomena, Vol. 145. (2009).
- [3] Snow, James T., Masanobu Sato, and Takayoshi Tanaka, Particle adhesion and removal (2015): 313-335.
- [4] Chen, Yufei, et al. "Post-CMP Cleaning of Copper/Hydrophobic Low-k Dielectric Films." ECS Transactions 19.7 (2009): 83-90.
- [5] Tamaddon, A. H., et al. "Role of Ambient Composition on the Formation and Shape of Watermarks on a Bare Silicon Substrate." ECS Journal of Solid State Science and Technology 3.1 (2014): N3081-N3086.
- [6] Belmiloud, N., et al. "Effect of the surface/water chemistry on the creation of watermarks." Solid State Phenomena. Vol. 195. Trans Tech Publications, (2012).

Extended-Nano Fluidic Devices and the Unique Liquid Properties

Kazuma Mawatari and Takehiko Kitamori

Department of Applied Chemistry, School of Engineering, The University of Tokyo, 7-3-1 Hongo,
 Bunkyo, Tokyo 113-8656, Japan

Email: kmawatari@icl.t.u-tokyo.ac.jp

Invited Paper

Keywords: nanofluidics, device, extended-nano space, liquid property

Abstract. Microfluidic devices are downscaling to 10-100 nm space, which we call extended-nano space. Because the extended-nano space is a space to bridge isolated molecules and normal bulk fluid, new solution chemistry can be expected. However, it was difficult to investigate due to the ultra-small space. Our group developed fundamental technologies for the extended-nano fluidics such as nanofabrication and bonding for glass substrates, aL-fL pressure driven fluidic control, partial surface modification, and single molecule detection. Based on these technologies, many unique liquid properties were found such as viscosity increase, enhanced proton mobility, lower dielectric constant. In addition, the liquid property changes depended on channel size, channel shape, and kinds of liquid. New analytical and energy devices are created utilizing the unique properties in the extended-nano space. In this talk, fundamental technologies and unique liquid properties found in this space are mainly presented, which would have impact not only on chemistry and biology but also on semiconductor industry.

Introduction

Integration of chemical processes on microchemical chips gained much attention in a past decade. Concepts were proposed to realize general micro-integration on a chip, which were micro unit operations (MUOs) and continuous flow chemical processing (CFCP) [1]. The bulk-scale chemical operations were integrated as MUOs and connected each other in parallel and serial by CFCP like an electric circuit (Figure 1). Multiphase laminar flows are unique liquid flow in microspace and used for fluidic control. In order to realize the basic concept, the fundamental technologies were developed

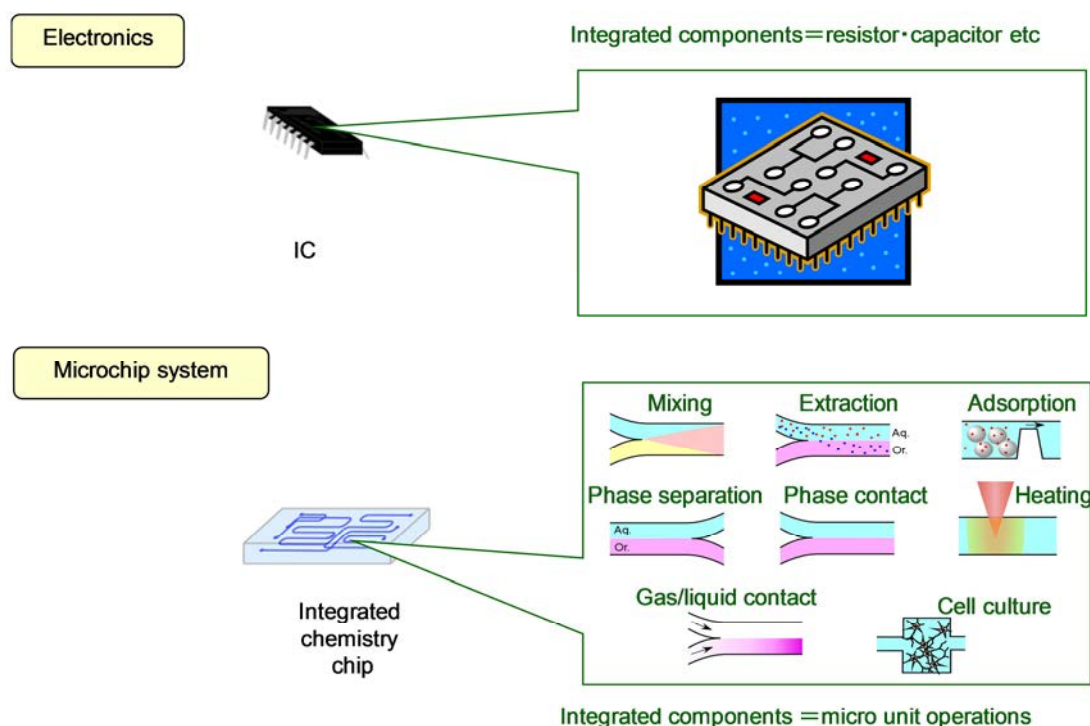


Figure1: Electronics and microchip system.

such as microfabrication, fluidic control, detection, surface modification, and cell culture methods. In contrast to conventional bunk-scale chemical tools, superior performances were demonstrated in shortening process time, dramatic decrease of sample and reagent volume, integration of multiple chemical functions, and easy operations. At present, the micro-technologies are moving toward practical applications by establishing devices and systems. Several companies commercialized the microsystems in biochemical analysis, cell analysis, electrophoretic separation, chromatographic separation, medical diagnosis, and chemical synthesis. We also developed several prototype systems (Figure 2), and some of them were commercialized in our venture company [2].

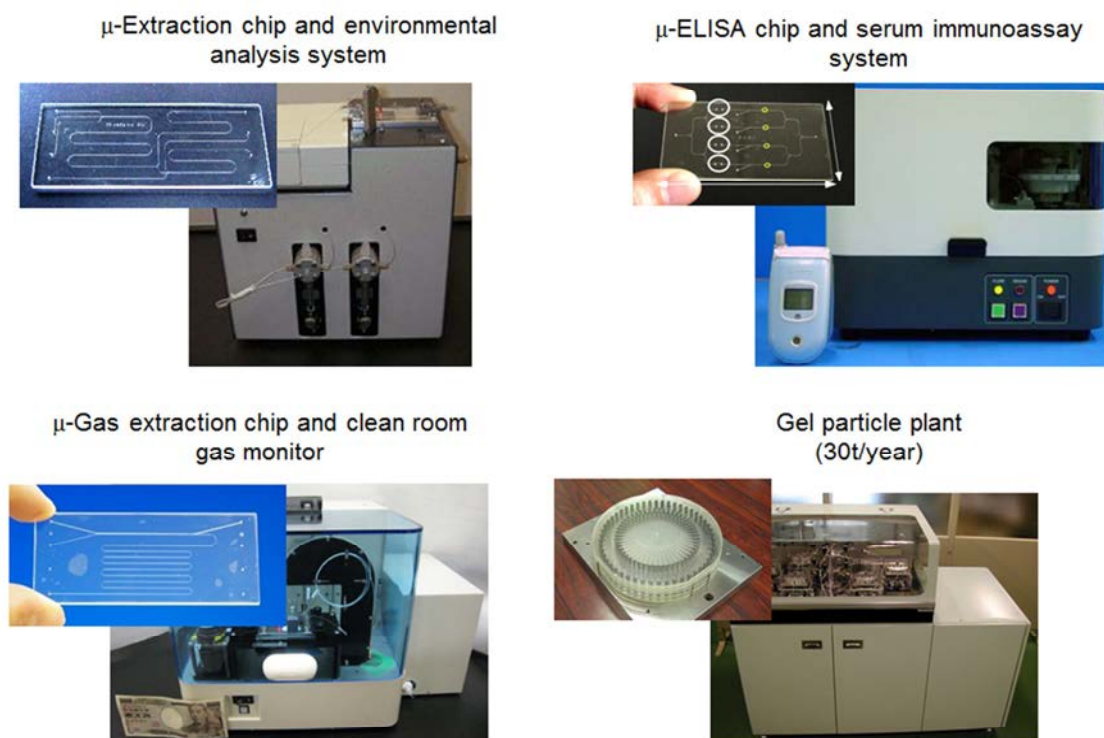


Figure 2: Microfluidic devices (chemical CPU) and systems.

Recently, the space is further downscaling to 10^1 - 10^2 nm scale, which we call extended-nano space (Figure 3) to distinguish the space from conventional nanospace treating 10^0 nm space in nanotechnology. The extended-nano space locates the gap between isolated molecules in the conventional nanotechnology and normal condensed fluid in microspace and bulk, and many unique properties can be expected. The surface-to-volume ratio is 10^3 times higher than the micro space, and the surface property will have great influence on the fluidic and chemical properties. However, it was quite difficult to investigate the liquid properties due to lack of fundamental technologies for this ultra-small space, which was even smaller than the wavelength of visible light. In order to overcome the barrier, many efforts have been made to establish the methodologies for this ultra-small space. Our group established many fundamental technologies for general integration of chemistry in the extended-nano space: top-down and bottom-up nano-fabrication methods, low-temperature bonding method, single molecule detection method for non-fluorescent molecules, partial surface modification method with spatial resolution less than optical diffraction

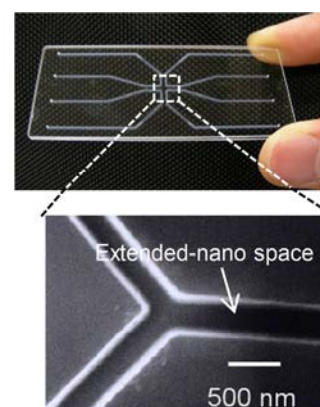


Figure3: Extended-nano fluidic device.

limit, and aL-fL pressure driven fluidic control method (Figure 4). Here, we show the low temperature bonding technology as a very important fundamental technology (Figure 5). Previously, a thermal bonding method was utilized for glass/glass substrate bonding [3].

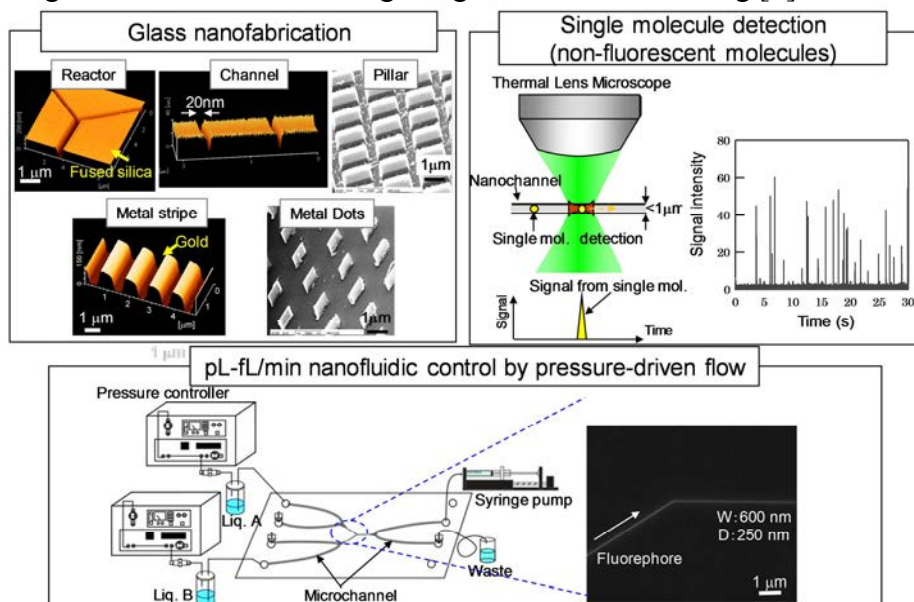


Figure 4: Fundamental technologies for extended-nano fluidic devices

The glass substrates were cleaned by piranha solution, and the two glass substrates were bonded in a furnace by raising the temperature to around glass transition temperature, which depended on the glass materials (more than 1000 °C for fused-silica). When the functional materials were modified on the surface before bonding for functionalization, the materials are burned out during the bonding process. That is why low temperature bonding method is very important for functionalization. For this purpose, we developed a surface treatment method for the low temperature bonding [4]. The glass surface was cleaned in an oxygen plasma chamber with a Teflon block to add F atom on the glass surface. Then, the two glass substrates were bonded at low temperature (room temperature to 100 °C) by applying high pressure (5000 N for 3 cm × 7 cm glass substrates)

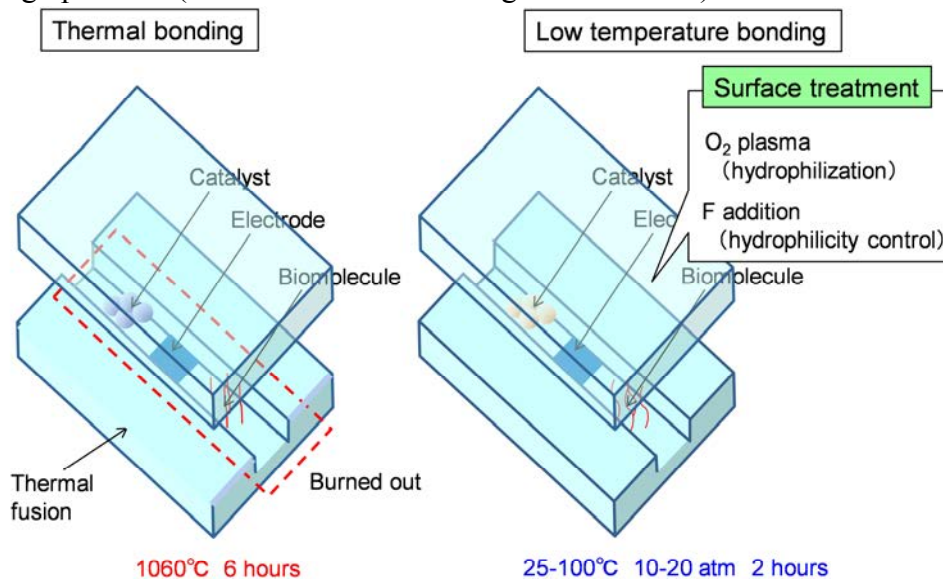


Figure 5: Thermal bonding and low temperature bonding methods for extended-nano fluidic devices

With these state-of-the-art technologies, many unique liquid and chemical properties were reported [5, 6], which were quite different with those in micro or bulk space (viscosity increase, proton mobility, dielectric constant, proton concentration, chemical reactions). Some properties can be expected by considering the characteristics of microspace and the size effect, and the others were

unexpected or difficult to predict. Also, the unique liquid properties were induced when the channel size became 10^2 nm scale both for depth and width. In conventional chemistry, the researchers were believing that the liquid properties changes only when the space size becomes molecular-scale, while there was no evidence of this assumption. Based on the results, we proposed a three-layer model. In this model, three phases of water are considered: the adsorption phase, the proton transfer phase, and the bulk phase. In the bulk phase, the water molecules have an ordinary liquid structure and freely translate and rotate. In the adsorption phase, the water has an ice-like structure in which both translation and rotation are inhibited. Intermediate to the adsorption phase and the bulk phase, a proton transfer phase of approximately 50 nm thickness exists and features loosely-coupled water molecules that keep a four-coordinated H_2O structure, which have slower translational motions, and possess high proton transfer capabilities resulting from proton hopping along a linear $\text{O}\cdots\text{H}-\text{O}$ hydrogen bonding chain. While this is still the assumption, we are trying to clarify the microscopic water structure by developing extended-nano X-ray diffractometry.

Now, chemistry and fluidics in the extended-nano space are forming a new research field and will contribute to understand the chemical and biological process in the small spaces (e.g. inter-cellular space in neuron, liquid in the bedrock, and slipping in the fluidic mechanics) and to realize a new chemical and bio devices.

In this presentation, we will introduce the fundamental technologies (fabrication, fluidic control, detection, and surface modification) and the unique liquid properties found in our laboratory. The device applications (single cell & single molecule analysis, self-charging fuel cell, etc.) utilizing the liquid properties are also included.

References

- [1] M. Tokeshi, T. Minagawa, K. Uchiyama, A. Hibara, K. Sato, H. Hisamoto and T. Kitamori: *Anal. Chem.*, **74**, (2002), P1565.
- [2] Website of Institute of Microchemical Technology, Co., Ltd.: <https://www.i-mt.co.jp/e00top/eindex.html>
- [3] B. Renberg, K. Sato, K. Mawatari, N. Idota, T. Tsukahara, T. Kitamori: Thermal bonding of nano- and microfluidic chips, *Microchimica Acta*, **166**, (2009), P177.
- [4] Y. Xu, C. Wang, Y. Dong, L. Li, K. Jang, K. Mawatari, T. Suga, T. Kitamori: Low-temperature direct bonding of glass nanofluidic chips using a two-step plasma surface activation process, *Anal. and Bioanal. Chem.*, **402(3)**, (2012), P1011.
- [5] T. Tsukahara, K. Mawatari, T. Kitamori: *Chem. Soc. Rev.*, **39**, (2010), P1000.
- [6] K. Mawatari, Y. Kazoe, T. Tsukahara, Y. Tanaka, D. Philip, T. Kitamori: *Extended-Nano Fluidic Systems for Chemistry and Biotechnology* (Imperial College Press, UK, 2012)

CHAPTER 6:

Mechanical Fluid Effects, Nanoparticles

Measurement of the Frictional Force Between PVA Roller Brushes and Semiconductor Wafers with Various Films Immersed In Chemicals

Kenya Nishio^{1, a}, Toshiyuki Sanada¹,
Satomi Hamada², Hirokuni Hiyama³ and Akira Fukunaga²

¹ Shizuoka University, 3-5-1 Johoku, Naka-ku, Hamamatsu, Shizuoka 432-8561, Japan

² Ebara Corporation, 4-2-1 Honfujisawa, Fujisawa, Kanagawa 251-8502, Japan

³ Ebara Corporation, 11-1 Haneda Asahi-cho, Ohta-ku, Tokyo 144-8510, Japan

^a nishio.kenya.15@shizuoka.ac.jp

Keywords: Post-CMP Cleaning, PVA roller brush, Friction, Thin films, Chemicals

Abstract. To better understanding the lubrication condition between a polyvinyl acetal (PVA) brush and cleaning surfaces, we measured the frictional force between the PVA roller brushes and the semiconductor wafers with various films immersed in chemicals. The frictional force showed different tendencies depending on the combination of chemicals and surface films. Especially, the large fluctuation of friction force was observed under the combination of Cu and NH₄OH.

Introduction

As microfabrication technology progresses supporting an increased integration of semiconductor devices, chemical mechanical polishing (CMP) is considered as part of the essential processes. However, a large number of nanoscale residues are generated by the CMP process, and this can cause a device yield loss. To achieve a defect-free post-CMP cleaning, polyvinyl acetal (PVA) roller brushes have been extensively used. However, the design and operation conditions of the PVA brushes have been determined based on experimental trial-and-error, and a variety of shapes of PVA roller brushes have been proposed [1]. This is because many researchers have proposed different cleaning mechanisms for PVA brushes, whereby the optimal condition is dependent on the cleaning mechanism. For example, Gu et al. [2] reported that the cleaning was achieved with the use of a fluid shear force or a direct brush contact at high or low brush rotation speeds, respectively. Hence, to clarify the contact condition between the PVA brush and the cleaning surface, many researchers have investigated the frictional forces.

Philipossian et al. [3] measured the coefficient of friction between the PVA roller brushes and silicon dioxide. They reported that the friction was decreased with an increase of the pH value of the chemicals used. Hara et al. [4] also measured the friction between the PVA roller brushes and several surfaces, and reported the effects of surface wettability and the roller kinematic condition. However, there is little information available on the study of the frictional force on films in chemical solutions other than those that are Si-based. In this study, we measured the frictional force between the PVA roller brushes and the semiconductor wafers with various films, such as W and Cu, which have been extensively used in recent semiconductor devices immersed in chemicals. Specifically, we focus on the effect of rotational speed and the pH value of the chemicals used.

Experimental setup, method, and conditions

Figure 1 shows the schematic of the experimental setup for the measurements of the frictional force of PVA brushes. We modified the experimental setup of a previous study [4] to measure the frictional force in chemicals. The frictional force F_s generated because of brush compression and rotation on wafers in the pool filled with chemicals was measured using load cells installed at the pool ends. The rotational speed N was controlled with a servomotor, and the compression distance d_n was controlled using a Z stage.

In this study, in order to decrease the influence of the eccentricity of the roller brushes [5], we used PVA brushes with four rows of nodules. The wafers with films were Si-based film1 (Si-1), Si-based film2 (Si-2), Si-based film3 (Si-3), W, and Cu. Here the Si-based films were different compound materials typically used for CMP process. The corresponding contact angles θ of each of the films were $12 \pm 2^\circ$, $10 \pm 1^\circ$, $46 \pm 2^\circ$, $21 \pm 6^\circ$, and $20 \pm 7^\circ$, respectively. The chemicals were ultra-pure water (UPW), citric acid aqueous solution (citric acid, 23%, pH = 2), and ammonium hydroxide (NH₄OH, 0.5%, pH = 11.4). The experimental conditions included the brush rotational speed, $N = 10\text{--}500$ rpm, and the compression distance, $d_n = 0.5\text{--}3.0$ mm.

Results

Figure 2 shows the frictional force variation of the PVA roller brushes on different films as a function of the rotational speed. The F_s values indicate the fluctuation of force with time [3, 6] due to the brush rotation and nodule existence. Correspondingly, we present and discuss the time-averaged value \bar{F}_s of the frictional force. As shown in the figure, \bar{F}_s decreased with increase in the rotational speed N in citric acid or UPW. On the contrary, \bar{F}_s increased with increase in N in NH₄OH.

Figure 3 shows the frictional force of the PVA roller brush on different films as a function of the pH of the chemicals. The error bar shows the range of variation of \bar{F}_s caused by the change in the rotational speed N as illustrated in Fig. 2 (e). Overall, \bar{F}_s on Si-based films decreased with increase in the pH values of the chemicals. This result exhibits a similar tendency to previous findings [3]. On the other hand, combinations of W or Cu and NH₄OH showed different tendencies.

Figure 4 shows the time series of the frictional force F_s of the PVA roller brush on different films in NH₄OH at $N = 500$ rpm. As shown in Fig. 4 (a)–(c), the fluctuation of the frictional forces on Si-based films was very small compared to the averaged value. On the other hand, the frictional force on W and Cu shows large fluctuations. F_s oscillated with a frequency of 8.33 Hz ($500/60 = 8.33$ Hz) as a function of rotational period in the case of W and oscillated at a frequency of 133 Hz ($8.33 \times 16 = 133$ Hz) as a function of the impact period of nodules in the case of Cu, respectively, as shown in the close-up view of Fig. 4 (f) and (g). Herein, the roller brush has 16 nodules.

Figure 5 shows the difference between the maximum and minimum values of the frictional force ΔF_s in chemicals [the definition is indicated in Fig. 4 (f)] as a function of rotational speed N . Figure 5 (a), (b), and (c), show results for the citric acid, UPW, and NH₄OH, respectively. ΔF_s has large values at rotational speed N up to 100 rpm, after which ΔF_s decreases to small values in UPW and citric acid. These large values are of the same order as the averaged value, \bar{F}_s . On the contrary, ΔF_s in NH₄OH exhibits different tendencies with films, as shown in Fig. 5 (c). ΔF_s on Si-based films show extremely small values. However, ΔF_s on Cu in NH₄OH drastically increased with increase in N . ΔF_s values in the case of W in NH₄OH were comparatively similar to the values obtained with the other chemicals.

Discussion

In the present study, the frictional force showed a different tendency as a function of the rotational speed and at different combinations of film and chemicals. As shown in Fig. 2, \bar{F}_s decreased with increase in the rotational speeds in citric acid or UPW. This result exhibits a tendency similar to our previous findings [4]. We speculated that this result was caused by the decrease in growth of the real contact area with decrease in contact time. We believe that this was mainly caused by mechanical actions. On the contrary, \bar{F}_s increased with increase in the rotational speed in NH₄OH. Furthermore, ΔF_s showed a different tendency with the combination of film and chemicals. We consider that this was caused by the chemical reaction on the surface of films because of the chemicals used. Herein, we focused on the effect of chemical reactions between films and chemicals.

The difference between the maximum and minimum values of the frictional force ΔF_s on Si-based films yielded extremely low values as shown in Fig. 4. As pointed out by Philipossian et al. [7], we believe that dissolution materials, such as silicic acid, act as lubricants. However, the reason why the \bar{F}_s of Si-based films increased with increase in the rotational speed in NH_4OH is not clear at the present stage.

As shown in Figs. 3–5, the frictional forces of W or Cu in NH_4OH were totally different. We consider that this was also caused by the chemical reaction on the surface of films. W will have low reactivity with oxygen because W must lose six electrons to become completely oxidized [8]. Therefore, we speculate that the surface condition of W was almost unchanged. Then \bar{F}_s and ΔF_s in the case of W in NH_4OH exhibited a tendency similar to UPW case. In contrast, \bar{F}_s and ΔF_s in the case of Cu in NH_4OH exhibited extremely large values. We consider that Cu is easy to react chemically, and the thin film of Cu is partially removed. Cu in NH_4OH react chemically as Equations 1 and 2 [9].



Cu in water is covered with $\text{Cu}(\text{OH})_2$ over wide range of pH [10]. On the other hand, $\text{Cu}(\text{OH})_2$ in NH_4OH is dissolved by NH_3 [11] and nascent surface of Cu, which is highly active is exposed. As a result, the frictional force increased with increase of real contact area between PVA brushes and nascent surface. In addition, the repetition of impact of PVA brush nodules enhanced the chemical reaction to accelerate a solution agitation. Stick-slip phenomena, which were observed in our earlier study [4], also occurred between the brush nodule and the bulk material. Therefore, large ΔF_s values were observed. It is known that such phenomena are a chemical reaction induced by friction or impact, called a tribochemical reaction [12]. The color change of the liquid during the experiments also supports our hypothesis.

Conclusion

We experimentally measured the frictional force between PVA roller brushes and semiconductor wafers with various films immersed in chemicals. The frictional force decreased with increase in the rotational speed in citric acid or UPW. In contrast, the frictional force increased with increase in the rotational speed in NH_4OH . Furthermore, the frictional force decreased with increase in the pH values of the chemicals used. On the other hand, combinations of W or Cu and NH_4OH showed different tendencies.

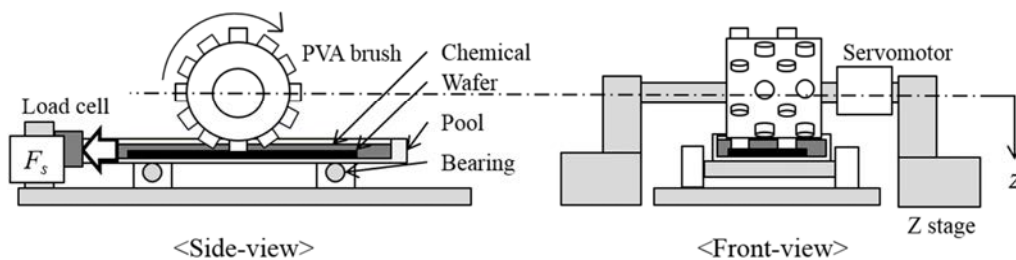


Figure 1: Experimental setup.

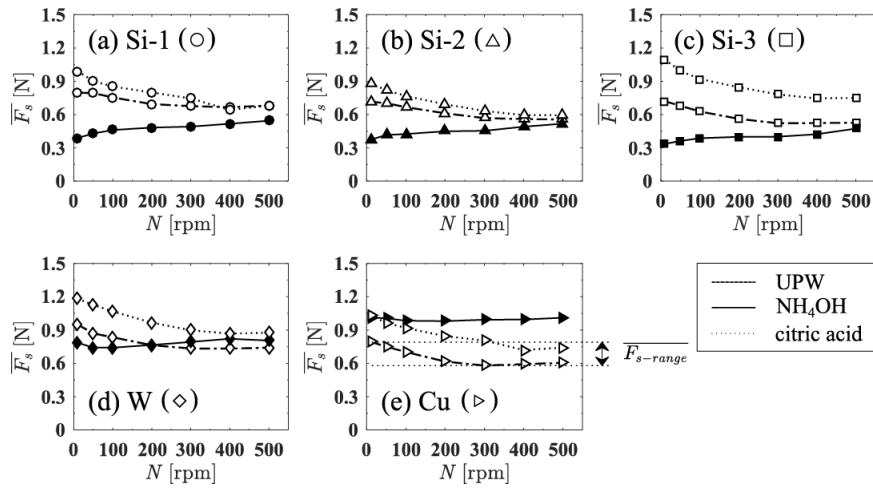


Figure 2: Frictional force of PVA roller brush on different films as a function of rotational speed N , (a) Si-1, (b) Si-2, (c) Si-3, (d) W, (e) Cu, $d_n = 3$ mm.

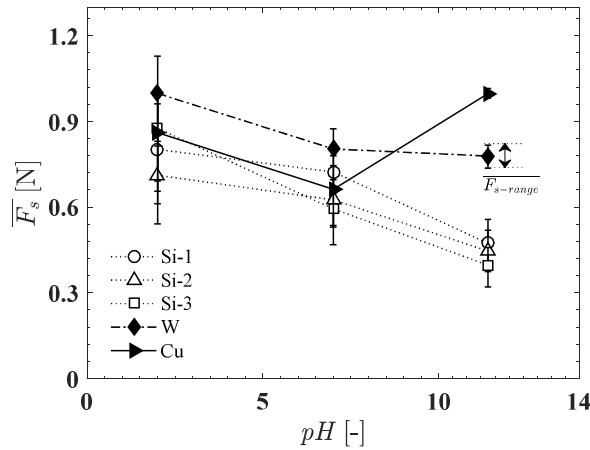


Figure 3: The average frictional force of PVA roller brush on different films as a function of the pH of the chemicals used for $d_n = 3$ mm, $N = 10$ –500 rpm (symbols: average value of F_s , citric acid: $pH = 2$, UPW, NH_4OH : $pH = 11.4$).

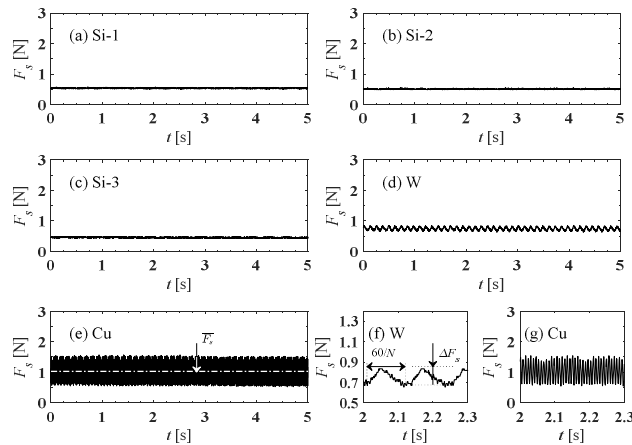


Figure 4: Frictional force F_s of the PVA roller brush on different films in NH_4OH as a function of time: (a) Si-1, (b) Si-2, (c) Si-3, (d) W, (e) Cu, (f) W (close-up view), (g) Cu (close-up view) $d_n = 3$ mm, $N = 500$ rpm.

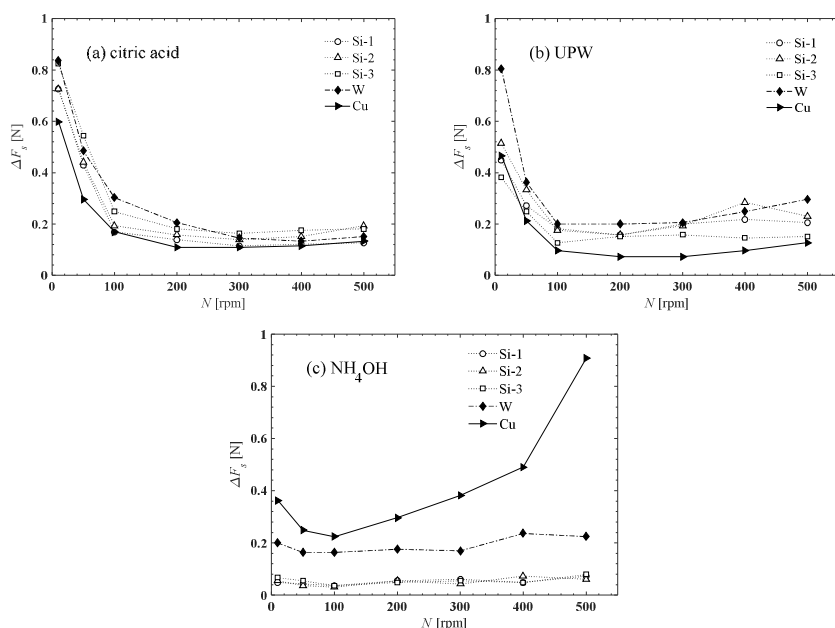


Figure 5: Differences between the maximum and minimum values of the frictional force in chemicals as a function of rotational speed N : (a) citric acid, (b) UPW, (c) NH_4OH , and $d_\eta = 3$ mm.

References

- [1] R. Singh, C. Patel, D. Trio, E. McNamara, and C. Wargo, ECS Transactions, 33 (10), 167–173 (2010).
- [2] X. Gu, T. Nemoto, A. Teramoto, M. Sakuragi, S. Sugawa, and T. Ohmi, Journal of The Electrochemical Society, 158 (11), H1145–H1151 (2011).
- [3] A. Philipossian, and T. Sun, Electrochemical and Solid-State Letters, 12 (3), H84–H87 (2009).
- [4] Y. Hara, T. Sanada, A. Fukunaga, and H. Hiyama, ECS Journal of Solid State Science and Technology, 4 (5), P141–P148 (2015).
- [5] T. Sun, Y. Zhuang, W. Li, and A. Philipossian, Microelectronic. Engineering, 100, 20–24 (2012).
- [6] Y. Hara, T. Sanada, A. Fukunaga, and H. Hiyama, ECS Transactions, 58 (6), 63–68 (2013).
- [7] A. Philipossian, and L. Mustapha, Journal of The Electrochemical Society, 151 (7), G456–G460 (2004).
- [8] Y. Seo, S. Park, and W. Lee, Transactions on Electrical and Electronic Materials, 7 (3) 108–111 (2006).
- [9] C. Sainio, and D. Duquette, Electrochemical Society Proceedings, 96 (22) 110–117 (1997).
- [10] K. Asare, and K. Mishira, Journal of Electronic Materials, 25 (10) 1599–1607 (1996).
- [11] K. Koyama, M. Tanaka, and J. Lee, Materials Transactions, 47 (7) 1788–1792 (2006).
- [12] F. Bowden, and D. Tabor, The Friction and Lubrication of Solids, Oxford, (1954).

Removal of Bull's Eye Signature by Optimizing Wet Cleans Recipe

Dhiman Bhattacharyya*, Pranesh Muralidhar, Mark Conrad

GLOBALFOUNDRIES, 400 Stone Break Road Extension, Malta, NY 12020, USA

*dhiman.bhattacharyya@globalfoundries.com

Keywords: Wet clean, photoresist strip, center signature, bull's eye defect, particle removal efficiency (PRE)

Abstract. As the semiconductor device technology is moving toward increasingly smaller nodes, it is becoming more challenging to keep the wafers free from contamination of even smaller particles. Wet cleaning process takes a major role in keeping the wafers clean, especially in post-RIE cleans. However, as every other process, wet cleaning also contributes some defects as adders which can potentially cause significant yield killer defects. A cluster of defects, classified as incomplete etch, was observed at the center of the wafer with a wet clean recipe (CIP1) since the adders from this recipe were not allowing the etch process and rendering incomplete etch defects. In this work, we optimized this CIP1 recipe to eliminate defects with the bull's eye signature at the wafer center and widened the process window of this type of wet cleaning process. The new recipe (CIP2) showed 100% success rate while CIP1 recipe had an occurrence of 35% failure for the bull's eye signature on the similar quality and quantity of wafers.

Introduction

Wafer cleaning process is increasingly becoming challenging as the size of the technology nodes are going down. The presence of a 45nm surface particle on sub 20nm gate would certainly have much bigger impact than it would have on 32 or 45nm gates. Therefore, a careful selection of wet chemical cleaning sequence is necessary for continuous improvement of cleaning recipes and their performance.

Photoresists are an integral part of the IC manufacturing photolithography process because these are used to create the patterns on the silicon wafers. Photoresist removal is commonly accomplished in a two-step process, (1) dry etch process followed by a (2) wet cleaning step. Plasma ashing removes most of the photoresists from wafer surface, however a wet cleaning is often required to remove leftover organic residues and surface particles and this clean is recommended to keep the wafer surface cleaner. The most commonly used aqueous chemistries for resist removal include SPM and SC1 or SC1 and SC2 or SC1 alone cleans or a combination of them [1,2].

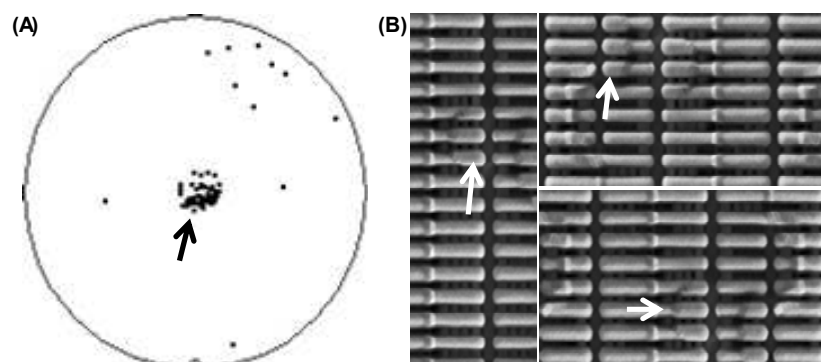


Figure 1: (A) Bull's eye signature of incomplete etch defect and (B) SEM images of the defects located at the center of the wafer.

A wet cleans process contributing too many particle adders, or inefficient removal of incoming organic residues and surface particles is a potential root cause for defects in the downstream processes. For example, the wafers which are reworked for lithography overlay mismatch or any other reasons, the resists are first stripped by dry ash followed by wet photoresist cleaning. The leftover defects from the dry rework are removed by the wet photoresist cleaning. Depending on the PRE of this cleaning process, the defects will stay on the wafer during the photoresist development and lithography process. The same defects can potentially block the post-litho etching process and finally yield to defects like incomplete etch. Since the kill ratio of these incomplete etch defects is close to 1, every occurrence of this defect is equivalent to loss of one individual dies. Therefore, an effective and optimized wet cleans process with very high particle removal efficiency (PRE) is desired during the wet cleans [3]. Complete surface cleaning can be achieved by combining the actions of previously mentioned chemistries, optimizing their flows and physical forces [4,5,6].

In this work, we evaluated two recipes (CIP1 and CIP2) in order to improve the PRE of the wet cleaning process during wet rework of photoresist coated wafers. The chemistries used in this work were a standard wet clean consisting of hot SPM and hot SC1 followed by cold SC1 nanospray. CIP1 recipe showed a significant difference in PRE performance based on the substrate surface property at the reworked layer. The CIP1 recipe caused a bull's eye signature of incomplete etch defects when used to rework at a layer with more oxide like surfaces [Figure 1]. However, the same CIP1 recipe did not show any defects at layers where the substrate surface is relatively more hydrophobic. Therefore, it was necessary to find the source of the defect and optimize the CIP1 recipe process window. The bull's eye signature of the defect that was observed in CIP1 was removed by optimizing the recipe in CIP2. Thus, the dies at the center of the wafers were protected from yield killer incomplete etch defects.

Experiments

CIP1 recipe was created following industry standard best known method (hot SPM-> hot SC1 -> SC1 nanospray chemistries) to maximize the PRE. It was then evaluated on blanket bare silicon wafers to verify its particle performance and then evaluated on patterned wafers. The defects were analyzed by dark field and bright field scans with scanning electron microscopy and electron dispersive X-ray spectroscopy. CIP2 recipe was created based on the CIP1 recipe; however a change in the recipe was made to optimize the chemical flow which helped to avoid the defects. The sequence of chemistries dispensed remains same in CIP2.

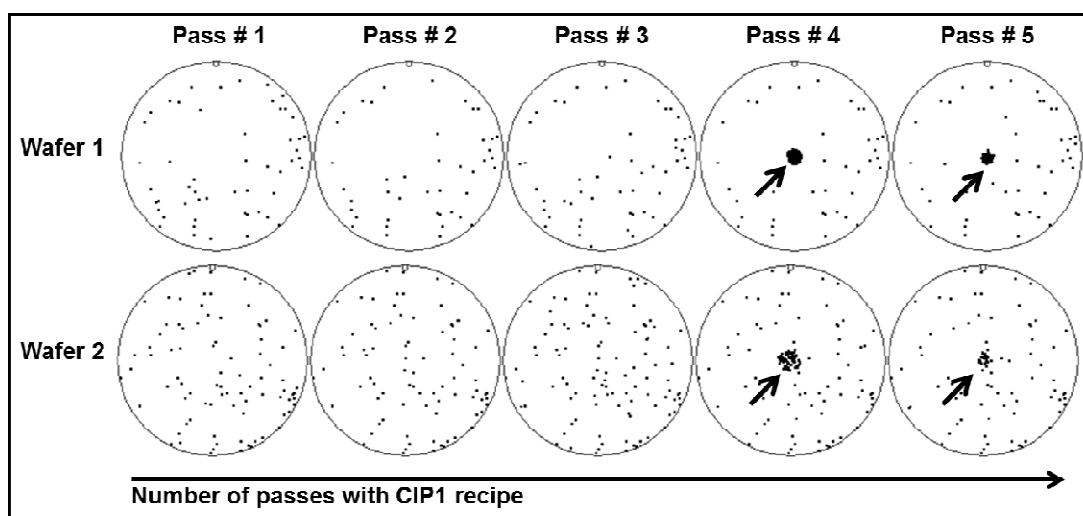


Figure 2: Examples of development of bull's eye defect on bare silicon wafers from the CIP1 recipe. Bare silicon wafers' surface become more and more hydrophilic as they go through several passes of SPM/SC1 chemistry. The bull's eye defect is found to be formed more frequently on hydrophilic surfaces than on hydrophobic surfaces.

Results and discussion

Initial testing on multiple bare silicon wafers ($N > 10$) did not reveal any bull's eye signature. However, a very strong signature of incomplete etch at the center of the wafers was observed when the recipe was evaluated on patterned wafer [Figure 1]. However, interestingly the identical recipe did not show any such defects at other production layers where relatively more hydrophobic surfaces were exposed during this wet cleaning process. After observing the defects on product wafers, repeated testing of the CIP1 recipe on the same set of bare silicon wafers was performed. The defect showed up at the center with the same CIP1 recipe after 3 to 4 consecutive passes on the same wafers [Figure 2]. It is believed that, consecutive passes of the SPM/SC1 chemistries on relatively hydrophobic silicon wafers turned the wafer surface hydrophilic [7] which facilitated the formation of the defects at the center of the wafer. Successive use of chemistries of higher temperature, such as hot SPM and hot SC1, heated up the wafer surface to higher temperature. This heated wafer surface was then exposed to high power nanospray consisting of more N_2 gas and less liquid flows which allowed the wafer to dry out from the center at a faster rate during the nanospray dispense.

The defects on the blanket wafer appeared to be residues and drying marks at the center of the wafer and composed of carbon and oxygen as observed under SEM and EDX [Figure 3].

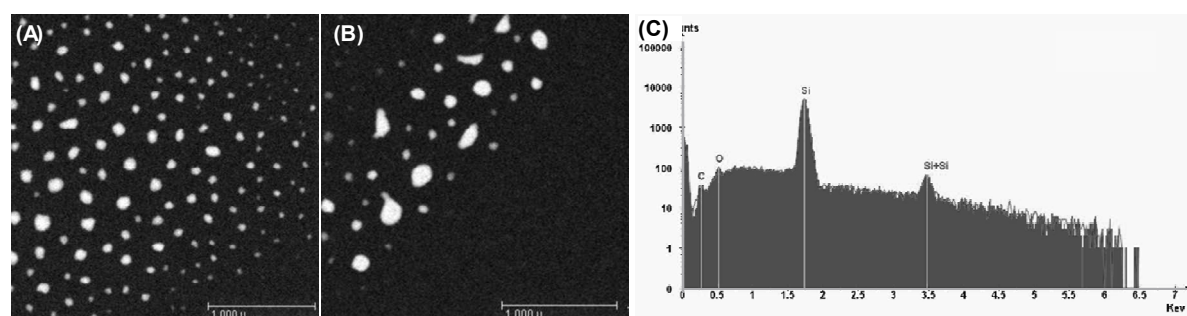


Figure 3: (A) and (B) SEM images of the defects at the center of the wafer, and (C) EDX analysis of the same defects.

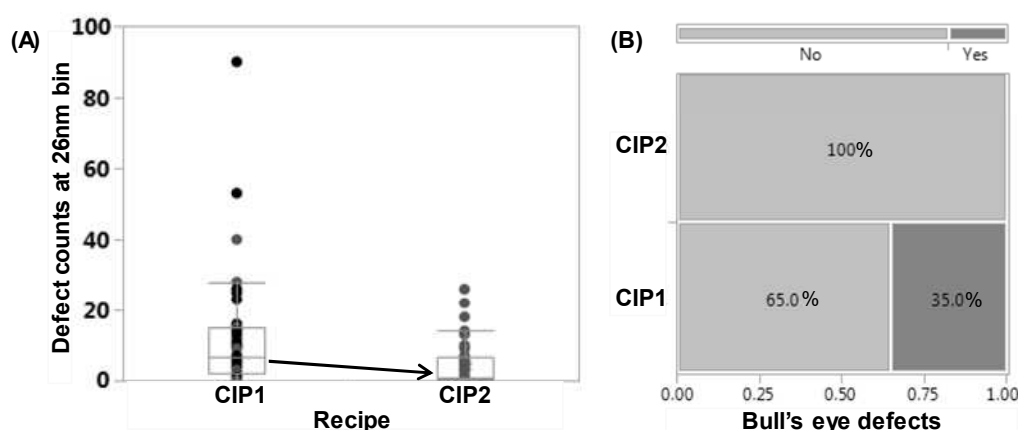


Figure 4: (A) Statistical comparison of the 26nm bin particle performance of CIP1 and CIP2 recipes, and (B) a mosaic plot of contingency analysis to correlate the two recipes to the bull's eye defect failure where $N = 40$.

Some adjustments to the recipe structure, SC1 and nanospray flows were made to the CIP1 recipe considering the probable causes of the bull's eye signature. An inclusion of cold SC1 dispense after hot SC1 helped reducing the wafer temperature before cold SC1 nanospray hit the wafer surface which allowed the wafers not to dry out during cold SC1 nanospray. An alternative solution was to insert an additional step of SC1 nanospray with lower N_2 gas flow after hot SC1 dispense (data is not reported here). SC1 nanospray with lower N_2 gas flow has higher proportion of liquid SC1 which can efficiently lower the wafer temperature before SC1 nanospray with higher N_2 gas flow is

dispensed. In cases where hot SC1 is followed by deionized water nanospray only, addition of cold deionized water dispense before the nanospray can act the similar way.

The new recipe (CIP2) with all these adjustments showed 100% success rate on unpatterned silicon wafers while CIP1 had an occurrence of 35% failure on the similar quality of wafers as shown in Figure 4B. In addition to elimination of the bull's eye signature, the mean particle counts (>26nm bin size) was also improved from CIP1 to CIP2 when compared within a sample size of 40 [Figure 4A].

Summary

A cluster of defects left at the center of the wafer with bull's eye signature after the wafers were processed with a wet cleaning recipe caused incomplete etch defects in the downstream. Root cause investigation revealed that the bull's eye signature was a result of the combination of wafer surface state and a transition from heated chemistry to high power nanospray. It is more frequent on hydrophilic surfaces and facilitated by faster drying of the wafer center. In order to eliminate the signature, adjustments to the chemical flows were made in the recipe which prevented the premature center drying and the new recipe did not show any similar defects.

References

- [1] M. Toofan and J. Toofan, Developments in Surface Contamination and Cleaning, Vol 8., Ch 5, R. Kohli & K.L. Mittal (Ed). (2015).
- [2] E. Kesters, Q. T. Le, I. Simms, K. Nafus, H. Struyf, and S. De Gendt, "Wet removal of post-etch residues by a combination of UV irradiation and a SC1 process", Solid State Phenomena, Vol. 195, (2013), p114.
- [3] P. Garnier, "Photo lithography – Surface preparation interactions", Solid State Phenomena, Vol. 219, (2015), p 177.
- [4] J. T. Snow, M. Sato, T. Tanaka, "Dual-Fluid Spray Cleaning Technique for Particle Removal" in Developments in Surface Contamination and Cleaning, Vol 6., Ch 3, R. Kohli & K.L. Mittal (Ed) (2013).
- [5] M. Sato, K. Sotoku, K. Yamaguchi, T. Tanaka, M. Kobayashi, S. Nadahara, Proc. 12th International Symposium on Cleaning and Surface Conditioning Technology in Semiconductor Device Manufacturing, Electrochemical Society, Pennington, NJ, (2011), p75.
- [6] K.N. Chauhan, V. Sih, T. Bhat, M. H. Kang, E. Kabutoya, G. Cheng, "Removing Organic Residues Using Backside Brush Scrubber Clean", ECS Trans, Electrochemical Society, Volume 69, (2015), pp. 109-115.
- [7] X. G. Zhang, Electrochemistry of Silicon and Its Oxide, Springer Science & Business Media, (2007).

Toward CO₂ Beam Cleaning of 20-nm Particles in Atmospheric Pressure

Joonoh Kim^{1,a}, Jae Hong Lee^{1,b}, Seungho Kim^{1,c}, Jinkyu Kim^{2,d},
Kihoon Choi^{2,e}, and Ho-Young Kim^{1,3,f*}

¹ Department of Mechanical & Aerospace Engineering, Seoul National University,
Seoul 08826, Korea

² R&D Center, SEMES Co., Ltd., Cheonan 331-814, Korea

³ Big Data Institute, Seoul National University, Seoul 08826, Korea

^ajoonohkim05@snu.ac.kr, ^bjay.lee@snu.ac.kr, ^ccyon0376@snu.ac.kr,

^djinkyu22.kim@semes.com, ^ekh1027.choi@semes.com, ^fhyk@snu.ac.kr

Keywords: Dry cleaning, Carbon dioxide solid particles, 20-nm contaminants

Abstract. We propose an optimal strategy for cleaning 20-nm contaminants in atmospheric pressure by using CO₂ solid particles injected from a supersonic nozzle. We found that an excessively small exit diameter of the nozzle results in the shock wave, which decreases the particle removal efficiency (PRE). Based on the incompressible flow theory, we developed a supersonic nozzle that can issue CO₂ solid particles without shock wave. The shape of CO₂ beam and PRE of the developed nozzle are compared with the results of a pre-existing nozzle for vacuum condition by analyzing scanning electron microscopy (SEM) image of substrates. The results show that when we use the newly developed nozzle in atmospheric pressure, PRE is above 95 % without pattern damage. This work can pave the way for cleaning nano-scale contaminants that occur during manufacture of semiconductor chips at little cost.

Introduction

As the size of the patterns in the semiconductor chips decreases below 100 nm, techniques for cleaning small contaminants are becoming an issue of more importance in the semiconductor industries. Several cleaning methods have been studied, such as megasonic cleaning [1], drop impact [2] and cryogenic aerosol cleaning [3], which have difficulties in dislodging sub-100 nm contaminants and bring about pattern damages by excessive cleaning forces. Kim et al. [4] has recently developed a new method in which CO₂ solid particles nucleated from a supersonic nozzle attack and dislodge contaminants. However, this method should be conducted under vacuum condition for drastic expansion of the CO₂ gas, which increases the complexity of system and the cost for manufacture. Here we present an enhanced cleaning scheme available under an atmospheric pressure condition.

Experimental apparatus

Experimental apparatus for generating CO₂ solid particles is schematically illustrated in Figure 1. CO₂ gas whose initial pressure ranges from 30 to 60 bar is supplied to the plenum chamber, and the flow rate is controlled by the mass flow rate controller. Because of the large volume of the plenum chamber, the gas velocity becomes temporarily zero resulting in the uniform pressure and temperature. Then, the gas passes through the supersonic nozzle. Due to the converging-diverging shape of the nozzle, CO₂ gas is accelerated above the sonic speed. As the kinetic energy of the CO₂ gas increases, the static pressure decreases, which causes adiabatic expansion of the gas. As a result, the temperature of the CO₂ gas decreases below the sublimation point, leading to the phase change toward CO₂ solid particles. The aggregated CO₂ solid particles are injected into the cleaning chamber. The issued CO₂ particles directly impact on the contaminants for detachment. The interior pressure of the cleaning chamber is controlled by a vacuum pump that sucks air in the chamber.

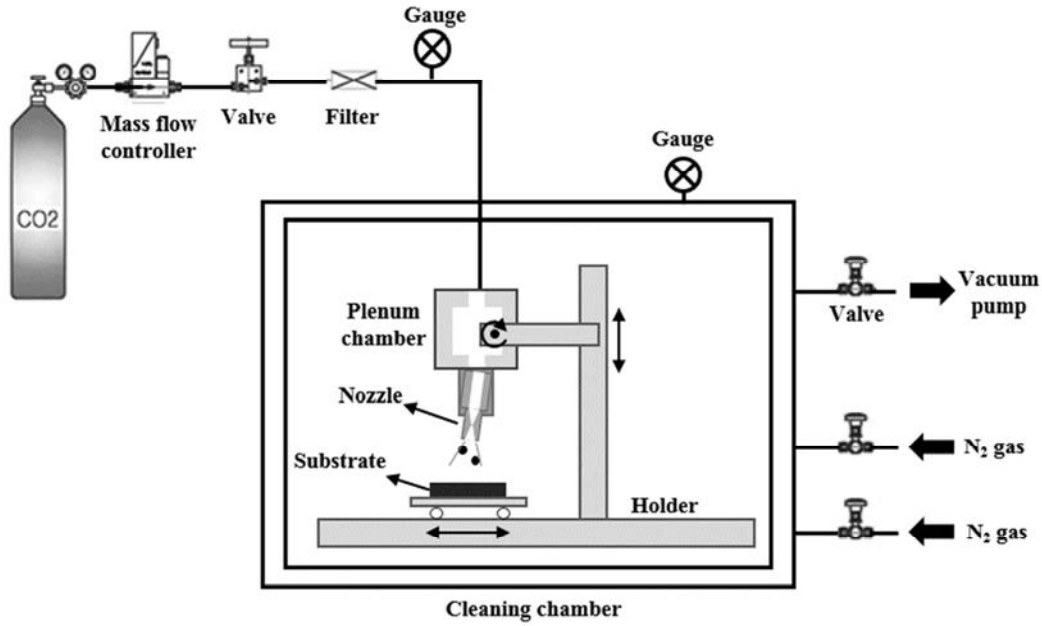


Figure 1: Schematic of the experimental apparatus.

Results

Optimal nozzle. We evaluated the shape of beam and cleaning efficiency depending on the pressure of cleaning chamber (P_b) and type of nozzle. We used two supersonic nozzles, one of which is a nozzle specialized for low P_b and the other is a developed one for cleaning in atmospheric pressure. The exit diameter of the developed nozzle, which determines the exit pressure, is larger than the one for vacuum condition. When the exit pressure is lower than the pressure of cleaning chamber, CO₂ beam is compressed and shock wave occurs. The shock wave causes unsteady velocity distributions of CO₂ particles, resulting in the decrease of impact force needed for dislodging the contaminants. The diameter of CO₂ beam becomes smaller because of the compression by high pressure of the cleaning chamber, which leads to the decrease of cleaning area. Therefore, supersonic nozzle should be designed to issue CO₂ beam without shock wave.

The pressure of the nozzle exit can be estimated using compressible flow theory. As the CO₂ gas flows through the converging-diverging nozzle, the velocity increases above the sonic speed and the pressure of the gas decreases drastically. The ratio of pressure at the inlet and outlet of the nozzle can be expressed as follows.

$$\frac{p_e}{P_i} = \left[\frac{1}{1 + \frac{(k-1)}{2} \text{Ma}^2} \right]^{\frac{k}{k-1}}. \quad (1)$$

P_e and P_i are exit and inlet pressure of the nozzle, respectively. k is the specific heat ratio of CO₂, and Ma is Mach number of the CO₂ gas at the exit of the nozzle. Substituting the inlet conditions and Mach number of CO₂ beam into Eq. 1, we can estimate the exit pressure which generates the shock wave. For instance, when using the nozzle specialized for low P_b with the inlet pressure of 40 bar, Mach number of the CO₂ beam becomes 3.9 by the acceleration through the nozzle. k of CO₂ gas is 1.3, and the exit pressure can be predicted to be 0.23 bar which is lower than 1 bar. Therefore, when we use this nozzle under atmospheric condition, CO₂ beam is compressed, leading to the shock wave. Using this estimation, we designed the nozzle that avoids the shock wave in the atmospheric pressure.

Cleaning experiments were conducted under three P_b conditions, 0.5 bar, 0.75 bar and 1 bar. To evaluate cleaning efficiency, we observed the wafer surface which is initially contaminated with cerium oxide particles as shown in Figure 2. The scanning SEM images of the substrates after the cleaning process were analyzed.

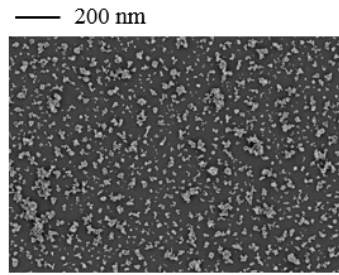


Figure 2: SEM image of contaminated Si wafer surface before CO₂ beam cleaning.

Figure 3 (a-c) shows that when using the nozzle for vacuum, particle removal efficiency (PRE) decreases with increasing P_b , because of the shock waves around the nozzle exit. However, when using the newly developed one, the contour of the beam is obviously stable and the PRE is over 95 % regardless of P_b , as shown in Figure 3 (d-f).

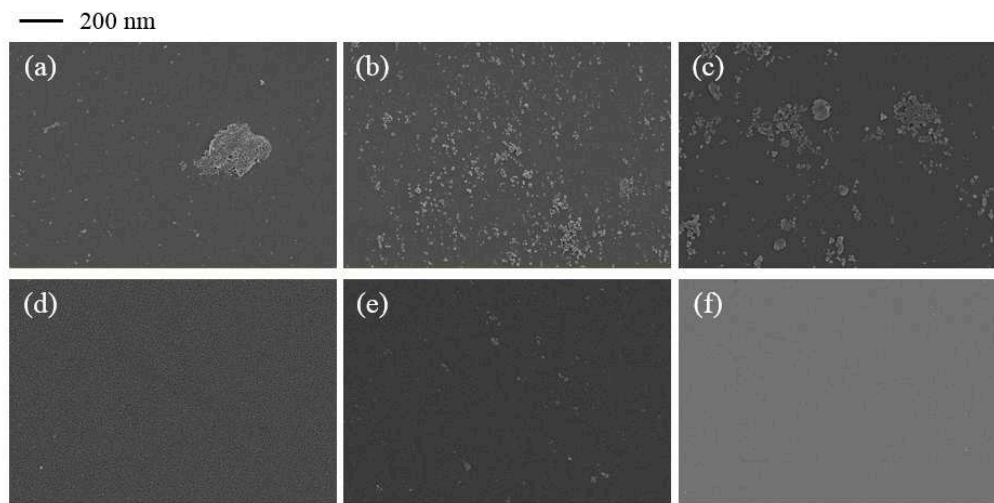


Figure 3: SEM images of Si wafer surfaces. (a-c) SEM images after cleaning process using the nozzle for vacuum (small exit diameter). (a) $P_b = 0.5$ bar. (b) $P_b = 0.75$ bar. (c) $P_b = 1$ bar. (d-f) SEM images after cleaning process using the developed nozzle (large exit diameter). (d) $P_b = 0.5$ bar. (e) $P_b = 0.75$ bar. (f) $P_b = 1$ bar.

Pattern damage. The pattern damages by the collision of CO₂ particles were assessed under optimum cleaning condition by using photoresist (PR) patterned substrate. The width and height of the patterns are 450 and 126 nm, respectively. The resulting damage was examined by analyzing SEM images of the substrates after the cleaning process. Figure 5 shows that when we use the developed nozzle for cleaning the PR pattern, no damages occur.

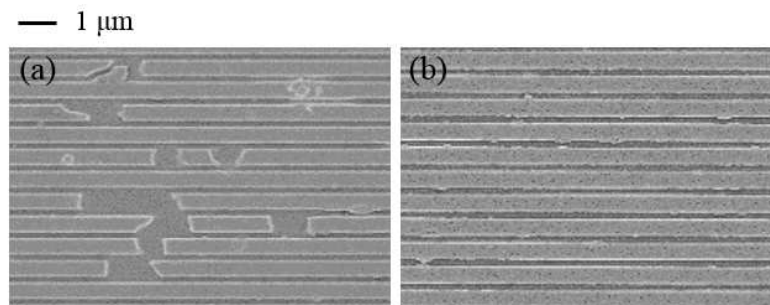


Figure 5: SEM images of PR patterns. (a) Collapse of patterns by excessive intensity of CO₂ beam. (b) SEM image after cleaning process using developed nozzle.

The collapse force of the PR pattern used in the experiments can be estimated based on the theoretical model by Lim et al [5]. When the incidence angle of the CO₂ beam is 90°, the minimum force to break a line pattern, F_c , is given by:

$$F_c = \frac{\sigma_Y LW^2}{6H} \quad (2)$$

σ_Y , L , W , and H are the yield strength, length, width and height of the pattern, respectively. As σ_Y of the PR pattern is 34 MPa, the collapse force is estimated to be approximately 210 nN.

Conclusion

We introduced a method to clean the 20-nm sized contaminants in atmospheric pressure without pattern damage. Using the compressible flow theory, the new supersonic nozzle that can issue the CO₂ beam without shock wave was developed. Cleaning efficiency of the developed nozzle was estimated to be above 95 % with no pattern damages observed.

Acknowledgments

This work was supported by National Research Foundation of Korea (Grant No. 2015001863) and SEMES via SNU IAMD.

References

- [1] W. Kim, T.-H. Kim, J. Choi and H.-Y. Kim, Appl. Phys. Lett. 94 (2009) 081908.
- [2] H. F. Okorn-Schmidt, F. Holsteyns, A. Lippert, D. Mui, M. Kawaguchi, C. Lechner, P. E. Frommhold, T. Nowak, F. Reuter, M. B. Piqué, Carlos Cairós and R. Mettin, J. Solid State Sci. Technol. 3 (2014) N3070.
- [3] N. Narayanswami, J. Electrochem. Soc. 146 (1999) 767.
- [4] I. Kim, K. Hwang and J. Lee, Nanoscale Res. Lett. 7 (2012) 211.
- [5] H. Lin, K. Chioujones, J. Lauerhaas, T. Freebern and C. Yu, IEEE Trans. Semicond. Manuf. 20 (2007) 101.

Liquid Cell Platform to Directly Visualize Bottom-Up Assembly and Top-Down Etch Processes inside TEM

Zainul Aabdin^{1,2,3,4,a}, XiuMei Xu^{5,b}, Utkarsh Anand^{1,2,3,4,c}, Frank Holsteyns^{5,d}
and Utkur Mirsaidov^{1,2,3,4,e*}

¹Department of Physics, National University of Singapore, 2 Science Drive 3, Singapore

² Graphene Research Centre, National University of Singapore, 6 Science Drive 2, Singapore

³ Centre for Bioimaging Sciences and Department of Biological Sciences, National University of Singapore, 14 Science Drive 4, Singapore

⁴ NUSNNI-Nanocore, National University of Singapore, 5A Engineering Drive 1, Singapore

⁵ IMEC, Kapeldreef 75, B-3001 Leuven, Belgium

^azainul.aabdin@gmail.com, ^bXiuMei.Xu@imec.be, ^cutkarsh.aanand@gmail.com,

^dFrank.Holsteyns@imec.be, ^emirsaidov@gmail.com

Keywords: In-situ TEM, Nanoscale liquid imaging, Hydration force, Steric force, Intermolecular force, Nanocrystal, Wet etching

Abstract. The assembly process of nanostructures from nanoparticles in solution is fundamental for bottom-up fabrication of functional materials and devices. In a similar way, bottom-down fabrication approach requires etching of materials. We take advantages of emerging in-situ liquid cell transmission electron microscopy (TEM) technique and explored several liquid processes such as: (1) nanoparticle-nanoparticle interaction in thin fluid layer, (2) wet etching of nanostructures and (3) pinning and de-pinning of nanodroplets at solid surface. Our approach is to directly visualize nanoscale liquid process, which is important for development of new nanofabrication processes for the design of next generation nanoscale devices. Our finding of nanodroplet pinning has important implications on surface cleaning at the nanoscale.

Introduction

Liquid cell dynamic TEM is an emerging technique that allows us to image nanoscale phenomena in liquids with subnanometer resolution inside TEM [1-3]. Liquid-phase processes are important over a wide range of areas in science and technology: one of these is bonding between nanocrystals in solution, which play an important role in structural organization for bottom-up fabrication and synthesis of new materials. However, bonding pathways of nanocrystals and its dynamics in liquid are poorly understood. In certain situations, few degree misalignment results in defect formation at bonding interface [4], and defect-free coherent bonding is only possible when bonding lattice planes of the two crystals are perfectly oriented. In recent studies, the pre-alignment of nanocrystals prior to attachment, post-bonding dipole-induced realignment of nanocrystals, and annealing of line dislocations in nanocrystals were observed [4,5,6]. However, two important key questions to nanocrystal bonding remain unresolved: 1) what are the necessary conditions for nanocrystal attachment in solution that will lead to defect-free coherent bonding? and 2) what is the likelihood of such coherent bonding? Furthermore, hydration forces play an important role in pre-alignment of nanocrystals. From earlier studies conducted at a macro and micro scale, it is known that these short-range repulsive forces may stall the approach of interacting surfaces [7]. However, the role of repulsive hydration forces on the interaction dynamics between nanocrystals remains unresolved. In this study, we will resolve the mechanisms and pathways of nanocrystal bonding. Further, we show that hydration forces form transient pairs by stalling nanocrystals in direct contact,

which may allow sufficient time for nanoscale bodies to reorient and explore optimal configurations prior to attachment.

Another phenomenon of liquid-solid interaction is wetting and dewetting of solid surfaces [8], which play an important role in surface cleaning. The phenomena of wetting and dewetting are dominated by pinning and de-pinning dynamics of the three-phase contact line on defect sites [9]. The practical problem of whether a droplet slides or stick on a surface depends largely on the underlying interfacial pinning forces [10]. The in-situ liquid cell TEM is ideally suited for exploring how the classical description of fluid behavior extends into the nanoscale. Here, we show our direct experimental observations of water nanodroplets in close proximity to gold nanoparticles, which act as pinning sites on an otherwise flat substrate. We describe the forces necessary for de-pinning nanodroplets from the nanoparticles, which is on the order of nanonewtons.

Materials and methods

Nanocrystal dynamic interaction and bonding was observed in solutions using in-situ TEM liquid cell platform. The liquid cell contains two micro-fabricated silicon (Si) chips, which sandwiches a thin layer (~ 100 nm) of the liquid specimen between two ultrathin electron transparent silicon nitride (SiN_x) membranes, which protected the liquid from the high vacuum within the TEM (Figure 1A). Approximately 400 nL of aqueous precursor solution containing 1 mM of chloroauric acid (HAuCl_4) (Sigma Aldrich Co., St. Louis, MO, USA: Cat# 254169) and 1 mM of cetrimonium bromide (CTAB) surfactant (Sigma Aldrich Co., St. Louis, MO, USA: Cat# H9151) was loaded into the liquid cell, which was in turn mounted onto a specimen holder that was inserted into the TEM [11,12]. For nanodroplet pinning and de-pinning study, water containing commercial gold nanoparticles of 10 nm size with concentration 10^{10} particles/mL (Nanocs Inc. New York, NY, USA: Cat#GP01-10-20) were loaded in the liquid cell after diluting in pure water (Sigma Aldrich Co., St Louis, MO, USA: Cat#30072) by 1:10 (v/v). Most of the gold nanoparticles get pinned to the SiN_x membrane and serves as pinning sites for nanodroplets formed by dewetting of thin film of loaded water.

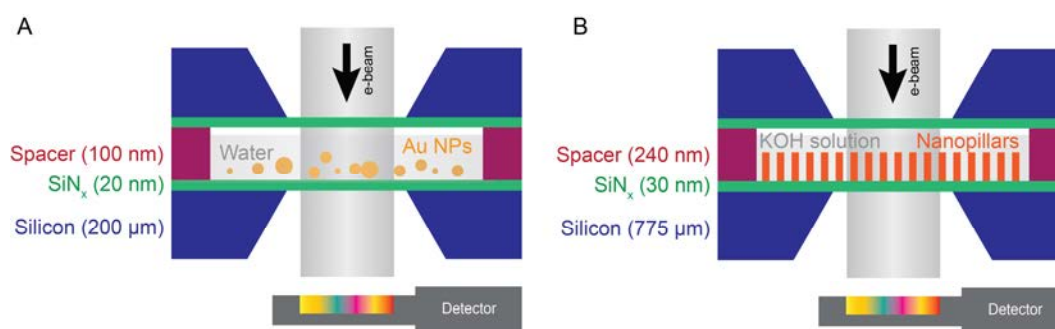


Figure 1: Schematic of in-situ TEM liquid cell platform for imaging (A) nanocrystals assembly in liquids and (B) nanoscale wet etch dynamics of semiconductor materials. Two ultrathin SiN_x membranes sandwich liquid layer and protect liquid specimen against the vacuum in the column of TEM.

Results and discussion

Figure 2A shows the coherent bonding of two nanocrystals initially separated by ~ 1 nm, and their (111) lattice planes misaligned by 10° (at $t = 6.9$ s) prior to contact. As the nanocrystals approach each other, their lattice misalignment decreases to 9° upon contact (not shown here, see ref. [11]), then visibly realigns into coherent bonding (Figure 2A; $t = 25.5$ s and 48.2 s). Here, the bonding was coherent because the common (111) lattice planes reflections of the nanocrystals merged into a single reflection with no visible defects (inset $t = 48.2$ s). Figure 2B shows another case of coherent bonding of two nanocrystals, misaligned by $\sim 15^\circ$ prior to attachment (Figure 2B; $t = 16.9$ s).

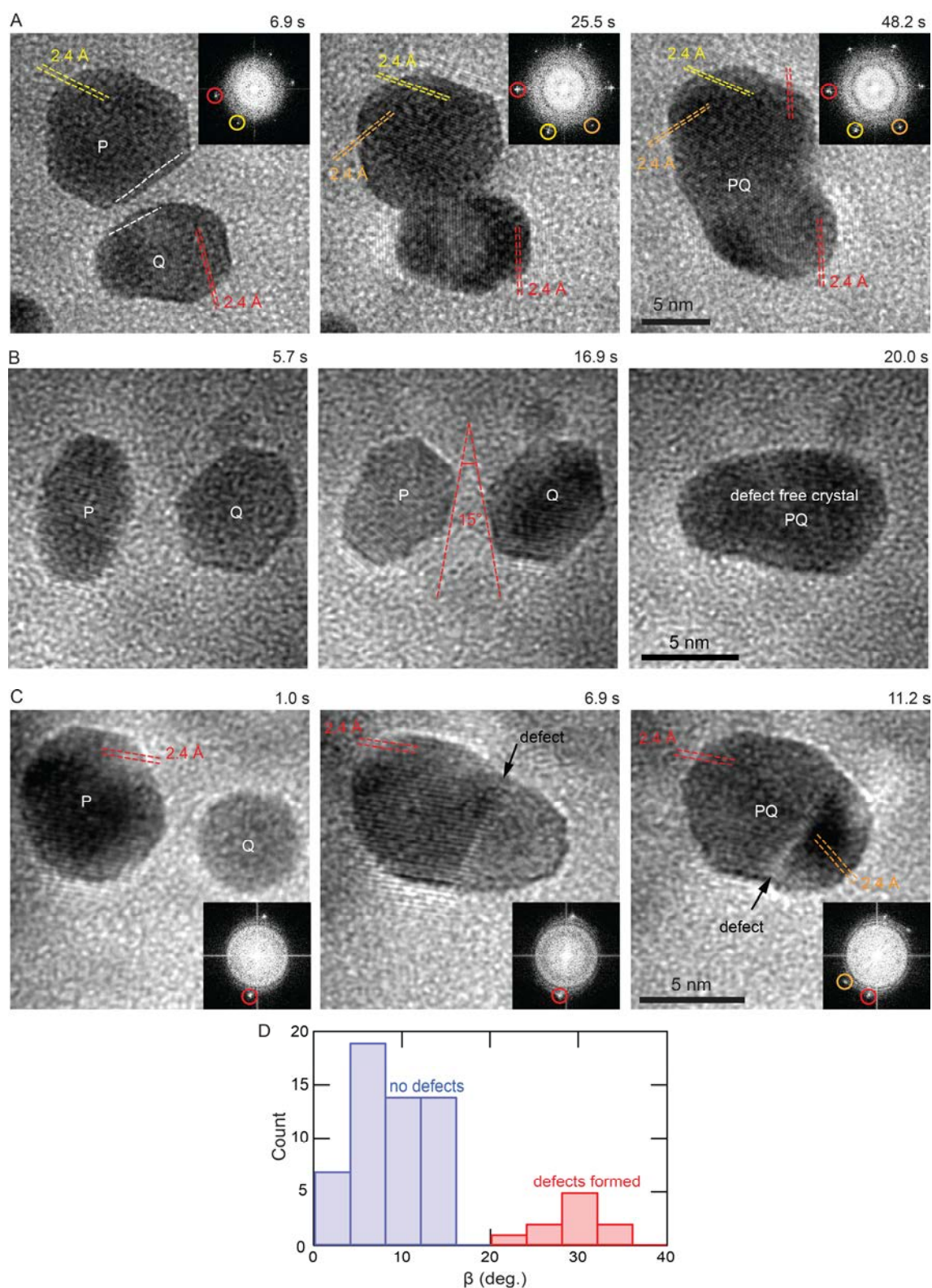


Figure 2: Time resolved TEM images of (A) and (B) coherent and (C) non-coherent bonding between two gold nanocrystals (P and Q). Coherent bonding shares common (111) lattice planes that are misaligned by angles less than 15° at contact and yields defect free nanocrystal PQ, whereas, for non-coherent bonding (111) lattice planes that are misaligned by 32° at contact yield a nanocrystal PQ with defect at the bonding interface. Lattice fringes along (111) plane with 2.4 Å spacing are marked by dashed parallel lines with corresponding reflections circled in the Fourier transform of the image as shown in the inset. All preceding images have same scale bar as right most image. (D) Histogram of experimental nanocrystal bonding events at different orientation angles (β) measured between the common (111) lattice planes showing that there is critical misalignment angle of $\sim 15^\circ$ which separates the two pathways. Adapted from reference [11].

Expectedly, defect-mediated bonding occurs when two nanocrystals meet with their (111) lattice planes initially misaligned by a large angle, for example by about 32° in Figure 2C. Here the nanocrystals do not realign upon bonding and a visible defect forms at their merging interface ($t = 6.9$ s, black arrow). Post bonding images and splitted Fourier reflections show that the newly formed nanocrystal is not a single crystal (Figure 2C; $t = 11.2$ s). The coherent and defect-mediated bonding sequences captured in Figure 2 are remarkable because upon contact the nanocrystals can reorient themselves to a limited extent, either to achieve coherent bonding when the two nanocrystals are initially misaligned by angles that are less than 15° , or rotate to a mutual configuration that allows defects to form. The experimental results in Figure 2D show that there is a critical misalignment angle ($\beta_{critical} \sim 15^\circ$) that separates two pathways for bonding: below this critical angle gold nanocrystals can realign for defect-free coherent bonding, and above which the defect are formed at the interface which mediate the bonding [11].

We track the separation between multiple interacting gold nanocrystals pairs in water. Figure 3A show time-resolved TEM image series of one such interaction between two nanocrystals. Tracking the spacing between nanocrystal surfaces as they interact reveals that the nanocrystals undergo a rapid approach when the corresponding pairwise distances reach ~ 5 Å, followed by a sudden jump to contact, which results in pairwise attachment (Figure 3B). The pairwise spacing indicates that pairwise attachment occurs immediately after surface-bound molecules (water with a molecular diameter of $\sigma_{water} \sim 3$ Å) are detached from the surface as these particles interact (Figure 3C).

Figure 3D show pairwise separations between nanocrystals approaching down to ~ 5 Å separation set by the combined thickness of the hydration layer of each nanocrystals, where nanocrystals form a sterically stabilized transient pair. Once the surface-bound water molecules between nanocrystals are drained, the nanocrystal surfaces come into contact at $t - t_0 = 0$ s, and coalesce, as schematically illustrated in the top panel [12].

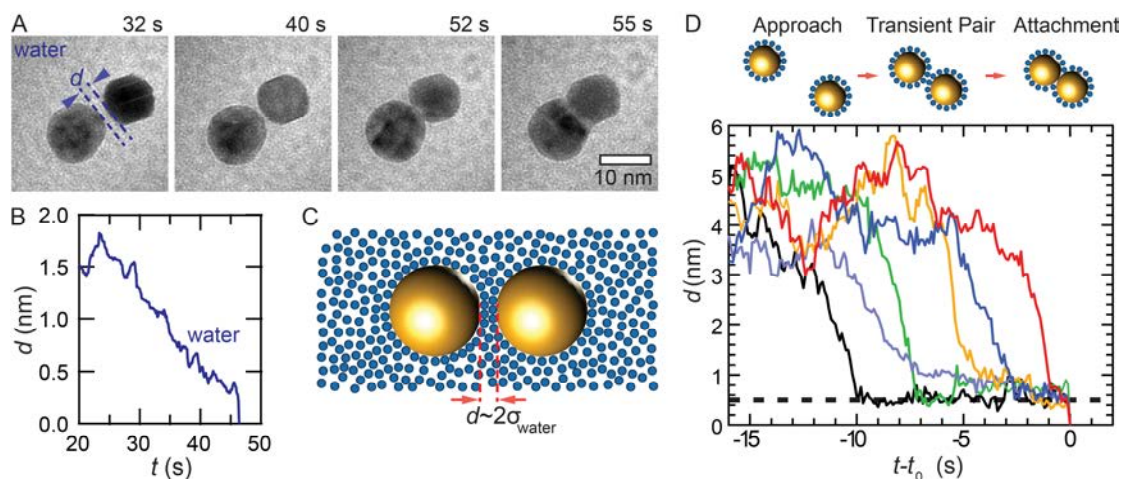


Figure 3: (A) Time-resolved TEM images of two gold nanocrystals undergoing coalescence in water. All preceding images have same scale bar as right most image. (B) Separation (d) between the two interacting gold nanocrystals; jump-to-contact occurs at a separation of ~ 5 Å. (C) The corresponding schematic of these nanocrystal interactions in water (blue spheres-water molecules, orange sphere-gold nanocrystal) that arise when gold nanocrystals come into contact with each other with their one-water-molecule-thick hydration layer. (D) Plots of pairwise separations between nanocrystals as a function of time showing the approach down to ~ 5 Å separation set by the combined thickness of the hydration layer of each nanocrystal, at which point the two nanocrystals form a sterically stabilized transient pair (top panel). Adapted from reference [12].

Further, we extended our study and observed the liquid interaction to pinned gold nanoparticles. Figure 4A shows a 30 nm diameter nanodroplet that translocates through a series of stick-slip steps, moving across the 10 nm gold nanoparticles. Once the nanodroplet comes into contact with the nanoparticle, it engulfs the particle and becomes pinned. While the nanodroplet remains pinned, its subsequent movements are restricted to the vicinity of this pinning site with its edge in constant

contact with the nanoparticle as shown in Figure 4C ($t = 6.1\text{--}7.7$ s). After de-pinning from nanoparticles, nanodroplet leaves behind a water film pinned on the nanoparticle, which then condenses into a smaller droplet, while a larger detached nanodroplet continues on its way. A crude estimate of the opposing capillary forces is made from the apparent width of the capillary bridge. Taking a semicircular arc length of $l \sim \pi w/2$, where the bridge width is $w \sim 15$ nm by inspection (red arrows in Figure 4C, $t = 7.6$ s), we estimate the capillary force to be $\gamma l \sim 1.65$ nN. More detailed discussion of de-pinning forces can be found in ref. [13].

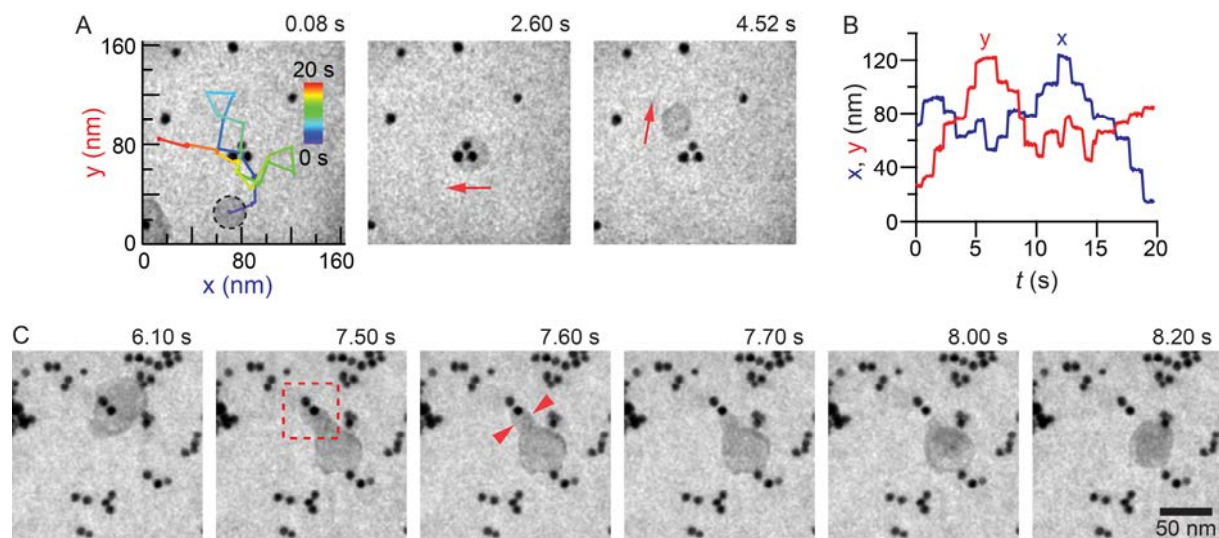


Figure 4: (A) Time series images showing nanodroplet at different stick position on gold nanoparticle coated SiN_x surface with stick-slip steps with its trajectory shown as the overlay on the left most image and (B) corresponding coordinates of its centre of mass. Red arrows indicate the direction towards which nanodroplet will move next. Dashed box at $t = 7.50$ s highlight features of the capillary bridge. All preceding images have same scale bar as right most image. Adapted from reference [13].

In addition, we will also describe our work on dynamics of wet etch processes of densely packed nanopillar arrays (not shown here) which has important bearing on fabrication of next generation transistors. Using the nanofluidic device and in-situ TEM platform (Figure 1B), we have for the first time visualized the real-time wet etch dynamics of nanoscale Si in aqueous KOH solution. Our findings reveal the detailed etch dynamics and its limitations and have important consequence for development of new fabrication methods.

Summary

In summary, our study reveals that gold nanocrystals bonding in solution can follow two distinct pathways: (1) coherent, defect-free bonding occurs when two nanocrystals attach with their lattices aligned to within a critical angle; and (2) beyond this critical angle, defects form at the interfaces where the nanocrystals merge. The critical misalignment angle for ~ 10 nm gold nanocrystals in CTAB is $\sim 15^\circ$. Further, we found that nanocrystals in water can form water-bonded transient pairs stabilized by steric hydration and attractive van der Waals forces. The formation of transient pairs with hydration shells in direct contact may allow sufficient time for nanocrystals to reorient and explore optimal configurations prior to attachment and it may play a crucial role in the oriented attachment of crystals as seen in this study. Our study of nanodroplet pinning and de-pinning from gold nanoparticles show that the nanodroplet stretches first, forming a short capillary bridge, followed by pinch-off, leaving behind a smaller residual nanodroplet attached to the nanoparticle. We find that the adhesion force that holds a 10 nm gold particle at a fixed point on the SiN_x surface is greater than ~ 1 nN, the force needed to de-pin the nanodroplet.

Acknowledgements

This work was supported by the Singapore National Research Foundation's Competitive Research Program funding (NRF-CRP9-2011-04). UM also acknowledges the support of the NUS Young Investigator Award (NUSYIA-FY14-P17).

References

- [1] N.D. Jonge and F. M. Ross, Electron microscopy of specimens in liquid, *Nat. Nanotechnol.* **6**, 695 (2011).
- [2] F.M. Ross, Opportunities and challenges in liquid cell electron microscopy, *Science* **350** (6267), 1490 (2015).
- [3] H. Zheng *et al.*, Observation of single colloidal platinum nanocrystal growth trajectories, *Science* **324** (5932), 1309 (2009).
- [4] R.L. Penn and J.F. Banfield, Imperfect oriented attachment: dislocation generation in defect-free nanocrystals, *Science* **281** (5379), 969 (1998).
- [5] H.G. Liao *et al.*, Real-time imaging of Pt₃Fe nanorod growth in solution, *Science* **336** (6084), 1011 (2012).
- [6] D. Li *et al.*, Direction-specific interactions control crystal growth by oriented attachment, *Science* **336** (6084), 1014 (2012).
- [7] J. Israelachvili, and H. Wennerström, Role of hydration and water structure in biological and colloidal interactions, *Nature* **379** (6562), 219 (1996).
- [8] D. Quéré, Wetting and Roughness, *Annu. Rev. Mater. Res.* **38**, 71–99 (2008).
- [9] N. Savva, G.A. Pavliotis, and S. Kalliadasis, Contact lines over random topographical substrates. Part 2. Dynamics, *J. Fluid Mech.* **672**, 384–410 (2011).
- [10] J. Wu *et al.*, Advanced understanding of stickiness on superhydrophobic surfaces, *Sci. Rep.* **3**, 3268 (2013).
- [11] Z. Aabdin *et al.*, Bonding Pathways of Gold Nanocrystals in Solution, *Nano Lett.* **14** (11), 6639 (2014).
- [12] U. Anand *et al.*, Hydration Layer-Mediated Pairwise Interaction of Nanoparticles, *Nano Lett.* **16** (1), 786 (2016).
- [13] Q. Liu *et al.*, Nanodroplet de-pining from nanoparticles, *ACS Nano*. **9** (9), 9020 (2015).

A Study on the Electrostatic Discharge (ESD) Defect in SOH Mask Pattern Cleaning

Dae-Wan KO, Tae-Ho HWANG, Sok-Hyung HAN, Chang-Hyun KIM,
Byung-Sul RYU

Samsung Electronics, San 14, Banwol-dong, Hwasung-City, Gyeonggi-Do 445-701, Korea

Keywords: SOH Film, Strip, SOH Mask Pattern, Rebounding, ESD, Electrostatic Discharge, semiconductor

Abstract. The application of the SOH Mask created a new defect. Defect image is similar to ESD defect, which occurred on POLY and METAL film. Stringent experiments were conducted in order to prove the correspondence principle of the defect of SOH and the mechanism of the ESD defect. Finally, it's concluded the defect of SOH is equal to the ESD defect. ESD defect occurred also on SOH film, like POLY or METAL film.

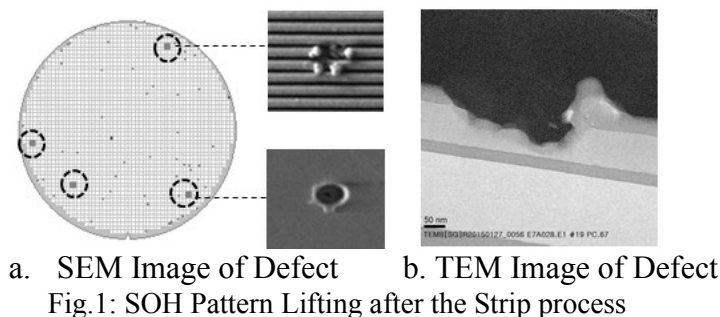
1. INTRODUCTION

This paper is about electrostatic discharge(ESD), during SOH film cleaning for pattern formation. SOH film is great worth the cost savings and process simplification compared with conventional hard mask. So, presently, SOH Film is important in the process of manufacturing semiconductor. But, the application of the new process(SOH Mask) created a new defect. Electrostatic discharge(ESD) defect is also one of those defects. This phenomenon occurred in the strip process after the step of SOH Etch. A lot of experiments were tried in order to prevent this defect. This paper is to investigate the way of preventing the electrostatic discharge defect, while cleaning SOH film, which is used to form patterns.

2. EXPERIMENT

2.1 Phenomenon of SOH Mask Pattern Defect

The process of Photo and Etch was applied on SOH film. And then, so as to remove by-products after the stage of Strip, the defects often occurred like Fig.1.



The defect appeared as if the pattern exploded.

The chemical used at the stage of STRIP is a kind of acid chemical to get rid of organic matters. The defect was found by Hitachi Co. SEM-Vision.

The defect was examined more in detail through TEM(Transmission Electron Microscope) equipment. In TEM image, SOH film exploded and the top SION layer peeled off. And, this defect is similar to ESD Defect, which occurred on POLY and METAL film. This defect caused on SOH Film influenced the following process.

As a result, the area in which the defect occurred was not able to function properly as Semiconductor.

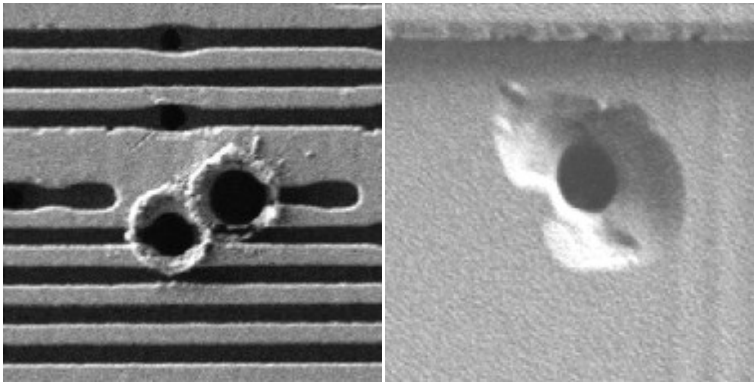
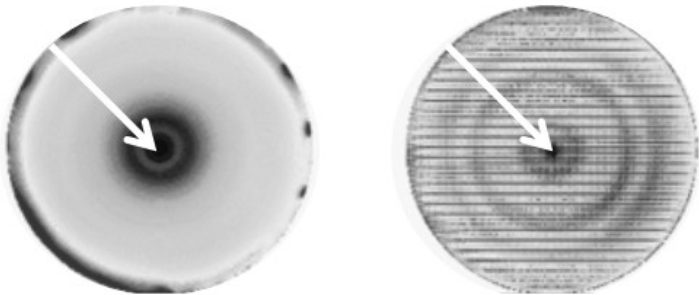


Fig.2: Exist ESD(Electrostatic Discharge) Defect

2.2 Defective Mechanism of SOH MASK Pattern

Fig.3 is the image measured by Q-Cept.
Before ETCH process, the electric charge is evenly located over the wafer surface.
But, neither it is, after ETCH process.
That is, before STRIP process, the state of the electric charge on the wafer surface is relatively unstable.

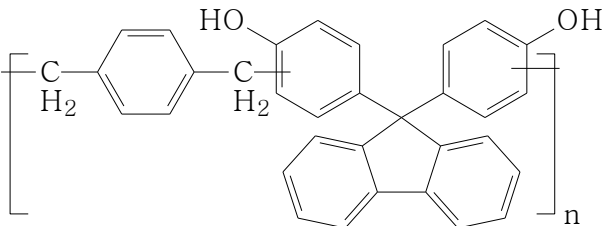
Q-Cept equipment : Qcept Technologies Inc. ChemetriQ3000



STEP	PRE ETCH	POST ETCH
Range	0.67V	1.10V

Fig.3: Surface Charge by Q-Cept

SOH film is a material that consists of the Carbon which electricity goes through. On the other hand, SIN, Oxide, and SION are an insulator.



The mechanism of ESD defect was applied to the defect, which was caused on SOH film.

The chemical droplets with a positive charge(+) fall on the front side of the wafer surface. And negative charges(-) are gathered on the SION film.

The exploding phenomenon of SOH film happens because of the energy by the gathered negative charges(-).

ESD defect gets to occur due to the phenomenon that the electric charge moves rapidly

In the end, the defect of SOH and the mechanism of the ESD defect are expected to correspond.

3. RESULT & DISCUSSION

- Stringent experiments were conducted in order to prove the correspondence principle of the defect of SOH and the mechanism of the ESD defect. There are three different methods tried on SOH pattern wafer.

First, a certain chemical for the step of Strip was sprayed only onto the front side of the wafer surface, second, only onto the back side of it. Lastly, it was sprayed onto the both sides of the wafer.

Then, it's been observed in which part of the wafer the defect happened.

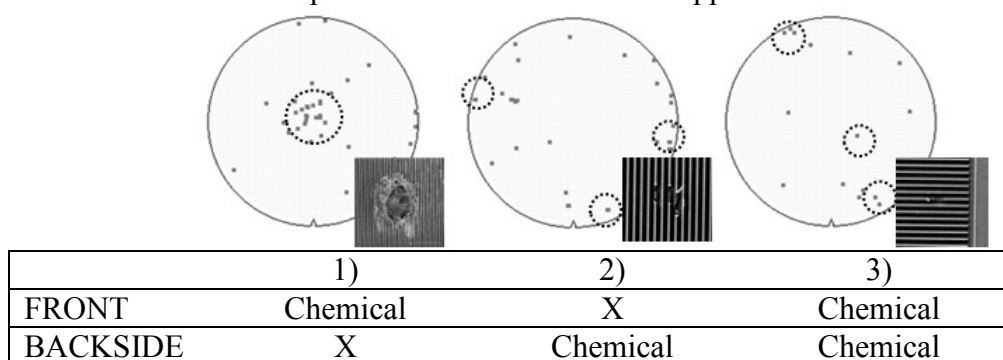


Fig.6: The evaluation for the defect verification

- Only on the front side; the defect occurred in the center of the surface. As the chemical was sprayed onto the very center of it.
- Only on the back side; the defect appeared in the edge of it. That's because the chemical sprayed on the backside rebounded on the front side of wafer, especially on the very outer edge.
- Both front and back side; the defect was found all around the surface.

In the condition of 1),2), and 3), the defect happened. The images of them were same as ESD defect.

Generally, the way to control ESD defect is to use Anti-static Chuck, CO2 rinse, and etc. The way was applied on SOH film. Consequently, ESD defect decreased just like POLY, METAL film, as well as SOH film.

ESD defect occurred also on SOH film, like POLY or METAL film.

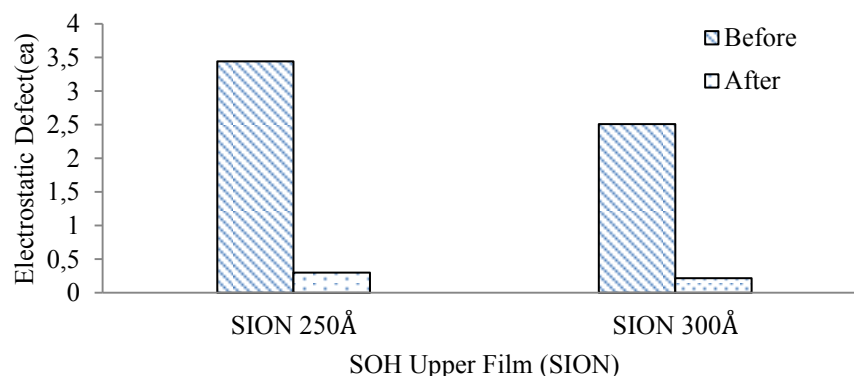


Fig.7: Electrostatic Discharge Defect (ESD) Trend

4. CONCLUSION

This paper is to discuss the way to control the new defect by introducing the SOH film.

The conclusion from this study is as follows.

Photo and Etch was processed on SOH film.

Then, the step of Strip(Cleaning) was conducted to remove by-products.

The electrostatic discharge defect was generated on the wafer surface due to the chemical sprayed in the strip stage.

ESD defect occurred also on SOH film, like POLY or METAL film.

Therefore, it is needed to control the ESD defect on SOH film.

It may be not available to get rid of ESD Defects in manufacturing semiconductor. The more important it becomes to solve it, the more technology has to be improved.

Literature References

- [1] J.K.LEE.Surface Resistance and Tensile Strength of Polyester Resin by Anti-static Agents (2010)
- [2] J.I.JUNG Control of Surface Charge Defect Cause by Spin Process (2011)
- [3] H.M.CHO. Materials for Nano Patterning in Semiconductor Fabrication; Organo silicon and High Carbon-Containing Materials for Spin Coating Hard mask. (2009)
- [4] C.G.PARK. EDS(Electrostatic Dissipation) Polymer. TCI Report (2006)
- [5] B.S.RYU Study on Absorption of Wet Chemical on the SOH and Treatment of Out-gassing(2013)
- [6] Yoshiya Hagimoto Defects of silicon substrates caused by electro-static discharge in single wafer cleaning process (2009)

Post-CMP Cleaners for Tungsten at Advanced Nodes

Ruben R. Lieten^{1,a}, Daniela White², Thomas Parson², Shining Jenq³,
Don Frye², Michael White², Lieve Teugels⁴, Herbert Struyf⁴

¹ Entegris, GmbH, Hugo-Junkers-Ring 5, Gebäude 107/W, 01109 Dresden, Germany

² Entegris, Inc, 7 Commerce Drive, Danbury CT 06810, US

³ Entegris, Inc, 1F, No. 669, Section 4, Chung-Hsin Road, Chutung Town, 31061, Taiwan

⁴ imec, Kapeldreef 75, 3001 Leuven, Belgium

^aRuben.Lieten@entegris.com

Keywords: Post-CMP formulations, tungsten 10 nm node, W/TiN barrier liners, SiO₂, silicon nitride, galvanic corrosion, particle-count defectivity, organic residue, XPS, Tafel, FTIR

Abstract. We discuss several mechanistic approaches and experimental data for improving post-CMP cleaning of W plugs with TiN as barrier liner, and dielectric substrates SiO₂ and Si₃N₄ for use at the 10 nm technology node (metal pitch of 40 nm). Particle charge in the low pH, W CMP slurries are usually positive, and the W surface is always negatively charged at pH >3. Therefore, a strong electrostatic attraction is expected to occur between the W surface and the residual particles during post-CMP cleaning. Two main approaches were chosen to break down the strong particles-W surface post-CMP electrostatic interactions, as well as particles dispersion and prevention of redeposition: (1) using cleaning additives able to adsorb at the W surface and reverse the W surface charge; (2) using organic additives to reverse the particle charge. The latter approach results in two strongly negative charged surfaces, which are able to repulse each other, and leads to the best cleaning.

Introduction

Currently, IC manufacturers strongly depend on Chemical Mechanical Planarization (CMP) processes to planarize and remove excess dielectric layers (ILD) between conducting metal layers, as well as in damascene processes involving metal interconnects lines (copper or tungsten) or plugs (tungsten). Polishing slurries used in these processes are usually aqueous, low or high pH nanodispersions containing abrasive particles (silica, alumina, zirconia, titania) and a variety of organic additives, such as ligands or complexants for the metals, oxidizers and surfactants^{1, 2}. Because of this, the probability of leaving post-CMP contaminated surfaces is very high and it is usually addressed by the post-CMP cleaning formulations^{3,4}. The main surface contaminants on the post-CMP planarized surfaces are: abrasive particles, organic residue, pad debris and metal cations - all of which negatively impact the wafer surface through covalent or hydrogen-bonding, electrostatic and hydrophobic/Van der Waals attractions.

Scope and approach

In this presentation, we discuss several mechanistic approaches (Figure 1) and experimental data for improving post-CMP cleaning of tungsten plugs with TiN as barrier liner, and dielectric substrates SiO₂ and Si₃N₄ for use at 10 nm technology node (metal pitch of 40 nm). In-depth characterization of the pre- and post-CMP cleaned surfaces, as well as the metals compatibility and their galvanic corrosion behavior, are based on multiple analytical techniques: Tafel plots (electrochemistry)⁵⁻⁷, zeta potential, scanning electron microscopy (SEM), Fourier transfer infrared - attenuated total reflectance (FTIR-ATR), contact angle. In-depth analysis of the cleaned surfaces and particle/organic residue defectivity review on post-CMP cleaned W, SiO₂ and silicon nitride surfaces improved our understanding of cleaning mechanisms on metal and dielectric surfaces, as

well as further helped develop continuous improvement process (CIP) formulations with highly reduced particulate defects and organic residue.

Historically, both W bulk and barrier CMP slurries were developed with a few key additives in mind: (a) abrasive particles (fumed alumina or silica: fumed or colloidal), (b) oxidizer (usually hydrogen peroxide), able to oxidize W metal to $W(VI)O_3$ later to be removed by chemical-mechanical interactions with the slurry abrasive, (c) H_2O_2 decomposition accelerator, (d) W corrosion protection additive, able to minimize the low pH stimulated W etch and recess during and after CMP.

Therefore, post-CMP W surface is always contaminated with slurry abrasive particles (dispersed or agglomerated), organic residue (slurry W corrosion inhibitor, particles stabilizers, pad debris, etc.) and metal ions. As mentioned before, particles charge in the low pH W CMP slurries are usually positive, since the isoelectric point, $pH_{IEP\ Al_2O_3} = 6-8$ and $pH_{IEP\ SiO_2} = 2-4$, and potentially > 4 due to surface modification by the slurry additives. Since W isoelectric point is @ $pH = 2-3$, W surface is always negatively charged at $pH > 3$, therefore, a strong interaction (electrostatic attraction) is expected to occur between the W surface and the residual particles during post-CMP cleaning.

Two main approaches were chosen by Entegris to break down the strong particles-W surface post-CMP electrostatic interactions, as well as particles dispersion and prevention of redeposition (see Figure 1): (1) **W surface charge reversal**, from $\zeta < 0$ mV to $\zeta \gg 0$ mV, by using cleaning additives able to adsorb at the W surface and reverse the charge, followed by strong repulsion expected between surface modified W surface and abrasive particles (either alumina, or positively charged silica from the CMP slurry), in addition other cleaning additives will prevent particles and organic residue redeposition after post-CMP cleaning.

(2) *Primary approach based on particles charge reversal and electrosteric protection* by using organic additives able to do it (*chemical formulae can't be disclosed here*), the result is two strongly negative charged surfaces ($\zeta \lll 0$ mV) able to repulse each other and achieve the lowest work of adhesion, W_{adh} , (calculated from the contact angle measurements, Van Oss theory), leading to best cleaning. Table 1 summarizes the main additives and their role in AG W-100 formulations.

Experimental conditions

Blanket W, plasma enhanced tetraethyl orthosilicate (PETEOS) and Si_3N_4 wafers were provided by Advantiv, W/TiN patterned wafers were provided by imec. All wafers used for full-wafer cleaning studies were provided by imec.

Zeta potential measurements on slurry particles and surface surrogates in contact with AG-W100 were done on a Beckman-Coulter DelsaMax Pro. Tafel Plots and Open-Circuit Potential experiments were performed using a Solartron 1285 Potentiostat. SEM measurements were performed using a Hitachi SU8000 w/ Bruker EDS. FTIR-ATR measurements of clean and post-CMP contaminated surfaces were performed using a Thermo Nicolet Magna 760 (FT-IR). W etch rates were measured by X-ray fluorescence (XRF) spectroscopy, on a Rigaku ZSX-400 XRF. TiN and dielectrics etch rates were measured by ellipsometry, using a JA Woolam M-2000D ellipsometer. Contact angle measurements were performed using a Krüss DSA 100 instrument. Several Entegris W post-CMP cleaners, (Entegris POR PlanarClean® AG W-100 and three new formulations, W105, CIP1 and CIP2), were evaluated at imec against diluted ammonia (dAmmonia) as commodity control, on W, SiO_2 and silicon nitride blanket wafers, previously polished with the imec POR slurries.

Cleaning performance on blanket wafers. In order to assess the cleaning performance, CMP + cleaning experiments have been done using 300 mm W, SiO_2 and silicon nitride blanket wafers. An AMAT Reflexion® LK polishing tool with integrated brush cleaner (Desica) was used. The CMP process consisted of one W polishing step. The following pad, slurry and conditioner were used: IC1010 pad, silica abrasive slurry (100 nm mean particle size), diamond pad conditioner (3M® Company A165). PVA brushes (Ripsey™ nanoShear™, TX5377) were used in the brush boxes.

Defect inspection was done by laser light scattering metrology (Surfscan® SP3, KLA-Tencor Corporation), with minimum defect size for W, SiO₂ and Si₃N₄ of 100 nm, 60 nm and 60 nm respectively. The cleaning formulation family, PlanarClean, is compatible with W and Ti/TiN liner/barrier combinations for advanced interconnects, more specifically for N10 (~40 nm metal pitch). The cleaners are designed to have a low, controlled, uniform and smooth W etch to undercut the particles and to maximize charge repulsion between silica particles and the tungsten.

Results and discussion

Galvanic corrosion. Usually, when a pattern wafer of the type: metal/barrier liner (e.g. Cu/Co, Cu/TaN, W/TiN) is subjected to being cleaned by a either low pH or high pH cleaning formulation, one of the substrates is more corroded at the interface (less noble) than the other one, as being reflected in the open circuit potential (OCP), E_{corr} difference between the galvanic couple (Figure 2, left). Ideally, OCP should be as close to zero as possible, and our continuous improvement formulations (CIP 1 and CIP 2) succeeded to do that (Figure 2, right). New and specific ligands added to CIP 1 and CIP 2 are easily adsorbed on one of the substrates (metal or barrier liner) and induce additional passivation on the less noble substrate, allowing both surfaces to have equal anodic or cathodic protection, and thus, minimizing the interfacial galvanic corrosion. Galvanic corrosion between W and TiN was evaluated by electrochemistry, generating *Tafel plots* for each individual cleaning formulation. No, or very low, E_{corr} difference between W and TiN was measured for all formulations tested. It was demonstrated that the nature of the pH adjustor, the pH and the type of organic additives used, can be tuned to drastically minimize E_{corr} difference between the galvanic couple (Figure 2).

Zeta Potential. Figure 3 shows the zeta potential values for various slurry nanoparticles (silica, alumina) and W/TiN/Dielectrics surfaces (silica, silicon nitride, Si₃N₄, silicon carbide, SiC). Since streaming potential measurements on flat wafer-like surfaces were not available in our labs, surface charges on W, Si₃N₄ and PETEOS solid surfaces were conducted as zeta potential measurements on the corresponding nanoparticles (WO₃, Si₃N₄ and SiO₂). Upon immersion/mixing with AG-W100, all nanoparticle dispersions either immediately reversed charges from positive to negative (Al₂O₃, WO₃, SiN) or became more negatively charged (SiO₂, SiC), indicating strong repulsion-type interactions between all surfaces to be cleaned (W/WO₃, TEOS, Si₃N₄, SiC) and CMP slurry particles (alumina, silica). For a TiN substrate, since isoelectric point, $\text{pH}_{\text{IEP}} \sim 4.5$, at the AG-W100 pH, this surface will also be negatively charged repulsive towards the slurry abrasive (either silica or alumina).

Organic residue characterization – contact angle measurements. It is well known that any bulk or buff W CMP slurry have to contain at least a W corrosion inhibitor, able to minimize the W etch and recess during polishing. Usually, these organic molecules are partitioned in the CMP slurry, between the abrasive particles surfaces and aqueous phase. Our experiments regarding on-purpose contamination of silicon nitride surfaces with slurry organic additives demonstrated that actually, the contamination takes places during post-CMP rinsing with DI water, pH ~6, rather than during polishing at low pH. Contact angle measurements with water, formamide and methylene iodide, on contaminated and clean silicon nitride surfaces, helped us identify, discern and ranked the most efficient AG-W100 cleaning formulations vs. % component D. Van Oss acid-base theory was used to calculate the surface energies of the clean and contaminated surfaces. Of all three solvents used for these measurements, formamide was the most sensitive to surface changes, due to specific H-bonding interactions with the N-containing organic contaminant.

Contact angle measurements on CMP slurry-contaminated silicon nitride wafers (polished or dipped, followed by DIW rinse) indicated that the main organic contamination occurs when the pH changes from acidic (CMP slurry) to neutral, during rinse. This behavior could be attributed to both silicon nitride isoelectric point (pH 5-7) - greatest surface instability/reactivity around pH 6, and also to the pK_a 's of the organic molecules used as W inhibitors in the CMP slurries.

We developed experimental techniques to monitor both organic contamination and surface post-CMP cleaning, based on FTIR-ATR and contact angle measurements (Figure 4). Most of our efforts were directed toward silicon nitride surfaces post-CMP contamination and cleaning, since the other surfaces involved (W and SiO₂) were much easier to clean.

FTIR-ATR. Small coupons of silicon nitride, Si₃N₄ were dipped in/or polished with a commercially available CMP W polishing slurry, rinsed with DI water and cleaned for one minute with AG-W100. The organic residue contaminated and cleaned surfaces were subsequently analyzed by FTIR-ATR, and the spectra presented in Figure 5. Organic contamination is clearly depicted in the 1650-1200 cm⁻¹ region, peaks corresponding to carboxylates or N-based molecules (amines, quaternary ammonium salts) and smaller ones in the aromatic region of 700-800 cm⁻¹. Upon cleaning for one minute with AG-W100 (light green spectrum), the peaks corresponding to the organic contamination disappeared, the spectrum being identical to the silicon nitride control (red baseline).

SEM data on 45 nm W/TiN Patterned Wafers. SEM data on post-CMP W/TiN pattern wafers surfaces showed already etched in the center W lines, with dirty, fuzzy TiN interfaces, Figure 6. Upon cleaning with AG-W100 and CIP formulations, the SEM top-down images have better resolution, sharper lines and more resolved W/TiN/dielectric interfaces (Figure 7). One more time, variable amounts of component D and competitive adsorption at the metals interfaces help with the contaminant removal and metal passivation.

Significant progress in the removal of the organic residue is reflected in the W, SiO₂ and silicon nitride SP3 pareto defectivity data, presented in Figure 8, 9 and 10. For TEOS blankets, dilute ammonia functions by dissolving some of the TEOS surface and silica particles. While effective in older nodes, tungsten and other metals are significantly etched to the point where tungsten recess is a serious issue. AG W-100 represents a significant improvement in cleaners. However, the cleaning additive in AG W-100 was replaced in CIP2 by a unique additive designed to disperse the silica and prevent reattachment to TEOS surfaces that allows defectivity statistically equal to dilute ammonia without damaging the tungsten. This feature enables advanced node W cleaning for memory devices. The type and number of defects on W, SiO₂ and silicon nitride surfaces cleaned with AG-W100 and CIP formulations can be controlled by varying several key factors: pH, addition of organic solvents, ionic strength control, charge screening by organic cations, dispersants for particles and organic residues able to prevent particles agglomeration and redeposition on the cleaned surfaces. CIP2 shows the best performance on W, SiN and SiO₂ blankets.

Summary

The performance of formulated W/TiN post-CMP cleaners for N10 has been evaluated. PlanarClean AG W-100 and several CIP formulations show excellent material compatibility and residue removal for W CMP with TiN barrier. Very low particulate and organic residue defectivity was additionally confirmed by different surface characterization techniques: FTIR-ATR, contact angle/surface energy. Very limited galvanic corrosion of the W/TiN liner (Tafel plots) indicated appropriate compatibility on patterned wafers, also evidenced by SEM measurements on 45 nm patterned wafers.

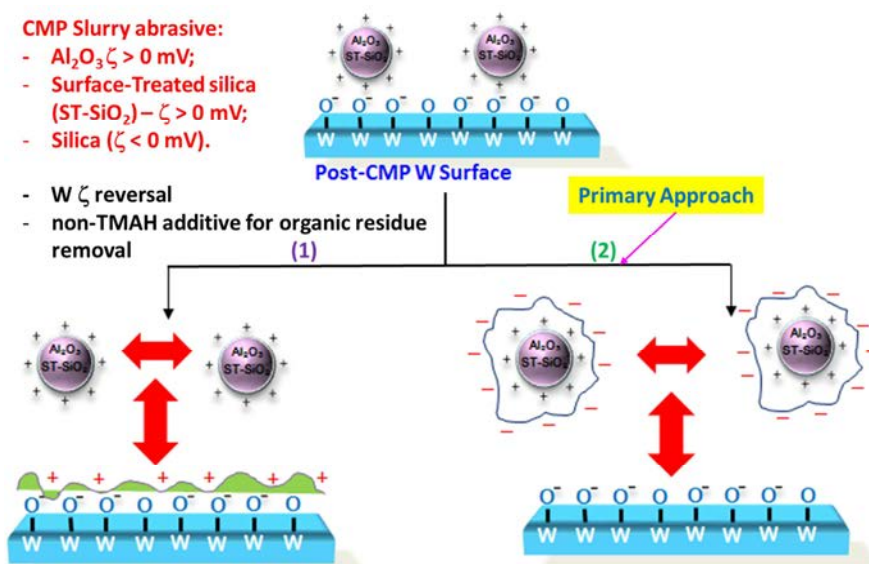


Figure 1 - W Post-CMP Cleaning Formulation – Mechanistic Design Concepts

Table 1 - PlanarClean® AG-W100 Formulation Additives List – Function and Mechanism

Component	Function	Mechanism
A	non-TMAH pH Adjustor	<ul style="list-style-type: none"> Provides the hydroxyl anions and adjust pH needed for W surface hydroxylation and good wetting Ensures negative surface charge on both wafer and contamination, by being adsorbed on inorganic and organic residues.
B & C	Complexing Agents	<ul style="list-style-type: none"> Surface Modification (ST-SiO_2 and Al_2O_3 complexants) Stabilization of particle with electrostatic repulsion (prevent agglomeration and re-precipitation)
D	Dispersing Agent	<ul style="list-style-type: none"> Interacts with particles and wafer surfaces to prevent aggregation and control etch rate.

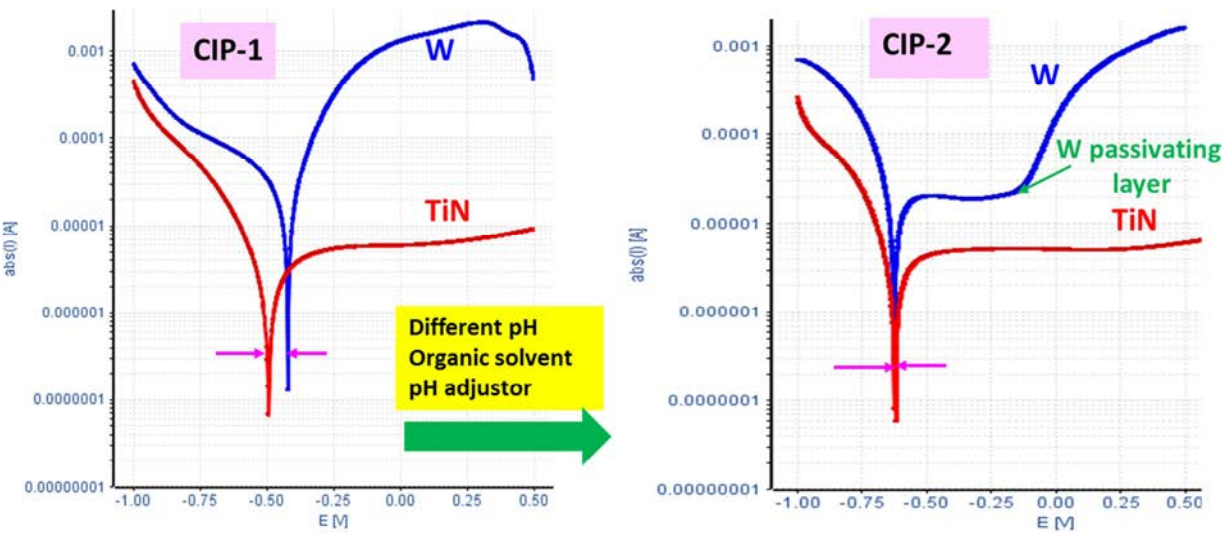


Figure 2 - Tunability of the galvanic corrosion W/TiN for PlanarClean AG W-100 type formulations

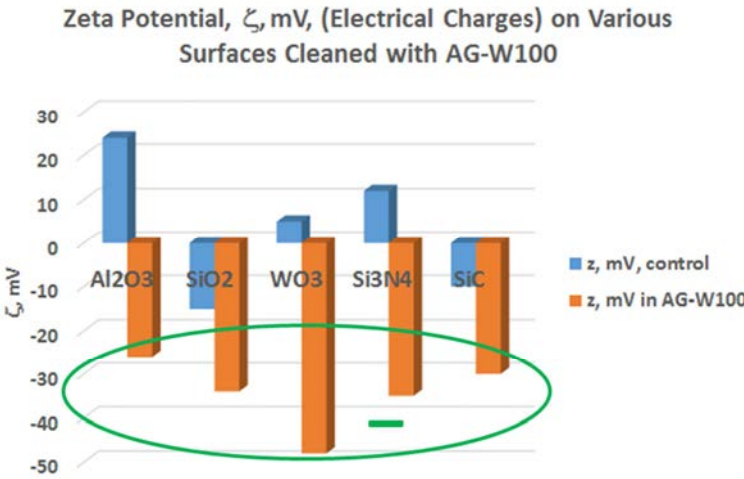


Figure 3 - Zeta Potential, ζ , mV, for slurry abrasives (alumina, silica), W and dielectrics surfaces in contact with AG-W100 formulation

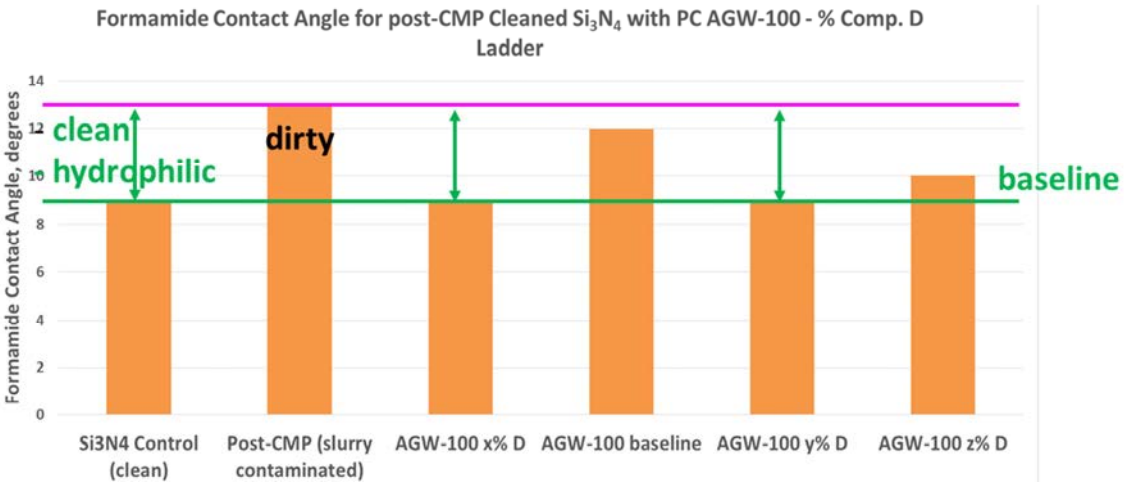


Figure 4 - Formamide contact angle measurements on contaminated and cleaned silicon nitride surfaces

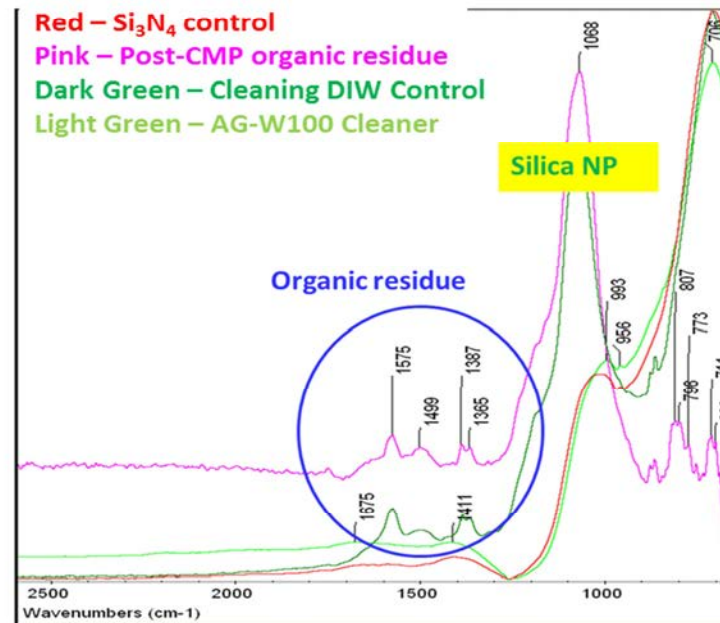


Figure 5 - FTIR-ATR spectra for contaminated and cleaned silicon nitride surfaces

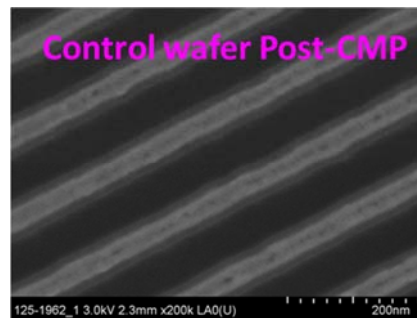


Figure 6 - SEM image of a 45 nm W/TiN patterned wafer control, post-CMP, before cleaning

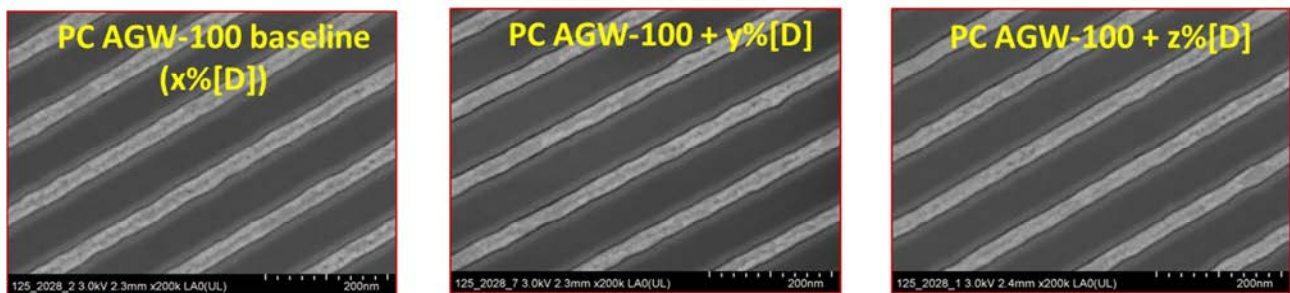


Figure 7 - Top-down SEM images for 45 nm W/TiN patterned wafers cleaned with AG-W100 and CIP formulations

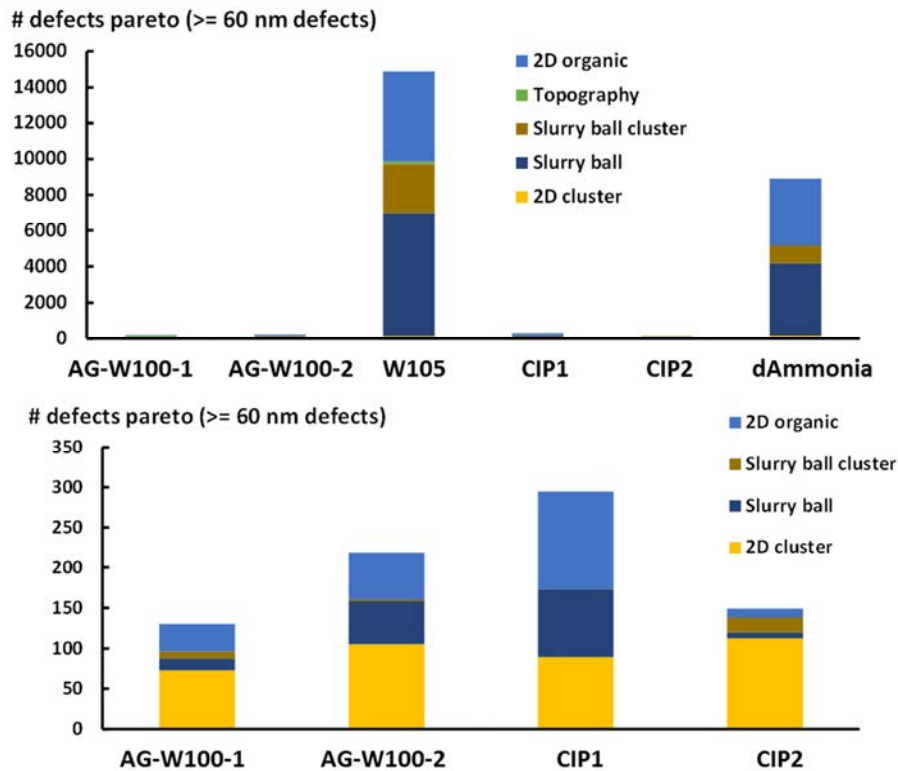


Figure 8 - # Defects (particles and organic residue) pareto on silicon-nitride blanket wafers (bottom figure is a zoom in of top figure)

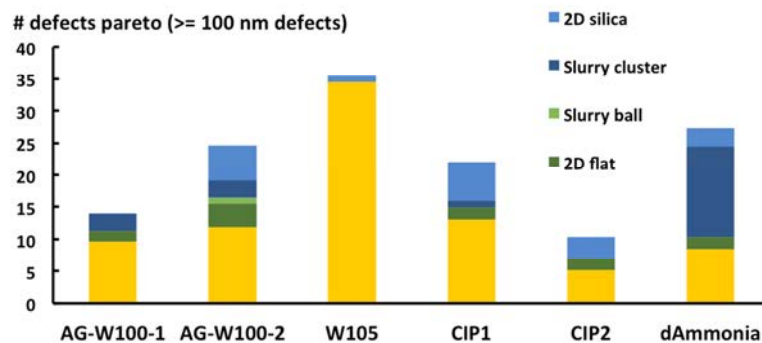


Figure 9 - # Defects (particles and organic residue) pareto on W blanket wafers

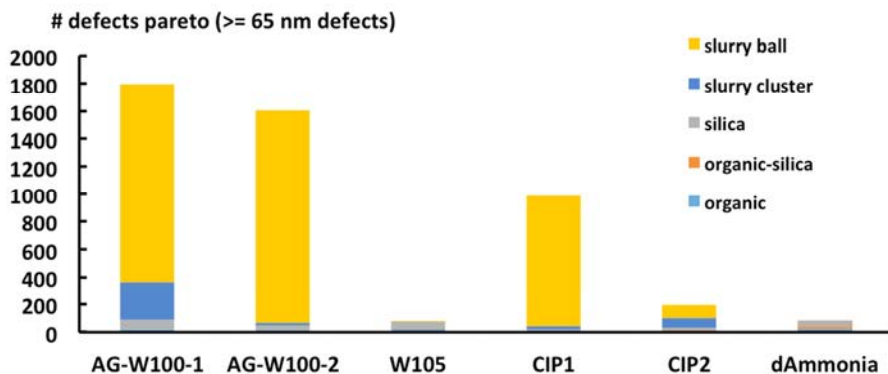


Figure 10 - # Defects (particles and organic residue) pareto on SiO₂ blanket wafers

Entegris® and PlanarClean® are trademarks of Entegris, Inc., Reflexion® is a trademark of Applied Materials, Inc., 3M® is a trademark of 3M Company, Rippey™ and nanoShear™ are trademarks of ITW Rippey and Surfscan® is a trademark of KLA-Tencor Corporation.

References

- [1] White, D., Parker, J. Polyoxometalate Compositions and Methods, US 8,057,561B2, **2011**.
- [2] Fu, L., Grumbine, S., Dysard, J., Li, T. Tungsten Chemical-Mechanical Polishing Composition, US 2015/0376462 A1, **2015**.
- [3] Bothra, S., Sur, H., Liang, V. A New Failure Mechanism by Corrosion of Tungsten in a Tungsten Plug Process. *Microelectron. Reliab.* **1999**, 39, 59.
- [4] Park, J., Kim, S., Lee, D. Novel Non-Oxidative Aqueous Cleaning Solutions for Tungsten Layers, *Meeting Abstracts Electrochemical Society – All Divisions*, **2008**, 2, 721.
- [5] Chen, B.H., Zhang, H., Chooi, S.Y.M., Chan, L., Xu, Y., Ye, J.H. Corrosive Behavior of Tungsten in Post Dry-Etch Residue Remover, *Ind. Eng. Chem. Res.* **2003**, 42, 6096.
- [6] Kneer, E.A., Raghunath, C., Raghavan, S., Jeon J.S. Electrochemistry of Chemical Vapor Deposition Tungsten Films in relevance to chemical Mechanical Polishing. *J. Electrochem. Soc.* **1996**, 143, 4095.
- [7] Stein, D.J., Hetherington, D., Guilinger, T., Cecchi, J.L. In-situ Electrochemical Investigation of Tungsten Electrochemical Behavior during Chemical Mechanical Polishing, *J. Electrochem. Soc.* **1998**, 145, 3190.

Advanced Cryogenic Aerosol Cleaning: Small Particle Removal and Damage-Free Performance

Chimaobi Mbanaso^{1, a*}, Jeffery W. Butterbaugh¹, David Scott Becker¹,
Wallace P. Printz², Antonio L. P. Rotondaro², Derek W. Bassett²,
Gregory P. Thomes¹, Brent D. Schwab¹, Christina Ann Rathman¹,
and Jeffrey M. Lauerhaas¹

¹TEL FSI, Inc., Chaska, MN 55318, USA

²Tokyo Electron America, Inc., Austin, Texas 78741, USA

^achimaobi.mbanaso@us.tel.com

Keywords: Cryogenic Nano Aerosol, Low-k, Damage-free, PRE, Hydrophobic, Haze

Abstract. The performance of a new cryogenic aerosol process was evaluated for cleaning nanoparticles and providing damage-free processing. Particle Removal Efficiency (PRE) tests conducted with wet deposited 40 nm, 30 nm and 18 nm silica particles on 300 mm wafers demonstrated cleaning efficiencies above 80%. Damage-free capability of the cryogenic aerosol process was evaluated with poly-silicon lines with an aspect ratio of approximately 9:1. These results highlight the potential of this new cryogenic aerosol to provide semiconductor device yield benefits by reducing small particulate contamination without causing pattern damage.

Introduction

Cryogenic aerosol cleaning, first developed in 1990 [1], is an enabling technology for defect removal on substrates where wet cleaning techniques are not practical or are difficult to implement. Example substrates are hydrophobic low-k films and films containing corrosion sensitive metals. Cryogenic aerosol defect removal from these substrates has been proven without any detrimental side effects [2,3]. Progress in IC manufacturing requires advances in cleaning technologies, particularly particle removal below 40 nm with minimal material loss and no change in film properties. Emphasis is placed on damage-free processing as well. In response to these requirements, cryogenic aerosol cleaning is being further developed to meet and exceed IC manufacturing requirements.

Formation of a cryogenic aerosol [4,5,6] can occur when gaseous argon and/or nitrogen is cryogenically cooled and then fed into an evacuated process chamber. The size and velocity of these cryogenic aerosols have been characterized with Malvern Fraunhofer diffraction and Phase Doppler Particle Analyzer (PDPA) systems [6]. Based on the reported measurements, the Sauter mean diameter of the aerosol was found to be in the 10 – 75 μm range with velocities on the order of 50 m/s [6]. In the present work, a cryogenically cooled inert gas was fed into a chamber via a nozzle located above the wafer surface. As the cooled gas exited the nozzle, an aerosol formed and removed particulate contamination via momentum transfer. Recent optimization of the process and advances in nozzle design resulted in an aerosol capable of efficient small particle removal without damage. These smaller cryogenic aerosols, which will be referred to as Cryogenic Nano Aerosols, cannot be characterized by PDPA because the size of this aerosol is below the detection limit of the PDPA technique. Instead, the properties of the Cryogenic Nano Aerosols were modeled based on a theory developed by Hagena [7]. Key process parameters such as temperature, pressure and density were extracted from fluid dynamic simulations using a commercial computation fluid dynamics (CFD) software package [8]. These modeling studies have calculated a smaller and faster aerosol with diameter on the order of 10 nm or less and velocities of 300 to 400 m/s.

To demonstrate PRE, blanket substrates intentionally challenged with 40 nm, 30 nm and 18 nm silica particles were processed with this Cryogenic Nano Aerosol process. Compatibility of this process with low-k films was also demonstrated by PRE experiments using 70 nm silica particles

and confirming no impact to the k-value of the film. A patterned substrate having poly-silicon lines with an aspect ratio approximately 9:1 was also processed to evaluate the potential of this Cryogenic Nano Aerosol process to maintain the structural integrity of features during cleaning.

Experimental

Blanket and patterned substrates were examined to investigate PRE and damage-free performance. Surface Particle Scanners (KLA Surfscan[®] SP2-XP, SP2 and SP5) and Scanning Electron Microscope (SEM) inspection were employed to quantify particle removal from substrates that were intentionally challenged with nano-sized particles and then cleaned with the Cryogenic Nano Aerosol process. The silica particles that were used for deposition on the blanket substrates originated from commercially available aqueous suspensions with nominal particle diameters reported as 40 nm, 30 nm and 18 nm. The nominal particle diameter of the silica particles used for the low-k PRE evaluation was specified as 70 nm. For the 40 nm and 30 nm silica particle PRE evaluation, light point defects were quantified using the KLA Surfscan[®] SP2-XP and SP5 respectively. Wafer inspection tools are typically calibrated using polystyrene latex (PSL) spheres, so sizing differences between silica particles and PSL spheres are to be expected. For further PRE evaluation, SEM inspection as well as monitoring the change in wafer haze signal as a result of intentional wet deposition of 30 nm and 18 nm silica particles was performed. Characterizing change in defect density using a haze response method has been previously reported [9,10]. For these blanket wafer studies, silica particles were deposited on the substrates by a wet deposition technique. Wet deposition was accomplished by using a particle suspension solution poured onto a spinning wafer. After the solution was poured onto the substrate, the substrate was spun dry, measured and allowed to age before Cryogenic Nano Aerosol processing. For PRE tests involving low-k wafers, dry particle deposition was accomplished with a commercially available MSP Corporation system.

The Cryogenic Nano Aerosol cleaning studies were performed in an automated single wafer cleaning system capable of processing 300 mm substrates. The cleaning system was equipped with mass flow controllers, a liquid nitrogen Dewar vessel and pressure transducers which were used to control and monitor the dispensing cryogenic fluid into the vacuum chamber via a nozzle. The substrate was scanned underneath the nozzle by using a chuck capable of simultaneously rotating and translating to allow for interaction of the cryogenic Nano Aerosols with the substrate. Processing time of the substrates underneath the nozzle was approximately 36 seconds for PRE and damage-free performance studies.

Results and Discussion

Particle Removal Studies on Blanket Substrates. For particle removal studies using surface scanning tools, 300 mm blanket silicon wafers were challenged by wet depositing either 40 nm or 30 nm silica particles, aging the wafers for a specified period of time before cleaning with the Cryogenic Nano Aerosol process. In the case of the 40 nm silica particles, the KLA Surfscan[®] SP2-XP was used for particle measurements while the KLA Surfscan[®] SP5 was used for 30 nm silica particle characterization. After 40 nm silica particle deposition and aging for six hours, ~ 99% removal efficiency was achieved after processing with the Cryogenic Nano Aerosol (Fig. 1). In the case of the 30 nm silica particles, ~ 97% removal efficiency was achieved (Fig. 2). A six hour aging time was evaluated to represent a typical FAB queue time.

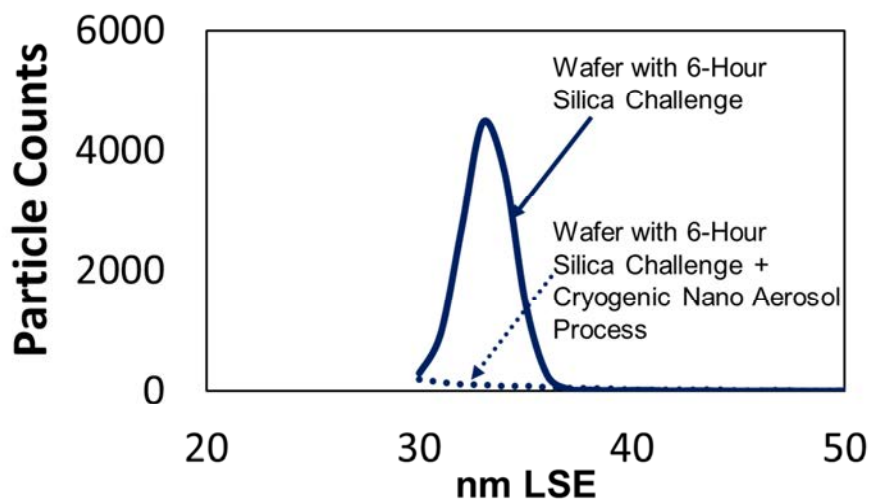


Figure 1: KLA Surfscan® SP2-XP scan data for 40 nm silica particles with and without the Cryogenic Nano Aerosol process. PRE was calculated as 99%.

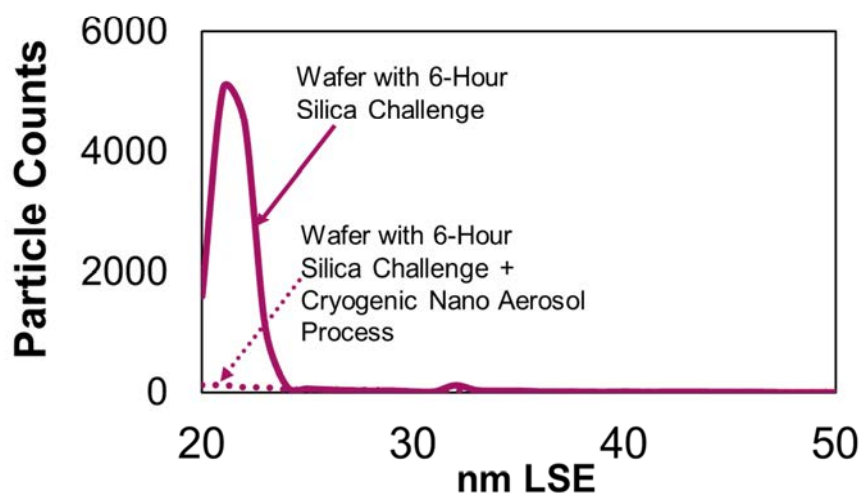


Figure 2: KLA Surfscan® SP5 scan data for 30 nm silica particles with and without the Cryogenic Aerosol process. PRE was calculated as 97%.

Additional studies to determine PRE of nano-sized particles were performed by SEM inspection. In this case, the particle density of a challenged blanket 300 mm wafer was compared to that of a wafer that was challenged, aged for six hours and then cleaned by the Cryogenic Nano Aerosol. 30 nm and 18 nm silica particles were used for this evaluation and the results are shown in Fig. 3 and Fig. 4 respectively. The particle densities at multiple inspection sites on the challenged sample were compared to the samples that were challenged, aged and then cleaned to determine the PRE. For the 30 nm silica experiment, a PRE of 100% was determined and 86% PRE was determined for the 18 nm silica particles.

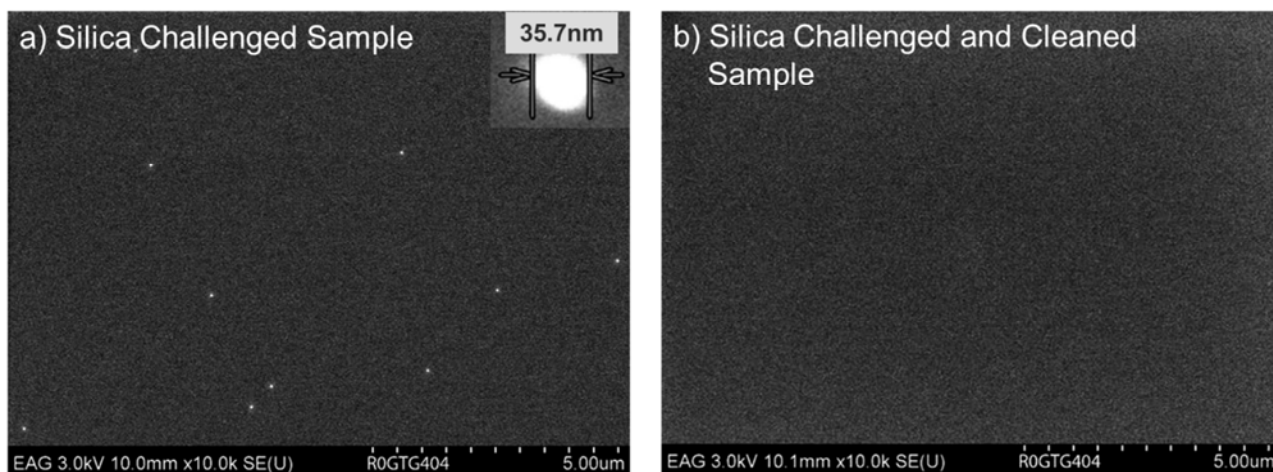


Figure 3: SEM images of a) 30 nm silica challenged sample and b) a sample that was challenged, aged for six hours and then cleaned. PRE was 100%.

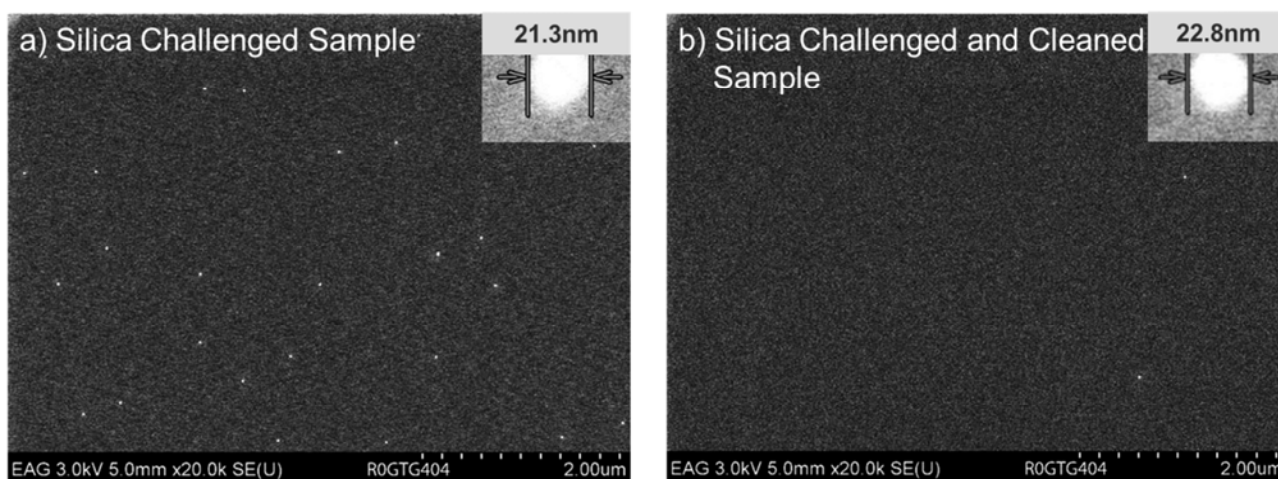


Figure 4: SEM images of a) 18 nm silica challenged sample and b) a sample that was challenged, aged for six hours and then cleaned. PRE was 86%.

Furthermore, the haze response as a result of challenging a blanket 300 mm wafer with a high concentration of a monodispersed particle distribution was monitored with a KLA Surfscan[®] SP2-XP haze recipe. In order to determine the cleaning efficiency, the reduction in the haze was measured after cleaning the challenged wafer with the Cryogenic Nano Aerosol process and then accounting for the haze of the wafer prior to the particle challenge. 30 nm and 18 nm silica particles were used for this evaluation and the results are shown in Fig. 5. For the 30 nm silica experiment, a haze removal efficiency of 99% was calculated and 86% for the 18 nm silica particles.

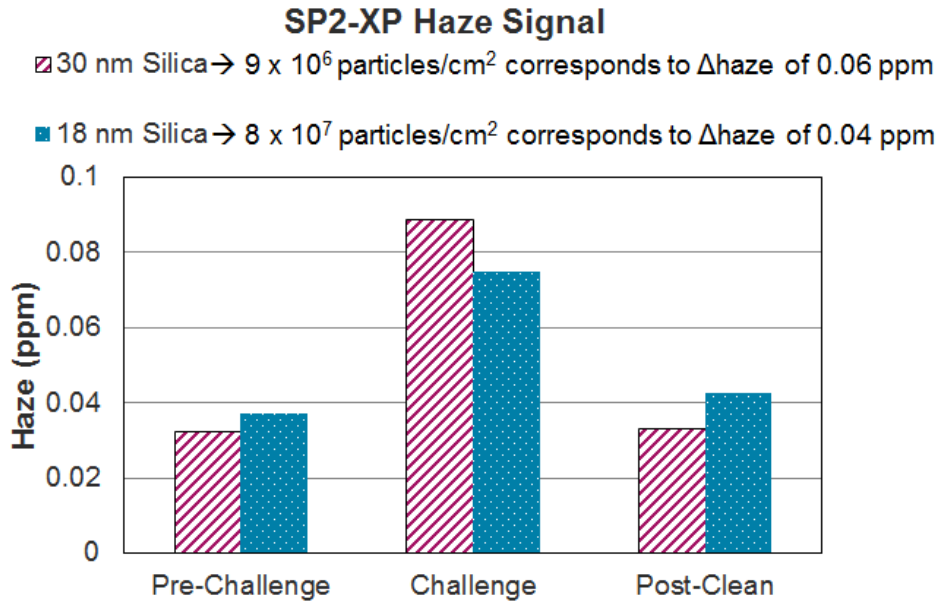


Figure 5: Haze measurements showing change in haze signal as a result of the 30 nm and 18 nm particle challenge and then cleaning with the Cryogenic Nano Aerosol process. The corresponding particle challenge densities were estimated based on SEM inspection experiments.

Particle Removal from Hyrdophobic Low-k Substrates. High PRE was also demonstrated on hydrophobic low-k films. Wafers with Black Diamond[®] 3 films (nominal k-value of 2.55) were purchased and evaluated for PRE and compatibility with the Cryogenic Nano Aerosol process. 70 nm silica particles were dry deposited on the low-k films; KLA Surfscan[®] SP2 sized the particles at 55nm. Particle measurement by KLA Surfscan[®] SP2 was limited to greater than 50 nm due to the background light scattering of the low-k films. Processing these wafers with the Cryogenic Nano Aerosol after six hours of aging removed greater than 99% of the silica particles without any change in k-value (Fig. 6). k-values were determined based on C-V (Capacitance-Voltage) measurements performed on MOS capacitor devices fabricated on each wafer used for this study.

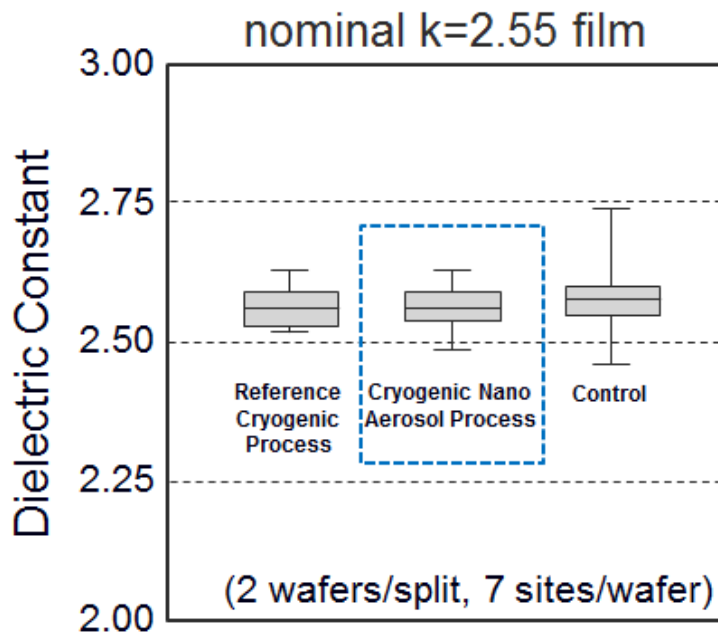


Figure 6: k-value measurement of low-k wafers processed with the Cryogenic Nano Aerosol and another reference Cryogenic Cleaning process. In comparison to an unprocessed wafer (control), no change in k-value was measured on any of the low-k substrates.

Damage-Free Processing. Poly-silicon lines with a 22 nm line width and 200 nm line height (IMEC DEF 45 wafers with aspect ratio of approximately 9:1) were processed with a Cryogenic Nano Aerosol capable of providing equivalent cleaning performance as demonstrated in the PRE on blanket studies. Full wafer KLA inspection confirmed damage-free processing was achieved.

Conclusions

An advanced Cryogenic Aerosol Cleaning process has been developed and tested for PRE with different particle challenges comprised of 40 nm, 30 nm and 18 nm silica particles. The Cryogenic Nano Aerosol process removed particles on the challenged substrates with an efficiency of >80%. PRE on low-k films was demonstrated without impacting the k-value. Damage-free performance was confirmed on a 300 mm full wafer with 22 nm poly-silicon lines and an aspect ratio of 9:1. This Cryogenic Nano Aerosol technology is expected to be applicable in advanced nodes for yield improvement on substrates with various on-wafer material and structure sensitivities.

Acknowledgements

The authors would like to thank Ryuichi Asako and Hiroyuki Nagai (Tokyo Electron Limited, Process Development Center), and Kaoru Maekawa (Tokyo Electron Technology Center America) for k-value measurement support, and Koji Kagawa (Tokyo Electron Kyushu Limited, SPE Process Technology Dept.) for SP5 measurement support.

References

- [1] W.T. McDermott, R.C. Ockovic, J.J. Wu, D.W. Cooper, A. Schwarz and H.L. Wolfe, US Patent 5,062,898 (1991).
- [2] J. Lauerhaas, L.T. Tan, A. Hamzah, Y.S. Kok and J. Kwang, Yield Improvement Using Cryogenic Aerosol for BEOL Defect Removal, ECS Trans. 11(2), 33-39(2007).
- [3] H. Lin, K. Chioujones, J. Lauerhaas, T. Freebern and C. Yu, Damage-Free Cryogenic Aerosol Clean Processes, IEEE Trans. Semi. Manuf. 20(2), 101(2007).
- [4] J. C. Patrin and J.M. Heitzinger, US Patent 5,961,732 (1999).
- [5] N. Narayanswami, Theoretical Analysis of Wafer Cleaning Using a Cryogenic Aerosol, J. Electrochem. Soc. 146(2), 767(1999).
- [6] N. Narayanswami, J. Heitzinger, J. Patrin, D. Rader, T. O'Hern and J. Torczynski, Development and Optimization of a Cryogenic-Aerosol-Based Wafer-Cleaning System, Particles on Surfaces 5 & 6: Detection, Adhesion and Removal, ed. K.L. Mittal, 251-266 . (1999)
- [7] O.F. Hagena, Nucleation and Growth of Clusters in Expanding Nozzle Flows, Surface Science 106, 101-116 (1981).
- [8] Computational fluid dynamics (CFD) software information <http://www.cd-adapco.com/>
- [9] S.H. Yoo, B. Y.H. Liu, J. Sun, N. Narayanswami and G. Thomes, Particle Removal Efficiency Evaluation at 40nm Using Haze Particle Standard, Solid State Phen. Vol 76-77, 259-262(2001).
- [10] K. D. Xu, R. Vos, G. Vereecke, M. Lux, W. Fyen, F. Holsteys, K. Kenis, P. W. Mertens, M. M. Heyns, C. Vinckier, Relation between Particle Density and Haze on a Wafer: a New Approach to Measuring Nano-Sized Particles, Solid State Phenomena, Vol. 92, 161-164 (2003).

Developments for Physical Cleaning Sample with High Adhesion Force Particles and Direct Measurement of its Removal Force

Emu Tokuda^{1, a}, Toshiyuki Sanada¹, Futoshi Iwata¹,
Chikako Takato², Hirokuni Hiyama³ and Akira Fukunaga²

¹ Shizuoka University, 3-5-1 Johoku, Naka-ku, Hamamatsu, Shizuoka 432-8561, Japan

² Ebara Corporation, 4-2-1 Honfujisawa, Kanagawa

³ Ebara Corporation, 11-1 Haneda Asahi-cho, Ohta-ku, Tokyo

^atokuda.emu.15@shizuoka.ac.jp

Keywords: Particle adhesion force, PVA brush, Particle removal rate

Abstract. We quantitatively evaluate the wet cleaning performance of particle contamination. We made particle sample which endure the wet cleaning and measured particle adhesion force by self-sensitive cantilever. The advantage of this method is that performed in both air and water. As a result, there were no significant differences between the air and water condition and the influence of particle size were dominant. Using this sample, we demonstrated particle removal rate of droplets impacts and PVA brush.

Introduction

In the semiconductor device manufacturing process, particle contamination is one of the critical problems. Especially after planarization (CMP) process, many slurry residues need to be removed. In these cleaning processes, physical cleaning such as PVA brush scrubbing and droplets impacts (two fluid jet) are widely used. However, some residues in the Post-CMP cleaning process have high adhesion forces compare to the particles of other processes because of high pressure and wet conditions during the CMP process. So, it is necessary to prepare a cleaning sample with high adhesion force particles for the evaluation of cleaning performance. The evaluation of cleaning forces on PVA brush scrubbing or droplets impacts are also important.

On the measurement of particle adhesion force, AFM was generally used. Park et al. [1] measured the vertical direction of the adhesion forces of silica particles on silicon wafers in IPA solutions. Kim et al. [2] measured the pattern strength in horizontal direction and proposed a concept of the cleaning process window. This window is effective for megasonic cleaning [3]. However, they measured the order of nN forces of particle adhesion and these are suitable for cleaning by air flows [4]. If we applied the wet cleaning methods such as PVA brush or droplets impacts, nN of the adhesion forces of the particles are easily removed so that the evaluation of the cleaning performance is difficult. In this study, first we have tried to make high adhesion force samples which can evaluate particle removal rate of PVA brush or droplets impacts. Second, we measured its removal force directly by using self-sensitive cantilever. Finally, we demonstrated particle removal rate of the samples by PVA brush scrubbing or droplets impacts.

Cleaning sample

We made a high adhesion force sample with resin (cross-linked polyacrylic acid ester) particles on a glass slide. Particle averaged diameter is 30 μm . In order to increase the adhesion force, we use the high moisture environment and a heater. The resin particles are sprinkled in high moisture atmosphere, after that the samples are heated. By changing the heating temperature and time, the adhesion forces were able to control. We believe that this is owing to the particle deformation and chemical reaction between glass and resin. In this study, the results of samples heated at 100, 200 and 290 $^{\circ}\text{C}$ for 10 or 60 min are reported. In addition, we compared the samples using glass particles on a glass plate.

Removal force measurement

We measured the adhesion force of the resin particles (heated at 290 °C for 60 min) by using self-sensitive cantilever (Hitachi High-Tech Science, NPX1CTP004) whose spring constant is 40 N/m. We developed this system by reference to measurement of cell adhesion force [5]. The cantilever has strain gage itself and can measure adhesion force F while removing particle so that the force of lateral direction can be measured. Figure 1 (a) shows experimental setup of direct measurement of particle adhesion force. The movements were controlled by picomotor (New Focus Technologies, 8301NF, 8353) and piezoelectric element (CEDRAT Technologies, APA120S) in coarse and micro motion, respectively. To control the piezoelectric element, a triangular waveform generated by function generator was used. The traverse speeds of the cantilever were able to control by changing the frequency of the signal. The output signal with bridge circuit from the cantilever was amplified by differential amplifier circuit. This method can be extended to measurements in liquids [5]. In the present stage we measured the forces in the atmospheric condition. In addition, for the evaluation of adhesion forces of glass particles on a glass plate, we used a centrifuge separation. Figure 1 (b) shows experimental setup of the measuring removal force of glass particles.

Results and discussion

Figure 2 (a) shows a typical example of output signal from the cantilever. This graph shows the relationship between measured force F and time t . Figure 2 (b) shows the visualization of removal process from the bottom. The measured force increases during contacting the cantilever with a particle. And a particle is removed then the force shows almost zero value. We define the maximum force as F_{max} . This F_{max} is corresponding to the particle removal force. As a result, F_{max} were above 100 μN in the present cleaning samples. In the early study [2], F_{max} were about 0.1~0.5 μN .

Figure 3 (a) shows the relationship between particle diameter D_p and F_{max} and Fig. 3 (b) shows schematic image of the forces acting on the particle. As shown in the figure, F_{max} does not depend on the traverse speed in the present experimental range. F_{max} decreases with D_p . We speculated that this is because the rolling moment is higher in the case of large D_p as shown in Equation (1). Here, $M_{rolling}$ is rolling moment, a_0 is contact area radius between particle and substrate, and F_A is the adhesion force (e.g. van der Waals force).

$$\frac{D_p}{2} |F_{max}| = a_0 |F_A| = M_{rolling} \quad (1)$$

We also measured the removal forces of glass particles on glass slide by centrifuge separation. We removed particles by applying centrifugal force by rotating the particle sample by changing acceleration. Figure 4 (a) shows the results of relationship between particle removal rate S_r and acceleration a by centrifuge separation and Fig.4 (b) shows the S_r and removal force F . We defined F_c as the force when particle removal rate reached 50 % by centrifuge separation. We fitted S_r by using error function and three vertical lines are estimated from the JKR model [4] (rolling mode). Figure 5 shows the results and comparison with Fig. 3 and Fig. 4. In the figure the removal force F_{JKR} estimated from the JKR model is also plotted. The F_{JKR} is expressed as Equation (2).

$$F_{JKR} = \frac{2a_0}{D_p} (F_{JKR,a} + F_g) \quad (2)$$

Here, $F_{JKR,a}$ is JKR adhesion model and F_g is gravity of acting on a particle. From the results, F_c is larger than $F_{JKR,a}$. From Fig. 4 (a), S_r of large D_p exhibited large value. This is because the rolling moment is higher in the case of large D_p as shown in Fig. 3 (a). On the other hand, there were no significant differences in F of each D_p of Fig. 4 (b). The most important point is that F_c of the typical particles of same size were about 0.1~0.5 μN . This means that adhesion forces of our new samples have about 10^3 times higher than glass particles sprinkled on glass slide. Note that the reason why F_c is ten times as high as F_{JKR} is because the liquid bridge force occurs by moisture in the air.

Dry cleaning methods such as air blowing can be evaluated by using particles which have F_c , in contrast, wet cleaning methods cannot be evaluated because the particles can be easily removed. Using new samples of this study, we evaluate particle removal rate S_r of wet cleaning.

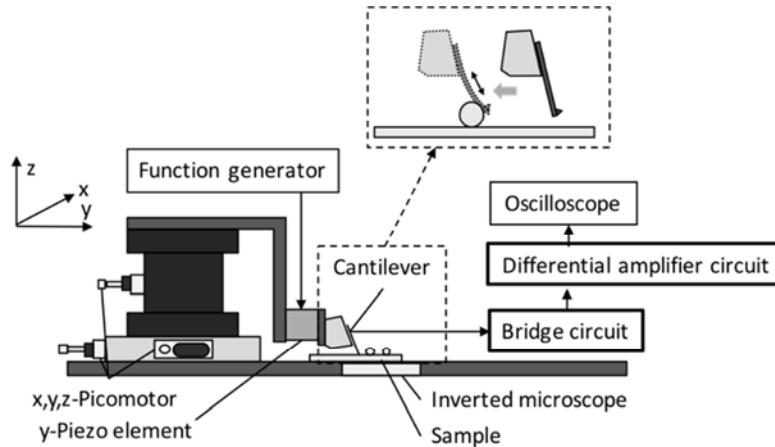
Figure 6 (a) shows a schematic of experimental setup to evaluate S_r by sliding a PVA brush nodule with sliding speed U_x . Figure 6 (b) and (c) show the results. As shown in the Fig. 6 (b), S_r of the samples which are heated low temperature has large dispersion. On the other hands, S_r does not depend on the U_x in Fig. 6 (c). The results indicate that the increase of heating time increases the adhesion force. The important point is that the results of Fig. 6 (c) shows the finite value of S_r . If the S_r shows 100 %, we can not evaluate the difference of cleaning condition.

In order to compare the physical action between PVA brush scrubbing and droplet impacts, particle removal rate by droplet train impacts was also measured using same samples. Figure 7 (a) shows the schematic of experimental setup to evaluate by applying monodispersed droplet train impact to present sample for 10 seconds. Figure 7 (b) and (c) show the results. Here f is the droplet generating frequency and Q is the water flow rate. In this experiment, particles of heating temperature at 290 °C were hard to remove. Especially, particles heating time for 60 min were not removed at all. These results indicate that the PVA brush is suitable for the high adhesion force samples.

Conclusion

We developed a cleaning sample with particles which has optimal adhesion force to evaluate wet cleaning. In addition, we measured the particle adhesion force by sliding self-sensitive cantilever. As a result, the adhesion force is above 100 μN . This force is about 10^3 times higher than glass particle sprinkled on glass slide. Using this sample, we demonstrate the cleaning performance of PVA brush scrubbing and droplets impacts.

(a)



(b)

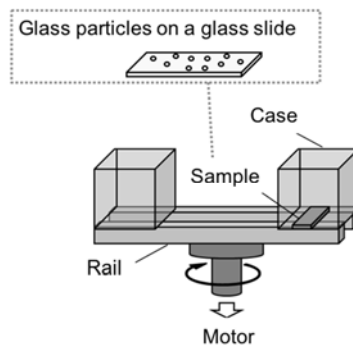


Figure 1: Experimental set up, (a) direct measurement of adhesion force for resin particles, (b) removal force measurement for glass particles by centrifuge separation.

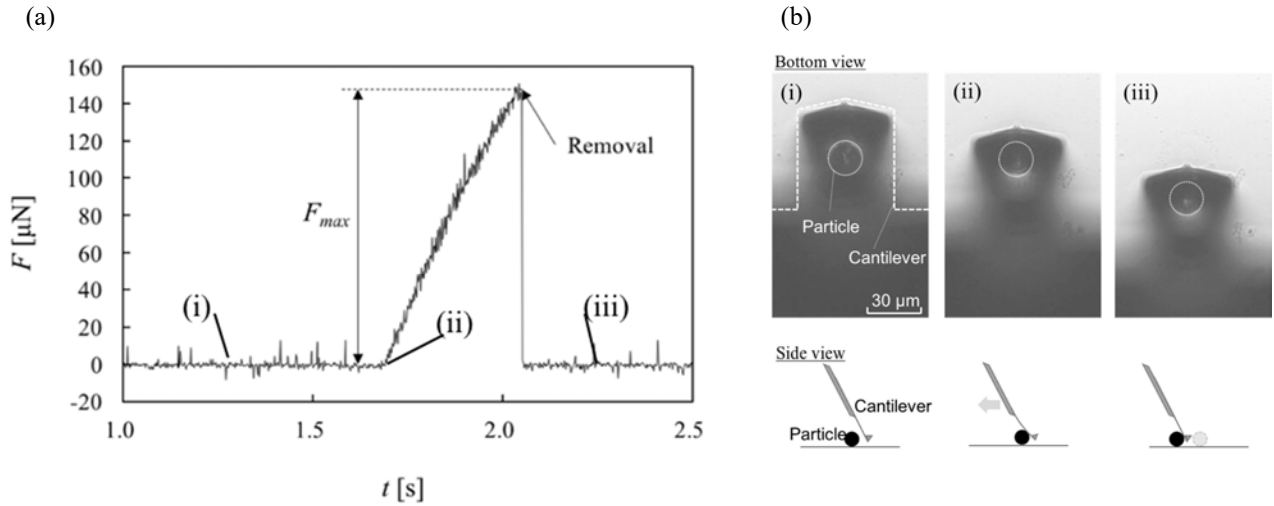


Figure 2: An example of measurement of removal force, (a) change of removal force. (b) images of removal process from bottom and side views, the symbols (i), (ii), (iii) correspond to the time of (a).

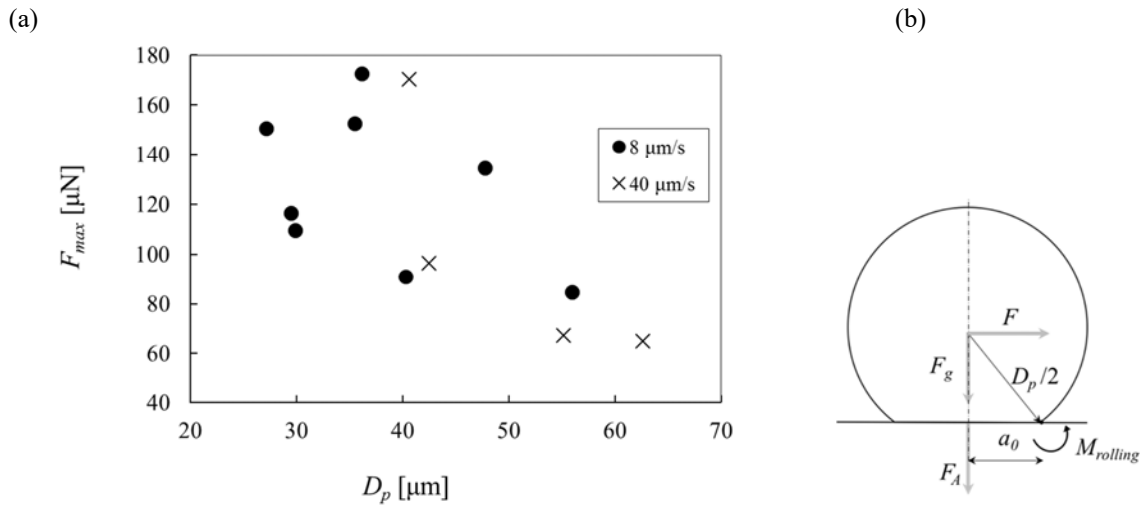
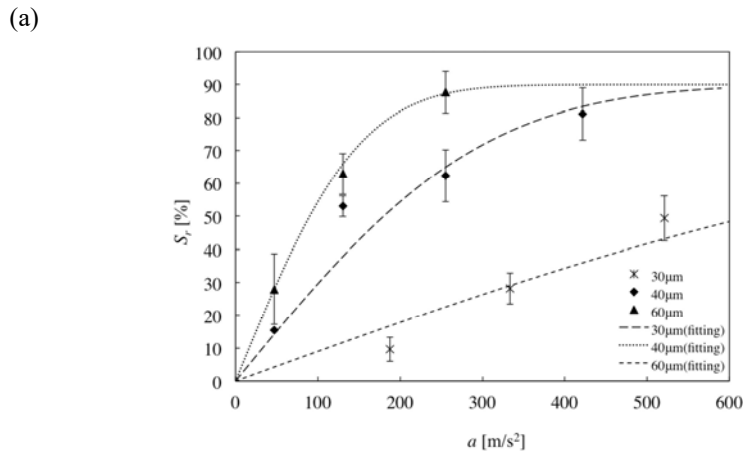


Figure 3: Particle removal forces, (a) relationship between particle diameter D_p and removal maximum force F_{max} . (b) schematic image of the forces acting on the attached particles.



(b)

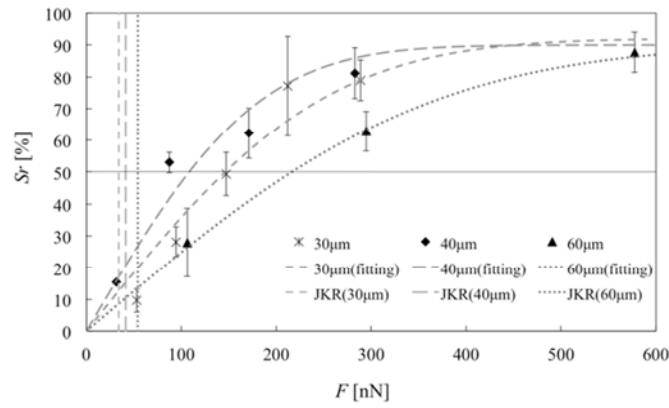


Figure 4: Particle removal rate S_r of glass particles (D_p are 30, 40 and 60 μm) by centrifuge separation (a) relationship between S_r and removal acceleration a . (b) relationship between S_r and removal force F .

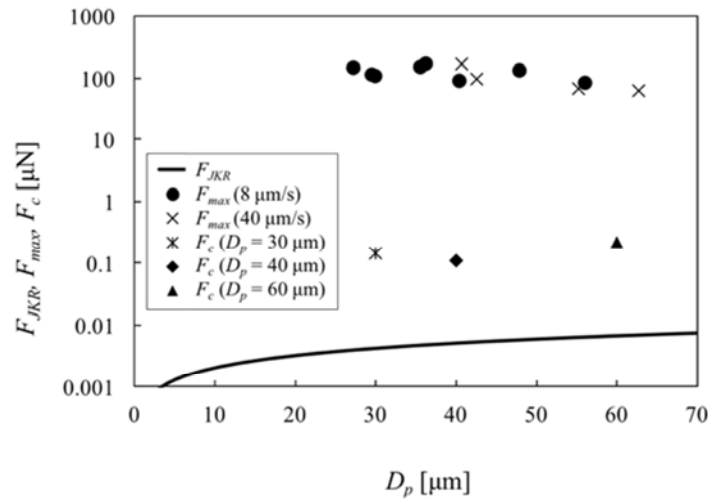


Figure 5: Glass particle removal force F_c and JKR model.

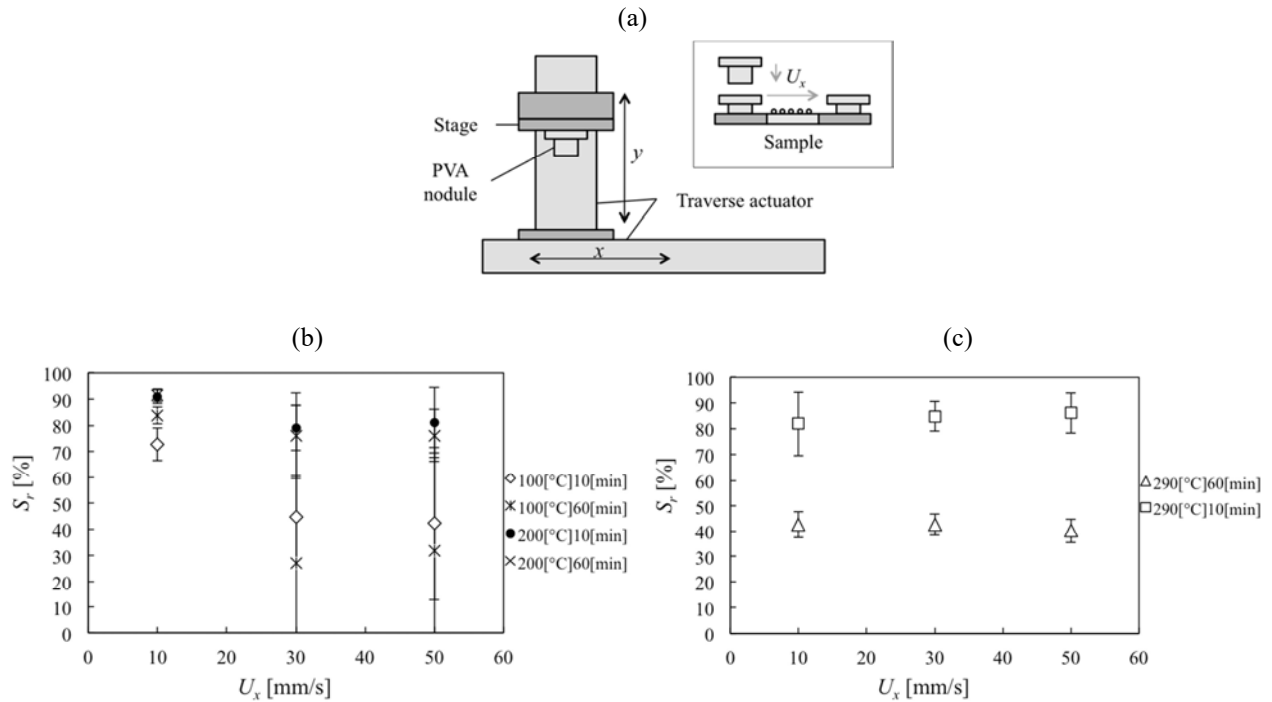


Figure 6: Measurement of particle removal rate by removed PVA brush nodule scrubbing, (a) Schematic of experimental setup, (b) Relationship between particle removal rate S_r and sliding speed U_x (heated at 100 and 200 °C), (c) Relationship between S_r and U_x (heated at 290 °C).

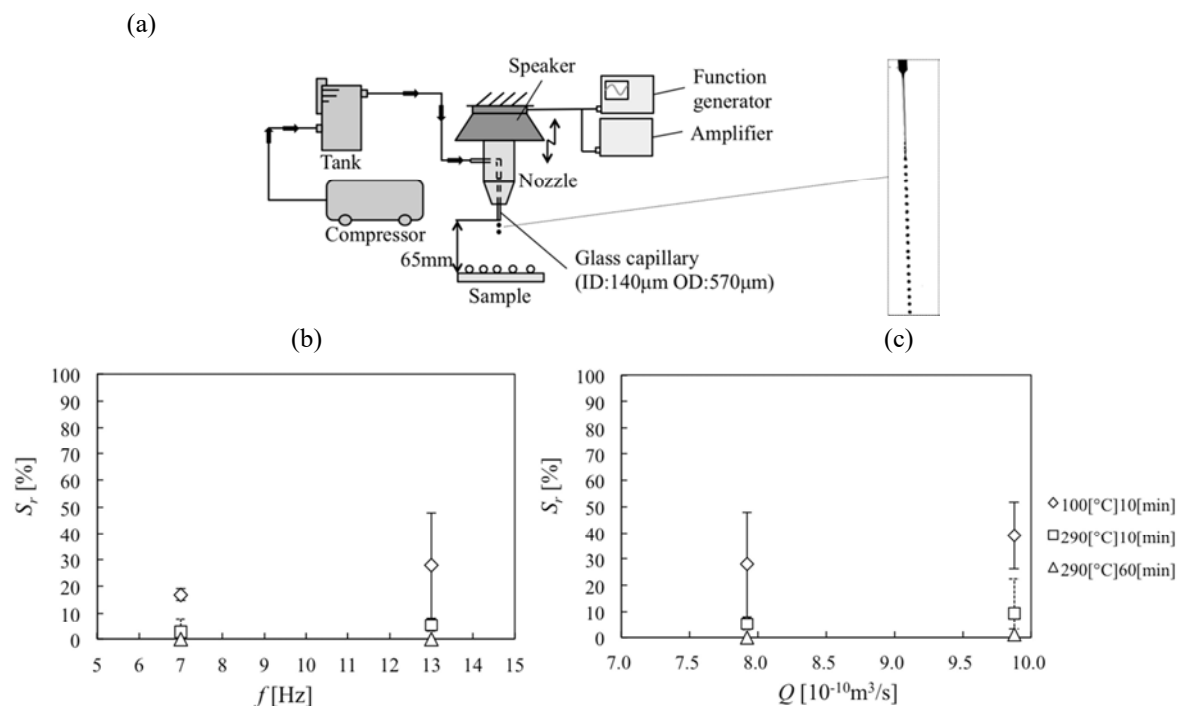


Figure 7: Measurement of particle removal rate by monodispersed droplet train impact, (a) Schematic of experimental setup (b) Relationship between particle removal rate S_r and droplet frequency f (Water flow rate $Q = 7.92 \times 10^{-10} \text{ m}^3/\text{s}$), (c) Relationship between S_r and Q ($f = 13 \text{ kHz}$).

References

- [1] J.G. Park, S.H. Lee, J.S. Ryu, Y.K. Hong, T.G. Kim and A.A. Busnaina, Journal of the Electrochemical Society, 153 (9) G811-G814 (2006).
- [2] T.G. Kim, K. Wostyn, T. Beard, J.G. Park, P.W. Mertens and M. Heyns, ECS Transactions, 25 (5) 203-210 (2009).
- [3] S. Brems, M. Hauptmann, E. Camerotto, A. Pacco, T.G. Kim, X. Xu, K. Wostyn, P. Mertens and S. De Gendt, ECS Journal of Solid State Science and Technology, 3 (1) N3010-N3015 (2014).
- [4] A.H. Ibrahim, P.F. Dunn, R.M. Brach, Aerosol Science, 34 (2003) 765-782.
- [5] S. Hashimoto, M. Adachi and F. Iwata, Japanese Journal of Applied Physics 54, 08LB03 (2015).

Characterization of Cavitation in a Single Wafer or Photomask Cleaning Tool

Xi Chen^{1, a}, Petrie Yam¹, Manish Keswani² Nagaya Okada³
and Claudio I. Zanelli^{1a}

¹ Onda Corporation, U.S.A.

² University of Arizona, U.S.A.

³ Honda Electronics Ltd., Japan

^aet@ondacorp.com

Keywords: Cleaning, Ultrasonic, Megasonic, Cavitation, Hydrophone, Sensor Array, Transient, Microstreaming, Photomask.

Abstract. A novel transducer for megasonic cleaning of photomasks presents an approach that differs from previous configurations, and appears to have unique features for cleaning while minimizing damage. As the cleaning and damage processes are determined by the presence of cavitation, a thorough acoustic analysis was performed on the device, by using a calibrated hydrophone scanned at the photomask location, and a quartz photomask with embedded sensors.

Introduction

The use of megasonics in semiconductor cleaning is well established. However, many fabrication facilities that routinely use megasonic cleaning have shied away from the method for some critical steps due to the difficulty in reaching process recipes that yield reproducible results. The main cause of this dubious status is the lack of control on cleaning performance and feature damage. Cleaning processes require the ability to accurately monitor and control each parameter that influences the particle removal efficiency and damage to delicate features. This includes the process time, temperature profiles, flow rate, pH, surfactant concentration, dissolved gas concentration, etc. Yet, typically the only parameters known in relation to the application of the sound field is the electric power and frequency delivered to the transducer. Implicitly, the assumption is that the acoustic pressure amplitude is proportional to the square root of the power. So if the power is fixed, so should the acoustic pressure. In other words, the efficiency of conversion from electric to acoustic energy is assumed constant over time. Another assumption generally made is that the acoustic field is uniform across the cleaning solution. Unfortunately, these assumptions are grossly inaccurate and are the cause of misguided effort throughout the industry.

The efficiency of transducers varies greatly with changes in temperature, as the components change dimensions upon which their resonant behavior rests. Although manufacturers design the electronics to compensate for this effect, the success in doing so varies widely. Similarly, the sound pressure field is not uniform in a vessel that contains localized transducers, reflecting substrate, and a surface of cleaning chemistry whose height and shape is continuously changing. As the wave travels through the liquid and encounters solid surfaces, it is reflected and (minimally) absorbed, whereas waves that impinge on a liquid-to-air surface are almost completely reflected. The presence of waves that travel in opposite directions results in standing -or stationary- waves, meaning oscillations in which no energy is transferred and consequently there are nodes -places where the oscillation is zero- and antinodes, where there the oscillation is intense. As a consequence of the waves being stationary, estimating the total acoustic power as proportional to integral of pressure squared over a plane in the water is incorrect, because that definition of power is based on the assumption of traveling waves that convey that energy. The locations of the nodes and antinodes can be altered by changes in the location of the reflecting surfaces. To minimize the intrinsic heterogeneities in the cleaning solution, some cleaning systems sweep the frequency of the waves.

Other tools move the transducer over the part, varying the angle of incidence or the distance, as a way to sweep the nodes and antinode locations. The extent of the sweeps in frequency or position are determined empirically and rarely based on simulations.

Fortunately, there are newly developed tools that allow direct measurement of the acoustic field at the location of interest. Traditionally the instrument of choice to measure acoustic fields is the hydrophone, a generic term for a point-like sensor that converts pressure to electric signals. However, such devices are intrinsically very sensitive and are easily damaged by the local high pressures generated during cavitation. Further investigation led to the two known forms of cavitation: stable and transient [1,2]. This prompted the development of rugged sensors and processing instruments to measure independently the direct -or driving- field, and the two forms of cavitation [3].

Cleaning Application

We present a set of pressure field and cavitation measurements for a novel single wafer or mask cleaning transducer, Model W-357-1MQB-SKC manufactured by Honda Electronics of Japan. The cleaning head consists of a quartz cone coupled to a transducer at its apex, where the cone is truncated at approximately 45 degrees of its axis (see Figure 1). The quartz cone typically translates over the surface to be cleaned, with cleaning solution flowing through its feed tube, while the object to be cleaned spins below.

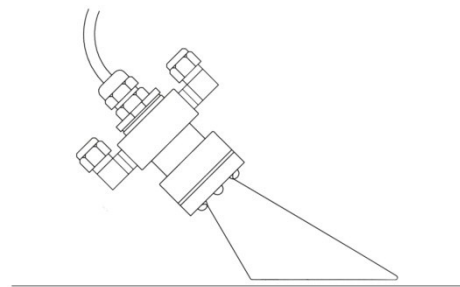
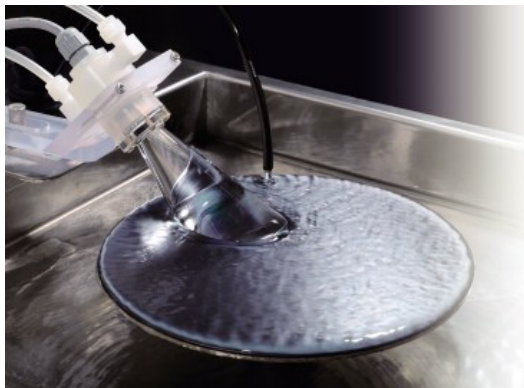


Figure 1. Conical cleaning transducer during operation, shown with a 200 mm wafer and in side view.

According to manufacturer's instructions, the flat surface of the quartz with an estimated area of 23.5 cm^2 must be kept parallel to the cleaned surface, separated by 1 to 2 mm. This device is available in different frequencies including 1, 2 and 3 MHz. We presently report measurements using the 1 MHz version, with a generator that can deliver power up to 12 W.

Measurements

In the cleaning application the sound waves between the transducer and surface reverberate and create standing waves, which result in a complex sound field. For this reason it is essential to first characterize the transducer in an open field such as a large scanning tank to minimize reflections from external surfaces, before characterizing it in the presence of a substrate such as a photomask, as shown in Figure 2.

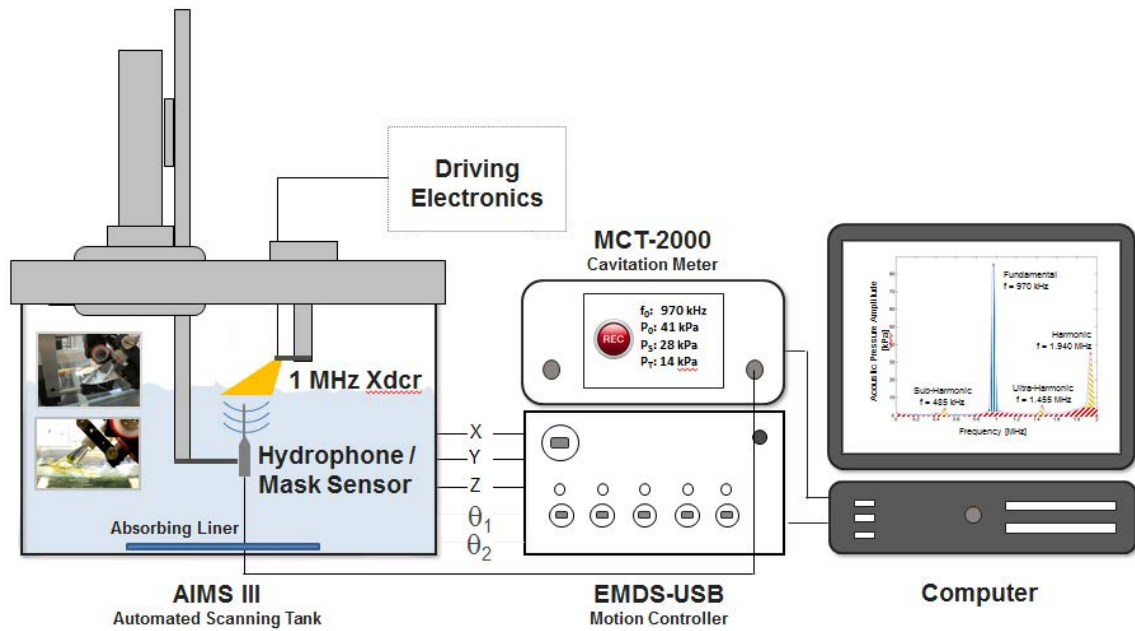


Figure 2. Hydrophone Measurement Setup. The flat surface of the cleaning transducer is parallel and in contact with the water surface. A hydrophone and a sensing photomask are scanned under the cleaning head.

The acoustic pressure distribution was mapped with a spatial resolution of 0.2 mm in the X-Y plane at 2 mm from the surface at nominal 3 and 12 Watts of electrical power, and linear scans in X and Y were obtained across the peak location near the center. This measurement was done by scanning a hydrophone and a standard 6 inch photomask with an embedded sensor. These measurements, shown in Figure 3, were done at a temperature of $21.0 \pm 0.5^\circ\text{C}$, using deionized water degassed to 3.6 ppm dissolved oxygen (DO). The complex (yet symmetric along the Y-axis) pressure pattern can be attributed to the considerable reverberations within the quartz cone.

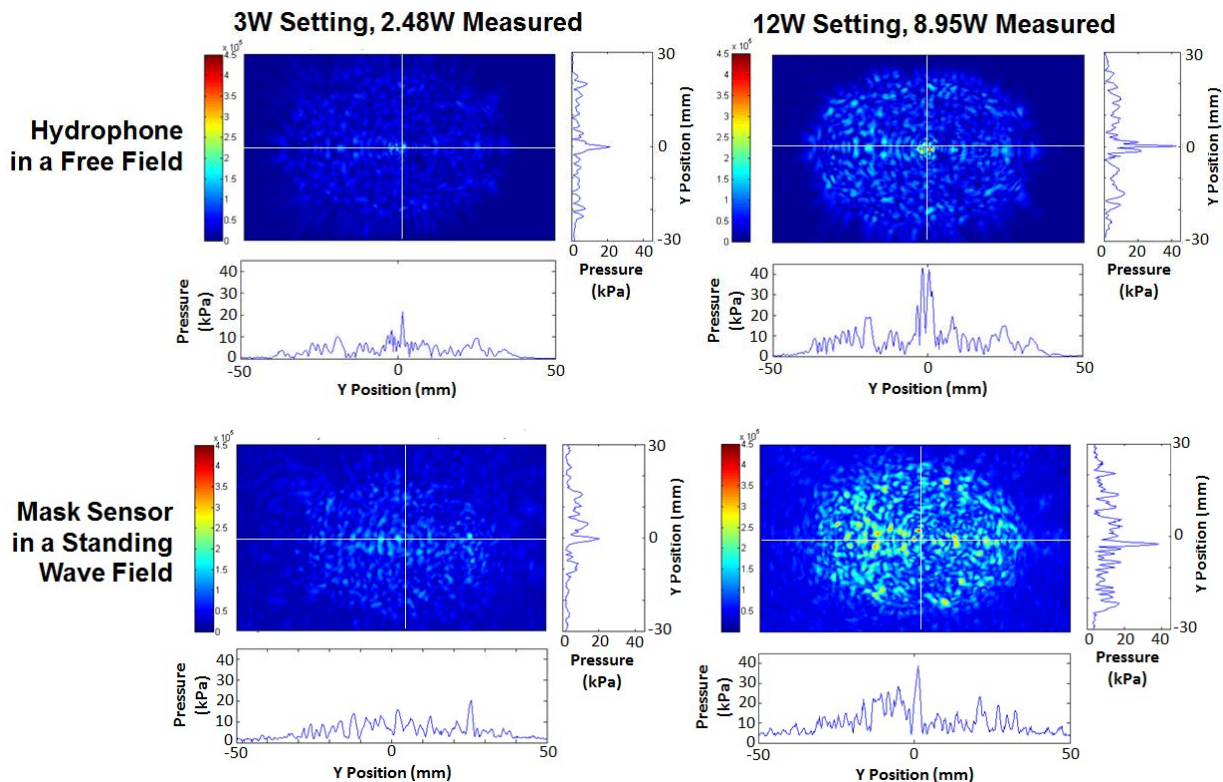


Figure 3. 2D pressure maps at 2 mm from the surface of the cleaning head, at different power settings, left is at nominal 3W and the right is at nominal 12W. The top two maps were obtained by scanning a needle hydrophone, and the bottom two maps used the mask with embedded sensor. Linear scans in X and Y were made across the location of the peak. Positioning accuracy in all 3 axes is 0.03 mm.

The 2D pressure maps were seen to change depending on the degree of immersion of the cone into the water, and care was taken to maintain the level at the face of the quartz cone.

Linear scans away from the transducer face were also acquired, comparing results from the hydrophone and mask sensor measurements (see Figure 4).

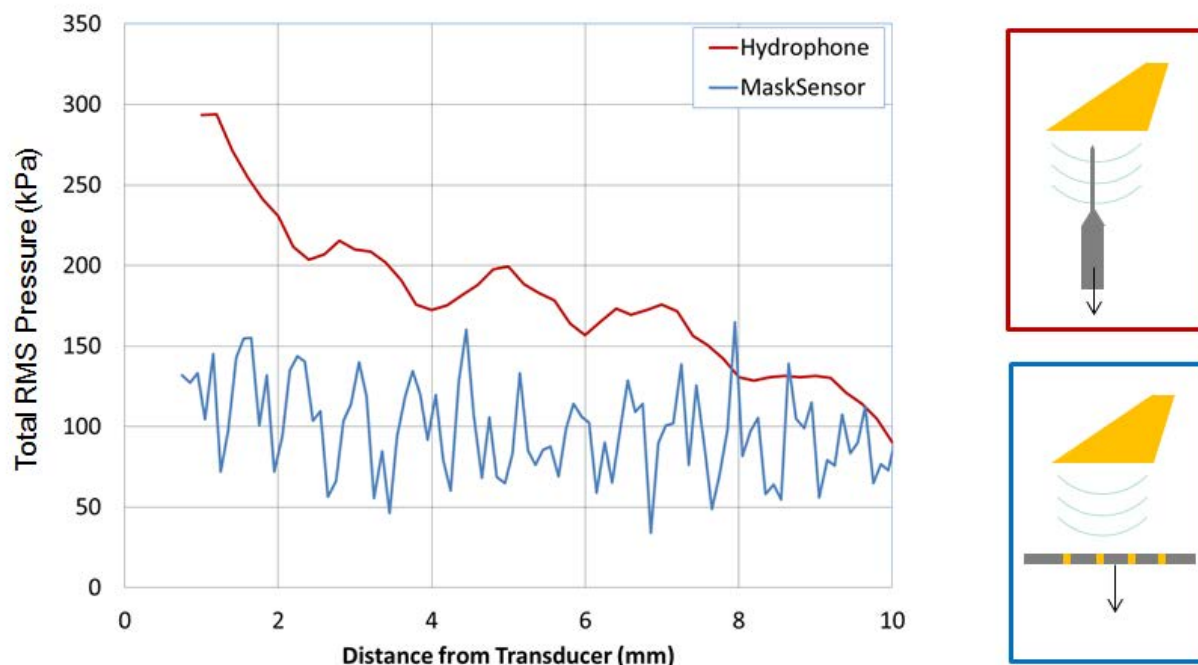


Figure 4. The effect of standing waves is evident when one compare the pressure plots as the distance between the hydrophone or mask sensor moves away from the conical transducer. With the hydrophone, the pressure decays quite monotonically with distance. The reflecting mask causes standing waves, which peak every half wavelength, or 0.75 mm.

Cavitation Detection

The method to quantify the cavitation pressure is based on the detection by spectral analysis of the hydrophone signal [1]. It can be found in three regimes: the direct field pressure P_0 , caused by the source, is predominantly present at the driving frequency (1 MHz in this case). Stable cavitation pressure P_s , which is due to stable (albeit microscopic) bubbles that oscillate at multiples of the fundamental frequency, appears in the spectrum as peaks at multiples of the driving frequency. Stable cavitation is believed to be responsible for somewhat gentle micro-streaming that disrupts the boundary layer and allows removal of particles. Transient cavitation, which occurs as micro-bubbles implode, is detected as broadband noise which is integrated as P_t . This form of cavitation has the potential to cause damage because of the high speed jets (and the corresponding shock waves) generated near hard surfaces [2].

Current wisdom indicates that cavitation is essential for particle removal. However, except near the location of the peak value in P_0 (approximately at $X=-2$ mm), where P_t also shows some increase, very little cavitation was detected with the hydrophone. While the hydrophone does not reflect acoustic waves, the presence of the mask generates regions of higher pressure because of the reverberations between the two flat surfaces. Not surprisingly, the mask measurements show a significant increase in stable and transient cavitation, concurrent with a slight decrease in direct field cavitation. Figure 5 shows these effects for a range of input power settings.

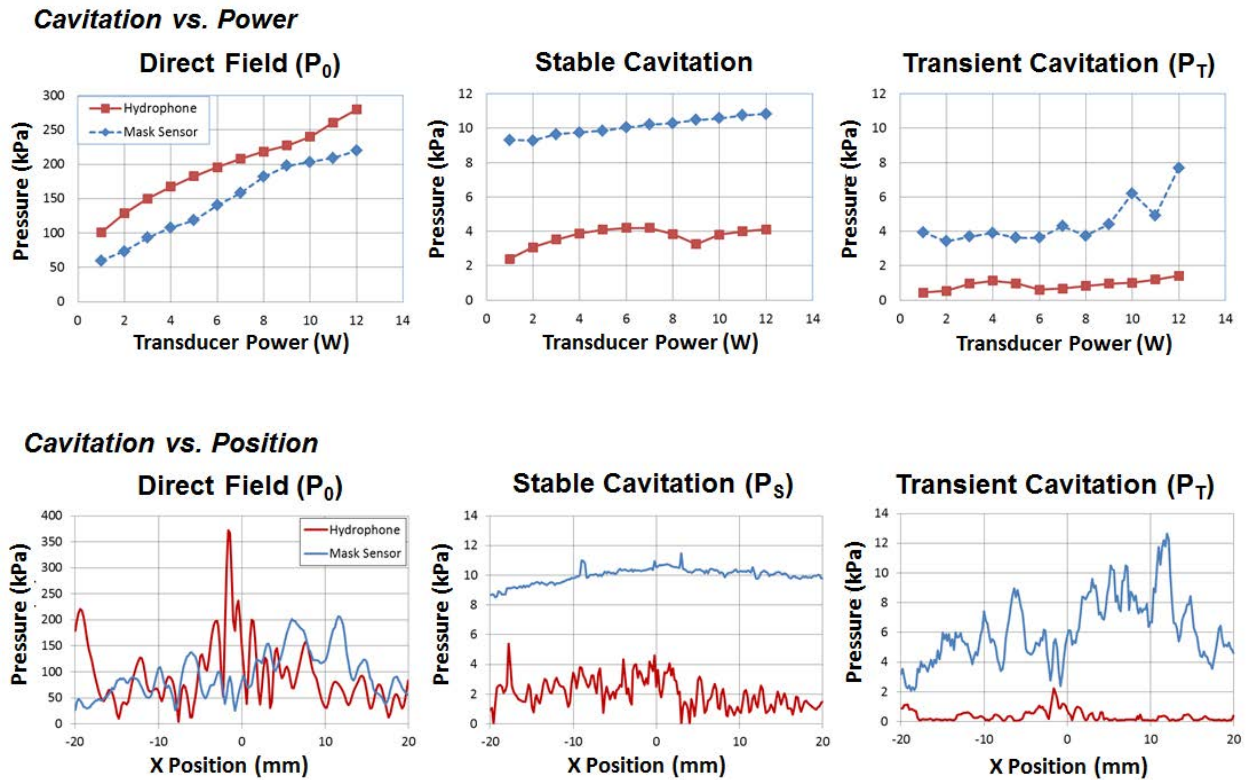


Figure 5. Pressure of the three sources of pressure in the liquid – direct field, stable cavitation and transient cavitation – as a function of power delivered to the transducer and position across transducer face.

Discussion

Measurements using a hydrophone show that the efficiency of the transducer (the ratio of acoustic power to displayed electrical power) is 83% at 3W setting and it drops to 75% at the 12W setting. However, the locations of maxima and minima stay in the same places, which would indicate that there are no structural changes as power changes. The power measured is also proportional to P_0^2 , as expected. The big surprise in the hydrophone field maps is in the pattern itself, which is by no means homogeneous, presenting a structure that rather resembles a brush with many points of high and low intensity. When the instrumented mask is used to measure the maps, the pattern widens beyond the profile of the source. This is because waves impinging on one part of the mask are carried by the mask (not by the water) to the embedded sensor, effectively creating an enlarged sensor. As expected, the pressure at the mask is enhanced in amplitude by the effect of reverberations between source and mask.

The amounts of stable and transient cavitation in the bulk water were very small, even at the 12W setting. However, when the hydrophone was replaced by the mask both cavitation levels increased by a factor of 5 while the direct field pressure decreased. This is attributed to a masking effect caused by the cavitation, where the high density of microbubbles is an effective scattering field for the waves launched by the transducer (P_0).

The dependency of pressure as one moves away from the source was studied too. Hydrophone measurements of pressure as a function of distance to the source revealed a generally monotonic decrease in amplitude, although not smoothly decreasing due to the complex pattern. This is in stark contrast with the effect of distance separation between the source and the mask. In this case, because we have a large component of standing waves, the pressure does not decrease, but instead it “beats” up and down with consecutive maxima separated by 750 μm , which is half of the wavelength in water. This effect must be considered when considering the position of the source above the mask. In fact, the amplitude changes by a factor of two when the separation changes by as little as 370 μm .

Conclusions

The two measurement types, hydrophone and sensing photomask, bring us closer to understanding the mechanism of action of this ultrasonic source. The hydrophone allows measurement of the true acoustic output of the device, and the mask sensor provides measurements from the standpoint of a particle on its surface. The enhancement of cavitation caused by the reflected energy is in complete agreement with the understanding of acoustics.

References

- [1] J. Frohly, S. Labouret, C. Bruneel, I. Looten-Baquet and R. Torguet. *J. Acoust. Soc. Am.* 108 (5), 2000
- [2] E. Camerotto, S. Brems, M. Hauptmann, A. Pacco, H. Struyf, P.W. Mertens and S. De Gendt. *J. Appl. Phys.* 112, 14322 (2012)
- [3] C.I. Zanelli, S.M. Howard, D. Giridhar and P. Yam, *J. Acoust. Soc. Am.* 134, 3993 (2013)
- [4] R. Balachandran, M. Zhao, P. Yam, C. Zanelli and M. Keswani, *Microelectronic Engineering* 133 (2015) 45–50

CHAPTER 7:

Interconnect Cleaning

Molecular Simulation Contribution to Porous Low-K Pore Size Determination after Damage by Etch and Wet Clean Processes.

Lucile Broussous^{1a}, Matthieu Lépinay^{1,2,3}, Benoit Coasne⁴, Christophe Licitra², François Bertin², Vincent Rouessac³, André Ayrat³

¹ STMicroelectronics, 850, rue Jean Monnet, 38926 Crolles cedex, France.

² Univ. Grenoble Alpes, F-38000, Grenoble. CEA, LETI, MINATEC Campus, 17 rue des Martyrs, 38054 GRENOBLE, France.

³ Institut Européen des Membranes, CNRS/ENSCM/UM2, place Eugène Bataillon, 34095 Montpellier, France

⁴ Laboratoire Interdisciplinaire de Physique (LIPhy), CNRS/Univ. Grenoble Alpes (UMR 5588). 140 rue de la Physique – Domaine Universitaire BP 87 – 38402 St Martin d'Heres, France

^aemail:lucile.broussous@st.com.

Invited Paper

Keywords: Porous low-k, micropores, molecular simulation, process damages, wet cleaning

Abstract Porous low-k materials used as insulator for interconnection levels in CMOS devices, are easily damaged during the patterning processes. Pore size characterization after material damage is challenging due to the chemical modification induced by the applied process. Numerical simulation of solvent adsorption on silica and functionalized silica surfaces was used to improve material pore size determination by ellipso-porosimetry, taking into account the modifications of surface/solvent interactions.

Introduction

Porous low-k materials are now widely used as insulator for Back End of Line interconnection levels in CMOS devices from 45nm down to 28/14 nm nodes. Material modifications due to plasma used for etching, or as pre-clean for metals and dielectric deposition, wet cleans and CMP processes were intensively studied in order to optimize process integration robustness [1, 2].

For the most recent generations, with 64nm minimum pitch, copper line width is equal to low-k insulator width, equal to 32nm. After line etching, 5 to 10nm depth low-k modification on each side corresponds to more than the half of the insulating line width, thus the impact of the degradation becomes very significant.

A number of publications highlight variations of low-k dielectric constant after various processes that induce damages or that aims to recover low-k properties [3-5], in good correlation with material surface properties. New methodologies were proposed, such as thin films surface energy measurements with OWRS method [6, 7]. Based on contact angle measurement with five different solvents, this method is easy to use on blanket thin films. Characterization techniques were improved in order to gain in sensitivity for surfaces analysis or to avoid the degradation of fragile thin films. For example FTIR used in Attenuated Total Reflection (ATR) mode or with Multiple Internal Reflection (MIR) apparatus [8] and low energy ToF SIMS coupled to multivariate analysis of the spectra [9, 10], were used to better identify chemical composition of the modified layer.

In this paper, we will focus on porosity characterization for porous low-k materials after process induced damages, in comparison with non modified material. Indeed, pore size physical characterization remains very challenging for these materials due to the chemical modification also induced by the applied process.

Ellipso-porosimetry (EP) is an easy and accurate technique to measure low-k thin films porosity [11]. However when applied to a modified material, it was not able to discriminate surface and bulk properties, because the surface modified layer, is very thin. Another approach was to use various solvents as probe molecules such as methanol, ethanol, toluene, iso-propyl alcohol [4,5, 12], for

solvent adsorption kinetic studies. Depending on solvent/material combination, we observed some delay to solvent adsorption, however no variation was evidenced on pore size distribution, by using standard models for microporous materials [4, 5] (Figures 1-3).

Depth resolved characterizations with Positron Annihilation techniques (PALS / DBAR) were then performed. Pore size evolution was investigated from material surface to 200 nm depth [4]. Material densification at the surface and at the interface with Si substrate was confirmed, in agreement with X-Ray reflectometry measurements. However pore size reduction at the surface was not evidenced. On contrary, average pore size increase was measured for the two samples showing toluene adsorption delay (Figures 2, 4).

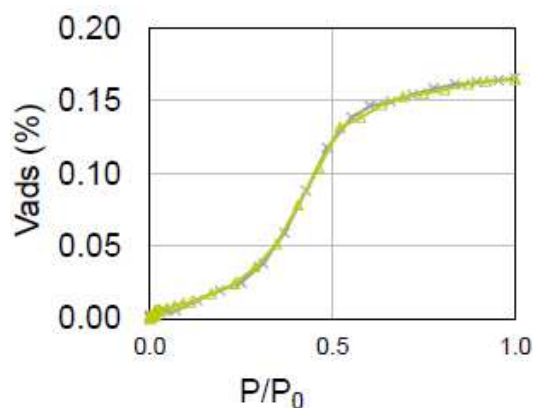


Figure 1 – Methanol adsorption/desorption isotherm for plasma treated samples.

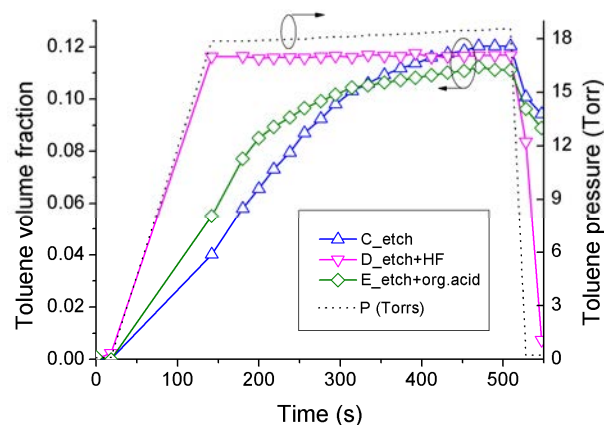


Figure 2 – Kinetics of toluene adsorption before and after cleaning chemistries.

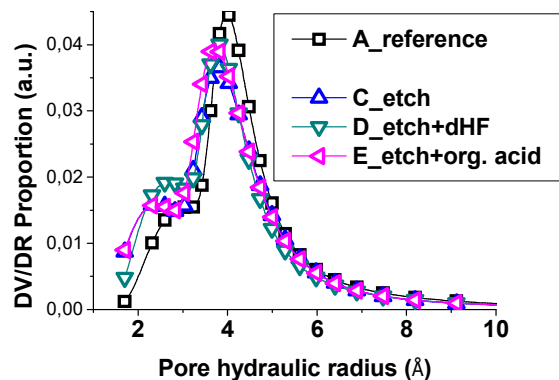


Figure 3 – Hydraulic pore radius distribution obtained from EP methanol isotherms with MP method.

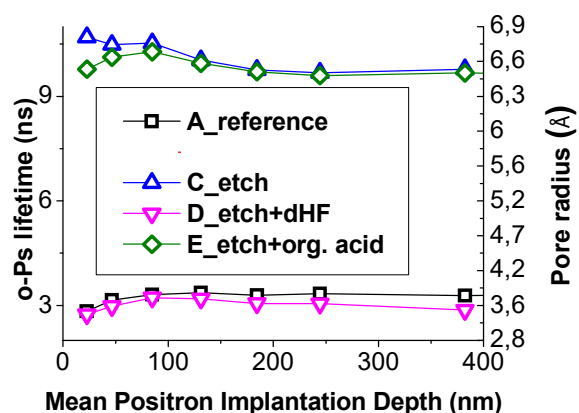


Figure 4 – o-Ps lifetime, and pore radius versus mean positron implantation depth (nm), measured by PALS. The error bars are of the order of the point sizes.

The modification of adsorption and diffusion behavior observed with toluene EP could arise from a modification of the properties at the top-surface (15 nm), where depth-averaged EP is not sensitive, and positroniums (Ps) tend to escape from the sample, thus rendering results exploitation difficult. In addition, we also need to consider both the possibility of closed porosity probed only by Ps, and a modification of affinity between the material and the toluene molecule, hindering toluene adsorption in the pores.

Thus, as ellipso-porosimetry technique can be sensitive to surface chemical composition variations, deeper understanding of the effect of pore surface chemistry is needed (i) to validate the selection of probe molecules depending on solvent/material affinity and (ii) to accurately measure micropores in modified low-k thin films (pore diameter around 2 nm).

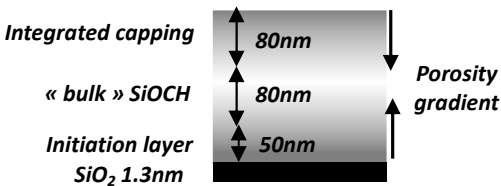
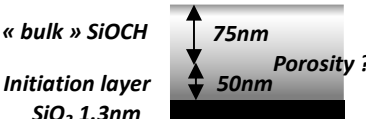
In this context, numerical simulations of the interactions between solvent probe molecules used in EP and functionalized silica surfaces were performed. Methylated, hydroxylated and fluorinated silica surface, aiming to have chemical composition close to low-k and modified low-k surfaces were studied. Adsorption isotherms were simulated then used in the treatment of experimental EP data with the Micropore Model (MP method), leading in a differentiation of sample pore size depending on the considered surface chemistry after etching and cleaning.

Experiments

The contribution of Statistical-Mechanics molecular simulations will be illustrated for low-k thin films modified by etching plasma and wet clean solutions.

Porous thin films samples. The samples were blanket thin films (200 nm) of porous low-k, SiOCH type material (BD2XTM, Applied Materials), as described in [5], and table 1. Sample A was the reference stack after deposition and anneal. Samples C, D and E were exposed for 30s at 350 °C to standard fluorinated plasma etching process used for line and via patterning [13]. Samples D and E were then exposed to wet cleaning chemistries containing respectively diluted HF (0.2%wt, 20°C, 50s) and glycolic acid (1%wt, 60°C, 120s).

Table 1 – Schematic information about SiOCH low-k samples.

	Treatment	Schematic representation
A	Reference. No treatment. “as deposited” ultra low-k stack. Initiation layer and surface “capping” are more dense than “bulk” porous material. Total thickness 215 +/- 1 nm	
C	Etch CxFy plasma Thickness 127 +/- 1nm	
D	Etch + dHF. CxFy plasma + wet clean HF 0.2%wt. 50sec. Thickness 124 +/- 1nm	
E	Etch + dHF. CxFy plasma + wet clean Glycolic acid 1%wt. 120sec. Thickness 128 +/- 1nm	

Ellipso-porosimetry. Methanol and toluene were used as adsorbents (probe molecules). Standard adsorption/desorption isotherms were recorded by EP, at wavelengths ranging from 270 to 805 nm (1.54–4.59 eV), using a Sopra “EP12” apparatus. “Type I” isotherms characteristic of microporous materials (Figure 1) were obtained for all the studied thin films (see IUPAC classification [14]). In this case, the MP method [15] is applied to estimate the micropore sizes. EP was also used to study the kinetics of methanol and toluene adsorption after a sudden increase of relative pressure, P/P_0 , from 0 to 0.8 in the sample chamber, as described in [11].

Molecular simulation. Three realistic models of bare and modified silica were prepared by means of molecular dynamics simulation, using the DL_POLY Classics package [16] and the CHIK potential [17], as described in [18, 19]. Hydrophilic Silica, with totally hydroxylated surface was first obtained from the simulation of a block of bulk silica (SiO_2), where the oxygen dangling bonds at the surface were passivated with H atoms (final OH surface density of 6.8 per nm^2).

In order to obtain methylated and trifluoromethylated surfaces, the Si-OH groups were then replaced with SiCH_3 and SiCF_3 groups. In each case, we considered two substitution ratios $n = 0.7$ and 1, in order to be close to as-deposited and damaged low-k surfaces.

Finally, the surfaces were allowed to relax by means of Molecular Dynamics simulation prior to start the simulation of methanol and toluene adsorption/desorption isotherms with Grand Canonical Monte Carlo simulations techniques (GCMC), as described in [13, 18].

In this first approach, we simulated plane surfaces of dense thin films, in order to compare the affinity of solvent molecules with hydroxylated silica and functionalized silica surfaces.

Results

Methanol and toluene adsorption isotherms were simulated on the five described surfaces. Figure 5 illustrate the adsorbed layer for final partial pressure $P/P_0=0.9$, and the thickness of adsorbed layer depending on partial pressure P/P_0 is reported in Figure 6.

It was confirmed that methanol has a good affinity with hydrophilic silica and methylated surfaces, but adsorption on fluorinated surfaces is lower. At low partial pressure ($P/P_0 < 0.4$), the presence of $-OH$ increases methanol adsorption on partially methylated surface (Figure 6a). For $P/P_0 > 0.4$, the formation of a continuous methanol film, then a multilayer is observed on the three types of surface. These results are in good correlation with EP experiments with methanol as probe molecule. In this case, no adsorption delay was observed in kinetic mode and it was possible to perform standard EP adsorption/desorption isotherms on most samples.

On contrary, it is evidenced that toluene has a very poor affinity with all surfaces, since maximum toluene adsorption is very low in comparison with methanol adsorption. On hydrophilic silica ($Si-OH$), saturation level is reached at very low partial pressure ($P/P_0=0.2$), with the formation of toluene monolayer ($t = 6\text{nm} \sim$ toluene molecular diameter). Even at high partial pressure, toluene never builds multilayer film on these surfaces. On fully methylated surface, that mimic “as deposited” low-k material, adsorption is slightly lower, but saturation at low partial pressure is not marked. On fluorinated surfaces, almost no adsorption occurs.

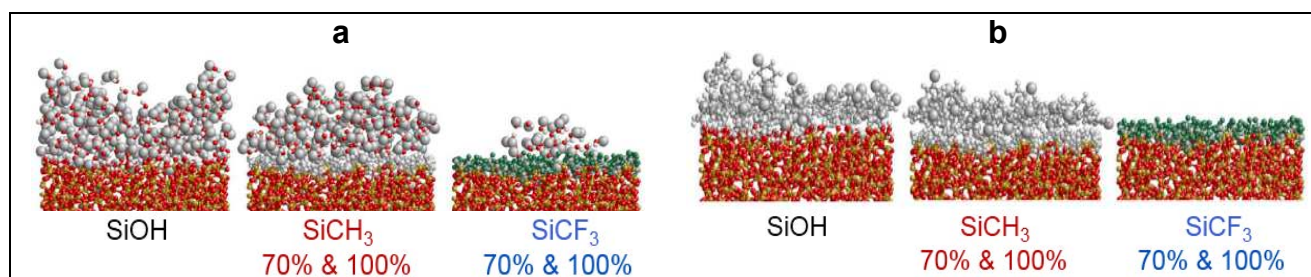


Figure 5 – Illustration of (a) methanol, and (b) toluene adsorption on functionalized silica surfaces.

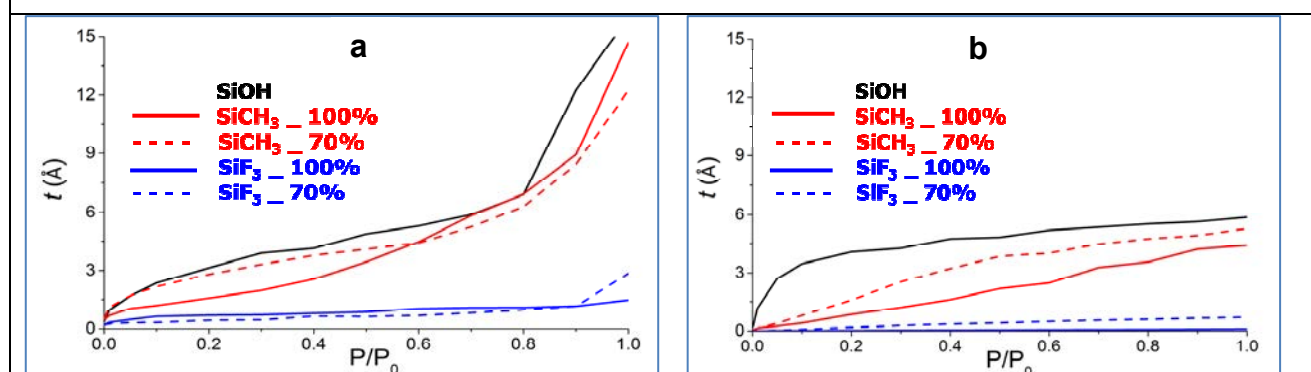
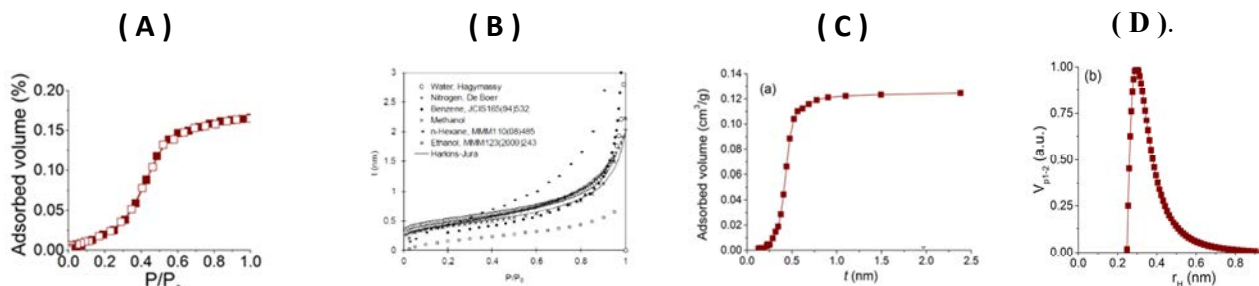


Figure 6 – Simulated adsorption of (a) methanol and (b) toluene on the five surfaces. Thickness of the adsorbed layer vs partial pressure P/P_0 .

At first order, these results are in good correlation with adsorption delay experimentally observed with toluene after etch plasma (sample C), because of carbon depletion and contamination with fluorine species. For the sample E, as the same adsorption delay is observed, we can state that the wet cleaning with glycolic acid is not efficient enough to remove surface contamination, neither change surface chemical composition. On contrary, no delay was observed after diluted HF wet clean (sample D), that maybe more efficient for the removal of fluorinated post-etch residues (slight etching of material surface).

Pore Size Distribution for Microporous materials (use of t-plot & MP Method) :

- Experimental Adsorption Isotherm (A) : type I in the IUPAC classification [22]
- Microporous Materials / pore size < 2nm / solvent adsorption saturation during micropores filling
- Dimensions of pore size close to probe molecule size → t = thickness of adsorbed layer
- MP method : $\%V_{ads} = f(P/P_0)$ (A) → Use Harkin Jura Equation (B) to plot $V_{ads} = f(t)$ (C)
- Pore Size Distribution $DV = f(R_h)$ (D). R_h = Hydraulic Radius. For cylindrical pore, pore diameter is $D_p = 4 \times R_h$



(B) : Theoretical t-curve (black) = Harkins and Jura equation for N₂ at 77 K, in correlation with Experimental t-curves for water on silica, nitrogen (at 77 K) on activated carbon, benzene on silica, methanol on oxide surfaces, n-hexane & ethanol on zeolites.

Figure 7 – Illustration of the methodology for pore size distribution by MP Method. The hydraulic radius r_H given by MP method represent the volume/surface ratio of the pore, and the equivalent pore radius (r_p) is dependent on the pore shape. For a cylindrical pore, $r_p = 2 r_H$; for a spherical pore, $r_p = 3 r_H$.

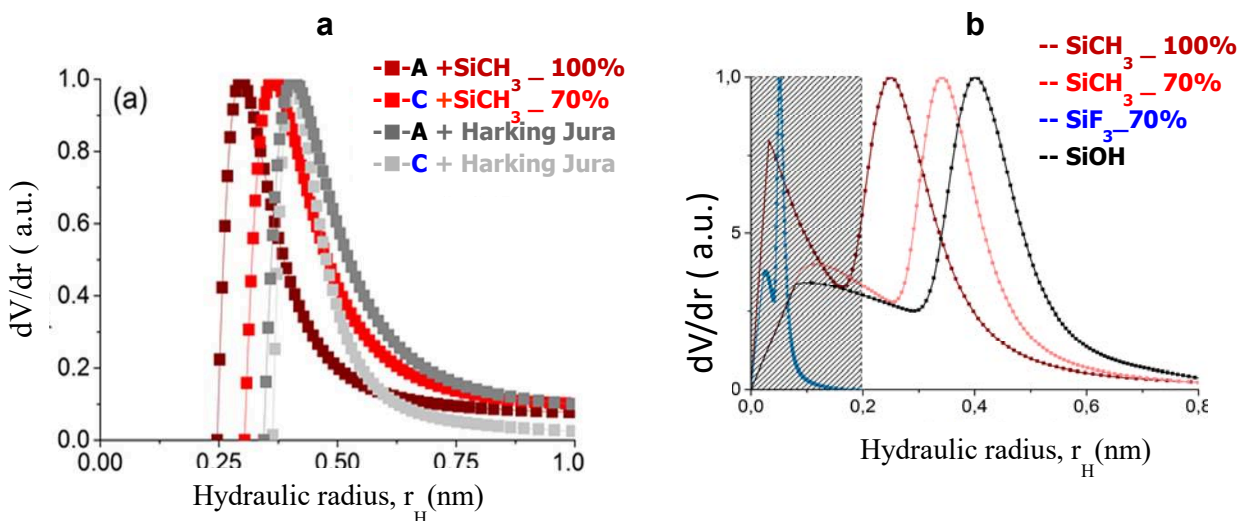


Figure 8 – Pore size distribution obtained from experimental methanol isotherm and simulated t-plot shown in Figure.6. for SiOH (black), SiCH₃ ($n=1$, brown ; $n=0.7$, red), SiCF₃ ($n=0.7$, blue). a_ samples A & C ; b_ sample C

Methanol simulated isotherms were then used to improve pore size determination from experimental EP measurement. Methodology is illustrated in Figure7 and described in detail in [19]. Figure 8 illustrate the pore size distribution obtained for sample A (as deposited low-k), and sample C (post Etch), by using MP method with specific t-plots for hydrophilic silica or functionalized surfaces, as well as the reference “Harkins-Jura” t-plot. Mean pore radius are given in table 2. We first note that pore size obtained with partially and fully methylated surfaces (Figure 8a) are lower than pore size obtained with standard Harkins-Jura t-plot. Thus, usual pore-size determined with standard MP method maybe over-estimated. We can note on Figure 8b that mean pore sizes obtained for fluorinated surface are very small and have no physical meaning. We also observe that hydrophilic silica and partially methylated silica surfaces exhibit higher pore size than fully methylated surfaces representative of low-k material. Thus, if we consider that etched samples

suffers carbon depletion and increasing OH dangling bonds, the use of t-plot simulated for partially methylated surfaces maybe more relevant. This will result in higher pore size than reference as deposited low-k, and better correlate with PALS experiments that highlight pore size increase after low-k damage by etch plasma (sample C).

Table 2 – Mean pore radii obtained from PALS, GISAXS and methanol EP, for a pristine “ref.” and a plasma-modified “etched” SiOCH low-k. The two mean pore sizes, extracted from PALS and EP adsorption isotherms, were determined by assuming cylindrical / spherical pore shapes (see [18] for detailed calculations).

Method	Mean pore radius (r_p , Å)	
	Sample A	Samples C, D
PALS	3.1 / 3.8	5.6 / 6.7
GISAXS	< 10	~ 10
Methanol EP (<i>t</i> -plot Harkins & Jura)	8.1 / 12.2	8.1 / 12.2
Methanol EP (<i>t</i> -plot on 100% SiCH ₃ surface)	5.9 / 8.9	
Methanol EP (<i>t</i> -plot on 100% OH surface)		8.1 / 12.2
Methanol EP (<i>t</i> -plot on 70% SiCH ₃ surface)		6.8 / 10.2
Methanol EP (<i>t</i> -plot on 70% SiCF ₃ surface)		1.7 / 2.6

Concerning wet cleans treatments, we can consider that due to the poor efficiency of organic acid, sample E surface composition is quite the same than etched sample (C). Same t-plot should be used and pore size remain the same than after etch process, in good correlation with PALS measurements.

For sample D, cleaned with diluted HF, PALS experiments highlight a pore size decrease in comparison with etched material (C). In this case, we emphasized that carbon depletion and oxygen enrichment are quite the same than after etch plasma [9, 10]. It was shown by advanced ToF SIMS measurements that Fluorine species are not fully removed with this cleaning process [10], however, etching residues and some contaminants maybe partially removed. Thus, after diluted HF cleaning, pore size reduction could be induced by dangling bond re-organisation and Si-O-Si bridge formation during the wet clean with diluted HF (Si-OH condensation). Indeed, very small variations in the range of 0.3 nm are consistent with a reduction of the distance between two adjacent Si atoms in silica network during Si-OH condensation (Figure 9), as reported in the literature [21].

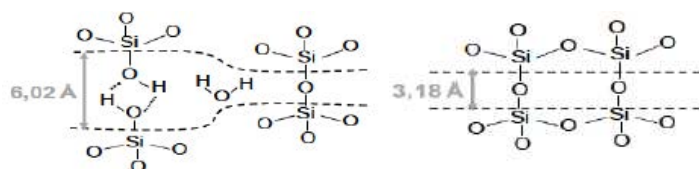
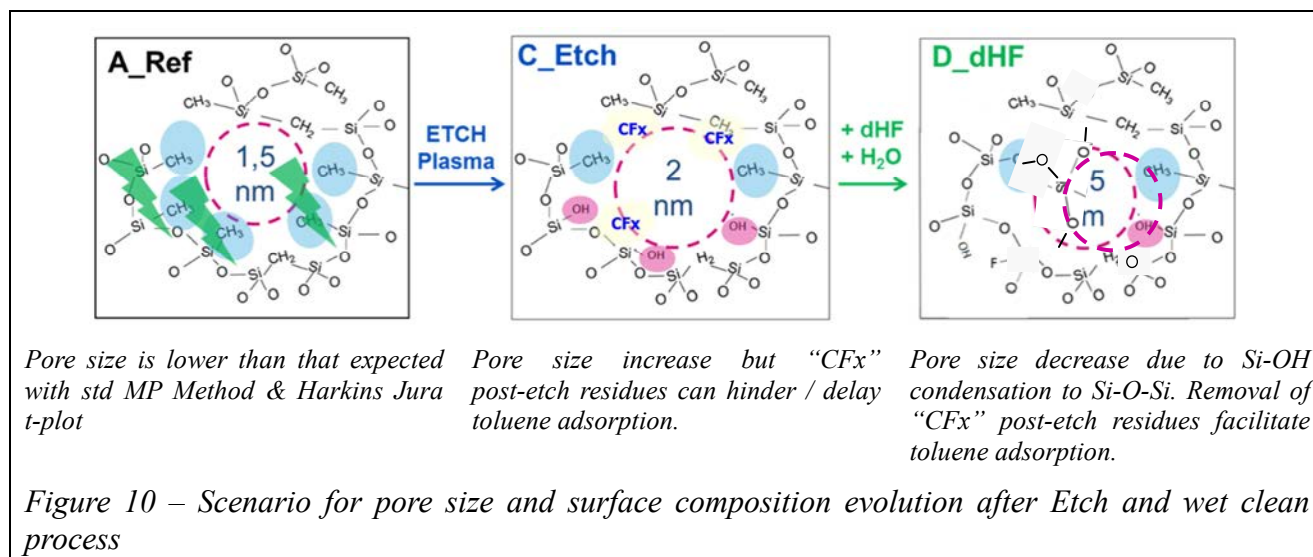


Figure 9 – Illustration of Si/Si distances in presence of Si-OH bonds and in fully reticulated silica network.

As a summary, a global scenario for pore size evolution is proposed in Figure10. Thanks to the contribution of molecular simulation, it was proposed that pore size determined with ellipso-porosimetry by using methanol maybe over-estimated for the as-deposited material. Pore size is slightly increased during etching process, due to carbon depletion, and Si-OH increase in the network. However, due to fluorinated post-etch residues, and the very low affinity of toluene with fluorinated surfaces, toluene adsorption maybe delayed. Then, it was shown that a cleaning chemistry such as diluted organic acid have a poor cleaning efficiency on the low-k material, and

induce no change in composition and porosity. On contrary, more reactive chemistry such as diluted HF is able to slightly etch the material, thus removing post-etch residues and inducing local condensation of Si-O-Si network. Pore size tends to be reduced in comparison with post-etch material, but accessibility to toluene is improved.



Conclusion

Numerical simulations of solvent adsorption on silica and functionalized silica surfaces highlighted solvent affinity variations depending on chemical surface compositions in good correlation with experimental EP measurements and known chemical and physical properties of the pristine and damaged materials. Pore size evaluation and toluene adsorption delay observed after specific treatments that induce small variations in materials structure and composition were found to be well explained thanks to the use of simulated adsorption isotherms on functionalized surfaces. Thus it seems mandatory to take into account the pore surface chemical composition in the determination of pore sizes by ellipso-porosimetry, due to modifications of surface/solvent interactions.

References

- [1] G.Dubois, et al. in Advanced Interconnect for ULSI Technology, Ed. By M.Baklanov (2012) p.1-33.
- [2] V. McGahay, Materials 3, 536–562 (2010)
- [3] M. Darnon, et al., J. Vac. Sci. Technol. B 31, (2013)
- [4] M.Lepinay, et al. proc. of AMC 2013 Conference (2013); ISBN 9781629938257
- [5] M.Lepinay, et al. J. of Porous Materials, 2014, 21, 475-484; DOI: 10.1007/s10934-014-9794-7
- [6] N. Ahner, et al, Solid State Phenomena 01/2009; 145-146
- [7] D.K. Owens, et al., J. Appl. Polym. Sci. **13** (1969) 1741.
- [8] N. Rochat, et al., J. Appl. Phys. **91**, No. 8, (2002) 5029.
- [9] R. Scarazzini, et al. Surf. and Interface Anal. 2014, 46, 213.
- [10] R.Scarazzini, PhD Thesis, Grenoble, France
- [11] M.R. Baklanov, et al. J. Vac. Sci. Technol. B 18(3), 1385 (2000)
- [12] W. Puyrenier, et al., Micro. Mesoporous Mat.. 106 (2007), 40-48.
- [13] M.Lepinay, PhD Thesis, Montpellier, France HAL Id: tel-01093980. /https://tel.archives-ouvertes.fr/tel-01093980
- [14] K.S.W. Sing, Pure Appl. Chem. 57 (1985) 603-619.
- [15] R.S. Mikhail, et al. J. Colloid. Interface Sci., vol. 26, no. 1, pp. 45-61, 1968.

- [16] W.Smith, et al The DL_POLY Classic User Manual, Version 1.0; STFC Daresbury Laboratory, 2010.
- [17] A. Carré, et al. Europhys. Lett. 2008, 82, 17001-17006.
- [18] M.Lepinay et al. *J. Phys. Chem. C* , 2015, 119 (11), 6009–6017.
- [19] M.Lepinay et al, *Micro.Mesoporous Materials*, 2015, v217, p.119-124.
- [20] Q. Y. Tong, U. Gösele, “Semiconductor wafer bonding: science and technology”, Wiley (1999).
- [21] F. Rieutord, J. Eymery, F. Fournel, D. Buttard, R. Oeser, O. Plantevin, H. Moriceau, B. Aspar, *Physical Review B* 63, p. 125408, (2001).
- [22] K.S.W. Sing, *Pure Appl. Chem.* 57 (1985) 603-619.

Rapid Recovery Process of Plasma Damaged Porous Low-K Dielectrics by Wet Surface Modifying Treatment

Akihisa Iwasaki^{1, 2 a}, Ayumi Higuchi¹, Kana Komori¹, Masanobu Sato¹
Els Kesters², Quoc Toan Le² and Frank Holsteyns²

¹ SCREEN Semiconductor Solutions Co., Ltd., 480-1, Takamiya, Hikone, Shiga, 522-0292, Japan

² imec vzw, Kapeldreef 75, 3001 Leuven, Belgium

^aa.iwasaki@screen-spe.eu

Keywords: plasma damage, porous low-k dielectrics, silylation, surface treatment, contact angle

Abstract A rapid repair process of plasma damaged SiCOH in combination with post-etch residue removal has been developed. The carbon depletion layer caused by plasma dry etching was repaired by subsequent surface modifying SAM treatment, which resulted in replenishment of carbon not only on the surface but also a few nm toward the bulk. This repairing technique provides a high-quality hydrophobic surface under conditions of low temperature and short process time. In addition, the SAM layer can be expected to act as an adhesion promotor with metal materials.

Introduction

Porous low-k dielectrics such as Spin-On-Dielectric (SOD) and Plasma-Enhanced Chemical Vapor Deposition (PECVD) porous SiCOH are required to reduce RC delays as integration in semiconductor devices becomes more challenging due to the decreasing feature size of devices. Two main concerns are carbon depletion resulting in low-k dielectric deterioration and polar group formation such as Si-OH in the dielectric layer from both plasma and wet clean processes. The plasma etching process causes surface roughening and densification of the dielectric in the beginning step leading to deposition of fluorocarbon polymer on the sidewall and bottom of the feature. A subsequent post-etch residue clean has to be introduced to remove the polymer in order to provide good adhesion of the following barrier metal deposition. However, the wet cleaned layer becomes hydrophilic, which facilitates unwanted moisture absorption on the surface.

Furthermore, patterning of sub-20 nm features on low-k dielectric suffers from the problems of etch-induced damage [1]. The thickness of the plasma damaged sidewall is a significant proportion of the feature size for narrow lines, which results in RC degradation and lower dielectric break down voltage issues. In a previous study, an approach to restore the damaged low-k was intensively studied with silylating agent such as hexamethyldisilazane (HMDS) and trimethylchlorosilane(TMCS) by either vapor or scCO₂ treatment [2-3]. However, these schemes required adverse conditions, e.g. high temperature, bake and low/high-pressure conditions, in addition to long reaction times for low-k restoration.

In this paper, we focus on the development of a wet cleaning process to restore the low-k dielectric combined with post-etch residue removal and carbon layer recovery. This is accomplished in part via a self-assembled monolayer (SAM) deposition using a formulated surface modification chemistry containing silylating agent.

Experimental

In this study, plasma-damaged low-k and thermal oxide blanket samples were prepared. 200-nm porous low-k films (SiCOH, k=2.4, porosity=20%) were deposited on 300-mm silicon substrates by PECVD, and then the surface was treated by 10 s C₄F₈-based plasma RIE etching. 200-nm thermal oxide control samples were used to compare the contact angle to the plasma-damaged low-k samples. Wet clean processes combined post-etch residue removal with low-k repair were executed in a beaker

set-up (Figure 1). Fluorocarbon polymers on the plasma-treated low-k layer were removed by 10 min exposure to a formulated chemistry at 50°C prior to application of silylating chemistry. Two types of formulated surface modification silylating chemistries (LKT-1 and LKT-2) were evaluated with application times of 10, 20, 30, 60 and 120 s at room temperature.

Carbon depletion, replenishment and elemental compositions into the porous low-k dielectric were analyzed by Fourier Transform Infrared spectroscopy (FTIR, JASCO FTIR-4100) and Transmission Electron Microscope - Electron Energy Loss Spectroscopy (TEM-EELS). The thickness of the SAM layer and surface morphology on Pt/SAM/plasma-damaged low-k were observed by bright field TEM images. The surface characteristics of plasma-damaged low-k were examined by Contact Angle measurement (CA, KYOWA DM701R).

Results and Discussion

FTIR was used to characterize chemical changes in the porous low-k films after the low-k repair process. Figure 2 shows transmission FTIR spectra with three different samples, (a) undamaged low-k, (b) damaged low-k, and (c) damaged low-k after repairing process. The result shows increases in the C-H asymmetric stretching at 2927 cm^{-1} and C-H symmetric stretching at 2880 cm^{-1} from CH_2 groups, indicating that SAM-comprising carbon chains were added to the film by reaction with the reactive surface modifying groups in LKTs. Other CH_3 peaks could not be assigned.

TEM-EELS was performed to investigate whether the added SAM molecules were uniformly distributed within the porous low-k film. Figure 3 (a) shows a typical example of TEM-EELS depth profile of carbon, oxygen and silicon for a plasma-damaged low-k sample. A 5-nm region of significant lower carbon concentration than bulk SiCOH is clearly observed under the low-k. Figure 3 (b) shows carbon depth profiles of three different damaged low-k samples: no repair, repair with 1 min LKT-1 and repair with 1 min LKT-2. LKT-1 showed slight improvement in the degree of carbon replenishment, while LKT-2 showed more carbon replenishment and sufficient carbon intensity than LKT-1. In addition, there was no change of the carbon content in the bulk low-k area, which indicates complete repair of the damaged layer by SAM and no penetration or residual SAM within the bulk layer.

Bright field TEM images of these three samples are presented in Figure 4. SAMs with thickness of 1-2 were observed in both LKT-1 and LKT-2. This layer was not observed for the no repair sample. Moreover the surface morphology on Pt was very smooth and densified on both LKT-1 and LKT-2 as compared to the untreated damaged low-k sample.

The hydrophobicity of surface damage low-k film was evaluated. Figure 5 shows water contact angle on SiCOH damaged low-k film as a function of repair process time applied with both LKT chemistries. LKT-1 showed a gradual increase in the contact angle with increase in the repair process time due to the reformation of methyl bonds. It increases from a hydrophilic state 12° for damaged low-k film (applied by 10 min formulated chemistry) up to 30° for one minute repair process time, indicating that the surface is partially recovered. In contrast, contact angle after LKT-2 treatment can be obtained higher than 80° of hydrophobicity in a quick 10 s process time and this value is almost saturated even after extending the process time to two minutes. The stable hydrophobicity was found to increase rapidly with 10 s repair time at room temperature, which enables a low-cost process for mass-production.

Conclusion

A rapid repair process of plasma damaged SiCOH in combination with post-etch residue removal has been developed. The carbon depletion layer caused by removal of the fluorocarbon-containing plasma was repaired by subsequent surface modifying SAM treatment, which resulted in replenishment of carbon not only on the surface but also a few nm toward the bulk. This repairing technique provides a high-quality hydrophobic surface under conditions of low temperature and short process time. In addition, the SAM layer can be expected to act as an adhesion promotor with metal materials.

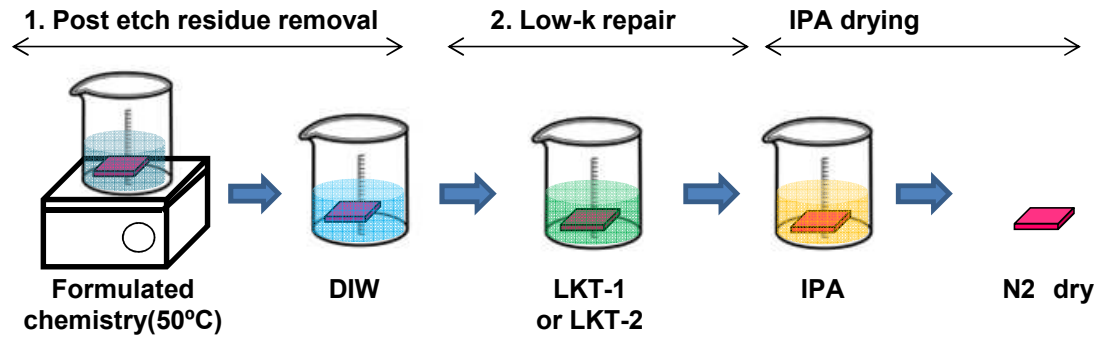


Figure 1: Schematic process sequence for combined post-etch residue removal and low-k repair

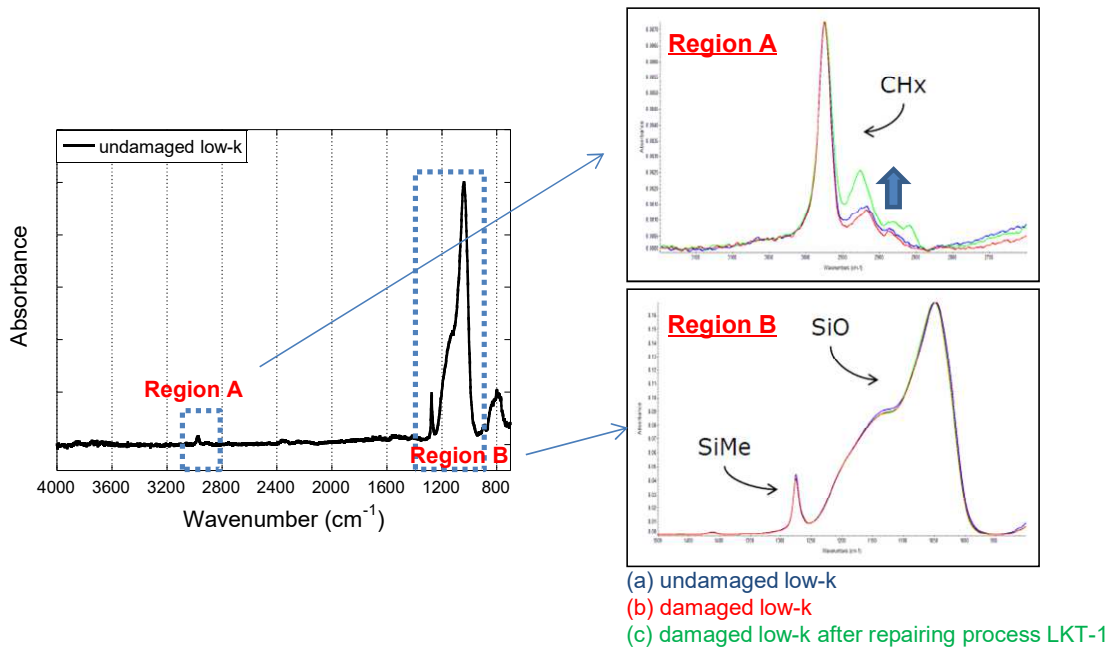


Figure 2: FTIR spectra of (a) undamaged low-k, (b) damaged low-k and (c) damaged low-k after repairing process

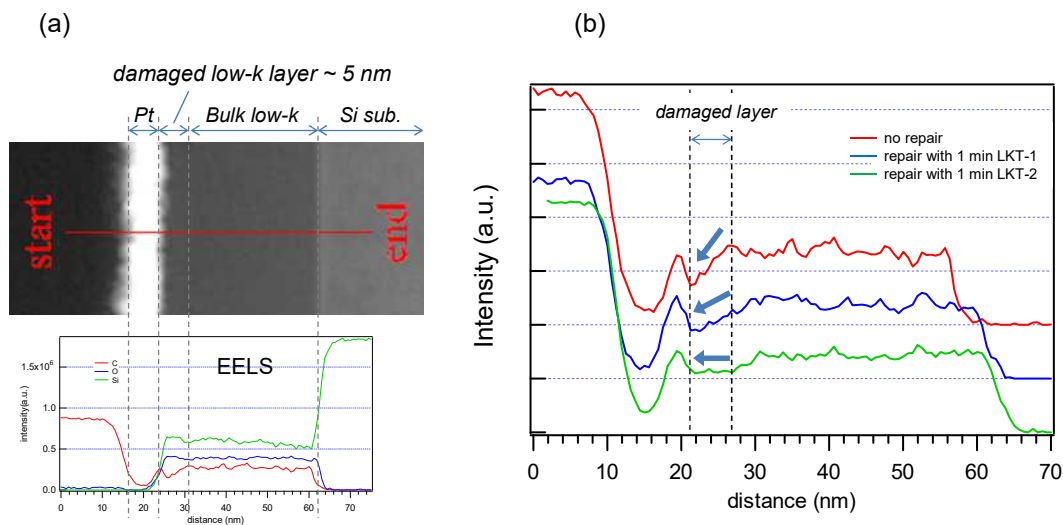


Figure 3: (a) TEM-EELS depth profile of carbon, oxygen and silicon for a plasma-damaged low-k sample, (b) Carbon depth profile for sample 1(no repair), sample 2(repair with 1 min LKT-1) and sample 3(repair with 1 min LKT-2)

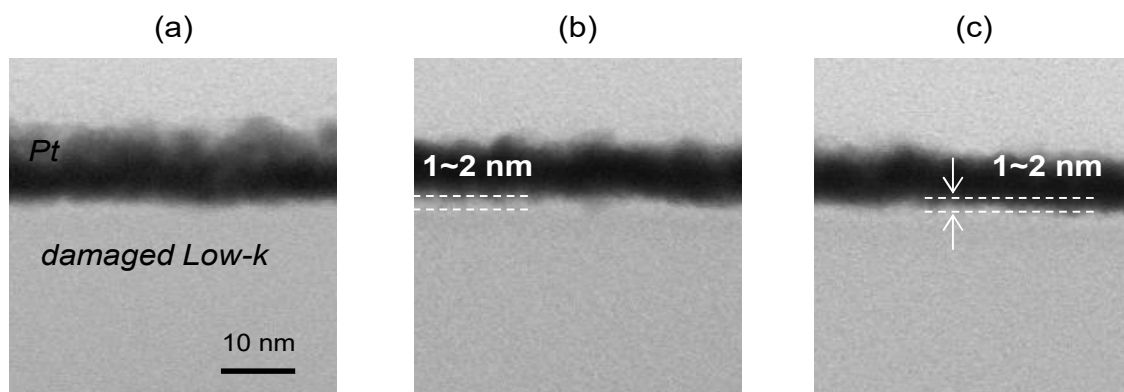


Figure 4: Bright Field TEM image of three damaged low-k samples with Pt deposition.(a) no repair, (b) repair with 1 min LKT-1 and (c) repair with 1 min LKT-2

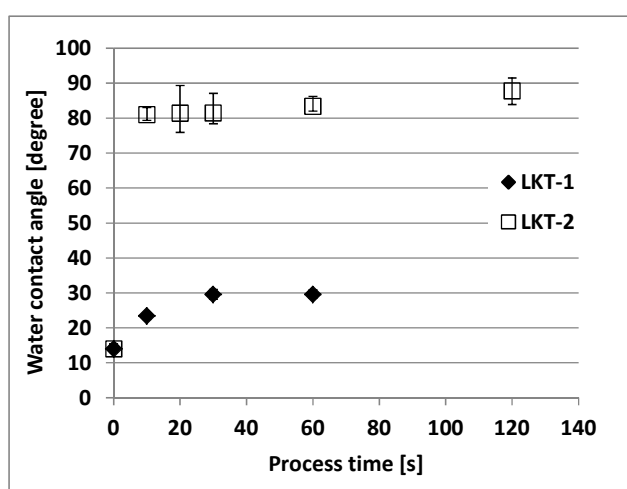


Figure 5: Water contact angle on SiCOH damaged low-k film as function of repair process time

References

- [1] Kanwal Jit Singh, Solid State Phenom. , Vol. 195 (2013), pp. 103-106.
- [2] Y. S. Mor, Journal of Vacuum Science & Technology B 20, 1334 (2002).
- [3] Jae Mok Jung: Microelectronic Engineering 87 (2010) 1680-1684.

Characterization of Etch Residues Generated on Damascene Structures

Q. T. Le^{1,a}, E. Kesters¹, I. Hofliijk¹, T. Conard¹, M. Shen², S. Braun²,
Y. Burk², and F. Holsteyns¹

¹ IMEC vzw, Kapeldreef 75, 3001 Leuven, Belgium

² BASF, Ludwigshafen, Germany

^a QuocToan.Le@imec.be

Keywords: Post-etch residues, Low-k dielectrics, Interconnects, Angle-resolved XPS.

Abstract. For patterned TiN/silicon oxide/low-k dielectric stack, fluorinated etch residues were detected on the TiN surface, the dielectric sidewall and bottom, regardless of the low-*k* material used in the stack. XPS results showed that they consisted of polymer-based (CF_x) residues deposited on trench sidewall and bottom, and metal-based (TiF_x) residues mainly deposited on top surface. In terms of post-etch residue removal, the efficiency of various wet clean solutions can be clearly distinguished for CF_x, and TiF_x using the same patterned porous low-*k* stack. These results also demonstrate that the removal of both TiF_x and CF_x residues generated during the plasma is possible in one step with optimized chemical and process.

Introduction

Porous dielectrics have been commonly used in micro- and nanotechnologies since the past decade. The dielectric layer is typically patterned by dry etching, through a photoresist or metal hard mask, using a fluorocarbon-containing plasma. A good balance between the etch of the dielectrics and the polymerization results in a vertical etch profile and also allows the deposition of a polymer film to passivate the sidewalls thereby minimizing the dielectric damage [1,2]. Prior to the deposition of subsequent materials (barrier layer, metal), this polymer must be removed to achieve good adhesion between the metal layer and dielectric sidewall, and good coverage.

This study focused on the characterization of the residues generated during the plasma patterning of a damascene structure of 45 nm $\frac{1}{2}$ pitch. Furthermore, a comparison was made for various wet cleans using patterned 45 nm $\frac{1}{2}$ pitch porous dielectrics as a test vehicle.

Materials and methods

The porous low-*k* dielectrics used in this study were CVD organosilicate glass (OSG) materials with the target *k*-values of 2.4 and 2.2, and porosities of 20 and 35%, respectively.

Typically, the stack of the 45 nm $\frac{1}{2}$ pitch test structure consists, from bottom to top, of Si substrate/OSG (80 nm)/oxide HM (30 nm)/TiN (25 nm). The TiN layer was first etched through a photoresist (PR) mask using a HBr/Cl₂ plasma. After the BARC and PR strip, the oxide HM and OSG etch was performed using a C₄F₈/CF₄-based plasma. The SEM image shown in Figure 1 was obtained after the dry plasma etch followed by the wet clean process, where the TiN layer was removed during the wet clean. All dies in the same wafer are fully covered with the same type of 45 nm $\frac{1}{2}$ pitch structure.

Two methods, which are commonly used for blanket layer characterization were applied for characterization of the patterned structure used in this study, including X-ray photoelectron spectroscopy (XPS) and Fourier-Transform Infrared spectroscopy (FTIR).

XPS measurements were carried out using a Thermo VG Scientific Theta 300 system equipped with an Al K α source (1486.6 eV) and simultaneous detection of photoelectrons at take-off angles (TOA) between 22 and 78 degrees. Take-off angle is defined as the angle between the surface normal and the axis of the analyzer lens system. Regarding the analysis mode, all the samples were analyzed following the perpendicular direction, i.e. the direction of the low-*k* lines and trenches

were perpendicular to the beam toward the XPS analyzer. FTIR (Thermo Fisher Scientific) spectra were recorded within the range of 400 to 4000 cm^{-1} using transmission mode with a resolution better than 2 cm^{-1} and averaged over 200 scans.

Cleaning experiments were conducted in a beaker set-up under constant agitation using a magnetic stirrer. HF 0.2 vol.% was used at room temperature. The cleaning experiments with tetramethylammonium hydroxide (TMAH): H_2O_2 : H_2O mixture (the concentrations of TMAH and H_2O_2 in the mixture are 1 and 5 vol.%, respectively), and the formulated mixture from BASF (FOTOPUR R, aqueous mixture, pH \sim 7-8) were performed at 50 and 55 $^\circ\text{C}$, respectively. The post-clean samples were then rinsed with DI water (2 min) and IPA (2 min) and finally dried with a nitrogen gun (1 min).

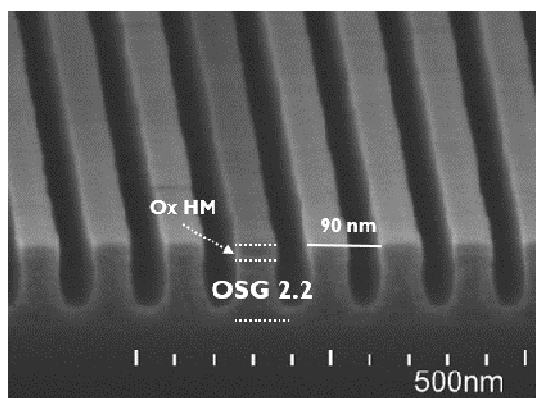


Figure 1: SEM image of the 45 nm $\frac{1}{2}$ test structure. The image was taken after the plasma etch followed by the wet clean using FOTOPUR R where the TiN hardmask layer was removed.

Experimental Results

Fluorinated etch residues were detected on the TiN surface, the dielectric sidewall and bottom, regardless of the low- k material used in the stack. For instance, the XPS F1s core-level spectra collected for the patterned OSG 2.2 consisted of two main components: the peak centered at \sim 684.6 eV corresponds to F-Ti bonds and the peak at 688.4 eV can be assigned to C-F bonds. For this damascene structure where the aspect ratio is \sim 1.8-1.95, the maximum take-off angle of photoelectrons which can escape from the trench bottom is estimated to be about 27 degrees. In other terms, the signals collected at TOA's larger than 27 deg. exclusively come from the top surface and sidewall of the low- k structure. The substantial change of the intensity of F-Ti/F-C peak ratio measured at 78 deg. (more surface sensitive) compared to the one at 44 deg. (both TiN surface and dielectric sidewall) indicates that Titanium fluoride-containing residues are exclusively detected at the top surface. In contrast to the F1s spectra, very similar Ti2p spectra were recorded regardless of the TOA's within the range of 22-78 deg., which in turn confirms the previous statement. The binding energies and the shape of the Ti2p spectra suggest that several types of Ti compounds are present at the surface, including TiO_2 , TiN, and TiFx [3,4]. The presence of the latter is strongly supported by the observed F1s spectrum as discussed above.

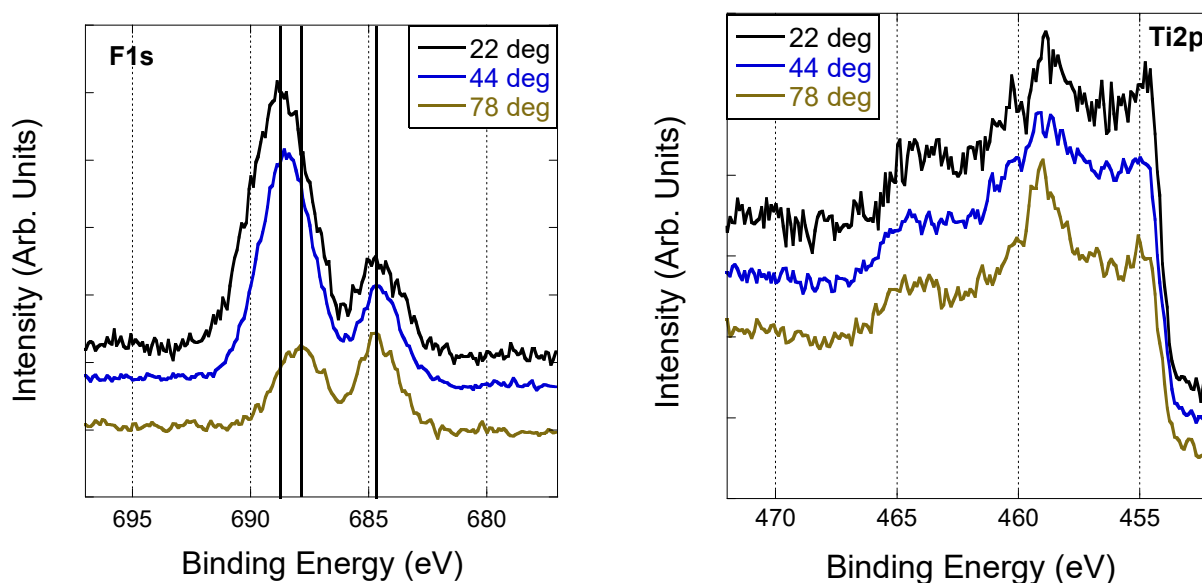


Figure 2: XPS F1s and Ti2p core-level spectra recorded after plasma patterning at various take-off angles,.

The presence of polymer residues at the dielectric sidewall was also indirectly detected using transmission FTIR. Figure 3 shows the *differential* transmission FTIR spectrum recorded for a patterned oxidized OSG film. The C=O and OH functional groups detected were the results of the polymer oxidation, where the C-C backbone was first fragmented and then oxidized in oxygen atmosphere.

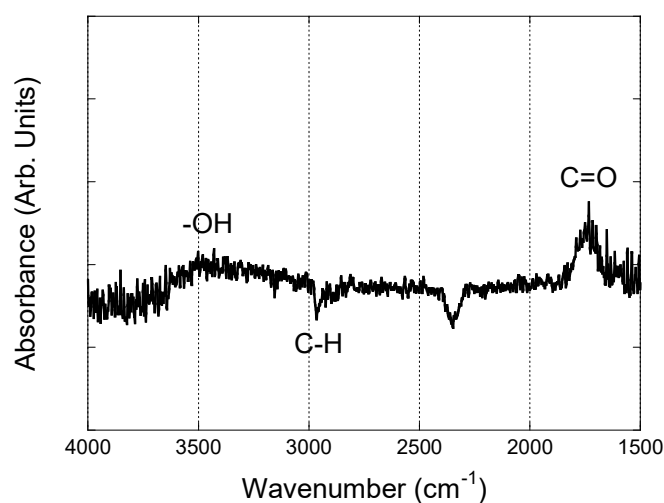


Figure 3: Differential transmission FTIR spectrum recorded for patterned oxidized OSG 2.2.

The efficiency of the removal/dissolution of CF_x and TiF_x by the wet chemistries can be clearly demonstrated using the patterned test structure. As shown in Figure 4, for both OSG 2.2 and OSG 2.4 stacks, dilute HF only showed a limited removal of fluorine-containing residues generated on the patterned structure. However, while dilute HF was relatively inefficient for removal of the fluorine-containing polymer (CF_x), it was significantly more efficient for removal of TiF_x-type residues (Figure 4c, OSG 2.4). Examination of the Ti2p spectra (Figure 4b and Figure 4d) suggests that the patterned TiN (after the plasma process) is covered by a TiO₂ layer at the surface. This TiO₂ layer is much thicker for the OSG 2.4 stack (Figure 4d), where the intensity of the component centered at ~455 eV (Ti-O) was substantially lower than the one at ~459 eV (Ti-N). The Ti2p spectrum recorded after the dilute HF clean indicates that the TiO₂ surface layer was partially removed by HF solution.

For both stacks, the TMAH:H₂O₂ clean resulted in a complete removal of the TiN layer as well as the TiFx residues. This mixture also showed relatively good dissolution of CFx polymer. Among the three chemical mixtures shown in Figures 4, the formulated mixture was most efficient for the dissolution of both CFx and TiFx residues. The Ti-F component in the F1s spectrum completely disappeared and the F-C component corresponding to F-C bonds was substantially decreased in intensity, where the concentration of fluorine changed from 22.4 to 2.7 at.%, and from 24.0 to 1.6 at.% after cleaning using the formulated mixture for the OSG 2.2 and OSG 2.4, respectively. The results shown in this paper also indirectly demonstrate that the removal of CFx polymer generated during the plasma is possible in one step with optimized chemical and process.

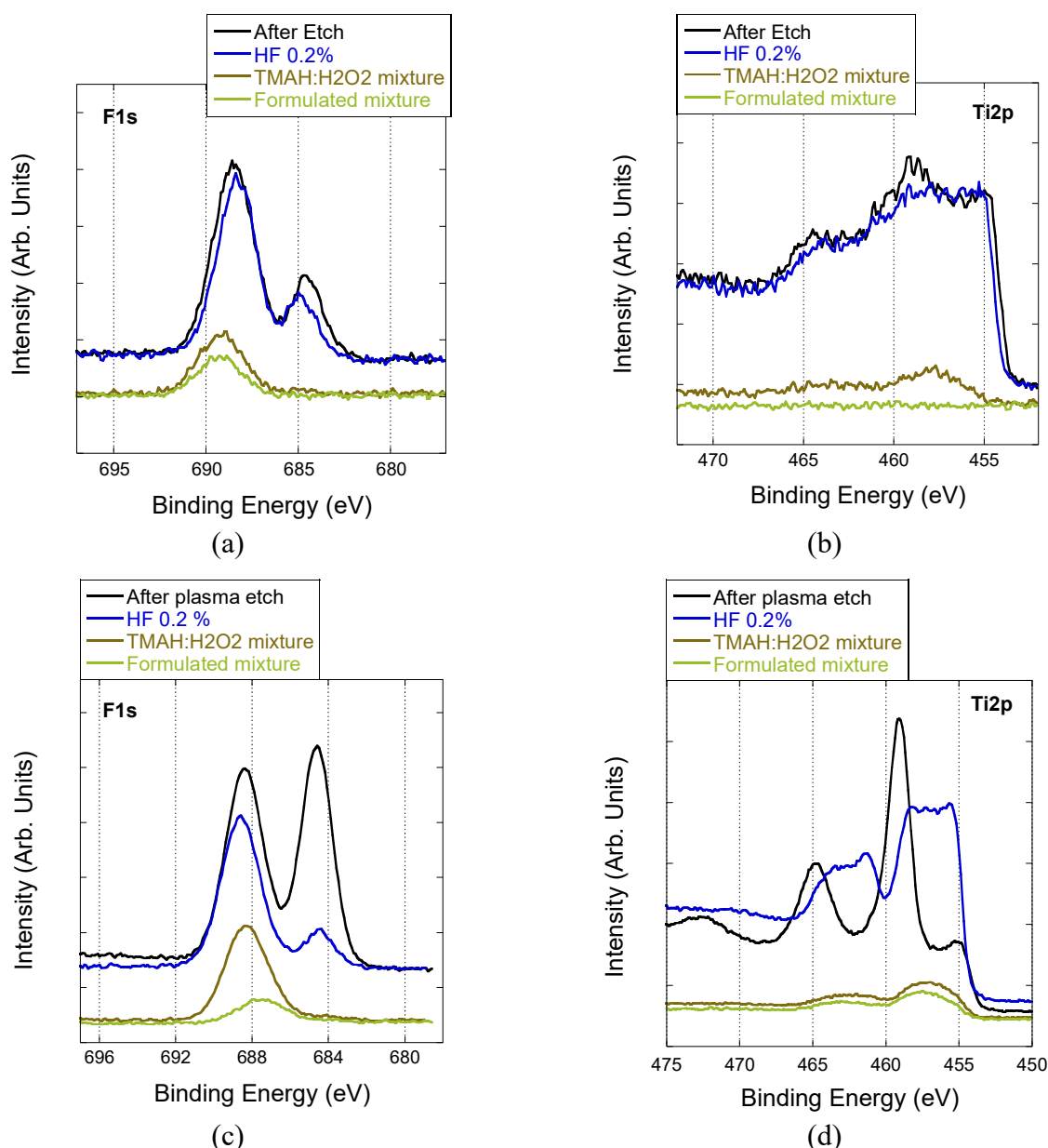


Figure 4: XPS Ti2p and F1s core-level spectra recorded after plasma etch and subsequent wet cleans for the 45 $\frac{1}{2}$ pitch OSG 2.2 stack [(a) and (b)] and OSG 2.4 stack [(c) and (d)].

Conclusion

The results shown and discussed in this paper demonstrate that the use of a relevant patterned test structure and its characterization represents an appropriate approach for optimization of the etch and cleaning processes in BEOL. With regard to the residues formed during, and after, a fluorocarbon-based dry etch plasma process on a patterned low-k/TiN hardmask stack, XPS characterization showed that they are at least of two types: polymer-based (CFx) deposited on trench sidewall and

bottom, and metal-based (TiFx) mainly deposited on top surface. For the same plasma process, the concentration of these residues appeared to depend on the type of the low- k material used in the stack. In terms of post-etch residue removal, the efficiency of various wet clean solutions can be clearly distinguished for polymer residues, CFx, and metal-containing residues, TiFx, using the same patterned porous low- k stack. These results also demonstrate that the removal of both TiFx and CFx residues generated during the plasma is possible in one step with optimized chemical and process.

Acknowledgement

The authors wish to thank S. Decoster (Imec) and D. Parnell (TEL) for their support and fruitful discussions on plasma treatment experiments.

References

- [1] H. Shi et al., “Plasma Processing of Low- k Dielectrics”, in *Advanced Interconnects for ULSI Technology*, Ed. M. R. Baklanov, P. S. Ho, and E. Zschech, John Wiley & Sons Ltd. (2012) Doi: 10.1002/9781119963677.
- [2] M. R. Baklanov, J.-F. de Marneffe, D. Shamiryan, A. M. Urbanowicz, H. Shi, T. V. Rakhimova, H. Huang, and P. S. Ho, *J. Appl. Phys.*, **113**, 041101 (2013).
- [3] P. J. Matsuo, T. E. F. M. Standaert, S. D. Allen, G. S. Oehrlein, and T. J. Dalton, *J. Vac. Sci. Technol. B* 17, 1435 (1999).
- [4] Q. T. Le et al., *ECS J. Solid-State Sci. Technol.* 5, N5 (2016).

Evaluation of Post Etch Residue Cleaning Solutions for the Removal of Tin Hardmask after Dry Etch of Low-K Dielectric Materials on 45 nm Pitch Interconnects

Makonnen Payne¹, Steve Lippy¹, Ruben Lieten^{2,a}, Els Kesters³,
Quoc T. Le³, Gayle Murdoch³, Victor V. Gonzalez³, Frank Holsteys³

¹ Entegris, Inc., 7 Commerce Drive, Danbury CT 06810, US

² Entegris, GmbH, Hugo-Junkers-Ring 5, Gebäude 107/W, 01109 Dresden, Germany

³ imec, Kapeldreef 75, 3001 Leuven, Belgium

^aRuben.Lieten@entegris.com

Keywords: PERR, interconnects, copper, tungsten, corrosion, BEOL

Abstract. In the BEOL, as interconnect dimensions shrink and novel materials are used, it has become increasingly difficult for traditional PERR removal chemicals to meet the evolving material compatibility requirements. As a result, formulated cleans that specifically target these unique challenges are required. Two formulated BEOL cleans were evaluated on blanket and patterned wafer coupons for their ability to wet etch titanium nitride (TiN) and clean post-plasma etch residue, while remaining compatible to interconnect metals (Cu and W) and low-k dielectric ($k = 2.4$). Both, showed an improvement in material compatibility relative to dilute HF, while simultaneously being able to remove the TiN hardmask and post-etch residue, leading > 90% yield on test structures of varying sizes.

Introduction

In the back-end of line (BEOL), dielectric materials are patterned by a dry etch process using a fluorocarbon based plasma, which leads to fluorinated polymer deposition on the dielectric sidewalls [1, 2, 3]. Prior to subsequent metallization, this polymer needs to be removed in order to achieve good adhesion between the metallization stack and dielectric and to prevent voiding. The required post-etch residue removal (PERR) wet cleaning step needs to be compatible with a variety of new materials that are introduced in advanced interconnect technology [4]. Furthermore, removal of the TiN hard mask (HM) with the same wet cleaning step may be desired. Removal of the TiN HM relaxes the aspect ratio and makes subsequent metallization steps more straightforward. Formulated cleans have been developed to address the complexity of having exposed dielectric, barrier, liner and line materials and to have as tunable TiN removal rate. In this work we evaluate two types of formulated PERR cleans from Entegris, Inc.: the first with compatibility to tungsten and the second with compatibility to copper for advanced interconnects, more specifically for the 10 nm technology node and beyond.

Scope

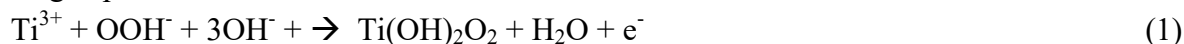
We will discuss the performance of two different formulated cleans that have been developed by Entegris, Inc. in order to effectively remove post-etch residues, have compatibility with interconnect level materials, a tunable TiN hard mask removal rate and acceptable cost of ownership. The first cleaner that will be evaluated, named TitanKlean[®] 10-X4 (TK10-X4), targets metallization level M1, where tungsten (W) is targeted as the metal of choice. The second cleaner to be evaluated, named TitanKlean[®] 9C (TK9C), targets metallization levels starting from M2 and beyond, where copper (Cu) is typically used. Although developed for the ≤ 10 nm technology nodes, the formulations are evaluated here on blanket films for material compatibility and on 45 nm $\frac{1}{2}$ pitch and 22 nm $\frac{1}{2}$ pitch structures for evaluating residue removal and electrical performance. A schematic overview of BEOL interconnect test structures used is shown in Figure 1

Approach

These formulated cleans are designed to have a high TiN etch rate, which is achieved by an oxidation-dissolution mechanism, where in an aqueous medium, we first oxidize the TiN via the general scheme:



More specifically, in the case of TK9C, which is an alkaline chemistry diluted with the oxidizing agent hydrogen peroxide, the TiN removal mechanism is as follows:



The HTiO^{3-} formed in step (2) is soluble in water, thus the TiN is removed. The rate of the removal is dependent on both the OH^- and hydrogen peroxide concentrations. In the case of TK10-X4, an acidic formulation, the oxidizing agent is contained in the formulation and the subsequently formed titanium oxide will, depending on the reaction medium, be soluble or will need to be further functionalized with components in the formulation to make the oxidized Ti species soluble in the reaction medium or in the rinse.

The selectivity of the formulations to the exposed contact metals W and Cu is tuned by taking advantage of corrosion behavior of the two materials relative to pH., where based on trends indicated on their respective Pourbaix diagrams, W is passivated in the acidic pH regime while Cu is passivated in the alkaline regime. Modulating the concentration of the other components in the formulations and by the use of corrosion inhibitors we further tune the selectivity of the formulations being evaluated here. Hence, TK10-X4 (pH 0.5-2) is targeted toward W based BEOL applications and TK9C (pH >13, undiluted) is targeted toward Cu interconnect levels.

Experimental

Material compatibility. Blanket and patterned wafer testing for TK10-X4 was performed on the SCREEN SU3200, a 300 mm single wafer tool, at 60 °C at a flow rate of 1.5 l/min.,. For TK9C, the concentrate was mixed with 30% H_2O_2 at a dilution ratio of 1:9 by mass to a total mass of 250 g and heated to 50 °C in a beaker with agitation (300 rpm). In both cases, a two-minute deionized water (DIW) rinse, three-minute IPA rinse and N_2 blow dry is performed after exposure to the process chemistry. The thickness of the tungsten and electroplated copper blanket films, before and after the experiments, was measured by calibrated XRF. Spectroscopic ellipsometry was used for measuring the thickness of the low-k material and TiN. The low-k material used in this work was an orthosilicate glass (OSG) type of material with a target k-value of 2.4 (~20% open porosity). The film etch rates were compared to a dilute aqueous hydrofluoric acid (dHF) solution with an HF concentration of 0.05% by weight. The dHF mixture was processed in a beaker at 25 °C for comparison to TK9C and TK10-X4.

Cleaning performance. To assess the performance on patterned structures, a 45 nm $\frac{1}{2}$ pitch test structure was used. Coupons were immersed in TitanKlean® 10-X4 at 60 °C for two minutes in a beaker with agitation (300 rpm), followed by two minutes DIW overflow rinse, three minutes IPA rinse and N_2 dry. The cleaning performance was then evaluated by SEM.

Electrical performance. The electrical performance and yield for TK10-X4 was evaluated using a 45 nm $\frac{1}{2}$ pitch test structure with OSG 2.55 dielectric, where the via contact and meander line resistances were measured. The electrical performance and yield for TK9C was evaluated at two different hydrogen peroxide dilutions using a 22 nm $\frac{1}{2}$ pitch test structure, where Cu line thicknesses varied from 22 nm to 32 nm.

Results

Material compatibility. The results of the blanket film etch rates are summarized in Table I for TK10-X4 and in Table II for TK9C; both formulations are compared to 0.05% (w/w) hydrofluoric

acid (dHF) solution, which is often used as a PERR chemistry at the BEOL. In the case of TK10-X4, it is clear that the W etch rate from TK10-X4 is similar to that of the dHF chemistry tested, where the etch rates were 0.12 nm/min and 0.09 nm/min, respectively. However, the etch rate of the low-k dielectric film in the dHF mixture is approximately 3 times that of etch rate in TK10-X4. Conversely, the etch rate of TiN in the dHF mixture was two orders of magnitude less than that of the etch rate in TK10-X4. In the case of TK9C compared to the dHF process, the compatibility of the chemistries with Cu and the OSG film are similar, however like the TK10-X1 case, there is a large disparity in the etch rates of TiN, where dHF had an etch rate of 0.7 nm/min, while the hydrogen peroxide diluted TK9C had an etch rate of 12.9 nm/min.

Cleaning performance. A cross-section SEM image before and after cleaning with TK10-X4 is shown in Figure 2. Before cleaning, the TiN hard mask is visible on top of the low-k material (Figure 2a). After cleaning, the TiN is removed (Figure 2b), with no residue evident in the cross section (b) and top view (c) images.

Electrical performance. In the case of TK10-X4, the electrical yield is 98% for 45 nm vias (Figure 3a) and 45 nm wide and 2 cm long meander lines (Figure 3b). The electrical performance of two different peroxide dilutions of TK9C was evaluated against an unprocessed wafer (Figure 4). It was determined that as the feature size decreased, the need for a chemistry increased, where on the 32 nm lines of each wafer tested had parity performance. However, the yield for the 22 nm lines (the smallest feature tested) showed 90% yield for the TK9C processed wafers as opposed to a 50% yield for the unprocessed wafer. Conceivably, this is result of the overall amount of the residue not changing with feature size, but becoming a more significant hindrance to electrical performance as feature sizes shrink. Extrapolating further, based on the slight difference in yield observed on the 22 nm and 23 nm lines when comparing the 1:3 to the 1:9 dilution, there exists a potential sensitivity to peroxide dilution as the feature sizes shrink. Further testing, with a larger sample set, additional hydrogen peroxide dilutions or with smaller features, would be necessary to understand the significance of these differences.

Summary

The performance of formulated PERR cleaners, TitanKlean[®] 10 and TitanKlean[®] 9, developed for < 10 nm interconnects has been evaluated. The solutions were specifically developed for W and Cu compatibility, respectively. They show excellent compatibility to OSG 2.4, excellent residue removal, as well as tunable TiN hardmask removal. Electrical evaluation of both formulations show yield > 90% on the structures tested, a significant improvement over unprocessed wafers.

Table I: Overview of etch rates for TitanKlean[®] 10-X4 at 60 °C compared to 0.05% (w/w) hydrofluoric acid at 25 °C

Film Type	Etch Rate (nm/min)	
	0.05% HF	TK10-X4
Plasma-exposed W	0.09	0.12
Plasma-exposed OSG 2.4	0.27	0.09
TiN	0.7	19.7

Table II: Overview of etch rates for TitanKlean[®] 9C at 50 °C compared to 0.05% (w/w) hydrofluoric acid at 25 °C

Film Type	Etch Rate (nm/min)	
	0.05% HF	TK9
Plasma-exposed Cu	0.2	<0.1
Plasma-exposed OSG 2.4	0.3	0.4
TiN	0.7	12.9

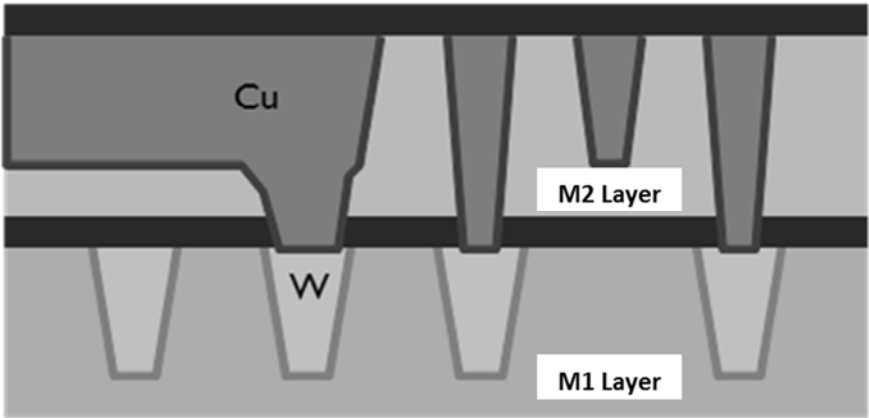


Figure 1: Schematic overview of a BEOL interconnect test structures used for N10 node (M1 and M2 levels). Schematics show the test structure after dry etching, PERR cleaning, metallization, CMP and capping.

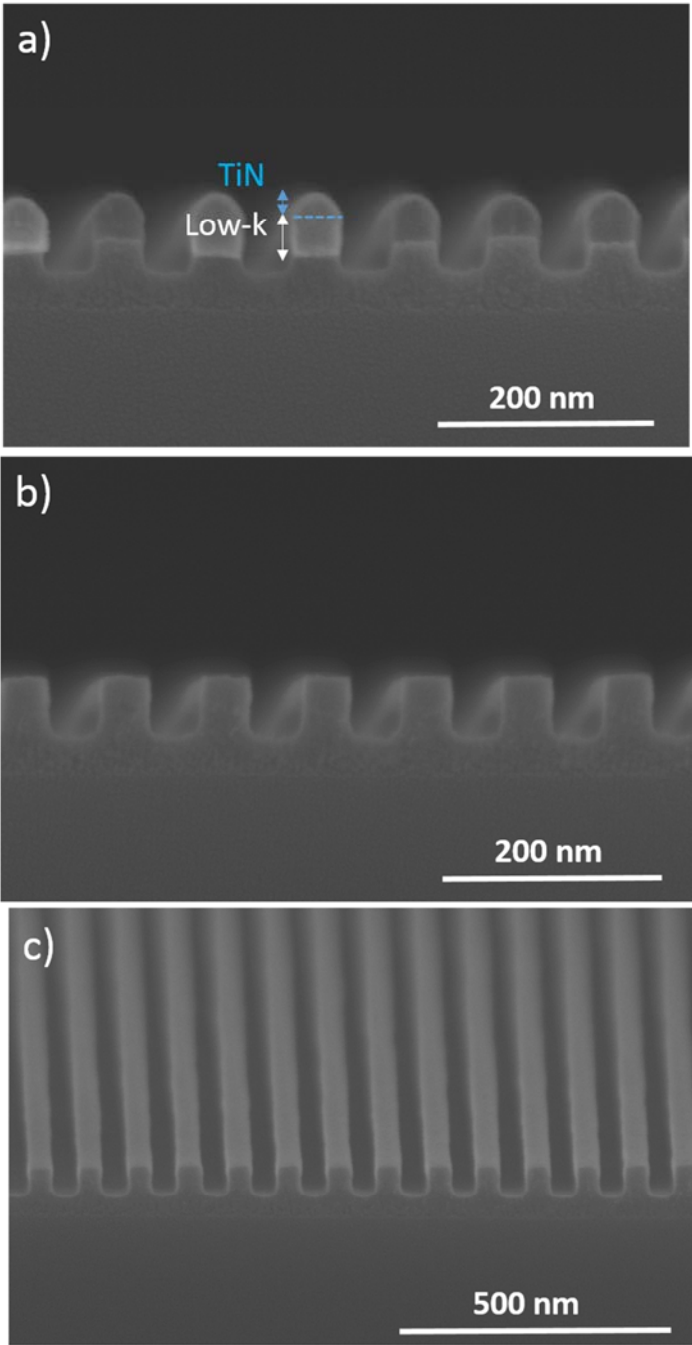


Figure 2: X-section SEM image of a) 90 nm pitch patterned wafer with TiN hard mask and low-k before cleaning; b) after cleaning and c) after cleaning (top view).

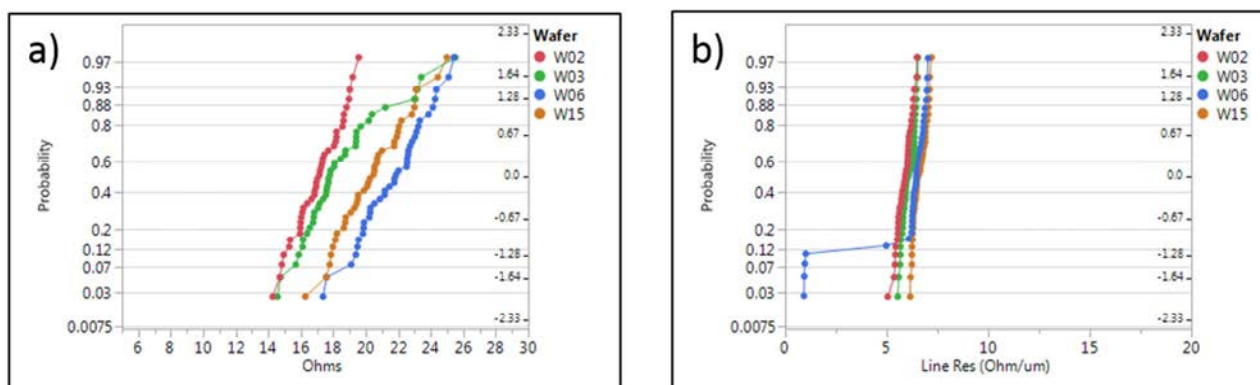


Figure 3: Electrical results for TitanKlean® 10-X4 using a 90 nm pitch test structure, highlighting a) via contact resistance and b) meander line resistance. Four wafers were processed with the same conditions.

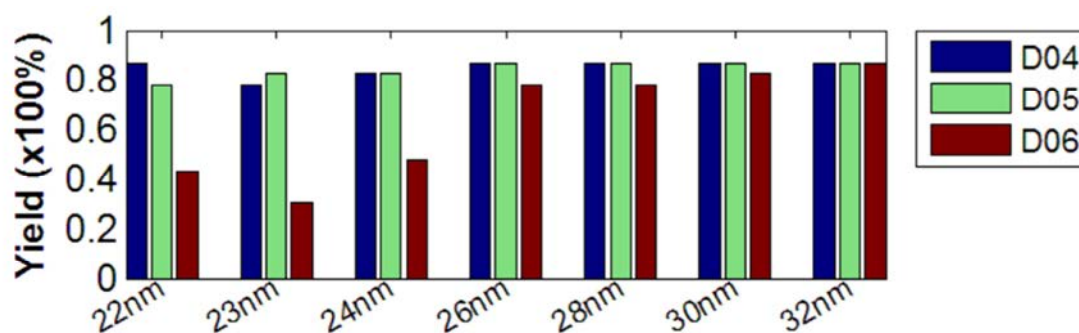


Figure 4: Electrical results for TitanKlean® 9C using a 45nm pitch test structure with CD lines of 22 nm and more. Significant yield improvement for D04 (TitanKlean® 9C:H₂O₂ 1:3, 50 °C, two minutes) and D05 (TitanKlean® 9C:H₂O₂ 1:9, 50 °C, two minutes) vs. no clean D06 (no clean): 90% vs. 50% for CD lines of 22 nm.

References

- [1] Y. Furukawa et al., Microelectron. Eng., 70, 267 (2003).
- [2] Q. T. Le et al., J. Electrochem. Soc. 159, H208 (2012).
- [3] T. Mukherjee et al., ECS Solid-St. Lett. 2, N11-N14 (2013).
- [4] E. Kesters et al., Solid State Phenomena, 219, 201 (2015).
- [5] Barnes, J. et al, US Application No. 20150027978 A1

Optimization of Cu/Low-k Dual Damascene Post-Etch Residue and TiN Hard Mask Removal

Alexander Kabansky^{1, a}, Glenn Westwood^{2, b}, Samantha Tan¹,
Frederic Kovacs¹, David Lou¹, Joe Han¹, Gerardo Delgadino¹
and H. W. Chang¹

¹ Lam Research Corporation, 4540 Cushing Parkway, Fremont, CA 94358, USA

² Avantor Performance Materials, 1904 J.T. Baker Way, Phillipsburg, NJ 08865, USA

^aalexander.kabansky@lamresearch.com

^bglenn.westwood@avantormaterials.com

Keywords: BEOL, dual damascene, vias, post-etch residue, wet clean, TiN hard mask removal

Abstract. For advanced technology nodes TiN hard mask integration into Cu/low-k via/trench DD process requires the mask to be fully stripped after DD etching. The one-step H₂O₂ containing wet chemical clean aiming to removing TiN mask often failed to simultaneously clean etch residue. We developed more reliable two-step wet chemical process combining a solvent-based post-etch residue clean followed by a solvent/H₂O₂ mixture strip for TiN mask removal. Bath lifetime optimization was also demonstrated.

Introduction

Copper (Cu) interconnect process integration for the 14 nm and beyond technology nodes requires post-etch residue (PER) removal and complete TiN hard mask (HM) strip. Wet chemical cleaning where hydrogen peroxide (H₂O₂) based TiN HM wet strip is performed after low-k via plasma etching down to SiCN etch stop followed by Cu open and PER wet clean is an option. The industry desires to avoid this complicated “dry-wet-dry-wet” approach by developing a mixture of a solvent-based PER remover with H₂O₂ to deliver a simple solution: residue clean and TiN strip at the same time after via fully etched down to Cu. Wet chemistry selection and process optimization are both critical. The requirements for wet chemistry include an effective removal of PER from high and low aspect ratio (AR) dual damascene features, effective strip of the TiN HM, and compatibility with low-k, Cu and other related materials. However, it is difficult to achieve all of them together and maintain reasonable chemical bath life. In this paper, we present another wet cleaning approach and our methodology for BEOL wet chemical characterization and clean process optimization for PER and TiN HM removal.

Experimental

The test vehicle for wet clean experiments contained a multilayer stack, Cu/SiCN/low-k (~2.5), with a SiO₂/TiN HM on top. The trench patterned HM was opened in Lam's Kiyo FXTM etcher followed by forming via patterned trilayer. The all-in-one coupon-based etch process was performed in Lam's Flex FLTM etcher to deliver ~20 nm via/trench dual damascene (DD) structures with ~6:1 AR vias and ~4:1 AR trenches along with other features used for wet clean study. The process was further stressed to generate heavy residue for evaluating the capability of different wet clean solutions.

The wet chemical cleaning tests were conducted in beakers where post-etched coupons were exposed to different chemicals at different temperature and exposure times (≤ 2 min), followed by DI water rinse and IPA/N₂ drying. Different wet chemicals were chosen based on chemical composition and physical properties (MSDS) to evaluate their ability to clean post-etch residue and remove TiN HM without structure damage and material losses.

Post-etch, post-clean residue characterization was done by SEM techniques and STEM/EELS analysis. TiN removal rates were measured with spectroscopic ellipsometry. Cu etch rates were determined by 4-point probe and Co etch rates were measured by cross-section SEM.

Post-etch and post-clean residue analyses and discussion

Fig. 1a presents SEM images of Cu/low-k DD vias formed by Lam's plasma etching process. Heavy post-etch polymeric residue was found at bottom of different types of vias by both SEM techniques: top down (CD-SEM) and tilted X-SEM inspection. The EELS analyses were used for characterization of residue formed inside of dense small diameter via/trench array structures. Cr-coating was applied for residue decoration. The chemical composition of bottom residue consists of fluorocarbon polymer, CF_x , with Si, O and N incorporated into it. Fluorine was not found because EELS is not sensitive to residual F. Residual Ti as a result of TiN HM plasma sputtering was found everywhere. Cu incorporated into bottom via residue as a result of plasma sputtering was observed inside wide vias but not inside narrow vias.

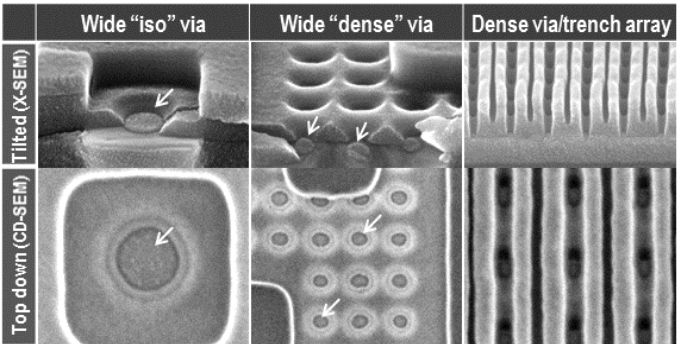


Fig. 1a: Post-etch residue assessment by SEM

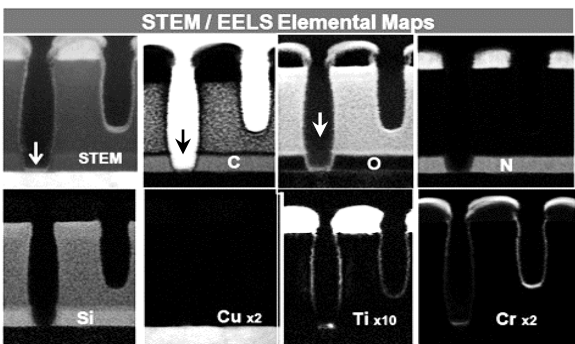


Fig. 1b: Via inspection by EELS analyses

Three wet chemicals mixed with hydrogen peroxide were evaluated on their ability to remove post-etch residue together with a TiN mask. The results are presented in the Fig. 2. No mixture of chemical/ H_2O_2 was able to clean heavy bottom residue but easily stripped TiN mask. The residue became less removable at higher H_2O_2 concentrations and temperatures due to chemical modification.

	Chem. A / H_2O_2 mixture	Dil. Chem. B / H_2O_2 mix	CLk-228 / H_2O_2 mixture	
Wide "Dense" Via				
Wide "Iso" Via				
Comments	Aqueous based solvent 2:1 mixture 55°C, 120 s Residue not removed TiN mask stripped	Aqueous based, fluoride cont. 1:8:5 (water) mixture 50°C, 120 s Residue not removed TiN mask stripped	Semi-aqueous solvent 2:1 mixture 65°C, 120 s Residue not removed TiN mask stripped	Semi-aqueous solvent 1:5 mixture 65°C, 120 s Residue not removed TiN mask stripped

Fig. 2: Post-etch residue and TiN mask removal in a mixture of chemical with hydrogen peroxide: none chemical was able to clean via bottom from heavy etch residue but fully stripped TiN mask

The J.T.Baker® CLk™-228 photoresist and post-etch fluoropolymer residue remover (pH 10.65 for 10% solution in water) was chosen as a promising chemical that has demonstrated good cleanability in removing heavy via bottom polymer formed in the “stressed” plasma etch process. The SEM images in the first row of Fig. 3 show no residue at the bottom of wide “iso” and “dense” vias as well as HAR narrow vias inside trenches. However, this chemical was not designed to etch TiN mask. We proposed and demonstrated 2-step cleaning process where post-etch residue removal (step 1) and TiN mask strip (step 2) were performed as two independent, sequential processes. In Fig. 3, the second row of SEM images shows the cleanability of this two-step process where the J.T.Baker® CLk™-228 residue remover was used to clean via residue and together with H₂O₂ to etch away TiN mask. This concept is considered as more flexible, better tunable, and a more reliable method in comparison with a one-step residue / mask removal.

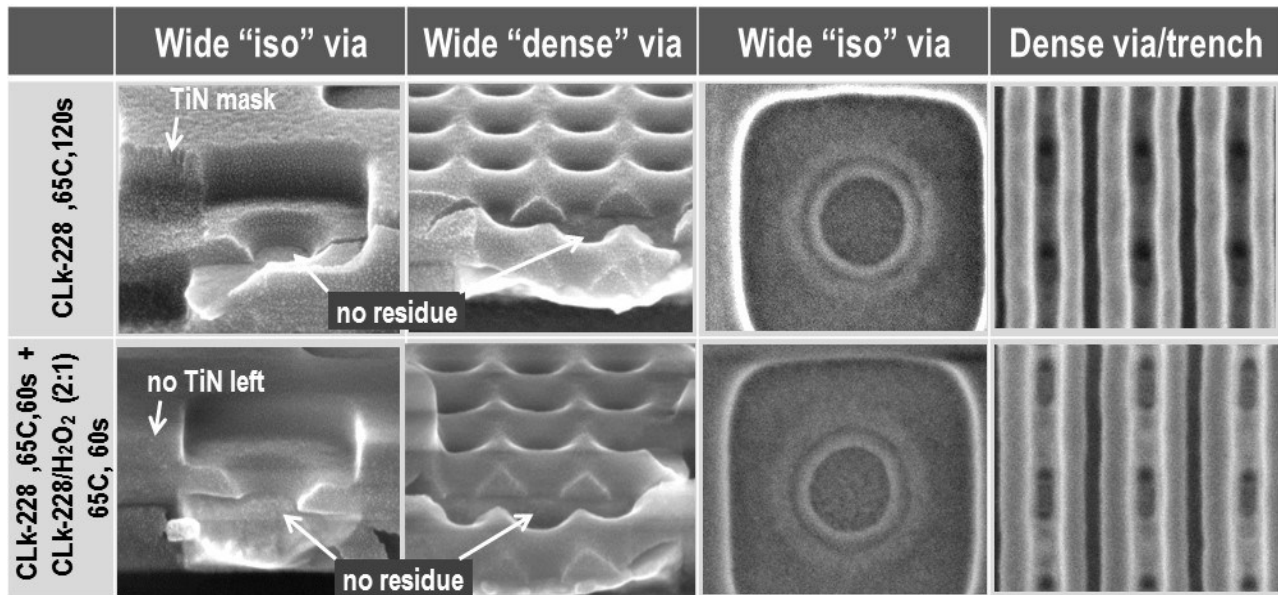


Fig. 3: The post-etch residue and TiN mask removal: one-step clean versus two-step sequential clean

Titanium nitride removal and bath life issues

To bring this concept to practice, the bath life of a mixture of J.T.Baker® CLk™-228 residue remover and H₂O₂ was investigated as a function of different temperatures and component ratios. TiN etch rate together with TiN:Cu etch selectivity was also investigated. Based on blanket wafer etch rates, as listed in Table 1, mixing ratios less than 1:2 (for J.T.Baker® CLk™-228 residue remover / H₂O₂ (30%)) are necessary to achieve the following targets: high TiN etch rates, low Cu and Co etch rates, and excellent (>100:1) TiN:Cu selectivity. All mixtures tested showed excellent TEOS compatibility as well.

Table 1: TiN, Cu and Co etch rates in mixtures of J.T.Baker® CLk™-228 residue remover with hydrogen peroxide (H₂O₂) at 55°C

CLk™-228: H ₂ O ₂ mixture	TiN Etch Rate [Å/min]	Cu Etch Rate [Å/min]	Co Etch Rate [Å/min]
1:10	>116	<1	<1
1:2	>116	<1	4
1:1	>116	1.4	4
5:1	35	3.8	5
20:1	1.3	3.6	2
1:0	<1	<1	1

All J.T.Baker® CLk™-228 residue remover / H₂O₂ mixtures were found to be unstable over time, and the challenge to maintain performance was one of controlling pH and H₂O₂ levels. For a 1:10 mixture at 55°C with no Ti loading, the pH drops from 6.7 to 6.3 within 3 hours (Figure 4.a). Under these conditions, the pH level and performance (TiN and Cu etch rates) can easily be maintained by regular additions of J.T.Baker® CLk-228, and the H₂O₂ concentration is little changed even without additional H₂O₂ spiking. In the case where Ti is loaded into the mixture, a significant decrease in H₂O₂ concentration is also detected over time. A decrease in the percentage of H₂O₂ in J.T.Baker® CLk™-228 residue remover/ H₂O₂ mixtures has an undesirable impact on TiN etch rates (Figure 4.b). In order to maintain the performance of J.T.Baker® CLk™-228 residue remover / H₂O₂ mixtures under real process conditions, regular spiking with both J.T.Baker® CLk™-228 residue remover and H₂O₂ is required.

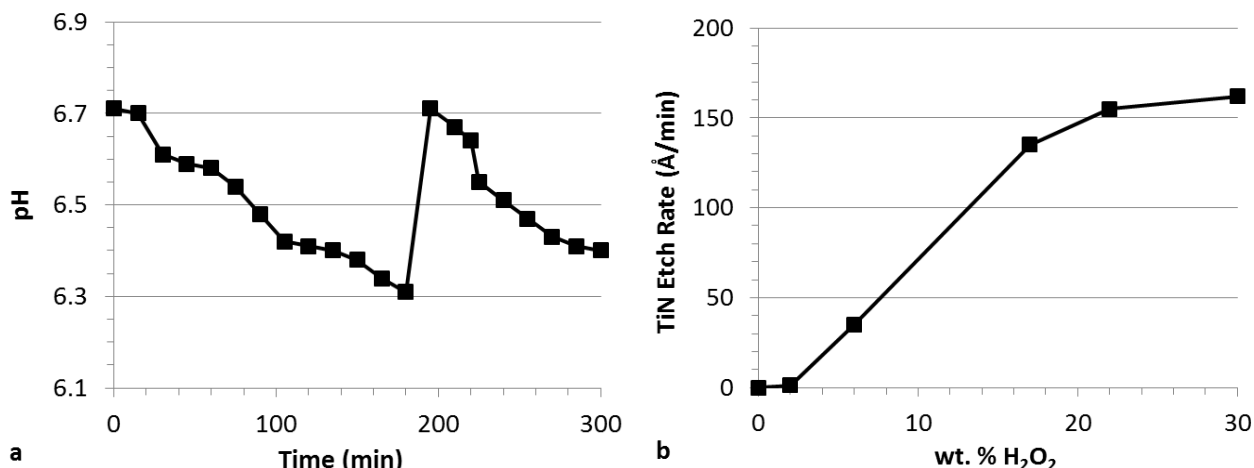


Fig. 4: Critical bath life factors for mixtures of H₂O₂ (30%) and J.T.Baker® CLk™-228 residue remover. (a) pH (additional J.T.Baker® CLk™-228 residue remover was added at 180 min.) and (b) hydrogen peroxide concentration. Data was collected from covered beaker experiments

Because of the short bath life of J.T.Baker® CLk™-228 / H₂O₂ mixtures, an optimal dump/fill process has been developed to extend the bath life of this system and make the process more useful in a high volume manufacturing setting. For a 1:10 J.T.Baker® CLk™-228 / H₂O₂ mixture at 55°C, a dump fill process has been developed to maintain pH as well as TiN, Cu, and TEOS etch rates. This process involves replacing 6.4% of the solution with a 1:6 J.T.Baker® CLk™-228 / H₂O₂ mixture every thirty minutes. A bath life experiment was performed using this dump/fill procedure under Ti loading conditions of ~4 ppm Ti/hour, as determined using spectrophotometric quantification of pertitanic acid formed *in situ* [1]. Figure 5 shows the stability of pH, TiN etch rate and H₂O₂ concentration while running this process over a period of 8 hours. TEOS etch rate and Cu etch rate were also stable over the duration of this experiment. Following the dump/fill procedure described herein for a 10:1 mixture over an 8 hour period, pH and % H₂O₂ are maintained within a 5% range and TiN etch rates are kept within 30% of the starting etch rate.

For comparison, a process involving the replacement of 6.4% of the solution with a 3:2:1 mixture of water / H₂O₂ / J.T.Baker® CLk™-228 is also presented. In this case, a decrease in H₂O₂ replenishment and a slight increase in CLk-228 spiking results in loss of control of the solution. After 4 hours the mixture reached a condition where TiN etch rate is decreased and Cu etch rate begins to increase. This comparison highlights the need for tight control of the dump/fill process to maintain good performance of the mixture.

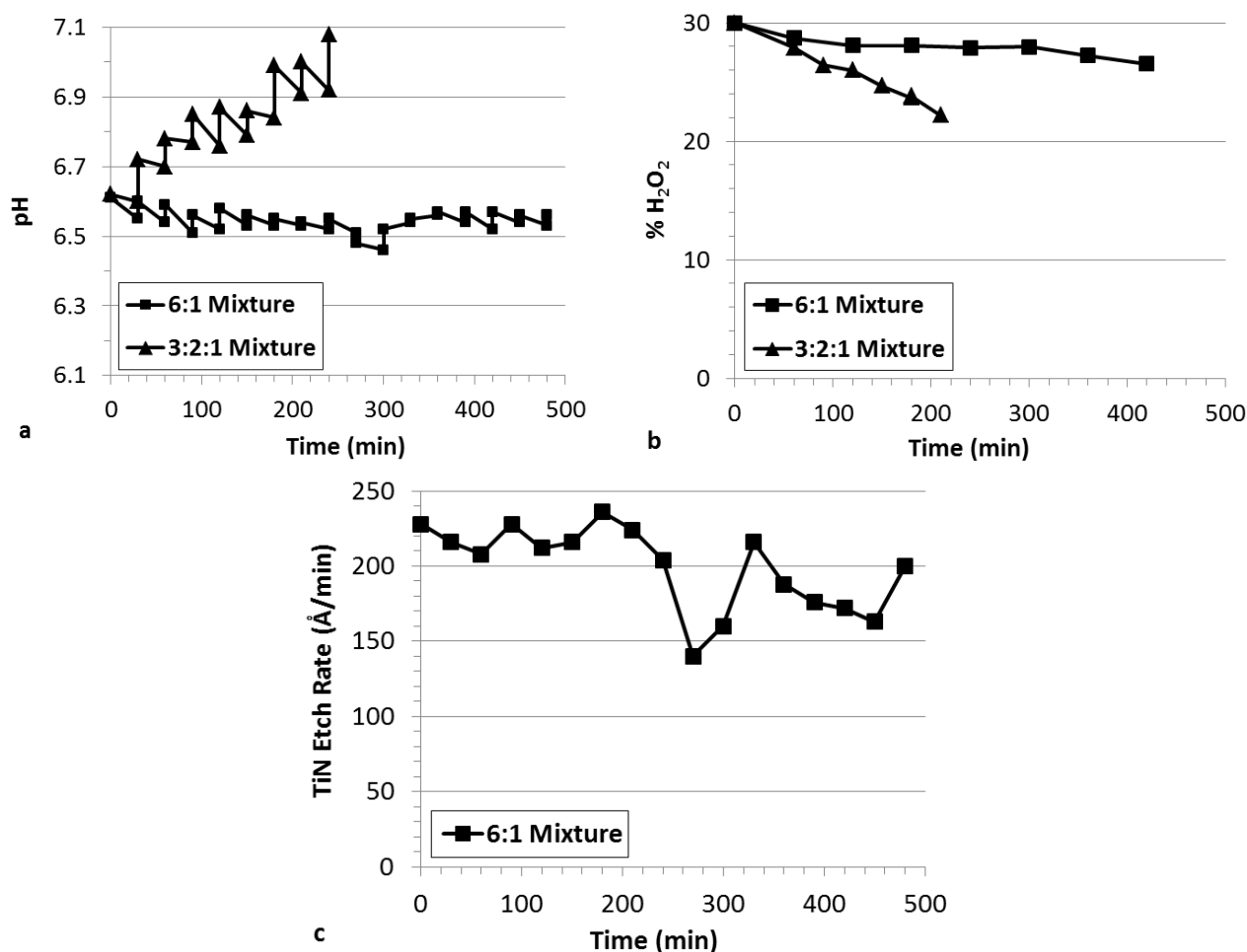


Fig. 5: Bath life extension experiment for 550g of 10:1 H₂O₂ (30%):J.T.Baker® CLk™-228 residue remover at 55 C in a covered beaker. Every 5 min, a 16 cm² TiN (~300 Å) was stripped in the mixture to simulate TiN loading. At each 30 min time point, pH (a), TiN etch rate (b), and H₂O₂ concentration (c) were measured and 6.4% of the mixture was dumped and refilled with a 6:1 mixture of H₂O₂ (30%) : J.T.Baker® CLk™-228 residue remover or 3:2:1 mixture of Water : H₂O₂ (30%) : J.T.Baker® CLk™-228 residue remover. At each time point, pH was measure before and after the dump/fill procedure.

Conclusions

Mixtures of solvent cleans and hydrogen peroxide are excellent removers of TiN, but they not capable of removing the tough fluoropolymer residues at the bottom of vias formed by plasma etching of low-k DD trenches and vias. A two-step process has been developed for removing both post-etch residues and a titanium nitride hard mask from Cu/Low-k DD structures. First, J.T.Baker® CLk™-228 residue remover is used to remove post-etch residue. Next, a mixture of J.T.Baker® CLk™-228 residue remover and hydrogen peroxide is used to remove the hard mask. A dump/fill sequence has also been identified to maintain more than 8 hours bath life while keeping high (>150 Å/min) TiN mask etch rate and excellent (>100:1) TiN:Cu and TiN:Co etch rate selectivity, which makes this process feasible in a HVM setting.

References

- [1] G. Eisenberg, Colorimetric Determination of Hydrogen Peroxide, Ind. Eng. Chem. Anal. Ed. 15 (1943) 327.

TiN Metal Hardmask Etch Residues Removal with AlN Etch

Hua Cui

DuPont Electronics & Communications, Hayward, CA, USA

Hua.Cui@DuPont.com

Keywords: Metal hardmask, etch residues removal, sidewall polymer, TiN, AlN etches, Cu/low-k

Abstract. A wet cleaning formulation with tunable AlN etch rate approach was developed. The formula is compatible with Cu, Co and low-k materials, is able to remove etch residues and does not contain fluoride.

Introduction

As the technology nodes advance to 10nm and beyond, AlN has been introduced as an etch stop layer replacing SiCN to gain better etch selectivity between low-k and etch stop layer. In this paper we report a recently-developed novel wet cleaning formulation approach in which the cleaning formulation HCX-AL (i) removes etch residues; (ii) is compatible with low-k, Cu and Co; (iii) provides a tunable AlN etch rate; and (iv) does not contain fluoride.

Fluorine-containing plasma gas chemistry is used to etch low-k, and the impact of the plasma dry etching with fluorine-containing etching gas on the AlN etch stop layer is also discussed.

Experiments

Residue removal experiments were conducted in beakers at 50 °C for 90 s. Etch rate experiments were conducted at 50 °C for 2 mins and 60 °C for 1 min for TiN, and 10 mins at 50 °C and 60 °C for Cu, Co and AlN. The residue removal efficiency was evaluated by SEM (Hitachi S-5500) in the areas of etched sidewall and via bottoms as shown in Figures 1 and 2. Cu and Co thickness was measured using a Four Dimensions Four Point Probe Meter 333A, whereby the thickness correlates to the resistivity of the film remaining. AlN thickness was measured with an Axios XRF spectrometer by PANalytical. Low-k (BDIII) material thickness was measured with an Auto SE Spectroscopic Ellipsometer by HORIBA JOBIN YVON. Etch rates were calculated based on the change in thickness (before and after chemical treatment) divided by the chemical treatment time. The AlN blanket wafer was treated with proprietary fluorine-containing gas plasma. The etch rates of plasma-treated and non-plasma-treated AlN blanket wafers in DI water were tested at room temperature (RT) for 2 mins. The XPS experiments were performed using a Physical Electronics (PHI) Quantum 2000 Scanning ESCA Microprobe. The XPS measurements on AlN were obtained using Monochromatic AlK α (1486.6eV) radiation. The acceptance angle was $\pm 23^\circ$ and the take-off angle was 45° .

Results and discussion

Figure 1 shows the etching residues after dry etching. Figure 2 shows the complete removal of the etching residues after treatment with HCX-AL at 50 °C for 90 s. Table 1 shows the etch rates of TiN, Cu, Co and AlN for HCX-AL. HCX-AL is compatible with Co, Cu and low-k at 50 °C, and the AlN etch rate increases from 24 to 41 Å/min as temperature increases from 50 °C to 60 °C; the etch rates of Cu and Co were only slightly increased at 60 °C. Figure 3 shows etch rates with various concentrations of compound A in the HCX-AL formulation at 50 °C; the etch rate of AlN increases with compound A concentration, but Co and Cu remain essentially unchanged. In this way the HCX-AL formulation provides a tunable AlN etch rate.

XPS was used to characterize the surface of plasma treated and non-plasma treated AlN blanket wafers, and the results are shown in Tables II and III. Table II shows that there was a significant

amount of fluorine (17.3%) on the surface of the plasma treated AlN wafer; AlF_3 (or AlxFy) is formed on the surface of plasma treated AlN^[1]. Table III shows that there is a very low atomic concentration of fluorine (0.3%) present on the surface of the non-plasma treated AlN blanket wafer. The presence of fluorine is likely due to contamination during handling.

Table IV shows the blanket AlN wafer etch rates in DI water. The plasma treated AlN blanket wafer shows an etch rate of 29 Å/min at RT. The AlF_3 (or AlxFy) that is formed is water soluble^[2], and the dissolution of soluble AlF_3 (or AlxFy) is responsible for the AlN etching in DI water. DI water has no impact on the non-plasma treated AlN wafer.

Figure 4 shows that the AlN (non-plasma treated) etch rate increases significantly with NH_4F . The AlN etch rate jumps from zero to 77.3 Å/min with an addition of 0.05% fluoride, and to nearly 250 Å/min with the addition of 0.15% fluoride.

The AlN etch stop layer in pattern wafers is exposed to fluorine-containing gas plasma and the AlN has been plasma damaged during the low-k etch Cu interconnects fabrication. It is very challenging to formulate a chemical remover that is compatible with AlN in pattern wafers, because the AlN will be etched by DI water due to the formation of water-soluble AlF_3 (or AlxFy).

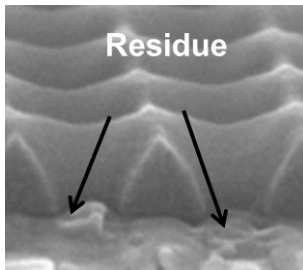


Figure 1: SEM wafer as received.

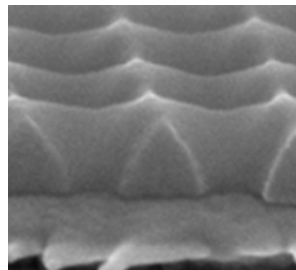


Figure 2: SEM after cleaning at 50°C for 90 s (HCX-AL: Residues are removed completely).

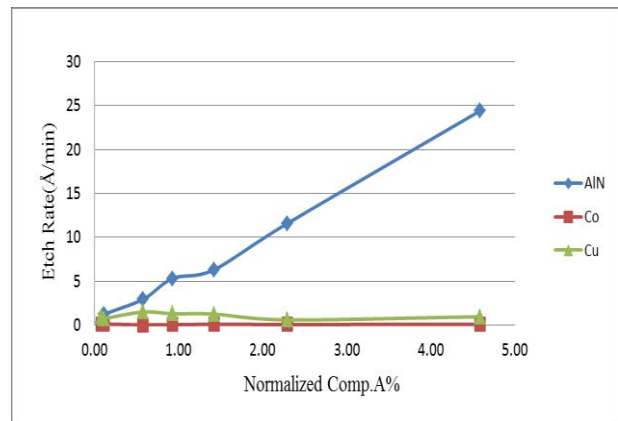


Figure 3: AlN, Co and Cu etch rate vs. Comp. A concentration at 50 °C for HCX-AL

Table I: Etch rate of Co, TiN, Cu, AlN and low-k at 50 °C and 60 °C

Chemical	Temp (°C)	TiN (Å/min)	Co (Å/min)	Cu (Å/min)	AlN (Å/min)	BDIII (Å/min)
HCX-AL	50	198	0.09	0.96	24	-0.55
	60	> 360	2.09	2.09	41	0.33

Table II: XPS atomic concentrations of plasma treated AlN blanket wafer

XPS Analysis: Plasma Treated AlN Wafer					
Atomic Concentrations [%]					
C	N	O	F	Al	Cl
36.2	8.6	20.1	17.3	17.6	0.3

Table III: XPS atomic concentrations of non-plasma treated AlN blanket wafer

XPS Analysis: Non-Plasma Treated AlN Wafer					
Atomic Concentrations [%]					
C	N	O	F	Al	Cl
31.9	8.7	39.7	0.3	19.1	0.3

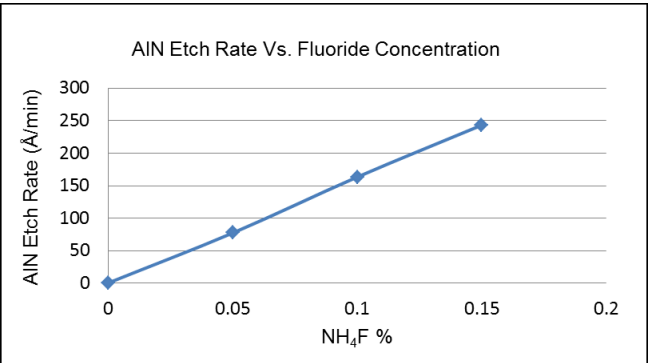


Figure 4: AlN etch rate as a function of ammonium fluoride concentration at 50 °C for HCX-AL

Table IV: Etch rate of plasma treated and non-treated AlN in DI water

Temp (°C)	Plasma Treated AlN (Å/min)	Non-Plasma Treated AlN (Å/min)
RT	29	0

Summary

The formulation, HCX-AL, with tunable AlN etch rate, has been successfully developed. The formula is compatible with Cu, Co and low-k dielectric materials, and is able to remove all etch residues. Although formulation compatibility with AlN blanket wafers is achievable, AlN compatibility in pattern wafers may be challenging due to the formation of AlF₃ (or AlxF_y), which is water-soluble.

References

[1] Da Chen, Jingjing Wang, Vacuum. 83 (2009) 282-285.

[2] Krumgalz, B.S., Mineral Solubility in Water at Various Temperatures, Israel Oceanographic and Limnological Research Ltd., Haifa, (1994).

High Throughput Wet Etch Solution For BEOL TiN Removal

Chia-Jung Hsu^{1, a}, Chieh-Ju Wang¹, Sheng-Hung Tu¹, Makonnen Payne²,
Emanuel Cooper² and Steven Lippy²

¹ Entegris, Inc., 1F, No. 669, Section 4, Zhongxing Road, Zhudong Town, Hsinchu County, 31061, Taiwan (R.O.C.)

² Entegris, Inc., 7 Commerce Drive, Danbury, CT, 06810, USA

^awisma.hsu@entegris.com

Keywords: non-TMAH, titanium nitride, wet etch, low-k compatibility, residue clean, TiN removal.

Abstract. Sub-10 nm technology node manufacturing processes may require the use of thicker and denser TiN hard mask for patterning at the BEOL. The modified TiN, which tends to be more chemically robust, must be removed using a wet etch process, while maintaining typical throughput - no extension of typical wet etch process times. To satisfy these needs, a new TiN etching accelerator was found that enhanced the activity of peroxide-related species in a wet etch chemical formulation that achieved increased TiN etch rate relative to formulation without TiN etch rate accelerator (Sample 1), while also minimizing the damage to ultra-low-k inter layer dielectric (ILD) layer by a strong base, also present in the formulation. We report here the result of a solvent based formulation, which adopted the TiN etching accelerator. The formulation was able to maintain TiN etch rate and remove post-etch residue, while remaining selective to ultra-low-k ILD, Co and Cu. The TiN etch rate of the accelerator enhanced formulation can be further tuned by modifying the process temperature or the hydrogen peroxide to formulation mixing ratio and has the potential capability to process > 400 wafers.

Introduction

To solve problems related to double patterning/double etching (2P2E) and RC-delay, TiN hard mask and low-k dielectrics were adopted in advanced nodes of BEOL [1]. TiN removal is required before wet clean to get better Cu filling in 10 nm node [2]. In addition, to get dry etch with high selectivity between TiN and low-k dielectric, a thicker high-density TiN film can prevent misalignment and improve yield for 2P2E process but makes removal more difficult. TiN removal rate will be important for wet cleaner because a new deposition technique of TiN is involved; the throughput in BEOL wet etch process can be impacted by those integration changes.

In general, a conventional chemical e.g., SC1, SC2 or SPM can meet the purpose of high TiN removal rate, but high selectivities between TiN, dielectric and metals are difficult to achieve [3]. While processes that do not expose some metals, e.g. Cu, Co, are feasible and can avoid the problem of metal incompatibilities, in formulations with very high or low pH it is hard to find the right balance between TiN removal, ILD compatibility, and post dry etch residue removal. In conventional formulations, a near-neutral pH is unfavorable for getting high enough TiN etch rates, so a new strategy in formulation development is needed for settling all these concerns. In this study, we report a TiN etch solution with a novel TiN-etching accelerator that can accomplish high etch rate of high-density TiN film, as well as provide the following advantages for BEOL wet cleaner: no TMAH, tunable TiN etch rate, compatible with ultra-low-k ILD, compatible with hydrogen peroxide so as to avoid exothermic decomposition, free of 0.1 um liquid particle count (LPC) problems, and suited for single wafer tool (SWT) process.

Experimental

The thickness of high-density TiN and dielectric films were measured by ellipsometer (M-2200D from JA Woollam Co.) or XRF (ZSX-400 from Rigaku Co.); 0.1 μm particle analyses were performed by liquid particle counter (KS-40AF and KE-40 from RION Co., Ltd); Ti concentration was determined by ICP-OES (Optima 8300, PerkinElmer Inc.). All etch rates were calculated by dividing the change in film thickness by process time. The ILD/ultra-low-k film, purchased from Advantiv Technologies Inc., was produced by plasma enhanced chemical vapor deposition (PE-CVD); k-value is 2.4. pH was measured by glass electrode, without applying a special peroxide correction.

Results

Because removal of the organic contaminants formed in the dry etch process was critical and to achieve high TiN etch rate purpose, the focus was on SC1-like formulations. In general, SC1-related systems rely on hydrogen peroxide and the HO_2^- ions, generated from hydrogen peroxide and base in Eq. 1, to etch TiN:



Following up on the mechanism showed in Eq. 2 and Eq. 3, both hydrogen peroxide and HO_2^- can coordinate to Ti^{4+} or titanyl (TiO^{++}) ions to form water soluble complexes, and HO_2^- is more active than hydrogen peroxide to achieve the purpose of TiN removal [4]; increasing pH in formulation should be a good idea to generate high enough HO_2^- for TiN etch rate enhancement. However, an SC1-like formulation with such high pH may raise safety concerns during wet etch; once the formulation dissolves TiN in high concentration, Ti ions or its complexes will catalyze decomposition of the remaining hydrogen peroxide, possibly causing process temperature to rise out of control. To resolve this issue, a TiN-etching accelerator “E” was introduced, which can generate peroxide-related highly active species at lower pH and possibly stabilize Ti complexes in the formulation, thus reducing the safety concerns related to accumulation of Ti species in solution during the process.

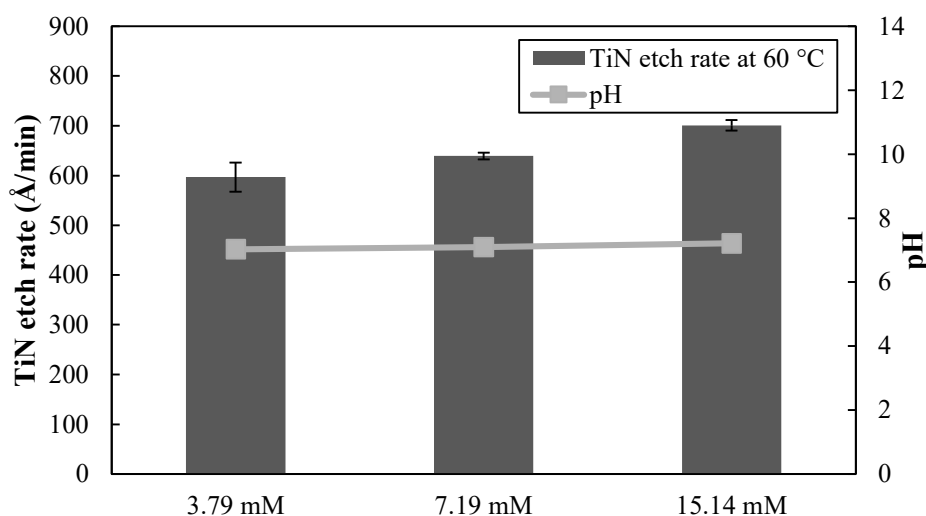


Figure 1: TiN etch rate and pH vs. TiN-etching accelerator “E” concentration change at 60 °C.

Table I: TiN, Co and Cu etch rates of selected aqueous examples at 60 °C.

Sample #	1	1a	1b	1c
Additional pH adjustor (mM)		7.71		
Additional TiN-etching accelerator “E” (mM)			7.19	
Additional corrosion inhibitor (mM)				7.51
pH	6.54	7.00	6.43	6.51
High-density CVD TiN etch rate (Å/min)	232	304	482	240
Cu etch rate (Å/min)	-0.05	0.02	0.29	1.07
Co etch rate (Å/min)	1.38	1.10	1.93	0.19
Ultra-low-k ILD etch rate (Å/min)	<0.5	<0.5	<0.5	<0.5

To understand the effects of the TiN-etching accelerator on etch rates and pH, the concentration of component “E” was increased from 3.79 mM to 15.14 mM (Figure 1). Component “E” in aqueous formulation, when mixed with H₂O₂ in 1:9 dilution ratio, boosted TiN etch rate from 597 to 701 Å/min without substantial pH change. Furthermore, it can be concluded from the data in Table I that component “E” is more effective than the pH adjustor in boosting the TiN etch rate. In Table I, sample 1 is included as baseline; sample 1 with additional 7.19 mM of component “E” and sample 1 with additional 7.71 mM pH adjustor are listed as samples 1a and 1b, respectively. The TiN etch rate difference between samples 1a and 1b indicates that the TiN-etching performance enhancement by component “E” is 1.6 times higher than that by the pH adjustor, increasing TiN etch rate with low impact on pH and on Cu and ultra-low-k ILD etch rates. Even though component “E” caused Co etch rate to increase to 1.93 Å/min in sample 1b, addition of 7.51 mM corrosion inhibitor in sample 1c can provide the needed metal protection for different customers’ integration flow for dual damascene.

Considering that hard-to-remove organic residues can be generated by fluorocarbon-based plasma during dry etch, solvents were introduced for residue removal in BEOL advance node. Functional tests for selected solvent-containing formulation are recorded on Table II. The TiN etch rates of formulations 2 and 3 are ≥285 Å/min with low damage for ultra-low-k ILD. To improve metal protection in formulation 4, process temperature was decreased from 60 to 55 °C deliberately, so TiN etch rate of formulation 4 was significantly lower than the other two formulations.

Table II: TiN, Co and Cu etch rates of selected semi-aqueous formulation for TiN removal.

Formulation	2	3	4
pH adjustor	Non-TMAH base	Non-TMAH base	Non-TMAH base
Solvent	Water + solvents	Water + solvents	Water + solvents
TiN-etching accelerator	Yes	Yes	Yes
H ₂ O ₂ stabilizer	Yes	Yes	Yes
Corrosion inhibitor	No	No	Yes
Formulation (Chemical) / 31%H ₂ O ₂	1:1	1:1	1:1
dilution ratio			
Process temperature (°C)	60	60	55
pH	7.29	7.55	7.96
High-density CVD TiN etch rate (Å/min)	418	481	170
High-density PVD TiN etch rate (Å/min)	285	365	133
Ultra-low-k ILD etch rate (Å/min)	<0.5	<0.5	<0.5
Cu etch rate (Å/min)			0.59
Co etch rate (Å/min)			0.05

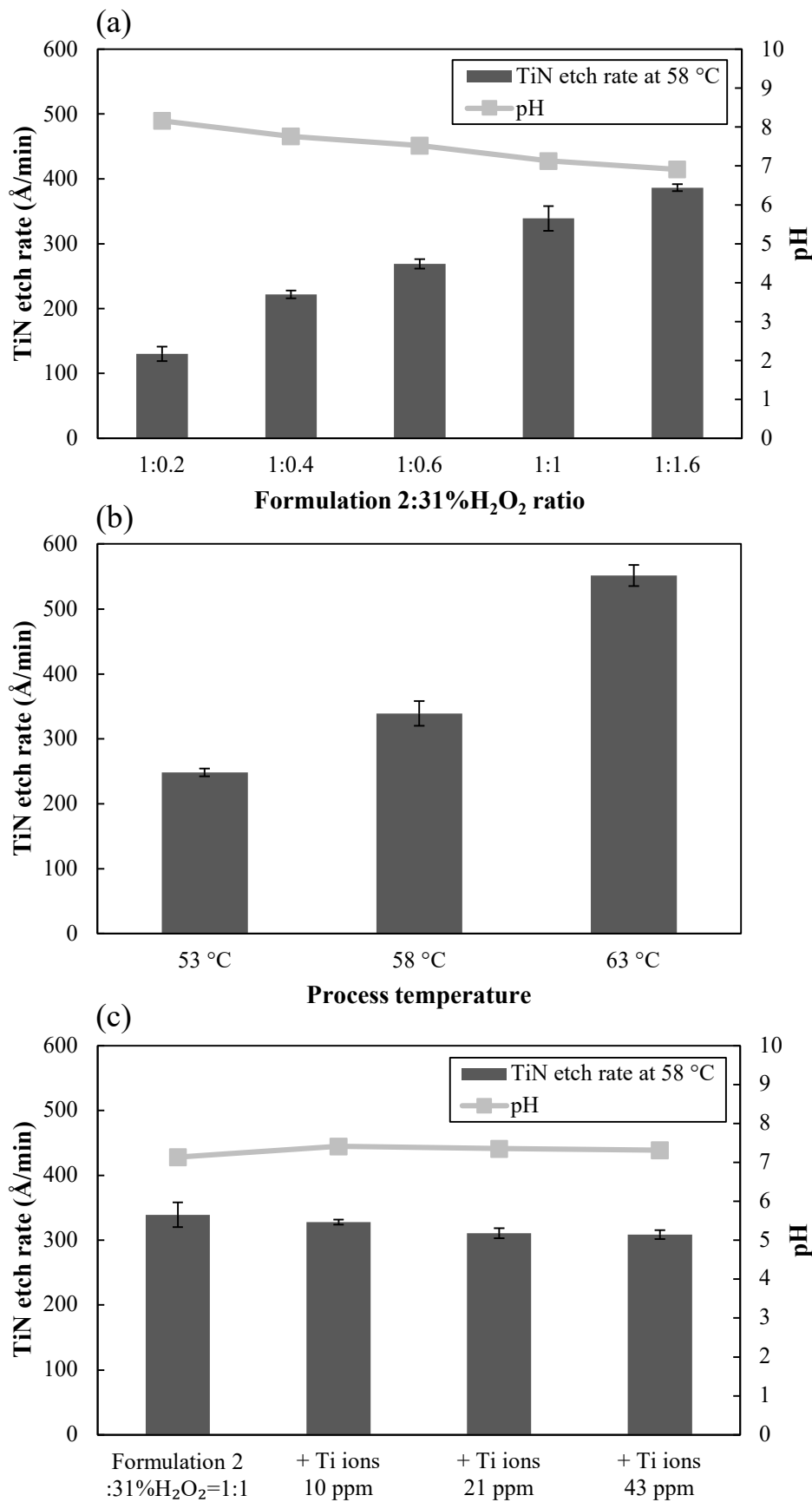


Figure 2: TiN-etching performance of formulation 2 can be controlled by (a) hydrogen peroxide or (b) temperature. (c) TiN etch rate and pH vs. formulation 2 with different concentration of TiN.

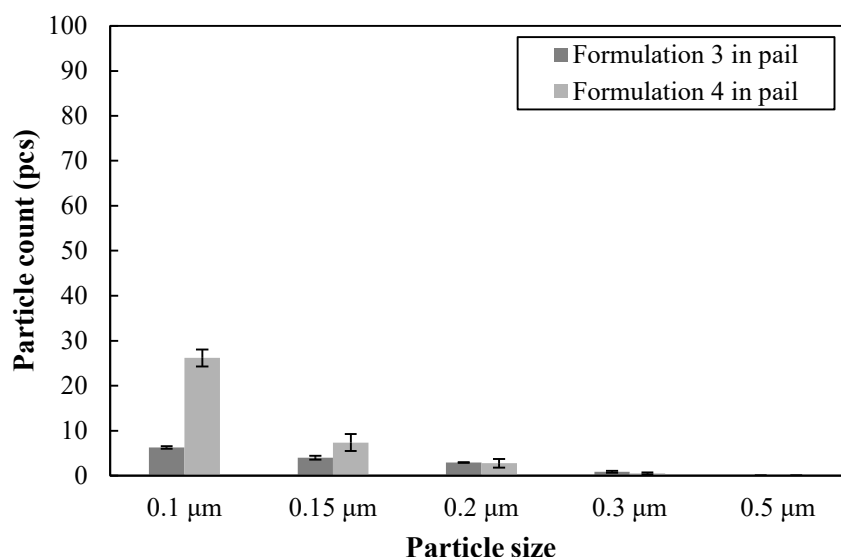


Figure 3: Liquid particle count results for formulations 3 and 4.

TiN etch rates of formulations 2-4 can be easily controlled by changing process temperature or H_2O_2 mixing ratio; examples for formulation 2's TiN etch rate tuning are summarized in figures 2a and 2b. TiN etch rates increase when the hydrogen peroxide concentration or the process temperature increase in formulation 2. Formulation 2's post-etch residues removal efficiency has been tested on key customer's sub-28 nm M2V1 via-trench structure. All visible residues on top of patterned structure can be removed by 2 mins, 60 °C process.

To understand how the TiN etch rate changed during pattern wafer clean, a TiN loading test was designed for formulation 2 (Figure 2c). In this simulated test, we assumed 300 Å TiN on 300 mm patterned wafer with coverage fraction of 50% would be totally removed during SWT clean. After TiN was dissolved in the chemical, the TiN etch rate and final Ti concentration were measured by ellipsometer and ICP-OES, respectively. Results in figure 2c show that the TiN etch rate of formulation 2 decreased from 339 to 308 Å/min due to dissolved Ti. When Ti ion concentration reached 43 ppm, corresponding to a loading of 490 patterned wafers, the TiN etch rate decreased by ca. 9% without significant pH change. To avoid the need for special particle containment during process, designed formulations can provide good 0.1 μm LPC performance for SWT demo; see examples in figure 3.

Conclusion

A series of formulations with TiN-etching accelerator have been developed for BEOL TiN removal for ≤ 10 nm nodes. The selected TiN-etching accelerator can promote TiN etch rate to overcome the difficulty from high-density TiN layer which was adopted as metal hard mask in dry etch process. The TiN etch rate of formulations in this study can be easily controlled by process temperature, hydrogen peroxide mixing ratio, and TiN-etching accelerator fine tune. More importantly, this series of formulation provides a pH-stable environment during simultaneous TiN removal and contaminant cleaning without ultra-low-k ILD damage. Selected solvents can improve wetting and cleaning for SWT; some of the formulations, which have been tested on patterned wafers, compatible with typical 10-nm technical node structures and support improved throughput of the wet etch process.

References

- [1] M. R. Baklanov, J. F. de Marneffe, D. Shamiryan, A. M. Urbanowicz, H. Shi, T. V. Rakhimova, H. Huang and P. S. Ho: *Journal of Applied Physics* **113** (2013), p. 041101.
- [2] A. Iwasaki, K. Courouble, S. Lippy, F. Buisine, H. Ishikawa, E. Cooper, E. Kennedy, S. Zoll and L. Broussous: *Solid State Phenomena* **219** (2015), p. 213.
- [3] E. Cooper, R. Rajaram, M. Payne and S. Lippy: *Solid State Phenomena* **195** (2013), p. 143.
- [4] S. Verhaverbeke and J. W. Parker: *MRS Proceedings* **477** (1997), p. 447.

Impact of Dissolved Oxygen in Dilute HF Solution on Material Etch

Els Kesters^{1,a,*}, Akihisa Iwasaki², Quoc Toan Le¹, and Frank Holsteys¹

¹ IMEC vzw, Kapeldreef 75, 3001 Heverlee, Belgium

² Screen, Kapeldreef 75, 3001 Heverlee, Belgium

^akesterse@imec.be

Keywords: dilute HF, low dissolved oxygen, post-etch residue removal (PERR) clean, low-*k* material, metals

Abstract. Using diluted HF (0.05-0.1%) as cleaning solutions, experimental results showed that the etching behavior of Cu strongly depended on the dissolved oxygen (DO) concentration and the chamber atmosphere conditions. On the contrary, the Cu etch rate was not affected by the HF concentration. A complete reverse trend was observed for plasma-treated OSG2.4. The etching behavior of plasma-treated OSG2.4 was not affected by DO concentration and chamber atmosphere conditions, but was strongly dependent on the HF concentration. The etch rate determined on patterned structure with low-*k* exposed, using CD measurements, confirmed the results obtained on blanket plasma-treated OSG2.4 material.

Introduction

A possible way to realize a 22.5-nm, ½-pitch and beyond BEOL interconnect structure within the low-*k* material is the partial-trench via first with self-aligned double patterning (SADP) integration approach. A scheme of this BEOL integration stack with the different materials used after patterning is shown in Fig. 1. In BEOL processing, fluorocarbon-containing plasma is commonly used to pattern silica-based dielectric layers. During the patterning of the low-*k* dielectric layer, a thin layer of fluoropolymer (CF_x-type residues) is intentionally deposited on the dielectric sidewalls to ensure anisotropic etching and prevent/minimize dielectric degradation. This polymer layer must be removed from the sidewall and the via bottom prior to the subsequent processing steps to achieve good adhesion and coverage of materials deposited in the etched features. The compatibility requirement is even more stringent for advanced low-*k* dielectrics, i.e. materials with a lower *k*-value and higher porosity. Therefore HF based low dissolved cleans are important. Related applications, are cleans for Post-Etch Residue Removal (PERR), CuOx removal and selective etches to control silica/low *k* recess (e.g. airgaps: selective oxide removal, Low *k* removal,...) and will require low-O₂ conc.: <20ppb for the liquid & <500ppm (air). The low-*k* material used in this work is an organo-silicate glass (OSG) type of low-*k* material with *k* = 2.4 (~20 % open porosity). Recent results clearly showed the presence of a highly fluorinated layer deposited on the trench sidewalls during the plasma etch based on a fluorocarbon plasma [1-4]. This study focused on the use of dilute HF with different dissolved oxygen (DO) concentrations on the material etch of the exposed materials in the stack structure. Depending on the purpose of the cleaning step, this dilute HF clean can be used alone or in combination with an aqueous post-etch residue removal (PERR) chemistry to enable the removal of TiO and TiF residues together with the top TiN HM and the post-etch residues generated during the plasma etch.

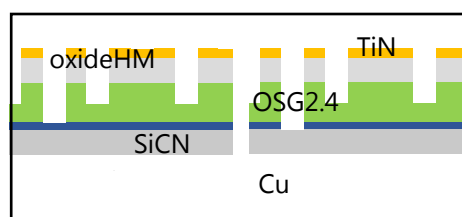


Figure 1: A partial-trench via first to realize 45-nm pitch by SADP approach on dual damascene compatible hardmask as TiN.

Materials and methods

All low oxygen, HF-based cleaning steps were performed on a SU-3200 platform, SCREEN single wafer cleaning tool. HF concentrations were varied from 0.05 - 0.1% in combination with DO concentrations in the range of 70 - 3000 ppb. HF cleaning processes were executed with two different chamber atmosphere conditions, controlled and non-controlled ambient oxygen. Material compatibility tests were done on 500-nm blanket PVD Cu and 65-nm blanket plasma-treated porous low- k ($k = 2.4$; OSG2.4). The effect of a wet clean on blanket low- k materials was evaluated by Spectroscopic Ellipsometry (SE) and Fourier Transform Infrared (FTIR) spectroscopy. The thickness variations of low- k and CuOx were determined by ellipsometry. For Cu the thickness measurement was done by a four-point probe (sheet resistance) measurement.

Results

Effect of Dissolved Oxygen Concentration in DHF Solution on Material Etch (Cu, OSG2.4).

The CuOx thickness before and after clean was measured by ellipsometry [5]. The CuOx layer formed on the as-deposited Cu surface was readily dissolved in diluted HF. Within 70 - 3000 ppb DO and for a clean of 2 min in dHF (0.05% or 0.1% - controlled ambient condition), the final CuOx thicknesses were found to be very similar. The CuOx thicknesses remaining on Cu after different HF cleans, were about 1.5-2 nm, which is most likely the native CuOx formed after clean (not shown).

The bulk Cu loss caused by 0.05% HF cleans for 1 min with 70 ppb, 200 ppb and 3000 ppb DO in controlled and non-controlled ambient conditions was also determined. In both ambient conditions, it seemed that the Cu loss increased with increasing DO concentration in dilute HF solution. The Cu loss obtained by dilute HF processing in the controlled condition was less compared to the Cu loss reached in the non-controlled condition. This can be explained by the air present in the non-controlled compared to the controlled condition. Less than 1 nm Cu loss was observed for 0.05% HF with 70 ppb and 200 ppb DO. Only using 3000 ppb DO in dHF in the non-controlled condition started to etch Cu. Higher dilute HF concentrations (0.1 and 0.2% HF) were also tested, but a similar trend was observed for higher [HF]. This means that the etching behavior of Cu strongly depended on the DO concentration and was not affected by the HF concentration. The etching behavior of Cu was also strongly dependent on the chamber atmosphere condition. From Fig. 2 it is clear that 10 ppb DO for the non-controlled and ~200 ppb DO for the controlled was required to reach a spec of less than 1 nm Cu loss.

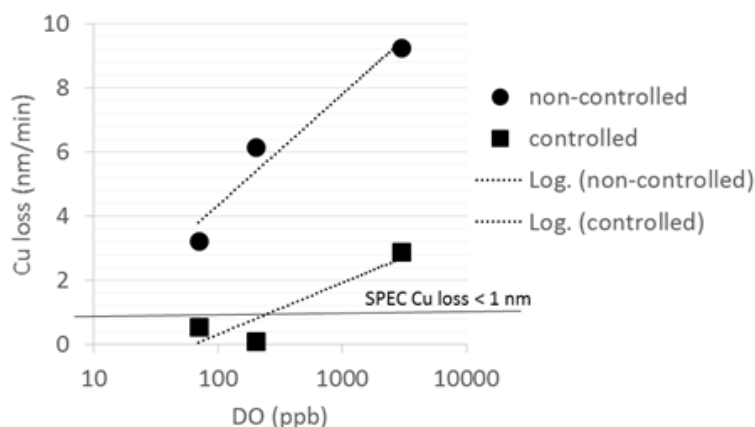


Figure 2: Cu loss as a function of DO in 0.05% HF for 1 min processing in non-controlled and controlled ambient condition.

For 1 min 0.05% and 0.1% HF processing in the controlled ambient, an increase in DO from 70 ppb to 3000 ppb did not show a noticeable impact on OSG2.4 etch. A similar thickness of damaged layer (~0.5 nm) was removed within 1 min. For 2 min processing, an increase in the [HF] from 0.05

to 0.1% resulted in a significant etch of damaged OSG2.4 layer. Negligible difference in OSG2.4 wet etch was observed for different DO (from 70 ppb to 3000 ppb) (Fig. 3). This means that the etching behavior was not affected by DO concentration but strongly depended on the HF concentration. The same phenomenon was also observed in the non-controlled ambient (not shown).

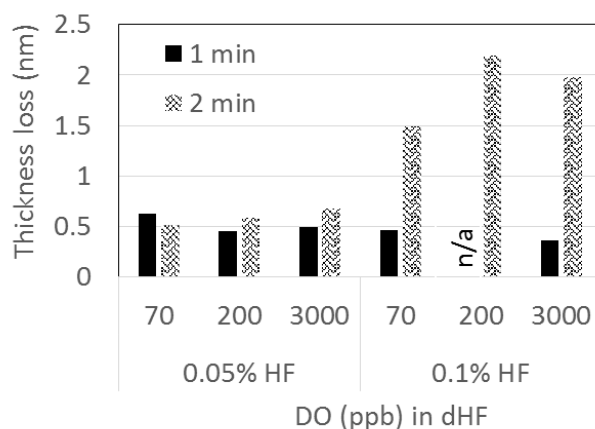


Figure 3: Thickness loss of plasma-treated OSG2.4 for 1 and 2 min processing in 0.05% and 0.1% HF for different DO concentrations.

Effect of Chamber Atmosphere on Material Etch (Cu, OSG2.4 and thermal oxide). The effect of bulk Cu loss was examined using 0.05% HF processing with 70 ppb DO in both the controlled and non-controlled ambient chambers. Based on a polar 49-point thickness measurement, the difference in bulk loss between center ($r=(0,0)$), middle ($r=(0,47.5\text{mm})$ and $r=(0,95\text{mm})$) and edge ($r=(0,142.5\text{mm})$) of the wafer was also studied for different dispense times (Fig. 4). Combined low oxygen ambient with low DO 0.05% HF did not attack bulk Cu, even after 2 min dispense and if edge exclusion (EE) 3 mm was included. For the non-controlled ambient using low DO 0.05% HF process, it seems that the Cu etch was faster toward the outer peripheral side of the wafer compared to the controlled ambient and also Cu loss increased with dispense time.

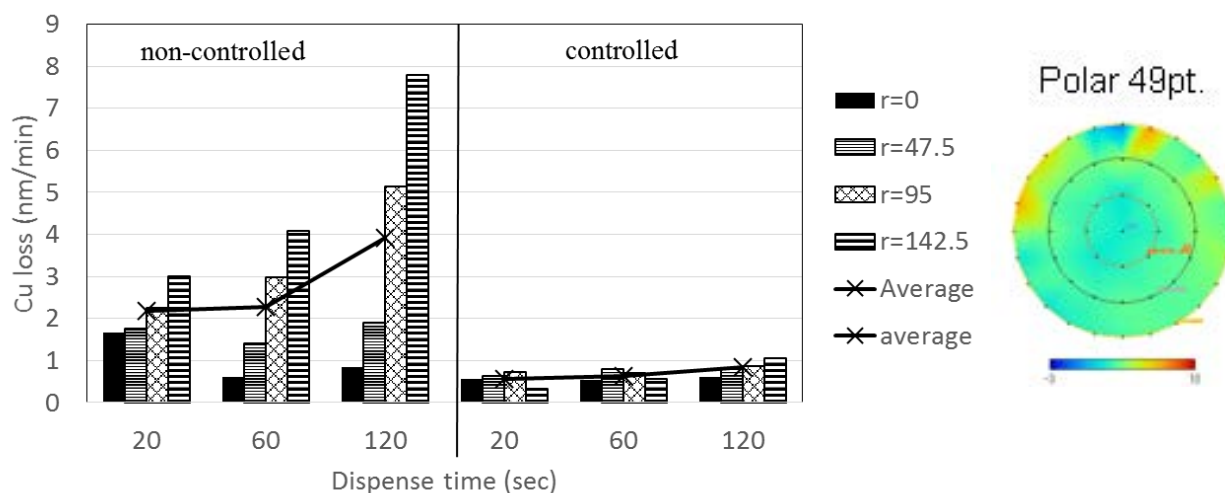


Figure 4: Cu loss as a function of dispense time using 0.05% HF with 70 ppb DO in controlled and non-controlled ambient chamber.

The effect of plasma-treated OSG2.4 and thermal oxide loss was examined using 0.1% HF processing with 70 ppb DO in both the chamber atmosphere conditions. For both OSG2.4 and thermal oxide no difference in material loss was observed between both conditions (Fig. 5). For plasma-treated OSG2.4, 2 different ERs were obtained. The damaged layer ($\sim 2.5\text{ nm}$) formed on top of the OSG2.4 material etched faster compared to the bulk OSG2.4 material (Fig. 5, left).

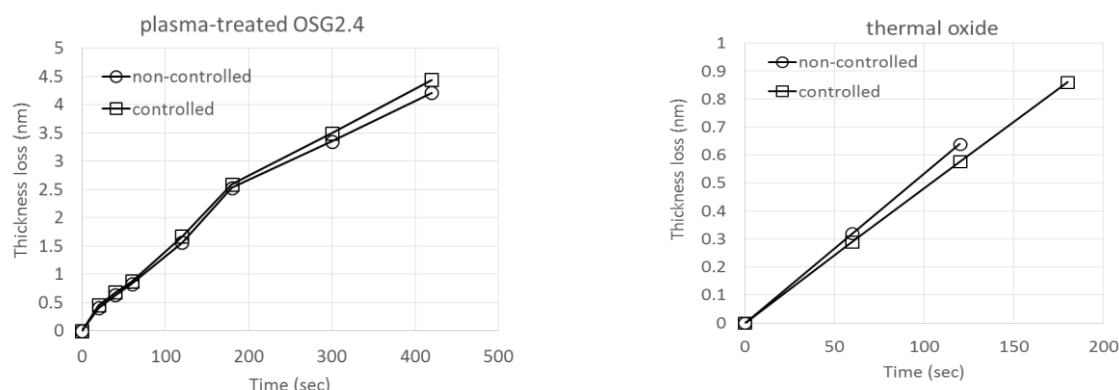


Figure 5: Thickness loss as a function of dispense time using 0.1% HF with 70 ppb DO in non-controlled and controlled ambient chamber for plasma-treated OSG2.4 (left) and thermal oxide (right).

Effect of Dissolved Oxygen in HF on CD Change of OSG2.4 Present in a Patterned Structure.

The ER of a blanket plasma-treated OSG 2.4 using 0.05%HF (DO = 70 ppb) was about 0.5 nm/min (Fig. 3). The same HF treatment (1 min 0.05%HF with DO = 70 ppb '3 cycles') was applied on a patterned wafer after low- k etch and TiN removal. TD-SEM (Fig. 6, left) and CD-measurements (Fig. 6, right) were performed after every cycle of 1 min clean. The CD loss is estimated to be ~2 nm for 2 min of HF 0.05 % clean, which also corresponds to an ER of 0.5 nm/min.

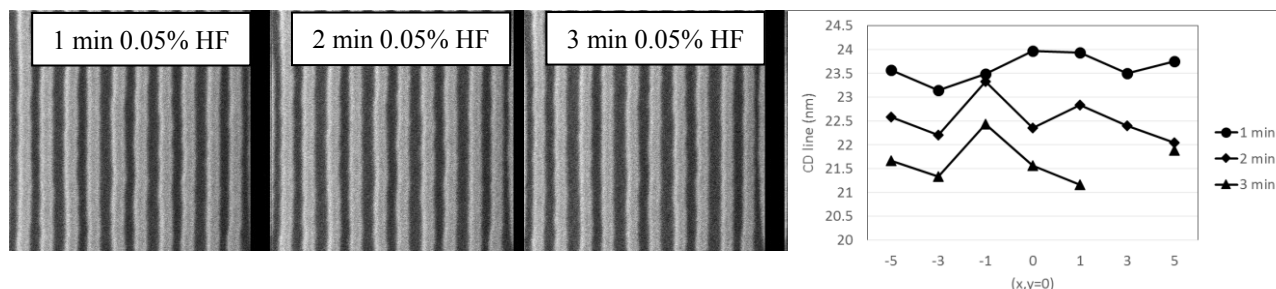


Figure 6: TD-SEM pictures (left) and CD-data (right) of low- k lines after different HF cleans (3* 1 min 0.05% HF – 70 ppb DO) on a patterned wafer.

Summary

The etching behavior of Cu strongly depended on the DO concentration and was not affected by the HF concentration. The Cu loss was also strongly dependent on the chamber atmosphere condition. More Cu loss was obtained in the non-controlled ambient condition. In the controlled oxygen condition, a uniform etching behavior of Cu was seen (center versus edge). For the plasma-treated OSG2.4, the etching behavior was not affected by DO concentration but strongly depended on the HF concentration, and was independent on chamber atmosphere condition. The ER on a blanket OSG2.4 material was also confirmed, using CD measurements, on a patterned structure with low- k exposed.

References

- [1] M. Darnon et al., Microelectron. Eng., 85, 2226 (2008).
- [2] Q. T. Le et al., J. Electrochem. Soc., 159, H1-H6 (2012).
- [3] T. Mukherjee *et al.*, ECS Solid-St. Lett., 2, N11-N14 (2013).
- [4] Q.T. Le *et al.*, JSST, 5 (3) N5-N9 (2016).
- [5] A. Satta *et al.*, JES 150, G300 (2003).

The Effect of Inhibitors on Co Corrosion in Alkaline Post Cu-CMP Cleaning Solutions

Ping Hsu^{1a}, Paul R. Bernatis², Kevin Huang¹, Chi Yen¹

¹ EKC Technology, DuPont Electronics & Communications, Hsinchu, Taiwan

² EKC Technology, DuPont Electronics & Communications,
2520 Barrington court, Hayward, CA, 94545, USA

^aping.hsu@dupont.com

Keywords: Post CMP, cobalt, impedance

Abstract. Corrosion of cobalt-contained metal line is one of critical defects during post-CMP cleaning process. Thus, the understanding of inhibitors is significant to eliminate corrosion. In this paper, we discuss the learning from etching rate and electrochemical measurement for the solutions using multiple corrosion inhibitors. Furthermore, TEM of cobalt pattern wafer and cleaning results are shown to demonstrate cleaning and cobalt compatibility performance.

Introduction

Post Cu CMP (chemical mechanical polishing) cleaning has become one of the most critical steps in the manufacturing of ultra-large-scale integrated (ULSI) circuit devices for Cu interconnects. Insufficient post-CMP cleaning could cause significant impact on device yield and reliability. As the minimum feature size has been reduced to <15 nm, new liner materials have been incorporated to replace Ta/TaN which has inadequate coating properties for very small high aspect ratio trenches. Cobalt has been introduced as one of the most promising candidates for TaN/Ta barrier layer replacement and as a conductive layer for the next-generation ULSI circuits due to its good adhesion to Cu and excellent conformal coverage. Furthermore, with these excellent features, its footprint is extending to the middle end of line as a conductive wire. As a result, it is becoming the remarkable material in ULSI circuits. However, a significant drawback with cobalt is that feasible oxidation during post-CMP cleaning and excess loss was expected to have a significant adverse effect on device reliability. Therefore, a new generation of post-CMP formulations with excellent cobalt compatibility was required to successfully integrate this metal into advanced chip manufacturing.

This study demonstrated how cobalt compatibility and cleaning efficiency were improved in formulations by adding multiple inhibitors to formulations. This alternative approach of adding more than one inhibitor dramatically enhanced passivation and the protection of cobalt surfaces during the post-CMP cleaning step. Detailed information about the interaction of the inhibitors with cobalt was obtained using electrochemical techniques [1] and these results have been described. Furthermore, the cleaning performance of the solutions which contained the corrosion inhibitors was evaluated.

Experimental

Materials. All chemicals are commercially available. Alkaline post-CMP cleaners were prepared based on EKC 2nd generation PCMP cleaner, PCMP5600 series.

Cobalt etch rate. Cobalt thickness was measured using XRF, Axios (Panalytical). Cobalt etch rates of each solution were calculated from the thickness loss and process time.

Electrochemistry. Electrochemical impedance spectroscopy was carried out using a three-electrode configuration with a saturated Ag/AgCl reference electrode, a platinum wire as a counter electrode, and Cu or Co wafer coupons as working electrodes.

CMP and post-CMP clean. Commercially available Cu/ULK patterned wafers (< 28nm node) were used for the cleaning test. The wafers were polished using a CMP wafer polisher with a standard polishing recipe. After polishing, the wafers were cleaned with the test formulations and rinsed with de-ionized water using wafer scrubber system with a standard cleaning recipe. Defects on the patterned wafer were measured using ultraviolet illumination laser-scanning patterned wafer inspection tool.

Result and Discussion

Five formulations S2-A, S2-B, S2-C, S2-AB and S2-AC were prepared with inhibitors A, B, C, A and B, A and C, respectively to assess their effect on cobalt compatibility. As shown in Figure 1, cobalt etch rates were collected to evaluate the Co compatibility of alkaline post-CMP cleaning solutions containing various corrosion inhibitors. Inhibitor A was the most effective cobalt inhibitor at reducing the cobalt etch rate. Interestingly, S2-AB shows the lowest Co etching rate, indicating the synergic effect of inhibitor A and inhibitor B to significantly improve the Co corrosion performance.

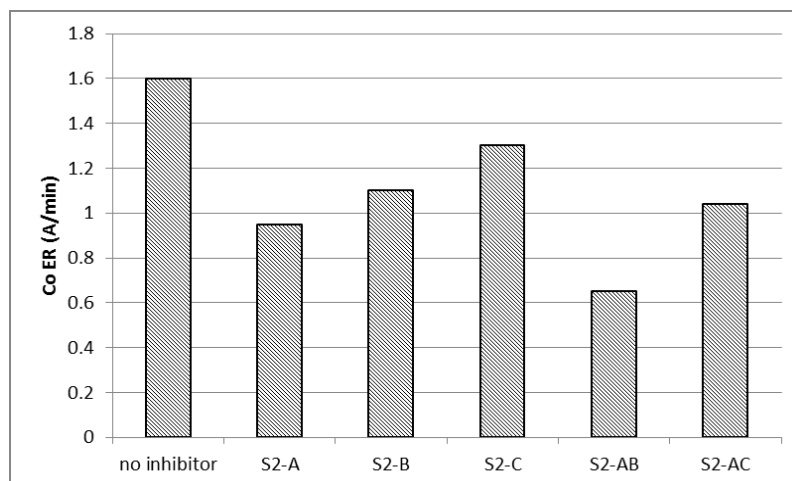


Figure 1: Cobalt etch rate (ER) of alkaline post-CMP cleaning solutions containing various corrosion inhibitors

Electrochemical impedance spectroscopy has been a powerful technique to probe in-situ surface properties at a solid-liquid interface. To understand the protection mechanism of inhibitor A and inhibitor B, impedance measurements were used to investigate how the electrochemistry of cobalt changed in solutions S2-A, S2-AB, and no inhibitor. The sizes of semi-circles observed in electrochemical impedance spectra represent the charge transfer resistance (R_p) between the electrodes and the solution. Nyquist curves were fit with a Randles circuit model [2]. Figure 2 shows the Nyquist plots collected for the formulation without inhibitor, and in the formulations S2-A with a single inhibitor and S2-AB which contains two inhibitors. Charge transfer resistance data that was calculated from the impedance data in Figure 2 has been plotted in the Figure 3.

The R_p of cobalt in the formulation with inhibitor A was larger compared to non-inhibitor solution. Increased charge transfer resistance was consistent with inhibitor A having formed a passivation layer on the cobalt surface. The R_p in the binary inhibitor system S2-AB was even larger compared to S2-A. If the inhibitors interact with different sites on cobalt or have a synergistic effect and can activate each other was not clear. Detailed studies to understand the role of each inhibitor in the binary systems is in progress. Importantly, the higher charge transfer resistance observed in impedance data correlated with cobalt metal loss data in Figure 1 and supported that the inhibitors were effective at passivating corrosion sensitive cobalt.

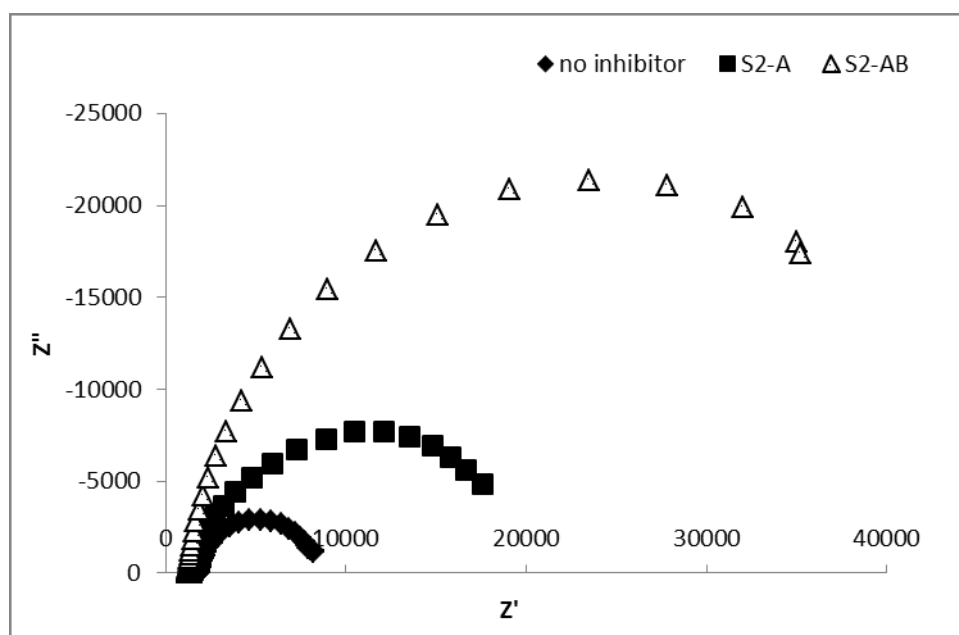


Figure 2: Nyquist plot obtained with a cobalt electrode in three post-CMP cleaning chemistries.

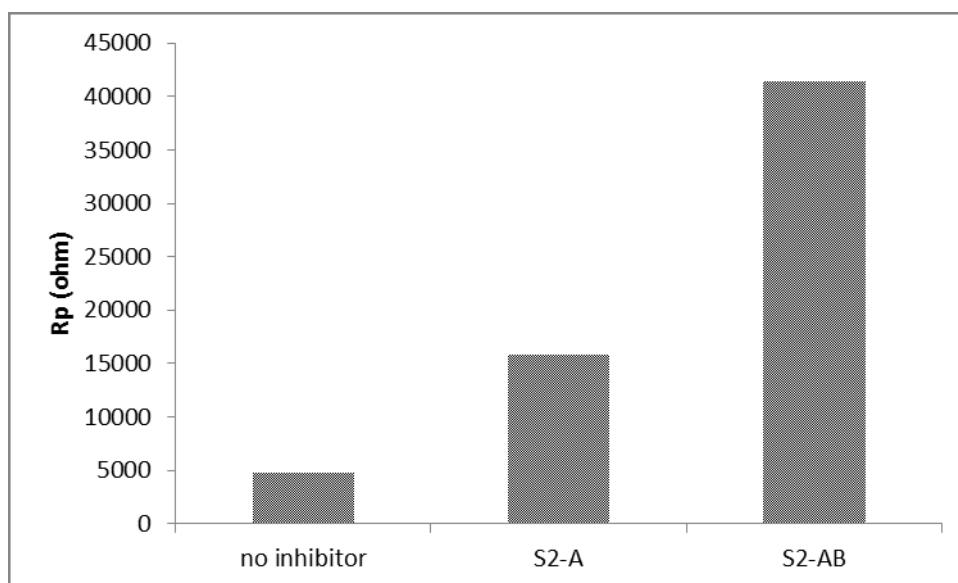


Figure 3: R_p (charge transfer resistance) of cobalt surfaces obtained by Nyquist plot fitting from Fig.2

Since both cobalt and copper have been concerned about galvanic corrosion in the advance node, it is crucial to minimize the driving force (potential gap between Cu and Co) for galvanic corrosion in the cleaning solutions. The formulation without inhibitor therefore has been tuned to minimize the open circuit potentials (OCP) gap between Cu and Co (Figure 4a). After adding inhibitors, the formulations S2-A and S2-AB did not change the electrochemical behaviors of the corrosion potential between Cu and Co. Figure 4 shows the Tafel plot for Cu and Co in the formulations S2-A and S2-AB. The small OCP gap between Cu and Co indicates that the driving force galvanic corrosion in this formulation has been almost completely eliminated.

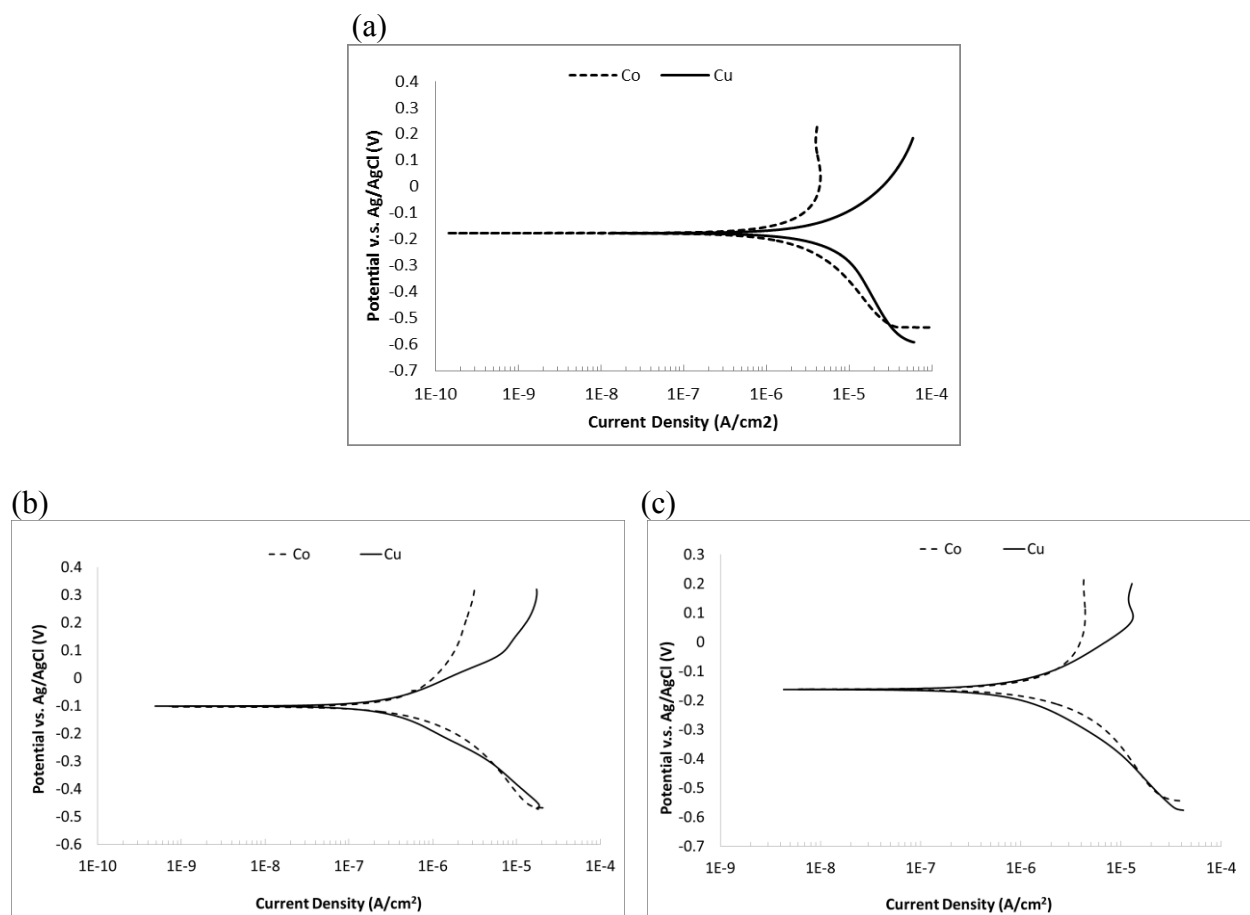


Figure 4: Tafel plots of Cu and Co in the 50 dilution ratio of (a) no inhibitor, (b) S2-A and (c) S2-AB

To further verify the Cobalt compatibility performance, patterned wafers with ILD structure containing copper vias and cobalt liners were tested in formulation without inhibitor and S2-AB. Coupons from the wafer were dipped in each solution for 2 minutes and the Co loss inspected by TEM. Figure 5a shows the TEM images of the wafer as received and of coupons from the wafer after they have been processed in solutions with no inhibitor (Fig. 5b) and in the system S2-AB with two inhibitors (5c). Figure 5b indicated that Co and Cu loss was observed due to the lack of protection from inhibitors. By the contrast, the TEM images clearly showed little or no Co liner loss after dipping in S2-AB. As a result, two inhibitor systems of S2-AB provide superior Co compatibility.

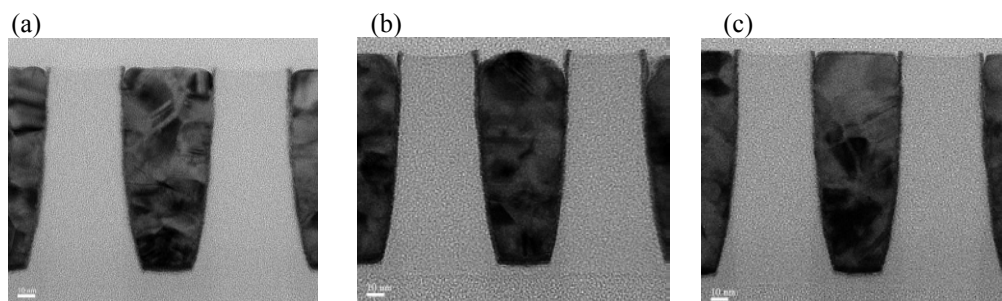


Figure 5: TEM images to evaluate the Co loss. (a) as received, (b) after dipping in solution without inhibitor, (c) after dipping in S2-AB

The cleaning ability of the formulations with the lowest cobalt etching rates were evaluated relative to the baseline formulation which was an established extensively used commercial alkaline post-CMP clean. As shown in Figure 6, S2-AB is better at removing CMP residues on copper blanket wafers than baseline.

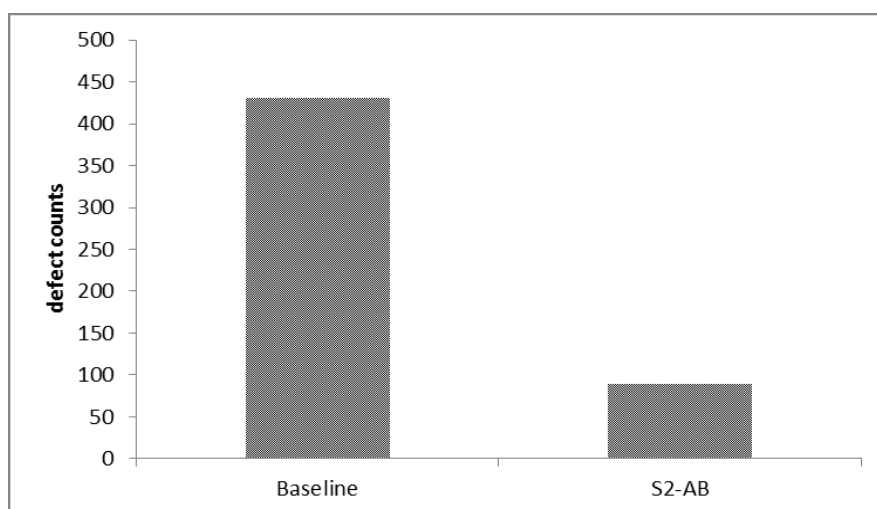


Figure 6: Defect number on copper blanket wafers after post-CMP cleaning.

Summary

New cobalt compatible post-CMP formulations have been prepared that was highly effective for removing CMP residues. After screening, formulations that contained a combination of two inhibitors were found to have the lowest cobalt etch rates and were the most efficient for post-CMP cleaning. The new formulation S2-AB had the best overall performance characteristics for post-CMP cleaning at advanced device nodes where a corrosion sensitive cobalt liner has been incorporated. The interaction between inhibitors continues to be studied in order to further improve post-CMP process yield and device reliability.

References

- [1] A. Otake, A. Kuroda, T. R. Luo and P. R. Bernatis, Proceedings of UCPSS, 2012, p.124
- [2] A. J. Bard, Electrochemical Method: Fundamentals and Applications, John Wiley & Sons, Inc. New York, 2001.

Oxygen Control for Wet Clean Process on Single Wafer Platform

Lucile Broussous^{1, a}, Kevin Hoarau¹, Come de Buttet²
and Stephane Zoll¹

¹STMicroelectronics, 850, rue Jean Monnet, 38926 Crolles, France

²Univ. Grenoble Alpes, F-38000, Grenoble. CEA, LETI, MINATEC Campus, 17 rue des Martyrs, 38054 GRENOBLE, France.

^alucile.broussous@st.com

Keywords: Low Oxygen process, Dissolved Oxygen meter, BEOL cleaning

Abstract. Wet processing with low oxygen content may provides some advantages, however, full control to avoid oxygen uptake during wafer processing remains a challenge for short process industrialization on single wafer tool. Inline oxygen concentration monitoring was used for process optimization. Then, cobalt etch in diluted HF solutions was evaluated depending on the recorded oxygen concentration and hardware available options for atmosphere control in the process chamber.

Introduction

The advantages of wet processing with low oxygen content in the liquid (rinsing water, diluted acids such as HF, HCl) and in the atmosphere (nitrogen flows, closed chambers), have been demonstrated both for FEOL applications [1-3] and BEOL applications [4-7], and the 2010 ITRS roadmap recommended 10ppb [O₂] in the ultrapure water provided by fab facilities to wet equipment. However, full control to avoid oxygen uptake during wafer processing remains a challenge for process industrialization on single wafer tool with very short process time.

In this work, we will focus on oxygen control in ultra diluted HF solutions. Indeed, it was already demonstrated that “HF budget” used for BEOL interconnections post-etch clean is continuously decreasing with technology nodes [7, 8], but may remain necessary to ensure low cost process with a good cleaning efficiency. In order to minimize lateral etching of the insulating porous dielectric, HF concentrations down to 0.05%wt were proposed even for 10nm node with improved control of oxygen concentration [7]. However, as process robustness may suffer from very short process time (<15 seconds for example), we studied solutions with lower HF concentration. The use of 0.025%wt HF solution, allowed us to maintain a very low etching of the dielectric with longer process time, so that cleaning process window should be slightly improved as well as in-line monitoring robustness (flows and temperature inline control). HF concentration reduction maybe also interesting in order to better control the etch-rate of sensitive metals such as Cobalt, used as copper “liner” and copper “capping” in advanced nodes[9, 10].

As we attempted to develop a stable low oxygen process, we pointed out the influence of some process parameters on oxygen concentration at the point of use, such as chemical flow rate, process time, process recipe structure and we investigated potential optimization thanks to inline oxygen concentration monitoring. Application to BEOL post-etch clean was then carried out. In particular, cobalt etch in diluted HF solutions was evaluated depending on the recorded oxygen concentration and hardware available options for atmosphere control in the process chamber.

Experimental

In this study, industrial single wafer platform SU3100 from SCREEN was used. Solutions were prepared in a mixing tank, located in the basement with ultrapure and deoxygenated water from facilities (< 0.5ppb [O₂]) and standard microelectronic grade chemistries, to reach a final concentration of 0.025%wt. HF mixing tank atmosphere was saturated with N₂, thanks to an N₂ flow and N₂ bubbling from the tank bottom at 10 l/min. An additional degassing unit was installed

on the chemistry line, before the point of use (membrane based oxygen separation unit). In the Hybrid Multi-Process Chamber (HMP) the ambient atmosphere is regulated thanks to additional N_2 flows. A “shield plate” allows watermark-less processing and reduced metals corrosion thanks to central nitrogen flow and short distance between the plate and the wafer (referred to as “ N_2 coverage” in the figures).

Oxygen concentration was monitored thanks to an Horiba system HD-960L, specially designed for HF solutions monitoring. Chemical flows were varied from 0.1 to 1.5 l/min.

Low Oxygen Process was evaluated on blanket cobalt wafers of 165 Å thick, deposited by PVD on 1000 Å SiO_2 . Cobalt thickness measurement was done by ellipsometry technique. Each result was the average of 6 wafers/run, with 17 measurements point/wafer.

Results

Low oxygen concentration at point of use is quite difficult to manage, in particular with preparation in the mixing tank because oxygen uptake may arise in several parts of the hardware (tank drain, PFA pipes, fluids suck-back in dispense lines...). First the variation of oxygen concentration during wafer processing was recorded for very long process time (20 minutes), as shown in fig.1. Under our experimental conditions, oxygen concentration was found to decrease with higher flow-rate. At first order the main parameters to be considered are the “refreshing rate” in the mixing tank (refill frequency with deoxygenated water from facilities) and the oxygen uptake due to the remaining air in the recirculation loop that prevents chemistry stagnation. Degassing unit efficiency and oxygen permeation through PFA pipes played a second order part in oxygen concentration variations.

Thus these first experiments allowed us to select the best conditions for low $[O_2]$ solution in our configuration (high chemical flow rate), and manage process evaluations with various O_2 concentration.

Process was then performed with shorter recipes, nonetheless adapted to monitor oxygen concentration: long pre-dispense to drain (3 minutes) followed by two minutes of chemical dispense. The recorded oxygen concentrations before and after recipe optimization are illustrated in figure 2. We confirmed that before processing each wafer, the long pre-dispense is necessary to flush the remaining oxygen in the line before to send the chemistry on the wafer. However, a small peak of oxygen increase was detected at the beginning of chemical dispense on the wafer (fig.2a). Comparison of real time oxygen monitoring and process recipe time sequence allowed us to identify that it was due to the additional pre-wetting step with water before chemistry dispense. Indeed, the oxygen content in the line slightly increased due to valve open/close. Stable oxygen concentration was then observed by removal of this pre-wetting step (fig. 2b).

Optimized process recipe, with short process time (20 – 60 seconds) was then used to perform metals etch-rate. Cobalt thickness variation as a function of process time and oxygen content in the solution is illustrated on fig.3. Thickness variation was linear with process time. For all process conditions, initial offset is due to cobalt oxide removal in the first seconds of the process, due to the low stability of cobalt oxide in acidic solutions. Interception of the line with the Y axis for $t=0$ allowed us to emphasize that native cobalt oxide was in the range 15-25 Å.

The cobalt etch decrease is clearly correlated with the oxygen concentration decrease in the solution (2000ppb/400ppb/200ppb). It is also interesting to note the effect of “atmosphere control” over the wafer by using the “shield plate” at a very close distance. This effect is evidenced by the highest cobalt etch recorded with the lowest $[O_2]$ (200ppb) in the fluid, but no atmosphere control.

The corresponding Cobalt etch rates (Å/min.) are reported in fig.4. The highest cobalt etch rate (80 Å/min) was recorded without atmosphere control, and it dropped down to 46 Å/min. with shield plate atmosphere, independently of $[O_2]$ in the solution. Thus, at first order, atmospheric control in the chamber allows to divide by ~2 the cobalt etch rate. Then, with the shield plate atmosphere control, additional fluid deoxygenation from 2000ppb down to 200ppb allowed to divide by 7 the cobalt etch rate. In the best conditions achieved in this study (200ppb $[O_2]$ with atmosphere control), an etch rate of 6 Å/min was obtained.

In fig.5, these results are compared to previous unpublished studies with 0.05%wt HF and 1%wt glycolic acid at room temperature, on a single wafer platform that allowed oxygen control (not exactly measured). It is interesting to note that without oxygen control, 1%wt. glycolic acid is less aggressive than both diluted HF solutions (0.05% and 0.025%wt.). HF concentration reduction from 0.05% to 0.025% does not impact cobalt etch rate, since same slope is observed for cobalt thickness variation vs process time. As soon as oxygen concentration decreases (in solution and atmosphere), the cobalt etch rate strongly decrease. However, no significant difference is observed depending on the nature of the acid and its concentration in solution (glycolic acid vs diluted HF 0.05% and 0.025%wt).

This significant decrease of cobalt etch rate is thus promising for low oxygen cleaning process with diluted HF solutions and short process time in presence of exposed cobalt. However, as initial cobalt oxide consumption may not be avoided, final process validation will also depend on integration scheme and potential cobalt oxidation during interconnections fabrication.

Conclusion

In conclusion, in line monitor for oxygen concentration in the chemistry was found to be very sensitive to small fluctuations of oxygen concentration over very short process time. For a given tool configuration, it allowed us to clearly identify some crucial parameters that may influence oxygen concentration at the point of use such as chemical flow rate, mixing tank preparation, initial oxygen content and recipes parameters (predispense time, suck back steps, ...). Process performance was validated with a drastic decrease of Cobalt etch rate in ultra-diluted HF solution.

Acknowledgements

This work was performed in the frame of a join development program with SCREEN. The authors wishes to thanks HORIBA for their active collaboration on Dissolved Oxygen monitoring in diluted HF solutions.

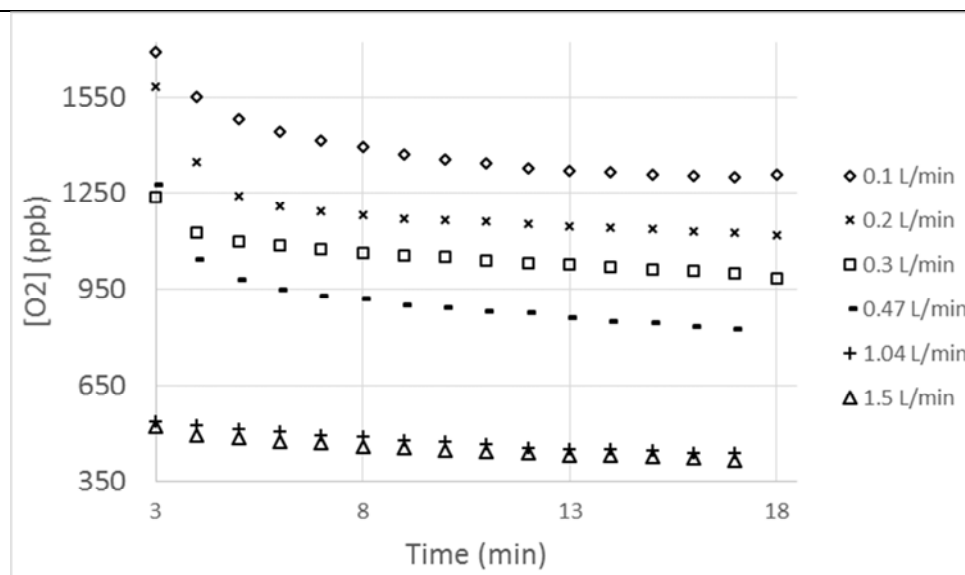


Fig. 1: Oxygen concentration depending on chemistry flow rate, recorded for 20min process recipe (1 wafer/run)

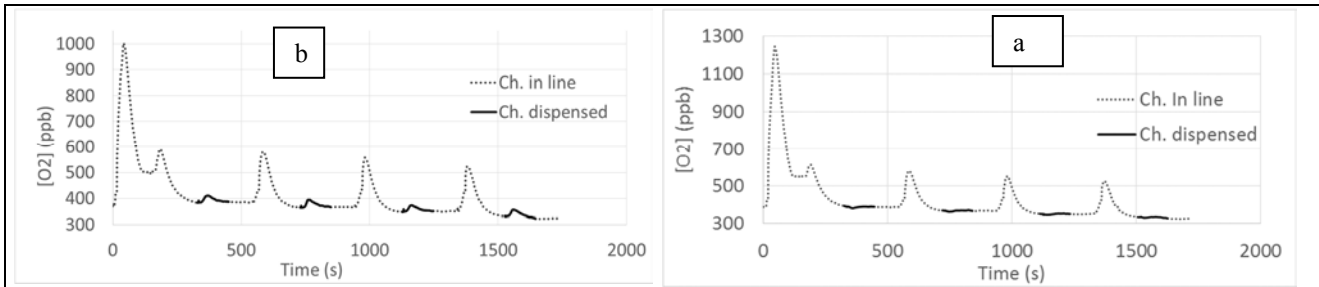


Fig. 2: Illustration of recipe optimization to avoid oxygen concentration increase during process. a_ initial recipe. b_ after optimisation/“Ch in line”: chemistry go to drain. “Ch dispensed” : chemistry dispense on wafer

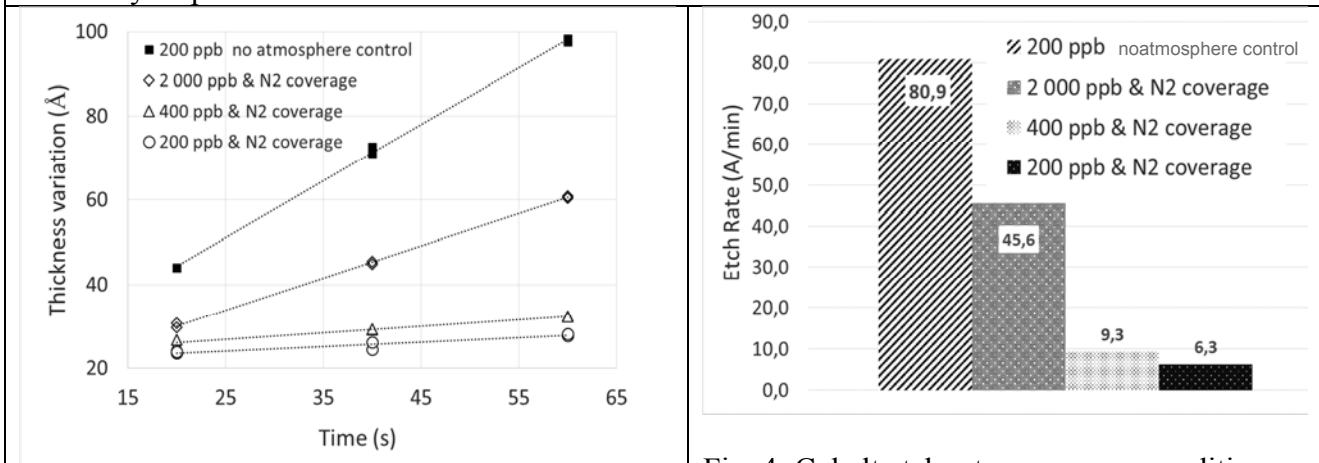


Fig. 3: Cobalt thickness variation in 0.025%wt.HF solution vs. process time and process conditions

Fig. 4: Cobalt etch rate vs process conditions

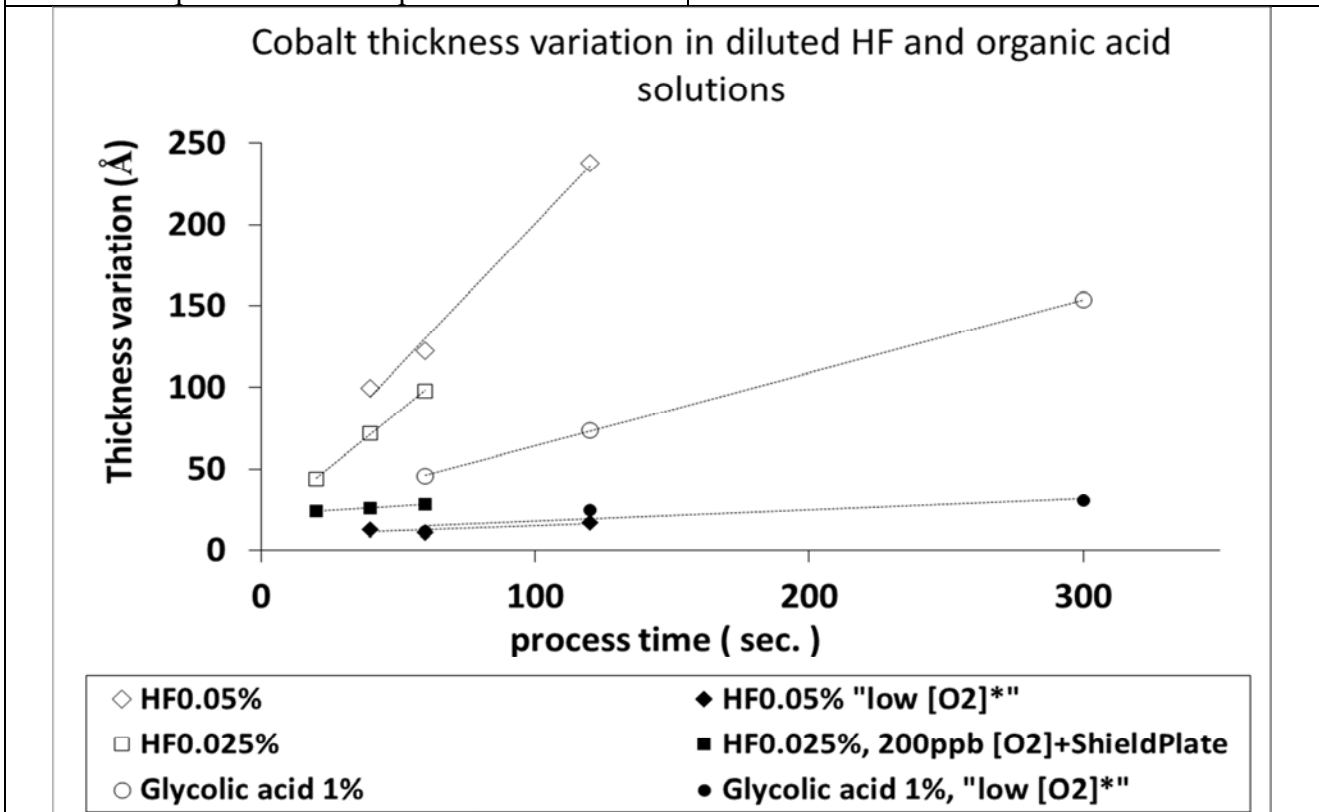


Fig. 5: Cobalt thickness removed in diluted HF (0.025% and 0.05%wt*) and diluted glycolic acid (1%wt)* solutions.

*experiments performed on CVD Co 1000A, measured by 4point probe resistivity, without exact monitoring of the oxygen concentration in the solution.

References

- [1] Y.Yagi, T.Imaoka, Y.Kasama, T.Ohmi, IEEE Transactions on Semiconductor Manufacturing 5(2) (1992) p.121-127
- [2] T.Yoshida, M.Otsuji, H.Takahashi, Solid State Phenomena 219 (2015) p85-88
- [3] F.Sebai, L.Witters, F.Holsteys, Y.Yukimi, P.Mertens, S. De Gendt, Solid State Phenomena 219 (2015) p.105-108.
- [4] L. Broussous, O. Hinsinger, S. Favier, P. Besson, Solid State Phenomena 92 (2003) p.263-266
- [5] D.Rébiscoul, N. Lopez, L. Broussous, D. Louis, G. Passemard, Solid State Phenomena 134 (2008) p.333-336
- [6] S. Bilouk, C. Pernel, L. Broussous, V. Ivanova, R. P.Nogueira, Solid State Phenomena 145-146 (2009) p. 343-346
- [7] B.Peethala, F.W.Mont, S.Molis, R.Knarr, B.L'lherron, C.Labelle, D.Canaperi, S.Siddiqui, Microelectronic Engineering 161 (2016) p.98-103
- [8] L.Broussous, W. Puyrenier, D. Rebiscoul, V. Rouessac, A. Ayral, Solid State Phenomena 145-146 (2009) p. 295-302
- [9] M.Hauschildt, B.Hintze, M.Gall, F.Koschinski, A.Preusse, T.Bolom, M.Nopper, A.Beyer, O.Aubel, G.Talut, E.Zschech, Jap.J.of Ap.Physics 53, 05GA11 (2014)
- [10] R.Galand, L.Arnaud, E.Petitprez, G.Brunetti, L.Clément, P.Waltz, Y.Wouters, IEEE transaction, IITC 2011 conference. DOI: 10.1109/IITC.2011.5940320

Study of TiW Conditioning through Different Wet and Dry Treatments to Promote Ni Electroless Growth

Ivan Venegoni ^{1a}, Fabio Scimè¹, Enrica Ravizza¹, Simona Spadoni¹,
 Francesco Pipia¹, Paolo Colpani¹, Mauro Alessandri¹

¹ STMicroelectronics, via Olivetti 2, 20041, Agrate Brianza, Italy

^aivan.venegoni@st.com

Keywords: TiW, Ni, W, Ti, tungsten, titanium, nickel, treatments, electroless, oxidation.

Abstract. Electroless Ni deposition is often used in presence of Cu, Ti and Au. Recently TiW has also started to be employed, but with this alloy the Ni deposition is not always neat. In our work we investigate the effect of different wet treatments on the Ni growth by means of XPS analyses and SEM inspections. It is found that an oxidized surface inhibits the activator deposition. The de-oxidized Ti atoms in TiW on the other hand are believed to act as the principal sites for Pd seed deposition and subsequent Ni growth.

Introduction

Ti and its alloys are commonly used in microelectronic devices thanks to their intrinsic properties that include good adhesion towards both silicon oxide and noble metals, low metal diffusivity and the ability to produce low resistance ohmic contacts. Within this class of materials, the TiW alloys recently found wide applications, in most cases combined with metals such as Cu, Ni and Au for RDL (Re-Distribution Layer), OPM (Over Pad Metallization), bumping and MEMS processes [1]. Usually the TiW is deposited by PVD techniques and immediately covered by the seed layers of these metals, avoiding the spontaneous oxidation of its surface [2]. Anyway, in most cases the TiW is usually patterned, resulting in an exposition of the sidewall to air and to the subsequent process steps, in general involving an electroless metal growth which could give birth to a spurious deposition on the TiW itself. Therefore it could be interesting to understand in which way the alteration of the TiW surface properties, made by different wet and dry treatments, could influence the subsequent electroless deposition step.

Experimental

The work has been divided in two phases: the first one dedicated to the characterization of the TiW surface after being subjected to different wet and dry treatments; the second one dedicated to the study of the effects of these treatments on the following Ni electroless deposition. Both phases involved the preparation of Si/Si₃N₄ flat substrates covered with 3000 Å of TiW by PVD process. The TiW deposition has been carried out on an Endura AMAT tool equipped with a TiW alloy target.

Table 1: Summary of the samples analyzed by XPS.

Substrate	Treatments			Equipment	Characterization
	Type	Time	Chemistry		
Si/Si ₃ N ₄ /TiW	/	/	/	/	XPS
	Wet	60s	H ₂ SO ₄	AMAT Raider Spray Acid	
	Wet	60s	HF	AMAT Raider Spray Acid	
	Wet	60s	H ₂ O ₂	AMAT Raider Spray Acid	
	Dry	60s	O ₂	Axcelis Gemini	

In the first phase these substrates have been conditioned by different wet and dry treatments, as reported in Table 1. Both acidic (H₂SO₄ 2%wt, HF 1%wt) and oxidizing (H₂O₂ 30%wt, O₂ plasma) chemistries have been tried. The wet treatments were performed on an AMAT single chamber spray tool, whereas the dry plasma treatment was performed on an Axcelis Gemini tool.

The effects of these treatments on the TiW surface have been investigated through XPS analyses, using a Physical Electronics 5600 tool, with 23.5V pass energy and 75° take-off angle. Since the TiW is spontaneously prone to oxidation and the increasing of native oxide thickness goes to saturation within very short time, we performed the XPS analyses 7 days after the treatments.

Table 2: Summary of the samples prepared for the electroless Ni growth trials.

Substrate	Treatment		Ni deposition	Characterization
	Type	Chemistry		
Si/Si ₃ N ₄ /TiW	/	/	30s	SEM / TEM / EDX
	Wet	HF 60s		
	Wet	H ₂ O ₂ 60s		
	Dry	O ₂ 60s		

In the second phase the substrates have been treated with the same chemistries already described and have been subjected to electroless Ni deposition, as reported in Table 2. The electroless process is composed by two steps: 1) substrate activation and 2) Ni deposition. For this work a very short (30s) Ni deposition recipe was used in order to highlight the metal growth morphology at the beginning of the reaction. Finally the samples on which the Ni growth was successful were characterized by TEM sections and EDX analyses, whereas the samples on which we didn't find the presence of Ni were characterized by SEM inspections and EDX analyses.

Results and discussion

The first phase of this work started with the XPS analyses on the TiW substrates. This technique collects 4 peaks related to W and 3 peaks related to Ti. Going into details, the peaks at 31.1 and 33.2 eV are assigned to the metallic W, while the peaks at 35.9 and 38.0 eV are assigned to the oxidized W in oxidation state of +6. Whereas regarding the Ti emission, we can assign the peak at 453.9 eV to the metallic Ti and the peak at 464.8 eV to oxidized Ti in oxidation status of +4. Finally the peak at 459.1 eV is the sum of signals coming from metallic and oxidized Ti. Therefore to evaluate the effect of treatments in terms of W and Ti oxidation we calculated the ratio between oxidized and non-oxidized signals after Gaussian fitting of W4f peaks and Ti2p peaks.

Table 3: Ratios between the oxidized and metallic signals for W and Ti.

Treatment	W oxidation		Ti oxidation	
/	0.35	REF	1.77	REF
H ₂ SO ₄	0.52	↑	2.53	↑
HF	0.32	≈	0.43	↓↓
H ₂ O ₂	1.02	↑↑	1.47	↓
O ₂	1.83	↑↑↑	12.27	↑↑↑

Starting from the XPS results for the TiW treated with acidic solutions, we can observe in Fig. 1 and Table 3 that the ratio between the oxidized and the metallic tungsten signals is increased after the H₂SO₄ treatment, while is almost unchanged after the treatment with HF. This result is coherent with the fact that the Pourbaix diagrams reported in literature give the WO₃ as the thermodynamically stable phase in low pH conditions, but it could also be an artifact made by the tendency of TiW surface to be quickly re-oxidized by air exposure. In this case the higher ratio showed in Table 3 (0.52 versus 0.35) could be simply explained by an higher surface reactivity produced by the H₂SO₄ treatment. Moving to the Ti signals (Fig. 2), we observed a reduction of the Ti metallic signal after the H₂SO₄ treatment, probably hidden by the higher amount of WO₃ present into the surface oxide. On the opposite, we saw a strong reduction of the oxidized Ti peak after HF. Therefore we can conclude for the acidic solutions, that H₂SO₄ produced an increase of TiW surface oxidation through the increase of tungsten oxide, while HF showed a significant deoxidizing capacity, almost completely removing the Ti oxide.

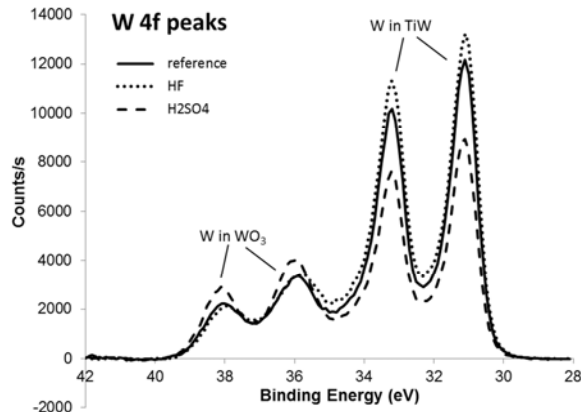


Fig. 1: W XPS peaks after acid treatments.

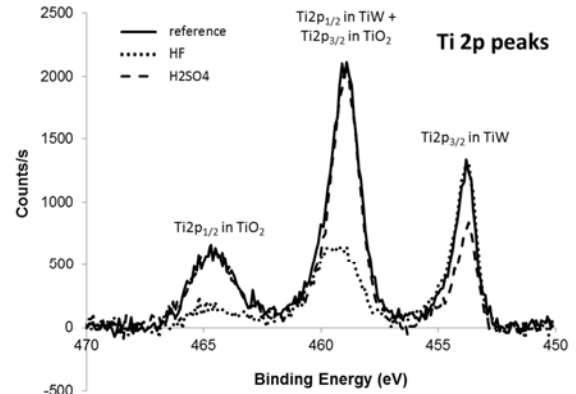


Fig. 2: Ti XPS peaks after acid treatments.

Continuing with the analyses of oxidizing treatments, we can observe by Fig. 3 that both the treatments gave origin to an increase of the oxidized peak intensities, and that the O_2 dry plasma was more effective than the H_2O_2 chemistry. This last one also gave origin to the formation of the WO_2 oxide where tungsten is in oxidation status of +4. Finally, collecting the XPS spectra in the Ti emission region (Fig. 4), we found that after the H_2O_2 all the peak intensities were decreased. We interpreted this result as a change of the TiW surface oxide stoichiometry, meaning that the oxide left after the H_2O_2 treatment is probably richer in W respect to the native oxide of the non-treated sample. On the opposite, the O_2 treatment strongly oxidizes also the Ti atoms, in the same way as we have already observed for the W ones.

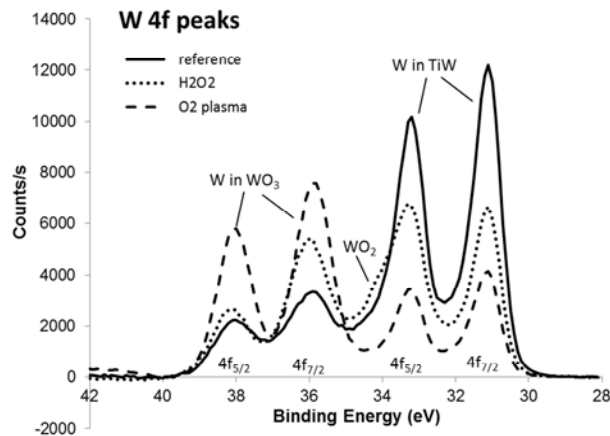


Fig. 3: W XPS peaks after oxidizing treatments.

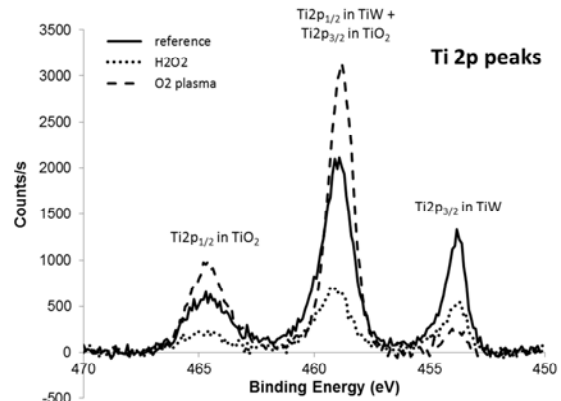


Fig. 4: Ti XPS peaks after oxidizing treatments.

Upon completion of the discussion on the XPS analyses, it is now possible to understand the results of the electroless Ni growth trials that has been run in the second phase. This deposition on TiW was successful only for the HF treatment, as reported in Table 4. This could be explained by the needing of the electroless Ni growth process to be applied on a deoxidized surface, able to give electrons to the Pd catalyst, which needs to be reduced before being deposited onto the TiW surface [3]. Thus both the samples subjected to oxidizing treatments and the non-treated one are not suitable as substrates for the electroless Ni growth. Therefore a SEM inspection with tilted view was performed on these three samples, while TEM section images have been collected to study the sample treated with HF.

Table 4: Ni electroless growth results.

Treatment	Ni growth
/	No
HF	Yes
H_2O_2	No
O_2	No

From SEM images reported in Fig. 5, we can observe that on the non-treated sample few bright particles are present. The EDX analysis performed on one of these particles confirmed that are made by Pd, probably deposited at the pinholes of the TiW oxide [3]. None of these particles have been observed on the samples treated with H_2O_2 or O_2 , probably because of their higher surface oxidation which doesn't leave Ti and W atoms able to donate electrons to the Pd ones. The surface of TiW appears rougher after the H_2O_2 treatment probably because it has been partially etched.

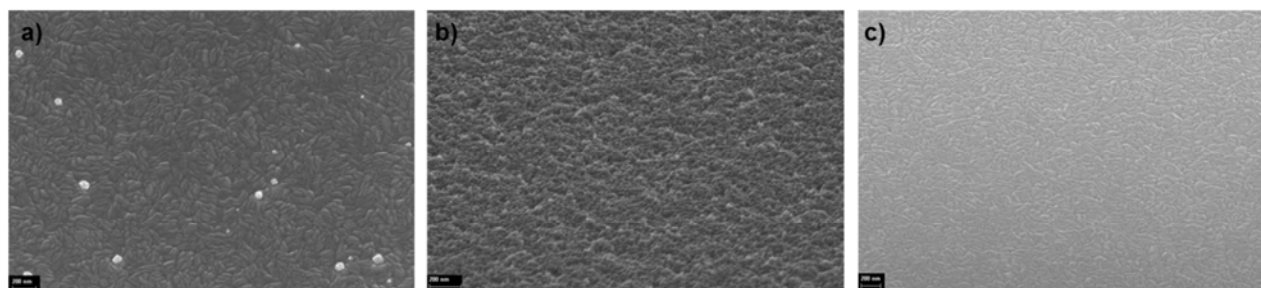


Fig. 5: SEM tilted images of a)TiW non-treated, b)TiW treated with H_2O_2 , c)TiW treated O_2 , after being subjected to the Ni electroless growth process.

The TEM section reported in Fig. 6 and taken from the sample treated with HF showed the presence of Ni, grown around the Pd seeds. In addition it is possible to observe that the Pd seed density on this sample is much higher than what we have seen on the non-treated sample. The increasing of Pd seed density has to be attributed to the deoxidizing effect of the HF treatment which produced an higher amount of Ti atoms freed from their initial bonds with oxygen and able to reduce Pd. Again from Fig. 6, it is possible to observe that the morphology of the Ni layer is not flat, probably because the Pd seed density was not high enough to produce an homogeneous deposition across the TiW surface.

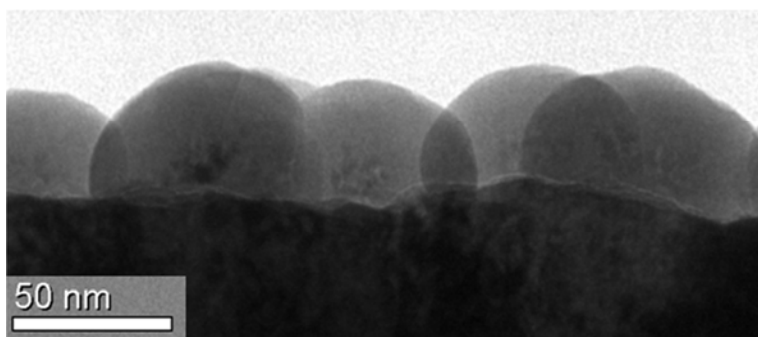


Fig. 6: TEM section of TiW treated with HF after being subjected to the Ni electroless growth process.

Conclusions

The importance of substrate conditioning before the electroless metal deposition process has been confirmed also for TiW, determining the growth morphology in the first phase of the deposition. In particular the effect of different wet and dry treatments on TiW has been explained through the XPS analyses and subsequently showed by the SEM and TEM images. These analyses want to shed a light on a process which is not well described yet, potentially opening the way to new applications involving the TiW material.

References

- [1] Frederic Battegay, Mickaël Fourel: *Barrier Material Selection for TSV Last, Flipchip & 3D - UBM & RDL Integrations*, 2015 Electronic Components & Technology Conference.
- [2] H.G. Tompkins, S. Lytle Green: *An investigation of the oxidation of Ti:W*, Journal of Applied Physics, 1988.
- [3] A.M.T. van der Putten: *Controlled Mechanical Adhesion of Electroless Cu Patterns*, Journal Electrochemical Society, 1993.
- [4] V.M. Dubin, S.D. Lopatin, V.G. Sokolov: *Selective electroless Ni deposition on a TiW underlayer for integrated circuit fabrication*, Thin Solid Films, 1993.

Post CMP Wet Cleaning Influence on Cu Hillocks

Annamaria Votta^{1, a}, Francesco Pipia¹, Luisito Livellara¹, Manuela Caminati¹
Simona Spadoni¹, Enrica Ravizza¹, Salvatore Grasso¹, Maddalena Bollin¹,
Maurizio Moroni¹, Mauro Alessandri¹, Paolo Colpani¹

¹ STMicroelectronics, via Olivetti 2, Agrate Brianza (Mi), Italy

^aannamaria.votta@st.com

Keywords: Cu wet cleaning, Copper Oxide removal, Copper kinetic

Abstract. Up to date, it is commonly reported in literature that the amount of copper hillocks is dependent on a) the total amount of residual Cu oxide after Cu CMP, and b) the Cu nitridation. The present work describes how that is only partially true: hillocks depend also on the kind of oxide and on the roughness of the surface after wet treatment. This contribution is even more important than what reported in literature. A tentative model for this behavior is proposed.

Introduction

In copper damascene architecture copper hillocks defect density can be generated when SiN is deposited after Cu-CMP due to Cu reorganization. This defectivity sometimes is reported to be responsible of electrical failures, such as for example the so called “black vias”. In addition it can saturate defectivity maps and, as a consequence, can mask other kind of post CMP defectivity [1]. In literature is reported that the removal of copper oxides grown post CMP through wet cleanings is able to reduce this kind of defectivity [2], but no satisfactory explanation is given for this finding. In this paper we have investigated the influence of different post CMP wet cleanings on copper hillocks reduction. The Cu surface has been analyzed through X-ray Photoelectron Spectroscopy (XPS), Time-of Flight Secondary Ion Mass Spectroscopy (ToF-SIMS) and Atomic Force Microscopy (AFM) in order to shed a light on the influence of the different copper oxides on hillocks formation. The effect of q-times between CMP- wet cleaning and wet cleaning-SiN deposition has been investigated as well.

Experimental

In order to investigate the influence of post Cu CMP wet cleanings on copper hillocks, defectivity analyses have been performed on copper dual damascene structures (SiO₂, Ta/TaN barrier, Cu) after SiN CVD deposition (380° C, SiH₄ and NH₃ precursors). Post CMP wet cleanings have been performed on single wafer tools (LAM SP223) with different chemicals: diluted citric acid @ 25°C, a monocarboxylic acid with pH 2.1 @ 30 °C (P 1), HF 0.5% @ 30 °C. Defectivity inspection has been performed on KLA Tencor tool. XPS, ToF-SIMS and AFM analyses have been done on flat copper substrates (TaN/Ta and Cu seed + ECD Cu 1.4 µm) deposited on TEOS 1000 Å and annealed (150 °C H₂/N₂). After the annealing these substrates have been processed with the same Cu CMP as the one performed on patterned wafers and then cleaned with different chemicals. XPS analyses were performed using a Physical Electronics 5600 tool, with Al monochromatic source, 23.5 V of pass energy and 45° of take-off angle, while ToF-SIMS depth profiles were acquired by a ToF-SIMS IV by IONTOF with Ga⁺ as primary ion gun 25 keV 2.5 pA and Cs⁺ 1 keV 60 nA. AFM analyses were acquired by a Bruker Dimension 3100.

Results and discussion

Influence of wet cleaning. In order to understand the impact of different wet cleanings, some patterned wafers have been processed with P1/ 60s, HF 0.5%/ 10s, citric acid/ 60s after CMP and defectivity analysis has been done on the wafers after SiN deposition. As can be seen in Figure 1, defectivity maps show that a significant hillocks reduction can be obtained with P1 or citric

(1-2 def/cm² vs 150 def/cm² without cleaning), whereas no reduction can be obtained with HF. Those numbers were obtained with cleaning performed immediately after CMP. P1 results were slightly more efficient than citric acid in reducing the defectivity. In order to better understand whether the impact on hillocks of the different cleanings was generated by different surface termination, XPS and ToF-SIMS analyses have been done on the unpatterned wafers.

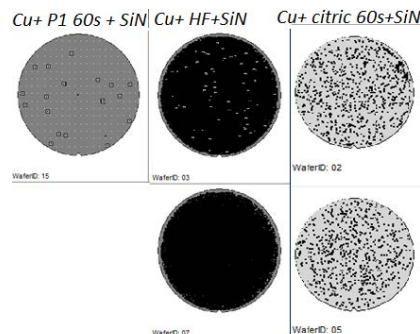


Figure 1: Defectivity maps after SiN deposition.

XPS analysis has been performed on flat Cu wafers immediately after the post CMP wet and has been repeated after 24 h in order to investigate the copper surface termination and evolution. As can be seen in Figure 2a where Cu LMM auger peaks are reported, both citric acid and P1 are able to reduce the Cu oxide grown immediately after CMP. Comparing the ratio of metallic Cu peak and Cu₂O/Cu(OH)₂ peak it can be seen that citric is more effective than P1 regardless of the time: no differences can be noticed between 60 s and 120 s. Anyway the mix of oxides present after wet is depending on the kind of wet performed on the copper surface: after citric acid the Cu surface is richer in Cu(OH)₂ than after P1 or after CMP as can be seen from O1s peak (Figure 2b).

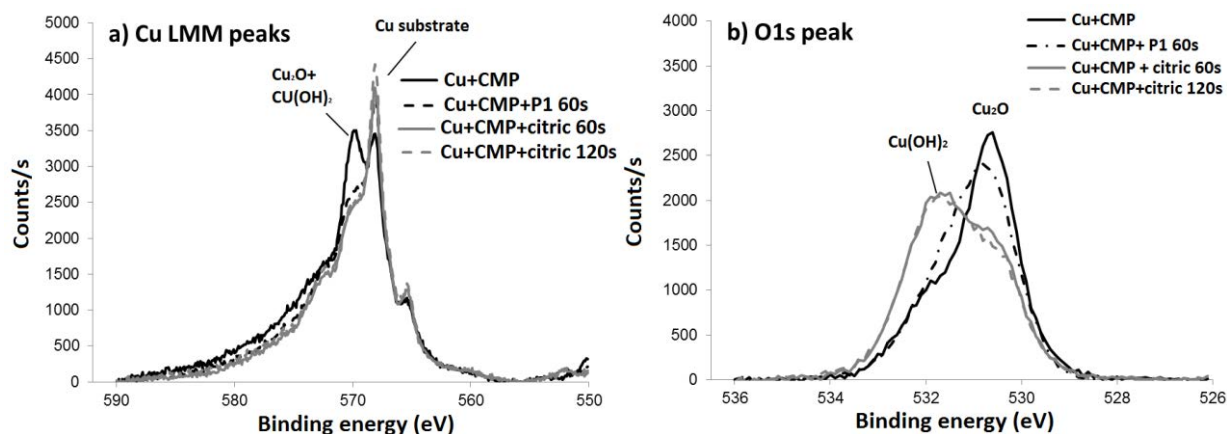


Figure 2: XPS peaks of Cu surface after CMP and different wet cleanings; a) Cu LMM auger peak; b) O1s peak.

On the contrary, HF treatment was less efficient than P1 in removing the oxide: it is very efficient in removing Cu(OH)₂ but less efficient than P1 in reducing the Cu₂O native oxide as can be seen in Figure 3.

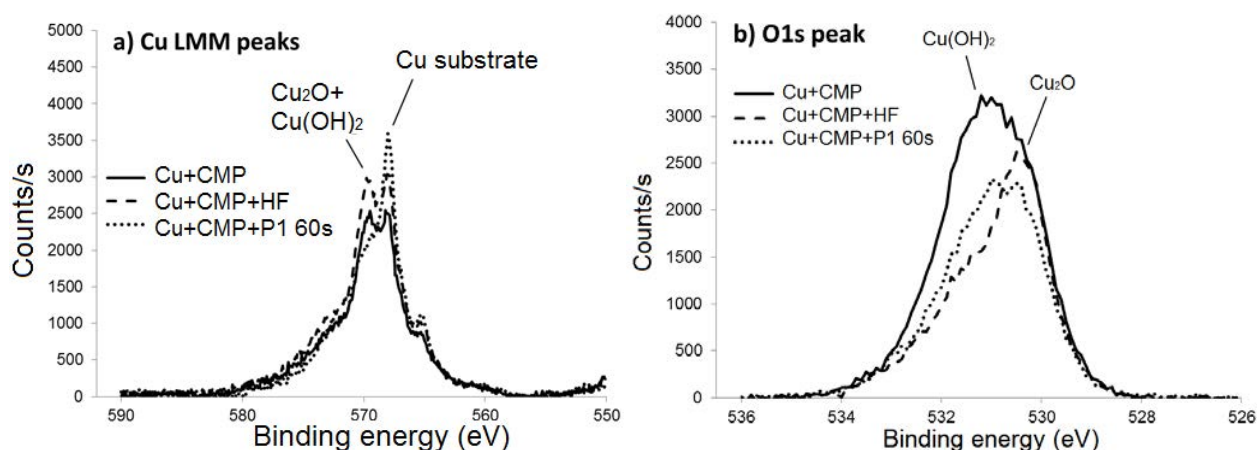


Figure 3: XPS peaks of Cu surface after CMP and different wet cleanings; a) Cu LMM auger peak; b) O1s peak.

AFM measurements have been done on the same wafers in order to understand whether copper oxide removal was able to influence the roughness of the surface. As expected the surface roughness is higher after wet cleans than after CMP (Table 1): copper oxide in fact is not a uniform layer grown on Cu surface, therefore when removing it the surface non-uniformity is enhanced. The roughness after HF is higher than the roughness after P1: HF increases the grain boundary surface.

Table 1: Summary of AFM analyses results

Wet	RMS(nm)
CMP	0.35
CMP+HF	0.63
CMP+ P1	0.53

Kinetic influence. Since different wet cleanings show different efficiency in removing the post CMP native oxide and since the kinetic of Cu oxides re-growth after wet is influenced by the cleaning, both factors have been investigated through defectivity, XPS and ToF-SIMS.

Some wafers have been treated with Cu CMP and then they have been cleaned 7 days after CMP with citric acid 120 s vs P1 60 s vs P1 15 s. SiN deposition has been performed immediately after cleaning. Defectivity analysis has shown that both chemicals are able to reduce the hillocks formation with respect to the wafers that have not been cleaned. Anyway, as can be seen in Figure 4, the reduction obtained with citric acid is not the same as the one obtained performing the cleaning immediately after the CMP (Figure 1) : the defect density is in this case 28 def/cm² vs 5 def/cm² found with citric done immediately after the CMP. With P1 on the contrary the hillocks' defect density is lower than 1 def/cm² for both 15s and 60s process times.

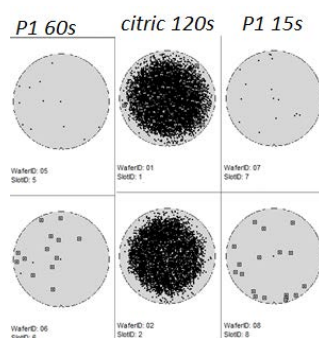


Figure 4: Defectivity maps of wafers with wet cleaning performed 7 days after CMP.

XPS and ToF-SIMS on flat wafers processed with the same recipes 7 days after CMP, as expected, show that the native oxide amount is higher than the one immediately after CMP. Citric acid is more effective than P1 in removing the native oxide (Figure 5) but, again the surface after citric is Cu(OH)₂ richer than P1 as can be seen in Figure 6.

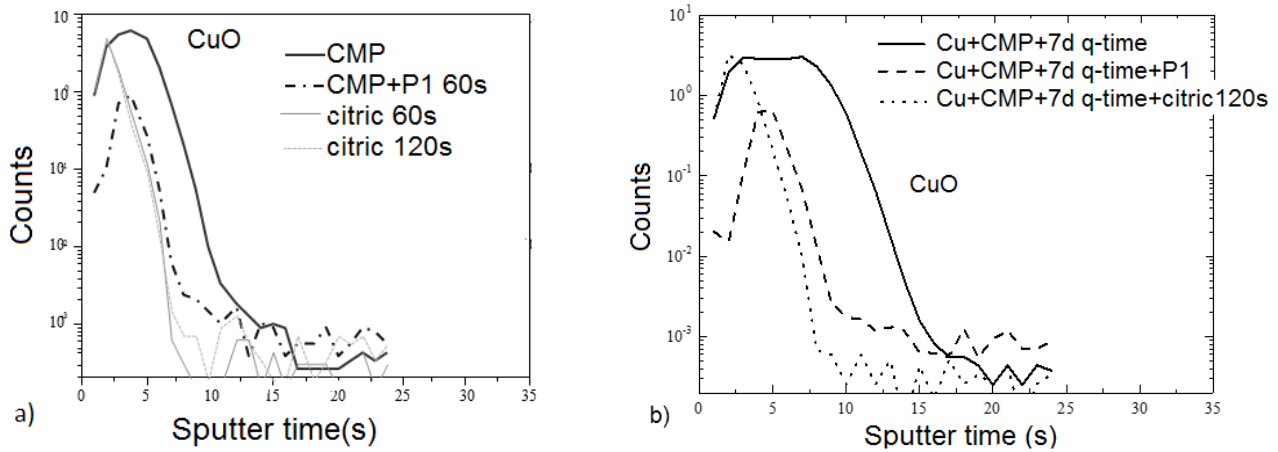


Figure 5: ToF SIMS analyses of Cu+ CMP a) wet after CMP; b) wet 7 days after CMP.

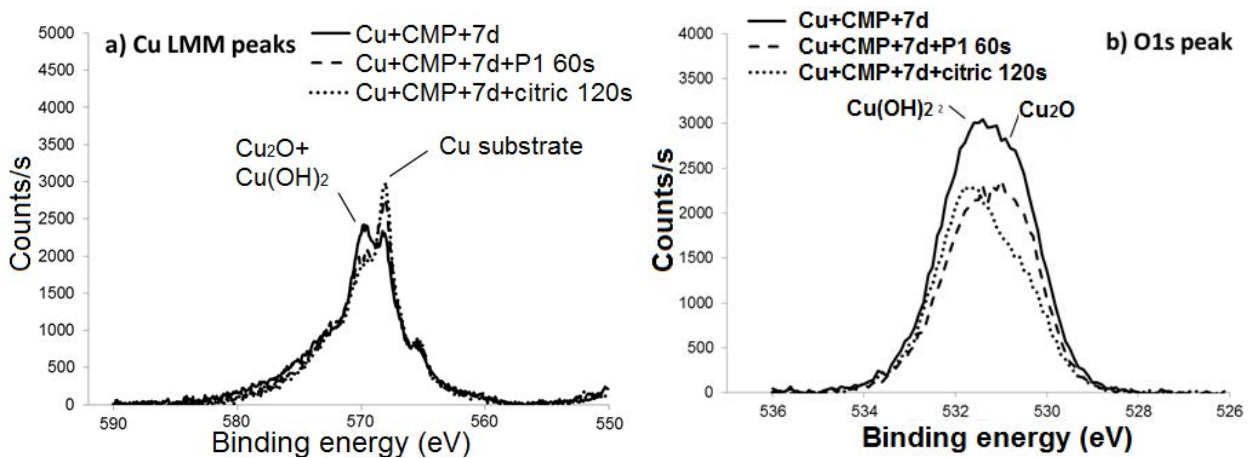


Figure 6: XPS peaks of Cu surface after CMP and different wet cleanings performed 7 days after CMP; a) Cu LMM auger peak; b) O1s peak.

These analyses show that the hillocks formation is related not only to the amount of oxide present, but also to the kind of oxide: $\text{Cu}(\text{OH})_2$ seems to promote the formation of Cu hillocks more than Cu_2O . The explanation of this can be due to different factors: the presence of H- radicals due to thermal decomposition of hydroxide during SiN deposition, the different behaviour of the oxides vs the nitridation during SiN deposition or the different stress of the oxides. In literature infact, several mechanisms are proposed to explain the formation of hillocks: a) the formation of Cu-N compounds at grain boundaries that generate stress in Cu when it is annealed [3], b) the different stress induced in Cu by copper oxide at grain boundaries, i.e. after HF, c) the H embrittlement in Cu during annealing [4]. Based on our measurements, the formation of Cu-N compounds does not seem to modulate the Cu hillocks formation after wet cleaning: ToF SiMS measurements done on flat wafers on which SiN has been deposited show no difference in terms of Cu-N compounds between wafers that have been cleaned with P1 or citric acid, as can be seen in Figure 7a. The only difference is in terms of oxide amount at Cu-SiN interface, as can be seen in figure 7b. In addition, the only Cu-N compound that is reported in literature to have some stability is Cu_3N , but also this compound is metastable: it is reported to decompose into metallic Cu + N_2 starting from 250 °C [5].

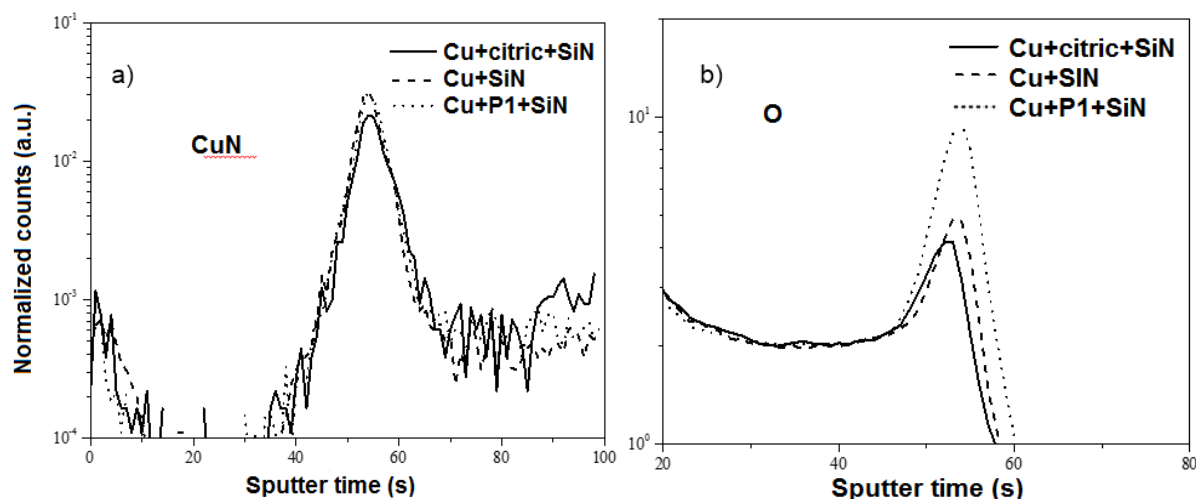


Figure 7: ToF-SIMS depth profiles a) CuN compounds at Cu-SiN interface; b) O content at Cu-SiN interface

Instead, the stress induced by different copper oxide growth or the H embrittlement seems to be the most likely mechanisms. Two experiments support these hypotheses: one is a q-time trial between Cu-CMP and SiN deposition. Defectivity analysis performed on wafers with different CMP-SiN q-times (between 24 h and 168 h) do not show any difference in terms of hillocks (Figure 8a), in spite of XPS data on flat wafers that show that already after 2 days post CMP the most part of the native oxide is already grown (Figure 8b).

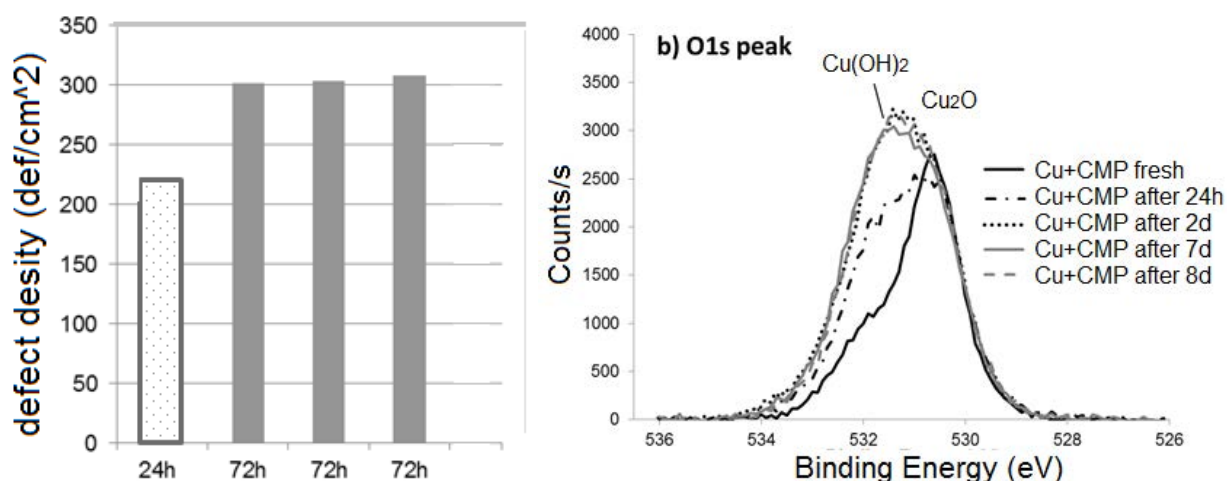


Figure 8: Defectivity analysis and XPS O1s peaks of wafer with different q-times after Cu-CMP a) defectivity analysis after SiN deposition; b) O1s XPS peak

If the total amount of oxide was the only parameter affecting the hillocks formation, defectivity should have shown an increasing hillocks defect density with longer Cu CMP-SiN q-times.

The other experiment is a q- time trial between post CMP cleaning and SiN deposition. Citric acid cleaning has been done on flat Cu wafers immediatly after CMP. Then on some wafers SiN has been deposited 24 hours after citric without any other treatment, on other wafers citric was repeated immediatly before SiN deposition. Defectivity analysis done on wafers cleaned with citric after Cu CMP that have waited 24 hours between citric and SiN deposition shows that the number of hillocks is quite high (30 def/cm²). The number instead is reduced again if a citric treatment is repeated before the deposition of SiN, as can be seen in Figure 9.

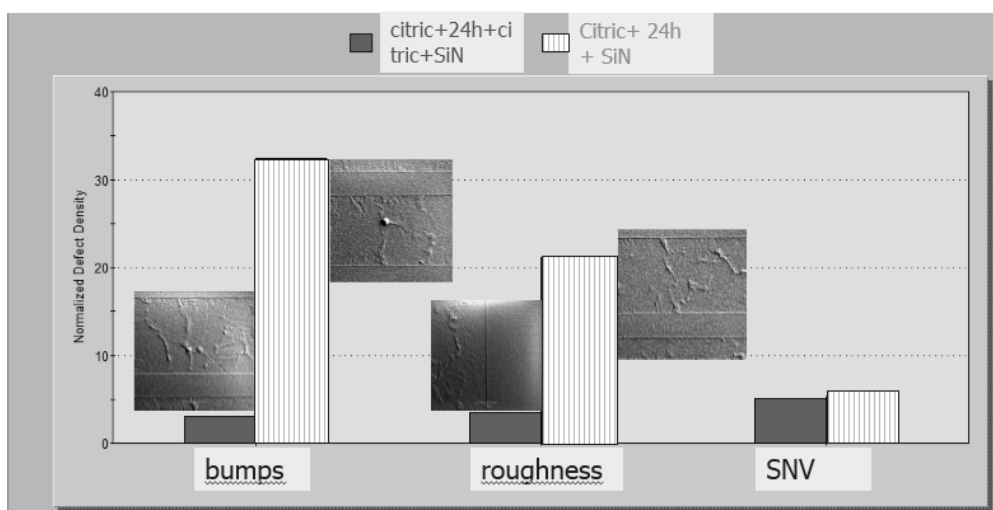


Figure 9: Defectivity analysis of wafers cleaned with citric after CMP and with 24 hours q-times before SiN deposition with and without citric rework.

The kinetic of Cu oxide regrowth after P1 and citric has been investigated using XPS, repeating the measurement after fixed times. Measurements show that after 24 hours the oxide re-grown after P1 is comparable to not-cleaned samples while after citric the oxide is lower but rich in hydroxide more than on wafers without cleaning, as can be seen in Figure 10. No difference instead has been observed by XPS analysis in terms of C adsorption between 0 and 24 h on both samples cleaned with citric or P1: so the organic acid adsorption on Cu does not affect the Cu nitridation and does not completely inhibit the oxide formation. As a consequence, C does not play a role in copper hillocks formation.

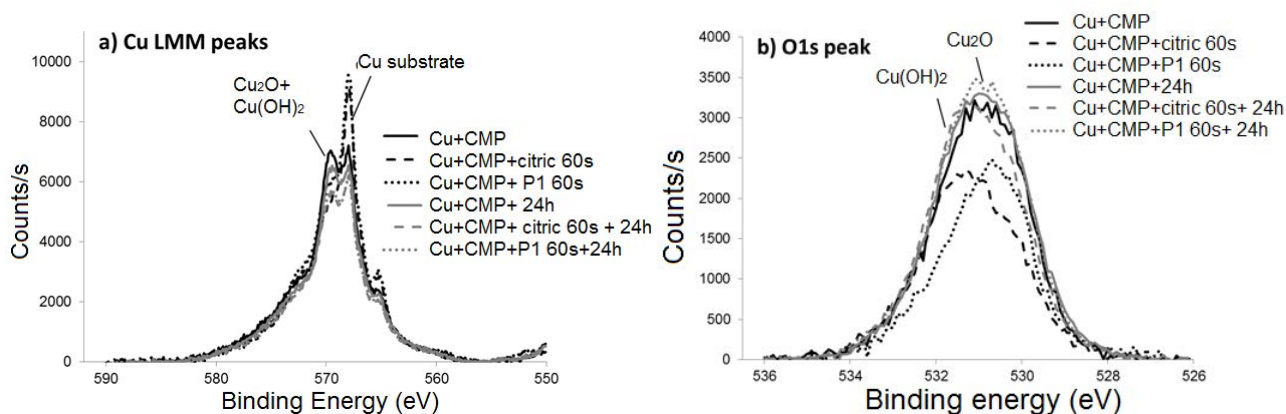


Figure 10: XPS peaks of Cu surface after CMP and P1/citric after the cleaning and 24 h after the cleaning a) Cu LMM auger peak; b) O1s peak.

Comparing XPS O1s peaks (Figure 11) it can be seen that for both citric acid and P1 the oxidation is very fast up to 4 hours, than it slows down, and the difference between 8 and 24 hours is not substantial.

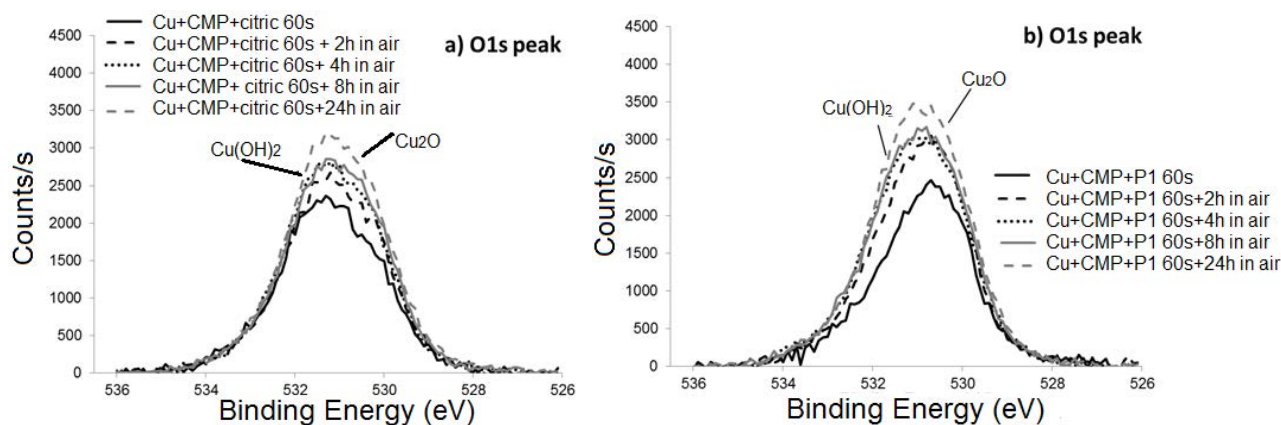


Figure 11: XPS O1s peaks of Cu surface after CMP after cleaning at different q-times after cleaning a) surface after citric; b) O1s surface after P1.

As a consequence it can be deduced that after wet cleaning the Cu hillocks formation is modulated both by amount of oxide and the kind of oxide grown. Probably, as reported in literature [6], the texture of the copper oxide grown after wet cleanings is also different from the one after CMP and this difference may be relevant for bumps formation too: this is under further investigation.

Conclusions

After Cu CMP, the total amount of residual oxide on Cu surface as well as Cu nitridation are reported in literature to be responsible for hillocks formation. Our results attribute the hillock formation after wet cleaning more to the kind of oxide and to the roughness of the surface than to the overall oxide or CuN formation. A tentative model for this behaviour is proposed.

References

- [1] Sangchul Kim et al.: ECS Transactions, **2** (1) (2006), p. 237-241
- [2] United States Patent Application Publication, Lin et al. , US 2006/0270227 A1, NOV. 30, 2006
- [3] Tsung-Kuei Kang et al: Journal of Electrochemical Society, **151**(6) (2004), p. G391-G395
- [4] G. Zhou et al. : Applied Surface Science **210** (2003), p. 165–170
- [5] Jianrong Xiao et al.: J. Mater. Sci. Technol., (2011), **27**(5), p. 403-407.
- [6] A.Hodgson, S. Haq: Surface Science Reports **64** (2009), p. 381-45

Minimizing Wafer Surface Charging for Single-Wafer Wet Cleaning for 10 nm and Beyond

Ken-ichi Sano, Rafal Dylewicz, Xia Man, David Mui, Ji Zhu,
 and Mark Kawaguchi

Lam Research Corp., 4650 Cushing Parkway, Fremont CA 94538 USA

Keywords: wafer charging, BEOL, ionizer, single-wafer clean, dilute NH_4OH , soft X-ray

Abstract. Wafer charging has become an issue since single-wafer wet clean has been introduced and multiple aspects could be potential root causes. In chemistry and DIW process factors, typical process parameters; flow rate and time were re-evaluated. As an alternative solution, dilute NH_4OH could reduce the wafer surface charging. Hardware parts were also investigated and wafer holding chuck-pin material was revealed to become a risk of discharging failure at edge of wafer. Ionizer has been known to discharge wafer surface; however, it is not enough to remove pre-existing charge from post DIW rinsed wafer. Soft X-ray is challenged to remove pre-existing charge and obtained initial positive result.

Introduction

Wafer charging becomes an increasingly important issue, thus being a key parameter in 10 nm and sub-10 nm technology nodes. Single-wafer cleaning equipment has various advantages over batch-type processes, and adoption has been widespread in both BEOL and FEOL manufacturing. Due to the materials used in constructing the process module being primarily made out of plastic for chemical compatibility, there are significant challenges in managing charge build-up to an acceptable level. Figure 1 summarizes three major modes of charging and issues in a single wafer cleaning. Liquid flow electrostatic charge – charge builds up on a wafer surface due to the advection of charge by the flow of a liquid, e.g., deionized water (DIW) on a wafer surface [1].

Incoming wafer charge: charges that exist on the wafer surface due to previous processing steps (e.g., dry etch or pre-clean) and are dissipated through conductive chemistry resulting in arcing [2].

Inductive charge: charged plastic parts such as chamber rings induce charges on the wafer surface when they are in close proximity to each other [3].

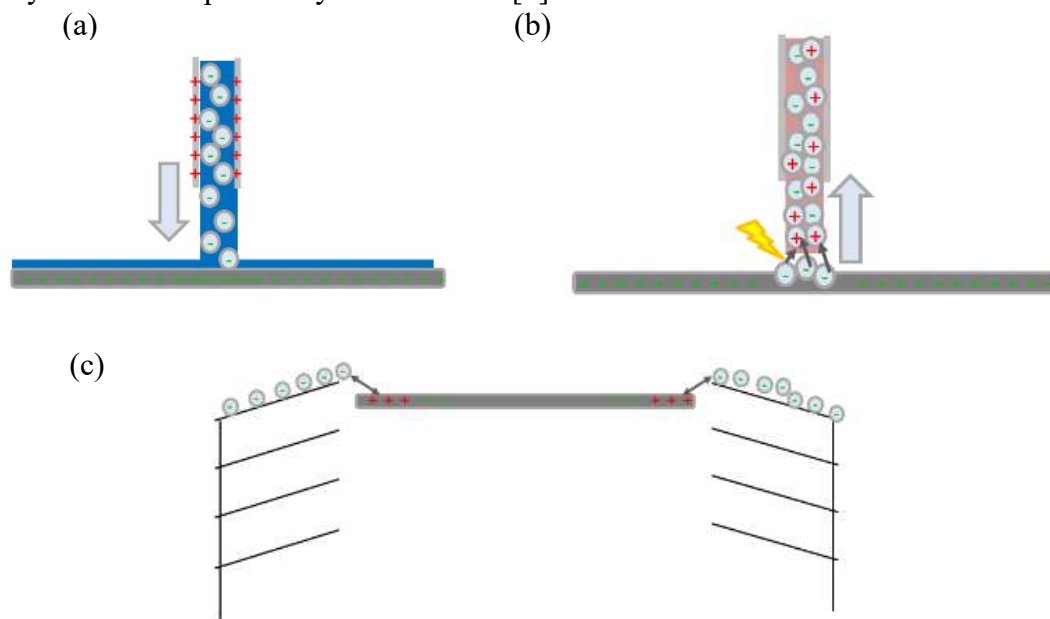


Figure 1. Single wafer charging models; (a) Liquid flow electrostatic charge; DIW dispense to wafer, (b) incoming wafer charge; pre-charged wafer, (c) Inductive charge; plastic material charges transfer induct wafer charging.

Amongst these three charging modes, arcing is the most destructive toward device yield. Hagimoto, Matz, and Halladay discovered that cleaning chemistries with different conductivity and film stacks generate different types of punch-through defects on the wafer surface. Dielectric layers such as SiO_2 and Si_3N_4 are where these charges are located. In the past, these charges could be dissipated by DI- CO_2 [4, 5, 6]. However, 10 nm BEOL process has a very tight specification on copper film loss limiting the use of a DI- CO_2 . Hayashi et al., reported that dilute NH_4OH has lower copper etch rate than DI- CO_2 , and which also maintains discharge capability [7].

In this study, two approaches are considered to eliminate the charging induced by these three charging modes. The first approach is to optimize the process parameters. The second approach is to optimize hardware. Consolidating these two approaches would lead to optimized processes and hardware for 10-nm BEOL processing.

Charging prevention approach (1): process optimization – DIW dispense

Charge advection caused by the flow of DIW has been known to be a source of charging in single wafer cleaning. Figure 2a shows the impact of liquid flow rate (all results collected with Qcept ChemetriQ tool). Center-negative charge has been found by increasing of DIW flow rate, which means the higher impinge pressure creates more charging. On the other hand, the result suggests to reduce DIW flow rate to minimize the charging issue. Comparing 0.7 lpm (liters per minute) and 2.3 lpm, 0.7 lpm shows 3~4 times lower charging. Figure 2b shows the impact of DIW rinse time, comparing 10 s, 60 s, and 300 s process time. Longer rinse time resulted in higher value of negative charges in center area. Shortening rinse time is required. Both data clearly suggests lowering DIW flow rate and/or process time can lead to reduced wafer charge.

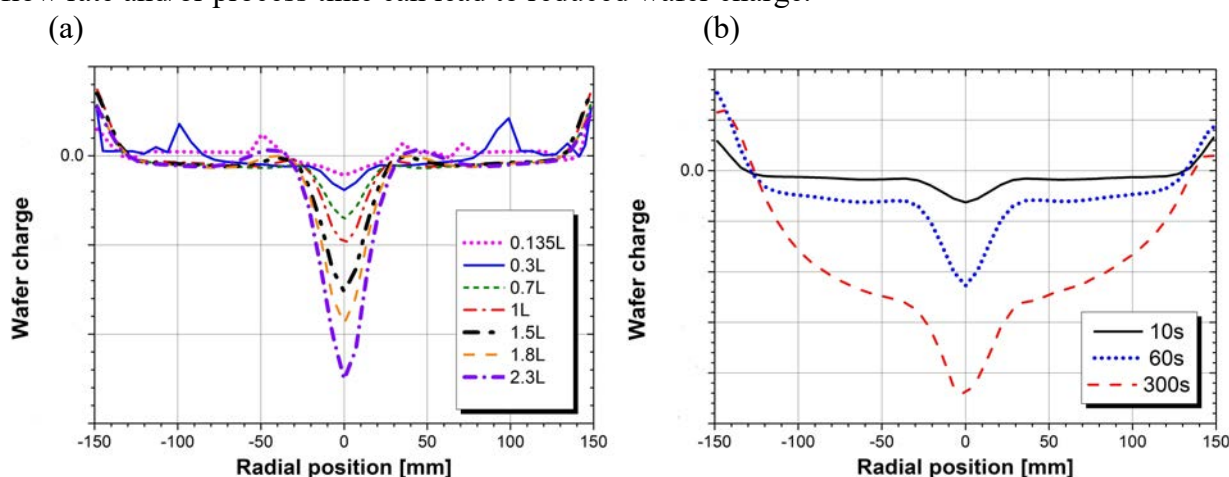


Figure 2. Impact of DIW process conditions on wafer charging: (a) DIW flow rate impact 0.135 to 2.3 lpm, (b) DIW process time impact; 1 lpm DIW flow rate and 200 rpm.

Charging prevention approach (2): process optimization – DIW dispense

Figure 3 shows beneficial effect of functional water effect. Even 5 $\mu\text{S}\cdot\text{cm}$, which is very dilute NH_4OH with 10 sec short process successfully eliminates center-negative charging. The results also matched the previous reports [7].

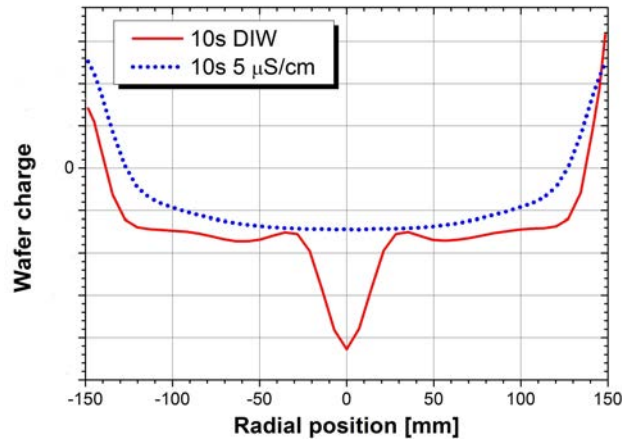


Figure 3. Effect of functional water rinse on wafer charging performance, 10s dispense time with 1 lpm liquid flow.

Fundamental study: charging study about 1V SiO₂

As shown in Figures 2 and 3, single-wafer wet clean process-related charging issues could be mitigated by process adjustment and/or liquid type. We have also studied to utilize gas phase approach to mitigate or remove the wafer charging.

To begin with a charging study, 1V static charge on a surface needs to be fully understood. Assuming that a surface of 100-nm thick SiO₂ surface is charged with 1V, it can be calculated how much charge is stored in a film. Based on Eq.1, it is calculated to be 3.4 E-8 F/cm², thus a charge density of 1V SiO₂ is 3.4 E-8 C/cm². Finally the 300 mm wafer surface total charge is calculated as 1.5 E+14 ions based on Q=CV where 1 electron has 1.6 E-19 C and considering a surface area of 300 mm wafer

$$C = \epsilon_r \epsilon_0 \frac{S}{d} \quad (1)$$

where C is the SiO₂ capacitance, ϵ_r is relative permittivity (3.9), ϵ_0 is permittivity of free space (8.85 E-12 F/m), S is surface of area and d is film thickness.

Conventional DC pulse ionizer generates 8.7 E+11 ions/s to our best knowledge, while we have simulated the efficacy of ionizer in Table 1. If an ionizer is located at close proximity to a wafer with 100% efficiency, 1V surface charge can be dissipated in 174 s; however, a conventional ionizer is located 300 – 400 mm away from a wafer, and this would significantly make discharging slower to more than 90 min. Therefore alternative discharging approach needs to be considered.

Table 1. Efficacy of ionizer

Case	Ionizer to wafer distance	Ionizer efficiency	Calculated 1V surface discharge time
Ideal	75 mm	100%	174 s
Conventional	380 mm	3%	5842 s

Charging prevention approach (3): ionizer improvement

In order to pursue an alternative approach, we have compared the performance of conventional DC pulse ionizer, AC pulse ionizer, and a soft X-ray ionizer. It is known that a soft X-ray hits molecules and ejects electrons, resulting in positively charged molecules and electrons. Then, the electron changes another molecule to be negative charge. This mechanism would provide very well balanced positive and negative ion counts.

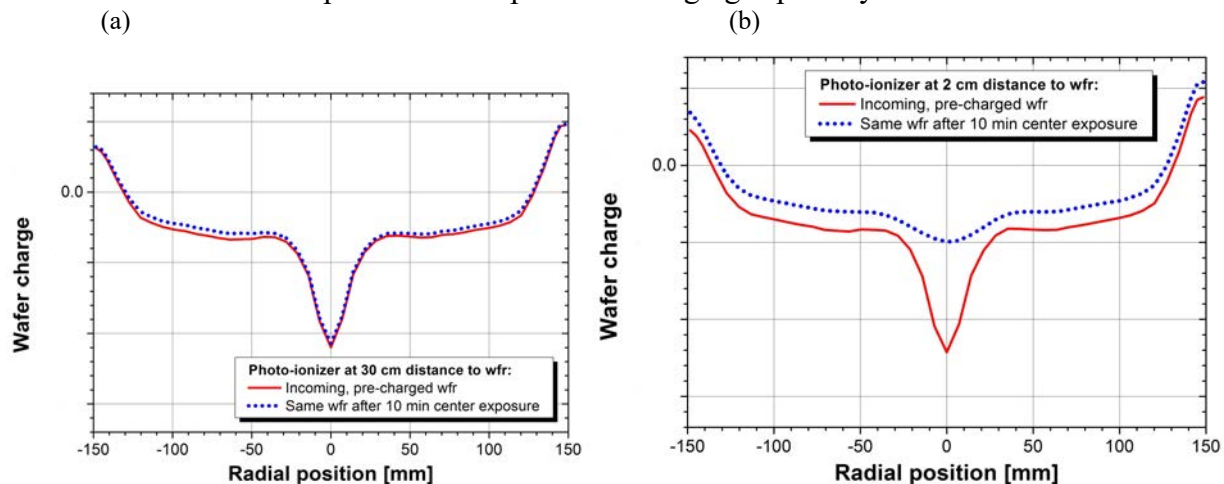
In Table 2, the basic performance parameters such as ion count and charge plate decay time are compared. Amongst them, soft X-ray produces the highest count of ions, and showed the best decay time performance as well.

Table 2. Ionizer performance comparison

	Ion count (10^6 ions/cm ³)		Charge plate decay time (sec)	
	Positive	Negative	+1000V→+100V	-1000V→-100V
DC pulse ionizer	0.9	0.6	3	2.2
AC pulse ionizer	2.1	2	0.7	1
Soft X-ray ionizer	3.7	4.6	0.6	0.6

These results show the soft X-ray ionizer is challenged to remove existing charging. In Figure 4, a thermal oxide wafer was prepared by DIW rinse to have pre-charging with 1.0 lpm DIW center dispense at 200 rpm for 60 sec. A typical center-negative and edge-positive profile has been obtained in the range of -12V ~ +4V. The charge profile in this pre-charged wafer was challenging to remove using the soft X-ray ionizer.

Figure 4a shows the data for which the ionizer was located 30 cm away from the wafer. No charging removal was observed even after 10 min exposure; however, if it was placed at a closer distance, 2 cm (Figure 4b), the discharging effect started to be observed. In Figure 4b, center-negative charge was reduced from -12V to -5V. Although it requires longer exposure and proper placement, soft X-ray ionization showed some potential to improve discharging capability.



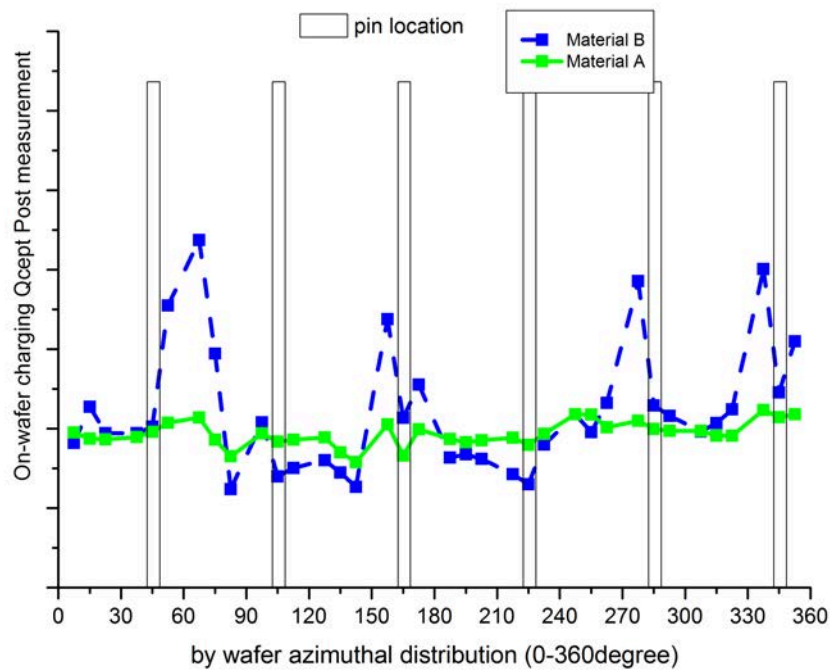
Figures 4. Pre-charged wafer discharge results using a soft X-ray ionizer at a distance of (a) 30 cm, (b) 2 cm from wafer.

Charging prevention approach (4): chuck pin improvement

In order to pursue an “edge-wing” charging profile, chuck pin materials also need to be qualified. Table 3 represents basic performance of two materials. Material B is expected to show better performance based on lower resistivity than Material A; however, Material A resulted in better wafer-edge charging result. Figure 5 shows the DIW wafer charging result, and there are 3~5 V lower charging gaps along 6 pin locations. This could have been explained by pin wettability. Both pin materials were compared in terms of contact angle. Material A showed some wettability while B was completely hydrophobic.

Table 3. Chuck pin material comparison

	Pin resistivity to ground	Contact angle
Material A	10,000~20,000 ohm	105°
Material B	20 ~ 50 ohm	>135°



Figures 5: Wafer edge charging result comparison of two materials after the process DIW 1.0 lpm, 200 rpm, and 60 s processing.

Summary

Single-wafer wet clean related charging issues has been discussed here from multiple aspects. Dispense conditions and functional rinse water usage have been revisited and tested. DIW process factors such as time and flow rate were observed to have a strong impact on center negative charging. In addition to reducing process time and DIW flow, minimizing the impinging pressure of DIW needs to be considered. Functional DIW rinse is a promising alternative to standard DIW rinse, as 5 \square S·cm dilute NH_4OH successfully removed center-negative charge.

In order to re-qualify hardware parts, ionizer and chuck pins were re-evaluated for the 10 nm node. Regarding pre-existing center-negative/edge-positive charging removal, soft X-ray has been tested as a new ionizer solution. Soft X-ray could remove the charging although it requires specific positioning and longer exposure time. Chuck pin materials needed to be selected carefully not only from resistivity but also wettability point of view. Both process and hardware need to be carefully optimized for 10 nm technology node.

Acknowledgements

This study was supported by the Hamamatsu Photonics, Mr. Suzuki and Mr. Mizuguchi. The author greatly appreciates their supports.

References

- [1] D. S. L. Mui, E. H. Lenz, C. Cyterski, K. Venkataraman and M. Kawaguchi, *IEEE Transactions on Semiconductor Manufacturing.*, 24, Issue 4 (2011), 552.
- [2] Y. Hagimoto, H. Iwamoto, Y. Honobe, T. Fukunaga and H. Abe. *Solid State Phenomena*, 145-146, (2009), 112.
- [3] M. Wada, T. Sueto, H. Takahashi, N. Hayashi and A. Eitoku, *Solid State Phenomena*, 134, (2008), 263.

- [4] T. Guo, T. Tsai, C. Chien, M. Chan, C. Yang and J. Wu, *Solid State Phenomena*, 187, (2012), 63.
- [5] J. Halladay, B. Teeter, R. Newcomb, W. Usry, J. Yoo, K. Lam, J. Lansford and B. Brennan, *Proceedings of SPCC08*, Austin, TX, April (2008).
- [6] P. Matz, T. Hurd, K. Cunningham et al., *Proceedings of the 212th ECS meeting*, 7-10 October, (2007).
- [7] Y. Hayashi, M. Kawakami, D. Yano and K. Yamanaka, *ECS Transactions*, 69 (8), (2015), 37.

CHAPTER 8:

3D Integrated Structures

Silica Formation During Etching of Silicon Nitride in Phosphoric Acid

Derek W. Bassett^{1, a}, Antonio L. P. Rotondaro¹

¹ Tokyo Electron America, Inc., 2400 Grove Blvd., Austin TX, 78741, USA

^a derek.bassett@us.tel.com

Keywords: silica, silicon nitride, phosphoric acid, nucleation, colloid gel, 3D NAND

Abstract. The etching of silicon nitride using phosphoric acid with silicon dioxide as a mask is an important process step used in the production of 3D NAND devices. This paper examines the theory of formation of a silica film onto the silicon dioxide surface during this etching step by performing a shell balance analysis of silica species in the etched out liquid volume of the 3D NAND structures. The method of moments is used to solve for the moments of the distribution of particle sizes, and this is used to solve for the potential energy barrier for silica particles to adhere to the silicon dioxide surface.

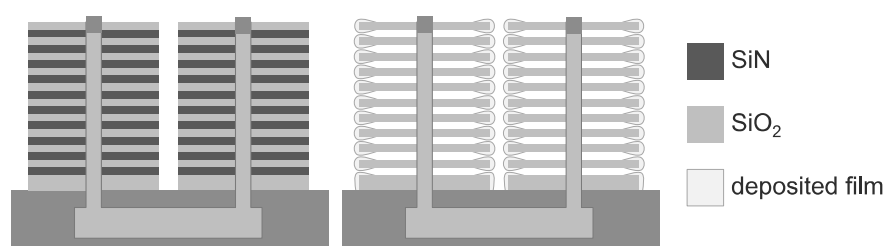
Introduction

3D NAND devices are the most recent iteration in high-density memory fabrication. In this technology, the gates are stacked on top of one another, with the potential for stacks of over one hundred gates in the near future. There are several integration schemes that are used in this process, many of which involve depositing alternating layers of silicon nitride (SiN) and silicon dioxide (SiO₂), with the SiN being etched in a phosphoric acid bath with the SiO₂ as an etch stop (Fig.1). The basic reaction (not stoichiometrically balanced) is:



As memory manufacturers have been transitioning to 3D NAND architecture, there are reports of a deposited layer that forms on the SiO₂ during the phosphoric acid SiN etch (Fig.1). In some cases, this film may be removed by continued exposure to the phosphoric acid bath after the SiN has completely etched away, but that leads to a process time significantly longer than what would otherwise be necessary. However, if continued exposure does not dissolve the film, then it becomes a defect that can hinder later device performance.

Figure 1: 3D NAND structures before and after phosphoric acid etch of SiN, with deposited film on SiO₂ structures.



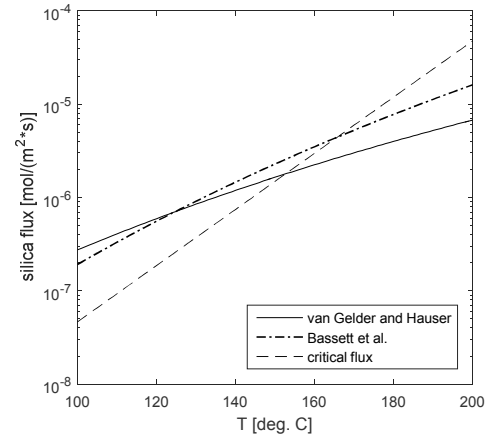
This paper proposes that this deposited film is low-density silicon dioxide that is formed from dissolved silica that enters into solution during the SiN etching. The film is formed by one of two possible mechanisms that will be explored in the paper. One possible mechanism of formation is the dissolved silica heterogeneously nucleating onto the SiO₂ surface [1]. The other possible mechanism is that the dissolved silica rapidly polymerizes via a hydrolysis reaction, forming silica sol particles. These sol particles then aggregate with each other and with the SiO₂ surface, forming a gel that coats the surface [2].

Iler [2] reports that even in conditions where the bulk silica concentration is below the equilibrium saturation concentration, colloidal silica can still be formed if the local rate of addition of silica to the solution is greater than a critical rate. The value for the critical flux rate of silica into the solution, above which silica will form colloidal silica, can be calculated from Iler's results:

$$N_{crit} = 2.31 \times 10^{-8} (2)^{(T-363)/10} \quad (2)$$

where N_{crit} is the critical flux of silica added to the solution in $[\text{mol}/(\text{m}^2\text{-s})]$, and T is the temperature in $[\text{K}]$. We can then compare this with the silica flow that results from known etch rates [3,4] of the SiN in the phosphoric acid bath, where etch rates have been converted to a molar flux. The results shown on Figure 2 predict that for typical operating conditions of 150°C to 170°C the flux of silica into the phosphoric acid due to etching of the SiN is very close to the critical flux for colloidal silica formation, and thus the formation of colloidal silica is a possibility.

Figure 2: Flux of silica due to etching of SiN in phosphoric acid as reported by van Gelder and Hauser [3] and Bassett et al. [4], compared with the critical flux of silica added to solution above which the silica will form colloidal silica [2].



The formation of colloidal silica can have a significant effect on the diffusivity of chemical species involved in the reaction including: phosphoric acid, water, silicic acid, and ammonium phosphate if the density of the colloidal silica is high enough. It has been showed that the etching of the SiN in phosphoric acid is a reaction-limited process [4]. However if the colloid density becomes high enough within the structures, it could significantly decrease the solution diffusivity and instead make the process diffusion-limited. If the silica forms colloidal particles, then the colloidal silica particles will have a diffusivity in the solution given by [5]:

$$D_{AB} = \frac{k_B T}{6\pi\mu R} \quad (3)$$

where D_{AB} is the diffusivity of the colloidal silica particles in the solution, k_B is the Boltzmann constant, T is the absolute temperature, μ is the viscosity of the solution, and R is the radius of the colloidal particles. Assuming that $R = 4$ nm for the colloid particles in the phosphoric acid bath [2], the diffusivity is $D_{AB} = 3 \times 10^{-11} \text{ m}^2/\text{s}$. This value is significantly lower than the typical value of $\sim 3 \times 10^{-9} \text{ m}^2/\text{s}$ for molecular species in liquids. This causes a higher concentration of silica near the SiN surface during etch, contributing further to potential formation of colloidal silica.

This paper uses nucleation theory [6-9] to examine the silica sol polymerization mechanism as a way to describe the formation of the silica film on the SiO_2 surface since this broader theory encompasses the heterogeneous nucleation case. The implications towards reducing or eliminating the silica deposition during the SiN etching process will be discussed.

Method and Results

In order to model the evolution of silica clusters and the deposition of silica onto the SiO_2 surface, a macroscopic balance on the volume of liquid inside the trench during the etching process was done. The macroscopic balance relies upon the assumption that the conserved property – in this case the number density of silica clusters – is uniform within the entire control volume. This is not strictly the case, but previous simulations [4] showed that the change in concentration inside the trench is much smaller compared to the change between inside the trench and the solution in the bath. This

simplified model lets us better understand the mechanisms causing silica particle growth and deposition, and make useful predictions from it.

The conservation equations for silica monomer and silica clusters of i -monomers are shown below:

$$V \frac{dN_1}{dt} = A_{\text{SiN}} J_1 - VK_{\text{coll}} \sum_{j=1}^{\infty} N_1 N_j - A_{\text{SiO}_2} G_{\text{coll}} N_1 - A_{\text{out}} k_m (N_1 - N_{1,\infty})$$

$$V \frac{dN_i}{dt} = \frac{1}{2} VK_{\text{coll}} \sum_{j=1}^{i-1} N_j N_{i-j} - VK_{\text{coll}} \sum_{j=1}^{\infty} N_i N_j - A_{\text{SiO}_2} G_{\text{coll}} N_i - A_{\text{out}} k_m (N_i - N_{i,\infty}) \quad (4)$$

Figure 3: Diagram of control volume for silica coagulation and deposition model. Volume is calculated as a cross-sectional area, and areas of the control volume are calculated as relevant wetted perimeters. Values are calculated by assuming a geometry with a main central trench of depth $H = 2000$ nm and width $L = 50$ nm, SiO_2 and SiN layer thicknesses $h = 20$ nm, and instantaneous etch depth ℓ varies from 0 to 300 nm.

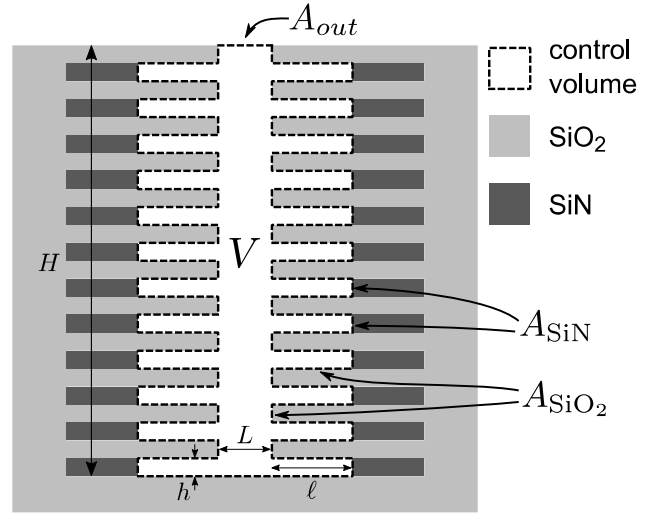


Table I: Variables of conservation equations (4) and their initial value at $t = 0$ s.

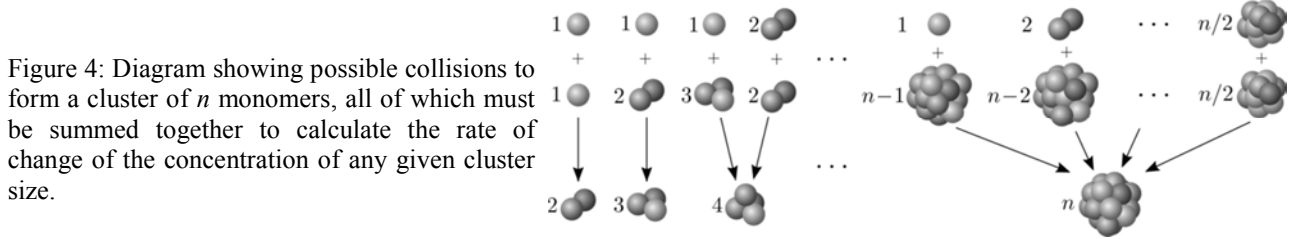
Variable	Unit	Description	Initial Value
N_i	L^{-3}	Number density of clusters comprised of i monomers	
t	t	Etch Time	0 s
V	L^2	Total volume of the control volume, neglecting the depth dimension	$0.1 \mu\text{m}^2$
J_1	$L^{-2} t^{-1}$	Flux of silica monomer into the control volume due to etching of SiN	$1.1 \times 10^{19} \text{m}^{-2} \text{s}^{-1}$
A_{SiN}	L	Total surface area of the etching SiN, neglecting the depth dimension	$2 \mu\text{m}$
K_{coll}	$L^3 t^{-1}$	Cluster collision coefficient which gives the rate at which clusters are colliding with each other to form larger clusters	see below
A_{SiO_2}	L	Total surface area of SiO_2 on which the silica is depositing, neglecting the depth dimension	$2 \mu\text{m}$
G_{coll}	$L t^{-1}$	Surface deposition coefficient, which gives the rate at which clusters collide with the SiO_2 surface and form colloidal silica	see below
A_{out}	L	Area of the outside of the control volume at the top of the trench that borders with the bulk of the solution, neglecting the depth dimension	50 nm
k_m	$L t^{-1}$	Overall mass transfer coefficient between the control volume and the bulk	$2.2 \times 10^{-8} \text{m/s}$
$N_{i,\infty}$	L^{-3}	Number density of i -clusters in the bulk of the solution	see below

This series of equations is actually a separate equation for each cluster size i . The variables of equations (4) and their initial values at $t = 0$ s are described on Table I.

Using the geometry as shown in Figure 3, the control volume (expressed in terms of planar area by neglecting the depth dimension) has an initial value of $0.1 \mu\text{m}^2$, and when the SiN reaches the etch stop it has a total volume of $0.7 \mu\text{m}^2$. The control volume is changing as a function of time, but because diffusion is very fast compared to the SiN etch rate [4] and cluster coagulation is primarily a diffusion-driven process, the quasi-steady-state solution can be used to decouple the cluster evolution rate and the change of the control volume. For initial conditions, the silica in the control volume is assumed to be identical to the bath, so that $N_{1,0} = N_{1,\infty} = 5.3 \times 10^{27} \text{m}^{-3}$ based on an assumed silica concentration of 40 ppm in the bath, and $N_{i,0} = N_{i,\infty} = 0$ for all $i > 1$.

The terms of Equation 4 for N_1 are as follows: 1st term - change rate for the number density of silica monomers; 2nd term - addition of monomers due to etching of SiN; 3rd term - consumption of

monomers due to collisions with other clusters to form larger clusters; 4th term - loss of monomers due to deposition on the SiO₂ surface; and 5th term - loss of monomers due to leaving the control volume via diffusion/convection. The terms in the N_i equation are similar, except that there is no addition of larger clusters due to the etching of SiN since it only creates monomers, instead there is an additional term for smaller j -clusters and $[i-j]$ -clusters colliding to form i -clusters. Figure 4 illustrates the accounting for the aggregation of monomers and clusters to form larger clusters.



Determining the collision parameters K_{coll} and G_{coll} is a much more involved process, which becomes the fundamental difficulty in modeling coagulation and deposition. The cluster collision coefficient K_{coll} was derived using work by Philipse [6], using the more accurate formulations for the van der Waals (VDW) attraction and electrostatic (ES) potential fields between two interacting spheres of different sizes from Birdi [10]. Although K_{coll} is a function of the sizes of the two colliding particles, the range in values is small and so an average value of $K_{coll} = 1.5 \times 10^{-18} \text{ m}^3/\text{s}$ was calculated. The same method cannot be used to calculate G_{coll} .

Equations (4) can be nondimensionalized by defining the dimensionless number density to be $n_i = N_i/N_{1,\infty}$, and the dimensionless time to be $\tau = K_{coll} N_{1,\infty} t$. The dimensionless equations then become the following:

$$\frac{dn_1}{d\tau} = \alpha - \sum_{j=1}^{\infty} n_1 n_j - \beta n_1 ; \quad \frac{dn_i}{d\tau} = \frac{1}{2} \sum_{j=1}^{i-1} n_j n_{i-j} - \sum_{j=1}^{\infty} n_i n_j - \beta n_i \quad (5)$$

With the dimensionless parameters α and β as the following:

$$\alpha = \frac{A_{\text{SiN}} J_1 + A_{\text{out}} k_m N_{1,\infty}}{V K_{coll} N_{1,\infty}^2} ; \quad \beta = \frac{A_{\text{SiO}_2} G_{coll} + A_{\text{out}} k_m}{V K_{coll} N_{1,\infty}} \quad (6)$$

α is the ratio of: (particles coming into the system by etching and convection/diffusion) to (particles being combined due to collisions). Substituting in the values we get $\alpha = 8.0 \times 10^{-12}$. Similarly, β is the ratio of: (particles leaving the system by deposition and convection/diffusion) to (particles being combined due to collisions). The value of β cannot be calculated *a priori* without first knowing the value of G_{coll} . However β can be estimated by making the assumption that the majority of particles leaving the control volume will do so by diffusion/convection, and only a small fraction will adhere to the SiO₂ surface. Indeed if that were not the case, etching would be impossible as the growing silica gel would completely fill the gap between the etching SiN layers, making further etching impossible. Therefore, for a first-order estimate for β we assume that $A_{\text{out}} k_m \gg A_{\text{SiO}_2} G_{coll}$, so that $\beta = (A_{\text{out}} k_m) / (V K_{coll} N_{1,\infty})$. From this initial estimate we get $\beta \approx 1.6 \times 10^{-12}$.

While the nondimensionalization simplifies the equations considerably, there is a potentially infinite number of ordinary differential equations (ODE) that must be solved simultaneously, one equation for each possible particle size. This is made solvable by following the method of moments first derived by Smoluchowski [11], with a detailed derivation of the method shown in [8]. In summary, the k -th moment of the distribution of the particles is defined to be:

$$M_k = \sum_{i=1}^{\infty} i^k n_i \quad (7)$$

By summing all the equations from $i = 1$ to ∞ , an equation in terms of the 0-th moment M_0 is obtained. Many of the terms in the double summations cancel each other out, and the remaining

terms can be expressed in terms of moments as well. By multiplying the i -th equation by i and then summing all the equations together we get an ODE for M_1 :

$$\frac{dM_1}{d\tau} = \alpha - \beta M_1 \quad (8)$$

In fact we can derive an ODE for any moment M_k by multiplying each equation by i^k and then summing them together and simplifying. A general formula is shown in [8]. The primary interest is in the 1st norm M_1 , and Equation 8 is easily solved to find:

$$M_1(\tau) = \frac{\alpha}{\beta} + \left(1 - \frac{\alpha}{\beta}\right)e^{-\beta\tau} \quad (9)$$

Analysis of Equation 9 shows that the steady-state value of $M_1 = \alpha/\beta$, and that M_1 reaches 95% of its change to steady-state at $\tau^* = 3.19 \times 10^{10}$, or $t^* = 4.0$ s. Since this is much smaller than the overall etch time (on the order of 1000 s), the steady-state value of $M_{1,ss} = \alpha/\beta = 4.1$ can be used, confirming the assumption of the quasi-steady state approximation. It is also of interest to note that the value of $M_{1,ss}$ does not depend upon the cluster collision coefficient K_{coll} , though the time it takes to reach steady-state does.

To find the growth rate of colloidal silica on the SiO₂ surface, the wall cluster deposition coefficient G_{coll} is multiplied by the volume of each silica cluster, and then the contribution for each cluster size is summed up resulting in:

$$GR = G_{coll} \sum_{i=1}^{\infty} v_i N_i = v_1 G_{coll} \sum_{i=1}^{\infty} i N_i = v_1 G_{coll} N_{1,\infty} \sum_{i=1}^{\infty} i n_i = v_1 G_{coll} N_{1,\infty} M_{1,ss} \quad (10)$$

where GR (units of L/t) is the growth rate, and v_i is volume of a silica particle comprised of i monomers. Since each monomer contributes the same volume of v_1 to the total particle volume we can substitute $v_i = i v_1$, which allows us to calculate the growth rate in terms of the first moment M_1 . The monomer volume $v_1 = 4.51 \times 10^{-29}$ m³ is calculated from the density of silica, 2200 kg/m³.

The estimate of G_{coll} is made by calculating the total number of cluster collisions that occur on the surface per area per time, and multiplying that by the fraction that are able to overcome the potential energy barrier and adhere to the surface. That is equated with G_{coll} multiplied by the concentration of clusters:

$$G_{coll} \sum_{i=1}^{\infty} N_i = \sum_{i=1}^{\infty} \sqrt{\frac{3kT}{4m_1 i}} N_i \exp\left(-\frac{\Delta g_{\max}}{kT}\right) \quad (11)$$

The summations can be converted to moments as before, and the estimate for the surface coagulation coefficient is

$$G_{coll} \approx \sqrt{\frac{3kT}{4m_1}} \left(\frac{M_{-1/2}}{M_0} \right) \exp\left(-\frac{\Delta g_{\max}}{kT}\right) \quad (12)$$

where m_1 is the mass of a single silica monomer, Δg_{\max} is the calculated potential energy barrier for the cluster to adhere to the surface, and $M_{-1/2} = \sum_{i=1}^{\infty} i^{-1/2} N_i$, the value of which is estimated using the interpolation method for fractional moments in [9]. Using the combined VDW and electric field potentials for a sphere and a planar wall, $\Delta g/kT$ is estimated to be equal to 1.15. This gives a value of $G_{coll} = 52$ m/s, which can be used to calculate the growth rate with Equation 10. However, this estimate comes out to be $GR = 130$ m/s, which is about 12 orders of magnitude too high. Therefore, the estimation of G_{coll} is also too high by the same 12 orders of magnitude.

This is not entirely unexpected, as classical nucleation theory (CNT) might be inaccurate to predict nucleation rates, and it is not unusual for predictions to be off by 10 orders of magnitude or more [12]. Much of this discrepancy is due to the failure of VDW and ES forces to predict the potential energy barrier for nucleation to occur. Additional factors such as molecular orientation, stearic

hindrance, and the complex reaction for the polymerization itself also impact the bonding to the silica surface.

The above analysis can also be used to look at the case of heterogeneous nucleation, where the only change is that in Equation 4 the cluster collision coefficient is set to $K_{coll} = 0$. This gives an ODE for monomer density $N_1(t)$, with a different time to reach steady-state than the clustering model, but still short enough to allow the quasi-steady state approximation.

Though prediction of the deposition rate cannot be accurately done from CNT, we can instead predict how large the potential energy barrier must be in order to give a reasonable deposition rate. For example by making the assumption that the silica deposition on the SiO_2 surface grows to a thickness of 5 nm in 20 minutes, then Equation 10 can be solved for G_{coll} , and then Equation 12 is solved for $\Delta g/kT$. This result in values of 1.7×10^{-12} m/s and 32.16 respectively, which is a much higher exponential term than the 1.15 that was estimated using CNT. This suggests that there is a high potential energy barrier for the cluster deposition to occur on the silicon dioxide surface.

Conclusions

Although CNT is unable to predict an accurate rate for silica deposition, it shows that the simultaneous silica particle clustering and deposition onto a surface can be modeled. The only undetermined parameter is the potential energy barrier associated with the surface deposition coefficient G_{coll} . This remaining parameter can be solved for with a series of experiments that measure the deposition rate while monitoring the silica concentration.

Furthermore, the analysis shows that both the clustering rate and the deposition rate depend directly on the concentration of silica monomer $N_{1,\infty}$, which shows that careful control of silica concentration will be necessary in order to control the deposition onto the surface.

In future work, the reverse process in which the deposited silica re-etches to be dissolved back into the solution will be included in the model to show how silica deposition and etching can occur depending on local properties of silica concentration, temperature, electrolyte concentrations, etc.

References

- [1] R.P. Sear, J. Phys.: Condens. Matter **19** 033101 (2007).
- [2] R.K. Iler, *Chemistry of Silica* (John Wiley & Sons, NY, 1979).
- [3] W. van Gelder and V.E. Hauser, J. Electrochem. Soc., **114** (8) pp. 869 (1967).
- [4] D. Bassett, W. Printz, and T. Furukawa, ECS Trans., **69** (8) pp. 159 (2015).
- [5] R.B. Bird, W.E. Stewart, and E.N. Lightfoot, *Transport Phenomena* (John Wiley & Sons, NY, 2002).
- [6] A.P. Phillipse, Colloid Polym. Sci. **226** pp. 1174 (1988).
- [7] T. Matsuoka and E. Gulari, J. Colloid and Interface Sci. **132** (1) pp. 13 (1989).
- [8] M. Frenklach, J. Colloid and Interface Sci. **108** (1) pp. 237 (1985).
- [9] M. Frenklach, Chem. Eng. Sci. **57** pp. 2227 (2002).
- [10] K.S. Birdi, *Surface and Colloid Chemistry* (CRC Press, NY 2009).
- [11] M. Smoluchowski, Physik. Z. **17** pp.557 (1916).
- [12] W.P. Schmelzer, *Nucleation Theory and Applications* (Wiley-VCH, Weinheim Germany 2005).

Low Undercut Ti Etch Chemistry for Cu Bump Pillar Under Bump Metallization Wet Etch Process

Simone Capecchi^{1, a}, Tanya Atanasova¹, Reiner Willeke¹
Michael Parthenopoulos², Christian Pizzetti³ and Jerome Daviot³

¹ GLOBALFOUNDRIES, Wilschdorfer Landstraße 101, 01109 Dresden, Germany

² Fraunhofer IZM, ASSID, Ringstraße 12, 01468 Moritzburg, Germany

³ Technic France, 15 rue de la Montjoie, BP79, F93212 La plaine St Denis France

^asimone.capecchi@globalfoundries.com

Keywords: Cu Pillar bumps, UBM etch, UBM Ti undercut.

Abstract. This paper demonstrates how a low undercut Ti etchant developed by Technic France can be successfully introduced in a high volume manufacturing Fab for etching the under bump metallization (UBM). The Ti etchant has been tested on 300mm wafer production equipment in GLOBALFOUNDRIES. The Ti etchant evaluation has been carried out in collaboration with the Fraunhofer IZM-ASSID institute.

Introduction

In advanced packaging technology, Cu pillar bumping has become a common approach for flip-chip bonding. Using Cu pillars allows achieving finer pitch (<60 µm) [1] than achieved with solder bumps. Because of the non-planarized passivation surface, often present on some recent technologies, wet etching is preferred to dry etching for under bump metallization (UBM) removal. However, the drawback of the wet etching approach is pillar undercut.

The aim of this work is to minimize the undercut created during the Ti barrier etch by using a novel H₂O₂ buffered etchant mix with a stabilizing complexing agent and to prove the manufacturability of this approach in a high volume production equipment.

Background

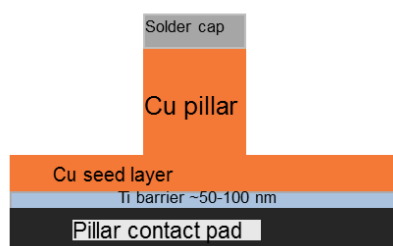


Figure1: Cu pillar before UBM etch



Figure2: Cu pillar after UBM etch

Figure 1 represents a Cu pillar bump structure before the UBM etch is performed. All bumps have been grown onto a seed Cu layer sputtered on the wafer. All the bumps at this stage are still electrically shorted. Wet etch is carried out to remove the metal layers (Cu seed and Ti barrier) to electrically isolate the bumps from each other. It is also important that metal residues are removed from the passivation surface to guarantee electrical isolation as well as good underfill adhesion in the packaging process. A problem arises when typical Ti etchants, such as dilute HF or BOE, are used to remove the Ti barrier, since they lead to larger undercut, normally in the range of 500-600 nm.

In order to reduce this undercut, TechniEtch TBR19 mix developed by Technic has been evaluated.

Experimental Work

Solution key attributes.

Based on the process limitations encountered with standard diluted HF for Ti based barrier etching, the specifications of the novel Titanium Barrier Remover were set to overcome most of the current etching mixtures drawbacks such as etch rate, undercut & pH control, bath ageing, metal compatibility, reclaimability, etc.

Product specifications:

Etch rate above 450Å/min for (Ti, TiN and TiW).

Compatible with Al, Sn, Cu, Ni (ER<10Å/min).

Possibility to be reclaimed over 6 hours.

Ready to use.

The mixture stability was monitored based on the British Standard 7546 & CEFIC Bulk Storage guideline (2012).

The stability tests involved the accurate measurement & monitoring of the hydrogen peroxide loss over a 16 h period at different temperatures (Figure 3). The same procedure has been used for estimating the shelf life of the ready-to-use version (TBR19 additives mixed with H₂O₂) in the different storage conditions of 10, 15 and 20 °C with results tending to confirm a great stability over 6 months.

The H₂O₂ loss monitoring was also a valuable mean to establish the best compromise between etching performance and stability while screening the chelating & stabilizers agents, hydroxyl alkali species, buffering additives, ingredients & hydrogen peroxide purity grade, additives ratios.

Figure 4, for instance is an example of how the stability test was directly used throughout the formulation stage to establish the final TechniEch TBR19 ingredient concentrations.

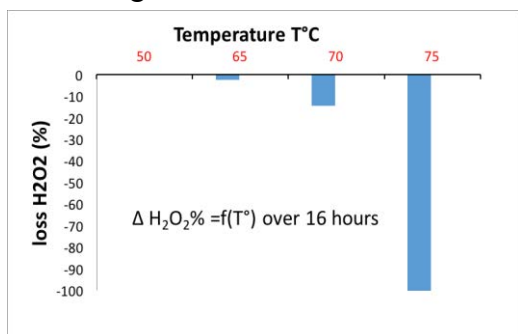


Figure 3: Peroxide concentrations loss vs temperature (16 h)

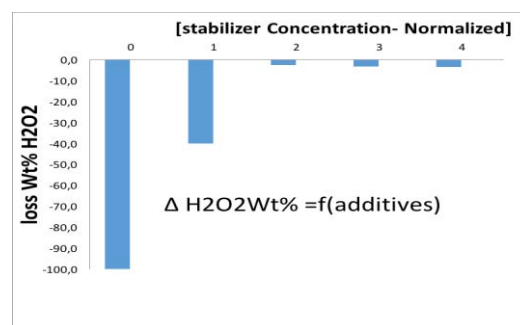


Figure 4: Peroxide loss vs stabilizer concentration

From the solution decomposition rate and Ti etching rate change with temperature, it is recommended to work at 50 °C to combine best bath ageing, metal etch rate, process control and solution stability attributes.

One extra singular attribute of the solution is the capability to etch several metals, such as W, TiW, Ti and TiN (Figure 5) likely to be stacked up as barrier and adhesion layers while being fully compatible with metal interconnections and contacts.

The following etching rate profile results (Figure 6) were collected on the tri metal layer stack (W/TiN/Ti) through four point probe measurements and confirmed the great etching stability and selectivity over a 6 hours process period. Similar process optimization were carried out on Ti/TiN/Ti stack, where the new etchant (TechniEch TBR19) permitted to significantly reduce the number of process steps from six (HF/SC1/HF + rinsing) to two (TBR19/Rinse) with better Ti undercut control.

Finally, investigations on single tool platform over 24 hours were also carried out with the new etchant where Ti barrier undercut was monitored. The results showed a 9% drop in Ti Etch Rate and a Cu Etch Rate remaining at $<3\text{Å}/\text{min}$ over the 24 hours. More interestingly, undercut monitoring on a copper pillar with a 200 nm thick Ti barrier while applying an overetch process of 50% led to a WIW feature undercut below $0.2\text{ }\mu\text{m}$ over the 24 hours period.

TechniEch TBR19	Etch Rate (Å/mins) @ 50C
Ti	$450 < E/R < 2000\text{ Å}/\text{mn}$
TiN	$120\text{ (low stress)} < E/R < 900\text{ Å}/\text{mn}$ (thick BEOL)
TiW	$1000 < E/R < 1400\text{ Å}/\text{mn}$

Figure 5: TechniEch TBR19 standard etch

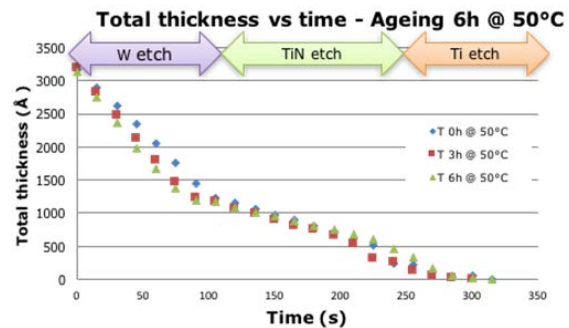


Figure 6: Etch rate stability over 6 hours for a trilayer W (2000Å) / TiN (700Å) / Ti (450Å) stack

The TBR19/ H_2O_2 mix can be prepared by Technic France and stored with a proven shelf life of 6 months. The ready-to-use mix represents an advantage in a manufacturing environment, as no mixing station is needed for this solution.

TBR 19 test method in a manufacturing environment

The etching chemical characterization has been carried out using a Raider AMAT tool in GLOBALFOUNDRIES. The tool has four single wafer chambers, two of which are connected to the tank containing TBR19 ready-to-use mix. This tank can be heated to $50\text{ }^\circ\text{C}$. During wafer etching, the chemical is sprayed onto the wafer through a series of nozzles and then reclaimed into the tank. Reclaiming the chemical after the etch step is necessary, otherwise single chemical use would lead to high consumption (up to $\sim 5\text{-}6$ liters per wafer), jeopardizing the process manufacturability.

The UBM etch (Cu and Ti) can be performed in sequence within the same chamber on each wafer. The equipment has an optical end point detector (EPD). The EPD can be used only in a passive mode, i.e. the EPD data was collected and analyzed post processing to assess the Ti etch time (Ti clearance time from the wafer passivation surface). The aim of this test was to prove that TBR19 can be used on a high volume manufacturing equipment, whilst achieving pillar Ti undercut less than 200 nm without Ti residue on the wafer passivation layer. Moreover the process has to be highly selective to Al, Cu, Ni, Sn and Ag.

The test was carried out on structured wafers with the complete Cu pillar stack on top of the passivation layer. Structured wafers have also been used to age the chemical bath.

The Cu pillar Ti undercut measurement was carried out with a SEM cross section. The UBM metal residues assessment was carried out with XPS analysis at the center, half radius and edge of the wafer.

A 12 runs screening design of experiment (DOE) was carried out taking into account the following 4 factors with their respective high and low values.

- Temperature: $47\text{ - }53\text{ }^\circ\text{C}$
- Concentration of TBR19 additive in H_2O_2 wt% : $5.7\text{ - }6.3\%$
- Nozzles spray pressure $14\text{ - }19\text{ psi}$
- Bath age 0-50 wafers: $0\text{-}6\text{ hours}$

The criteria of these high and low parameters values are as follows.

The equipment is capable of controlling the temperature and the pressure at least within $\pm 2^\circ\text{C}$ and ± 2 psi, respectively. Also the concentration of the TBR19 mix can be controlled well within $\pm 0.3\%$. Therefore, a wider screening process window would assess the manufacturability of the process.

The 12 runs that have been carried out are shown in the table below:

Table1: 12 DOE runs conditions

	Temperature	concentration	pressure	bath age
1	47	5.7	19	fresh
2	47	5.7	14	fresh
3	53	5.7	14	fresh
4	47	5.7	14	old
5	53	5.7	19	old
6	53	5.7	19	old
7	53	6.3	14	fresh
8	53	6.3	19	fresh
9	47	6.3	19	fresh
10	53	6.3	14	old
11	47	6.3	19	old
12	47	6.3	14	old

The DOE output was Ti clearance time (s) measured with the chamber end point detector.

Results

The DOE Effect summary table shows that temperature and bath age have a statistically significant effect. Pressure and concentration (at least for the assessed process window) can be ignored as modulator of the Ti etch time (see Figure7).

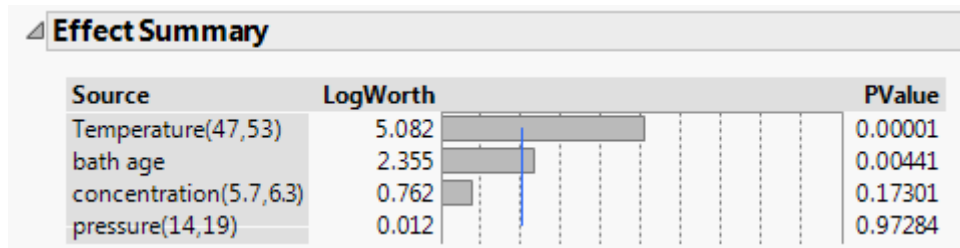


Figure 7: Parameters showing a p Value less than 0.05 have a statistically significant effect on the output (Ti etch time)

Figure 8 shows the shift in etch time due to the TBR19 bath ageing: the Ti etch time shifts upwards of about 20s at the end of the 50 wafer (6 h) bath life.

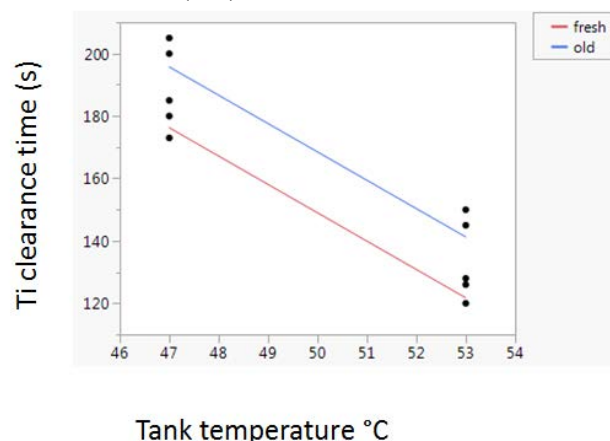


Figure 8: The Ti etch time shifts of about 20 s at the of the TBR19 bath life

Figure 9 shows the time needed to clear the Ti from the surface as a function of the bath temperature when the bath is at the end of life (50 wafers and 6 hours).

At 50°C roughly 170s of Ti etch time is needed to completely remove the Ti from the passivation of the wafer. The complete Ti removal was confirmed by XPS analysis that showed no Ti residue present on the wafer with an accuracy of less than 0.1% at.

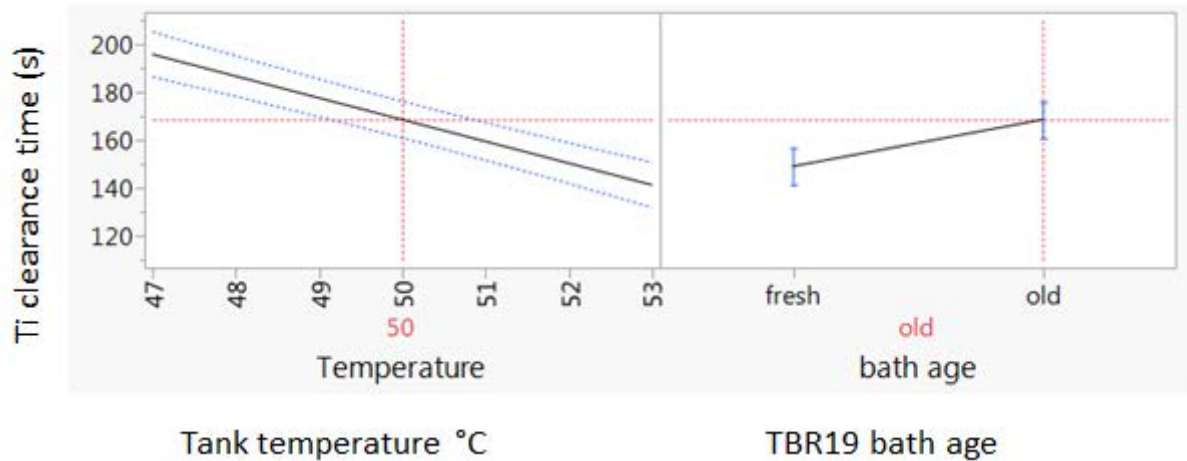


Figure 9: Ti clearance time vs Temp for aged bath

The undercut has been also measured by etching a wafer with a fresh bath. Etching a wafer with a fresh bath is the worst case scenario for undercut as the etch rate is at its highest point. Figure 10 shows that, even with an etching time of 200 s at 50 °C, the undercut is still less than 200 nm.

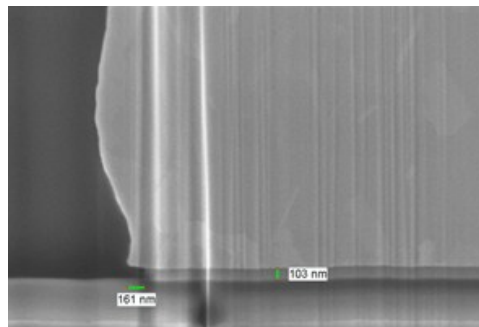


Figure 10: Ti undercut ~160 nm on micropillars with etch time of 200 s at 50 °C in fresh TBR19 bath

Conclusions

The possibility of achieving a pre-mixed H_2O_2 based solution (TBR19 ready-to-use mix) to etch Ti with an undercut less than 200 nm has been demonstrated. Through stabilizers screening and pH control performed by Technic France, it has been possible to develop a H_2O_2 based mix that is stable enough to be used in a manufacturing environment. The possibility of reclaiming and re-using the solution ensures a consumption of less than 0.5 L per wafer. The tests performed in GLOBALFOUNDRIES show that the Cu pillar Ti undercut is greatly reduced compared to conventional HF based solutions.

Moreover, this solution has also proven good selectivity to other metals exposed in the Cu pillar process, such as Cu, Ni, Sn and Al. Figure 11 shows an overview of pillars after reflow at the end of the Cu pillar process. Neither cap nor pillar attack have been observed.

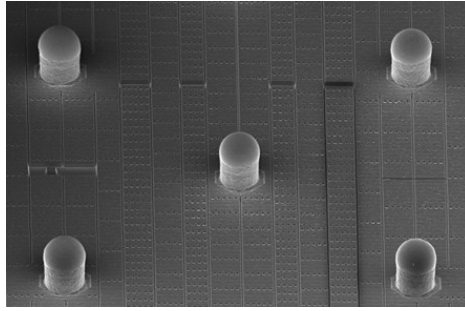


Figure 11: Overview of Cu pillar post UBM etch and post solder cap reflow

References

- [1] Minjae Lee, Min Yoo, Jihee Cho, Seungki Lee, Jaedong Kim, Choonheung Lee, Daebyoung Kang, Curtis Zwenger, Robert Lanzone: *Study of Interconnection Process for Fine Pitch Flip Chip* (2009 Electronic Components and Technology Conference).

CHAPTER 9:

Metrology, Specification and Control of Contamination

Electrical Characterization of As-Processed Semiconductor Surfaces

Jerzy Ruzyllo^{1, a} and Patrick J. Drummond²

¹ Department of Electrical Engineering, School of Electrical Engineering and Computer Science
Penn State University, University Park, Pennsylvania 16802, USA

² Department of Engineering, Penn State University, Altoona, Pennsylvania 16828, USA

^ajrzylo@psu.edu

Invited Paper

Keywords: Surface charge, surface recombination lifetime, Surface Photovoltage (SPV), Photoconductance Decay (PCD), chemical composition, physical damage

Abstract. The paper is concerned with electrical characterization of as-processed semiconductor surfaces and near-surface regions for the purpose of process development and monitoring. The methods of electrical characterization based on Surface Photovoltage (SPV) and Photoconductance Decay (PCD) effects are discussed as being particularly conducive with the needs of as-processed semiconductor surface characterization and experimental results demonstrating merits of the proposed methodology are presented.

Introduction

With wafer surfaces playing key role in defining characteristics of semiconductor devices and circuits, surface characterization and monitoring processes in semiconductor device engineering are increasingly important. This includes in particular wafer cleaning operations and other surface conditioning steps that need to be closely monitored. Methods of semiconductor surface characterization that can be used in surface processing characterization and monitoring include (i) chemical/physical surface analysis involving methods such as SIMS, XPS, TXFR, SEM, AFM, (ii) optical methods such as spectroscopic ellipsometry, FTIR and others, and finally (iii) electrical methods which allow identification of the surface-related electrically active centers representative of the condition of the wafer surfaces. While not qualitative the last type of methods is of particular interest as they unravel surface characteristics which are directly affecting performance of the final device.

The methods of electrical characterization of semiconductor surface and near-surface region fall into two categories. The first is based on the use of test devices with permanent contacts (e.g. MOS capacitors or metal-semiconductor diodes) allowing I-V and C-V measurements from which key electronic properties of semiconductor surface can be obtained. Second category involves characterization methods which do not require permanent contact to the surface, and hence, allow measurements of selected electrical parameters of the as-processed surfaces, i.e. surfaces resulting from any given operation without wafer exposure to any additional processing steps.

In this overview methods of electrical characterization which allow characterization of as-processed semiconductor surfaces are discussed. The focus is on non-contact Surface Photovoltage (SPV) and temporary contact based Photoconductance Decay (PCD) method. The overview presented is not attempting to show a broad picture of the field of electrical characterization methods used in surface cleaning monitoring. Instead, its goal is to illustrate effectiveness of selected methods in establishing a direct link between electronic properties of semiconductor surfaces and their chemical composition and/or physical condition, and hence, their relevance in the monitoring of surface cleaning operations. This point is being made in this contribution with the help of experimental results obtained by the authors over the years.

Surface Photovoltage (SPV) based method

The SPV method represents non-contact methods of semiconductor surface characterization. It involves the absorption of photons featuring energy higher than semiconductor bandgap which penetrate sub-surface region of semiconductor wafer to the depth dependent on the wavelength of the light used for surface illumination. Resulting generation of electron-hole pairs alters surface photovoltage and allows, by means of Surface Charge Profiling (SCP) methodology [1], determination of the surface charge, near-surface dopant concentration, as well as surface recombination lifetime.

Figure 1 shows significant depletion of boron concentration at the Si surface in as manufactured wafers [2]. An anneal at the temperature above 150°C is needed to restore near-surface boron concentration to its value in the bulk. The detrimental effect demonstrated in Figure 1 is a result of boron deactivation by copper introduced in the course of the wafer polishing process. Figure 2 shows direct correlation of the surface recombination lifetime measurements using SCP methodology with wetting angle measurements in identifying changes in the Si surface characteristics resulting from the anhydrous HF:CH₃OH native/chemical oxide etching [3]. Figure 3 confirms the increase of the surface recombination lifetime with oxide etching time by monitoring changes in the oxygen O_{1s} count by means of XPS [4]. The results in Fig. 4 show evolution of the surface charge on p-type Si surface in the course of thermal oxidation in dry oxygen for three different oxidation temperatures [5]. As seen, evolution of surface charge proceeds in stages and only for the oxides thicker than 3 nm a final positive charge associated with thermally oxidized Si surface is established.

Photoconductance Decay (PCD) based method

The Photoconductance Decay (PCD) measuring set-up using temporary contacts (tungsten probes) is shown in Fig. 5a. Generation of minority carriers is stimulated by the light-pulse of 10 μs duration produced by laser diode featuring peak emission wavelengths of 405 nm. The results are obtained in the form of the decay curve reflecting gradual surface-driven recombination of the minority carriers. As illustrated in Fig. 5b shape of the decay profile is indicative of the physical/chemical characteristics of the measured surface. The details regarding analysis of the photoconductance decay profiles obtained are available in Ref. [6].

Figure 6 shows the effect of the time of immersion of silicon wafers both bulk (Fig. 6a) and SOI (Fig. 6b) in HF (1%): H₂O solution on near-surface minority carrier lifetime and wetting angle. Gradual increase of the minority carrier lifetime with Si surface changing from hydrophilic to hydrophobic remains in agreement with the results of dilute HF exposure obtained using SPV based surface charge profiling (Figs. 2 and 3). Essentially the same results obtained for the bulk Si wafer (Fig. 6a) and SOI wafers with 205 nm thick active Si layer (Fig. 6b) further support the notion the recombination events monitored occur in the region immediately adjacent to the wafer surface.

The results of experiment discussed above demonstrate ability of the PCD measurements to follow changes in the chemical composition of Si surface. Figure 7 reflects sensitivity of the PCD measured near-surface minority carrier lifetime to the changes in surface morphology of multi-crystalline Si in response to the HF:HNO₃:H₂O etch [7]. Exposure of the sawed wafer (etch time $t = 0$) to etch chemistry for 1 minute improves significantly characteristics of the m-c Si surface as indicated by the increase of the minority carrier lifetime (Fig. 7). However, longer etch time results in significant alteration of the m-c Si surface resulting in the gradual decrease of the minority carrier lifetime.

To further investigate performance of the PCD method in the characterization/monitoring of the SOI wafers surface a physical damage to the SOI surfaces was inflicted by Ar⁺ ion etching [8]. As the variations in the PCD decay profiles in Fig. 8 demonstrate, prolonged exposure of SOI surface to high energy Ar⁺ ions leads to excessive physical damage and creation of the additional recombination centers at the surface.

Summary

The goal of this review was to demonstrate very high sensitivity of the photovoltage and photoconductance decay based electrical characterization to the subtle changes in the chemical and/or physical condition of as-processed semiconductor surfaces. What needs to be pointed out is that the same performance of the PCD methodology developed for the purpose of as-processed semiconductor surface characterization was demonstrated for bulk and SOI silicon wafers. In the separate experiments not reported here, ability of the temporary contact PCD method (Fig.5) to characterize surfaces of semiconductors other than silicon, including germanium, gallium arsenide and indium phosphide, was demonstrated.

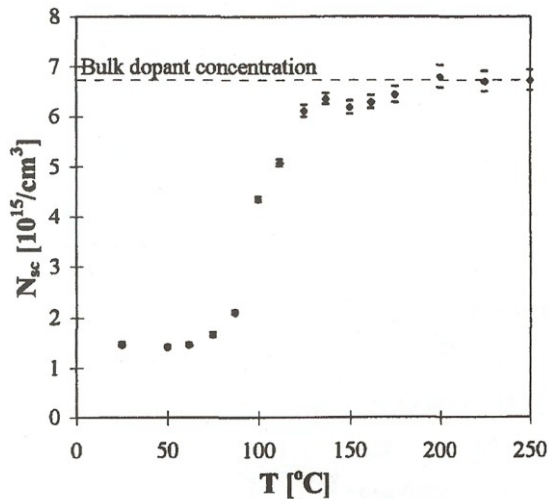


Figure 1 Surface dopant concentration in polished p-type Si wafers.

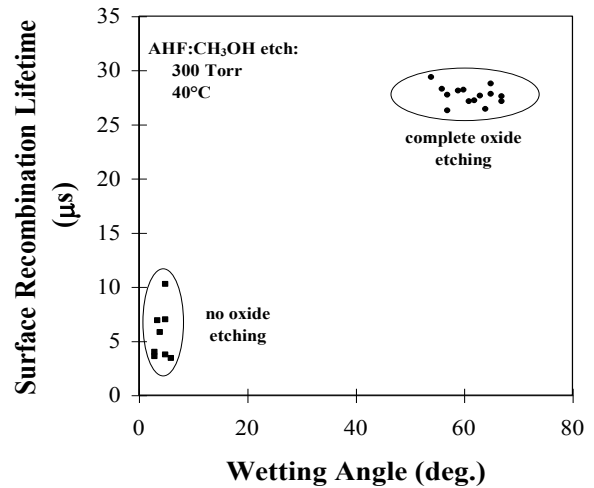


Figure 2 Surface recombination lifetime vs. wetting angle of Si wafers on anhydrous HF etched and not etched Si wafers.

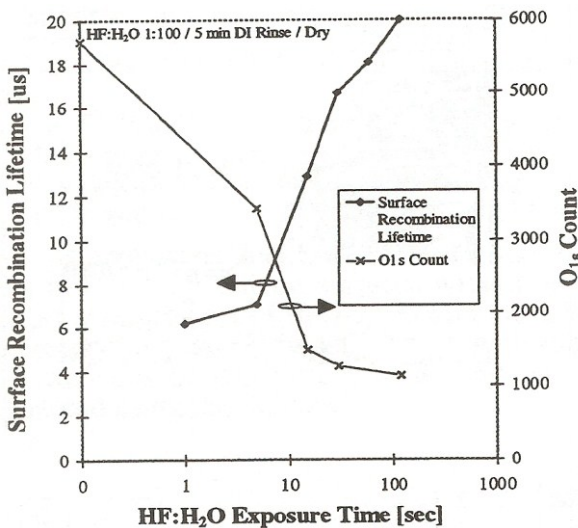


Figure 3 Surface recombination lifetime and O1s XPS count vs. HF/water (1:100) exposure time.

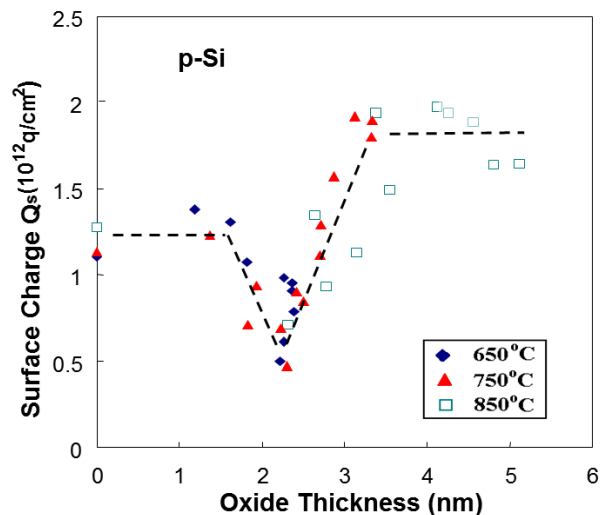


Figure 4 Monitoring of charge evolution during thermal oxidation of Si using SCP (SPV) method.

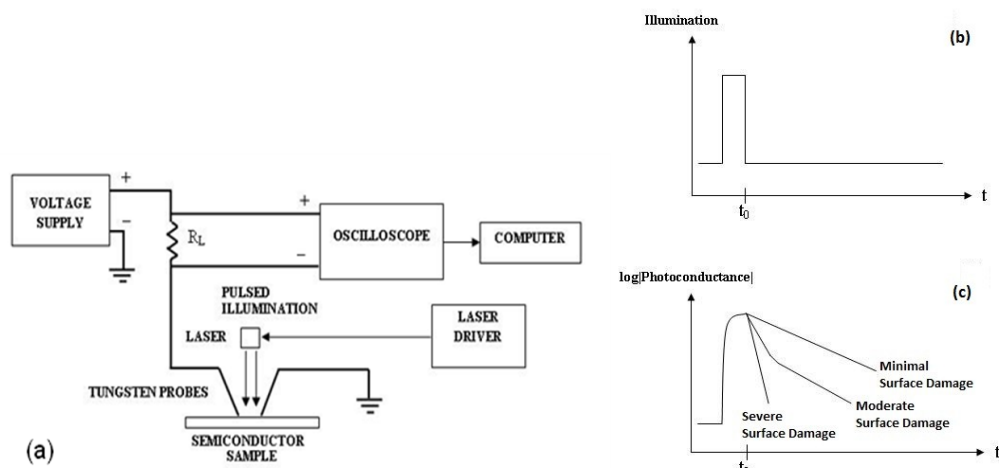


Figure 5 (a) Experimental set-up for PCD measurements and (b) light pulse and (c) possible photoconductance decay plots.

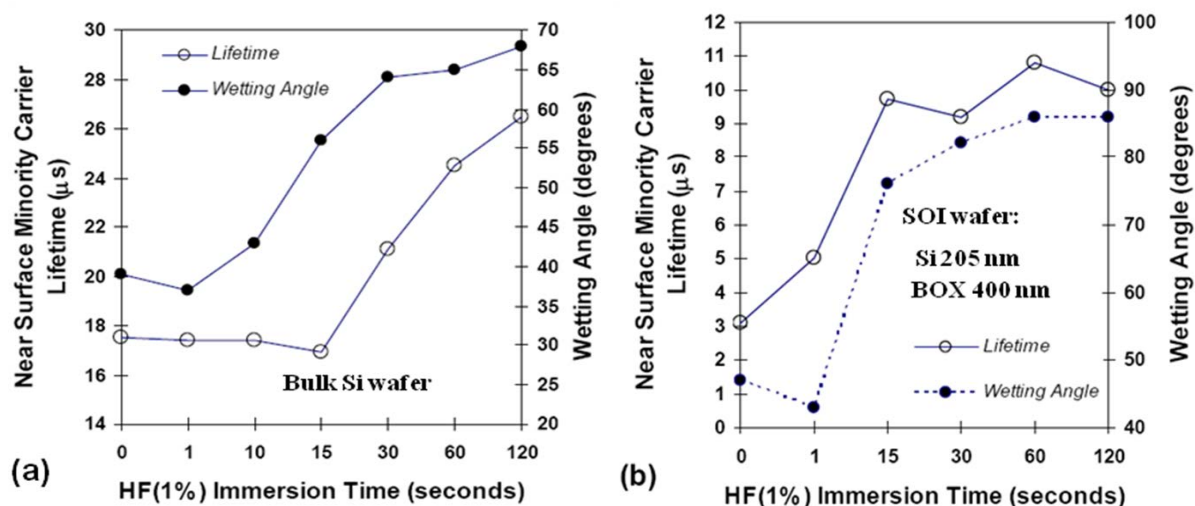


Figure 6 Variation of near-surface minority carrier lifetime and wetting angle as a function of HF (1%) immersion time for (a) bulk and (b) SOI silicon wafers.

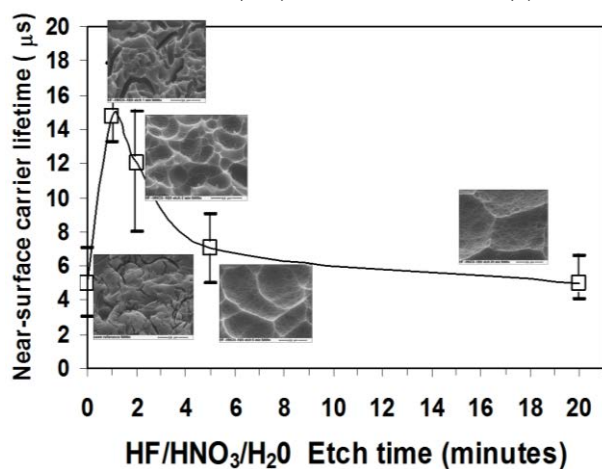


Figure 7 Near surface minority carrier lifetime and SEM micrographs of the surface of microcrystalline Si as a function of time of HF/HNO₃/H₂O (14:1:5) etch

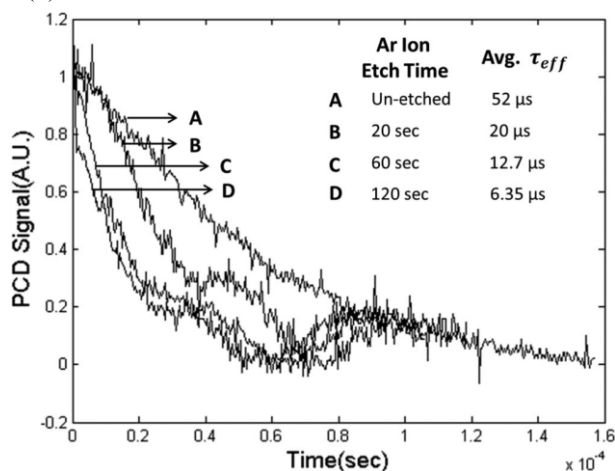


Figure 8 Normalized PCD curves for SOI wafers subjected to Ar⁺ ion etch for different times.

References

- [1] J. Ruzyllo and P. Roman, *Electrical Characterization of c-Si Surfaces* (Properties of Crystalline Silicon, Ed. R. Hull, INSPEC Publication, IEE, London, 1999).
- [2] P. Roman, J. Staffa, S. Fakhouri, M. Brubaker, K. Torek, E. Kamieniecki, and J. Ruzyllo, *J. Appl. Phys.*, **83** (1998), p. 538.
- [3] M. Brubaker, P. Roman, S. Staffa, and J. Ruzyllo, *Electrochem. and Solid St. Letters.*, **1** (1998), p. 130.
- [4] J. Ruzyllo, P. Roman, J. Staffa, I. Kashkoush, and E. Kamieniecki, *SPIE Proc. Vol.* **2876** (1996), p.162.
- [5] J. Wang, P. Roman, e. Kamienicki, and J. Ruzyllo, *Electrochem. and Sol. St. Letters*, **6** (2003), p. G63.
- [6] P. Drummond, A. Kshirsagar, S. Ramani, and J. Ruzyllo, *Thin-Solid Films*, **519** (2011), p. 7621.
- [7] P. Drummond, D. Bhatia, and J. Ruzyllo, *Solid-State Electronics*, **81** (2013), p. 130.
- [8] A. Arora, P.J. Drummond, and J. Ruzyllo. *ECS. J. Sol. St. Sci. and Technol.*, **5** (2016), p. P3069.

Atomic Resolution Quality Control for Fin Oxide Recess by Atomic Resolution Profiler

Tae-Gon Kim^{1,2,a}, Heon-Yul Ryu², Karine Kenis¹, Ah-Jin Jo³,
Sang-Joon Cho³, Sang-Il Park³, Sebastian Schmidt⁴, Bernd Irmer⁴

¹ Imec vzw., Kapeldreef 75, Leuven, B-3001, Belgium

² Hanyang University, Hanyangdaehak-ro 55, Ansan, 426-791, South Korea

³ Park Systems, Iui-Dong 906-10 Suwon, 443-270, South Korea

⁴ Nanotools GmbH, Reichenbachstrasse 33, Munich, 80469, Germany

^a Tae-Gon.Kim@imec.be

Keywords: FinFET, Oxide recess, Atomic resolution profiler, In-line monitoring, Metrology, Atomic force microscopy

Abstract. A non-destructive metrology technique for critical dimension of Fin structure is important for better device characterization and development for improving yield. Due to extremely small dimension with high complexity in FinFET a new metrology solution needs to be evaluated. In-line atomic resolution profiler was performed to provide a suitable metrology for oxide recess metrology in Fin process. The technique could measure accurately the height and CD of Fin structures, which has the space with of 25 nm and the height of 60 nm. The uniformity of recess height could be measured, which could be interpreted by loading effect of etch process. High long term repeatability of the technique was achieved for process monitoring purpose.

Introduction

Oxide recess control in fin fabrication process is a key quality factor for better FinFET device performance and yield, and the specifications of its control parameters such as fin height, oxide footing and oxide recess level are getting tighten and require atomic resolution due to device scaling [1]. In-line metrology methodologies such as CD-SEM and scatterometry (or OCD) shows a strong value in CD and fin height monitoring in terms of throughput. The techniques require a dedicated metrology structure for monitoring and it is hard to provide an oxide recess footing and oxide recess level and so on. FIB and TEM inspection therefore are employed in order to investigate these parameters. However, these techniques lead sample damage during sample preparation and provide insufficient information in terms of monitoring because a section of structure is seen. As a result, a new in-line metrology technique is needed to fulfill all requirements of in-line monitoring for oxide recess process. In this study, we investigated a new metrology technique, which is atomic resolution profiler (ARP) for oxide recess control in fin fabrication process. ARP is a similar technique as atomic force microscopy (AFM) but it was reconstructed for this purpose. AFM is a well known technique, but it only uses in limited process area due to low throughput and low reliability, which is caused by probe wear during measurement. Profiler is being used very much for in-line process monitoring, but it used less and less due to unsuitable stylus dimension. ARP is a technique, which was integrated strength of AFM and profiler in order to developed for in-process monitoring metrology by resolving these issues.

Experimental

Samples. Self-aligned double-patterned (SADP) Fin, which has the width of 10 nm and the pitch of 45 nm was used as shown in Figure 1. The sample was treated at various oxide recess process conditions and Fin height and oxide footing shape were measured.

Measurement Technique. The measurements were done by in-line atomic resolution profile measurement tool (NX-3DM, Park Systems). In order to measure accurate Fin height and oxide footing shape AFM probe should access the Fin trench, which has about the space width of 25-35 nm. Its shape and dimension are, therefore a key component to make this measurement technique possible for oxide recess monitoring. For this reason electron beam deposited carbon fiber, which has a diameter of 10 nm and a height of 100 nm (M-CNT-100, Nanotools) was used. For within wafer uniformity investigation, the target Fin structures were measured at 27 dies and in order to achieve this capability pattern recognition with sub-nanometer precision was provided.

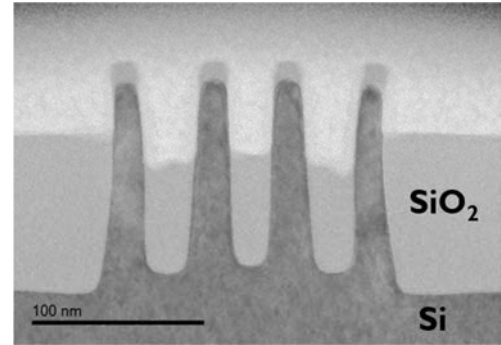


Figure 1: TEM image of an example of SADP Fins with the width of 10 nm and the pitch of 45 nm after SiO₂ recess process

Results and Discussion

Fin Profile Metrology. Fin profiles, which were measured from single line over the Fins treated at different oxide recess conditions was shown in Figure 2. It clearly shows that Fin height, oxide profile and oxide footing shape at the inside and outside Fins varied at different oxide recess conditions. It proves that the dimension of the AFM probe is enough to access the bottom of the trench without problem. Figure 2a shows that oxide inside the Fins was removed faster than outside Fins, on the other hands, Figure 2b shows opposite oxide recess behavior and oxide inside Fins remained more than outside Fins. After oxide recess process optimization, flat oxide recess profile was achieved as shown in Figure 2c. These results show that this technique is effective for determining and monitoring the loading effect.

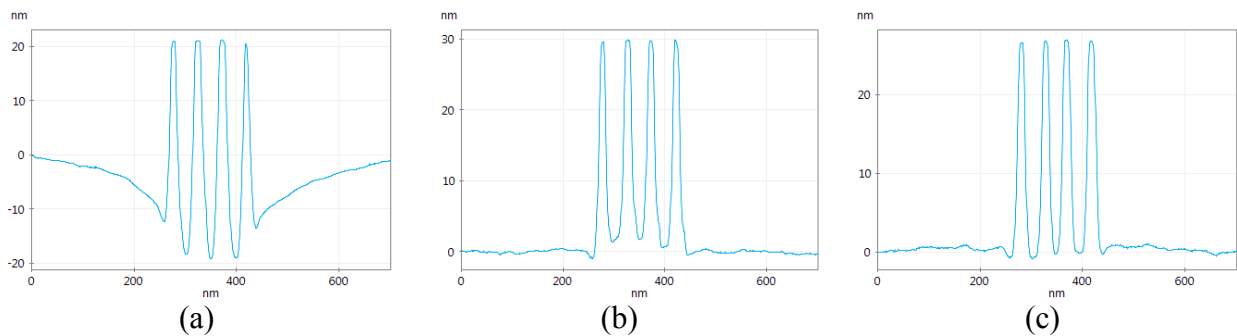


Figure 2: Fin profiles, which were treated at different oxide recess condition of (a), (b) and (c)

Oxide Recess Variation within Fins. When a Fin was scanned with multiple lines and their profiles were plotted on top of each other, oxide recess variation was observed as shown in Figure 3a. The profile along the Fin trench was characterized as the cross section of A-A' and the oxide recess variation was observed as shown in Figure 3b. The variation might be caused by non-uniform wetting property of Fin sidewall. This information is a key quality factor for FinFET performance which any other metrology techniques such as TEM, FIB, CD-SEM and scatterometry could not provide. Thus, oxide recess variation within Fins should be measured by taking multiple lines and the variation should be represented by standard deviation of Fin height.

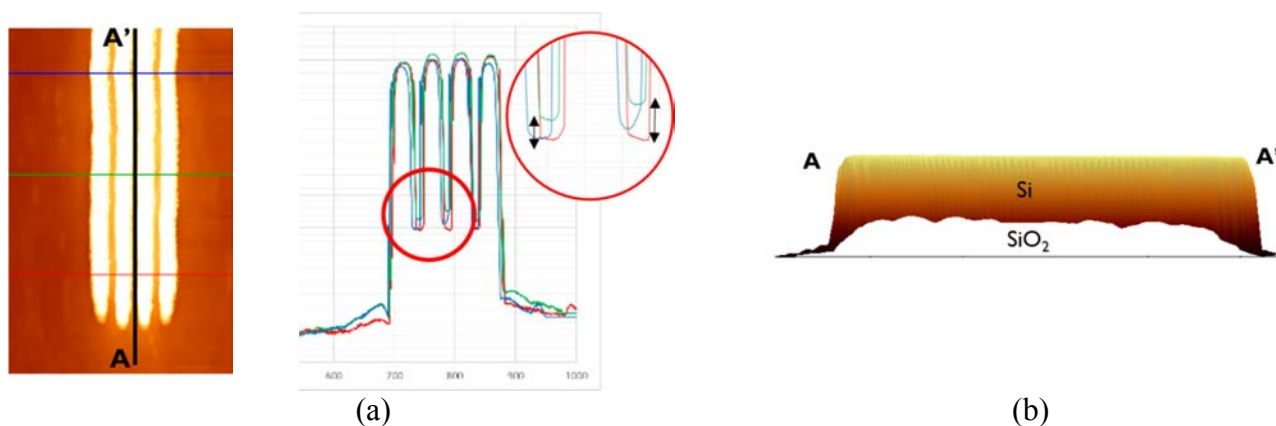


Figure 3: (a) Area image of a Fin structure and its profile graph, which was plotted multiple lines on top of each other and (b) cross section image of the Fin trench as A-A'

Verification by HRTEM. Fin profile measurements were performed at the same location by ARP and HRTEM in order to verify truth and accuracy of ARP result. Figure 4 shows cross section image of HRTEM and profile measured by ARP. It proves that Fin height value from ARP agrees well with the one measured by HRTEM. Because x and y axis scale in the profile from ARP was not 1:1 scale and the result was stretched in y axis, the profile shape was exaggerated especially in y scale. Thus, oxide footing shape at outer Fins looks like severe etched, but the information could not be verified due to not enough field of view of the HRTEM image for this case.

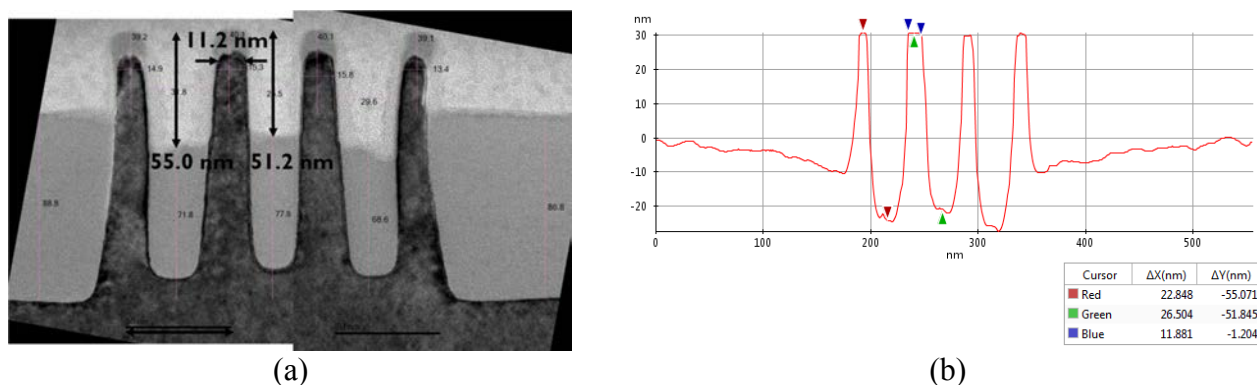


Figure 4: Cross section image and profile image that measured at the same location by (a) HRTEM and (b) by ARP

Within Wafer Oxide Recess Uniformity. Fin structures were measured at 27 dies across wafer as shown in Figure 5. It allows to check the uniformity of Fin height, oxide recess profile and oxide footing shape across wafer. It also proves that pattern alignment performed accurately without missing measurement. The wafer map shows that the remaining oxide height of inner Fin at the wafer center is smaller than the one at the wafer edge. Figure 6 shows that the wafer uniformity map of height of inner and outer Fins. It also shows that oxide recess variation within Fins and large spread was observed at wafer edge compared to at wafer center. It means that higher non-uniformity of oxide recess presented at the edge.

Long Term Reliability. Long term reliability of metrology tool is an essential key feature that metrology should be fulfilled. Especially metrology tool, which uses delicate consumable such as AFM probe or stylus, which could be worn or damaged during measurement, should provide a good reliability. For monitoring of Fin oxide recess, which has a pitch of 45 nm ARP should carefully control CNT probe, which has a diameter of 10 nm in order to minimize any unexpected damage and wear. To evaluate this long term reliability of ARP Fin wafer was measured at the same location over 90 times and Fin height was recorded as shown in Figure 7. It shows that 3σ of Fin height was achieved below 0.6 nm and peak to valley of the Fin height value was less than 1 nm. It proves that ARP achieved a good long term reliability by maintaining extremely delicate CNT probe.

Conclusions

We successfully demonstrated that ARP could be used for in-line process monitoring of oxide recess process in FinFET device fabrication and the technique provided unique metrology solution especially atomic resolution oxide footing shape, oxide level and non-uniformity of oxide level, which other metrology tool could not provide. The measured values were verified by HRTEM and it shows a good agreement with ARP results. ARP also provides a unique value, which is non-destructive atomic resolution in die measurement. When ARP is used together with CD-SEM and OCD as a complementary technique it could provide a best quality control solution for oxide recess process in FinFET device fabrication process.

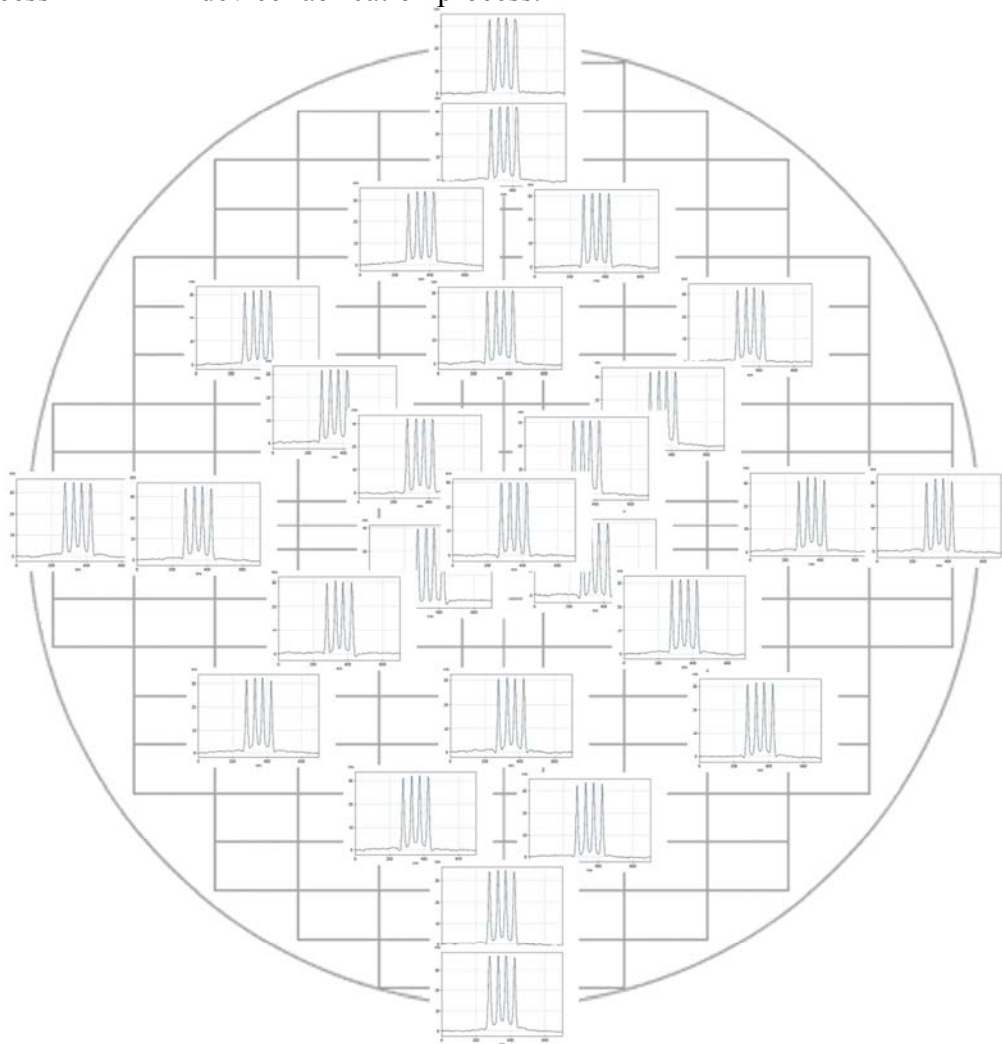


Figure 5: Fin profile map measured at 27 dies across wafer

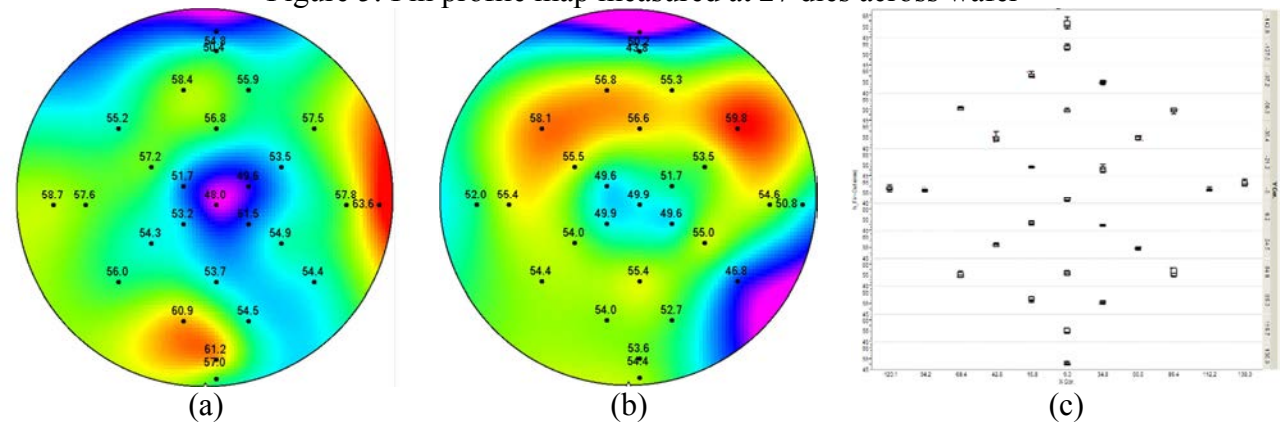


Figure 6: Wafer uniformity map of height of (a) inner Fins and (b) outer Fins and (c) non-uniformity of oxide recess within Fins.

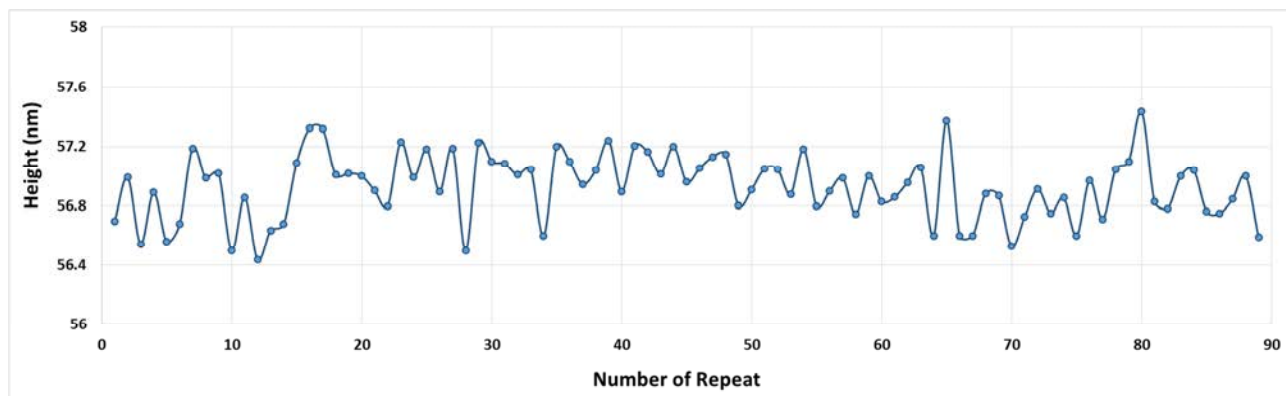


Figure 7: Long term reliability graph of ARP. Fin height was measured over 90 times at the same location

References

- [1] A. Redolfi, E. Sleenckx, K. Devriendt, D. Shamiryan, T. Vandeweyer, N. Horiguchi, M. Togo, J.M.D. Wouter, M. Jurczak, T. Hoffmann, A. Cockburn, V. Gravey, D.L. Diehl: Ultimate Integration on Silicon (ULIS), 2011 12th International Conference on (2011) p. 1.

Specification of Trace Metal Contamination for Image Sensors

Paul W. Mertens, Simone Lavizzari and Stefano Guerrieri

Imec, Remisebosweg 1, 3001 Leuven

paul.mertens@imec.be

Keywords: specification, trace metal contamination, image sensor, trap-assisted generation current, dark current.

Abstract. CMOS image sensors can suffer from background noise in absence of any light. In order to suppress this it is important to keep this noise, referred to as dark-current low. This implies that the internal generation current should be very low. Trace metal impurities have been reported to increase the generation current. In this study the trap-assisted generation current contributions due to 7 different metal impurities have been calculated. It was concluded that Cu and Mn impurities yield the highest generation current contribution.

Introduction

The ITRS roadmap has focused on the most advanced scaled CMOS technology, mostly for logic applications. The critical contamination levels, specified in the roadmap, are most often, interpreted as the most severe, in the sense that critical levels for any other type of technology with larger geometric feature size would be equal or higher.

Some specific type of “bipolar” devices, however, may require more severe specifications, with respect to contaminants (such as trace metals) that contribute to recombination or generation leakage current.

Particularly silicon photodiodes in state-of-the art CMOS image sensors (CIS), have been reported to be very sensitive to trace metal contamination [1, 2]. The light sensing components of a silicon CMOS image sensor are reverse biased photo-diodes [3]. The photons absorbed in the silicon excite electrons from the VB to the CB (which is referred to as *external* generation of free charge carriers). Simultaneously there is a small “natural or thermal” flux of electrons from the VB to the CB (referred to as *internal* thermal generation of free charge carriers). It is this spontaneous generation current that acts as a back-ground noise signal, which is named the leakage current or dark-current (I.e. the signal produced in total dark conditions).

The lower the noise the better the sensor can operate under low time-integrated illumination dose (i.e. in conditions of high spatial resolution, under limited illumination or where high-speed imaging is desired or combinations of these). Lowering the noise dramatically improves the performance under critical conditions and thus the market value of an image sensor.

The dark current specification (at room temperature) ranges from the order of 100 pA/cm², for commodity cameras to below 1 pA/cm², for very advanced professional camera applications. More detailed analysis deals with specifications for the leakage current of one pixel and the related statistics.

The probability of a spontaneous electron excitation is largely enhanced by the presence of trap centers, providing a “step-stone” with an energy level, close to midgap (E_i) in the junction space charge layer [4]. Some metallic impurities present in silicon are known to introduce electron defect-traps some of which have an energy level close to midgap that largely contribute to the generation leakage current.

In this study the trap-assisted thermal generation current is calculated for different metal contaminants as a function of the concentration of metal atoms present in the photodiode space charge layer. The calculations are based on published values for “simple” metal-induced electron states, neglecting potential interactions such as formation of clusters or larger complexes.

Basic model

The trap-assisted generation current originating from different metal contaminants in silicon, is calculated using the basic Shockley-Read-Hall (SRH) model.

In a simplified case where the capture cross-section for electrons and holes are take equal, the trap-assisted thermal generation current introduced by one single trap, i_1 , is given by [4, 5]:

$$i_1 = \frac{qn_i A_{\min} \cdot v_{th}}{2 \cosh\left(\frac{E_t - E_i}{kT}\right)} \quad (1)$$

Where:

- $q = 1.6 \times 10^{-19} \text{C}$
- n_i = intrinsic carrier concentration = $1.45 \times 10^{10} / \text{cm}^3$
- A_{\min} = minority carrier capture cross section of the defect state.
- v_{th} = thermal velocity of the minority carriers
- E_t : the electron energy level of the impurity-defect
- E_i : the intrinsic electron energy level = level at midgap

The characteristic values for different metal related traps, taken from Refs [5-7], and the resulting values of i_1 , according to eq. (1) are shown in table I.

Table I: Overview of properties of dominant carrier generation traps for different metals in silicon at 20C [5-7].

quantity	units	Cu	Mn	Co	W	Ni	Fe	Mo
$A_{\min} \cdot v_{th}$	(cm ³ /s)	2e-8	5e-8	2e-8	5.94E-09	9e-10	3.00E-10	1.10E-08
$E_t - E_i$	(eV)	-0.10	0.13	0.15	-0.151	0.18	-0.18	-0.28
i_1 eq. (1)	(A)	9.63e-19	7.5e-19	1.39E-19	4e-20	1.95E-21	6.50E-22	6.50E-22

From table I it can be seen that the energy level of the Mo-defect is not very close to the center of the bandgap. This explains why a Mo-trap yields the lowest generation current. For the other 6 metals the trap capture cross-section is the dominant difference.

The trap-assisted thermal generation current per unit volume due to a volume concentration of metal atoms in the space charge layer (SCL), C_{SCL} , is then given by, I_V :

$$I_V = C_{SCL} i_1 \quad (2)$$

Using these equations in combination with the values shown in Table I, the leakage current generated per unit volume can be calculated as a function of the metal volume concentration, shown in Figure (1).

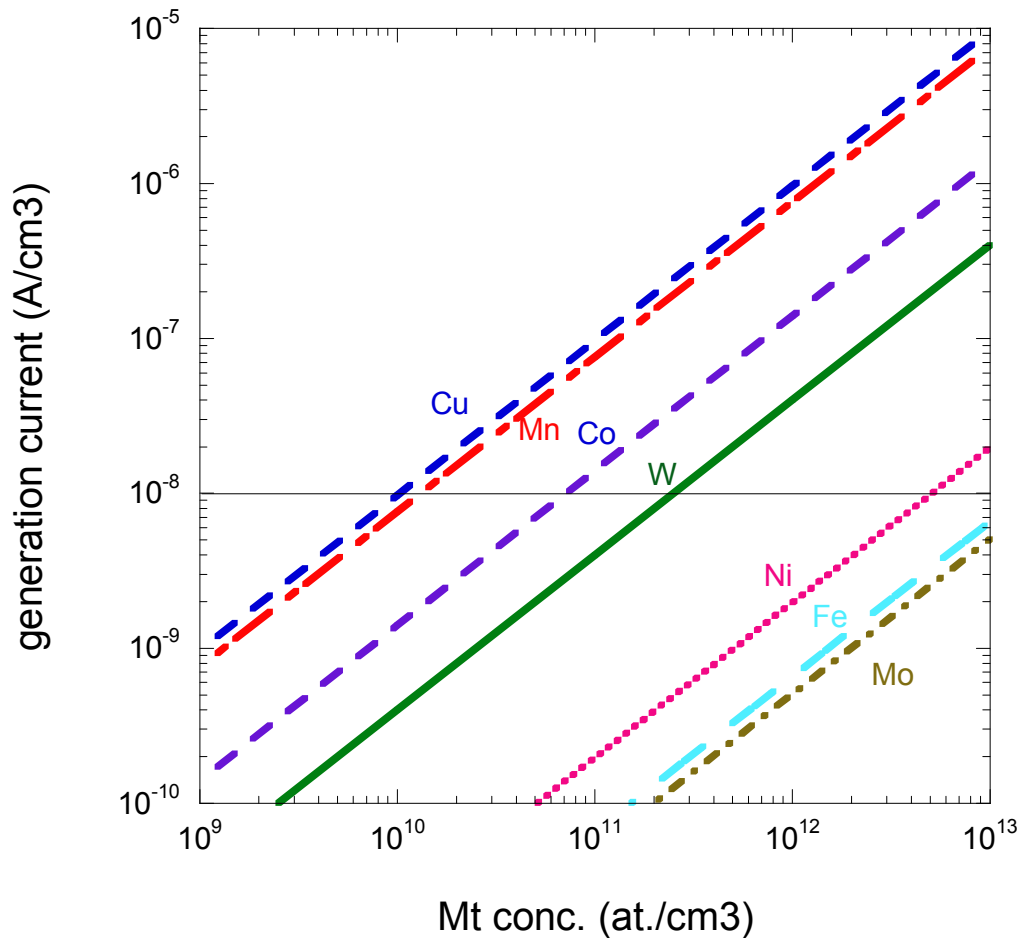


Figure 1: The calculated contribution of different metal impurities to the trap-assisted dark current generated per unit volume as a function of the volume concentration of metal-impurities in silicon (according to eq.(2)).

Clearly the contaminants resulting in the highest trap-assisted generation current from this selection are Cu and Mn. Followed by Co and W. Significantly less detrimental are Ni, Fe and Mo contamination.

The horizontal line in Figure 1 represents a specification for a dark current of 10^{-8} A/cm³. In case of an active SCL with a thickness of 1 μ m this would correspond to a leakage current of 1 pA/cm². Using this specification level for the leakage current, this would imply that the Cu contamination should be kept below 10^{10} at /cm³. If the Cu contamination would be uniformly distributed throughout the wafer thickness this would correspond to an integrated dose as low as 10^9 at/cm². This is significantly lower than the specification levels for advanced logic CMOS.

Discussion

The graph of Fig. 1 is based on simple SRH calculations, and one may question the accuracy and validity of such calculations.

It should be noted, however, that the parameters that are used for these calculations are extracted from measurements on samples with controlled intentional metal contamination. As such the result shown in Fig. 1 can be interpreted as a kind of interpolation or extrapolation or transformation of experimental results obtained for the state of metal incorporation as they occurred in these experimental studies rescaled in an appropriate range and format.

Potentially the metal impurities incorporate in a real CMOS imager may have a different chemical and electronic state (e.g. cluster to other “point-defects” such as intrinsic point defects, dopants etc....) [8]. The current study neglects the potential effect of such phenomena

It should be noted that some of the metals with large impact, such Cu, Co and W, are commonly used in state of the art logic CMOS processing. Therefore manufacturing CMOS image sensors should be well segregated from those sources of metal contamination and protective layers should be applied where possible [9].

Conclusion

Metal impurities in Silicon are known to introduce trap levels in the energy bandgap. The Trap assisted generation current contribution was calculated based on published electronic characteristics of these metal impurities of Cu, Mn, Co, W, Ni, Fe. It was found that the contribution due to Cu and Mn are dominant. For a typical photodiode device and if the generation current needs to be kept below 10^{-8} A/cm³, the Cu and Mn contamination on the surface should be kept below 10^9 at/cm².

References

- [1] F. Domengie, J. L. Regolini, D. Bauza, and P. Morin, IEEE Int. Reliab. Phys. Symp. Proc. 2010, 259–264.
- [2] F. Russo et al, Solid-State Electronics 91 (2014) 91-99.
- [3] T. York, R. Jain, *Fundamentals of Image Sensor Performance*
<http://www.cse.wustl.edu/~jain/cse567-11/ftp/imgsens/index.html#sec1>
- [4] A.S. Grove, *Physics and Technology of Semiconductor Devices*, (Wiley , New York 1967) p 129, 174.
- [5] J van Hellemont and E. Simoen, JECS 2007, 154, p. H572.
- [6] E. Simoen *et al.*, *ECS Journal of Solid State Science and Technology*, 5 (4) P3001 (2016).
- [7] H. Lemke, ECS proceedings 1994, ed. Huff et al., PV94-10, p.695.
- [8] T. Iwasaki, K. Sueko, J. Komachi, K. Saga, Japan Society for Simulation Technology (2011).
- [9] K. Saga, S. Kobayashi and K. Sueoka, Solid State Phenom. 219 (2015) 265.

Metal Removal Efficiency in High Aspect Ratio Structures

Philippe Garnier^{1, a*}, Herve Fontaine²

¹ STMicroelectronics Crolles2, 850 rue Jean Monnet 38921 Crolles, France

² Univ. Grenoble Alpes, F-38000 Grenoble, France - CEA, LETI, MINATEC Campus, F-38054 Grenoble cedex 9, France

^a philippe-e.garnier@st.com

Keywords: Metal removal efficiency, deep trenches, SPV, VPD & LPD ICPMS, CMOS Image sensors

Abstract. An extremely low level of metal contamination is required for specific devices like memories and CMOS Image sensors. Most of past work in the literature has focused on blanket wafer decontamination, since metrology is mostly adapted to flat surfaces. Metal removal efficiency has been compared between blanket wafers versus high aspect ratio deep trenches wafers. Two different metrology technics enable a quantitative and spatial metal removal determination on patterned wafers. Efficient cleaning in high aspect ratio structures requires much longer cleaning recipes than on flat surfaces.

Introduction

Metal contamination in integrated circuits fab has always been a source of severe yield degradation. Whereas its impact on transistors and removability has been widely studied on flat surfaces these last twenty years, extremely low focus exist on patterned wafers, mainly due to lack of relevant methodologies. The wet cleaning consists in successive steps: structures wetting, contaminants removal and wafer drying. In this paper, they are deeply discussed comparing blanket versus high aspect ratio patterns. Plus, an analytic methodology for deep trenches is given.

Even if metal contamination affects every semiconductors plant, its severity depends on the produced technology. The most sensitive one is the CMOS image sensor. Pixels performance is degraded (white pixels) with a $1\text{E}+8\text{at}/\text{cm}^2$ contamination (i.e. Mo and W) [2] [3]. Memories (DRAM and Flash) reliability is degraded from some contaminants at $1\text{E}+9\text{at}/\text{cm}^2$ level. Logic is less sensitive and can still follow ITRS roadmap. Finally MEMs are only sensitive to high contamination levels.

Metal contamination can degrade the dies in various ways: gate oxide reliability [4], white pixels for imagers, device degradation (i.e. diode leakage), but also yield loss linked with physical defects. Indeed, metal contamination can generate some silicon corrosion [5] or some catalytically grown defects made of Si or SiO₂ (figure 1) during epitaxy or CVD (Chemical Vapor Deposition) processes.

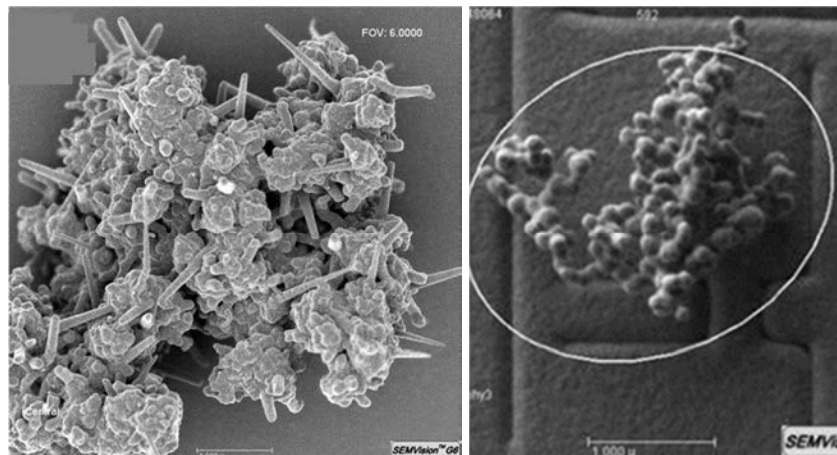


Figure 1: CVD catalytic grown defects

Left: Si whisker grown during Si LPCVD; Right: SiO₂ nanowire grown on Si during SiO₂ CVD

Whereas cleaning recipes are usually developed and characterized on blanket wafers, patterns can drastically reduce their cleaning efficiency. The cleanliness depends on three complementary steps of the cleaning recipe: structure wetting, cleaning and drying performances, hereby discussed.

Experimental

15 to 30:1 high aspect ratio structures are made of a silicon DTI (Deep Trench Isolation) network (figure 2). In a CMOS Image sensor device, these trenches isolate each pixel from each other. Therefore they require a perfect cleanliness. On the tested product, the DTI represent 20% of the total surface of the wafer.

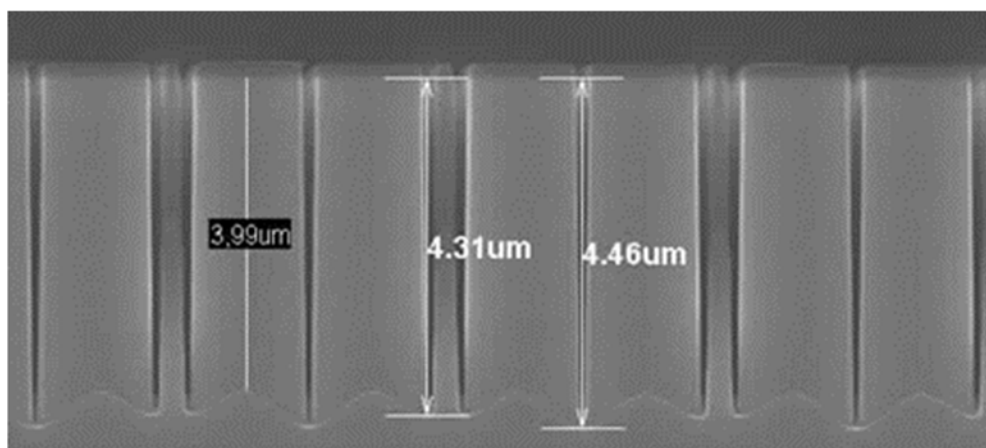


Figure 2: Studied silicon deep trenches network

Both blanket and patterned wafers have been intentionally contaminated on a spin dryer with a slightly acidified solution made of 14 metal ions mixture to get about $1\text{E}+12\text{at}/\text{cm}^2$ contamination, checked by TXRF. A comparison of the cleaning efficiency is made between various cleaning platforms: from a batch spray tool to a single wafer spin dry tool. The evaluated chemicals range from conventional FEOL chemicals (SC1, HCl, and HF) or their combination, to a commercial alkaline formulation with a chelate and a surfactant. MRE (Metal removal efficiency) is determined by complementary methods: VPD (Vapor Phase Decomposition) ICP-MS (Inductively Coupled Plasma - Mass Spectrometry) for blanket wafers, SPV (Surface Photo Voltage) for both blanket and patterned wafers and LPD (Liquid Phase Decomposition) ICPMS for patterned wafers.

Otherwise mentioned specifically, chemicals conditions are: 30s SC1 (Standard Clean 1) 1/2/80 ratio at 65°C , HCl 1/100 at RT (Room Temperature), 30s m-SC1 (modified SC1 with chelate and surfactant), HF concentration is at 0, 5%. A cleaning sequence on a spray batch tool is also tested with a HF 0,7% 15s room temperature, HF 0,02% 40min 65°C , SC1 1/4/32 40°C 2 min.

Results and discussion

Structures wetting by wet chemicals

The first and big challenge is to bring the chemicals down to the bottom of the high aspect ratio structure (deep holes or trenches). This wetting depends on several parameters. Whereas some chemicals (i.e. HF) exhibit an excellent wetting [6] some other ones (i.e. SC1) show poor wetting [7]. Indeed, first the wetting corresponds to the replacement of the trapped gas into the structures. Therefore, chemicals containing high dissolved gas trigger off bad wetting. Secondly, the material surface tension affects the wetting. Polar liquids demonstrate a better affinity and wetting of hydrophilic surfaces [8] than non-polar ones. Last, low viscosity chemicals are preferred or require a surfactant to efficiently fill a deep trench or hole. Moreover, the higher the aspect ratio, the worst the wetting [9]. To check the wetting efficiency of most used chemicals in FEOL cleans, deep trenches will be filled with various materials and etch rates in these structures will be performed along the depth of these structures and results presented at the conference.

Structures cleaning by wet chemicals

Whereas metal contamination on blanket is common, few methods exist to analyze it on patterned wafers. Studied DTI network has been made into silicon thanks to a SiN hard mask patterning that is completely removed for the study to only deal with silicon surfaces. First, localized LPD ICPMS analysis with HF/HNO₃ droplet has been attempted. Nonetheless it has been quickly abandoned due to chemicals spread through DTI (figure 3). Full wafer LPD ICPMS is then successfully tried but having higher detection limit and no contamination mapping inputs.

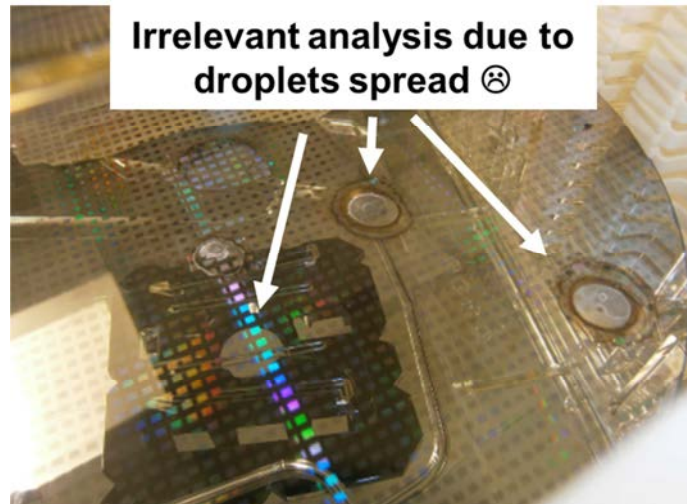


Figure 3: Localized LPD ICPMS on patterned wafers: HF/HNO₃ droplets spread through deep trenches

Whereas blanket wafers have been analyzed with VPD ICPMS, deep trenches with LPD ICPMS, explaining the difference of respective LLD (Lower Limit Detection) (figure 4). A SC1 HCl recipe on a spin dry single wafer tool is tested. Although MRE (Metal Removal Efficiency) is excellent on flat surfaces, poor MRE is obtained in deep trenches.

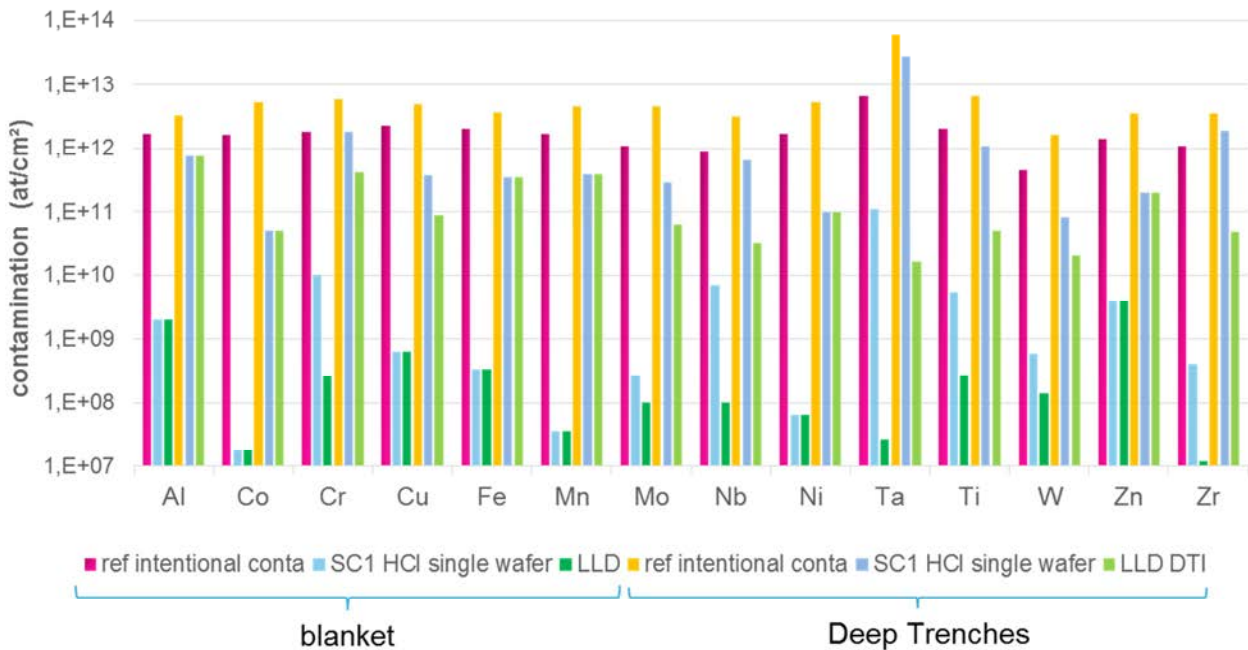


Figure 4: MRE of a 30s SC1 1/2/80 65°C - 30s HCl 1/100 25°C: blanket versus deep trenches

The MRE of some elements (Cr, Mo, Nb, Ta, Ti, W and Zr) is especially poor. This can be due to several reasons: poor chemical wetting in DTI, metal oxide precipitation, slow desorption kinetics [10], or elements trapped into the chemical silicon oxide [11].

Various cleaning sequences are compared looking at their MRE in DTI (Figure 5). First a focus is done between SC1 SC2, SC1 HCl and HCl. Whereas the two first sequences give similar results, HCl is much less efficient on some metals. Indeed some cations need to be oxidized before chlorine can remove them. Then a comparison is made between SC1 HCl and the modified SC1 (including chelate and surfactant). Performances are similar, excepted for Al. The chelate is not efficient for this element, and HCl duration is key. The cleaning sequence has only 10s HCl dispense compared with 30s for the SC1 HCl sequence. Finally, a complete chemical silicon oxide removal with HF-SC1-HCl sequence has been tested with success, bringing all elements down to the detection limits. This is true for both single wafer and batch spray toolset.

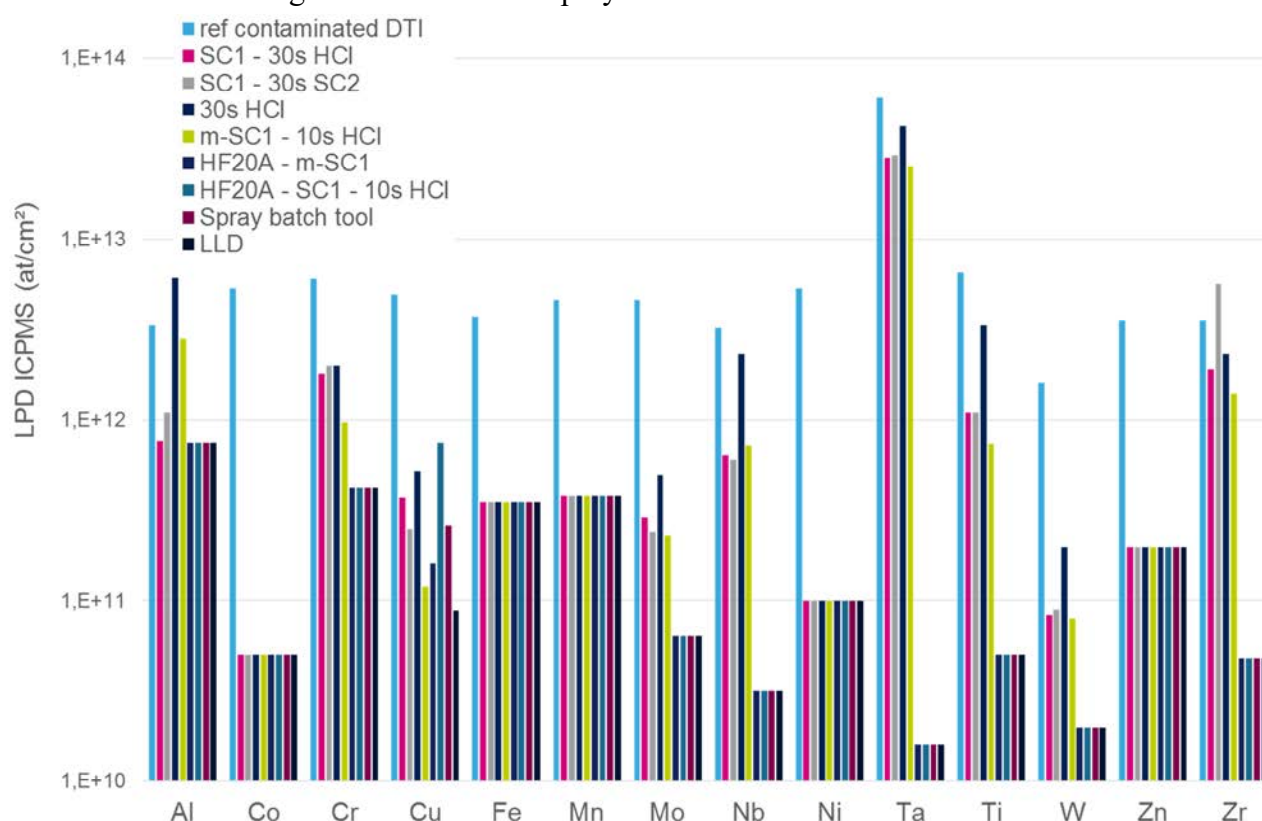


Figure 5: MRE of various recipes on wafers with 4μm deep trenches

Although LPD ICPMS is a relevant method for such study, two drawbacks remain: high detection limits and absence of contamination mapping. SPV is an alternative method. Although it's developed for blanket wafers, it perfectly works for patterned ones with an excellent detection limit, when the measurement is made on the wafer upside down and for elements measurable by SPV. Figure 6 demonstrates a huge difference in iron cleaning efficiency (up to 2 decades difference) between blanket and patterned wafers. Moreover unexpected MRE difference is noticed between SC1 SC2 and SC1 HCl. This difference could be linked with a worse wetting ability in deep trenches of SC2 than HCl due to increased dissolved gas content. The higher the dissolved gas concentration is the worst the wetting, so the cleaning efficiency. Deeper work is ongoing to validate such hypothesis. Last, the contamination removal is much poorer on the patterned wafer edge (closer to the 6 chuck pins of the cleaning tool) than the center.

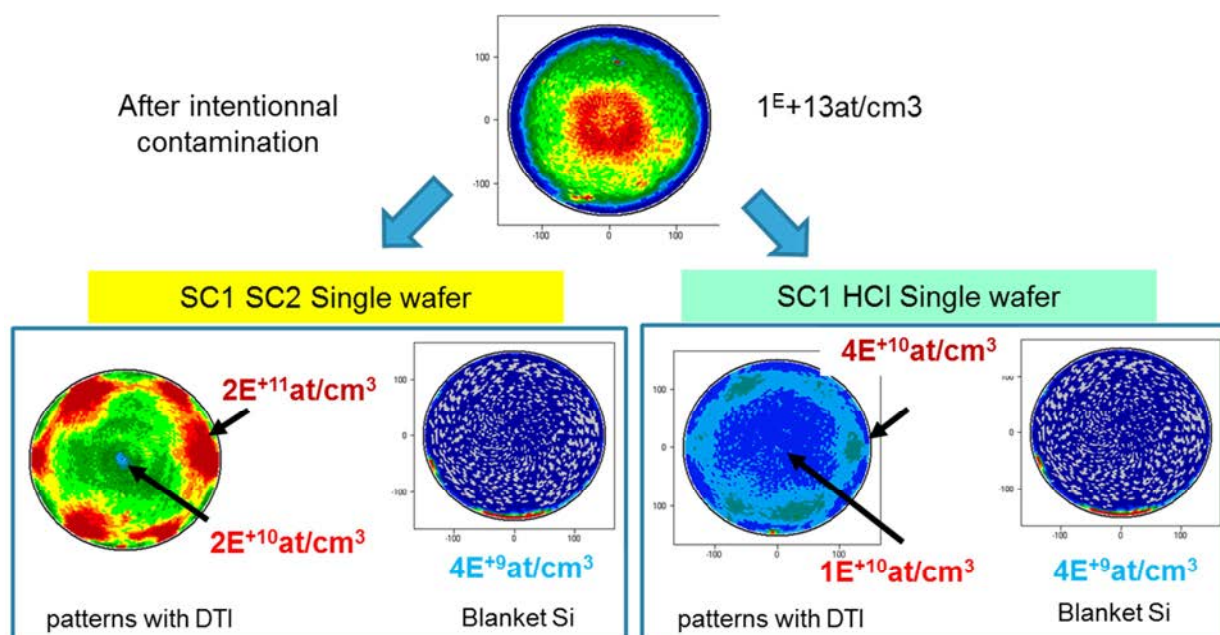


Figure 6: Fe SPV mapping before and after cleaning: blanket versus deep trenches

All these data indicate conventional recipes on single wafer tools need to be redesigned with an improved wetting of the high aspect ratio structures. HF-SC1-HCl recipes enable a good MRE but probably only on the top of the DTI. Indeed the intentional contamination has been made with contaminated water. Hence doubts exist on the wetting of the trenches till their bottom. Ongoing work aims at such characterization.

Drying by wet chemicals

After removing contaminants in DTI, their recontamination must be avoided during their drying. Two challenges are depicted on figure 7. Watermarks can trap all kind of contaminants including metals. Therefore IPA wafer drying is to be preferred to spin drying methods. Moreover a special care to IPA quality is to be considered since it's the last step of a cleaning recipe and cations adsorption is quite easy in such step with a very thin boundary layer.



Figure 7: Watermarks in DT (left) & pattern collapse of silicon features (right)

Not only patterns collapse can occur during final drying step but also during chemical and rinse transitions due to wafer de-wetting. One can wonder if alternative drying methods could even lower the metal contamination level.

Summary

Metal removal efficiency has been compared between blanket and high aspect ratio structures. To perform such study, a methodology has been proposed relying on both SPV and LPD ICPMS, bringing different kind of inputs. Whereas SPV presents an excellent LLD and mapping data but

limited to high diffusivity elements, LPD ICPMS is universal but only brings an average data and high detection limits. Cleaning recipes developed for flat surfaces aren't always suitable to clean high aspect ratio patterns. Whereas soft SC1-HCl recipes aren't able to perfectly clean metal contamination in deep trenches, a complete native silicon oxide removal brings down the contamination to a more acceptable level. Further work is required to enable a good wetting of patterns and a perfect metal contamination removal.

References

- [1] D. Gui, 15th International Symposium on the Physical and Failure Analysis of Integrated Circuits, IPFA 2008.
- [2] P. Garnier, Metal removal efficiency in deep submicron trenches by wet chemicals. Solid state phenomena, Vol. 219, 2014, pp 32-35
- [3] F. Domengie, Study of Metal Contamination in CMOS Image Sensors by Dark-Current and Deep-Level Transient Spectroscopies, journal of electronic materials, Vol. 39, N°6, 2010
- [4] S.Verhaverbeke, the effect of metallic impurities on the dielectric breakdown of oxides and some new ways of avoiding them, IEDM, 1988, pp 71-74
- [5] J. L. Baltzinger, Correlation of metallic contamination with gate disturb failure mechanism on EEPROM cell: data analysis and process robustness improvement for contamination free manufacturing, ASMC, 2007, pp 133-138
- [6] I. Nakao, a simulation model for wet cleaning of deep trenches, J. Electrochem. Soc., Vol. 137, 1990, pp 2303-2305
- [7] K. Ota, Liquid infiltration mechanism for cleaning in deep microholes, ECS Trans. Vol 11, 2007, pp 299-306
- [8] C. Virgilio, Wetting characterization of high aspect ratio nanostructures by gigahertz acoustic reflectometry, International journal of medical and health sciences Vol:3, No:3, 2016
- [9] H. Aoki, cleaning for deep submicron structures, J. Electrochem. Soc., Vol. 99, pp 102-113
- [10] D. Zamani, Surface cleaning of small structures during spin rinsing of patterned substrates, Microelectronic Engineering, 2013, Vol. 108, pp 57-65
- [11] P. Boelen, Metal contamination removal evaluation for single wafer processing, Solid State Phenomena, Vol. 92, 2003, pp 49-52

Quantitative Analysis of Trace Metallic Contamination on III-V Compound Semiconductor Surfaces

Koichiro Saga^{a*} and Rikiichi Ohno^b

Sony Corporation

4-14-1, Asahi-cho, Atsugi 243-0014, Japan

^aKoichiro.Saga@jp.sony.com, ^bRikiichi.Ohno@jp.sony.com

Keywords: metallic contamination, analysis, TXRF, III-V compound semiconductors

Abstract. We studied the detection by TXRF of several transition metals on the surface of III-V materials for high mobility channel. It has been found that the lower limits of detection of some transition metals on the surface of III-V materials become higher than that on the Si surface because the sum peaks or Raman scattering peaks as well as the fluorescent X-ray main signals from the materials themselves partially cover those from the transition metals.

Introduction

To compensate the high switching speed and low operating voltage of CMOS transistors, a new channel material that has much higher carrier mobility than silicon is required [1]. III-V compound semiconductors such as InP, InAs, InGaAs, GaAs, and GaSb are candidates for n-MOS channel materials [1, 2]. Controlling the metallic contamination on the III-V channel has become important, the same as it has on Si. Total reflection X-ray fluorescence spectroscopy (TXRF) has been widely used for detecting and quantifying trace metallic contamination on silicon surfaces. It has been reported that when III-V compound semiconductor materials are measured using ordinary TXRF, some noble metals such as Pt and Au cannot be detected because the main signals of the elements such as Ga and As composing materials such as GaAs cover the signal of the noble metals in the same fluorescent energy range [3].

In the present study, we examined the detection of metallic contamination on the surface of five different III-V compound semiconductor materials to clarify the lower limits of detection of several transition metals on these surfaces by TXRF.

Experimental

10 μ L of solutions including Cr, Mn, Fe, Ni, Cu, Zn, W, and Mo of 1 ppb and 10 ppb were deposited on two groups of InP, InAs, InGaAs, GaAs, and GaSb surfaces. The solutions were prepared by diluting the standard solution for atomic absorption spectroscopy (AAS) with ultrapure water. The diameter of dropping area and dried area was within 10 mm. The amounts of the metals dropped with 1 ppb and 10 ppb were theoretically 1×10^{11} atoms/cm² and 1×10^{12} atoms/cm², respectively. These surfaces were measured by TXRF (Rigaku, TXRF 310). W-L β line (9.67 keV) and W-high energy line (24 keV) was used for incident X-ray beams to detect transition metals and heavier metals, respectively. The power of the X-ray was 35 kV, 200 mA. Measuring time was 300 sec.

Results and discussion

Figure 1 shows TXRF spectrum of the InGaAs surface contaminated with metals whose concentration is equivalent to 1×10^{11} atoms/cm². The magnified spectrum of the energy range between 6.2 and 7.2 keV is shown in Fig. 2 (b). The sum peaks corresponding to In-L α + In-L α and to In-L α + In-L β are observed at 6.57 keV and 6.77 keV. The Fe-K α peak (6.4 keV) is adjacent to the sum peak corresponding to In- α + In- α and the Fe-K α signal is partially covered with the sum peak. This phenomenon affects the lower limit of detection of Fe on InGaAs surfaces. In contrast, no sum peak is observed on the Si surface, as shown in Fig. 2 (a).

Figure 3 shows the magnified TXRF spectra of the energy range between 7.0 and 9.6 keV, for the (a) GaAs surface and (b) GaSb surface contaminated with metals whose concentration are equivalent to 1×10^{11} atoms/cm². The resonance Raman scattering broadly appeared at 7~8.7 keV by interference of Ga-K absorption edge (10.386 keV) and W-L β line (9.67 keV). The broad Raman scattering fully covered the Cu-K α peak. The sum peak of Sb-L α + Sb-L β (7.4 keV) partially covered Ni-K α signals (7.473 keV), as shown in Fig. 3 (b).

Figure 4 shows the magnified TXRF spectrum of the energy range between 7.0 and 9.6 keV for the InP surface contaminated with metals whose concentrations are equivalent to 1×10^{11} atoms/cm². Sum peak corresponding to In-L α + P-K β is observed at 5.42 keV and the sum peak of In-L γ 1 + P-K α is observed at 5.93 keV. The Cr-K α peak (5.41 keV) and Mn K α peak (5.9 keV) are partially covered with the sum peak.

The lower limits of detection of the Cr, Mn, Fe, Ni, Cu, Zn, W, and Mo on the InP, InAs, InGaAs, GaAs, and GaSb surfaces have been determined by considering the interfering peaks such as sum peaks and resonant Raman scattering peaks. The lower limit of detection has been defined in the following three cases:

- If the signals from the contaminated metals are clearly observed in the spectra without any interfering peaks, the lower limit of detection was given by

$$\text{LLD} = 3 C / I_{\text{net}} \times (I_{\text{bg}} / t)^{1/2}, \quad (1)$$

where C is a theoretical concentration of the contaminated metal (in atoms/cm²), I_{net} is a net intensity of the signal from the metal (in cps), I_{bg} is a background intensity (in cps), and t is measurement time (in sec).

- If the signals from the contaminated metals are observed in the spectra, but partially covered with the interfering peaks, the peaks for the contaminated metals were separated from the interfering peaks. The lower limit of detection (LLD) was then given by equation (1). When the correlation curve between the peak intensity and the metal contaminant concentration becomes non-linear, the concentration at the inflection point is LLD.
- The signals from the contaminated metals are not observed in the spectra by fully covering the signals with the interfering peaks. The lower limits of detection go to 1×10^{12} atoms/cm².

The results are summarized in Fig. 5. The lower limits of detection of metals on Si are also shown. The lower limits of detection of Fe on the materials including In (InAs and InSb as well as InGaAs) are significantly higher than those on the others. The lower limits of detection of Cu on the materials including Ga (GaAs, GaSb, and InGaAs) are significantly higher than those on the others due to the resonance Raman scattering peak generated by interference of the Ga-K α edge and W-L β line. The lower limit of detection of Ni on the material including Sb (GaSb) is significantly higher than those on the others due to the partial covering of Ni-K α signals with the sum peak of Sb-L α + Sb-L β . The lower limit of detection of Cr and Mn on the material including In and P (InP) are significantly higher than those on the others due to the partial covering of Cr-K α and Mn-K α signals with the sum peak of In-L α + P-K β and the sum peak of In-L γ 1 + P-K α , respectively.

Summary

We have found that the lower limits of detection by TXRF of some transition metals on the surface of III-V materials for the high mobility channel become higher because the sum peaks or Raman scattering peaks as well as the fluorescent X-ray main signals from the materials themselves partially cover those from the transition metals. Improving the limitations of trace metal detection on III-V compound semiconductors is required.

Acknowledgements

We thank Nadine Collaert and Robert Langer of IMEC for providing InAs and GaSb wafers. We also thank Yuki Miyunami and Masashi Nakazawa for supporting our research.

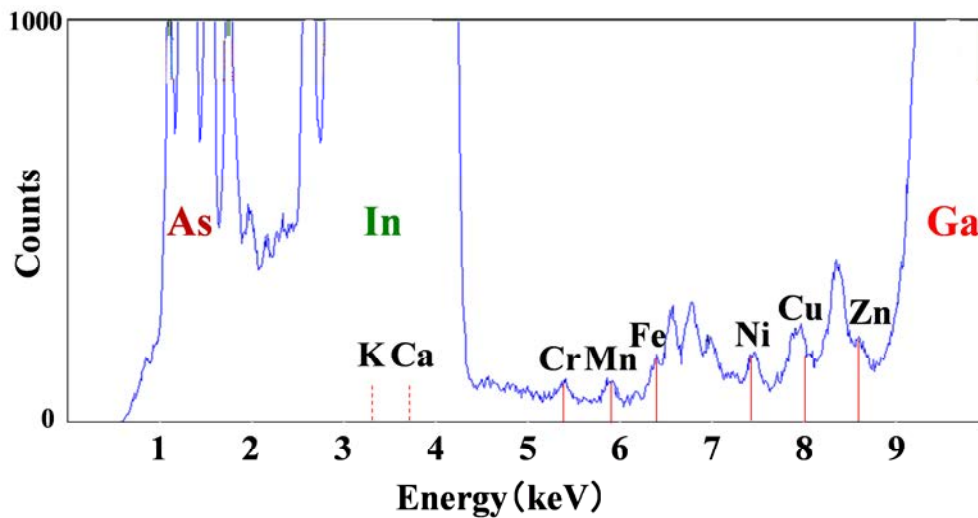
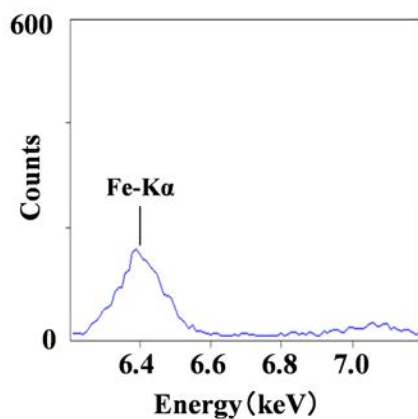
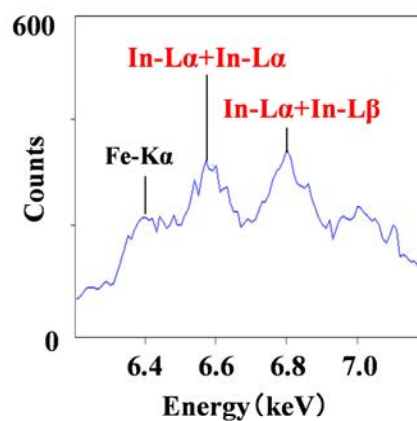


Figure 1: TXRF spectrum of InGaAs surface contaminated with the metals, whose concentration are equivalent to 1×10^{11} atoms/cm².

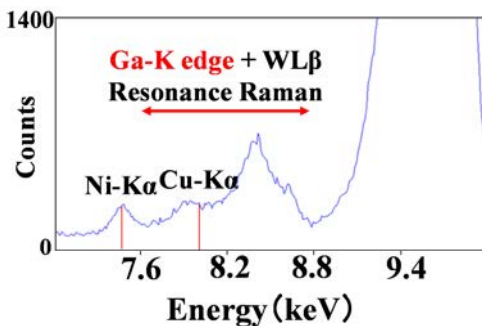


(a) Si surface

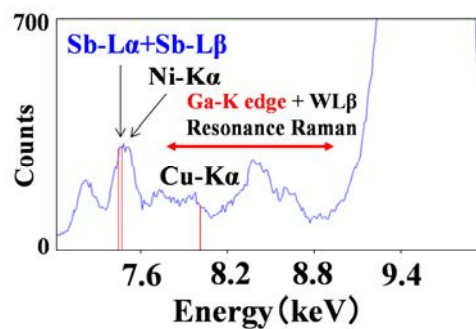


(b) InGaAs surface

Figure 2: TXRF spectra of (a) Si surface and (b) InGaAs surface contaminated with the metals, whose concentration is equivalent to 1×10^{11} atoms/cm² (magnified at 6.2 keV ~ 7.2 keV).



(a) GaAs surface



(b) GaSb surface

Figure 3: TXRF spectra of (a) GaAs surface and (b) GaSb surface contaminated with the metals, whose concentration are equivalent to 1×10^{11} atoms/cm² (magnified at 7.0 keV ~ 9.6 keV).

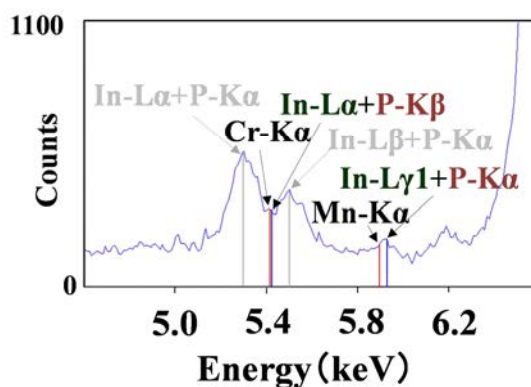


Figure 4: TXRF spectra of InP surface contaminated with the metals, whose concentration are equivalent to 1×10^{11} atoms/cm² (magnified at 4.6 keV ~ 6.6 keV).

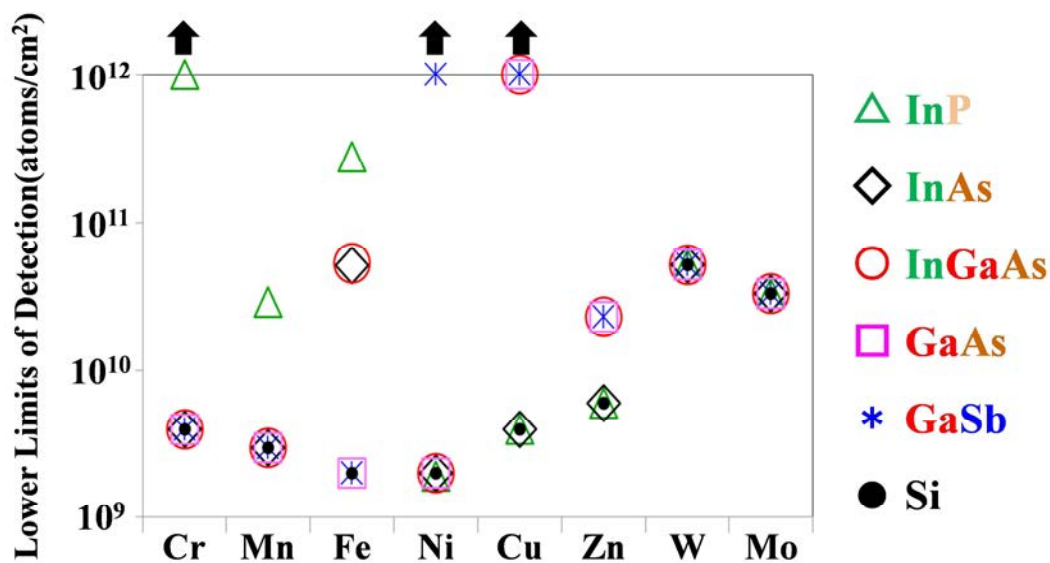


Figure 5: Lower limits of detection of the transition metals on the III-V compound semiconductor surfaces.

References

- [1] J. A. del Alamo, Nature, 479 (2011) 317-323.
- [2] S. Zaima, Jpn.J. Appl. Phys., 52 (2013) 030001-030012.
- [3] H. Fontaine and T. Lardin, ECS Transactions, vol. 58 (6) (2013) 327-335.

A Mathematical Model Forecasting HF Adsorption onto Cu-Coated Wafers as a Function of the Airborne Concentration and Moisture

Fernando Herrán¹, Hervé Fontaine¹, Paola González-Aguirre^{1,2},
Carlos Beitia¹, Jim Ohlsen², Jorgen Lundgren²

¹ Univ. Grenoble Alpes, F-38000 Grenoble, France - CEA, LETI, MINATEC Campus, F-38054 Grenoble cedex 9, France

² Entegris, SAS, Parc Centr'Alp Ouest, 196 rue du Rocher de Lorzier, 38430 Moirans, France
fernando.herran@cea.fr, herve.fontaine@cea.fr, paola.gonzalez@entegris.com

Keywords: AMC, molecular, cross-contamination, volatile acids, desorption, water

Abstract. In order to better understand and model the whole sorption behavior of the HF when in contact with a Cu surface inside a FOUP and thus control the related yield losses, Cu-coated wafers have been exposed to varying HF (ppbv) and H₂O (% RH) airborne concentrations. These experiments have yielded a HF-Cu sorption empirical-mathematical model that may be used as an industrial tool for queue-time or fluoride surface concentration predictions. Besides, the formation of CuF₂ only in case of corrosion is evidenced by the XPS measurements whereas the key role of the H₂O is further confirmed by the desorption experiments. The H₂O retained by the surface is actually responsible for promoting the HF adsorption/desorption onto/from Cu and enables a HF threshold concentration that separates the two well differenced uptake regimes; adsorption and corrosion.

Introduction

Semiconductor manufacturing technologies have evolved to the point where molecules, such as water, oxygen and airborne molecular contaminants (AMCs), have become critical in specific process conditions. Front Opening Unified Pods (FOUPs) are designed as controlled microenvironments (MEs) that protect processed wafers from contamination during transport and storage inside a cleanroom. However, it has been demonstrated that FOUPs are susceptible to AMC accumulation when exposed to freshly processed wafers that release process gases. Such contaminants are subsequently able to be released and transferred to other sensitive wafers leading to diverse detrimental impacts [1, 2]. This cross-contamination path from FOUP to wafer has already been evidenced for HF, which is responsible for yield losses due to severe corrosion issues or crystal growth on Cu, Al or TiN materials [1, 3, 4].

Wafer defectiveness is strongly linked to storage conditions, which, in this case, correspond to the environment inside the FOUP. In particular, parameters such as contaminant airborne concentration, moisture and time must be controlled since they turn out to be key in the defect creation process. In order to drastically reduce wafer defectiveness due to AMC, it may indeed be useful to know minutely the sorption kinetics of various critical molecules onto sensitive wafer surfaces and the influence of each of the three parameters previously mentioned.

This work addresses therefore the HF sorption onto 200 mm Cu-coated wafers varying the environmental moisture content and HF airborne concentration. The experimental results are discussed and analyzed in order to build up a mathematical model based on a 1st order adsorption equation (Langmuir type), which may either predict threshold storage times for avoiding corrosion issues due to excessive F⁻ levels onto Cu layers or serve for the preparation of controlled MEs.

Experimental

A constant air flow characterized by its moisture content (Relative Humidity RH between < 1% RH and 60% RH) and a HF airborne concentration ($60 \text{ ppbv} < [\text{HF}]_{\text{air}} < 240 \text{ ppbv}$) is generated under cleanroom conditions ($45\% \pm 5\% \text{ RH}$, $21^\circ \text{ C} \pm 2^\circ \text{ C}$) and led to a specifically dedicated chamber holding 200 mm wafers. The HF airborne concentration is checked by air bubbling in DIW (DeIonized Water) + Ionic Chromatography (IC). A temperature/humidity sensor (TR-77Ui) monitors the RH in the range of 0% to 90% RH with a precision of $\pm 2.5\% \text{ RH}$. Cu-coated (100 nm PVD deposition) 200 mm silicon wafers are exposed inside the pod for a time between 15 minutes and 6 days. The HF molecules adsorbed on the Cu-coated wafers are collected following a Liquid Phase Extraction (LPE) protocol: the surface of the wafer is evenly wetted using a fixed DIW volume and the solution is then analyzed by IC. LPE-IC quantifies HF as fluoride ions (F^-) and features a detection limit of $5.0 \cdot 10^{11} \text{ ions cm}^{-2}$ [2].

Moreover, the X-ray photoelectron spectrometry (XPS) technique (Al K_α X-rays, $E_{\text{photon}} = 1486.7 \text{ eV}$, take-off angle = 80°) is used to analyze the orbital energy emitted by the elements potentially bound to the copper onto the surface of the wafer (fluorine, oxygen and carbon). The samples are prepared so that the waiting time before XPS analysis is minimized, keeping the state of the surface as close as possible to the reality when exposed to the experimental environment (% RH, $[\text{HF}]_{\text{air}}$). These XPS measurements carried out onto copper samples presenting different contamination levels ($\sim 10^{14}$ and $\sim 10^{15} \text{ ions cm}^{-2}$) obtained under either dry or humid environments (40% RH and <1% RH) are assessed and compared.

Desorption experiments have also been carried out in order to find out whether HF-Cu adsorption is a reversible phenomenon. Cu-coated wafers are firstly exposed to a HF airborne concentration and humidity for a given time yielding a known fluoride surface concentration. This wafer is then transferred to an adapted HF-free container swept by a constant air flow (either 40% RH or < 1% RH) in order to evaluate the impact of humidity on HF desorption from Cu-coated wafers. Vacuum desorption is also tested and compared to the atmospheric pressure cases.

Results & discussion

Figures 1.A and 1.B show an unconditional acceleration of the HF uptake kinetics onto copper as % RH and $[\text{HF}]_{\text{air}}$ increase and exhibit two different uptake regimes:

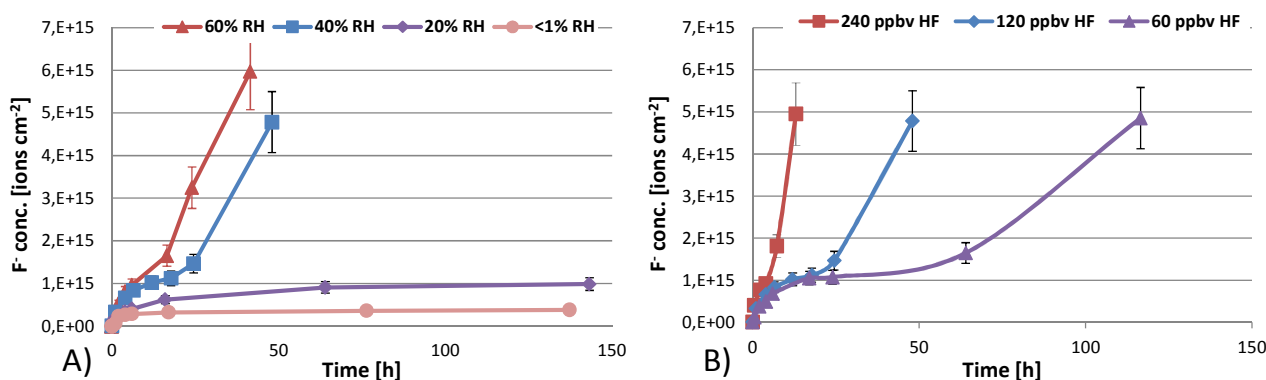


Figure 1. HF uptake kinetics onto Cu A) for $[\text{HF}]_{\text{air}} = 120 \text{ ppbv}$ varying % RH and B) for 40% RH varying $[\text{HF}]_{\text{air}}$.

Firstly, a typical Langmuir-type adsorption behavior i.e. a rapid increase up to a saturation level corresponding to $[\text{HF}]_{\text{air}} - [\text{F}^-]_{\text{surf}}$ balance is observed for low moisture content environments (< 1% RH and 20% RH) in figure 1.A, coinciding with previously reported works [5] under dry conditions (< 1% RH).

Secondly, a deviation from the expected plateau is observed when $RH \geq 40\%$. In fact, this sharp increase enhanced by both % RH and $[HF]_{air}$ (figures 1-A and 1-B) appears as the HF uptake slows down and reaches the $\sim 10^{15}$ ions cm^{-2} surface concentration level. At this stage ($> 10^{15}$ ions cm^{-2}), the slope of the HF uptake is proportional to $[HF]_{air}$. The copper surface darkens and corrosion traces appear (see figure 2), putting in evidence that an irreversible detrimental process is triggered and dominates the whole HF uptake dynamics onto copper.

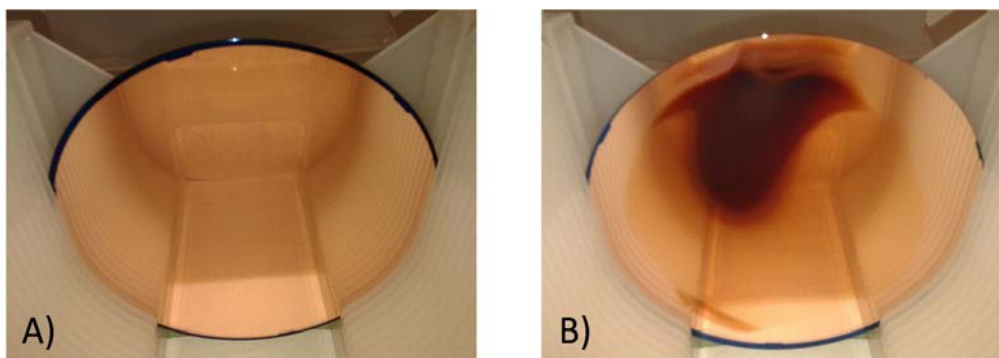


Figure 2. Cu-coated wafer corrosion due to HF A) Non-exposed wafer B) Extensively corroded wafer (240 ppbv, 40% RH, $t = 13h$).

It may therefore be concluded that HF is bound to Cu whatever the % RH is (including the dry air case, $< 1\%$ RH). It is therefore evident that moisture, whose impact becomes inescapable as % RH increases, plays a key role in the HF – Cu interactions.

According to [6], the $[H_2O]_{surf}$ is below the monolayer (ML) at 20% RH ($\theta = [H_2O]_{surf}/[H_2O]_{surf-ML} < 1$) but is exceeded at 40% RH ($\theta > 1$) and beyond. This indicates that the plateau deviation requires the formation of at least the first H_2O ML to occur. The threshold time at which the plateau deviation starts (only if $RH \geq 40\%$) is progressively reduced as $[HF]_{air}$ and % RH rise.

Furthermore, $[F^-]_{plateau}$ shows a much more significant dependence on % RH rather than $[HF]_{air}$, indicating the likely existence of a threshold fluoride concentration in the volume of the adsorbed H_2O multilayer film from which the uptake regime changes definitely.

The potential HF reservoir, namely the $[H_2O]_{surf}$ onto copper, increases as the H_2O partial pressure rises since the H_2O dynamic equilibrium established between the molecules adsorbed onto copper and the surrounding gas phase exhibits a larger molecular exchange due to the increasing molecular flow impinging on the surface. This would progressively ease the integration of HF molecules in the H_2O multilayer film given their strong affinities [7] intensified by the formation of H-bonds. Due to the polar nature of the involved HF and H_2O molecules, the HF retained within the H_2O multilayer film ($RH \geq 40\%$) would be partially ionized as it diffuses towards the copper surface, favoring thus the fluorine uptake.

The HF uptake experimental data may be empirically modeled as a function of the HF and H_2O airborne concentrations for $[F^-] < 1.5 \cdot 10^{15}$ ions cm^{-2} by means of a 1st order-Langmuir type equation:

$$[F^-] = [F^-]_{plateau}(1 - \exp(-k't)) \quad (1)$$

where $[F^-]$ and $[F^-]_{plateau}$ are expressed in [ions cm^{-2}], k' in [h^{-1}] and the exposure time t in [h]. Parameters $[F^-]_{plateau}$ and k' may be obtained after fitting Eq. 1 to the experimental data for each case (% RH, $[HF]_{air}$) by means of the least squares method (see figure 3).

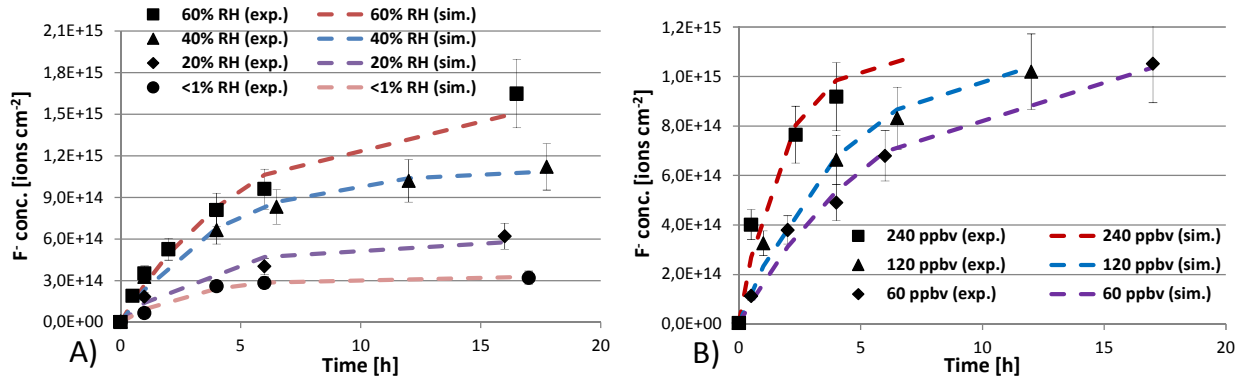


Figure 3. Experimental data fitting: HF sorption onto Cu at A) fixed $[HF]_{air} = 120$ ppbv varying % RH and B) fixed RH = 40% varying $[HF]_{air}$.

The modeling surface concentration range excludes intentionally the regime change ($[F^-] \geq 1.10^{15}$ ions cm^{-2} , $RH \geq 40\%$) when forecasting the HF uptake as a function of time, given that the threshold fluoride level on exposed Cu-surfaces in manufacturing area according to ITRS [8] is fixed at 10^{14} ions cm^{-2} . Parameter fitting results are presented in figure 4:

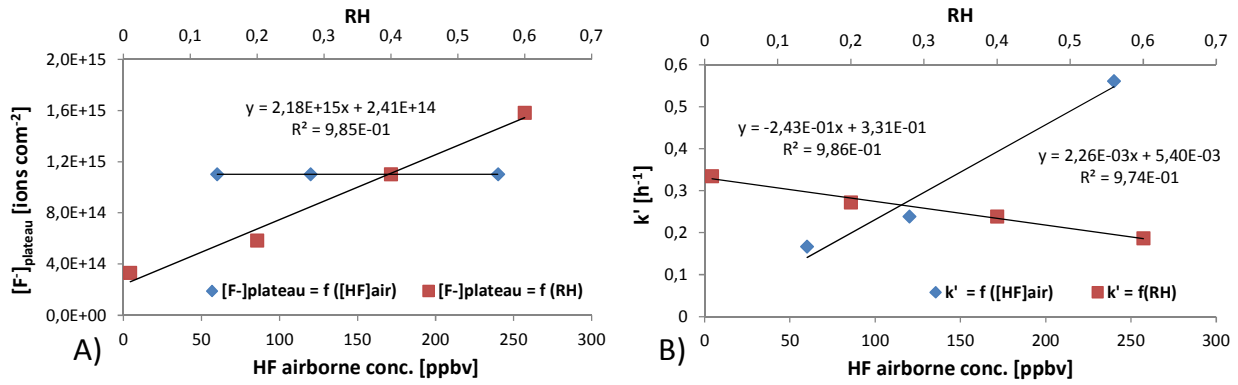


Figure 4. Parameter evolution resulting from the experimental data fitting: A) $[F^-]_{plateau} = f(RH, [HF]_{air})$ and B) $k' = f(RH, [HF]_{air})$.

According to figure 4, $[F^-]_{plateau}$ depends only on the moisture content (RH, varying between 0 and 1) whereas k' depends on both moisture content and HF airborne concentration ($[HF]_{air}$ in ppbv). $[F^-]_{plateau}$ may be then expressed as follows:

$$[F^-]_{plateau} = 2.2 \cdot 10^{15} RH + 2.4 \cdot 10^{14} \quad (2)$$

If the slope characterizing the dependence on moisture for the k' parameter (square points) is extrapolated to the other HF airborne concentrations ($[HF]_{air} \neq 120$ ppbv), the variation of the ordinate at the origin as a function of $[HF]_{air}$ is obtained (linear equation, $R^2 = 0.97$) and added to the k' parameter equation in order to have both contributions, yielding:

$$k' = (2.3 \cdot 10^{-3} [HF]_{air} + 1.0 \cdot 10^{-1}) - 2.4 \cdot 10^{-1} RH \quad (3)$$

$[F^-]_{plateau}$ and k' parameters in Eq. 1 may be thus substituted by Eq. 2 and Eq. 3 in order to estimate the HF uptake onto copper under different conditions of moisture and HF airborne concentration outside the experimental range. Thus, a robust mathematical model (cf. figure 3) is obtained in order to forecast the HF uptake onto Cu surfaces as a function of both environmental humidity and HF airborne concentration in the range of $< 1\%$ RH – 60% RH and 0 - 500 ppbv respectively. Given the large difference in terms of HF uptake dynamics onto copper between the two regimes shown in figure 1 and the extensive corrosion phenomenon driven by the airborne HF and H_2O concentrations, differently contaminated samples (dry/humid environment) have been analyzed by the XPS technique in order to characterize the chemical compounds formed onto the copper surface:

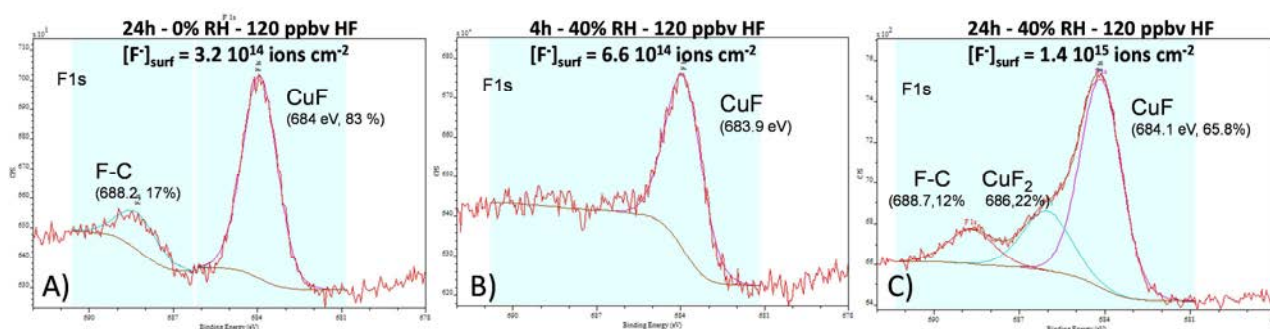


Figure 5. Fluorine 1s X-ray photoelectron spectra onto Cu-wafers exposed to 120 ppbv HF airborne concentration and A) $t = 24\text{h}$, $<1\%$ RH, B) $t = 4\text{h}$, 40% RH and C) $t = 24\text{h}$, 40% RH. A similar F-C peak appears on the reference spectrum (non-exposed Cu layer).

As shown in figure 5, the formation of CuF is detected whatever the exposure conditions are (dry/humid environment, below/above the $[F]_{\text{plateau}}$ threshold level). It may therefore be assumed that fluorine substitutes the oxygen atoms within the native oxides ($\text{CuO}/\text{Cu}_2\text{O}$) onto the wafer surface regardless of the moisture content in the surrounding environment. In addition, the presence of CuF_2 has been detected onto extensively corroded wafers, which means that the formation CuF_2 is preceded by the formation of CuF, whose concentration increases as shown by figures 5.B and 5.C between the 4h and the 24h exposure cases. Moreover, given the relative intensities of the CuF peaks in the dry-wet 24h exposure cases (figures 5.A and 5.C), it may be concluded that a significant HF fraction of the total uptake is bound to the H_2O multilayer film rather than Cu.

In order to evaluate the reversibility of the HF uptake by the copper surface or, otherwise said, the removable fluoride fraction in each case, other similarly contaminated samples (120 ppbv HF, RH = 0%, 40%, $t = 4\text{h}$, 24h) have been exposed to three different desorption environments: humid (40% RH) air flow, dry ($<1\%$ RH) air flow and primary vacuum (cf. Table 1). Contrarily to what may be expected, a dry flow is less efficient than a humid flow in terms of HF desorption in spite of the H-bonds between H_2O and HF and the H_2O removal due to surface drying. Desorption is actually enhanced in case of exposing the sample to a humid air flow rather than a dry air flow. This evidences the key role of H_2O and its dynamic equilibrium between the gas phase and the surface, which favors the HF adsorption or desorption according to its airborne concentration in the surrounding environment ($[\text{HF}]_{\text{air}}$). The removable fraction of the HF molecules retained by the copper surface when exposed to a humid air flow seems to be time-dependent. Furthermore, vacuum desorption and dry air flow desorption barely impact the HF surface concentration level when the sample is contaminated in a dry environment for 24h.

Table 1. Desorption efficiencies obtained under vacuum, dry air flow and humid air flow conditions over differently contaminated samples (4h/24h, dry/humid environment, 120 ppbv HF) characterized by LPE-IC (uncertainty: $\pm 15\%$).

Exposure conditions	Initial $[F]_{\text{surf}}$ [ions cm^{-2}]	$t = 24\text{h}$, desorption flow 40% RH [ions cm^{-2}]		$t = 24\text{h}$ desorption flow 0% RH [ions cm^{-2}]		$t = 20\text{ mins}$ desorption, 1 ^{ary} vacuum [ions cm^{-2}]	
4h, 40% RH	6,6E+14	2,3E+13	-96%	4,0E+14	-40%	3,3E+14	-50%
24h, 40%RH	1,4E+15	5,4E+14	-63%	8,3E+14	-43%	5,7E+14	-61%
24h, 0%RH	3,2E+14	2,0E+14	-40%	3,0E+14	$< \pm 15\%$	3,7E+14	$< \pm 15\%$

Two hypotheses are then plausible. The first one refers to the actual presence of physically adsorbed HF molecules onto the copper surface at every moment prior to the CuF formation, either directly bound only to the copper in a dry environment (HF-Cu) or besides interacting with the H_2O molecules if applicable (HF- H_2O -Cu). The second one assumes that every HF molecule retained by a dry copper surface is chemically bound to copper (CuF then CuF_2). The later arrival of a humid air flow would induce a H_2O surface concentration onto the copper surface previously contaminated by HF (CuF formed). The interaction of the physically adsorbed H_2O molecules with the CuF

would take the fluoride back to the H₂O multilayer film. This fluoride would be finally desorbed due to the H₂O concentration gradient through the multilayer film and the H₂O dynamic equilibrium between the copper surface and the surrounding environment.

Conclusions and perspectives

It has been demonstrated that HF uptake onto copper presents two different regimes that manifest or not according to H₂O and HF adsorbed on the surface. The first one responds to a Langmuir-type behavior featuring a strong dependence on % RH and [HF]_{air} since the prevailing molecular interactions switch from HF-Cu to HF-H₂O as the H₂O surface coverage (θ) rises. The second one puts in evidence the detrimental corrosion occurring when $\text{RH} \geq 40\%$ ($\theta > 1$) after attaining a threshold volume concentration of fluoride ions within the H₂O multilayer film, which corresponds to a surface concentration of $\sim 1.10^{15}$ ions cm⁻² at 40% RH (HF monolayer). The threshold time at which this concentration is attained is progressively reduced as % RH and [HF]_{air} increase. Finally, the HF adsorption onto copper as a function of % RH and [HF]_{air} has successfully been modeled using a Langmuir-type relation for $[\text{F}^-]_{\text{surf}} < 1.10^{15}$ ions cm⁻² enabling HF uptake estimations throughout an industrial environment. On the other hand, the XPS analysis have evidenced that the formation of CuF whatever the exposure conditions are (% RH, [HF]_{air}), followed by the formation of CuF₂ in case of extensively corroded copper surfaces ($\text{RH} \geq 40\%$). The results yielded by the desorption experiments have confirmed the key role of the H₂O in the behavior of HF sorption and desorption due to the dynamic equilibrium state of the H₂O molecules retained by the copper surface and the surrounding environment that accelerates the molecule exchange with the gas phase. More experiments must however be carried out in order to characterize thoroughly the HF-Cu interactions in the gas-solid interface, especially the kinetics of the CuF formation and the intermediate compounds participating in the chemical reaction(s) as well as the influence of H₂O on it.

References

- [1] H. Fontaine et al., Plastic containers contamination by volatile acids: accumulation, release and transfer to Cu-surfaces during wafers storage. *Solid State Phenom*, 134 (2008), 251-254.
- [2] H. Fontaine et al., Study of the volatile organic contaminants absorption and their reversible outgassing by FOUPs. *Solid State Phenom*, 145-146 (2009), 143-146.
- [3] T.Q. Nguyen et al., Identification and quantification of FOUP molecular contaminants inducing defects in integrated circuits manufacturing, *MEE*, 105 (2013), 124-129.
- [4] P. González-Aguirre et al., FOUPs against AMCs: The HF case, *Future Fabs International*, 42 (2012), 80-86.
- [5] H. Fontaine et al. Deposition behavior of volatile acidic contaminants on metallic interconnect surfaces, *Solid State Phenom*, 103-104 (2005), 365-368.
- [6] F. Herran et al., Validation, improvement and implementation of sorption mathematical models using a quartz crystal microbalance (QCM), *MEE*, 149 (2016), 106-112.
- [7] W.D. Lamb, "SO₂ in Aluminum Reduction-Cell Dry Scrubbing Systems", *Journal of Metals*, 2 (1979), 32-37.
- [8] International Technology Roadmap for Semiconductors (ITRS), Yield Enhancement, 2013. (www.itrs.net).

CHAPTER 10:

Photovoltaics

Oxidation of Si Surfaces: Effect of Ambient Air and Water Treatments on Surface Charge and Interface State Density

Heike Angermann^{1, a *}, Patrice Balamou^{2, b}, Wenjia Lu^{1, c}, Lars Korte^{1, d},
Caspar Leendertz^{1, e}, and Bert Stegemann^{2, f}

¹Institute of Silicon Photovoltaics, Helmholtz Center Berlin, Kekuléstr. 5, 12489 Berlin, Germany

²HTW Berlin - University of Applied Sciences Berlin, Wilhelminenhofstr. 75a, 12459 Berlin, Germany

^aangermann@helmholtz-berlin.de, ^bpatrice.balamou@gmail.com, ^clu.wenjia@hotmail.com,
^dkorte@helmholtz-berlin.de, ^eleendertz@gmail.com, ^fbert.stegemann@htw-berlin.de

Keywords: Silicon solar cell substrates, wet-chemical oxidation, ultra-thin oxide layer, surface photovoltage SPV, surface charge, interface state density, Effective Lifetime Analysis ELifAnT

Abstract. Surface sensitive methods, UV-VIS spectral ellipsometry (SE), surface photovoltage (SPV) measurements, and X-ray photoelectron spectroscopy (XPS) measurements were combined to investigate in detail the Si substrate oxidation and resulting interface electronic properties. Various wet-chemical oxidation methods utilizing hot deionized water with different HCl or Ozone content were optimized in order to prepare ultra-thin oxide layers with reproducible oxide thicknesses ($d_{\text{ox}} > 0.3$ to 3.5 nm), low values of interface state densities and well-defined interface charges. The simulation tool ELifAnT (Effective Lifetime Analysis Tool) was utilised to analyse experimental excess minority charge carrier density (Δn) dependent charge carrier lifetimes $\tau_{\text{eff}}(\Delta n)$, and to establish correlations between preparation induced interface charges Q_{it} and defect densities D_{it} on both p- and n-type substrates.

1. Introduction

The concomitance of oxygen and humidity causes the initial oxidation of silicon surfaces during all steps of electronic device manufacturing. In order to avoid un-stoichiometric mixed phases of native Si oxides (SiO_x) at wet-chemically treated interfaces, the native oxidation of Si substrates was thoroughly investigated as an undesirable side effect of wafer storage and water rinsing procedures [1]. On the other hand, the initial oxidation of Si surfaces and the preparation of ultra-thin silicon oxide layers in deionized water (DiW) or diluted solutions of ozone or HCl can be utilized to optimize surface morphology and surface electronic properties with respect to the subsequent processing steps. Numerous technological applications of ultra-thin oxide layers on Si substrates have been reported, e.g., to improve the surface wettability prior to inline doping and diffusion for improved emitter formation [2], as passivation interlayer on contacts [3,4] in n^+ -SIPOS/p-silicon heterojunction solar cells [5], prior to the deposition of all-PECVD $\text{AlO}_x/\text{a-SiN}_x$ passivation stacks [6] or in amorphous/crystalline a-Si:H/c-Si heterojunction solar cells [7].

Essential requirement for all applications is the reproducible preparation of uniform ultrathin oxide layers with a thickness of < 2 nm and interfaces with low densities of defect states and defined interface charges. Thus, the goal of this study is the development of simple and surface sensitive tools for controlling and monitoring the initial oxidation processes during Si solar cell manufacturing. The understanding of the related modification of surface electronic properties is considered as a precondition to achieve Si substrate conditioning by ultra-thin wet-chemical oxides with defined interface charge and low interface state densities.

2. Preparation and experimental methods

Initially H-terminated polished p- and n-type Si(100) and Si(111) substrates were exposed in (i) cleanroom air (25°C, humidity 50%), (ii) deionized water (DiW: dissolved oxygen concentration D.O.C.~ 8 ppm) at 80°C, and (iii) diluted HCl solutions (HCl : H₂O, 1:10, 1: 100 and 1:1000).

Simultaneous UV-VIS spectral ellipsometry (SE) [8], surface photovoltage (SPV) measurements, and x-ray photoelectron spectroscopy (XPS) measurements were performed to monitor the change of oxide coverage and of the electronic surface properties during the exposition times ranging from 5 min to 180 h in air, and from 5 min to 6 h in DiW solutions, respectively.

UV-VIS spectral ellipsometry (SE) measurements in the ultraviolet and visible (UV-VIS) spectral range (angles of incidence of 70°, 60° and 50° in the wavelength range of 250 nm to 800 nm) were carried out immediately after preparation and surface oxidation. Assuming appropriate models values for the surface micro-roughness $\langle d_r \rangle$ and the thickness of the ultra-thin oxide $\langle d_{ox} \rangle$, respectively, were calculated. The optical effect of a microscopically rough surface can be described accurately [9] by a Bruggeman effective medium [10] (EMA) layer. For microscopically rough wafers a two layer model was used consisting of bulk c-Si [11] and a Bruggeman EMA layer consisting of 50% bulk c-Si and 50% voids. Wafers with an ultra-thin oxide layer $\langle d_{ox} \rangle$ were modeled by a layer of SiO₂ [12] on top of c-Si. Here, the data from the initially H-terminated sample before oxidation were used to include a small fraction of surface roughness $\langle d_r \rangle$ remaining after the H-termination procedure.

X-ray Photoelectron spectroscopy (XPS), which is a well-established technique for obtaining quantitative information on the interface composition and stoichiometry by analysis of the chemical shift of the Si 2p core-level electrons [13] was applied to characterize the chemical properties of the SiO_x/Si interface.

Field-dependent SPV is a very surface sensitive method, measuring the surface photo voltage U_{ph} as a function of the external bias voltage as recently described in detail in [14] using a mica foil dielectric spacer. A laser diode (902 nm, 150 ns pulse length) was used as a light source. The photovoltage pulses, as shown in Fig. 3a, were recorded with a transient recorder (resolution time 5 ns). The determination of the interface state density $D_{it}(E)$ by a pulsed field modulated SPV method was first published in 1968 by Heilig [15]. To determine the interface state density $D_{it}(E)$ (see Fig. 3b) a varying electric field perpendicular to the surface was applied, which changes the surface potential Φ_s continuously as a function of the field voltage U_F . Due to screening effects the influence U_F on the surface potential Φ_s depends on the charge Q_{it} trapped in interface states.

The simulation tool ELifAnT is a semianalytical simulation model, implemented in Mathematica®, that calculates the c-Si band bending and recombination rates at a c-Si hetero-interface such as the a-Si:H/c-Si interface, or the SiO₂/c-Si interface investigated in the present study. Briefly, band bending is calculated based on charge neutrality between c-Si (charge Q_{cSi}), interface states (Q_{int}) and the charge in the film forming the heterojunction to the c-Si substrate (Q_f), i.e. SiO₂ in the present case:

$$Q_{cSi}(\Delta n, \psi) + Q_{int}(\Delta n, \psi) + Q_{fix}(\Delta n, \psi) = 0 \quad (1)$$

Here, ψ is the c-Si band bending. The charge in the space charge region $Q_{cSi}(\Delta n, \psi)$ is calculated following Girisch et al. [16]. For the interface defect charges $Q_{int}(\Delta n, \psi)$, a Gaussian distribution centred around c-Si midgap is assumed, while the charge in the film is assumed to be fixed at a level of $+2 \times 10^{11} \text{ cm}^{-2}$, based on literature findings for thick SiO₂ films [17].

To calculate charge in interface defects $Q_{int}(\Delta n, \psi)$ the injection-/band bending dependent carrier concentrations at the surface are determined from the standard Shockley-Read-Hall equations, integrating across the energetic distribution of the defects and using the approximation of flat quasi-Fermi levels throughout the junction. Thus, solving Eq. (1) numerically for ψ , the band bending is obtained for different injection levels Δn . This yields the positions of the quasi-Fermi levels at the c-Si/SiO₂ interface, enabling to calculate the effective interface recombination rate $U_{int}(\Delta n)$ based on Sah and Shockley's model [18] and thus the effective interface recombination rate $S_{eff} = U_{int}/\Delta n$.

This is then combined with a calculation of the injection level dependent minority carrier lifetime τ_b , yielding an effective carrier lifetime $\tau_{\text{eff}}(\tau_b, S_{\text{eff}}, \Delta_n)$: For good interface passivation, $1/\tau_{\text{eff}} = 1/\tau_b + 2 S_{\text{eff}}/W$, W being the wafer thickness.

Varying the interface defect parameters and the fixed charge in the SiO_2 , these τ_{eff} curves can be fitted to experimental data obtained from photoconductance decay (PCD) measurements, which were carried out on a commercial Sinton WCT-100 setup. For the present study, we are mainly interested in extracting the c-Si/ SiO_2 interfacial charge Q_{it} [cm^{-2}] from these fits.

3. Influence of substrate properties and preparation conditions on surface oxidation rate

The native oxidation of Si surfaces in ambient air at room temperature (RT) is a long-lasting process. As shown by our recently reported results, during an initial phase ranging from 2 to 48 hours, the appearance of the first monolayer of silicon oxide causes a strong increase of the interface states density $D_{\text{it}}(E)$ about two orders of magnitudes.

The further native oxide growth is characterized by significant decrease of $D_{\text{it}}(E)$ and a continuous change of the surface charge Q_{it} . It takes at least 6 months and was found to be limited at oxide thicknesses $\langle d_{\text{ox}} \rangle$ 1.5 ... 3.0 nm [19]. A very fast oxide growth can be achieved at RT in diluted solutions of O_3 (3 ... 50 ppm), but the rapid process causes high D_{it} values which in most cases are not suitable as passivation layer [2].

In order to optimize the wet-chemical oxide preparation without O_3 initially H-terminated p- and n-type Si(100) and Si(111) substrates were exposed in ultra-pure DiW at 80°C . In Fig. 1 $\langle d_{\text{ox}} \rangle$ is shown as determined from SE measurements as a function of the immersion time in clean room air (a) and in DiW at 80°C (b and c).

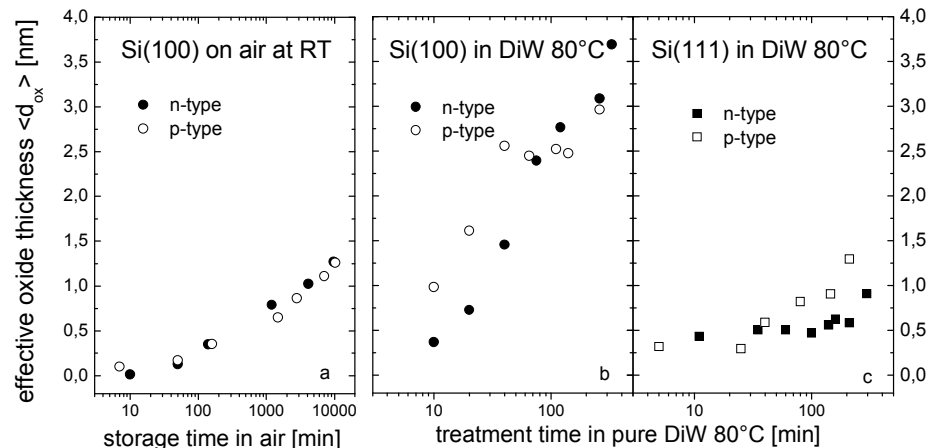


Fig. 1 Effective oxide thickness $\langle d_{\text{ox}} \rangle$ on initially H-terminated p- and n-type Si(100) determined from UV-Vis SE measurements as function of immersion time in clean room air (a) and in DiW at 80°C (b and c).

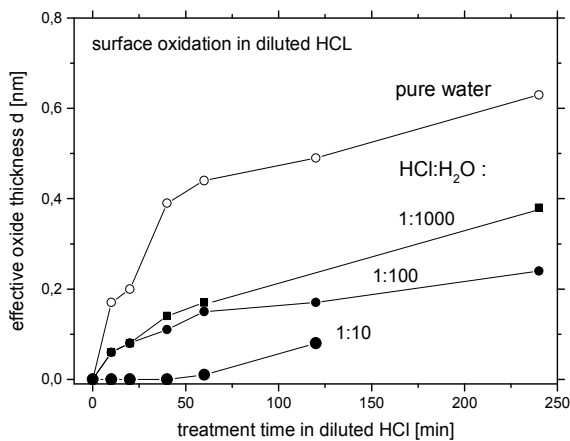


Fig. 2 Effective oxide thickness on initially H-terminated n-type Si(111) as function of immersion time in pure DiW at 80°C with increasing HCl content.

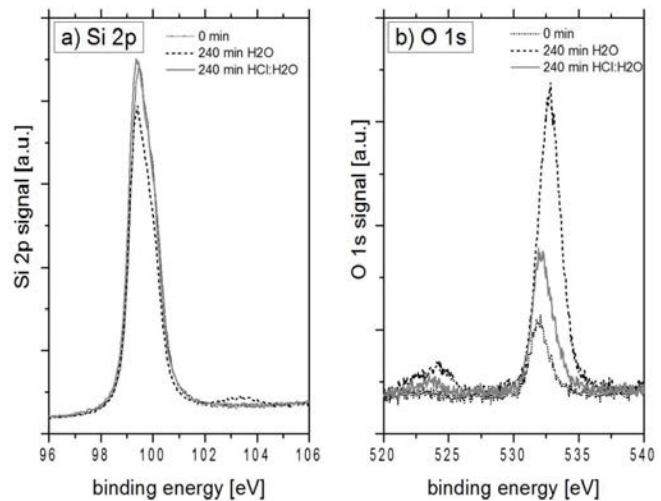


Fig. 3 XPS (a) Si 2p and (b) O 1s spectra of a Si(111) wafer, as cleaned, oxidized in H_2O and oxidized in $\text{HCl}:\text{H}_2\text{O}$.

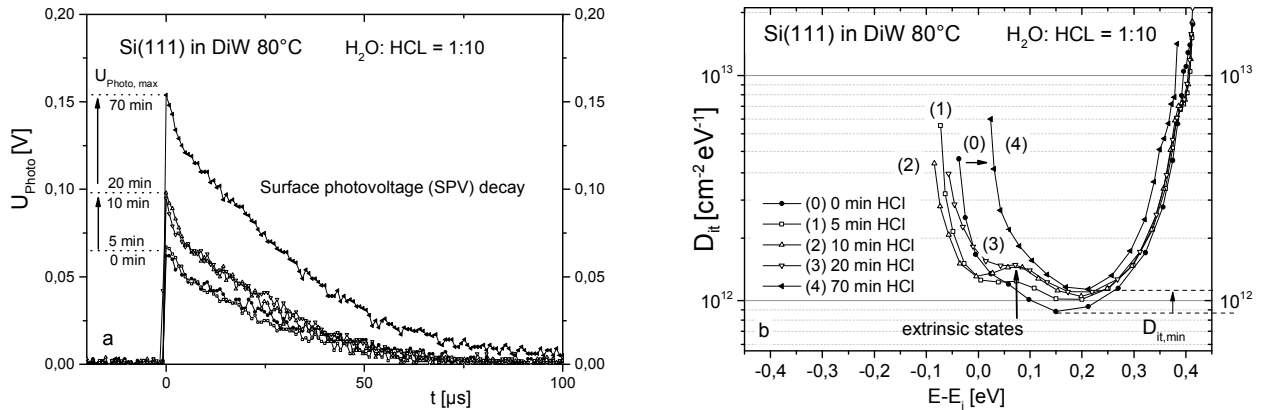


Fig. 4 SPV transients (a) measured without bias voltage and the determined $D_{\text{it}}(E)$ (b) on polished H-terminated n - Si surfaces after increasing exposition duration in HCL:H₂O = 1: 10.

The growth rate in ultrapure water was found to be significantly higher compared to the native oxidation on air, and results in ultra-thin oxide layers of 1 ... 3.5 nm thickness for Si(111) and Si(100), respectively [20]. The faster oxidation and higher final oxide thickness were obtained on Si(100), which can be explained by a higher O₂ diffusion rate due to greater Si atom distance compared to Si(111) [21].

In contrast to results obtained by ozone containing solutions [2], the addition of HCL results in a slower oxidation process of the Si surface and is superior to oxidation in pure H₂O with respect to a low $D_{\text{it}}(E)$. The influence of increasing HCL content on the evolution of effective oxide thickness on n-type Si(111) and on the XPS Si 2p and O 1s as function of immersion time in pure DiW at 80°C are shown in Fig. 2 and 3. Typically, by means of XPS the amount of interfacial Si suboxides, i.e. oxidation states (i.e., Si¹⁺, Si²⁺, Si³⁺), that are present at the SiO₂/Si interface can be determined. However, in the present case of oxidation in HCL:H₂O apparently just a very thin surface oxide is formed, yielding an XPS Si⁴⁺ 2p signal which was just above the detection limit. Thus, the amount of interfacial suboxides can be considered as negligible. Moreover, by comparison of the presented curves it is concluded that the presence of HCL decelerates the wet-chemical oxidation in hot water allowing for very precise oxide layer thickness control [22].

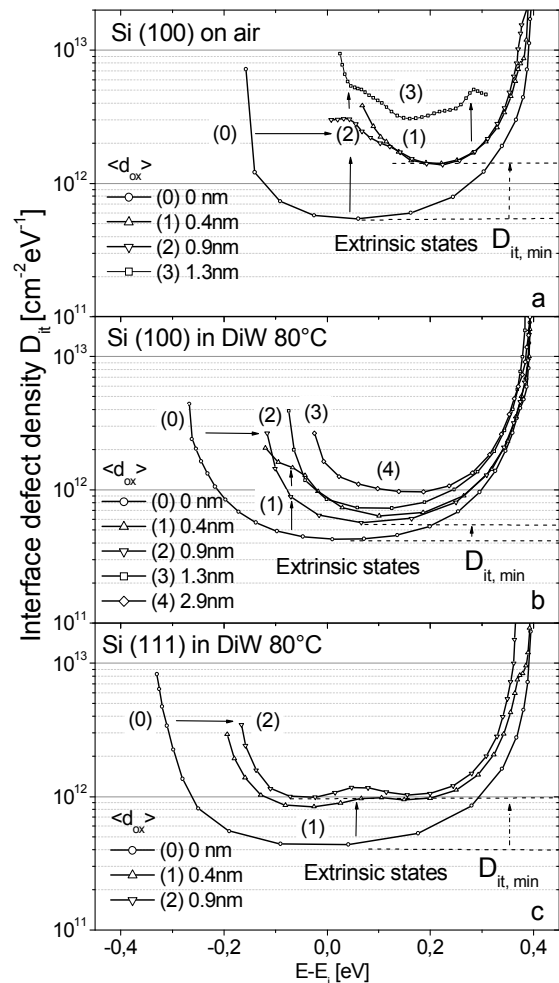


Fig. 5 $D_{\text{it}}(E)$ on initially H-terminated Si (curves 0) after preparation of ultra-thin oxide layers $\langle d_{\text{ox}} \rangle$ 0.4 nm (curves 1), $\langle d_{\text{ox}} \rangle$ 0.9 nm (curves 2), $\langle d_{\text{ox}} \rangle$ 1.3 nm (curves 3) and $\langle d_{\text{ox}} \rangle$ 2.9 nm (curve 4)

4. Evolution of interface state densities during silicon surface oxidation

In Fig. 4 are given the SPV transients (right) measured on n-type Si(111) substrates without bias voltage and the determined $D_{\text{it}}(E)$ (left) on initially H-terminated n -type Si after increasing exposition duration in HCL:H₂O = 1:10. The wet-chemical oxidation of Si leads to an increase of $D_{\text{it}}(E)$ with immersion times and oxide thicknesses. Independent from the minimal value $D_{\text{it, min}}$ the appearance of extrinsic states - caused by dangling bond defects on Si atoms with lower stage of

oxidation - increases the density of rechargeable states in the lower part of the gap. As recently reported, this process was found to be strongly related to the O_3 or HCl content [20,23].

Fig. 5 shows for n-type Si substrates the effect of Si(100) and Si(111) surface orientation and oxidation conditions, which are investigated in detail by exposition in air at RT (Fig. 5a) and in pure DiW at $80^\circ C$ (Fig. 5 b and c). During the initial phase of oxidation on the U-shaped $D_{it}(E)$ distribution of intrinsic states obtained on H-terminated surfaces (Fig. 5 a,b,c curves 0) different Gaussian distributed groups of extrinsic states additionally appears [24]. States in the lower part of the gap, related to defects on Si^{+1} were observed on Si(100) substrates (Fig. 5a,b, curves 1,2,3). The initial oxidation of Si(111) causes extrinsic states in the higher part of the gap (Fig. 5 c, curves 2,2) due to Si^{+2} defects [25]. On ultra-thin tunneling oxides ($\langle d_{ox} \rangle \pm 0.9$ nm) prepared in DiW at $80^\circ C$ (Fig. 5 b,c curves 2) significantly lower values of interface states in were observed, compared to native oxides grown on ambient air (Fig. 5a curve 2).

Lowest minimum values $D_{it,min} \leq 5 \cdot 10^{11} \text{ cm}^{-2} \text{ eV}^{-1}$ were achieved on Si(100), whereas on Si(111) least densities of rechargeable states in lower part of the gap were obtained.

5. Evaluation of surface charge on wet-chemically oxidized Si surfaces

To investigate the relation between the individual peaks in the D_{it} distributions of wet chemical oxides and the effective charge, the D_{it} values at energy levels of $E-E_i = -0.1$ eV and $E-E_i = +0.2$ eV in the Si band gap are extracted from $D_{it}(E)$ curves such as the ones depicted in Fig. 5. Furthermore, the ELifAnT tool was used to calculate the effective interface charges Q_{it} from TrPCD carrier lifetime data obtained from symmetrical samples with the same oxide passivation. The two D_{it} values and the effective interface charge Q_{it} are plotted as functions of the oxide thickness in Fig. 6. To see the correlation more clearly, the range of the tunneling interlayer thickness is here broadened to 0-2 nm.

It is apparent from Fig. 6 that no pronounced correlation exists between Q_{it} and D_{it} . A detailed understanding and a simulation is complicated because the D_{it} values do not increase over the whole band gap and separate defect peaks at different energy positions are present, as can be seen in Fig. 5 (middle panel). Note that the situation is different from what we find in native oxide growth in c-Si (data not shown): An increase of D_{it} from $\sim 0.5 \cdot 10^{12} \text{ cm}^{-2} \text{ eV}^{-1}$ to $\sim 3 \cdot 10^{12} \text{ cm}^{-2} \text{ eV}^{-1}$ during native oxide growth is accompanied by a change of Q_{it} from $\sim 4 \cdot 10^{10} \text{ cm}^{-2}$ to $-4 \cdot 10^{10} \text{ cm}^{-2}$, i.e. even including a sign reversal of the charge.

In order to assess their suitability as tunnel layers, we discuss the properties of the best (low $D_{it,min}$) chemically grown oxides with thicknesses < 1 nm: For the oxide on (100) oriented (n)c-Si, an oxide thickness of 0.7 nm is reached after 20 minutes of oxidation, with a D_{it} of $5.6 \cdot 10^{11} \text{ cm}^{-2} \text{ eV}^{-1}$. $Q_{it} = -2.6 \cdot 10^{10} \text{ cm}^{-2}$ is rather low for this surface orientation. For the chemically grown oxides on (111) n-type c-Si, after 100 min oxidation we find an oxide thickness of 0.5 nm, with a slightly higher $D_{it,min}$ value of $7.6 \cdot 10^{11} \text{ cm}^{-2} \text{ eV}^{-1}$. However, in this case the fixed charge is increased to $-7.7 \cdot 10^{10} \text{ cm}^{-2}$, which is beneficial if this oxide is used as an tunnel layer in a hole collecting contact, e.g. in a (p)a-Si:H/SiO₂/(n)c-Si emitter structure.

It should be noted, that for the usual random pyramid surface texture used in monocrystalline silicon solar cells, the (111) surface is the technologically relevant one, since the facets of the random pyramids exhibit this surface orientation.

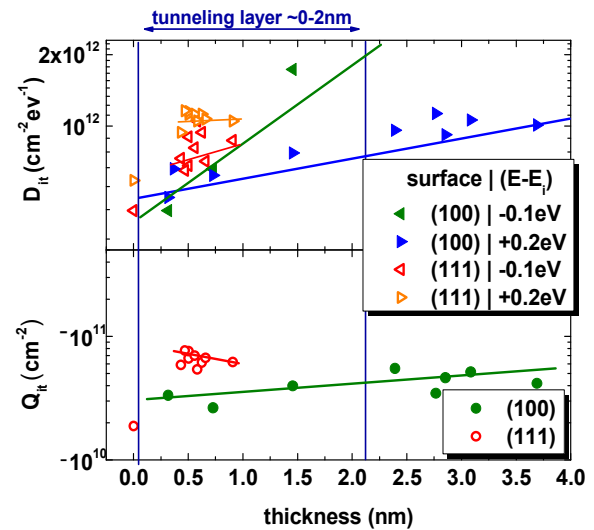


Fig. 6 Effective interface charge Q_{it} for oxides on n type Si(100) and Si(111) as functions of $\langle d_{ox} \rangle$. The lines are guides for the eye.

6. Summary

By simultaneous determination of several oxide parameters, i.e. oxide coverage, interface charges Q_{it} and density of interface states D_{it} , correlations were established between the substrate properties, the process parameters, the kinetics of oxide formation and the evolving surface electronic properties. The detailed understanding of the initial oxidation processes could be used to optimize wafer storage, cleaning and rinsing processes in order to avoid contaminations with undesirable un-stoichiometric native oxides. It was shown that ultra-thin oxide layers ($\langle d_{ox} \rangle 0.3 \dots 3.5$ nm) with low interface state densities $D_{it,min} \sim 5 \dots 9 \cdot 10^{11} \text{ cm}^{-2} \text{ eV}^{-1}$ and well defined surface charges can be prepared by wet-chemical oxidation in DiW at 80° C .

The addition of HCl lowers the oxidation rate, however, a short oxidation in presence of chlorine (high dilution preferable i.e. 1:100 ... 1:1000) and an immediate oxide removal offers the possibility to eliminate further metal contaminations and to improve the electronic interface properties [22]. For the chemically grown oxides on the technologically relevant (111) n-type c-Si surface, a 0.5nm tunnel oxide can be grown within 100 min, yielding a $D_{it,min}$ of $7.6 \cdot 10^{11} \text{ cm}^{-2} \text{ eV}^{-1}$ and a fixed charge Q_{it} of $-7.7 \cdot 10^{10} \text{ cm}^{-2}$. This charge can support the band bending if the oxide is used as a tunnel layer in a hole collecting contact, e.g. in a (p)a-Si:H/SiO₂/(n)c-Si emitter structure.

Application of this results e.g. in the realization of tunnel oxide-based solar cell concepts allows for the selection of the proper oxidation techniques to obtain high-quality SiO₂/Si interface and, thus, contributes to further improvements of the conversion efficiency.

References

- [1] D. Gräf, M. Grundner, R. Schulz, J. Vac. Sci. Technol. A7 (1989) 808.
- [2] K. Wolke, Ch. Gottschalk, A. Moldovan, A. Oltersdorf, H. Angermann, In: H. Ossenbrink, [u.a.] [Eds.] : 26th European Photovoltaic Solar Energy Conference 5 - 9 September, Hamburg, Germany. München: WIP, 2011.
- [3] A. Moldovan, F. Feldmann, M. Zimmer, J. Rentsch, J. Benick, and M. Hermle, *Solar Energy Materials and Solar Cells*, SI: Proceedings of the 5th International Conference on Crystalline Silicon Photovoltaics (SiliconPV 2015), 142 (November 2015): 123–27.
- [4] U. Römer, R. Peibst, T. Ohrdes, B. Lim, J. Krügener, E. Bugiel, T. Wietler, and R. Brendel. *Solar Energy Materials and Solar Cells*, SI: SiliconPV 2014, 131 (Dezember 2014): 85–91. doi:10.1016/j.solmat.2014.06.003
- [5] W. Füssel, H. Eschrich, L. Elstner, M. Schmidt, N.D. Sinh, W. Henrion, H. Angermann, H. Flietner, R. Henschel, G. Krageler, G. Willeke, Proc. 13 Europ. PV Solar Energy Conf., Stephens Ed. (1995) 45.
- [6] A. Laades, H. Angermann, H.-P. Sperlich, U. Stürzebecher, C. Álvarez, M. Bähr, A. Lawerenz, *Solid State Phenomena* 195 (2013) 310.
- [7] R. Varache, H. Angermann, M.-E. Farret, J.P. Kleider, L. Korte, Proc. of the 27th EU PVSEC - European Photovoltaic Solar Energy Conference and Exhibition Frankfurt / Main, Germany, (2012) 1582 – 1585.
- [8] W. Henrion, M. Rebiën, H. Angermann, A. Roeseler, Appl. Surf. Sci. 202 (2002) 199.
- [9] D.E. Aspnes, Phys. Rev. B41 (15) (1990) 10334.
- [10] D.A.G. Bruggeman, Ann. Phys. (Leipzig) 24 (1935) 636.
- [11] T. Yasuda and D.E. Aspnes, Appl. Opt. 33 (1994) 7435.
- [12] B. Brixner, in: E.D. Palik, ed., Handbook of Optical Constants of Solids, (Academic Press, New York 1985), 759.
- [13] B. Stegemann, D. Sixtensson, T. Lussky, A. Schoepke, I. Didschuns, B. Rech, M. Schmidt, *Nanotechnology* 19 (2008) 424020.
- [14] H. Angermann, Anal. Bioanal. Chem. 374 (2002) 676.
- [15] K. Heilig, Experimentelle Technik der Physik 14 (1968) 135.
- [16] R. Girisch, R. Mertens, and R. D. Keersmaecker, IEEE Trans. Electron Devices 35(2) (1988) 203–222.

-
- [17] Aberle, A. G., Glunz, S. & Warta, W. J. Appl. Phys. 71, (1992) 4422.
 - [18] C. T. Sah and W. Shockley, Phys. Rev. 109(4) (1958) 1103.
 - [19] H. Angermann, W. Henrion, M. Rebien, A. Röseler, Solid State Phenomena Vol. 92 (2003) 179-182.
 - [20] Lu, W.; Leendertz, C.; Korte, L.; Töfflinger, J.A.; Angermann, H.: Energy Procedia 55 (2014) 805-812.
 - [21] H. Angermann, W. Henrion, A. Röseler, M. Rebien, Materials Science and Engineering B73 (2000) 178.
 - [22] P. Balamou, H. Angermann, B. Stegemann, In: Photovoltaic Specialist Conference (PVSC) New Orleans, LA, 2015 IEEE 42nd. IEEE Journal of Photovoltaics 5,(2015) 1-5.
 - [23] Angermann, Heike; Wolke, Klaus; Gottschalk, Christiane; Moldovan, Ana; Roczen, Maurizio; Fittkau, Jens; Zimmer, Martin; Rentsch, Jochen: Apl. Surf. Scie. 258 (2012) 8387-8396.
 - [24] J. P. Campbell, P. M. Lenahan, Appl. Phys. Lett. 80, (2002) 1945.
 - [25] T. Hattori, Critical Reviews in Solid State and Materials Science 20 (4) (1995) 339.

Surface Optimization of Random Pyramid Textured Silicon Substrates for Improving Heterojunction Solar Cells

Bert Stegemann^{1,a*}, Jan Kegel^{1,2,b}, Lars Korte^{2,c} and Heike Angermann^{2,d}

¹ HTW Berlin - University of Applied Sciences Berlin, Wilhelminenhofstr. 75a, 12459 Berlin, Germany

² Helmholtz Center Berlin for Materials and Energy (HZB), Kekuléstraße 5, 12489 Berlin, Germany

^a bert.stegemann@htw-berlin.de, ^b kegel_j@yahoo.de ^c korte@helmholtz-berlin.de,
^d angermann@helmholtz-berlin.de

Keywords: a-Si:H, heterojunction, passivation, charge carrier lifetime, density of interface states, silicon, solar cell, texture

Abstract. Key steps in the fabrication of high-efficiency a-Si:H/c-Si heterojunction solar cells are the controlled pyramid texturing of the c-Si substrates to minimize reflection losses and the subsequent passivation by deposition of a high-quality a-Si:H layer to reduce recombination losses. This contribution reviews our recent results on the optimization of the wet-chemical texturing of crystalline Si wafers for the preparation of heterojunction solar cells with respect to low reflection losses, low recombination losses and long minority carrier lifetimes. It is demonstrated, that by joint optimization of both saw damage etch and texture etch the optical and electronic properties of the resulting pyramid morphology can be controlled. Effective surface passivation and thus long minority charge carrier lifetimes are achieved by deposition of intrinsic amorphous Si ((i)a-Si:H) layers. It is shown, that optimized (i)a-Si:H deposition parameters for planar Si(111) wafers can be transferred to a-Si:H layer deposition on random pyramid textured Si(100) wafers. Statistical analysis of the pyramid size distribution revealed that a low fraction of small pyramids leads to longer minority charge carrier lifetimes and, thus, a higher V_{oc} potential for solar cells.

Introduction

Silicon heterojunction solar cells have the advantages of very high conversion efficiencies, low temperature coefficients and a high stability [1]. Key feature of this solar cell concept is a thin layer of intrinsic amorphous hydrogenated silicon, i.e. (i)a-Si:H, which forms the heterocontact with the crystalline silicon (c-Si) wafer and provides passivation of the a-Si:H/c-Si interface [2]. High quality surface passivation is essential to obtain high charge carrier lifetimes and, thus, high open-circuit voltages (V_{oc}). In addition, random pyramid texturization of the Si wafer surfaces is utilized to reduce reflection losses and to increase the absorption probability with the aim to increase the short-circuit current density (j_{sc}) [3]. However, adequate cleaning and passivation of pyramid textured Si wafers is more difficult to achieve due to the increased effective surface area, which impedes the removal of solvent residues from the pyramid valleys and a higher number of crystallographic imperfections, which might facilitate undesired side reactions during subsequent cleaning, etching and rinsing processes. Thus, the goal of this study is to combine random pyramid surface texturing with appropriate interface passivation that the density of interface defect states is effectively reduced, and thereby highest carrier lifetimes and thus open-circuit voltages are obtained. To achieve this goal wet-chemical texture etching conditions and subsequent surface conditioning were systematically varied and the properties of the textured Si wafer and of the a-Si:H/c-Si interface were thoroughly evaluated, optimized and preserved during successive solar cell processing.

Methods and experimental procedures

Conventionally, random pyramid textures are fabricated by wet-chemical etching of monocrystalline Si(100) wafers in KOH solution containing isopropyl alcohol (IPA) as an additive.

Due to procedural and environmental concerns the float-zone grown n-type c-Si wafers were textured in a novel IPA-free solution, that random pyramids with (111)-oriented facets are obtained [3, 4]. To separate the influence of saw damage removal and preparation-related size distribution of pyramids, the respective etching times of a two-step process were systematically varied with respect to low reflection losses as determined by UV-Vis spectroscopy and to low surface recombination losses. The respective recombination data were derived from the determination of the energetic distribution of interface state densities $D_{it}(E)$ by field-dependent surface photovoltage measurements (SPV) [5] and from the effective minority charge carrier lifetime τ_{eff} by transient photoconductance decay measurements (TrPCD) performed after (i)a-Si:H layer deposition and passivation with hydrogen. To evaluate the influence of saw damage etch (SDE) on the subsequent texturization, the SDE depth was systematically varied from 5 to 20 $\mu\text{m}/\text{side}$, while keeping the anisotropic pyramid texture etching step constant (i.e. etching time 20 min). To reveal the influence of the texturization time on the surface morphology and on the resulting electronic properties, samples with constant SDE (i.e. 10 $\mu\text{m}/\text{side}$) but with varying texturization times ranging from 5 to 40 min were analyzed.

By systematic variation of the etching time, random pyramids with different size distributions were obtained. The pyramid size distribution and, particularly, the fractions of small pyramids were determined by statistical analysis of scanning electron micrographs (SEM). After subsequent RCA cleaning and etching in HF (1%), 10 nm (i)a-Si:H layers were deposited by standard plasma-enhanced chemical vapor deposition (PECVD). After (i)a-Si:H layer deposition the samples were annealed at 200°C and treated in hydrogen plasma at 190°C to improve the passivation effect [2, 6].

Results and Discussion

Saw damage etching and random pyramid texturing of as-cut crystalline silicon wafers were successively optimized with respect to low reflection losses, low recombination losses and long charge carrier lifetimes. Thus, preparation conditions were systematically varied, as described in the previous section, and each time, the following three parameters were determined: R_{min} representing the absolute minimum of the reflection curve (in the range from 250 to 1600 nm), $D_{it,min}$ representing the minimum value of the interface state distribution $D_{it}(E)$ and τ_{eff} representing the minority charge carrier lifetime.

Saw damage removal. The complete removal of saw damages is an essential prerequisite for the reduction of recombination losses in Si solar cell substrates. The results, summarized in Table 1, clearly show, that optimal values with respect to low reflection losses, low densities of defect states and high carrier life times are obtained at intermediate SDE removal of about 10 $\mu\text{m}/\text{side}$. Too low etching times (5 $\mu\text{m}/\text{side}$) lead to incomplete saw damage removal, and thus high recombination losses, while too long etching times (20 $\mu\text{m}/\text{side}$) result in a very inhomogeneous texture, which also facilitates enhanced recombination losses [4].

Table 1. Reflection minimum R_{min} , minimum of the density of interface defect states $D_{it,min}$, and charge carrier lifetime τ_{eff} for different SDE removals and subsequent texture etch (20 min each).

SDE removal [μm]	R_{min} [%]	$D_{it,min}$ [$\text{cm}^{-2} \text{eV}^{-1}$]	τ_{eff} [ms]
5	12.5	$5.4 \cdot 10^{11}$	2.8
10	11.4	$5.2 \cdot 10^{11}$	3.9
20	11.6	$5.2 \cdot 10^{11}$	2.4

Texturization. Advanced IPA-free texturization was performed and compared to conventional texturization in KOH/IPA. Typical pyramid morphologies for both texturing processes are shown in the SEM images in Fig. 1. Accordingly, conventional etching in KOH/IPA (Fig. 1a) results in

morphologies with larger pyramids as compared to the IPA-free texturization (Fig. 1b). A detailed look at the pyramid facets in the KOH/IPA-etched sample reveals several dark lines which are not present at the IPA-free etched sample and which can be attributed to surface micro-roughness (i.e., crystallographic defects) leading to an increase of the density of interface defect states $D_{it}(E)$.

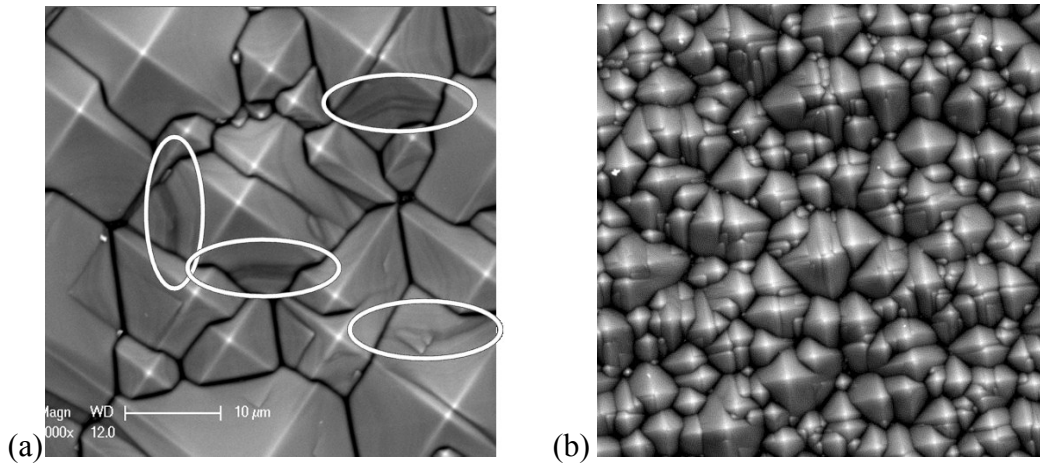


Figure 1. Scanning electron micrographs of c-Si wafers after (a) texturization in KOH + IPA (featuring crystallographic defects), (b) IPA-free texturization. Scanning size of both images: $45\ \mu\text{m} \times 45\ \mu\text{m}$, tilt = 0° .

The corresponding defect densities show generally a nearly intrinsic U-shaped energy distribution of surface states $D_{it}(E)$ around mid-gap. However, low $D_{it,min}$ values on the KOH/IPA textured sample can only be achieved by an additional wet-chemical smoothing step using e. g. $\text{H}_2\text{SO}_4:\text{H}_2\text{O}_2$, indicating some micro-roughness on the pyramid facets after the preceding texturization (see Fig. 2) [7]. In contrast, optimized etching in IPA-free solution directly yields smooth surfaces with low defect densities that are comparable to defect densities obtained on polished Si substrates. Accordingly, IPA-free texturization is advantageous for obtaining low surface state defect densities [4], which will systematically be investigated in the following.

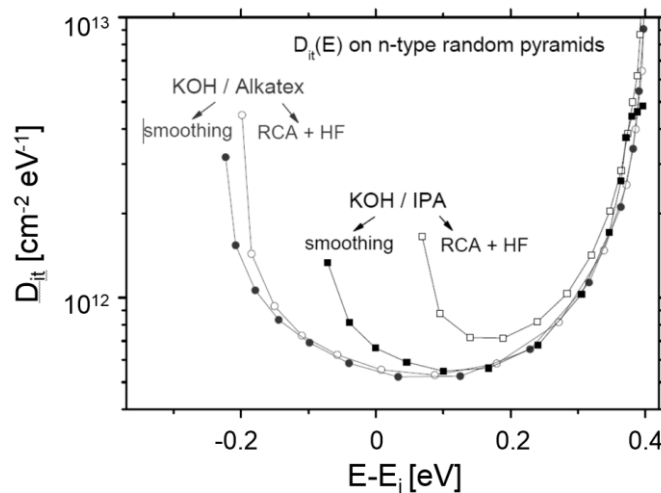


Figure 2. $D_{it}(E)$ for Si wafers after wet-chemical texturing in KOH + IPA and in KOH + Alkatex (IPA-free). In addition, the effect of subsequent wet-chemical smoothing in $\text{H}_2\text{SO}_4:\text{H}_2\text{O}_2$ is shown.

For optimization of the random pyramid texture a sample series with an optimized SDE of $10\ \mu\text{m}/\text{side}$ and a varying texture etching time was investigated with respect to morphology as well as to optimized optical and electronic properties. As the results show (cf. Table. 2), varying the texture etching time clearly influences the surface morphology as well as the reflection and recombination properties. Minimal reflection is observed for the sample with intermediate etching time (20 min),

whereas for shorter and longer texture etching times the reflection losses increase. In particular, at long etching times pyramid-free areas occur, which have an unfavourable influence on the reflection behaviour. Accordingly, longest charge carrier lifetimes were found at intermediate texture etching and typically correspond to lower defect density at the interface. Short etching times lead to an uneven surface with smaller pyramids. At longer times the number of strained and dangling bond defects is increased due to a higher number of crystallographic imperfections inherent to small pyramid morphologies.

From the results obtained by systematic variation of the SDE and the texture etching time it is concluded that there is an interplay and both steps of wet-chemical treatment need to be optimized and evaluated with respect to reflection losses and recombination losses. Both, lowest reflection losses and lowest recombination losses are obtained at intermediate etching times. By taking into account a desirably short processing time a SDE of 10 $\mu\text{m}/\text{side}$ and a texture etching time of 20 min, corresponding to a removal of 5.7 μm , is recommended.

Table 2. Reflection minimum R_{\min} , minimum of the density of interface defect states $D_{it,\min}(E)$, and the charge carrier lifetime τ_{eff} , average pyramid size and fraction of small pyramids for different random pyramid texture times after constant SDE (10 μm / side).

Texture time [min]	Texture removal [μm]	R_{\min} / [%]	$D_{it,\min}(E)$ / [$\text{cm}^{-2}\text{eV}^{-1}$]	τ_{eff} [ms]	Average pyramid size [μm^2]	Fraction of small pyramids [%]
5	2.2	12.4	$5.6 \cdot 10^{11}$	2.2	3.3	70
20	5.7	11.6	$5.2 \cdot 10^{11}$	3.9	5.4	33
40	8.5	13.8	$6.4 \cdot 10^{11}$	2.5	1.9	85

Statistical analysis of the SEM images was carried out to reveal the influence of the pyramid morphology and the size distribution on both the optical reflection and charge carrier lifetime. As shown in Fig. 3a, there is a nearly linear dependence of the normalized reflection on the fraction of small pyramids. Also samples with significantly larger average pyramid sizes (cf. Fig. 1a) fit well with the trend. Samples with mainly smaller pyramids have a higher reflection than samples with larger pyramids. Lowest reflection corresponds to a fraction of small pyramids below 20 %. In this case there is a higher probability of light absorption due to the occurrence of multiple reflections at the surface. It is important to note that for the occurrence of multiple reflections smaller pyramids surrounded by bigger ones are necessary [8]. The increase of reflection at higher fractions of small pyramids is due to the larger amount of horizontal facets and pyramid valleys at small pyramids, which reflect more light directly [9].

For further evaluation of the influence of the pyramid size distribution on the electronic properties of the interface, textured samples were passivated with (i)a-Si:H layers and subsequently annealed in hydrogen plasma. The dependence of τ_{eff} on the fraction of small pyramids is summarized in Fig. 3b. This graph can be roughly divided into two parts. Whereas samples with a large fraction (> 50 %) of small pyramids show lower carrier lifetimes of $\tau_{\text{eff}} < 2.5$ ms, samples with a fraction of small pyramids of < 50 % reach higher lifetimes of up to 4.2 ms. At high fractions of small pyramids the lifetime is limited due to the increased influence of the valleys and edges. τ_{eff} rises with increasing fraction of larger pyramids due to the lower density of plane areas with (100) orientation, pyramid valleys and edges which are known to be centers for epitaxial growth as well as for local cracks of the (i)a-Si:H layer [4]. Above a certain threshold, a further increase in pyramid size does not lead to a concomitant increase in charge carrier lifetime and it is suggested that on textures with large pyramids the recombination processes at defects on the pyramid facets dominate the overall recombination at the interface [10].

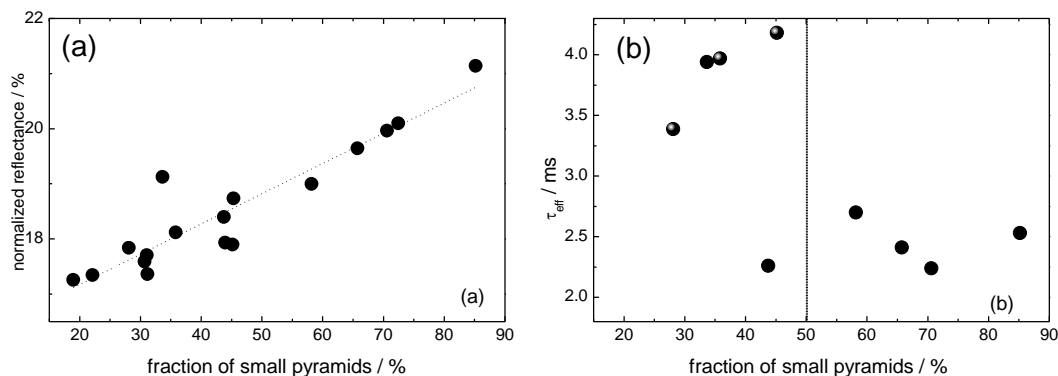


Figure 3. Dependence of the (a) normalized reflectance and the (b) effective charge carrier lifetime on the fraction of small pyramids.

Passivation. Excellent passivation of the hetero-interface can be achieved by deposition of (i)a-Si:H layers, due to the resulting very low interface defect densities. The deposition processes onto planar c-Si wafers are well-established and the influence of substrate temperature T_{sub} during deposition and post-deposition treatments on the resulting layer properties is well understood. The transferability of these recipes to the controlled deposition of (i)a-Si:H layers on textured c-Si wafers will be demonstrated in the following. As shown in Fig. 4, increasing the temperature up to 190°C leads to an increase of the charge carrier lifetime up to 9.5 ms at planar Si(111) wafers, which is due to the excellent interface passivation produced by the highly mobile hydrogen. At 190°C a trade-off between hydrogen concentration and mobility is reached. At lower temperatures diffusion is limited and interface passivation is suppressed, which results in low charge carrier lifetimes. Beyond 190°C τ_{eff} decreases, due to the lower hydrogen concentration and the increased interface recombination caused by local epitaxial growth, which is known as being detrimental for passivation [3]. On the textured wafer, the same qualitative behavior is observed. As expected, the maximum lifetime of 3.3 ms is lower than in the planar case, but found at the same temperature of 190 °C resulting in a well-passivated interface. Thus, know-how gathered from passivation of planar substrates by (i)a-Si:H layer deposition can be transferred to the passivation of random pyramid textured substrates.

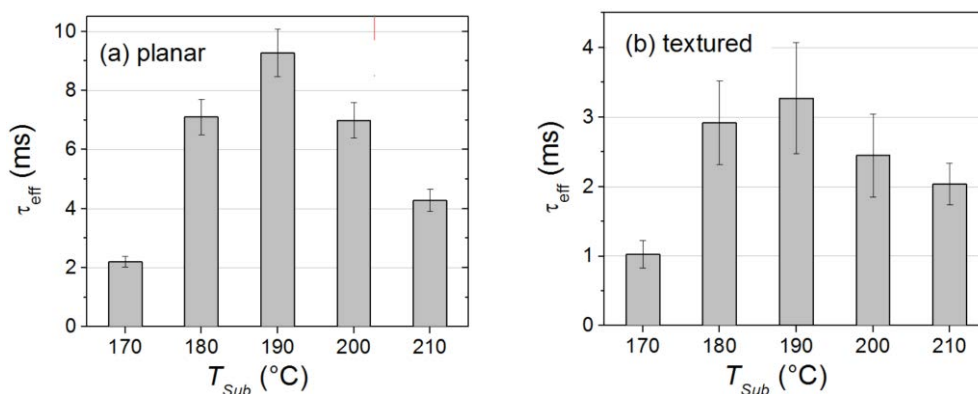


Figure 4. Dependence of the charge carrier lifetime on the (i)a-Si:H deposition temperature for (a) planar and (b) textured Si wafers (after thermal annealing), both with (111) termination.

Conclusions

Substrate texturization and interface passivation was further optimized with the aim to improve Si heterojunction solar cells. Optimal pyramid textured surface morphologies with respect to low reflection and recombination losses are obtained at a balanced distribution of small and large pyramids by IPA-free texturization, which was carefully optimized with respect to SDE and pyramid size distribution. Furthermore, atomically smooth, low-defect pyramid facets are formed upon optimization of the etching time, which can be effectively passivated by wet-chemical

treatment. For further efficient surface passivation knowledge from (i)a-Si:H layer deposition on planar substrates was successfully transferred to (i)a-Si:H deposition on random pyramid textured substrates. Application of these processes in the fabrication of complete Si heterojunction solar cells led to efficiencies above 20 % [3]. Further improvement of interface passivation might be possible by, e.g. implementing a silicon oxide tunnel layer at the a-Si:H/c-Si interface [11, 12].

Acknowledgements

The authors thank Uta Stürzebecher (CiS Institut für Mikrosensorik und Photovoltaik Erfurt), Erhard Conrad, Kerstin Jacob and Thomas Lussy (Helmholtz-Zentrum Berlin) for experimental support. This work was supported by the HTW Berlin (project “ μ -Tex”)

References

- [1] K. Masuko, M. Shigematsu, T. Hashiguchi, D. Fujishima, M. Kai, N. Yoshimura, T. Yamaguchi, Y. Ichihashi, T. Mishima, N. Matsubara, T. Yamanishi, T. Takahama, M. Taguchi, E. Maruyama, S. Okamoto, *IEEE Journal of Photovoltaics* 4 (2014) p. 1433-1435.
- [2] B. Stegemann, J. Kegel, M. Mews, E. Conrad, L. Korte, U. Stürzebecher, H. Angermann, *Energy Procedia* 38 (2013) p. 881-889.
- [3] J. Kegel, H. Angermann, U. Stürzebecher, E. Conrad, M. Mews, L. Korte, B. Stegemann, *Applied Surface Science* 301 (2014) p. 56-62.
- [4] J. Kegel, H. Angermann, U. Stürzebecher, B. Stegemann, *Energy Procedia* 38 (2013) p. 833-842.
- [5] H. Angermann, *Applied Surface Science* 312 (2014) p. 3-16.
- [6] B. Stegemann, J. Kegel, M. Mews, E. Conrad, L. Korte, U. Stürzebecher, H. Angermann, *Energy Procedia* 55 (2014) p. 219-228.
- [7] H. Angermann, A. Laades, J. Kegel, C. Klimm, B. Stegemann, *Solid State Phenomena* 219 (2015) p. 291-206.
- [8] N. Bachtouli, S. Aouida, R.H. Laajimi, M.F. Boujmil, B. Bessais, *Applied Surface Science* 258 (2012) p. 8889-8894.
- [9] E. Fornies, C. Zaldo, J.M. Albella, *Solar Energy Materials & Solar Cells* 87 (2005) p. 583-593.
- [10] S. Olibet, C. Monachon, A. Hessler-Wyser, E. Vallat-Sauvain, S.D. Wolf, L. Fesquet, J. Damon-Lacoste, C. Ballif, in: *Proc. 23rd European Photovoltaic Solar Energy Conference* (2008) p. 1140-1144.
- [11] K.M. Gad, D. Vössing, P. Balamou, D. Hiller, B. Stegemann, H. Angermann, M. Kasemann, *Applied Surface Science* 353 (2015) p. 1269-1276.
- [12] B. Stegemann, K.M. Gad, P. Balamou, D. Sixtensson, D. Vössing, M. Kasemann, H. Angermann, *Applied Surface Science* (2016), <http://dx.doi.org/10.1016/j.apsusc.2016.1006.1090>.

‘Just-Clean-Enough’: Optimization of Wet Chemical Cleaning Processes for Crystalline Silicon Solar Cells

M. Haslinger^{1,a}, M. Soha², S. Robert¹, M. Claes¹, P. W. Mertens¹, J. John¹

¹ IMEC, Kapeldreef 75, Leuven, Belgium

² University of Debrecen, Faculty of Science and Technology, Institute of Physics 4026, Bem square 18/b, Debrecen, Hungary

^amichael.haslinger@imec.be

Keywords: Silicon surface clean, silicon solar cells, metal contamination, Langmuir adsorption isotherm.

Abstract. Advanced concepts for photovoltaic silicon solar cells, especially high-efficiency n-type solar cells, requires appropriate wet cleaning treatment in order to remove metallic contamination prior to high temperature processes like diffusion and passivation [1]. The cost of the cleaning process should be as low as possible that requires an optimized usage of the chemicals by increasing process tank lifetimes and developing dedicated feed and bleed recipes. The just clean enough concept has been developed to fulfil the needs of PV industry to minimize the consumption of chemicals. When the dominant contamination metal is identified in quality and quantity, a dedicated wet chemical cleaning process can be applied to remove the metal concentration from the semiconductor surface under a specified limit with the minimum volume on cleaning solution. The paper describes how to optimize a dedicated wet cleaning process for prominent metal impurities like Fe, Cu, Cr, Ti, Co and Zn. For each metal an exchange volume is determined to develop a feed and bleed recipe. The accumulation of the metal impurities in the process tank is calculated and process tank lifetimes are predicted.

Introduction: The just-clean-enough concept

A given cleaning solution can be described by two main effect [2]. Firstly, the capability to remove the contamination initially present on the silicon surface, later on referred as “loading” of the cleaning solution. This property can be characterized by a specification on the amount of metal allowed to remain on the wafers after the clean. Secondly, a cleaning solution should also prevent the contamination to go from the solution back to the silicon substrate, this is referred as the “out-plating behavior” of the solution. Very often for silicon photovoltaic, new cleaning processes are evaluated by comparison tests. The aim of such an approach is to compare electrical data (lifetime, Joe or cell results) of a process flow using different cleaning solutions [3]. While the metal removal capability can be successfully assessed by such a method, the accumulation of metal in the cleaning solution, bath lifetime and the cost of the cleaning step cannot be modeled quantitatively.

In this paper, we present a practical implementation of the just-clean-enough concept. We were able to model the out-plating behavior of various transition metals for diluted HCl solutions. This model was then used to calculate the minimum volume of liquid required to clean a contaminated silicon surface to a desired specification.

Experimental approach and results

Experimentally, controlled contamination tests for metals suspected to have a detrimental impact on lifetime, namely Fe, Cu, Cr, Ti, Co and Zn, were performed. The wafers used for the experiment were [100] Cz-Si 8inch mirror-polished wafers¹. All experiment were performed in Imec’s class 1000 cleanroom, using ULSI quality chemicals and ultra-pure DIW.

¹ Similar out-plating behavior was observed for Cz-Si 8inch mirror-polished wafers and Cz-Si 6inch solar cell n-type wafers after saw damage removal.

All these precautions are important as controlled contamination experiment can strongly impact and be impacted by the environment. Therefore, dedicated set of beakers, rinse bathes and dryers were used to perform these experiments. All materials and tools were decontaminated between every iteration of the experiment.

First of all, the wafers were cleaned using Imec standard clean based on DIW:O₃ + HF:HCl mixtures (10ppb O₃, HCl 1%, HF 1%). The clean was then followed by an extra DIW:O₃ treatment in order to create a clean chemical oxide and therefore have a stable hydrophilic surface. The wafers were then processed in a diluted HCl solution (pH 1.3) spiked with an increasing amount of metallic impurities. The solutions used to spike the contamination are ICP-Standard solution at 1000ppm and were diluted to the desired concentration. The amount of impurities injected in the cleaning solution were 0ppb (clean d-HCl solution), 30, 100, 300, 1000 and 3000ppb. The wafers were immersed in the contaminated solution for 5min and received a subsequent DIW overflow rinse for 5min. The wafers were then dried using a spin-dryer. After this contamination process, the wafers were measured using the combined method of VPD-DC (Vapor Phase Decomposition – Droplet Collection) and TXRF (Total Reflection X-Ray Fluorescence) as described by Hellin et al [4].

The relation between the amount of metal diluted in an acidic liquid C_{liq} [at/cm³] and the concentration of metal at the silicon surface C_{surf} can be approximated by Langmuir adsorption isotherms [5,6] and can be fitted by a three-parameter equation [7] :

$$C_{surf} = \frac{b}{[H^+]^a} \times C_{liq}^d \quad (1)$$

The amount of surface metal will depends on the amount of metallic impurities in the liquid, the pH of the solution and is specific for every metals. The measurement results obtained from the TXRF measurement C_{surf} [at/cm²] and the amount of metallic impurities were fitted on a logarithmic scale in order to avoid an excessive effect of the large contamination amount and plotted on semi-logarithmic scale (see figure1). The fitting parameters were extracted and are reported in the table 1.

Table 1: Transition metals, legend and fit parameters a,b,d.
The fit parameters are extracted from fig 1.

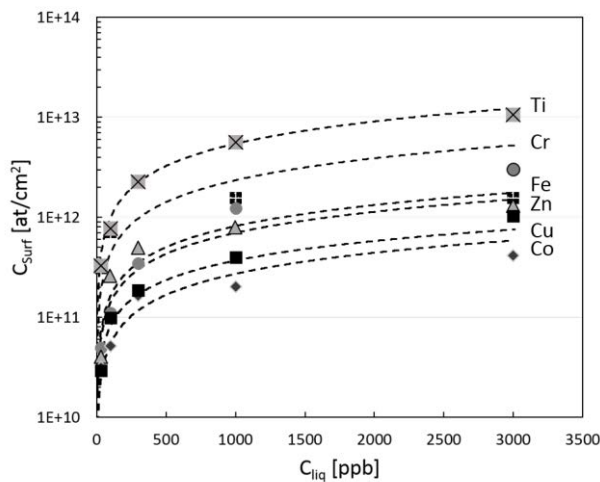


Fig. 1: Langmuir adsorption isotherms of different transition metals (Fe, Cu, Co, Zn, Ti, Cr) in hydrochloric solution of pH 1.3.
The markers depicting measured values the dashed lines are the corresponding fitting curves.

Metal	Symbol	a	b	d
Ti	⊗	0.25±0.02	3.16±0.18	0.74±0.00
Cr	⊠	0.26±0.06	2.03±0.37	0.73±0.01
Fe	●	0.3±0.06	2.00±0.34	0.70±0.01
Zn	▲	0.30±0.06	1.90±0.36	0.70±0.01
Cu	■	0.35±0.03	5.35±0.18	0.65±0.00
Co	◆	0.31±0.04	0.67±0.08	0.7±0.00

Estimation of the exchange volume and optimization of the cleaning process

Based on the model presented above, the exchange length L_{ex} for a specific cleaning mixture can be calculated as showed by Mertens et al. [6]. The exchange length can be defined as the minimum

liquid film thickness required to hold metallic impurities, in order to guarantee a certain surface metal concentration.

$$L_{ex} = \frac{C_{surf1}}{C_{surf2}} \times \frac{b}{[H^+]^a} \times C_{liq2}^{d-1} \quad (2)$$

With L_{ex} the exchange length [cm]

$C_{surf,1}$ the surface contamination of the incoming surface (to be cleaned) [at/cm²]

$C_{surf,2}$ the expected surface contamination after clean [at/cm²]

$C_{liq,2}$ the liquid concentration after a surface contamination clean from $C_{surf,1}$ to $C_{surf,2}$ [at/cm³]

$[H^+]$ the concentration of protons (pH) [at/cm³]

Furthermore, by multiplying the exchange length by the wafer surface, the minimum volume of solution required to clean the silicon surface from C_{surf2} (incoming surface) to C_{surf1} (cleaning specification), can be calculated. The calculation was done for $C_{surf,2} = 10^{12}$ at/cm², $C_{surf1} = 10^{10}$ at/cm², a pH of 1.3 and a standard square 6inch solar cell wafer (243cm²). The results are showed in table 2. As expected the metals that have the highest out-plating behavior will require the highest amount of cleaning solution in order to reach a similar surface cleanliness.

Table 2: Calculated values of the exchange length and exchange volume per wafer and per 50 wafers cassette for different metals.

Metal	Co	Cu	Zn	Fe	Cr	Ti
L_{ex} [um]	15	20	65	70	280	800
V_{ex} [ml/wafer]	0.74	1.11	3.15	3.39	13.5	38.1
V_{ex} [ml/50wafers]	37	56	158	170	676	1906

Broadly used in industry, a cost-effective way to design a cleaning process is the use of a feed and bleed method. After processing a defined amount of wafers, a part of the contaminated solution will be drained (“bleed”) and replaced by fresh chemicals (“feed”). By using the cleaning specifications defined above and the minimum exchange volume required to clean a wafer, it becomes possible to simulate the contamination build-up of such an optimized system by an iterative method.

$$C_{liq}(n+1) = C_{liq}(n) + C_{load} - R_{bleed}C_{Bleed} + R_{Feed}C_{Feed} \quad (3)$$

With $C_{liq}(n)$ and $C_{liq}(n+1)$ [at/cm³] correspond to the metal concentration after n and n+1 cassettes

C_{load} the amount of metals loaded in the solution during the clean

$R_{bleed} \cdot C_{Bleed}$, the amount of contamination drained during the bleed

$R_{Feed} \cdot C_{Feed}$ the amount of contamination added by the feed, assuming non pure chemicals.

C_{load} can be approximated, taken into account the initial contamination of the wafers and the metal specification, by $C_{load} = [(C_{surf,1} - C_{surf,2}) * N * A * 2] / V_{tot}$ with N the number of wafers per cassette, A the surface of the wafers and V_{tot} the total volume of the tank. We will also approximate R_{bleed} and R_{feed} to be identical and the ratio of the exchange volume and the total volume drained and spiked after each cassette, so $R_{bleed} = R_{feed} = V_{ex} / V_{tot}$. Finally we consider that the “bleed” will occur after the loading of the cleaning solution $C_{bleed} = C_{liq}(n+1)$ and that the “feed” is performed with clean chemicals, or $C_{feed} = C_{liq}(0)$.

The model presented above can be applied to simulate the accumulation of metals in a cleaning tank. Figure 2 shows the amount of metallic contamination as a function of the number of cassettes processed in the cleaning solution. For this example, the initial contamination was set to 1E12at/cm² and our metal specification is 1E10at/cm². As calculated previously and shown in table 2, the optimized Feed&Bleed recipe to guarantee a certain surface cleanliness is specific for every metal and given by the exchange volume V_{ex} . The solution is similar to the previous calculation (dHCl, pH1.3) as showed in table 2. Applying this volume for the different metals to our cleaning process results in different metal equilibrium values that will be reached after a certain number of batches.

Depending on the volume of solution added after every cassette, the maximum contamination will vary. As an extra example, the case where the solution is not spiked is also plotted for Fe, showing that metallic contamination will build-up and eventually trigger a bath change that could have been avoided by the use of spiking.

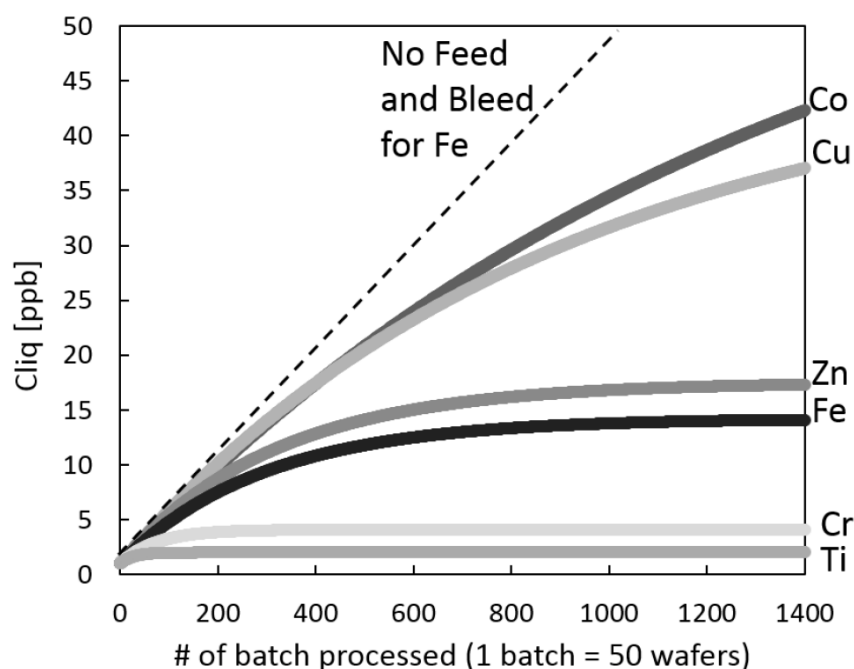


Figure 2: Metallic concentration as a function of the number of 50 wafers (6inch square) cassettes processed for an initial contamination of 10^{12} at/cm², a cleaning specification of 10^{10} at/cm² in a cleaning solution based on HCl and pH 1.3 and a total tank volume of 50L. The applied Feed&Bleed volume is based on the exchange volume V_{ex} (see Table2).

Conclusion

In this work we show the just clean enough methodology for some the most prominent transition metals. From the determination of the Langmuir adsorption functions, the extraction of the exchange volume, up to the accumulation of metal impurities in the processing tank in function of the incoming wafer batches. These calculations are done taking the optimized Feed&Bleed recipe into account, meaning that the tank will accumulates the maximum amount of metals but still guarantee a certain surface cleanliness after process. This method and the overall optimization scheme can be further elaborated to include other parameters such as the impact from the environment (contamination coming from another source) or the carry-over from other tanks, etc.

References

- [1] Rentsch J. et al., Proceedings of the 24th EU PVSEC (2009), p. 1113
- [2] Wostyn et al.: Solid State Phenomena Vol. 195 (2013), pp 293-296
- [3] Kuzma-Filipek I. et al.: Proceedings of the 6th International Conference on Silicon Photovoltaics (2016), accepted.
- [4] Hellin, D. et al.: Spectrochimica Acta Part B: Atomic Spectroscopy 59(8), 1149-1157.
- [5] Loewenstein, Lee et al.: J. Electrochem.Soc. 146:719 (1999)
- [6] Langmuir I.: Surface Chemistry. Nobel Lectur (December 14, 1932). In: Nobel Lectures, Chemistry 1922-1941 p.308. (Elsevier Publishing Company, Amsterdam, 1966)
- [7] Mertens et al.: Proceeding of SEMICON/WEST 1995 Technical Seminar: Cleaning Technology for the Submicron Era (1995)

Progress in Cleaning and Wet Processing for Kesterite Thin Film Solar Cells

Bart Vermang^{1,2,a}, Aniket Mule^{1,3}, Nikhil Gampa^{1,4}, Sylvester Sahayaraj^{1,2},
Samaneh Ranjbar^{1,5}, Guy Brammertz^{1,6}, Marc Meuris^{1,6}
and Jef Poortmans^{2,6}

¹ imec division IMOMEC – partner in solliance, Diepenbeek, Belgium

² Department of Electrical Engineering, KU Leuven, Heverlee, Belgium

³ Department of Mechanical and Process Engineering, ETH Zurich, Zurich, Switzerland

⁴ Department of Engineering, Université Claude Bernard Lyon 1, Villeurbanne, France

⁵ Department of Physics, Universidade de Aveiro, Aveiro, Portugal

⁶ Inst. for Material Research (IMO) Hasselt University – partner in Solliance, Diepenbeek, Belgium

^a bart.vermang@imec.be

Keywords: Photovoltaics, PV, thin film, kesterite, CZTS, wet processing, alkali, surface, cleaning, etching, passivation, chalcopyrite, CIGS.

Abstract. Copper indium gallium selenide/sulfide (CIGS) and copper zinc tin selenide/sulfide (CZTS) are two thin film photovoltaic materials with many similar properties. Therefore, three new processing steps – which are well-known to be beneficial for CIGS solar cell processing – are developed, optimized and implemented in CZTS solar cells. For all these novel processing steps an increase in minority carrier lifetime and cell conversion efficiency is measured, as compared to standard CZTS processing. The scientific explanation of these effects is very similar to its CIGS equivalent: the incorporation of alkali metals, ammonium sulfide surface cleaning, and Al₂O₃ surface passivation leads to electrical enhancement of the CZTS bulk, front surface and reduced front interface recombination, respectively.

Kesterite solar cells, the new kid on the block

The photovoltaic module manufacturing market is booming and presently dominated by Si modules, but also thin film (TF) photovoltaics (PV) remain very interesting due to their high potential for new applications and markets. TF PV can be completely processed on large rigid (e.g. glass) or flexible and thus lightweight substrates (e.g. steel) by use of monolithic integration (P1, P2 and P3 scribes). This is an interconnection technology that leads to a dark smooth appearance and is free of classic size limitations. Hence, such modules bring many exciting architectural choices with regards to size, shape, color and function; all important characteristics for building integrated PV (BIPV), a key future market. Additional advantages of TF PV are (i) the high energy yield and outstanding outdoor performance, (ii) the low energy consumption, short energy payback time and minimized material consumption, (iii) its proven reliability, (iv) the high productivity at the GW production level, and (v) the low production costs [1].

Cadmium telluride (CdTe) and CIGS are the two main TF PV technologies, together they represent the largest TF PV market share and the highest energy conversion efficiencies, but unfortunately also toxicity and abundance concerns. Indeed, two thirds of the TF PV market is provided by the two largest TF companies: First Solar (CdTe) and Solar Frontier (CIGS). Both companies are very successful in the development of their technologies, as demonstrated by their presence in the TF PV world record efficiency charts. These up-to-date record efficiencies are 21.0 % at cell level, as obtained by First Solar and Solibro (CIGS), and respectively 18.6 % (obtained by First solar) or 17.5 % (obtained by Solar Frontier) at module level. However, these technologies also embody clear toxicity (the use of poisonous Cd in CdTe PV) and abundance (the use of rare elements In and Ga in CIGS PV) concerns [2].

CZTS kesterite is a non-toxic and earth-abundant alternative with great potential, but material and device improvements are essential. A novel (first solar cell developed in 1996) TF PV material is CZTS, which is derived from the related CIGS compound by substitution of In and Ga for Zn and Sn. This isoelectronic substitution produces a material with many similar properties of the parent compound. Indeed, the CZTS kesterite and CIGS chalcopyrite structures are known to be associated, where the advantage of CZTS lays in its composition of non-toxic and abundant materials. At present, top conversion efficiencies for small-area CIGS solar cells are typically above 20 % (e.g. NREL, ZSW, HZB, EMPA, Solibro, Solar Frontier, etc.), whereas CZTS solar cells are limited to efficiencies slightly above 10 % (e.g. IBM, Imec, IREC, Solar Frontier, etc.). The main reason is that the CZTS technology is not as mature, where many difficulties need to be addressed to increase electrical performance. Typical issues are secondary phase formation, fluctuating potentials, reproducibility and stability, and also cell architecture [3,4]. A typical kesterite solar cell structure is shown in Fig. 1, as taken from [5].

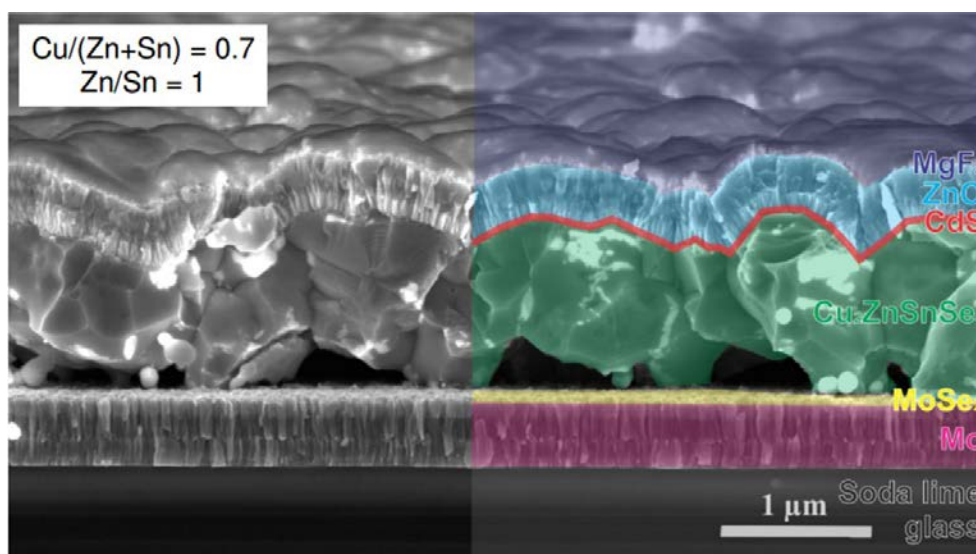


Figure 1: Scanning electron microscopy cross-section image of a typical kesterite solar cell, where the different layers are highlighted in different colors (taken from [5]).

In this work, three new processing steps – which are well-known to be beneficial for CIGS solar cell processing – are developed, optimized and implemented in CZTS solar cells. These three steps are known to improve the CIGS absorber layer by (i) the incorporation of alkali metals, (ii) cleaning of its surface, or (iii) the electrical passivation of its surface. (i) The incorporation of sodium (Na) and potassium (K) in and its positive influence on CIGS solar cells is well-studied. Na is reported to influence crystallinity, hinder inter-diffusion of In and Ga, change preferential crystal orientation, and increase the free carrier concentration of the CIGS absorber [6]. And the presence of K is shown to increase junction depth and band-gap (higher Ga content), and enhance passivation (grain boundaries and donor-like defects) [7]. (ii) It has been proven that both potassium cyanide (KCN) and ammonium sulfide (AS = $(\text{NH}_4)_2\text{S}$) treatments are successful in removing detrimental secondary phases in CIGS, where the focus is on the removal of Cu_xSe – which is known to increase the shunt conductance. Both wet treatments are found to selectively etch Cu_xSe phases, but lower etching rates are observed for the AS solution. Nevertheless, the AS treatment is shown to passivate the CIGS surface by incorporation of sulfur (as proven by an increase in minority carrier lifetime), which results in a solar performance enhancement [8]. (iii) Rear and front surface passivation approaches have already been introduced in CIGS solar cells. Therefore passivation layers are combined with nano-sized point openings, where the purpose of the passivation layer is to reduce charge carrier recombination at the CIGS surface, while the point openings serve as electrical contacts. Various approaches have been reported: Al_2O_3 rear surface passivation [9], and the spray-ILGAR[®] or SALT front surface passivation methodologies [10,11].

Advances in cleaning and wet processing for kesterite solar cells

Fig. 1(a) shows the effect of Na and K on CZTS absorber layer quality. In standard kesterite solar cell processing soda lime glass (SLG) substrates are used, wherefore it is known that Na (and very little K) diffuses – in an uncontrolled manner – from the glass into the CZTS absorber layer. Therefore, in the case of alkali treated samples these SLG substrates have been covered with a (silicon nitride) barrier layer to prevent this diffusion process from the SLG. Fig. 1(a) gives an overview of alkali treated CZTS layers grown on such SLG substrates with barrier layer. This figure gives an estimation of the average minority carrier lifetime of simplified devices, as obtained by time-resolved photoluminescence (TRPL). This minority carrier lifetime is derived using an exponential fit to the PL decay curve, where the slowest decay time is reported to be related to the low injection minority carrier lifetime. Hence, this figure clearly shows the potential absorber layer quality improvement in case of a well-controlled supply of Na and K. The effects of Na and K on CZTS solar cells are not yet well-understood, but other initial studies indicate a positive impact in both cases. Besides affecting the size of grains, Na has been shown to mainly decrease the defect and trap densities within the absorber bulk and at interfaces. The presence of K has been related to an increase in bulk crystallinity (and enhance the (112) preferred orientation), and a reduction in zinc sulfide (ZnS) secondary phase formation. Note that – amongst the other alkali metals – also Li seems to be a promising dopant, as far as optoelectronic properties are concerned [12].

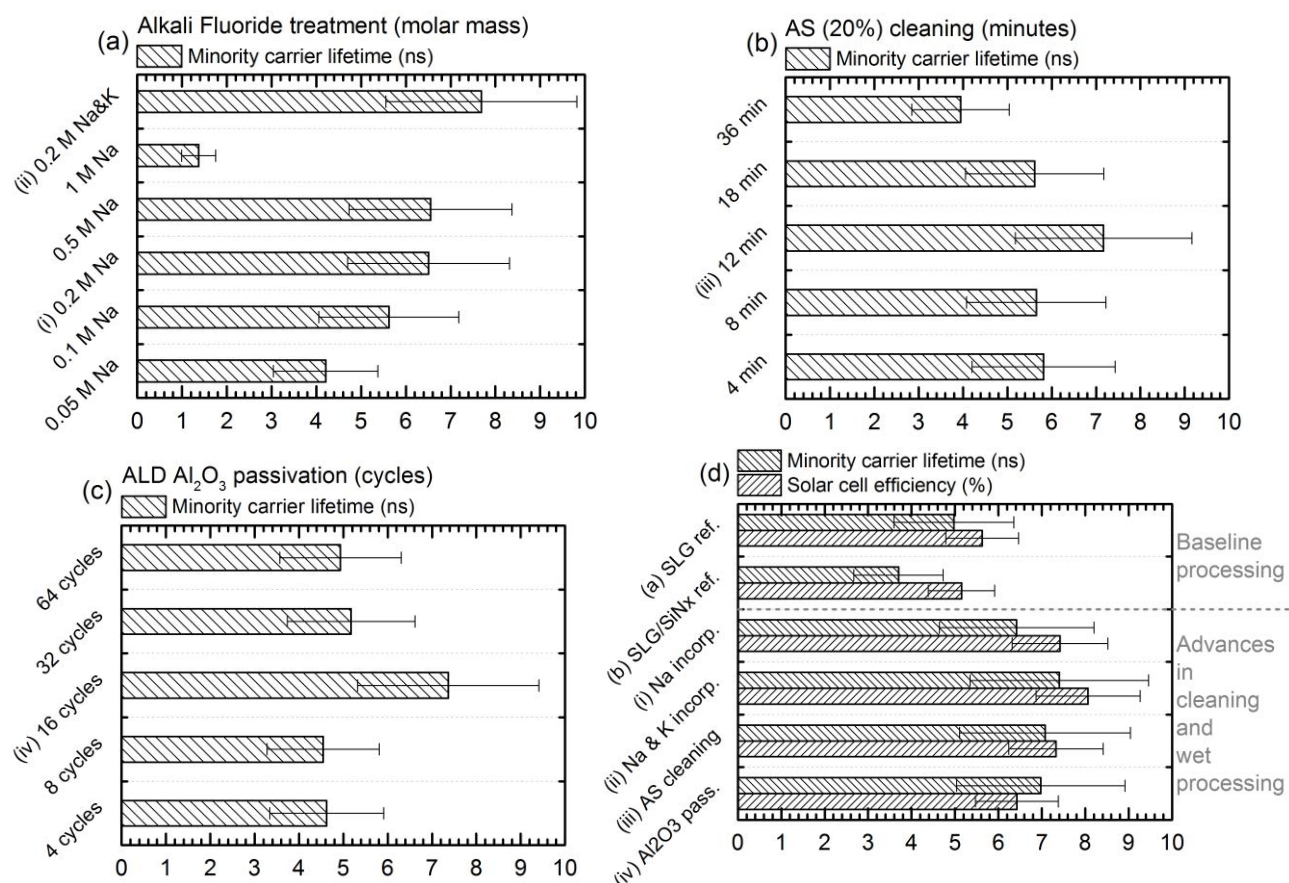


Figure 2: Average minority carrier lifetime for simplified kesterite devices, (a) grown on soda lime glass (SLG) / barrier-layer (thus without the supply of Na and K) substrates combined with an additional alkali (Na and/or K) fluoride treatment step, or (b) or (c) grown on SLG substrates combined with an extra surface cleaning ($(\text{NH}_4)_2\text{S}$) or passivation (Al_2O_3) step, respectively. (d) Average minority carrier lifetime and cell efficiency for complete kesterite solar cells fabricated on the same substrates and using the optimized processing steps as used in (a), (b) and (c).

Fig. 1(b) shows the effect of AS cleaning on CZTS surface quality. At present, KCN chemical etching is the standard method to remove secondary phases from the surface of the kesterite crystals, which is one of the major CZTS challenges. As compared to CIGS, there is only limited control of the composition and microstructure in the fabrication of CZTS materials. Hence, various secondary

phases, such as $\text{Zn}(\text{S},\text{Se})$, $\text{Cu}_x(\text{S},\text{Se})$, $\text{Sn}(\text{S},\text{Se})_x$ or $\text{Cu}_2\text{Sn}(\text{S},\text{Se})_3$, are typically formed during the processing of the absorber layer and eventually hinder the electrical performance of solar cell devices. The KCN treatment is found to clean the CZTS absorber surface from most of these secondary phase, and consequently became a characteristic kesterite solar cell processing step. On the one hand, standard KCN (5 wt% in aqueous KOH) immersion of the CZTS absorber up to 2 minutes appears to etch away most of these secondary phases. On the other hand, longer KCN etching times does result in the systematic damage of the CZTS surface [13]. A similar optimum is seen for 12 minutes of AS surface cleaning, as is shown in Fig. 1(b). The advantage of AS as compared to KCN, would be its safety, less toxic nature and potential to passivate the CZTS surface by incorporation of sulfur [8].

Fig. 1(c) shows the potential of Al_2O_3 passivation on the CZTS interface quality. Recently, capacitance-voltage profiling and quantum efficiency measurements have revealed that Al_2O_3 can lead to reduced interface recombination and a wider depletion width in kesterite solar cells [14]. In addition, the Al_2O_3 layer may also passivate pinholes and grain boundaries [15]. In this work, very thin Al_2O_3 front surface passivation layers are grown on a rough and unfavorably terminated CZTS surface, by use of atomic layer deposition (ALD). Hence, these layers should (a) be thin enough so that the photo-excited electrons could effectively tunnel through the layer, or (b) have nano-sized openings due to the surface-inhibited growth. Fig. 1(c) shows the positive impact of such Al_2O_3 passivation layers on the CZTS surface, where the thickness (and surface coverage) of the layers are tuned by varying the amount of ALD cycles. Note that – previously – similar results have been obtained by use of a TiO_2 front surface passivation layer [16], and an Al_2O_3 rear surface passivation layer with nano-sized point contacts [17].

In Fig. 1(d) the most optimized procedures (in terms of realized minority carrier lifetime) of these Na, Na & K, AS and Al_2O_3 processing steps are tried in actual CZTS solar cells, to show their full potential. The Na and Na & K incorporation procedures are implemented into CZTS solar cells fabricated on SLG / barrier-layer substrates, while the AS cleaning and Al_2O_3 passivation procedures are implemented on standard SLG substrates. As a reference, also regular solar cells have been fabricated on both SLG and SLG / barrier-layer substrates. This figure shows that all these novel cleaning and wet processing successfully increase solar cell performance, as compared with the references. Hence, it also supports our approach to use TRPL to screen and optimize new processing steps in a time-efficient manner, before applying them in tangible solar cell devices.

In summary, three new processing steps are successfully integrated into CZTS solar cells. For all these novel processing steps an increase in minority carrier lifetime and cell conversion efficiency is measured, as compared to standard kesterite processing. The scientific explanation of these effects is very similar to its CIGS equivalent: the incorporation of alkali metals, AS surface cleaning, and Al_2O_3 surface passivation leads to electrical enhancement of the CZTS bulk, front surface and reduced front interface recombination, respectively.

Experimental section

Baseline kesterite solar cell processing: Standard kesterite solar cells have a SLG/Mo/CZTS/CdS/i-ZnO:Al/Ni/Al device structure. First, Sn, Zn and Cu metal layers are e-beam evaporated on a standard SLG/(SiN_x)/Mo substrate. These stacked metal layers are then selenized in a rapid thermal anneal oven in vacuum, where a continuous flow of 10 % H_2Se in N_2 is supplied. The ramp up speed is 1 °C/s, and the anneal time is 15 minutes at a temperature of about 450 °C. Hence, a pure selenide p-type CZTS absorber layer of about 1 μm is fabricated. Next, two wet steps are performed: a KCN etch (5 wt% in H_2O), followed by chemical bath deposition of a n-type CdS buffer layer of 50 nm. The n-type front contact is deposited by sputtering: 100 nm of intrinsic ZnO followed by 400 nm of Al-doped ZnO. Finally, a front contact Ni/Al grid is deposited while cell isolation is made with needle scribing [4].

Advances in cleaning and wet processing: (i) *Incorporation of alkali metals:* Alkali metals are spin-coated onto the CZT metal stack (before selenization). First, the fluoride salts of alkali metals are dissolved in water. Next, this solution is spin coated onto the Sn/Zn/Cu metal stack, with a rotational speed of 1000 rpm and an acceleration of 1000 rpm/s², for 6 minutes. Finally, the alkali metals are incorporated into the CZTS layer during the selenization step. In [12] is presented that the alkali metals have effectively diffused into the absorber, and that the diffused quantity is related to the concentration of alkali metal solution, which demonstrates the controllability of the technique. (ii) *Surface etching/cleaning by (NH₄)₂S:* The AS treatment uses as-received ammonium sulfide dissolved in water (20 wt%). The SLG/Mo/CZTS samples are dipped into this solution, followed by 2 min of rinsing in deionized water. (iii) *Al₂O₃ surface passivation:* ALD of Al₂O₃, grown at low temperature ($\leq 150^{\circ}\text{C}$), is used as a one-step front surface passivation layer. In addition, this layer is grown on a rough and unfavorably terminated CZTS surface, and thus might lead to non-conformal surface-inhibited growth, also called island growth [18].

Characterization: (i) The metallic composition of the studied absorber layers is determined by *X-ray fluorescence (XRF)*. Absorber layers are prepared under Cu-poor ($[\text{Cu}]/([\text{Zn}]+[\text{Sn}]) \sim [0.7;0.9]$) and Zn-rich ($[\text{Zn}]/[\text{Sn}] \sim [1.0;1.25]$) conditions. In such case, the Zn excess is found to form Zn-rich secondary phases mainly located at the grain boundaries and at the free surface of the CZTS grains. In most cases, however, the CZTS layer is found to also contain some residue of the other secondary phases, even if their formation was prevented by using optimal precursor compositions and synthesis conditions [19]. (ii) *TRPL measurements* are acquired with a near infrared compact fluorescence lifetime measurement system. A circular area with 3 mm diameter is illuminated with a 15 kHz, 1.2 ns pulsed 532 nm laser. Hence, the minority carrier lifetime can be derived using an exponential fit to the photoluminescence decay curve (PL intensity as a function of time). The slowest decay time is reported to be the low injection minority carrier lifetime whereas the faster decay time(s) is/are linked to the charge separation time [20]. The minority carrier lifetime (at zero bias voltage) in standard finished kesterite solar cells is of the order of 4.0 to 6.0 ns. (iii) Solar cells are characterized by *illuminated current-voltage (J-V)* using a standard AM1.5G spectrum with an illumination intensity of 1000 W/m². To date, the best kesterite solar cell fabricated at Imec has an efficiency of 10.4 % [21], while the typical baseline efficiency lays in the range of 4.5 to 6.5 %. Note that a MgF₂ anti-reflection coating has been used for the record cell, which is not part of the baseline processing explained above.

Acknowledgments

This work is funded by the Flemish government (Department Economy, Science and Innovation) and the European Union (Horizon 2020 grant agreement No 640868). B. Vermang acknowledges the financial support of the Flemish Research Foundation FWO (mandate 12O4215N).

References

- [1] White paper for CIGS thin film solar cell technology, e.g. <http://www.solarpowerworldonline.com/wp-content/uploads/2016/01/CIGS-WhitePaper.pdf>, retrieved June 6th (2016).
- [2] M.A. Green, K. Emery, Y. Hishikawa, W. Warta and E.D. Dunlop: Prog. Photovolt: Res. Appl. 24(1) (2016), p. 3–11.
- [3] X. Liu, Y. Feng, H. Cui, F. Liu, X. Hao, G. Conibeer, D.B. Mitzi and M. Green: Prog. Photovolt: Res. Appl. 24(6) (2016), p. 879–898.
- [4] G. Brammertz, S. Oueslati, M. Buffière, J. Bekaert, H. El Anzeery, K. Ben Messaoud, S. Sahayaraj, T. Nuytten, C. Köble, M. Meuris and J. Poortmans: IEEE J. Photovoltaics 5(2) (2014), p. 486–492.

-
- [5] G. Brammertz, M. Buffière, S. Oueslati, H. El Anzeery, K. Ben Messaoud, S. Sahayaraj, C. Köble, M. Meuris and J. Poortmans: *Appl. Phys. Lett.* 103 (2013) p. 163904.
- [6] P.M.P. Salomé, H. Rodriguez-Alvarez and S. Sadewasser: *Solar Energy Mater. Solar Cells* 143 (2015), p. 9–20.
- [7] A. Chirilă, P. Reinhard, F. Pianezzi, P. Bloesch, A.R. Uhl, C. Fella, L. Kranz, D. Keller, C. Gretener, H. Hagendorfer, D. Jaeger, R. Erni, S. Nishiwaki, S. Buecheler and A.N. Tiwari: *Nature Materials* 12 (2013), pp. 1107–1111.
- [8] M. Buffière, A.-A. El Mel, N. Lenaers, G. Brammertz, A.E. Zaghi, M. Meuris and J. Poortmans: *Adv. Energy Mater.* 5 (2015), p. 1401689.
- [9] B. Vermang, J.T. Wätjen, C. Frisk, V. Fjällström, F. Rostvall, M. Edoff, P. Salomé, J. Borne, N. Nicoara and S. Sadewasser: *IEEE J. Photovoltaics* 4(6) (2014), p. 1644–1649.
- [10] Y. Fu, N.A. Allsop, S.E. Gledhill, T. Köhler, M. Krüger, R. Sáez-Araoz, U. Blöck, M.Ch. Lux-Steiner and C.-H. Fischer: *Adv. Energy Mater.* 1(4) (2011), p. 561–564.
- [11] P. Reinhard, B. Bissig, F. Pianezzi, H. Hagendorfer, G. Sozzi, R. Menozzi, C. Gretener, S. Nishiwaki, S. Buecheler and A.N. Tiwari: *Nano Lett.* 15(5) (2015), p. 3334–3340.
- [12] A. Mule, B. Vermang, M. Sylvester, G. Brammertz, S. Ranjbar, T. Schnabel, N. Gampa, M. Meuris and J. Poortmans: *Thin Solid Films* XX (2016), under review.
- [13] M. Sylvester, G. Brammertz, B. Vermang, M. Meuris, J. Vleugels and J. Poortmans: *Thin Solid Films* XX (2016), under review.
- [14] M.E. Erkan, V. Chawla and M.A. Scarpulla: *J. Appl. Phys.* 119 (2016), p. 194504.
- [15] Y.S. Lee, T. Gershon, T.K. Todorov, W. Wang, M.T. Winkler, M. Hopstaken, O. Gunawan and J. Kim: *Adv. Energy Mater.* XX (2016), early view, DOI: 10.1002/aenm.201600198.
- [16] W. Wu, Y. Cao, J.V. Caspar, Q. Guo, L.K. Johnson, R.S. Mclean, I. Malajovich and K.R. Choudhury: *Appl. Phys. Lett.* 105 (2014), p. 042108.
- [17] B. Vermang, Y. Ren, O. Donzel-Gargand, C. Frisk, J. Joel, P. Salomé, J. Borne, S. Sadewasser, C. Platzer-Björkman and M. Edoff: *IEEE J. Photovoltaics* 6(1) (2015), p. 332–336.
- [18] S.M. George: *Chem. Rev.* 110 (1) (2010), p. 111–131.
- [19] M. Buffière, G. Brammertz, S. Sahayaraj, M. Batuk, S. Khelifi, D. Mangin, A.-A. El Mel, L. Arzel, J. Hadermann, M. Meuris and J. Poortmans: *ACS Appl. Mater. Interfaces* 7(27) (2015), p. 14690–14698.
- [20] A. Kanevce, D.H. Levi and D. Kuciauskas: *Prog. Photovolt: Res. Appl.* 22 (2014), p. 1138–1146.
- [21] S. Oueslati, G. Brammertz, M. Buffière, H. El Anzeery, O. Touayar, C. Köble, J. Bekaert, M. Meuris and J. Poortmans: *Thin Solid Films* 582 (2015), p. 224–228.

CHAPTER 11:

Non-Wafer Cleaning, Mask Cleaning

Optimization of EUV Reticle Cleaning by Evaluation of Chemistries on Wafer-Based Mimic Test Structures

A. Pacco^{1, a}, D. Dattilo², R. Jonckheere¹, J. Rip¹, U. Dietze³, J. Kruemberg² and F. Holsteys¹

¹ imec Kapeldreef 75 B-3001 Leuven, Belgium

² SUSS MicroTec Photomask Equipment GmbH & Co. KG, Ferdinand-von-Steinbeis-Ring 10, 75447 Sternenfels, Germany

³ SUSS MicroTec Inc., 220 Klug Circle, Corona, CA, 92880, USA

^apacco@imec.be

Keywords: EUV, reticle, litho mask cleaning, molybdenum, silicon, TMAH, ammonia, passivation

Abstract. In order to evaluate the effect of repeated cleaning on EUV reticles, specifically, on the etched Mo/Si multilayer, wafer-based test structures with a mimic of this etched Mo/Si multilayer (“black-border”) were fabricated. The resistance of Mo and Si towards alkaline chemistries was tested and quantified using these test structures. The initial passivating film on Mo seems to play a role in delaying the Mo to further oxidize and dissolve in alkaline solutions. For the cleaning times used (minutes) the Mo surface, and thus the black-border edges, will probably stay passivated by that protective oxide in alkaline solution (pH 11), with no or only very limited Mo loss. Stirring and the amount of oxygen or other oxidizing species like H₂O₂ in solution could increase the oxidation rate of the Mo and/or Mo oxides into soluble Mo(VI) species.

Introduction

Pellicles are used for the protection of the frontside of reticles from possible contamination leading to printing errors during lithographic processes. However, for extreme UV lithography, a pellicle approach is not ready yet due to the very stringent requirements imposed by the extreme UV conditions [1-2]. Whereas this pellicle approach is strongly required for EUV based IC manufacturing, and therefore a key focus item under development, the need for an EUV reticle front side clean will still very likely persist: for example after situations where a pellicle needs to be replaced due to its relatively limited lifetime in high source power conditions required for high-volume manufacturing. A lot of requirements are imposed on a reticle cleaning step: it is clear that no added contamination whatsoever that could affect the printing performance of such a reticle can be allowed: i.e. cleans should be particle neutral. Besides that, the target contamination should be effectively removed, leaving the reticle unaffected. A typical EUV reticle is composed of many materials, including a Mo/Si multilayer to create the EUV mirror on the frontside, a Ru cap for protection of this mirror and a Ta-based absorbing layer to define the non-reflective regions. However, the latter is not completely blocking the reflection of the light, leading to partial reflection of the EUV light and consequently, an undesired exposure of neighboring fields (Fig. 1). One option that has been adopted to tackle this, is through removal of the entire Mo/Si multilayer in the border regions to mitigate reflection. The resulting etched Mo/Si multilayer is known as “black-border”. Since the Mo/Si multilayers are not protected anymore by the Ru capping layer in these black-border regions, they will be exposed to cleaning media used to clean the frontside of such reticles. In this work the effect of different cleaning media on this black border was investigated.

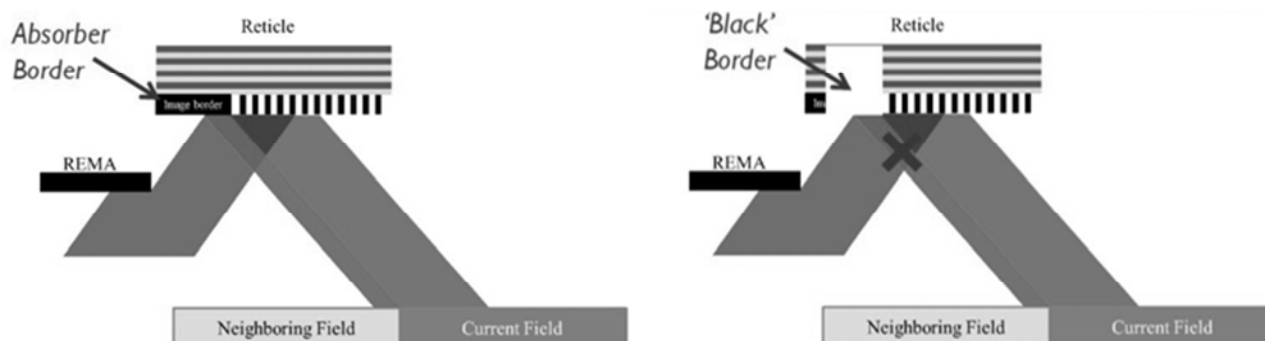


Figure 1: Schematic representation and purpose of the “black border”: without black border a portion of the light, is reflected by the image/absorber border (left); this unwanted effect is mitigated by etching away the entire absorber and multilayer (right).

Approach

Since EUV reticles are extremely expensive, especially those comprising an etched Mo/Si multilayer (“black-border”), test structures that are wafer-based were developed. 300 mm wafers with an adapted Mo/Si multilayer stack were fabricated. Test structures comprising a multilayer were preferred over blanket test films because chemical, as well as potential electrochemical, galvanic corrosion effects, were subject of interest. However the number of Mo/Si layers was significantly reduced for the sake of simplicity: the test samples were composed of 3 bi-layers of Mo/Si versus approximately 40 bilayers on a genuine EUV reticle (Fig. 2). Also the thickness of the layers was significantly increased: each Mo and Si layers was 40 nm thick versus the 3/4 nm thin Mo/Si layers for a genuine EUV reticle. This was done for the ease of inspection of the “black-border”: if only 3/4 nm layers would have been deposited, they wouldn’t have been resolved by conventional XSEM but then more time-consuming XTEM analyses would have been necessary. A mimic of the “black-border” was obtained by patterning the Mo/Si multilayer. Like that trenches and mesas with different widths were patterned into the Mo/Si multilayer.

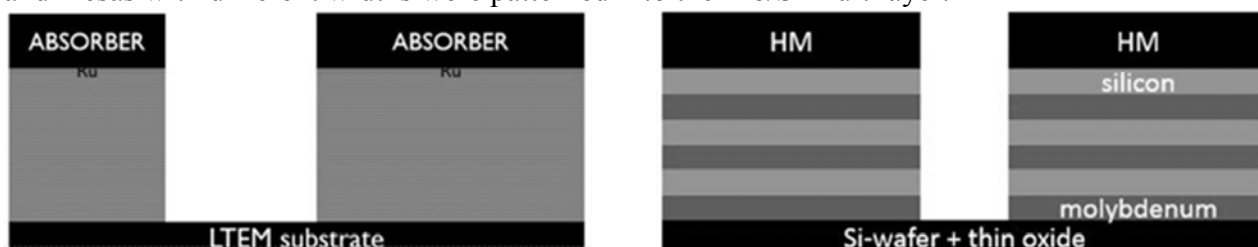


Figure 2: Schematic representation (approximate scaling) of a genuine EUV reticle with the black border etched into the Mo/Si multilayer consisting of many (≈ 40) thin (3-4 nm) Mo and Si layers (left), and test structures consisting of 3 double layers of Mo/Si, each layer being 40 nm thick, mimicking a black border (right).

Experimental

The starting substrates were 300 mm Si wafers with a thin 40 nm oxide film. The multilayer was deposited on top of the oxide film by CVD deposition of alternating films of Mo and Si (3x), starting with Mo. This multilayer was then patterned by using an Al_2O_3 hardmask. A $\text{SF}_6/\text{CH}_2\text{F}_2$ based plasma was used in order to obtain an isotropic etching and thus a vertical profile of the Mo/Si trenches. The last step in the fabrication of the Mo/Si multilayer test structures is the wet removal of the Al_2O_3 hardmask used for the dry etching of the Mo/Si trenches. Although the hardmask removal is not required for our purposes, residues were observed after some cleaning tests that could be originating from etch-by-products from this Al_2O_3 hardmask. Those residues can block the contact of the Mo/Si multilayer with the cleaning solution and/or blur SEM observation of possible Mo/Si multilayer degradation. Hot (50°C) H_3PO_4 (85%) was selected as etch solution since it is selective to the bottom oxide film, to the silicon layers, as well as to the molybdenum layers. All test evaluating the effect of different cleaning media on this black border were done in beakers at RT using standard electronic grade chemicals and with control of the pH.

Results and discussion

Proof of concept of the mimic test structures. Preliminary tests were done on the test structures in diluted APM in order to evaluate the method. APM was selected as a first test chemistry since an adverse effect on the Mo/Si layer is expected, more particularly, etching of the Mo metal [3]. Molybdenum in air is passivated by its oxides, but once in solutions with $\text{pH} > 2$, and in the presence of peroxide, these oxides can further oxidize and form soluble species: this behavior is called transpassivity [4]. Several samples were immersed in diluted APM for increasing times and then analyzed by XSEM (Fig. 3). No significant etching of the Si layers was observed, however, lateral etching of the Mo layers was observed and a rough estimation of the etch rate of the Mo could be made. This proves that the test structures can be used for the evaluation of different cleaning chemistries through a qualitative and quantitative inspection of the Mo/Si multilayer after immersion in the respective chemistries.

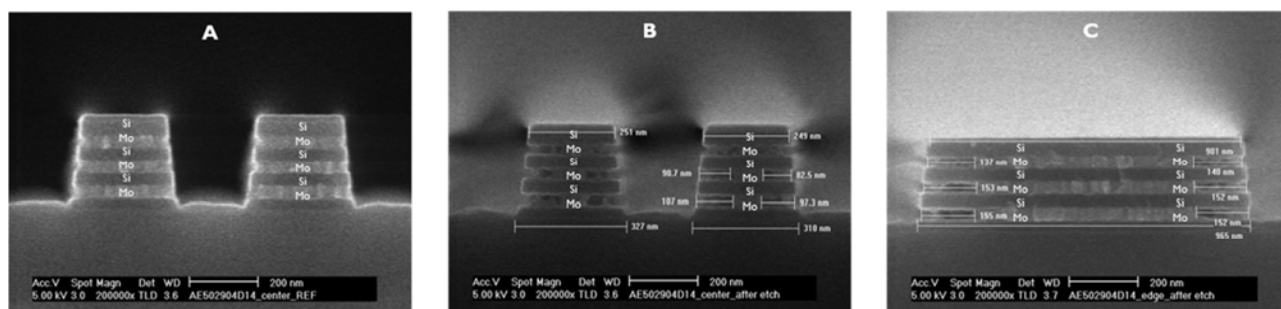


Figure 3: Mo/Si multilayer test structures, the brighter layers are the Mo layers: reference sample (A), sample after 20 min. of APM dip showing lateral degradation of the Mo (B), sample after 40 min. APM dip showing lateral degradation of the Mo layer (C).

Evaluation of Mo/Si multilayer in alkaline solutions. The degradation of the Mo layers was also evaluated in alkaline solutions without addition of peroxide. Two alkaline solutions: diluted NH_4OH and diluted TMAH, both at $\text{pH} 11$, were compared. The pH was set at 11 in order to be in a repulsive zeta potential regime (negative zeta potentials for particles as well as substrate) and thus to have good particle removal efficiency [5-6]. Although no peroxide was present in solution no significant Si etching was observed in all the tests. When samples were dipped in NH_4OH for 100 min no significant lateral etching of the Mo was neither observed. In TMAH, on the other hand, some degradation of the Mo layers was observed after 100 min (Fig. 4). Surprisingly, no degradation of the Mo layers was observed for shorter dipping times in TMAH (Fig. 5).

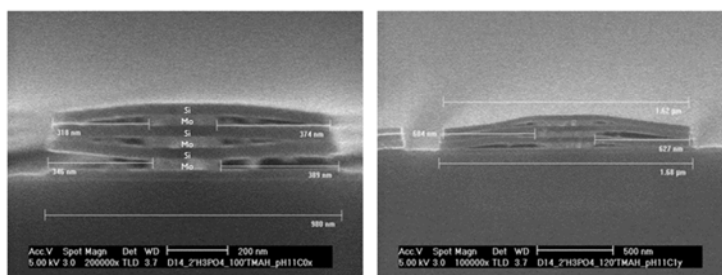


Figure 4: Mo/Si multilayer after 100 and 120 min TMAH: lateral degradation of the Mo layers.

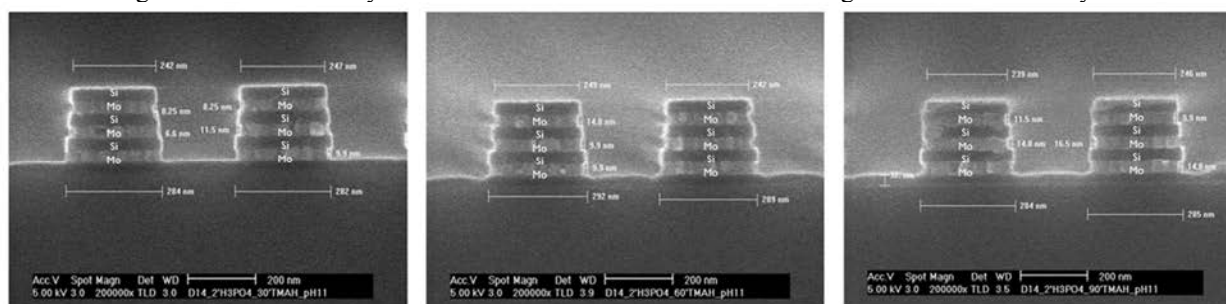


Figure 5: Mo/Si multilayer after 30, 60, and 90 min TMAH: very limited or no degradation of the Mo layers.

These results suggest that there is some delay in the etching of the Mo, but after this onset, the etching proceeds quite fast. It is known that in aqueous media, Mo is passivated by a film consisting of mainly of MoO_2 or their hydrated oxides. But passivation of the Mo metal by its oxides is not effective in alkaline media due to the formation of soluble species: MoO_4^{2-} and/or HMoO_4^- [7]. Badawy et al. [8] pointed out that the most stable anodic oxide film, MoO_3 is formed either in H_3PO_4 or H_2SO_4 . So it is very probable that during the hardmask removal in H_3PO_4 , a more stable MoO_3 is formed. The delay in the onset of etching suggests that the so formed initial passive film, probably consisting of the more stable MoO_3 , is not readily dissolved or undergoes a structural change towards a less stable oxide (e.g. MoO_2) before it starts to dissolve. This process needs time and could explain the observed delay in the etching of the Mo. Previous authors [9], observed a similar behavior by measuring the open-circuit-potential (OCP) of Mo in basic solution: the OCP initially decreased and after approximately 2 hours the OCP increased again. This was assumed to reflect the dissolution of the initial oxide and the probable subsequent formation of a new film. Interestingly, the time frame of their observations matches the delay observed in our work.

Conclusions

The initial passivating film on Mo seems to play a role in delaying the Mo to further oxidize and dissolve. Treatment of the samples with H_3PO_4 could transform the initial oxide into a more stable/passivating oxide. For the cleaning times used (minutes) the Mo surface, and thus the black-border edges, will probably stay passivated by that protective oxide in alkaline solution (pH 11), with no or only very limited Mo loss. Stirring and the amount of oxygen or other oxidizing species like H_2O_2 in solution could increase the oxidation rate of the Mo and/or Mo oxides into soluble Mo(VI) species.

References

- [1] C. Wagner, N. Harned, *Nature Photonics* 4, **24 - 26** (2010).
- [2] Y. A. Shroff, M. Goldstein, B. Rice, S. H. Lee, K. V. Ravi, D. Tanzil, *Proc. SPIE, Emerging Lithographic Technologies X*, 615104 (2006).
- [3] A. Zambova, L. Zambov, K. Stantchev, *J. Electrochem. Soc.*, **139**, 2470-2477 (1992).
- [4] A.G. Tyurin, *Protection of Metals*, **39**, 367–373, (2003).
- [5] S. H. Lee, Y. K. Hong, J. H. Song, J.G. Park, A. A. Busnaina, G. Zhang, F. Eschback and A. Ramamoorthy, *J. J. of App. Phys.*, **44**, 5479-5483 (2005).
- [6] I. K. Kim, B. G. Cho, T. G Kim, J. G. Park, *Int. Conf. of Planarization/CMP Tech.*, Verlag GMBH, Dresden (2007).
- [7] W. A. Badawy, F. M. Al-Kharafi, *Electrochimica Acta.*, **44**, 693-702, (1998).
- [8] W. A. Badawy, A. G. Gad-Allah, H. A. Abd El-Rahman, M. M. Abou-Romia, *Surface and Coatings Tech.*, **30**, 365-373, (1987).
- [9] L. De Rosa, C. R. Tomachuk, J. Springer, D. B. Mitton, S. Saiello and F. Bellucci, *Materials and corrosion*, **55**, 602-609, (2004).

Ultra-Trace Sulfate Ion Removal on Photomasks for Haze Reduction

Eric Guo¹, Crystal Wang¹, Sandy Qian¹, Mars Wang¹, Harry Zhang¹,
Keanu Wu¹, Jian Shen² and Wei Jiang², Fei Xu^{2,a}

¹ Semiconductor Manufacturing International Corporation, No. 18 Zhangjiang Road, Pudong,
Shanghai, China

² Changzhou Ruize Microelectronics, Co., Ltd. West wing of 1st floor, No. 25 Changjiang North Road,
Changzhou, Jiangsu, China

^a feixu@recmicro.com

Keywords: Residue sulfate ion concentration, Haze, MoSiN_xO_y, Quartz, Sulfuric Peroxide Mixture (SPM) cleaning, O₃ cleaning, Ion Chromatography

Abstract. Sulfuric Peroxide Mixture (SPM) showed excellent cleaning efficiency for organic contamination as well as metal or metal oxide particles on photomask surface. In order to reduce haze formation during litho process for ArF photomask, it is necessary to remove any ion sources on photomask, such as sulfate ion, ammonium ion, etc. In this paper we reported a new cleaning method, treating photomask with 172nm UV followed by hot DI rinse, reduces residual sulfate ion in MoSiN_xO_y surface and quartz surface by 50% and 80% respectively comparing to traditional cleaning process. We believe that this new process has the potential to greatly alleviate the haze issue caused by sulfate ion and helps increase the lifetime of photomasks

Introduction

Given its supreme cleaning efficiency for most types of contaminants, Sulfuric Peroxide Mixture (SPM) has been widely used in photomask fabrication processes, such as quartz blank cleaning, photoresist stripping, final cleaning and glue mark removal. However, residual sulfate ions left on the photomask surface are a main cause to haze formation with 193 nm reticles [1]. Various cleaning processes have been developed, such as hot DI water rinse, ozonated DI water rinse, in-situ UV process, etc., to remove sulfate ion residue from photomask. Osborne et al. reported using ozonated DI water and H₂ water to avoid ion residues [2]. Kang et al. reported using thermal treatment followed by hot DI rinse to remove sulfate ion [3]. It is believed that the heat could accelerate the formation of (NH₄)₂SO₄ and the formed salt is much easier to be removed by water rinse than sulfate ion itself. Eschbach et al. reported to expose photomask with 172 nm UV in N₂/O₂ mixture gas environment and then rinse the photomask with SC1 solution. This combined processes could reduce SO₄²⁻ residue to 8~10ppb [4]. Osborne et al. reported using sublimation principle, i.e. high temperature baking combined with UV process to remove sulfate ions to ~1.8ppb [5,6]. Haze formation is clearly still an issue all wafer fabs face. Acid-free methods have been tried with less optimal cleaning efficiency and do not exclude haze either. We hypothesize that the increased energy in 193 nm photons breaks S-O bonding of sulfate ion to form SO₂, which over the time combines with basic substance to form salt crystals, i.e. haze. We report here that treating photomasks with 172 nm UV further eliminates 80% or 50% of the residual sulfate ion on quartz or MoSiN_xO_y-coated surface, respectively, and thus potentially reduces haze formation in wafer fabs.

Materials and methods

The photomask cleaner PMC2500 was manufactured by REC (Changzhou Ruize Microelectronics, Changzhou, China), a single substrate spin spraying processor with megasonic nozzles for cleaning with SPM (sulfuric acid and hydrogen peroxide mixture), HDI (80 degree C hot DI rinse), SC1 solution (Standard cleaning solution 1), as well as 172 nm UV exposure in N₂ pressurized chamber. Quartz substrates with and without MoSiN_xO_y coating were used.

Three cleaning processes were tested, i.e. Process A (SPM clean only), Process B (SPM followed by HDI and SC1), Process C (Process B followed by UV and HDI and SC1). To measure residual sulfate

ion concentration on photomask surface, 500 mL of ultra clean DI water was preheated to and maintained at 90°C by using a water bath. After 25 mL of DI water was taken out for baseline measurement, the testing substrate was soaked in 90°C DI water for 2 hours to leach the SO_4^{2-} ion out of the substrate before 25 mL DI water was sampled.

The SO_4^{2-} ion concentration was measured using a Thermo-Fischer's ICS2100 ion chromatography system, with a detection limit of 0.05ppb.

Results and discussion

Post SPM cleaned MoSiN_xO_y substrates are expected to have high concentrations of SO_4^{2-} ions. We first tested UV exposure, SC1 rinse and HDI rinse respectively, for their efficiency of SO_4^{2-} removal. Figure 1 shows that the hot DI water rinse step has the highest SO_4^{2-} removal rate, and UV exposure is the least effective among the three methods.

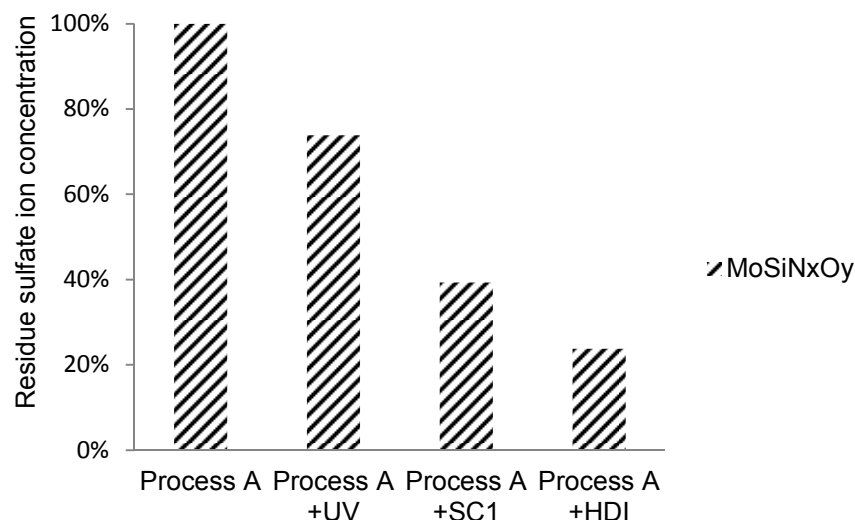


Figure 1: Relative residual SO_4^{2-} concentrations on MoSiN_xO_y surface after Process A vs. with an additional step of UV exposure, SC1 rinse or HDI rinse.

We then tested process B, which combined process A and an additional HDI rinse and SC1 rinse. As expected, the additional HDI and SC1 rinses drastically reduced sulfate ion concentration on substrates post process B cleaning. We added UV exposure and HDI rinse steps individually and sequentially after process B. Figure 2 shows that UV exposure followed by hot DI water rinse further reduced SO_4^{2-} concentration on MoSiN_xO_y surface after process B but either step alone had little effect on SO_4^{2-} concentration.

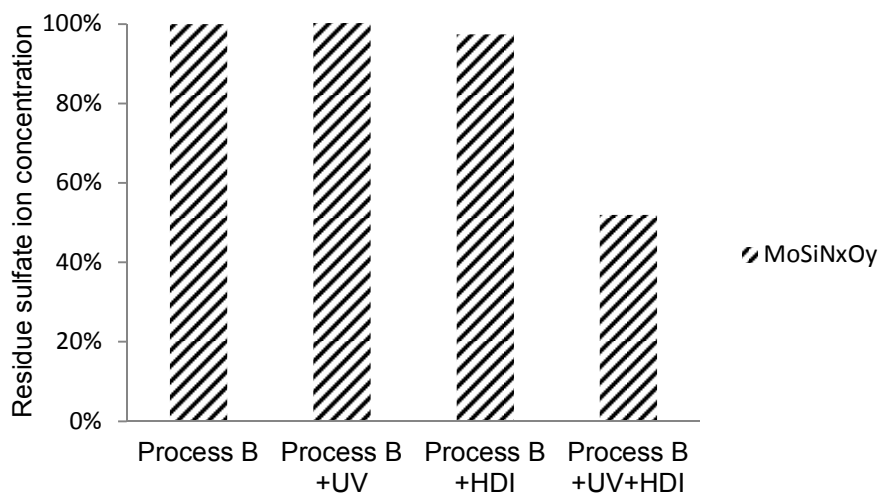


Figure 2: Relative residual SO_4^{2-} concentrations on MoSiN_xO_y surface after Process B vs. with an additional step of UV exposure, HDI rinse or UV exposure plus HDI rinse.

We then tested further adding a SC1 rinse. Interestingly, sulfate ion removal efficiency is dependent on length of UV exposure. Figure 3 showed 3 min of UV exposure combined with hot DI rinse and SC1 rinse is optimal for SO_4^{2-} removal on MoSiN_xO_y surface after Process B. We term the combined steps process C.

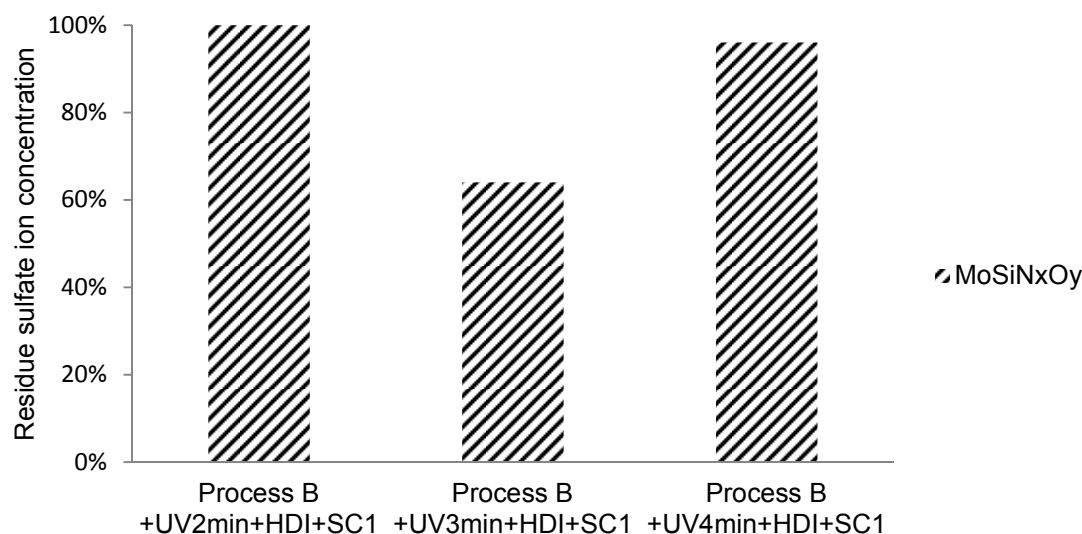


Figure 3: Residue SO_4^{2-} after different UV cleaning time for MoSiN_xO_y surface after Process B.

We repeated the same processes on quartz surface, which represents areas without MoSiN_xO_y coating on a photomask. Figure 4 showed process C has the best SO_4^{2-} removal efficiency for both MoSiN_xO_y and quartz surfaces. The residue sulfate ion concentration for quartz surface after process C is less than 0.1ppb.

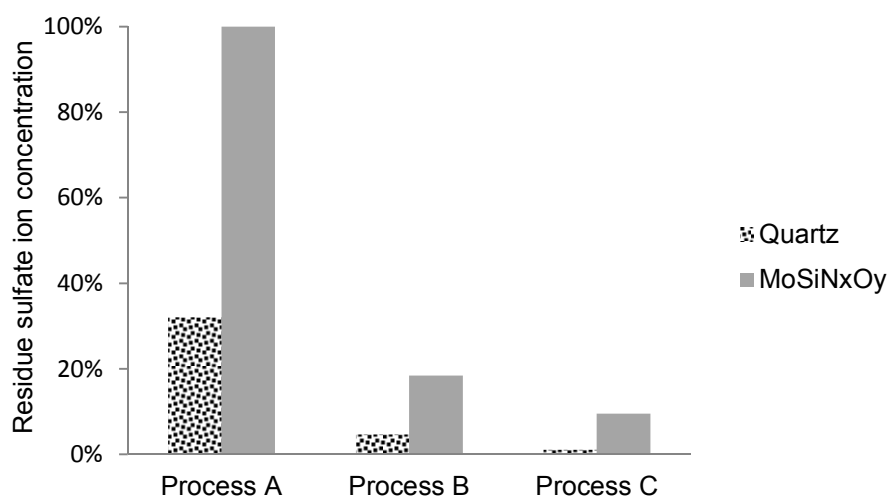


Figure 4: Relative residual SO_4^{2-} after each cleaning process on quartz and MoSiN_xO_y surfaces, normalized to that of process A on MoSiN_xO_y surface.

The relatively lower cleaning efficiency on MoSiN_xO_y than quartz surface may be due to the fact that MoSiN_xO_y layer is deposited by a sputtering process and the amorphous structure of MoSiN_xO_y allows SO_4^{2-} to diffuse below the surface while quartz crystal is more resistant to penetration. We hypothesize that a SO_4^{2-} concentration distribution model for MoSiN_xO_y surface after process B (shown in Figure 5). Various levels of diffusion of SO_4^{2-} ion is achieved at different depth, and we randomly divide the MoSiN_xO_y coating into 5 layers for illustration purpose here. The energy of a 172 nm UV photon is 700kJ/mol, which is higher than the S-O bonding energy at 580kJ/mol. Upon 172nm UV exposure, the sulfate ion could dissociate into SO_2 and O_2 , which could diffuse slowly towards the surface of substrate. The surfaced SO_2 could act as a crystal seed to attract basic substance from surrounding environment to form salt crystals. The energy of a photon of KrF and ArF light is 485kJ/mol and 630kJ/mol respectively. A SO_4^{2-} ion can be dissociated by an ArF photon

but not a KrF photon, which may explain why the industry experiences sudden increasing of haze formation when ArF was introduced into the semiconductor production process flow.

In this model, it is assumed that the room temperature DI water only can rinse away the SO_4^{2-} in the 1st layer. The 80 degree DI water can extract SO_4^{2-} ion out of 2nd layer as well as 1st layer. The 90 degree DI water can extract SO_4^{2-} ion out of 3rd layer and layers above. The temperature of SPM in process B reaches 130 degree C, and the SO_4^{2-} may diffuse to 4th layer and beyond. After process B, the SO_4^{2-} ions in the first 2 layers are effectively removed by the 80 degree HDI rinse. There is still quite some SO_4^{2-} in 3rd layer which can only be leached out by the 90-degree water bath soaking. When the process B cleaned substrate was exposed in the UV light, the SO_4^{2-} ions are dissociated into SO_2 and O_2 . Some of SO_2 could diffuse into upper layers slowly. When SO_2 is leached into water, it can be oxidized back to SO_4^{2-} quickly.

Based on this model, in figure 2, after the UV exposure, some SO_4^{2-} in 4th layer can be excited to SO_2 and could diffuse into 3rd layer. Some SO_4^{2-} in 3rd layer can be excited to SO_2 and could diffuse into 2nd and 1st layer. Depending on the amount of SO_4^{2-} in 4th layer diffusing into 3rd layer and the amount of SO_4^{2-} in 2nd layer diffusing into 1st layer which can be rinsed away by the following cold DI rinse, the total SO_4^{2-} concentration in the 3rd layer and layers above could remain unchanged. This explains why UV exposure followed by cold DI rinse did not reduce SO_4^{2-} concentration significantly. Since there already has HDI treatment in process B, the additional 80 degree HDI will not be able to leach much more SO_4^{2-} out of 3rd layer and beyond. However, after process B, the 80 degree HDI rinse after UV exposure can remove the SO_4^{2-} ion in 2nd layer and above. This explains UV exposure followed by HDI rinse can further reduce SO_4^{2-} for process B treated substrate, but not UV or hot DI rinse alone.

In figure 3, in the beginning of UV exposure, the amount of SO_4^{2-} diffusing into 3rd layer from 4th layer is less than the amount of SO_4^{2-} diffusing out of 3rd layer into 2nd and 1st layer. This results less SO_4^{2-} ion in 3rd layers and the layers above with more UV exposure time. With more UV time, the amount of SO_4^{2-} diffusing into 3rd layer from 4th and 5th layers become more than the amount of SO_4^{2-} diffusing out of 3rd layer into 2nd and 1st layer. This can explain why 3min UV exposure have the minimum detection of SO_4^{2-} .

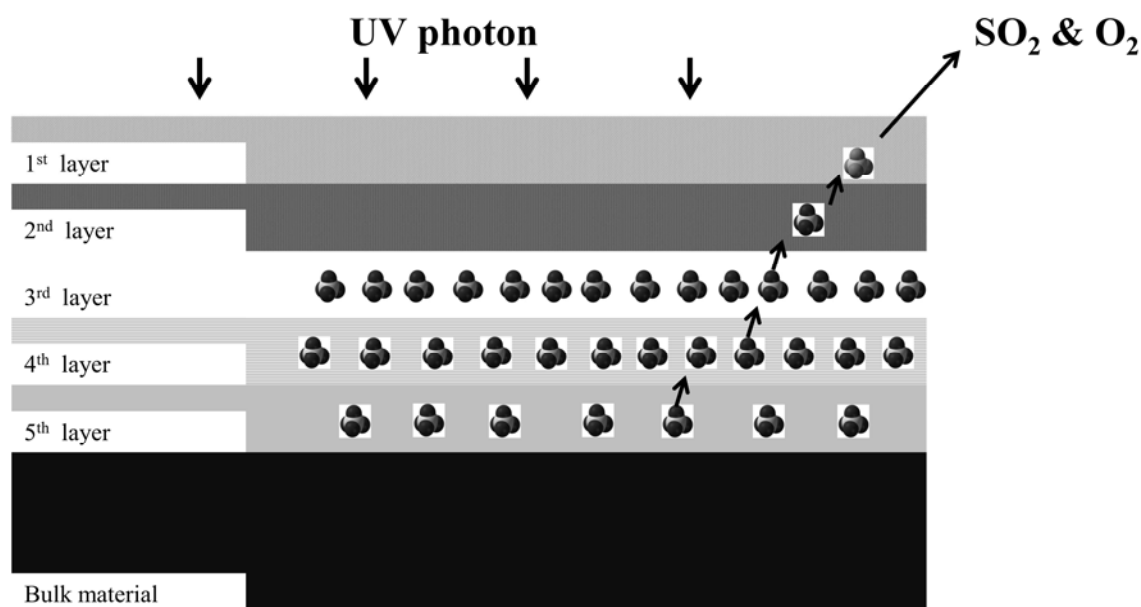


Figure 5: SO_4^{2-} distribution model on MoSiN_xO_y surface after process B.

Conclusions

Our new cleaning method, i.e. process C mentioned above, reduces residual sulfate ion in MoSiN_xO_y surface and quartz surface by 50% and 80% respectively comparing to traditional cleaning process, i.e. process B mentioned above. We believe that this new process has the potential to greatly alleviate the haze issue caused by sulfate ion and helps increase the lifetime of photomasks.

Acknowledgement

Many thanks to the management and technical support from Semiconductor Manufacturing International Corporation and Ruize Microelectronics Co., Ltd. Also thanks to the sponsorship by Program of Shanghai Subject Chief Scientist.

References

- [1] Eric V. Johnstone, Laurent Dieu, Christian Chovino, Julio Reyes, Dongsung Hong, Prakash Krishnan, Dianna Coburn and Chris Capella: SPIE USE, V. 2 5256-48 (2003)
- [2] Steve Osborne, Matthias Nanninga, Hidekazu Takahashi, Eric Woster and Carl Kanda: Proc. SPIE 5992, 25th Annual BACUS Symposium on Photomask Technology (2005)
- [3] Han-Byul Kang, Jong-Min Kim, Yong-Dae Kim, Hyun-Joon Cho and Sang-Soo Choi: Proc. of SPIE Vol.5853 (2005)
- [4] Florence Eschbach, Daniel Tanzil, Mike Kovalchick, Uwe Dietze, Min Liu and Fei Xu: Photomask and Next-Generation Lithography Mask Technology XI, edited by Hiroyoshi Tanabe, Proceedings of SPIE Vol. 5446 (2004)
- [5] Steve Osborne, Hidekazu Takahashia and Eric Wostera: Photomask and Next-Generation Lithography Mask Technology XIII, edited by Morihisa Hoga, Proc. of SPIE Vol. 6283, 628325 (2006)
- [6] Steve Osborne, Matthias Nanningab, Hidekazu Takahashia and Eric Wostera: Proc. SPIE 5992, 25th Annual BACUS Symposium on Photomask Technology, 59923H (2005)

172 nm Excimer Radiation as a Technology Accelerator for Bio-Electronic Applications

Andreas Schäfert^{1, a}, Hartwig Wiesmann²

¹ Ushio Deutschland GmbH., Münchener Str. 10, 85643 Steinhöring, Germany

² Ushio Europe B.V, Breguetlaan 16-18, 1438 BC Oude Meer, The Netherlands

^aandreas.schaefer@ushio.de

Keywords: 172 nm excimer, radiation, VUV, cleaning, surface activation, bonding, adhesive free attachment, polymer microchip, ship production, electro static erasing, grouting,

Abstract The publication reviews recent applications of 172nm excimer radiation in bio-electric fields. It shows the broad field which already profit from the technology and also illustrates possible potentials.

The principle of erasing static electricity from polyimide surfaces is explained as one application. The effect as a function of the dose is presented both for positive and negative charge and typical materials.

In addition the VUV cleaning mechanism with 172nm excimer radiation is demonstrated by the mass spectroscopy of contaminations on the surface of a Si wafer.

Surface energy changes of polyamides, glass and metal as a function of dose are presented as well as the change of the contact angle of water on the surface.

Another application of surface energy enhancement is the polymer microchip production. Due to the surface activation, the bonding strength for the PMMA-Si combination is significantly enhanced. The results are presented in comparison to other surface treatment methods.

Another presented application which profits from the surface activation is adhesive-free coupling. The mechanism of this application is explained and the adhesion strength as a function of material combination is presented. For 2 typical applications, the bonding strength is shown as a function of applied dose. A glance at other applications and an outlook is given as well.

Introduction

Treatment with excimer radiation is already standard in many fields of electronic production like flat panel display production or cleaning of silicon wafer before and after edging processes [1]. It is also used in biologic applications like the photofunctionalization of human implants for an enhanced healing pace [2]. Having advantages like no thermal stress on the substrates, high efficiency, high process safety, no damaging of the substrate as well as no production of disturbing residues the technology opens a wide field of applications for cleaning and surface preparation for bio-electronic applications. It can be used for the production of polymer microchips, as well as to erase static electricity from polymers. It offers a residue free removal of organic contamination, enhances the quality of grouting and can improve the coupling of organic molecules on Si-surfaces by an extreme enhancement of the surface energy.

Overall 172 nm excimer radiation can enhance and stabilize the quality of existing bio-electric applications as it has been doing in the field of electronic production before. In addition it enables completely new possibilities for products and processes.

Excimer lamp radiation

Excimer lamps are based on many plasma discharges within an atmosphere of noble gases or a noble gas halide compound which are excited to an excimer state and decay by the emission of photons of a characteristic wavelength [1].

Most widely used is xenon gas which results in the emission of narrow band radiation at 172 nm spectral distribution. Next to the short wavelengths the technology stands out for its high efficiency theoretically up to 67% [3].

172 nm excimer radiation to erase static electricity

When working with polyimides for electronic applications, static electricity is always a risk for sensitive components. However, with 172 nm excimer radiation there is a fast and easy way to erase this static electricity, both for negative as well as positive charge. This process is based on the photoelectric effect as sketched in Fig. 1. The photoelectric effect means that the 172 nm radiation has enough energy to eject electrons from the surface. In case the overall surface is charged positively the erased electron is again attracted by the surface. For a negatively charged surface the erased electron is rejected by the surface and therefore the charge is reduced. As the photoelectric effect takes also place in atmospheric conditions negatively charged ions are produced out of the air. They are either attracted by a positively charged surface or rejected by a negatively charged surface. In this way a positive charge is reduced while a negative charge is not affected by this effect.

Fig. 2 shows the required 172 nm-dose for typical polyimides. It can be seen, that a minimum dose is required to achieve an effect. For both types the static electricity can be erased completely while Kapton 150EN is easier to treat than Petec6010. It can be seen that with high-power excimer systems [400 mW/cm²] a reduction of static electricity can be achieved in less than a second depending on the type and the initial potential.

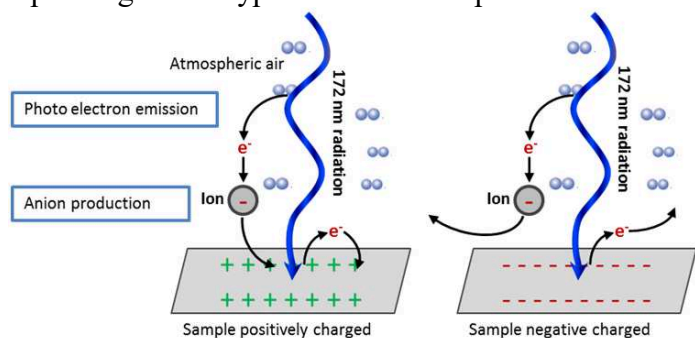


Fig. 1: Principle of static electricity erasing from polyimide surface by photo electric effect with 172 nm radiation.

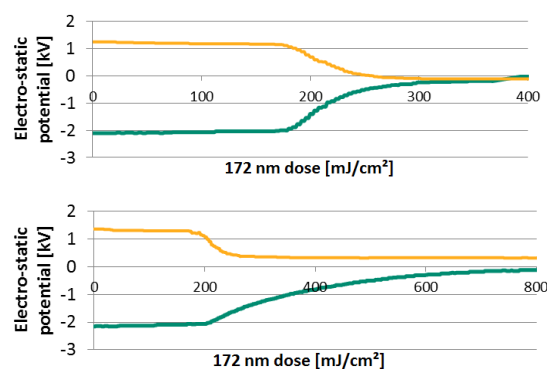


Fig. 2: Static electricity erasing of Kapton 150EN (top) and PETEC6010 (down) as a function of the 172 nm dose

172 nm excimer radiation to clean and activate surfaces of Si-layers, glass and polyamides to improve process quality

One of the main applications of 172 nm radiation is called VUV cleaning or VUV surface activation. By a two-step process biological contaminants are removed residue-free from all kinds of surfaces. In a first step the chemical bindings of the organic molecules are directly cracked by 172 nm radiation. In a second step the residues from the split molecules is removed from the surface by radical oxygen and ozone which is generated by the 172 nm radiation out of the thin air layer between the module and the surface. The principle of this process is shown in Fig. 3. The quality of the cleaning process can be displayed with mass spectroscopy at the contaminations of ø8" Si wafers extracted from the surface before and after 172 nm -excimer treatment.

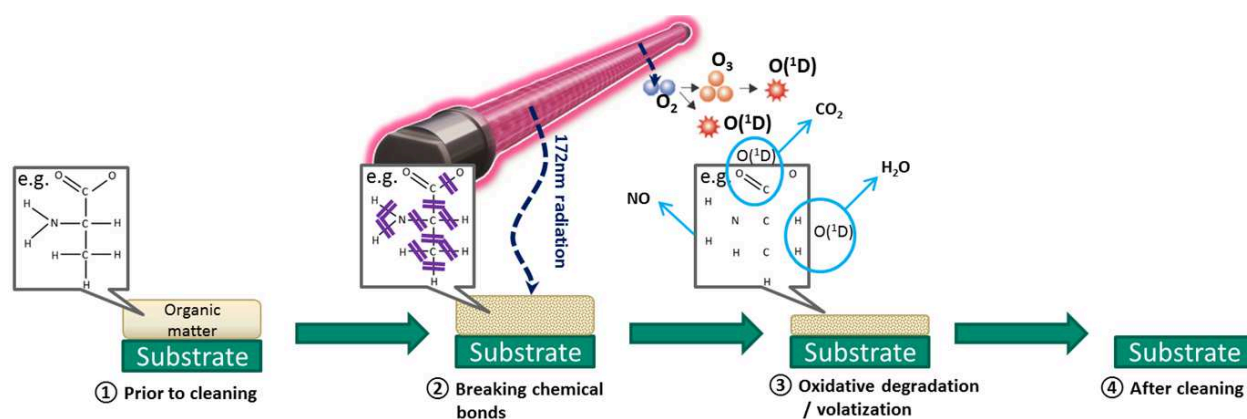


Fig. 3: Principle of VUV cleaning (based on [1])

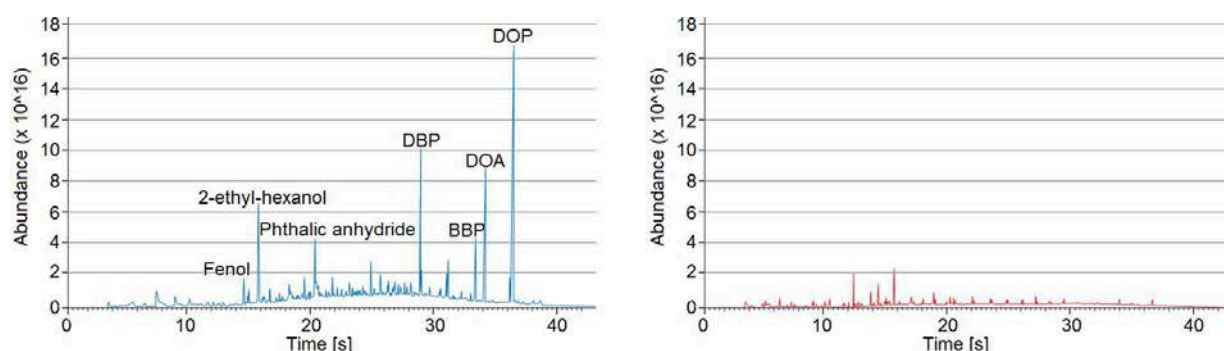


Fig. 4: Mass spectroscopy of surface contaminations of $\phi 8''$ Si wafer in production before (left) and after (right) a treatment with 172 nm excimer radiation in atmospheric air (based on [1])

By this cleaning the active layers of the substrates (glass, Si, polyamides) are exposed which significantly enhances the surface energy and therefore reduces the contact angle of liquids (Fig. 5). For polyamides, not only the actual contaminants can be removed, but also the adsorption layers of gas, dust or humidity. As from polyamide layers are removed constantly, there is a perfect illumination time during which the ideal bonding layer is exposed. When removing more material the surface energy and therefore the bonding strength is reduced. For materials like different metals (e.g. Si) or glass even hydrophilization is possible.

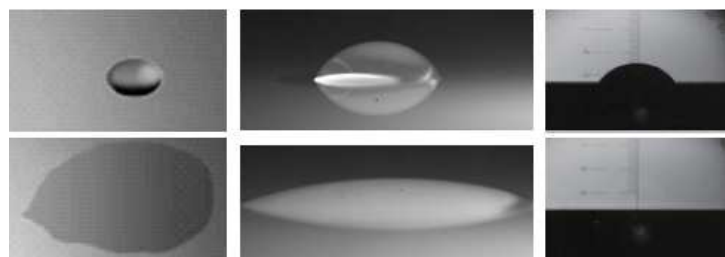


Fig. 5: Contact angle of purified water on Si-wafer (left), PMMA (middle) and alkali glass (left) before (up) and after (down) a treatment with 172 nm excimer radiation (100 mJ/cm^2).

In addition the bonding strength and wetting quality of technical lacquers, grouting compounds adhesives as well as solders is significantly enhanced. A better wetting quality and a cleaned surface means significantly reduced leaking currents due to remaining organic contaminants and air inclusions.

The influence of the 172 nm radiation on the surface energy of different polymers, metals and glass is investigated by a measurement of the contact angle of purified water on the substrate which is dependent on the surface energy. Fig. 6a shows the effect of high doses on polyamide surfaces. It can be seen clearly, that for all polyamides the contact angle is strongly reduced and there the surface energy enhanced. For low doses the surface energy was measured directly with test inks (Fig. 6b). The measurement shows that already with short radiation time surface energies which are similar to those of other surface activation techniques like plasma or corona [4] can be achieved, while no damaging of the surface occurs. In comparison to corona or plasma treatment, with excimer radiation no charges are applied onto the surface and therefore this technique can also be used for printed electronics or organic electronics applications.

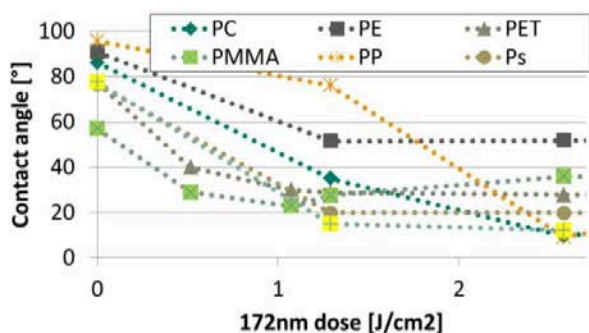


Fig. 6a: Contact angles of purified water for different polyamides

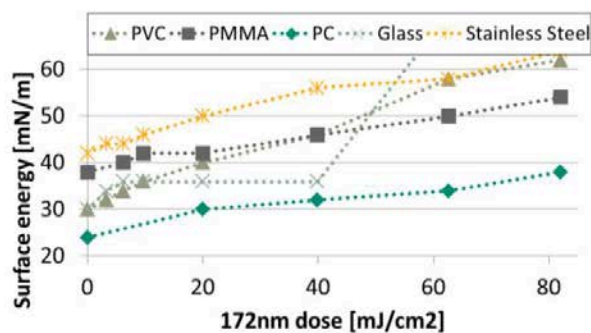


Fig. 6b: Short time activation of polyamides, glass and metal measured with test inks according to DIN 53364

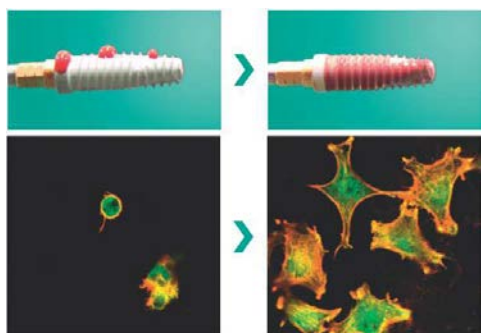


Fig. 7: Hydrophilization of titan implants with excimer radiation (left untreated, right treated) and enhanced osteoblast attachment due to the surface treatment. [5]

If attaching biological molecules on a metal surface is required this process can be strongly enhanced by a previous treatment with 172 nm radiation. One field of use of this technology is the treatment of implants before the surgery to enhance the bio-integration into the bones by a 2-5 times increased osteoblast attachment [5] (see Fig.7).

Application: 172 nm excimer radiation to improve the process of polymer microchip production

One of the major steps in polymer microchip production with microchannels is the attachment of a thin PMMA layer on a Si-substrate. Since bonding with adhesive reduces the product quality due to an additional optical layer a direct bonding has to be applied. The two layers have to be compressed under heat and it has been shown [6], that with a surface activation of the PMMA with 172 nm excimer radiation even under atmospheric conditions a reasonable bonding strength was achieved without a deformation of the microchannels or a damaging of the PMMA layer. The process is based on a combination of the direct 172 nm radiation and the oxygen radicals, which are formed out of the air in the layer between the excimer module and the substrate.

The technology was compared to similar technologies such as atmospheric plasma treatment, vacuum plasma treatment and a treatment with a low pressure UV lamp with 185 and 254nm radiation. As a result not only the bonding strength was superior for excimer radiation under reasonable conditions but in addition less time, less annealing temperature and less pressure was needed. This leads to a reduced stress for the components and a higher production quality. The results are displayed in Fig. 8. To show that the procedure does not affect the micro channels microscopy photographs of the manufactured chips were taken. This series is presented in [6].

Surface energy enhancement and a better wetting are not specific for bio-electric applications. However, especially with the usage of polyamides which have naturally a very low surface energy and therefore are difficult to handle the surface energy enhancement makes production much more stable.

In addition especially if bio-materials are combined with Si to form bio-electrical components a clean and activated contact layer significantly improves product quality.

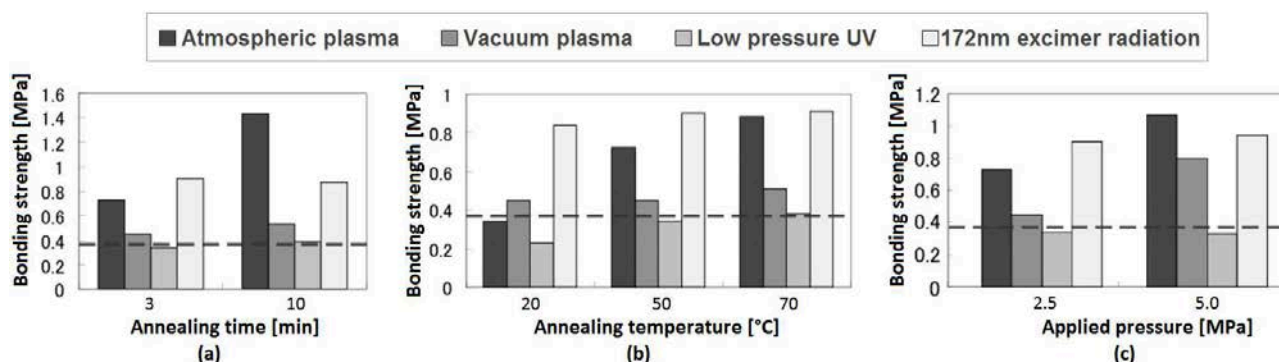


Fig. 8: Comparison of bonding strength for the PMMA-Si combination after treatment with atmospheric plasma (black), vacuum plasma (dark grey), low pressure UV (mid grey) as well as 172 nm excimer radiation (light grey). The impact on annealing time (a), annealing temperature (b) and applied pressure (c) is visualized [6]

These results were very promising under laboratory conditions, but a 3 minutes treatment with excimer radiation is not applicable for mass production processes. However, in 2006 the measurements were done with a low power excimer radiation with 10 mW/cm². With the recent high-power excimer units providing up to 400 mW/cm² similar results can be achieved after only some seconds of radiation.

The surface energy plot (Fig. 6a) shows that the highest surface energy and therefore bonding strength for PMMA can be achieved with around 1.0 J/cm² which corresponds with a radiation length of 2 s to 3 s. However, the low intensity results show that even with little radiation significant effects can be achieved and allow an optimization between required bonding strength and radiation time.

Application: adhesive-free coupling due to enhanced surface energy

A new application of 172 nm radiation is adhesive-free coupling which have been published first in 2011 [6]. With the combination of 172 nm radiation and slight pressure, a safe and long-lasting bond can be achieved. While many combinations have very good results for many polymers and glass, there are also combinations which cannot be coupled with the combination of excimer radiation and pressure. In Table 1 to Table 2 is shown, which combination of materials are bonding.

Table 1: Bonding of combinations of glass, sapphire, PDMS and silicon rubber

	Quartz Glass	Sapphire	PDMS	Silicone rubber
Quartz	○			
Sapphire		○		
PDMS	○	×	○	
Silicone rubber	○			○

○ : Strong
 △ : Weak
 × : No bond

Table 2: Bonding of combination of transparent polymers and quartz glass

	COC	Quartz Glass	PP Film (un-stretched)	PET Film (stretched)	PMMA
COC	○	○			
Quartz Glass		○			△
PP Film (un-stretched)			○	○	
PET Film (stretched)		×		×	×
PMMA		△			○

The general function is described in Fig. 9, presented for the example of bonding PDMS on glass. In the initial state, the capping layer of the PDMS substrate surface consists of CH₃ groups. With the excimer radiation, the Si-C, as well as the C-H bonding is cracked and the residuals are removed by the oxygen radicals. The Si-O bonding of the surface cannot be cracked. Combined with one oxygen atom from the oxygen radicals and a hydrogen atom from the original compound, the substrate surface becomes activated. When pressing together the activated PDMS substrate with a cleaned glass, the surface molecules bond while H₂O compounds are released.

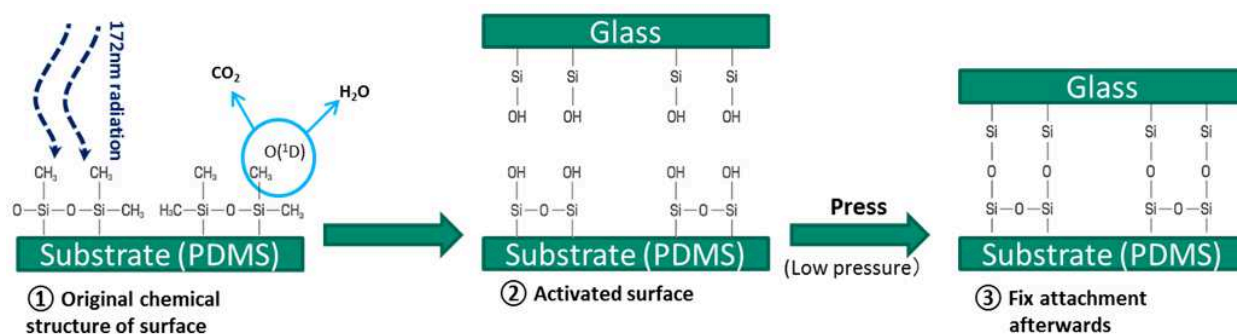


Fig. 9: General function of adhesive-free coupling, presented on the bonding of quartz glass onto PDMS

The bonding strength as a function of the 172 nm radiation dose as well as the pressure is displayed in Fig. 10. With an optimal 172 nm dose, a good bonding strength does not need high pressures and higher pressure is partly even reducing the bonding strength. After the optimal dose, the bonding strength is reduced again with additional 172 nm radiation.

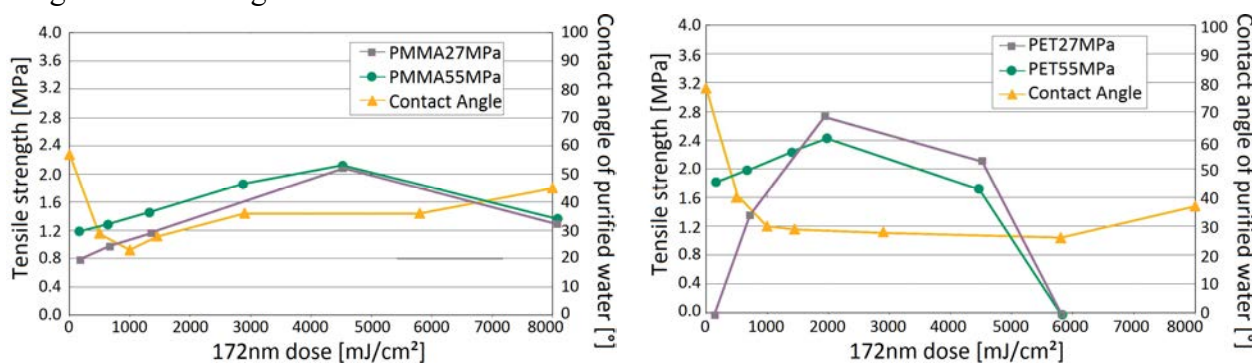


Fig. 10: Bonding strength as a function of 172 nm radiation and pressure for PMMA (left) and PET (right) measured with a peel test. In addition the contact angle of purified water on the surface is displayed to demonstrate the change of surface energy.

Beside the fact, that with adhesive free coupling no kind of curing is necessary and no additional chemicals are applied a main advantage is, that the optical properties of the bonded components are significantly improved compared to a version with an adhesive.

Application: enhanced encapsulation of organic solar cells

A test series was performed with commercial and prototype barrier foils for organic cells. These barrier foils are agglutinated with UV curing cationic adhesive.

By now, problems appeared as the glue didn't attach properly to the foil surface and therefore the two foils could be pulled apart easily while the adhesive film just stays as an individual layer.

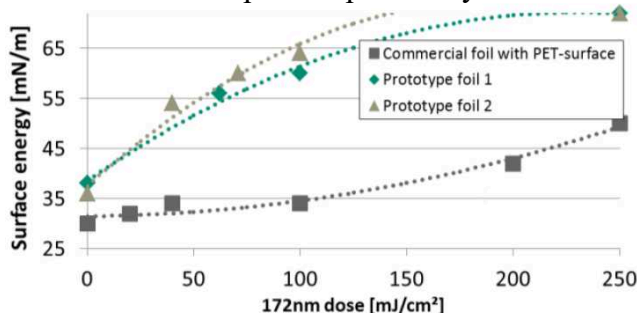


Fig.11: Surface energy of commercial and prototype barrier foils for organic solar cells

By applying excimer radiation, the surface energy could be enhanced for all foils tested (see Fig. 11). With 250 mJ/cm^2 radiation dose, the bonding strength on the surface was high enough, that under high tension not the adhesive film was peeled off but the adhesive film broke internally as the inner resistance was lower than the adhesion.

Summary and outlook

172 nm excimer radiation offers possible solutions for recent topics in bio-electronic applications. Especially the attachment of organic materials on Si-substrates by 172 nm surface activations offers the chance for new type of sensors. The erasing of static electricity of polyimide components as well as the enhanced quality of grouting compounds and adhesive processes results in increased production quality as well as enhanced reproducibility.

As 172 nm radiation can be monitored in real time with sensors in the excimer module a stable quality can be ensured easily. However, 172 nm excimer processes are sensitive to distances, kind and thickness of contamination. Thus the required dose has to be investigated for each specific application to receive best possible results.

References

- [1] USHIO Inc.: Excimer irradiation unit, Tokyo, 2011
- [2] H. Aita et al., *Biomaterials* **30** (6), 83 (2009)
- [3] Sz. Beleznai et. al., *J. Phys. D: Appl. Phys.* **41** (11), 6 (2008)
- [4] C. Mangipudi et. al., *Langmuir* **11** (1), 19 (1995)
- [5] F. Iwasa et. al., *Biomaterials* **31** (10), 2717 (2010)
- [6] H. Shinora et. al., *IEEJ Trans. SM* **2** (3), 301 (2007)
- [7] W. Okada et. al., *IEEJ Trans. SM* **131** (4), 159 (2011)

CHAPTER 12:

Contamination Control of Wafer Ambient

Electrolyzed Water for Efficient Metal Removal

John Oshinowo^{1, a}, Ann- Kristine Neelsen¹, Matthias Fryda¹,
 Lutz Rebstock² and Ulrich Quarti²

¹ CONDIAS GmbH, Fraunhofer Strasse 1 b, 25524 Itzehoe (Germany)

² BROOKS Automation (Germany) GmbH, Im Wiesengrund 17, 78315 Radolfzell (Germany)

^aemail: oshinowo@condias.de

Keywords: Electrolyzed water, Cathode water (CW), Anodic water (AW), FEOL wet clean, Anodic water chloride (AW-Cl), Oxidation Reduction potential (ORP), pH-value, HCl, SC2, FOUP

Abstract. This work demonstrates the efficient removal of various metals from the plastic surface of wafer storage cassettes (FOUP's) by using electrolyzed water. The studies are ruled out for Anodic water chloride. This new wet cleaning technology is a powerful application, not for FOUP's only, but also for innovative semiconductor surface preparation and FEOL cleaning applications.

Introduction

The fabrication of high-speed logical devices makes it necessary to use highly innovative FEOL wet chemical cleans. Electrolyzed cathode water (CW) cleans, for the removal of particles of silicon wafers, are already used since several years, by several notable device manufactures, especially in Asia [1- 4]. The cross-contamination of silicon wafers in storage cassettes and FOUP's (Front opening unified pods), leads to significant yield losses. The classical way, to remove particle contamination from FOUP's, is a DI-water clean. DI-water alone is not suitable for an efficient metal removal. For the first time – we are using electrolyzed water, for the removal of metals, from the FOUP plastic surface.

Red Ox[®] cell technology

Table I displays the various kinds of electrolyzed water for different process specifications and applications. The cathodic water process allows the production of cathodic water (CW), hydrogen water (HW) and ozonized water (OW). These processes are used mainly for particle removal and oxidation [5, 6].

Table I: Various types of electrolyzed water (EW) produced for different wet cleaning applications. The major process specifications are the oxidation reduction potentials (ORP) and pH-values.

	ESA	DESA	AW- F	AW-Cl	AW-SO ₄	OW	HW	CW
	Electrolyzed sulphuric acid	Diluted electrolyzed sulphuric acid	Anodic water fluoride (DHF)	Anodic water chloride (DHCl)	Anodic water sulphate	Ozonized water	Hydrogenated water	Cathodic water
Spec.	pH 0- 0.5 ORP 1800 - 2000mV	pH 1- 2.5 ORP 1220 - 1600mV	pH 2.5- 5 ORP 750 - 1400mV	pH 2.5- 5 ORP 750 - 1250mV	pH 2.5- 5 ORP 750 - 1400mV	pH 6.5- 7.5 ORP 800 - 1400mV	pH 9.5- 10.4 ORP -500 - -750mV	pH 10.5- 11.5 ORP -750 - -900mV
Appl.	Photo resist etching; Polymer removal	Soft and defined photo resist etching	Metal etching; SiO ₂ etching; surface conditioning	Metal etching	Organic removal; very soft resist etching	Soft Organic removal; defined surface oxidation	Soft particle removal; Oxidation prevention	Particle removal; Etching prevention

The anodic water (AW) process leads – depending on the feed chemistry – to anodic water fluoride (AW-F), anodic water chloride (AW-Cl) or anodic water sulphate (AW-SO₄). Major applications are metal etch. Photo resist removal will be done by ESA (Electrolyzed sulphuric acid) [7].

This paper shows the metal removal efficiency of electrolyzed water for zinc, iron and nickel. FOUP plastic materials, like for example, Polycarbonate (PC) and Polyetheretherketon (PEEK) are used. The metal free cell type (Red Ox[®] cell) was developed by CONDIAS and designed for Anodic water (AW) production [5]. An electrochemical reaction is induced by boron doped diamond electrode and a small amount of (ammonia) chloride is used to produce anodic water (AW-Cl).

Process Results

For the wet chemical tests, the FOUP material was rinsed, by using a spray nozzle setup, similar to the standard 300mm-FOUP cleaning equipment from BROOKS Automation (Germany). The results were compared with the metal removal efficiency of diluted SC2 and DIW, respectively.

For production of anodic water (AW-Cl) from DI water the cathodic electrolyte consists of 100 – 10000 ppm of chloride (NH₄Cl or HCl) in DI water. For our metal removal applications on FOUP's we used AW-Cl at pH values ranging from 2.6 to 3.1 and oxidation reduction potential (ORP) values ranging from 880 to 1100 mV.

Figure 1 displays the associated ORP as a function of pH-value for various chemicals and solutions. The conventional SC1 (APM) and SC2 (HPM) mixtures (squares) as well as OW, DIW and Hydrogen terminated water (HW) are shown (large circles). By tuning the cell current, the grade of oxidation can be enhanced or reduced (arrow bar on the left hand side) and the pH-value can be changed from acid to alkaline (arrow bar on the bottom). Cathode water (CW) as well as anode-water (AW) are created, with an accurately specified ORP/pH-value.

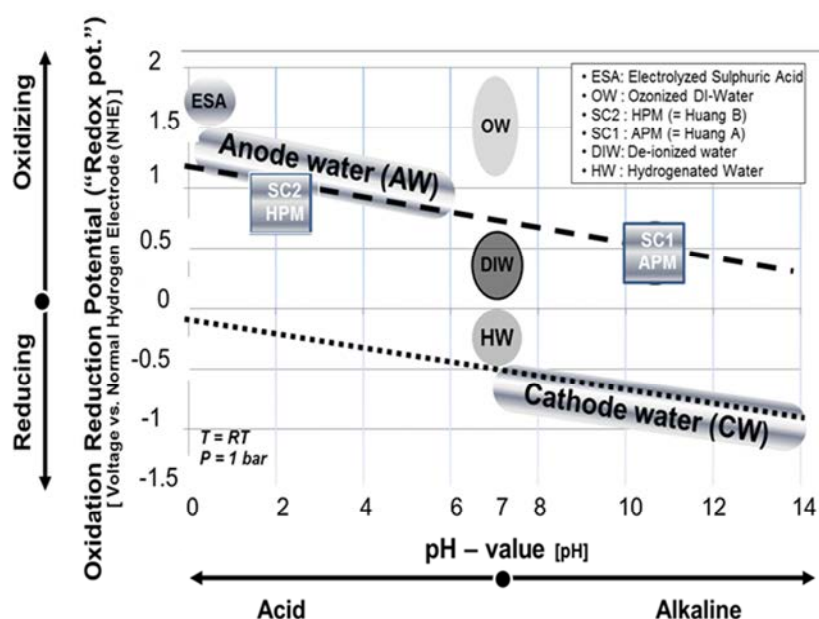


Figure 1: Overview of the oxidation reduction potential (ORP) as a function of pH-value for various FEOL cleaning chemistries. By simply tuning the Red Ox[®] cell current, the grade of oxidation can be enhanced or reduced (arrow bar on the left hand side) and the pH-value can be changed from acid to alkaline (arrow bar on the bottom). For the current study we are focusing on the Anodic water (AW) regime.

Figure 2 shows the major chemical reactions in the cell along the ion exchange membrane, by using DI water, NH_4Cl or HCl . During electrolysis chloride ions (Cl^-) will move through the anion exchange membrane into the anodic anolyte. Concentrations of 100 – 10000 ppm of chloride (Ammonia chloride or hydrogen chloride) are necessary to stabilize acidic water. Parallel ORP will be increased above +880 mV.

Catholyte process: input: DI water plus 100 – 10000 ppm chloride acid; main electrochemical reactions: $2\text{H}_2\text{O} + 2\text{e}^- \rightarrow \text{H}_2(\text{g}) + 2\text{OH}^-$ and main substance (output): H_2O , H_2 , NH_4^+ and OH^- .

Anolyte process: input: DI water; main electrochemical reactions: $\text{H}_2\text{O} - \text{e}^- \rightarrow \text{H}^+ + \text{OH}^\bullet$ and $\text{OH}^\bullet \rightarrow \text{O}_3 + \text{H}_2\text{O}$. The main substance (output): H^+ , Cl^- , H_2O and O_3 .

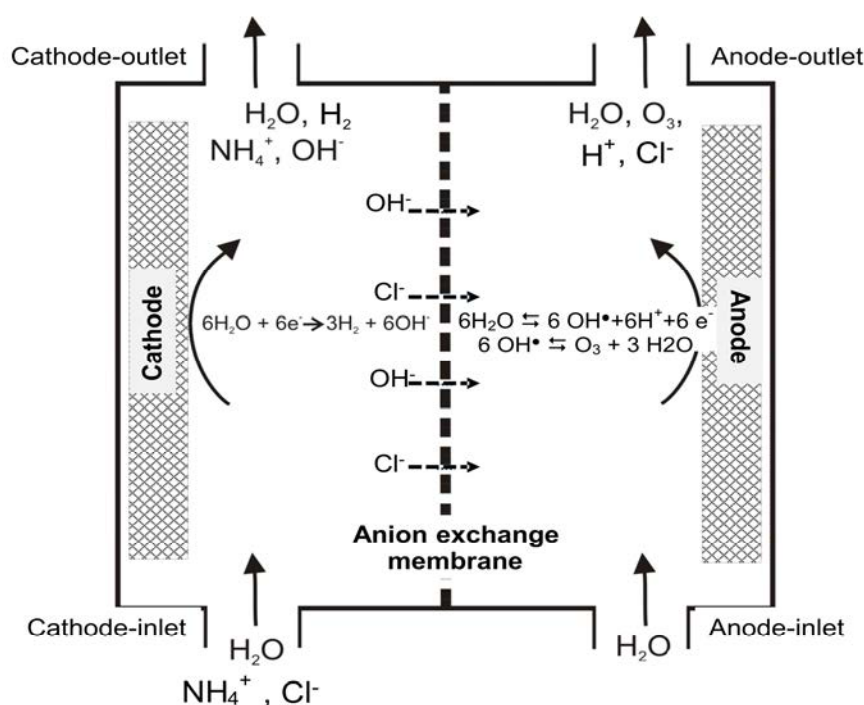


Figure 2: Main chemical reactions for AW-Cl production, in the Red Ox[®] cell along the anion exchange membrane, by using DI water and NH_4Cl or HCl .

Figure 3 shows the results of AW-Cl production: the ORP values versus pH value are shown for different chloride feed concentrations and electrical current (Ampere). For high chloride feed concentration of 10000 ppm (white symbols) the AW-Cl can be changed for a large ORP as well as pH-value range. The ORP can be tuned from about 860 mV up to more than 1150 mV by ranging from pH-value of 3.9 to 2.2. All measurements were performed at room temperature of $T = 22^\circ\text{C}$.

Most of the data are aligned on one straight line. For a fixed ORP value a fixed pH-value is given. For process optimizations reasons of the metal etch, it's more attractive to work with a larger process window, in order to tune the grade of oxidation as well as the etching rate; e.g. having for one ORP (pH) value various pH (ORP) values available.

We are able to enlarge the process window by decreasing the Cl -feed concentration to 100 ppm (black symbols). For a pH- value of about 3.7 we received ORP values from 860 mV (black dot), 900 mV (black square) and 950 mV (black triangle).

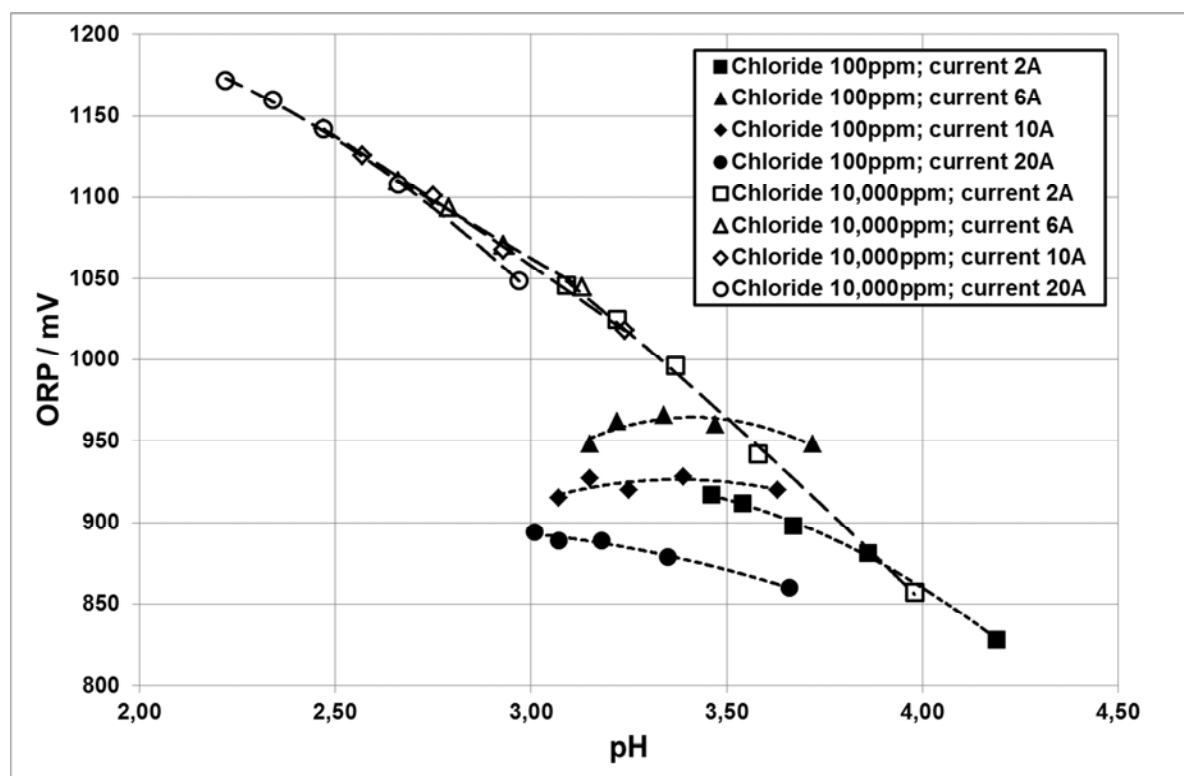


Figure 3: Oxidation reduction potential ORP [in mV] versus pH-value for the Anode water (AW-Cl) regime for different chloride feed concentrations of 100 ppm (black symbols) and 10000 ppm (white symbols). The electrical current [in Ampere] is displayed for 2 A (square), 6 A (triangle), 10 A (diamond) and 20 A (circle). All measurements were done at room temperature ($T = 22^{\circ}\text{C}$).

This result demonstrates the high potential of the electrolyzed water chemistry. By simply adjusting the ORP as well as the pH-value (in seconds only) and tuning the current of the cell device, in combination with the amount of chemical solution (at constant DIW flow), gives the EW technology a major advantage, compared to the conventional chemical/DIW mixture.

For the further process we choose one AW-Cl solution with a high ORP- (and low pH-) value and one with a low ORP- (and higher pH-) value.

Figure 4 displays the metal removal efficiency (in percentage) for three different metals: Nickel (Ni), Iron (Fe) and Zinc (Zn) and four (4) cleaning solutions are used at room temperature ($T = 20-22^{\circ}\text{C}$) for a spray time of 180 s. For the AW-Cl clean, two different chemical solutions with different pH/ORP-value are used. For comparison a diluted SC2 ($\text{HCl} : \text{H}_2\text{O}_2 : \text{H}_2\text{O} = 1:1:20$) clean as well as a simple DIW rinse is used.

The highest metal removal efficiency – for all 3 metals – is observed for the AW-Cl at pH-value 2.6 and $\text{ORP} = 1110\text{ mV}$ (black bar). A metal removal efficiency of up to 69% is reached for Zn, up to 58% for Fe and 40% for Ni. Similar metal removal rates, for Zn and Fe, are achieved with the other AW-Cl at pH-value 3.1 and $\text{ORP} = 880\text{ mV}$ (grey bar), with a metal removal of up to 69% for Zn and 60% for Fe.

The diluted SC2 at pH-value 2.5 and $\text{ORP} = 550\text{ mV}$ (striped bar) shows a significant lower metal removal rate for all three metals, compared to the best AW-Cl ($\text{pH} = 2.6$; $\text{ORP} = 1110\text{ mV}$). Even though, both solutions, having an almost similar pH-value, the higher ORP-value of 1110 mV of the AW-Cl leads to the higher metal rate removal compared to the diluted SC2 ($\text{ORP} = 500\text{ mV}$).

The metal removal efficiency of the DIW rinse at pH= 7, ORP= 400 mV (white bar) is just 18% for Zn and only 2% for Fe and Ni. The low ORP-value and high pH-value leads to a negligible metal removal rate.

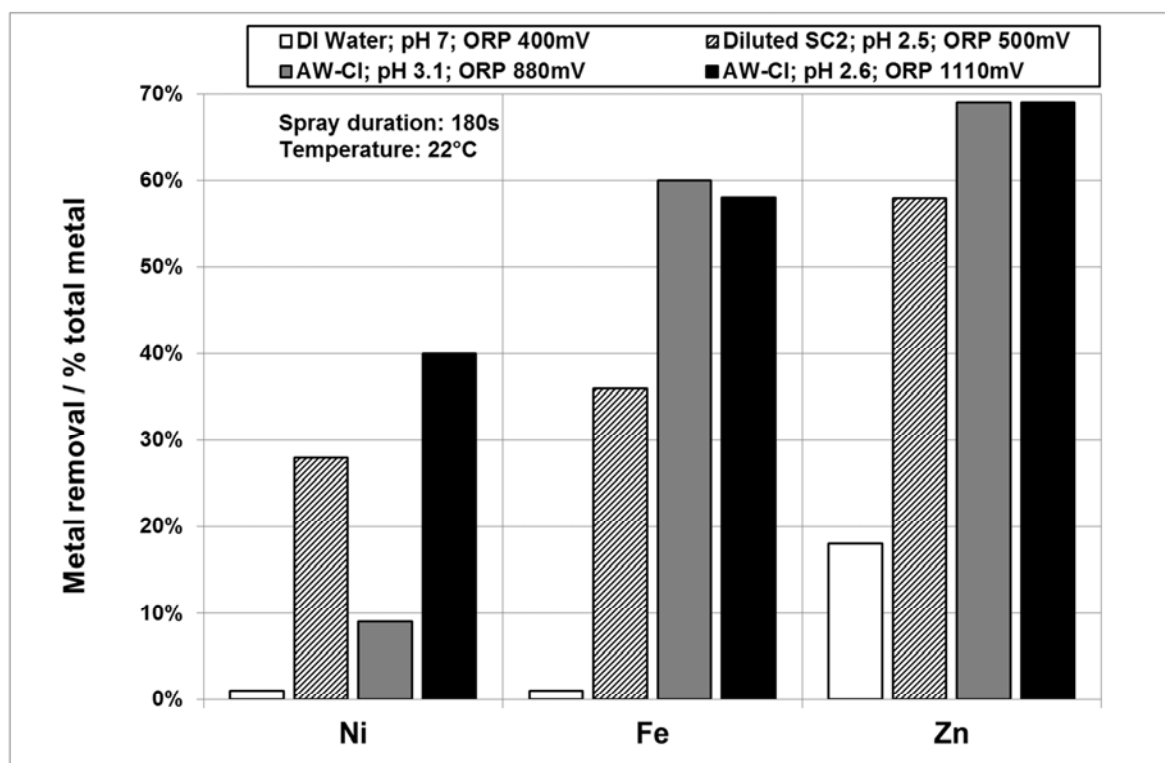


Figure 4: Metal removal efficiency for three different metals: Nickel (Ni), Iron (Fe) and Zinc (Zn) for 4 cleaning solutions, at room temperature ($T=20-22\text{ }^{\circ}\text{C}$) and spray time of 180 seconds. The wet cleaning solutions are electrolyzed anodic water (AW-Cl) for pH= 2.6/ ORP = 1110 mV (black bar) and AW-Cl for pH= 3.1/ ORP= 880 mV (grey bar). For comparison a diluted SC2 (striped bar) and DIW rinse (white bar) were used.

The results demonstrating the high metal removal efficiency of the AW-Cl, compared to diluted SC2 and DIW rinse, indicating that the electrolyzed water chemistry with a dedicated combination of ORP/pH-value, is a powerful solution for metal removal.

Additional investigations showing, that a shorter process time of only 60 s, leads still to a very good metal removal rate of 60% (for zinc), compared to a removal rate of 69% (at 180 s). Further investigations regarding metal removal rates for various AW-Cl etching times, for other metals (e.g. Cu, Zn, Ni and Ti) are under preparation. All studies shown in this paper are ruled out for AW-Cl (Anodic water chloride) based on diluted HCl. Additional studies for AW-F (Anodic water fluoride), based on DHF, are on our short term roadmap.

We have to highlight that the adjustment of the ORP/pH-value for the electrolyzed water can be executed digital (in seconds) at POU (point-of-use). Therefore it's an excellent candidate for fast and accurate process adaption. This innovative wet cleaning technology is a powerful application, not for FOUP's only, but also for semiconductor surface preparation and FEOL cleaning applications.

Conclusions

The highly efficient removal of metal contamination by wet chemical cleaning, on electrical and optical semiconductor devices, with ultra small pattern size, is still a challenge. Due to the fact that different metal ions having a different electrochemical potential and etching rates, the wet chemical clean on various semiconductor surfaces (e.g. covered by oxide, carbon, etc.) plays an important role.

Conventional wet chemical cleans, like SC2 or diluted HCl and DHF, having their limitations in ion/anion removal efficiencies, because their dedicated pH-value and ORP-value, respectively, is limited on a very small process window (e.g. SC2: pH= 2.5 and ORP= 500 mV), compared to Electrolyzed water-based cleans.

The usage of AW-Cl or AW-F will offer the chance, to tune the pH value from pH 2 up to pH 5 and the ORP-value from ORP= 750 mV up to 1400 mV. This very large process window of AW-cleans, might allow, to use more efficient wet cleans, with higher metal removal rate, compared to the conventional wet cleaning chemistry.

References

- [1] K. Ryoo, B. Kang, Electrolyzed water as an alternative for environmentally-benign semiconductor cleaning chemicals, *Clean Technology* 7 (3), 2001, pp. 215-223.
- [2] J.H. Bae, Flat Panel Display (2006), University of Suwon, South Korea.
- [3] G. Choi, Necessity of cleaning and its Application in Future Memory Devices, *Solid State Phenomena*, Vol. 219 (2015), pp. 3-10.
- [4] J. Kim, J. Lee, D. Sheen, B. Lee, Electrolyzed water, *Cleaning Technology Symposium* (2015), Hanyang University, South Korea.
- [5] G. Zwicker, M. Fryda, T. Matthée, 5th International Workshop for Diamond Electrodes (2002), Germany.
- [6] M. Fryda, Th. Matthée, J. Oshinowo, D.H. Baek, H.J. Förster, G. Heinze, Operation of a new electrolyzed cell using Boron Doped Diamond electrodes, *Solid State Phenomena*, Vol. 2192 (2015), pp. 40-43.
- [7] D. Hilscher, C. Thaft, S. Merrit, T. Nagai, T. Otsu, D. Harris, *Sematech Conference* (2010), Austin (USA).

Contamination Control for Wafer Container Used within 300 mm Manufacturing for Power Microelectronics

Germar Schneider¹, Thi Quynh Nguyen², Matthias Taubert¹,
Julien Bounouar², Catherine Le-Guet², Andreas Leibold³, Helene Richter³,
Markus Pfeffer³

¹ Infineon Technologies, Dresden, Germany

² Pfeiffer Vacuum SAS, Annecy, France

³ FhG IISB, Erlangen, Germany

germar.schneider@infineon.com

thi-quynh.nguyen@pfeiffer-vacuum.fr

Keywords: AMC, particle contamination, FOUP, FOSB

Abstract. This paper gives an overview about all activities performed within a common project between industrial and academic partners to define clean room concepts for the first worldwide high volume semiconductor front end facility IFD for 300 mm power semiconductors. The investigation within this study is the base for the 300 mm container strategy resulting in new innovative manufacturing and automation concepts.

Introduction

The equipment standard 300 mm front end wafer fab for microelectronics requires strictest specifications to the clean room and the standard minienvironment to fulfill ISO-class 2 or even better. Wafer container, Front Opening Unified Pod (FOUP), used within a typical front-end fab need also iso-class-2 specifications and special FOUP cleaning procedures are defined for a regular wet cleaning of the FOUPs depending on the production time, the door cycle times or after defined process steps where cleaned FOUPs are required.

FOUP cleaning performed by standard processes using deionized-water (DI-water) can remove particles and water soluble contaminants such as sodium or calcium, but are not 100% efficient to remove Airborne Molecular Contamination (AMC) or noble metals. Another effect which is driven by contaminants out of the container is metal corrosion for aluminum or copper wires within the microchip structure which is detected during defect density inspections. Those effects can lead to yield loss on the wafer. In case of contamination of the wafer inside the FOUP, an economic impact can already happen to the Integrated Circuit (IC) supplier if the defects are even detected several process steps later.

The aim of the study is to perform optimized controlling methods and analyses of the FOUPs for particles and AMC assuring quality and cost of ownership of FOUP cleaning and monitoring strategies within the fab. For a 300 mm fab, manufacturing power semiconductors working with different new materials like organic components, it is necessary to get a deep understanding about the components and impurity levels before and after the cleaning steps for all container types and process steps used within the fab to achieve optimized container cleaning and controlling strategies with low efforts within fab operation.

Description

Within this work monitoring of the particle level and AMC in wafer container using online systems are investigated which can be integrated into the cleanroom of the wafer facility with direct connection to the automation system of the fab. Over the last years, Infineon Dresden (IFD)

established 300 mm wafer pilot lines which will be ramped up to high volume manufacturing using various dedicated FOUP types for the different process flows assuring highest yield and quality level avoiding contamination or corrosion of the wafer out of the process or wafer container. Even for fab manufacturing of power semiconductors which is not focusing on technologies below 50 nm nodes, the cleanroom specifications for the minienvironment of the fab are similar compared to classical 300 mm fabs. At special process sequences, wafer outgassing and organic materials can contaminate the inner parts of the wafer container or the air inside the FOUP by a high particle level or airborne molecular contamination. Therefore, all wafer containers are regularly cleaned using commercial FOUP cleaning systems and analytics for free acids and ions are performed manually by the experts of the laboratory with a high manual effort. The cleaning of the FOUPs are automatically controlled by standing times or door cycles of the container and automated transportation of the containers to the FOUP cleaner. After special etch steps using aggressive fluorine or chlorine gases an automatic container exchange is triggered by the automated material handling system of the fab and purified containers are sent to the equipment. IFD has tested two different systems for analysis of FOUPs within various front end process steps studying the level of particles and AMC within the different container types. A particle counter, ADPC (adixen Dry Particle Counter), was used as a unique way to monitor the particular contamination inside FOUPs and FOSBs. The fully automated patented process removes, localizes and counts particles from the pod surfaces, including the door. The limit of detection of a standard counter is 0.1 μ m. A standard recipe measures each face of FOUP and takes 6 minutes. Then data will provide the total number of particle per FOUP as well as the particle distribution by size (0.1; 0.2; 0.3 and 0.5 μ m) and by FOUP internal faces (rear, top, bottom, right, left, and door).

Another equipment for monitoring AMC, APA (adixen Pod Analyzer), was used as a unique in-line monitoring tool for advanced chip manufacturing in clean room environment. This innovative equipment measures the AMC (HF, NH₃, total acids, SO₂, total VOC and H₂O) in both empty and filled carriers and in the surrounding environment. The measurement occurs in real-time with a high sensitivity in the ppbv-range. The measurement time takes only two minutes. By using data from this system, high contamination processes can be identified; FOUP cleaning efficiency can be evaluated. Moreover, to go further in molecule identification, a new option was developed. This option enables the fab operator to safely and automatically trap FOUP and wafer contamination in using impingers and Tenax tubes.

The use of the FOUP analyzer within the clean room of the fab is a highly efficient method to improve the transparence of the real time status of the FOUPs at any time within a high mix high volume fab with a very low effort if the system is connect to OHT (Overhead Hoist Transportation) and running in an automated mode.

Innovation

The level of particle impurities and AMC within FOUPs and FOSBs as well as the impurity levels at the different process steps like lithography, dry etch, wet, deposition or special thinning processes for manufacturing of power semiconductors was unknown so far. The contaminants could hardly be investigated by standard analytical methods. New demonstrator equipment designed for this purpose offers the possibility of analyzing many different containers before and after FOUP cleaning. The tests also provided important information about the impurity levels within the whole process of record which could not be detected yet. Additional tests by controlled contamination of the containers followed by different cleaning procedures were performed to achieve optimized cleaning procedures. The results out of the FOUP monitoring offer a very clear and optimized container strategy in terms of dedication and FOUP cleaning. Particles and AMC level can be easily detected without high laboratory efforts.

Results

A demonstrator equipment was developed to analyze the particle level before and after cleaning within different container types. Using this demonstrator equipment more than 100 FOUPs and FOSBs were selected and analyzed to determine the particle level inside the container.

Fig. 1 gives an overview about the level of particles before the container clean for particles $> 0.1 \mu\text{m}$.

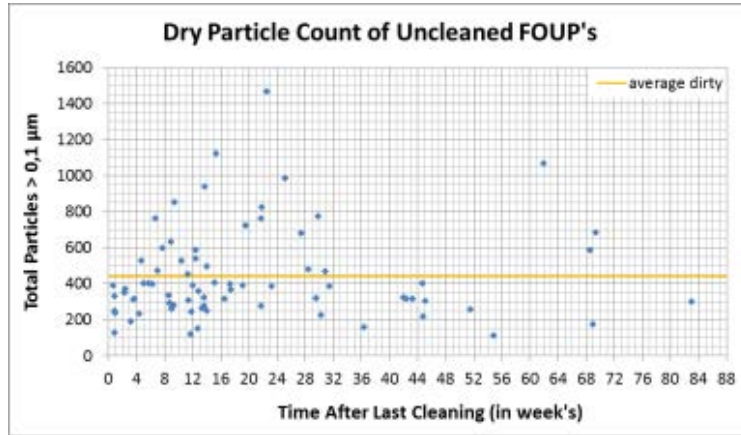


Fig.1: Particle level of the FOUPs dependent from stand time

The average particle level within the FOUP before the cleaning step was at around 400 particles $> 0.1 \mu\text{m}$. There was no dependency seen from the stand time of the FOUP within the fab. Similar tests were performed regarding the number of door cycle times showed also no correlation. Even some of the FOUPs are still at the same particle level after up to hundred days used within the fab. Out of these first results different types of FOUPs used within the fab were analyzed to understand the special behavior of different container types and to select the best container type.

Therefore, three different types of FOUPs were investigated for the particle level. In addition to the investigation of the FOUPs, a FOSB (front opening shipping box) was also analyzed and compared to the FOUPs. FOSB are only used for shipping wafers from one site to the other and are cheap compared to the FOUPs. Therefore, it was not surprising that the particle level of the FOSB was much higher compared to FOUPs used within front-end wafer production. Fig.2a showed that there are different particle levels also between the three FOUPs used within the fab, but after the cleaning process a quite similar particle level is achieved even for the FOSB, see Fig. 2b.

Another possibility was to study the distribution of the particles within the container such as bottom, door and rear site. This was possible because the demonstrator system uses a sucking unit with multiple valves for trapping and counting the particles. Therefore, the local distribution of the particles can be visualized. Fig.3 shows the distribution in percentage in-site the four different containers.

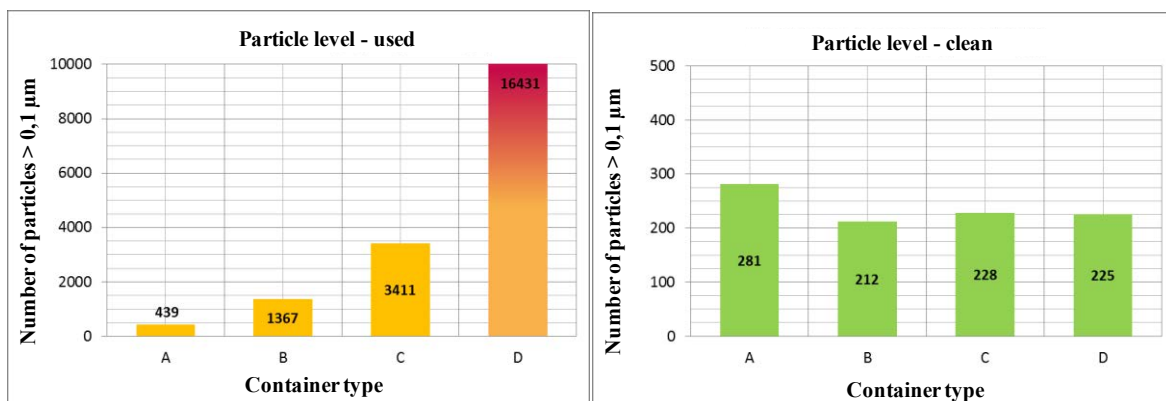


Fig. 2: Comparison of the detected particle levels within different wafer container types before (left) and after cleaning (right)

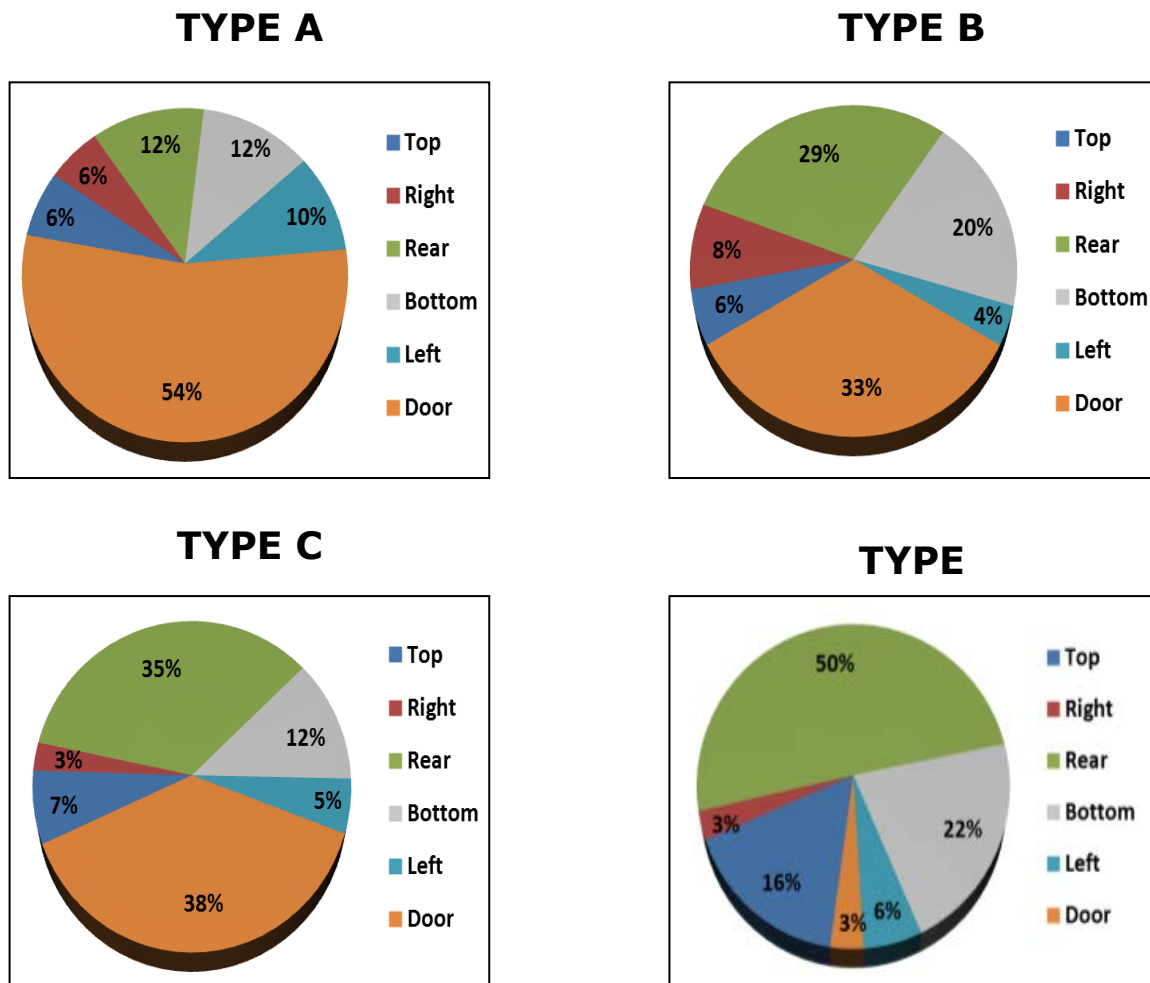


Fig.3: Distribution of particles within the container (A-C: FOUP, D: FOSB)

The diagram shows that the most of the particles within FOUPs (around 30-55%) are at the bottom of the container, whereas in a FOSB, the rear site is the most contaminated part. This means that one focus of the cleaning process for FOUPs must be spent on a perfect cleaning of the doors.

One of the main goals of the work was to study the particle level after several process steps like lithography, dry etch, ashing or special wafer thinning processes. Production wafers after the different steps were immediately transferred out of the FOUP and the empty process container analyzed for the particle level after the process step.

Fig.4. gives the overview of the results out of this test comparing the different FOUPs after the process.

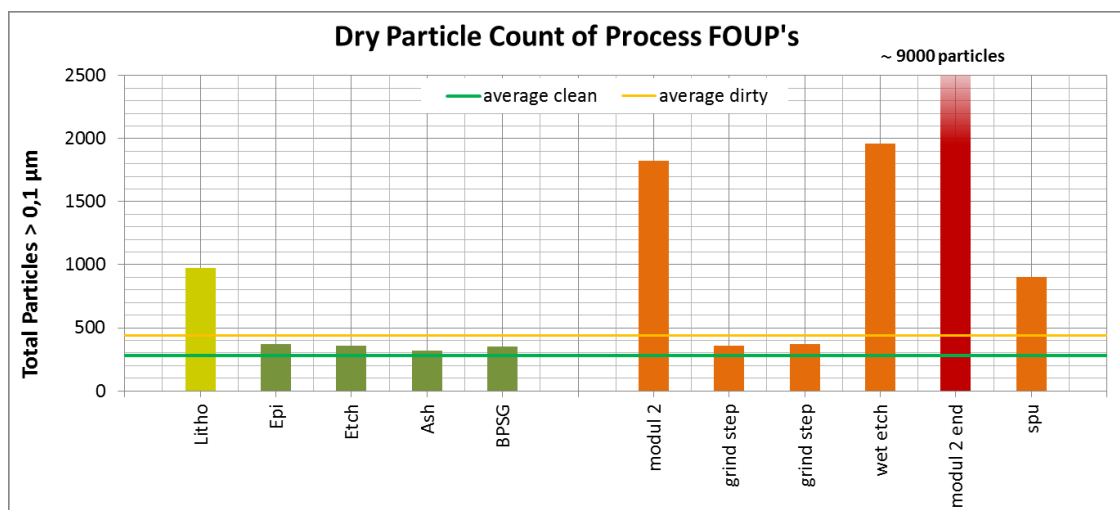


Fig.4: Particle level within FOUPs after different process steps

The green bars are processes used within the front end process flow which was compared to steps performed within the wafer thinning flow, orange bars.

The results showed that steps like lithography or thin wafer technologies induce the highest particle levels compared to steps used for dry etch or ashing processes using aggressive gases. So, the idea was to check the FOUPs especially if organic chemistry is used like within the litho process or the thin wafer flow for the AMC level.

The AMC demonstration tool (lab tool for R&D) was equipped with LabinFab option which allows connection of impingers for collecting free molecular inorganic and Tenax tubes for trapping organics. For analyzing the free acids like fluoride, chloride, nitrate and sulphate an ion-chromatography system by Dionex was used within the clean room at IFD. Organic components trapped using the Tenax tubes were analyzed by TD-GC MS at the laboratory of Fraunhofer IISB, Erlangen. Fig.5 shows a typical diagram of the organic impurities within standard FOUPs in a 300 mm front end fab. The results of the studies helps to define special FOUP cleaning and transfer steps ensuring highest quality of wafers released within the front end manufacturing process.

As a result of the study, an additional exchange of the FOUPs within the process flow was defined and the FOUPs are cleaned immediately after steps with a high level of AMC. Next steps are performing tests for purging the FOUPs lowering the AMC content and implementation of fully automated controlling and cleaning procedures within the whole process flow for a power semiconductor fab.

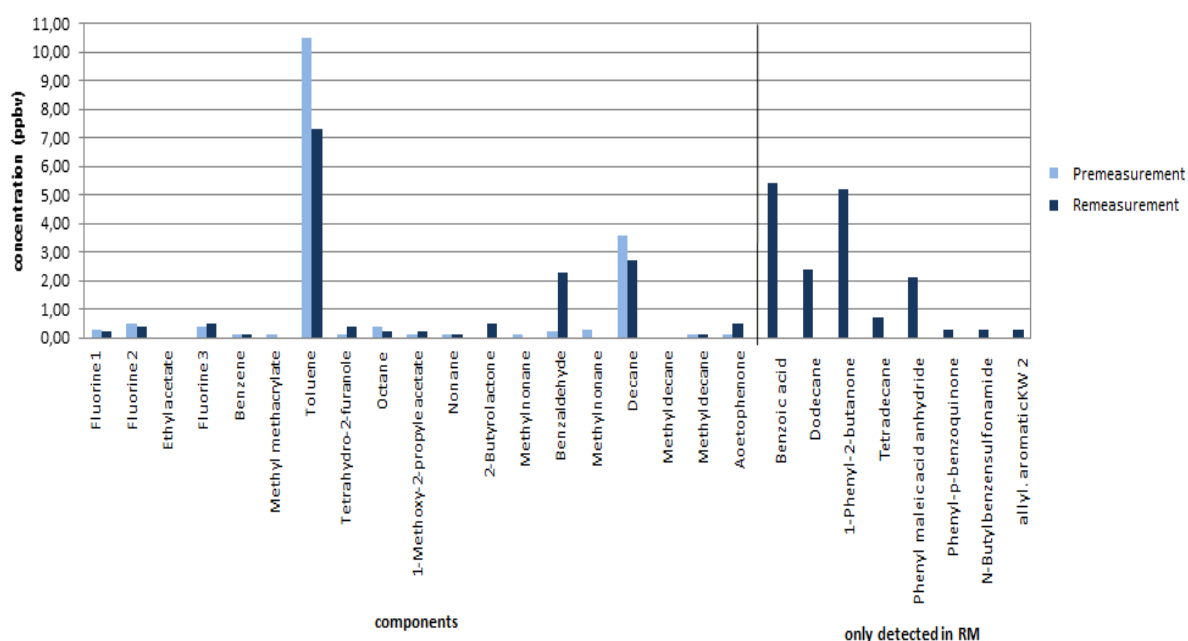


Fig. 5: Organic impurities (fingerprint) of a FOUP used within a 300 mm power fab

Conclusion

The goal of the study was the research about the particle and AMC level within the process flow of a 300 mm power production line by online monitoring of the different FOUPs and FOSBs used in the pilot production lines. Using the demonstrator for particle counting, the level in the container was determined and locally visualized at any time within production. This offers the possibility to save costs by optimized FOUP cleaning cycles saving process time, DI-water and electrical power. The equipment for monitoring the AMC level was used to identify critical process steps within the manufacturing area with a higher level of AMC concentrations or sources for organic contamination which can lead to corrosion or other defects on the wafers and yield loss. IFD worked on online analyses using the demonstrator equipment and also on cleaning concepts for particles and AMC level inside the container to achieve a stable yield level within the power pilot lines avoiding any

losses by higher particle levels or corrosion events. The results out of this work will be used to define the next steps of the equipment roadmap for the container strategies and cleaning concepts of the future Infineon fabs for high mix high volume manufacturing of power semiconductors.

Acknowledgement

The project EPPL is co-funded by grants from Austria, Germany, The Netherlands, France, Italy, Portugal and the ENIAC Joint Undertaking and is coordinated by INFINEON Technologies Austria AG. This activity has been done within the project “Enhanced Power Pilot Lines” (EPPL), (Grant Nr. 16ES0037K). The project is co-funded by the Federal Ministry of Education and Research of Germany.

References

- [1]. Sara Case, Stephanie Waite, John Barker, Wei Zhao, Jong Soo Kim, Joshua Moore, Eswar Ramanathan; Impact of FOUP Environment on Product Yield in Advanced Technologies ; IEEE, 2016; p. 168-171
- [2]. Thi Quynh Nguyen, Hervé Fontaine, Yannick Borde, Véronique Jacob, Identification and quantification of FOUP molecular contaminants inducing defects in integrated circuits manufacturing, Microelectronic Engineering, vol. 105, 2013, pp. 124-129.
- [3]. Hervé Fontaine, H. Feldis, A. Danel, S. Cetre, C. Ailhas, Impact of the volatile Acid Contaminant on Copper Interconnects, Electrical Performances. ECS Transactions, 25(5), 2009, pp. 78-86.
- [4]. K. Mikkelsen and T. Niebeling, “Characterizing FOUPs and evaluating their ability to prevent wafer contamination, Mirco journal, March 2001
- [5]. J. Bounouar, T. Q. Nguyen, O. Le-Barillec, A. Favre, E. Veran, I. Stassen, A. Gettel, FOUP Material Influence on HF Contamination during Queue-Time, Solid State Phenomena (Volume 219); pp 251-255
- [6]. Schneider, G., Wagner, T., Kraft, M. (2015). Use of Simulation Studies to Overcome Key Challenges in the Fab Automation of a 300 mm Power Semiconductor Pilot Line Comprising Thin-Wafer Processing. Proceedings of the 26th SEMI Advanced Semiconductor Manufacturing Conference (ASMC), Saratoga Springs, New York, USA.
- [7]. S. Rank, C. Hammel, G. Schneider, T. Schmidt: REDUCING SIMULATION MODEL COMPLEXITY BY USING AN ADJUSTABLE BASE MODEL FOR PATH-BASED SYSTEMS – A CASE STUDY IN THE SEMICONDUCTOR INDUSTRY, Proceedings of the 2015 Winter Simulation Conference

Inline FOUP Cleaner - The New Type FOUP Cleaner for the Next Generation

Prof. Gwon Sagong^{1,3,a}, Kwang-bong Lee², Byoung-jun Lee²,
and Geunmin Choi²

¹Hanseo University, Research Institute Catalyst Technology, Seosan City, Korea.

²SK hynix, 2091 Gyeongchung-daero, Bubal-eub, Icheon City, Korea.

³ISTe, 7-6 Yeongtong-ro 50beon-gil, Hwaseong City, South Korea.

^asagongjin@korea.com

Keywords: Inline Foup Cleaner (IFC), Stocker, Sorter, Vacuum

Abstract. The existing methodology for Front Opening Unified Pod (FOUP) cleaning, storage, and transfer is inherently flawed in three areas: a) equipment layout, b) intra-process wait time, and c) human handling. In each area, improved solutions are suggested and a new approach is developed and named In-line FOUP Cleaner (IFC). IFC is a new, singular approach accomplished via total integration of multiple equipment types including sorter, FOUP cleaner, stocker, particle counter, and the FDC monitoring system. Utilizing the IFC approach, significant improvements have been documented with respect to all three areas of concern. Overall cost savings, as well as a side benefit of improved fume removal, are carefully observed. It appears to be an interesting approach to solving the problems associated with FOUP cleaning, storage, and transfer for the next generation semiconductor fab.

Introduction

The next generation semiconductor fab requires improved solutions for FOUP cleaning and handling [1]. The need for improvement is evident and calls for an integrated approach combining sorter, FOUP cleaner, stocker, particle counter, and the FDC monitoring system within a single piece of equipment having a significantly reduced footprint. This new piece of equipment has been aptly named Inline FOUP Cleaner (IFC). The first IFC was designed and installed in the state of the art 300mm Fabrication Line. Three entire processing steps for the FOUP Cleaning have been skipped. In addition, four (4) minutes per FOUP exchange cycle have been saved. Finally, full automation has been achieved with complete elimination of human handling. Twenty-four (24) personnel were made available for other work assignments, dramatically improving overall human resources. Significant cost savings were realized by the integration into a singular piece of processing equipment and by savings of time, footprint, and personnel. In addition, fume management was dramatically improved through equipment integration and the addition of vacuum technology.

Experimental

The conventional type FOUP cleaner is composed of four (4) steps as shown in Figure 1, below. As you can see, a round trip with four (4) steps is required from sorter to stocker and stocker to FOUP cleaner and back again to the sorter from the FOUP cleaner through the stocker. The most critical concern should be with the two (2) steps between the stocker and FOUP cleaner and FOUP cleaner back to the stocker again. In these two (2) steps, forty-two (42) people are involved in FOUP transport.

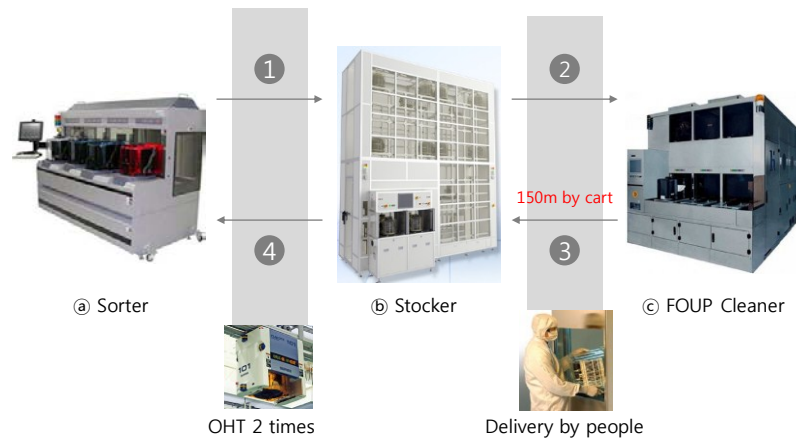


Figure1. Conventional FOUP cleaning sequence.

The new type FOUP cleaner, IFC, is one singular piece of equipment designed to receive, manage, transport, and retrieve the FOUP all within one self-contained chamber. The sorter, stocker, and FOUP cleaner are completely integrated within the IFC. An optional vacuum system can be applied to this singular chamber for maximum results in fume and moisture management. Another important aspect of the inline, integrated approach is realized with instantaneous measurement of particles within the FOUP. The IFC approach is shown by the integrated design as can be seen in Figure 2, below.

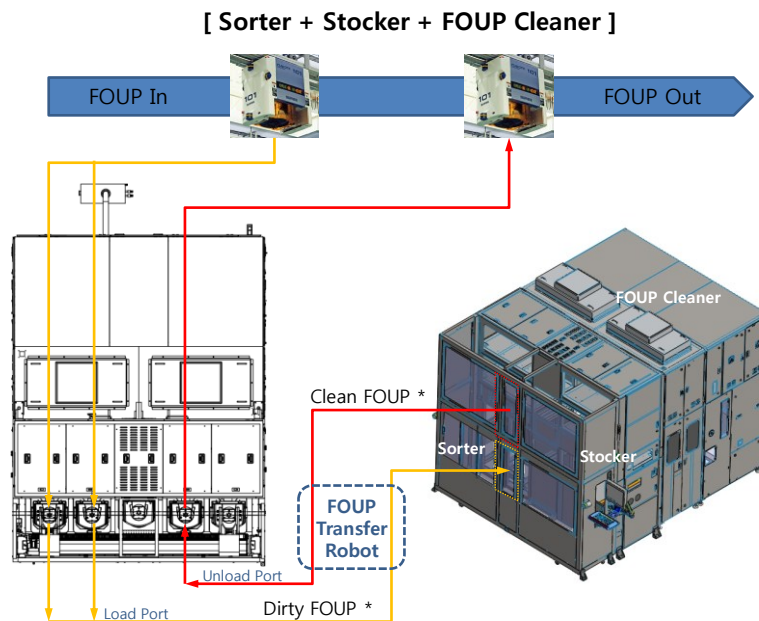


Figure2. A newly developed FOUP cleaning system.

Results and Discussion

The first IFC was designed and installed in the state of the art 300mm Fabrication Line. Significant cost savings were realized by the integration into a singular piece of processing equipment and by savings of time, footprint, and personnel. In addition, fume management was dramatically improved through equipment integration and the addition of vacuum technology. Three entire processing steps for the FOUP Cleaning have been skipped. In addition, four (4) minutes per FOUP exchange cycle have been saved. Twenty-four (24) personnel were made available for other work assignments, dramatically improving overall human resources. Finally, full automation has been achieved with complete elimination of human handling. This represents a significant improvement over the old method of blowing with clean dry air (CDA). A thirty percent (30%) improvement in fume management has been realized using this approach at DRAM fabrication line. The summary Table 1. provide the details of reduction and improvement.

Table 1. Comparison and results between 2 FOUP cleaners.

Items	Old FC	IFC	Result
Sub step	3 steps	1 step	(-) 2 steps
Footprint	20.1 m ³	11.7 m ³	(-) 8.4 m ³
Personnel	42 people	18 people	(-) 24 people
OHT(numbers)	12,000 trips	4,000 trips	(-) 8,000 trips
OHT (time loss)	4 min/trip	0 min/trip	(-) 4 min/trip
Fume Removal (Method)	Clean Dry Air Blowing	Vacuum	30% improvement

As previously mentioned, footprint reduction saves on clean room space and equipment maintenance estimated in the range of 1.3 MU\$. The total footprint was reduced 8.4 m³ (20.1 to 11.7). In addition, OHT related expenses (OHT trip time and OHT trip numbers) and sub-step reductions provided another 1 MU\$ cost savings. Personnel expenses are also saved by approximately 300 KU\$ with a headcount reduction. Initial equipment investments are virtually identical as compared between the current, conventional approach and the new, inline and integrated IFC approach. The IFC is a strong candidate for FOUP Cleaning Method in terms of cost saving and human safety.

Reference

- [1] G. Choi: *Necessity of cleaning and its Application in Future Memory Devices*. Solid State Phenomena, Vol. 219, p. 3-10 (2015)

Keyword Index

1-Eicosanethiol.....	55
172nm Excimer.....	366
172nm Radiation.....	122
20-nm Contaminants.....	172
248nm Deep UV Resist.....	117
3D NAND.....	285
III-V Compound Semiconductors.....	319
III-V Materials.....	61

A

A-Si:H.....	338
Acoustic Reflectometry.....	129
Activation Parameters.....	36
Adhesive Free Attachment.....	366
Alkali.....	348
Alkaline.....	3
Alkaline Conditions.....	3
AlN Etches.....	242
AMC.....	323, 381
Ammonia.....	357
Analysis.....	319
Angle-Resolved XPS.....	227
Anodic Water (AW).....	375
Anodic Water Chloride (AW-Cl).....	375
Atomic Force Microscopy.....	304
Atomic Layer Etch.....	41
Atomic Layer Etching.....	51
Atomic Resolution Profiler.....	304
ATR-FTIR.....	136, 141

B

Back-Grinding.....	97
BEOL.....	232, 237, 277
BEOL Cleaning.....	260
Bevel Particles.....	105
BHF.....	117
BOE.....	117
BOE Solution.....	75
Bonding.....	366
Bull's Eye Defect.....	168

C

Carbon Dioxide Solid Particles.....	172
Carbonated Water.....	22
Cassie-Baxter.....	136
Cathode Water (CW).....	375
Cavitation.....	207
Center Signature.....	168

Chalcopyrite.....	348
Channel Materials.....	51
Charge Carrier Lifetime.....	338
Chemical Composition.....	299
Chemical Passivation.....	55
Chemicals.....	163
CIGS.....	348
Cleaning.....	31, 51, 86, 207, 348, 366
CMOS.....	3
CMOS Image Sensors.....	313
CMP Defects.....	105
CO ₂ Gas.....	141
Cobalt.....	255
Colloid Gel.....	285
Concave-Convex Shape.....	97
Contact Angle.....	136, 223
Contact Cleans.....	105
Copper.....	232
Copper Kinetic.....	270
Copper Oxide Removal.....	270
Corrosion.....	232
Cross-Contamination.....	323
Crust Layer.....	111
Cryogenic Nanoaerosol.....	195
Cu Pillar Bumps.....	291
Cu Wet Cleaning.....	270
Cu/Low-k.....	242
CZTS.....	348

D

Damage-Free.....	195
Dark Current.....	309
Deep Trench Isolation.....	129
Deep Trenches.....	313
Density of Interface States.....	338
Desorption.....	323
Device.....	157
Digital Etching.....	61
Dilute NH ₄ OH.....	277
Diluted HF.....	251
Discharge Chemistry.....	41
Dissolved Oxygen Meter.....	260
Dry Cleaning.....	86, 172
Dry Strip.....	111
Dry Treatments.....	265
Dual Damascene.....	237

E

Effective Lifetime Analysis ELifAnT	331
Electro Static Erasing	366
Electroless	265
Electrolyzed Water	375
Electrostatic Discharge	182
Epitaxy	13
ESD	182
Etch Residues Removal	242
Etching	348
Etching Rate	97
EUV	357
Excimer	122
Extended-Nanospace	157

F

FEOL Wet Clean	375
FinFET	304
Fluid Velocity	97
Fluoride	75
FOSB	381
FOUP	375, 381
Friction	163
FTIR	186

G

GAAFETs	3
Gallium Arsenide	55, 61
Galvanic Corrosion	186
Gas-Phase HF	69
Gas Phase Surface Preparation	31
Gate-All-Around	3
Gate Oxide Reliability	8
Ge Nanowire	3
Ge Selectivity	3
Germanium	36
Germanium Surface	22
Grouting	366

H

Hard Mask	91
Haze	195, 361
HCl	375
Heterojunction	338
HF	117
HF Based Solutions	8
HF Last	13, 27
HF-Solution	86
HF/HNO ₃	97
High Aspect Ratio	129

High Aspect Ratio (HAR) Structures	136, 147
High Aspect Ratio Patterning	41
High Dose	111
Hydration Force	176
Hydrazine	31
Hydrogen Peroxide	27, 31
Hydrophobic	152, 195
Hydrophone	207

I

Image Sensor	309
Impedance	255
Implant	111
In-Line Monitoring	304
<i>In Situ</i> Passivation	31
<i>In Situ</i> TEM	176
Indium Antimonide	55
Indium-Gallium Arsenide	55
InGaAs	31
Inline Foup Cleaner (IFC)	387
Interconnects	227, 232
Interface State Density	331
Intermolecular Force	176
Ion Chromatography	361
Ionizer	277

K

Kesterite	348
Kinetics	36

L

Langmuir Adsorption Isotherm	344
Layer Modification	69
Light Ion Implantation	69
Liquid Property	157
Liquid Simulation	97
Litho Mask Cleaning	357
Low Dissolved Oxygen	251
Low-k	195
Low-k Compatibility	245
Low-k Dielectrics	227
Low-k Material	251
Low Oxygen Process	260
Low Temperature Etching	81
LPD ICPMS	313

M

Megasonic	207
Metal Contamination	344

Metal Hardmask	242
Metal Removal Efficiency	313
Metallic Contamination	319
Metals	251
Metrology	81, 304
Micropores	215
Microstreaming	207
Middle of Line	105
MoL	105
Molecular	323
Molecular Dynamics (MD)	
Simulations	147
Molecular Model	36
Molecular Simulation	215
Molybdenum	357
MoSiN _x O _y	361

N

Nanocrystal	176
Nanofluidics	157
Nanoscale Liquid Imaging	176
Nanostructures	141
Near Infrared (NIR)	81
NF ₃ -Based Gas Cleaning	86
NF ₃ +H ₂ O Dry Cleaning	86
Ni	265
Nickel	265
NMR Spectroscopy	36
Non-TMAH	245
Nucleation	285

O

O ₃ Cleaning	361
Optimized Semi-Aqueous Chemistry	3
Organic Residue	186
Organo-Silicon	81
Oxidation	265
Oxidation Reduction Potential (ORP)	375
Oxide Film Etching	86
Oxide Recess	304
Oxygen	18

P

PALS	117
Particle Adhesion Force	201
Particle Contamination	381
Particle-Count Defectivity	186
Particle Removal Efficiency (PRE) ..	168, 195
Particle Removal Rate	201
Particles	152

Passivation	31, 338, 348, 357
Pattern Collapse	136, 147
Pattern Transfer	41
PERR	232
pH-Value	375
Phosphoric Acid	81, 285
Photo-Conductance Decay (PCD)	299
Photomask	207
Photoresist	111
Photoresist Residue Removal	122
Photoresist Strip	168
Photovoltaics	348
Physical Damage	299
Plasma Damage	223
Polymer Microchip	366
Porous Low-k	215
Porous Low-k Dielectrics	223
Post CMP	255
Post-CMP Cleaning	163
Post-CMP Formulations	186
Post-Etch Residue	227, 237
Post-Etch Residue Removal (PERR)	
Clean	251
Pre-Epi Clean	27
Process Damages	215
PV	348
PVA Brush	201
PVA Roller Brush	163

Q

Quartz	361
--------------	-----

R

Radiation	366
Rebounding	182
Residue Clean	245
Residue Sulfate Ion Concentration	361
Residues	111
Resist Free Volume	117
Resist Lift off	117
Reticle	357
Rinse Effect	22

S

Salicidization	105
SC2	375
Selective Etching	91
Selective Removal	69
Selectivity	41, 81, 86
Self-Assembled Monolayer	55

Self-Limiting Oxidation	31	Surface Treatment.....	223
Semiconductor	182	T	
Sensor Array	207	Tafel	186
Ship Production.....	366	Texture.....	338
Si _{0.3} Ge _{0.7} Isotropic Etch	3	Thin Film	163, 348
Si _{0.5} Ge _{0.5}	3	Thin Layer Etching.....	69
Sidewall Polymer	242	Through Silicon via	129
SiGe	31	Ti	265
Sigma Wet Etching	18	TiN	242
Silica.....	285	TiN Hard Mask Removal.....	237
Silicon	338, 357	TiN Removal	245
Silicon (111).....	27	Titanium.....	265
Silicon Nitride.....	69, 75, 186, 285	Titanium Nitride	91, 245
Silicon Nitride Etch.....	81	TiW	265
Silicon Oxide.....	75	TMAH	18, 357
Silicon Solar Cell Substrates.....	331	Trace Metal Contamination	309
Silicon Solar Cells.....	344	Transient	207
Silicon Surface Clean.....	344	Trap-Assisted Generation Current.....	309
Silicon Surface Passivation.....	8, 13	Tungsten	91, 232, 265
Silylation	223	Tungsten 10 nm Node.....	186
Single-Wafer	152	TXRF	319
Single-Wafer Clean.....	277	U	
SiO ₂	186	UBM Etch.....	291
Soft X-Ray	277	UBM Ti Undercut.....	291
SOH Film	182	Ultra-Thin Oxide Layer	331
SOH Mask Pattern	182	Ultrapure Water	27
Solar Cell.....	338	Ultrasonic.....	207
Solvent	75	V	
Sorter.....	387	Vacuum.....	387
Spacer.....	69	Vertical Step	97
Specification.....	309	Vias	237
Spray Clean	152	Volatile Acids	323
SPV	313	VPD	313
Steric Force	176	VUV	366
Stocker	387	VUV Cleaning	122
Stress Relief	97	W	
Strip	182	W	265
Structural Strength	147	W/TiN Barrier Liners	186
Sulfur.....	36	Wafer Charging	277
Sulfuric Peroxide Mixture (SPM)		Wafer Edge	97
Cleaning	361	Wafer Edge Particles	105
Superhydrophobic	141	Water	323
Surface	348	Watermarks.....	13
Surface Activation.....	366	Wenzel	136
Surface Charge.....	299, 331	Wet-Chemical Oxidation.....	331
Surface Modification.....	136	Wet-Chemical Treatment.....	22
Surface Passivation	36, 61		
Surface Photovoltage (SPV)	299, 331		
Surface Preparation	31, 51		
Surface Recombination Lifetime	299		

Wet Clean.....	105,168, 237
Wet Cleaning.....	215
Wet Etch.....	245
Wet Etching.....	75, 97, 176
Wet Processing.....	348
Wet Treatment.....	265
Wetting.....	136, 141
Wetting Kinetics	129

X

X-Ray Photoelectron Spectroscopy	55
XPS	186

Z

Zeta-Potential	152
----------------------	-----

Author Index

A

Aabdin, Z.	176
Abrenica, G.	51
Ah-Leung, V.	69
Alessandri, M.	265, 270
Alvarez Jr, D.	31
Anand, U.	176
Angermann, H.	331, 338
Arnauts, S.	51
Atanasova, T.	291
Ayral, A.	215

B

Bai, C.N.	81
Bal, S.	136
Balamou, P.	331
Bassett, D.W.	195, 285
Becker, D.S.	195
Beitia, C.	323
Belmiloud, N.	152
Bernatis, P.R.	255
Bertin, F.	215
Besson, P.	61, 129
Bhattacharyya, D.	168
Bilodeau, S.	3
Bollin, M.	270
Borowik, L.	61
Bounouar, J.	381
Brammertz, G.	348
Braun, S.	227
Broussous, L.	129, 215, 260
Bruce, R.	41
Burk, Y.	227
Butterbaugh, J.W.	195

C

Caminati, M.	270
Campistron, P.	129
Campo, A.	111
Capecchi, S.	291
Carrier, J.	129
Chang, H.W.	237
Chen, X.	207
Cho, S.J.	304
Choi, G.M.	387
Choi, K.H.	172
Claes, M.	344
Coasne, B.	215

Colpani, P.	265, 270
Conard, T.	227
Conrad, M.	168
Contreras, Y.	55
Cooper, E.	3, 75, 91, 245
Croisy, M.	111
Cui, H.	242

D

Dattilo, D.	357
Daviot, J.	291
de Buttet, C.	260
de Gendt, S.	136, 141
Debruyne, H.	141
Delgadino, G.	237
Dietze, U.	357
Doumen, G.	136
Drummond, P.J.	299
Dylewicz, R.	277

E

Edmonds, M.	31
Engelmann, S.	41
Engesser, P.	36
Enyedi, V.	61

F

Fischer, R.	36
Fontaine, H.	313, 323
Fryda, M.	375
Frye, D.	186
Fujimura, Y.	27
Fukunaga, A.	163, 201

G

Gabette, L.	129
Gampa, N.	348
Gan, N.	27
Garcia Barros, M.	69
Garnier, P.	8, 13, 117, 129, 313
González-Aguirre, P.	323
Gonzalez, V.V.	232
Grasso, S.	270
Guerrieri, S.	309
Guiheux, D.	111
Guo, E.	361
Gwon, S.G.	387

H

Hagimoto, Y.....	97
Haigermoser, C.	18
Hamada, S.	163
Han, J.	237
Han, S.H.	182
Haslinger, M.	344
He, Y.G.	18
Herrán, F.	323
Higuchi, A.	223
Hiyama, H.	163, 201
Hoarau, K.	260
Hofliijk, I.	227
Holmes, R.	31
Holsteys, F.	3, 22, 27, 51, 136, 141, 147, 176, 223, 227, 232, 251, 357
Hsu, C.J.	245
Hsu, P.	255
Huang, K.	255
Hwang, T.H.	182

I

Irmer, B.	304
Iwamoto, H.	97
Iwasaki, A.	223, 251
Iwata, F.	201

J

Jenny, C.	111
Jenq, S.N.	186
Jiang, W.	361
Jo, A.J.	304
John, J.	344
Jonckheere, R.	357
Joseph, E.A.	41

K

Kabansky, A.	237
Kang, S.M.	86
Kawaguchi, M.	277
Kegel, J.	338
Kenis, K.	304
Kenkare, N.	152
Kesters, E.	223, 227, 232, 251
Keswani, M.	207
Kim, C.H.	182
Kim, H.Y.	172
Kim, J.K.	172
Kim, J.N.	172

Kim, S.H.	172
Kim, T.G.	304
Kim, T.H.	86
Kim, T.S.	86
Kitamori, T.	157
Ko, D.W.	182
Komori, K.	223
Korte, L.	331, 338
Kovacs, F.	237
Kruemberg, J.	357
Kummel, A.C.	31

L

Lauerhaas, J.M.	195
Lavizzari, S.	309
Le-Guet, C.	381
Le, Q.T.	223, 227, 232, 251
Lee, B.J.	387
Lee, J.H.	172
Lee, K.B.	387
Leendertz, C.	331
Leibold, A.	381
Lépinay, M.	215
Liang, G.	81
Licitra, C.	215
Lieten, R.R.	3, 186, 232
Lippy, S.	232, 245
Liu, F.	18
Liu, H.X.	18
Liu, J.L.	18
Livellara, L.	270
Lou, D.	237
Lu, W.	18
Lu, W.J.	331
Lundgren, J.	323

M

Mallabar, S.	105
Man, X.	277
Mancheno-Posso, P.	55
Marchack, N.	41
Martinez, E.	61
Masaoka, T.	27
Mawatari, K.	157
Mbanaso, C.	195
Mertens, P.W.	309, 344
Meuris, M.	348
Mirsaidov, U.	176
Miyazoe, H.	41
Moroni, M.	270

Mui, D.	277
Mule, A.	348
Muralidhar, P.	105, 168
Murdoch, G.	232
Muscat, A.J.	55

N

Neelsen, A.K.	375
Neyens, M.	117
Nguyen, T.Q.	381
Nishio, K.	163
Nongaillard, B.	129

O

Ogawa, Y.	27
Ohlsen, J.	323
Ohno, R.	319
Okada, N.	207
Okorn-Schmidt, H.	36
Okorn, G.	36
Okuyama, A.	97
Oshinowo, J.	375

P

Pacco, A.	27, 357
Papalia, J.	41
Pargon, E.	111
Park, S.I.	304
Parson, T.	186
Parthenopoulos, M.	291
Payne, M.	232, 245
Pfeffer, M.	381
Pipia, F.	265, 270
Pizzetti, C.	291
Pollet, O.	69
Poortmans, J.	348
Possémé, N.	69, 111
Pourtois, G.	147
Printz, W.P.	195

Q

Qian, S.	361
Quarti, U.	375

R

Ranjbar, S.	348
Rathman, C.A.	195
Ravizza, E.	265, 270
Rebaud, M.	61
Rebstock, L.	375

Richard, C.	111
Richter, H.	381
Rip, J.	3, 357
Robert, S.	344
Rotondaro, A.L.P.	195, 285
Rouessac, V.	215
Roure, M.C.	61
Ruzyllo, J.	299
Ryu, B.S.	182
Ryu, H.Y.	304

S

Saga, K.	319
Sahayaraj, S.	348
Saito, S.	97
Sanada, T.	163, 201
Sano, K.	277
Sardashti, K.	31
Sato, M.	22, 223
Schäfert, A.	122, 366
Schmidt, S.	304
Schneider, G.	381
Schwab, B.D.	195
Scimè, F.	265
Scott, S.	105
Sebaai, F.	3, 22
Sergeant, S.	136
Shalyt, E.	81
Shen, J.	361
Shen, M.	227
Singh, S.	105
Snow, J.	22
Soha, M.	344
Spadoni, S.	265, 270
Spiegelman, J.J.	31
Stegemann, B.	331, 338
Steller, B.	36
Struyf, H.	186
Suhard, S.	147

T

Takahashi, H.	22
Takato, C.	201
Takeo, K.	97
Tan, S.	237
Taubert, M.	381
Terryn, H.	136
Teugels, L.	186
Thomes, G.P.	195
Thomy, V.	129

Tokuda, E.	201
Toselli, L.	61
Toubal, M.	129
Tu, S.H.	75, 91, 245

V

van Dorp, D.H.	51
Venegoni, I.	265
Vereecke, G.	136, 141, 147
Vermang, B.	348
Virgilio, C.	129
Votta, A.	270
Vrancken, N.	136, 147

W

Wang, C.	361
Wang, C.J.	245
Wang, M.	361
Westwood, G.	237
White, D.	186
White, M.	186
Wiesmann, H.	122, 366
Willeke, R.	291
Witters, L.	3
Wolf, S.	31
Wostyn, K.	3, 27
Wu, H.C.	75, 91
Wu, J.G.	18
Wu, K.	361

X

Xu, F.	361
Xu, X.M.	136, 141, 147, 176

Y

Yam, P.	207
Yang, M.C.	75, 91
Yen, C.	255
Yoshida, Y.	22, 27
Yukifumi, Y.	3

Z

Zanelli, C.I.	207
Zhang, H.	361
Zhou, M.S.	18
Zhu, J.	277
Zoll, S.	260